The Älgliden Ni-Cu-Au sulfide deposit, Skellefte Belt, Sweden : a magmatic Ni-Cu deposit in a subduction setting

Kévin Coin

Communauté
UNIVERSITÉ Grenoble Alpes

THÈSE

Pour obtenir le grade de

DOCTEUR DE LA COMMUNAUTE UNIVERSITE GRENOBLE ALPES

Spécialité : **Sciences de la Terre et univers, environnement**

Arrêté ministériel : 25 mai 2016

Présentée par

Kévin COIN

Thèse dirigée par **Nicholas T. Arndt, Professeur, ISTerre**, et codirigée par **Carole Cordier, Maître de conférence, ISTerre**
préparée au sein du **Laboratoire ISTerre**
dans **l'École Doctoral Terre, univers, environnement**

Le gisement de sulfures à Ni-Cu-Au d'Älgliden, ceinture de Skellefte, en Suède : un gisement magmatique de Ni-Cu en zone de subduction

Thèse soutenue publiquement le **8 novembre 2017,**
devant le jury composé de :

M. Laurent TRUCHE
Professeur à l'université Grenoble Alpes, Président du jury
M. Wolfgang MAIER
Professeur à l'université de Cardiff, Rapporteur
Mme. Kathryn GOODENOUGH
Géologue principal au centre de recherche de Lyell, Rapporteur
M. Clément GANINO
Maître de conférences à l'université Sophia Antipolis, Examinateur
Mme. Giada IACONO-MARZIANO
Maître de conférences au CNRS, Examinatrice
Mme. Carole CORDIER
Maître de conférences à l'université Grenoble Alpes, Directrice de thèse
M. Nicholas T. ARNDT
Professeur à l'université Grenoble Alpes, Directeur de thèse

Communauté
UNIVERSITÉ Grenoble Alpes

THÈSE

Pour obtenir le grade de

DOCTEUR DE LA COMMUNAUTE UNIVERSITE GRENOBLE ALPES

Spécialité : **Sciences de la Terre et univers, environnement**

Arrêté ministériel : 25 mai 2016

Présentée par

Kévin COIN

Thèse dirigée par **Nicholas T. Arndt, Professeur, ISTerre**, et codirigée par **Carole Cordier, Maître de conférence, ISTerre**
préparée au sein du **Laboratoire ISTerre**
dans **l'École Doctoral Terre, univers, environnement**

The Älgliden Ni-Cu-Au sulfide deposit, Skellefte Belt, Sweden : a magmatic Ni-Cu deposit in a subduction zone setting

Thèse soutenue publiquement le **8 novembre 2017,**
devant le jury composé de :

Prof. Laurent TRUCHE
Professeur à l'université Grenoble Alpes, Président du jury
Prof. Wolfgang MAIER
Professeur à l'université de Cardiff, Rapporteur
Dr Kathryn GOODENOUGH
Géologue principal au centre de recherche de Lyell, Rapporteur
Dr Clément GANINO
Maître de conférences à l'université Sophia Antipolis, Examinateur
Dr Giada IACONO-MARZIANO
Maître de conférences au CNRS à Orléans, Examinatrice
Dr Carole CORDIER
Maître de conférences à l'université Grenoble Alpes, Directrice de thèse
Prof. Nicholas T. ARNDT
Professeur à l'université Grenoble Alpes, Directeur de thèse

Acknowledgments

First, I would like to express my deepest thanks to my supervisors, Carole Cordier and Nick Arndt. Carole was extremely prepared to listen, to help and to guide me, whatever the nature of the issues I faced. We had many active and fruitful debates, always in a deep mutual respect. Her pregnancy was absolutely not felt in my work, quite the contrary, I have gained from her care all along the thesis. I am also very grateful to Nick who allowed me to find my first job in mineral exploration as well as this PhD project. He has shared his huge experience and high-quality expertise, in a great humility, hence symbolizing a beautiful image a research. His dual culture was also really rewarding. Together, Nick and Carole have managed to build a propitious atmosphere for working. I have learnt a lot from them and I have benefited from a good chemistry between an experienced man and a young woman, each having their respective fields of expertise.

I would like to thank to the jury members, Wolfgang Maier, Kathryn Goodenough, Giada Iacono-Marziano, Clément Ganino and Laurent Truche for the evaluation of my work, from the manuscript to the oral defense, with such a involvement.

I also would like to express my gratitude to the Boliden staff. First, thanks to Rodney Allen who accepted to provide the financial support of this PhD project. Anders Zettergren and Peter Svensson are thanked for their warm reception at Boliden, giving access to Boliden datasets and drill cores.

I am grateful to Sarah Bureau and Sylvain Campillo for their help, availability, technical expertise and cheerfulness at the clean room and for the use of the mass spectrometers. I also would like to thank Catherine Chauvel for the use of the clean lab and her critical mind regarding the validation of the chemical data.

Valentina Batanova and Valérie Magnin are thanked for their availability and assistance on the use of the microprobe and the Eagle instrument. Thanks also to Anne-Marie Boullier for the managing of the microscope.

I would like to thank Pierre Cartigny and Nelly Assayag for their warm reception at the IPGP and their dynamic assistance for the S isotope analyzes.

I thank all my PhD colleagues, especially Fanny, Anthony, Cyril, Chloé and Camille, for the nice moments we have shared.

I am very grateful to my family and close friends who support(ed) me before, during and after this project. Special thoughts go to my father, my flat mates, mon Crâne, Kaï, Lucky, Didi, Ben, and Chris and his father.

Résumé en français

Dans un contexte où la demande en nickel (Ni) et en cuivre (Cu) pour la production de véhicules électriques est en pleine expansion, la recherche de nouveaux gisements de sulfures magmatiques à Ni-Cu est primordiale. Les gisements de sulfures magmatiques à Ni, Cu et éléments du groupe du platine (EGP) sont généralement générés à partir de magmas mafique-ultramafiques dérivés du manteau. Un gisement se forme par immiscibilité d'un liquide sulfuré et d'un magma silicaté, concentration des éléments chalcophiles tels que Ni et Cu dans le liquide sulfuré et accumulation de ce liquide. Le processus d'immiscibilité se produit dès lors que le magma est saturé en soufre (S). Cette saturation est atteinte par réduction de la solubilité du S et/ou augmentation de la concentration en S dans le magma silicaté, deux processus qui ont généralement lieu suite à l'assimilation de roches crustales riche en silice et/ou contenant du S. Les gisements de Ni-Cu sont principalement issus de magmas komatiitiques ou tholéiitiques associés à des panaches mantelliques, mais certains gisements ont été découverts depuis les années 2000 en association avec des magmas calco-alcalins, traduisant une mise en place des gisements en contexte de zone de subduction. C'est le cas du gisement d'Älgliden situé en Suède, qui montre, en comparaison avec l'ensemble des gisements mondiaux, des teneurs en or (Au) élevées et un faible rapport Ni/Cu. Le dyke d'Älgliden, dans lequel est porté la minéralisation à Ni-Cu-Au, recoupe un gisement porphyrique à Cu-Au contenant des sulfures, laissant ainsi suggérer que la minéralisation d'Älgliden résulte de l'assimilation des roches encaissantes (Bejgarn et al., 2013).

Le dyke d'Älgliden est situé dans la ceinture de Skellefte qui correspond au district miner le plus prospectif de Suède, en comptant plus d'une centaine de gisements, principalement des gisements de sulfure massif volcanogènes, mais seulement une mine de Ni-Cu. La ceinture de Skellefte est interprétée comme ayant été un arc volcanique, accrété au craton Archéen au moment de l'orogenèse Svecofenienne il y a environ 1.9 Ga, au même titre que la ceinture de Kotalahti en Finlande (Nironen, 1997), qui elle, contient plusieurs gisements de Ni-Cu. Le dyke d'Älgliden, dont la géométrie a été déterminée par des campagnes de forage et des levés électromagnétiques aéroportés, est orienté SO-NE et s'étend verticalement sur 3 km, avec une épaisseur maximale au centre et minimale aux terminaisons. L'intrusion comporte toujours des zones sous-explorées dans sa partie NE et en profondeur, constituant ainsi le potentiel d'exploration. De précédentes études ont montré que le dyke d'Älgliden se met en place dans un encaissant composé principalement de granodiorite et tonalite, elles même recoupées par des dykes de porphyre à quartz-feldspath, autour desquels la minéralisation à Cu-Au s'est développée en association avec zones d'altération hydrothermale avec ou sans sulfures (e.g. Weihed, 1992*b;* Bejgarn, 2012). Les contacts entre l'encaissant et le dyke varient de francs à

progressifs, avec des zones mixtes caractérisées par la présence de nombreux xénolithes de l'encaissant, préférentiellement dans les parties étroites de l'intrusion. Des dykes tardifs de composition basaltique à intermédiaire ou aplitique recoupent le dyke d'Älgliden et son encaissant.

Les objectifs de la thèse sont d'examiner les processus à l'origine de la formation du gisement d'Älgliden et d'en déterminer les implications au regard de la prospectivité du gisement, et plus généralement, de mieux comprendre la formation des gisements de sulfures magmatiques à Ni-Cu en contexte de zone de subduction. Ce projet de recherche, financé par la compagnie Boliden qui détient le gisement d'Älgliden, a été mené au sein du laboratoire de l'Institut des Science de la Terre, à Grenoble. Il inclut l'étude pétrologique du minerai et de ses roches hôtes, la détermination de compositions minérales, l'analyse des éléments majeurs et traces sur roche totale et enfin des analyses des isotopes du soufre, afin de répondre aux problématiques soulevées. Les échantillons ont majoritairement été prélevés et analysés à partir de deux sondages carottés, l'un situé au niveau de l'épaisse partie centrale du dyke, l'autre au niveau d'une partie étroite de l'intrusion.

L'altération minéralogique est préférentiellement localisée aux contacts lithologiques (i.e. paragenèse à talc-trémolite-carbonate) mais elle devient omniprésente (i.e. paragenèse à chlorite-actinote) à proximité des contacts ou sur l'ensemble de la largeur du dyke lorsqu'il est plus étroit. Les roches les plus fraiches sont situées au cœur du dyke là où le dyke est le plus large. L'observation de roches non ou faiblement altérées montre que les roches d'Älgliden sont principalement composées de norites à olivine parsemées de corps de leucogabbros formant des patches informes ou plus compacts dispersés au sein des norites ou par des veines.
Les norites à olivine sont composées de 15 à 40 vol.% de grains d'olivine sub-automorphes à automorphes. Les minéraux interstitiels sont, par ordre d'abondance, l'orthopyroxène, montrant des textures poecilitiques, le plagioclase, sous forme de lattes sub-automorphes, l'hornblende et la biotite, tous deux xénomorphes et parfois poecilitiques, et enfin les oxydes de fer (chromite, ilménite, titanomagnétite). Les leucogabbros sont composés à plus de 75 vol.% par des grains de plagioclase sub- à automorphe, d'hornblende et de biotite, de rare d'oxydes de fer et de quartz et carbonates secondaires. Certains leucogabbros peuvent également contenir de l'orthopyroxène. Les sulfures sont volontairement décrits plus tard. Les compositions sur roches totales montrent que certains dykes tardifs ont une composition proche de celle des leucogabbros. Ils s'en distinguent cependant par leur texture porphyrique et par la composition du plagioclase et de la biotite.
La texture des norites, leur teneur élevée en MgO, ainsi qu'en éléments compatibles dans l'olivine (e.g. FeO), et leur teneur faible en éléments incompatibles dans l'olivine (e.g. Al_2O_3,

La) indiquent que les norites sont des cumulats à olivine. Les données montrent que les norites à olivine se sont formées par accumulation de 20 à 60% de cristaux olivine au sein d'un liquide intercumulus de composition basaltique. Les compositions similaires des plagioclases et orthopyroxènes les plus primitifs chez les norites et les leucogabbros ainsi que les spectres d'éléments en traces incompatibles parallèles de ces deux types de roche montrent que le liquide intercumulus est également à l'origine des leucogabbros. La corrélation négative entre le MgO et le La des leucogabbros, cohérente avec la teneur en anorthite de leur plagioclase, suggère que les leucogabbros correspondent à des liquides produits par cristallisation fractionnée de plagioclase et d'orthopyroxene à partir du liquide intercumulus, avec ou sans accumulation de ces minéraux. Les compositions les plus évoluées sont observées dans les veines de leucogabbros, reflétant leur caractère plus différentié.

La gamme de composition très restreinte des olivines cumulatives sur la largeur du dyke suggère l'injection au sein d'un dyke d'une seule bouillie cristalline, riche en olivine. Ceci est confirmé par les faibles variations de composition d'orthopyroxène à travers le dyke, reflétant une composition homogène du liquide intercumulus à partir duquel l'orthopyroxène a cristallisé. Il y a donc peu d'évolution minéralogique et géochimique des norites à travers le dyke. Cependant, aux abords des contacts, la proportion d'olivine et la teneur en MgO diminuent. Ce profil est caractéristique du processus de différentiation par flux défini par Komar (1972) et Barrière (1976). Il est à noter que ce type d'évolution est aussi observé au niveau d'un contact avec un dyke tardif divisant le dyke d'Älgliden en deux parties, une partie dite NO, une autre dit SE. Les norites de la partie NO sont légèrement plus riches en chromite, avec des teneurs plus élevées en Cr_2O_3. Il est donc possible que le dyke se soit mis en place en deux injections successives de bouillies cristalline riches en olivine.

Les compositions sur roches totales des norites, la composition des olivines et des modélisations de cristallisation fractionné réalisées à partir du logiciel Petrolog3 (Danyushevsky & Plechov, 2011), ont permis d'estimer que la magma parent des norites est un basalte évolué, avec une teneur en MgO d'environ 6 wt.%. Les spectres de concentrations en éléments en traces incompatibles des norites et leucogabbros sont caractéristiques des magmas de zone de subduction avec des anomalies positives en U et Pb, et négatives en Nb-Ta (Perfit et al., 1980 ; Tatsumi et al., 1986). La contamination d'un magma d'arc par les encaissants du dyke par le processus d'assimilation couplée à la cristallisation fractionnée ne permet pas de reproduire les caractéristiques géochimiques des roches d'Älgliden, même en considérant des processus extrêmement favorables à l'assimilation. De même, il est exclu que la contamination ait pu avoir lieu après l'injection de la bouillie cristalline dans le dyke, au cours de la différentiation du liquide intercumulus, puisque les spectres des leucogabbros et des norites sont parallèles. Cela indique que le magma parent d'Älgliden est un magma évolué formé en contexte de subduction, et n'ayant pas subi d'interaction significative avec son

encaissant. Le rapport $\delta^{34}S$ des sulfures de la minéralisation d'Älgliden (3.8-4.6‰) et de l'encaissant (3.8-6.2‰) ne permettent pas de démontrer ni d'infirmer une quelconque contamination mais indique cependant une origine commune, à partir du coin mantellique métasomatisé au sein d'une zone de subduction. Ces conclusions poussent donc à réviser l'origine de la minéralisation du dyke d'Älgliden, jusque-là considérée comme résultant de l'assimilation de roches encaissantes.

L'assemblage minéralogique des sulfures, composés de pyrrhotite, pentlandite, chalcopyrite et parfois pyrite, est caractéristique de celui des sulfures magmatiques. Dans les trois-quarts du dyke, les sulfures sont disséminés, soit localisés préférentiellement aux jonctions entre les grains d'olivine des norites ou sous forme de globules de taille plus conséquente dans les leucogabbros. Des concentrations modérées de sulfures se présentent sous la forme de sulfures en réseaux, de veines de sulfures et de rares sulfures massifs de dimension relativement réduite (généralement quelques centimètres). Ces concentrations de sulfures sont spatialement associées aux leucogabbros (i.e. les liquides les plus différentiés) et aux xénolithes de l'encaissant et montrent des texture de remplacement où les sulfures semblent s'être développés aux dépens des minéraux de la roche hôte. Les sulfures ont des teneurs faible en Ni et en Cu, suggérant ainsi que le liquide sulfuré n'a que faiblement interagi avec un magma silicaté riche en Ni, Cu. Le faible rapport Ni-Cu de la minéralisation, l'association préférentielle des concentrations de sulfures avec les leucogabbros et la prépondérance de sulfures disséminés indiquent que l'immiscibilité du liquide sulfuré s'est produite tardivement au cours de la différentiation du magma d'Älgliden. Ce timing, en inhibant à la fois l'interaction entre les liquides silicaté et sulfuré et l'accumulation du liquide sulfuré, n'est pas favorable à la formation d'un gisement économique.

Le processus de d'assimilation de l'encaissant n'est pas considéré comme ayant joué un rôle majeur dans la formation du liquide sulfuré, *de facto* dans la formation de la minéralisation d'Älgliden. En revanche, le caractère évolué et oxydé du magma d'Älgliden apportent des contraintes significatives au regard du processus minéralisateur. Les fortes teneurs en Au et le faible rapport Ni/Cu s'explique par l'apparition tardive de la phase sulfuré au cours de la différentiation du magma d'Älgliden, dans la mesure où l'Au et le Cu sont incompatibles dans l'olivine à l'inverse du Ni qui y est incorporé préférentiellement. Les valeurs positives de $\delta^{34}S$ des sulfures du dyke suggèrent que le magma Älgliden dérive de la fusion partielle du coin mantellique métasomatisé dans une zone de subduction. Par comparaison avec les magmas d'arc actuels, ce magma était donc oxydé. L'importante fugacité en oxygène du magma lui confère un degré de sous-saturation en S significatif (Jugo, 2009). Atteindre la saturation par apport de S nécessiterait l'assimilation massive de roche encaissante, hypothèse qui n'est pas soutenue par les données géochimiques obtenues. L'hypothèse alternative est que la saturation

en soufre soit atteinte par réduction du magma. Ce processus de réduction a lieu au cours la différentiation des magmas d'arc oxydés (Kelley & Cottrell, 2012). Il a pu se produire au cours de la cristallisation de magnétite (Jenner et al., 2010), comme le suggère l'appauvrissement brutal en TiO_2 et V - éléments incorporés dans la magnétite - entre la formation des norites et des leucogabbros. La réduction peut également résulter du dégazage du magma (Longpré et al., 2017), en accord avec son caractère hydraté (e.g. présence de phases hydratées telles que l'amphibole et la biotite) et de sa faible profondeur de mise en place (<4 km). Les deux processus de réduction considérés ont lieu tardivement au cours de la mise en place du dyke et de la différentiation du magma. La minéralisation d'Älgliden n'apparait donc pas comme un cas d'étude exemplaire pour la formation de gisements à haute valeur économique en contexte de zone de subduction. En revanche, puisque les magmas d'arc sont capables de dissoudre de large quantité de S de par leur caractère oxydé, si un processus de réduction (e.g. assimilation de matériel réductant) opère relativement tôt au cours de la différentiation cela pourrait conduire à la formation de gisements économiquement rentables.

Les travaux de cette thèse ont ainsi permis de caractériser les modalités de formation et de mise en place des roches hôtes, et d'en définir les implications sur la prospectivité de la minéralisation d'Älgliden. Ils renseignent également sur la formation des gisements de sulfures magmatiques à Ni-Cu en contexte de zone de subduction.

L'intrusion d'Älgliden est principalement composée de norites à olivine formée par accumulation d'olivine et injection de cette bouillie cristalline au sein d'une structure verticale. Localement, des quantités mineures de leucogabbro se sont formées par ségrégation et différentiation du liquide interstitiel.

Le magma parent de l'intrusion était un basalte hydraté et évolué dont les concentrations en éléments traces indiquent qu'il s'est formé dans une zone de subduction. La contamination de ce magma par l'encaissant minéralisé de l'intrusion n'a pas été significative, si elle a eu lieu. Elle n'est donc pas considérée comme déterminante dans la formation de la minéralisation à Ni-Cu-Au. Les teneurs élevées en Au et le faible rapport Ni/Cu résulteraient du caractère évolué et oxydé du magma parent.

Les sulfures, disséminés à travers la grande majorité du dyke et les concentrations modérées en sulfures associées aux leucogabbro et aux xénolithes témoignent d'une ségrégation tardive du liquide sulfuré ne permettant pas au liquide sulfuré de s'accumuler. Le processus le plus probable de déclencher la saturation en sulfure est la réduction du magma oxydé par cristallisation de magnétite et/ou dégazage.

Les magmas d'arc apparaissent comme prospectifs pour la formation de gisements de sulfures magmatique en raison de leur capacité à dissoudre de grande quantité de S, à condition que le la saturation en sulfure soit atteinte précocement au cours de la différentiation.

Abstract

Most major sulfide Ni-Cu deposits originated from komatiitic or tholeiitic magmas that formed in association with mantle plumes. Their genesis involves the segregation of a immiscible sulfide liquid, reaction of the sulfide liquid with silicate melt to upgrade the sulfide in chalcophile elements, and the concentration of the sulfide liquid in economic amounts. Saturation in sulfide is commonly achieved by lowering the sulfide solubility via assimilation of siliceous wall rock or by increasing the S content by adding S-bearing materials.

The Älgliden dike in the Skellefte Belt in Sweden contains currently uneconomic Ni-Cu sulfide mineralization. The Älgliden mineralization is atypical insofar as it contains a significant amount of Au, has a low Ni/Cu ratio and formed in a subduction-related geodynamic setting. The host intrusion intrudes Cu-Au porphyry mineralization which led to the suggestion that the Älgliden Ni-Cu-Au mineralization was linked to the assimilation of sulfide-bearing wall rocks.

The goals of this research project were to investigate the ore forming processes of the Älgliden mineralization and its ore potential, as well as to improve our understanding of the genesis of Ni-Cu deposits in subduction zones. The work is based on a petrological study of the ore and its host rocks, determination of mineral compositions, analyses of major and trace elements in bulk rocks, and sulfur isotope analyses. This was supported by the Boliden company which owns the deposit.

The dike is composed mainly of olivine norites with minor leucogabbros. Bulk rock compositions, magmatic textures and mineral compositions suggest that the olivine norites formed by accumulation of olivine and that the leucogabbros represent residual melts with or without cumulus plagioclase ±orthopyroxene. The norites are interpreted to form by one or two injections of an olivine-rich crystal mush and subsequent fractional crystallization. The parental melt of the Älgliden rocks was a hydrous and evolved basalt estimated to contain ≈6 wt.% MgO.

The sulfide ore is mainly disseminated throughout the whole Älgliden intrusion. Some weak ore concentrations occur as network to vein and massive sulfides that are spatially associated with the leucogabbros and wallrock xenoliths. The association between the leucogabbros and the concentrations of sulfide, their low ore grade and Ni/Cu ratio suggest that the sulfide segregated late in the differentiation process. This timing appears unfavorable for the Älgliden mineralization because it inhibited both sulfide-silicate liquid interaction and the accumulation of sulfide.

Contamination of the Älgliden magma by its wall rocks is excluded by trace element data and S isotope compositions. Instead these data indicate that the Älgliden magma was emplaced above a subduction zone and sulfide saturation is thought to occur by reduction of the oxidized

and volatile-rich magma by magnetite fractionation and/or by degassing. Positive $\delta^{34}S$ ratios suggest addition of slab-derived material which is thought to be responsible for the oxidized character of the Älgliden magma.

The oxidation state of arc magmas allows them to carry large amounts of S and Au. Their evolved character is also responsible for their relatively high Au contents and low Ni/Cu. Such characteristics are likely to occur in sulfide mineralization in subduction zone settings, and if sulfide liquid segregation had occurred earlier than at Älgliden the process may have produced economic sulfide deposits.

Keywords: Älgliden dike, Ni-Cu-Au mineralization, Skellefte district, subduction zone, oxidized mafic magmas, reduction-induced sulfide saturation.

Table of contents

1. Introduction

To meet the increasing demand for electric vehicles in coming decades will require a substantial increase in the production of nickel and copper. These metals are partly supplied from magmatic sulfide deposits. In the last decade, the proportion of the world's Ni production coming from this type of deposit has not increase because only a few major deposits account for the global Ni production and because Ni tends to be more and more extracted from Ni-lateritic deposits. In a context of increasing Ni and Cu demand, this encourages to explore other economic magmatic sulfide deposits.

Magmatic Ni-Cu-platinum-group element (PGE) mineralization is associated with mantle-derived mafic-ultramafic magmas. Ore deposits form when the magma becomes saturated in S and segregates an immiscible sulfide liquid in which Ni, Cu and/or PGE, the chalcophile ore metals, are concentrated (e.g. Naldrett, 2004; Arndt et al. 2005). If the sulfide liquid can be concentrated in economic abundances, it will form a Ni-Cu-(PGE) deposit. Grade and metal ratios in magmatic sulfide deposits are variable and are used to distinguish sulfide-rich and Ni-Cu-rich deposits from sulfide-poor and PGE-rich deposits (Naldrett, 2004).

Worldwide, most of Ni-Cu deposits derived from tholeiitic or komatiitic magmas in association with mantle plumes. They are found in large igneous provinces or associated with Archean ultramafic lavas. Notable examples are the Norilsk-Talnakh deposits in Russia, which are associated with the Siberian large igneous province (Czamanske et al., 1995, Naldrett, 1996) and the Kambalda deposits in Australia, which are hosted in 2.7 Ga komatiites (Lesher & Keays, 2002). Some deposits, however, occur in a setting quite different from that of a mantle plume. For example, a number of relatively small deposits in Finland (Vammala, Kotalahti; Papunen & Gorbunov, 1985), Spain (Aguablanca; Tornos et al., 2001) occurs in subduction settings. Deposits from this type of geodynamic setting are poorly studied due to their restricted occurrences, but their interest is growing due to the increasing demand of Ni and Cu. In subduction zone settings, magmas are calk-alkaline and more oxidized than tholeiitic or komatiitic magmas (e.g. Ballhaus, 1993; Kelley & Cottrell, 2009), which increases the S solubility (Carroll and Rutherford, 1985, 1987; Luhr, 1990; Jugo et al., 2005), a key parameter in the formation of an immiscible sulfide liquid. Subduction zones are thus considered as unfavorable for the formation of magmatic sulfide deposits.

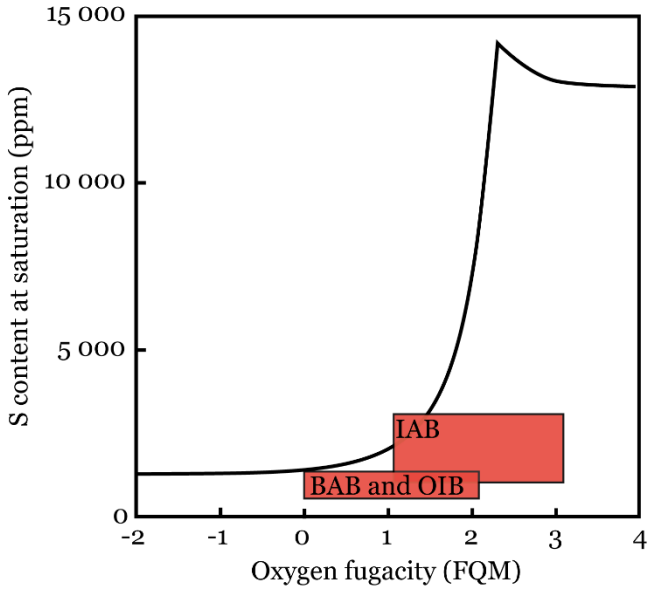

Figure 1.1 S content at sulfide and sulfate saturation from island arc basalts (IAB), back-arc basalts (BAB) and oceanic-island basalts (OIB) and mid-ocean ridge basalts (MORB). After Jugo (2009).

Sulfide saturation, which allows the formation of an immiscible sulfide liquid, is reached in response to two main processes, i.e. the increase of the S content and/or the decrease of the S solubility of the magma. The S solubility depends on several parameters including pressure, temperature, the redox conditions and the activity in SiO2 and in FeO (Naldrett et al., 2004 and reference therein). Sulfur, dissolved as sulfide (S^{2-}) in the magma, has a limit of solubility above which the magma becomes saturated in sulfide and exsolves a FeS-rich immiscible sulfide liquid (Mathez, 1976; Czamanske & Moore, 1977). Shima & Naldrett (1975) use the term "sulfur content at sulfide saturation" or SCSS to express the threshold of S content at which sulfide appears as a separate. The solubility of sulfide negatively correlates with pressure (Wendlandt, 1982; Keays, 1995; Mavrogenes & O'Neil, 1999) so that when mantle-derived magmas arrive near the surface, they are undersaturated in sulfide. Redox conditions have a strong effect on the S speciation leading to higher sulfide solubilities at increasing oxygen fugacities (Carroll and Rutherford, 1985, 1987; Luhr, 1990; Jugo et al., 2005). Jugo (2009) showed that oxidized magmas are strongly undersaturated, with SCSS up to ten times higher in island arc basalts than in mid-ocean ridge basalts (Figure 1.1).

The felsification of mafic/ultramafic magmas, by magma mixing or assimilation of siliceous material, increases the activity of SiO_2 and lowers the sulfide solubility (Li & Ripley, 2005; Ripley & Li, 2013; Naldrett, 2004). Decreasing temperature and related fractional crystallization, also cause the magma to approach sulfide saturation for two dependent reasons

Firstly, decreasing temperatures tends to reduce the sulfide solubility (Haughton et al., 1974; Wendlandt, 1982). Secondly, because S is incompatible during fractional crystallization of silicate minerals, its concentration increases in the residual melt.

The last main factor is the FeO content of magmas which have contrasting effects on sulfide solubility, producing a positive correlation at high FeO content, and a negative correlation when FeO combine with S^{2-} to form a FeS sulfide phase (O'Neil & Mavrogenes, 2002; Wykes et al. 2015). This combination of factors allows magmas to reach sulfide saturation after 20 to 40 wt.% of fractional crystallization, but this process is unlikely to produce economic magmatic sulfide deposits because the sulfide saturation occurrs late in the crystallization sequence and accumulated crystals prevent sulfide droplets from concentrating in large amounts (Arndt et al., 2005; Ripley & Li, 2013). Arndt et al. (2005) indeed pointed out the critical importance of the early triggering of sulfide saturation in the formation of economic deposits. The widely accepted model for the formation of magmatic sulfide deposit commonly requires assimilation of wall rock which lead to early sulfide saturation of mafic magmas (Keays, 1995; Naldrett, 2004; Li et al., 2009). Associated with this process, the sulfide solubility can be lowered by adding of siliceous materials or S can be added to the magma by assimilation of S-bearing rocks (e.g. Naldrett, 1992; Naldrett, 1999; Lightfoot & Keays, 2005; Ripley & Li, 2013). In most Ni-Cu deposits one of both processes occurred (e.g. Kambalda, Noril'sk).

In this manuscript, we* studied the Älgliden Ni-Cu-Au mineralization, located in the Skellefte belt of Sweden. The Skellefte belt has been interpreted as a volcanic arc (Rickard & Zweifel, 1975; Claesson, 1985; Vivallo & Claesson, 1987; Wilson et al., 1987; Gaál, 1990; Weihed et al., 1992; Öhlander et al., 1993; Allen et al., 1996; Billstrom & Weihed, 1996; Juhlin et al., 2002), and this offers the opportunity to study a magmatic sulfide mineralization in subduction zone setting. Moreover, the Skellefte belt is a highly prospective district hosting hundreds of deposits (i.e. mostly volcanic-hosted massive sulfide deposits). However, until now only one Ni-Cu deposit has been mined. In contrast, the Kotalahti Belt, the Finnish ewtension of the Skellefte Belt, hosts several Ni-Cu deposits.

The Älgliden mineralization occurs in a small, near-vertical, mainly gabbroic dike and consists of disseminated and minor concentrations of Ni-Cu sulfides. Peculiarities of the mineralization are their unusual metal grades: it shows a high Au content and a low Ni:Cu ratio relatively to other Ni-Cu deposits (Figure 1.2). The Älgliden dyke intrudes granitoids containing porphyry-type Cu-Au mineralization which led Bejgarn et al. (2013) to propose that assimilation of these wall rocks by the gabbroic magma was instrumental in the formation of the ores and responsible for the relatively high Au and Cu content of the Älgliden mineralization.

*In this thesis, the plural pronoun is used, following French conventions

In this study, we report the results of a detailed petrological and geochemical study of the Älgliden dike and its mineralization. We describe in detail the geological and tectonic setting, the lithology and mineralogy of the silicate rocks and the ores, and their geochemical compositions.

We then use this information to propose new ideas about the controls on the likely distribution, the composition and abundance of sulfides within the dike. Finally, we develop a new model for the formation of Ni-sulfide mineralization in calk-alkaline magmas in a subduction-related geodynamic setting.

The research was supported by the Boliden company who provided most of the research funding, access to core and abundant background information. Most of the research and analytical work was conducted in the ISTerre laboratories of the University Grenoble Alpes.

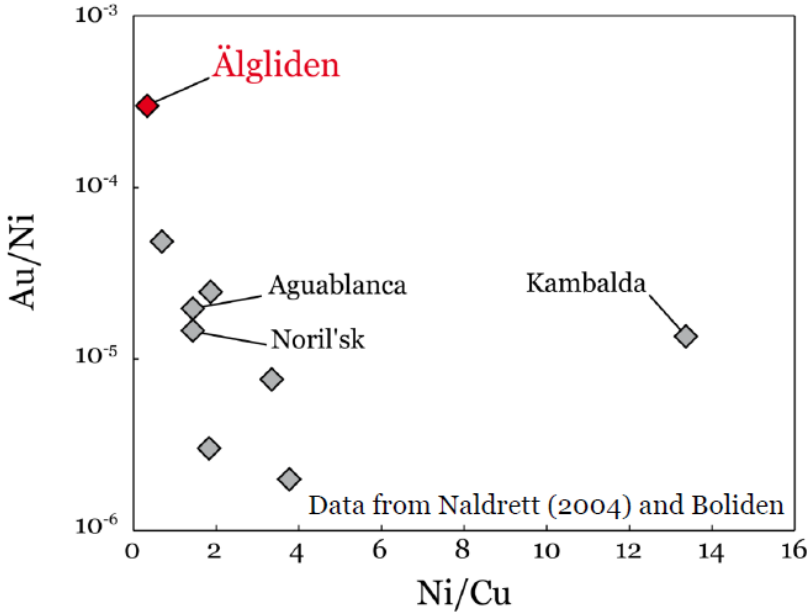

Figure 1.2 Au/Ni *vs.* Ni/Cu for some Ni-Cu deposits.

2. Geological context

2.1. Fennoscandian shield

The Fennoscandian shield (also called the Baltic shield) extends from Norway to NW Russia (Figure 2.1). It mainly consists in an Archean domain to the NE and a Paleoproterozoic domain, traditionally called the Svecofennian domain, to the SW. The Archean crust is divided into the Karelian, Belomorian, Kola and Norbotten provinces which are separated by Paleoproterozoic thrust faults (Gaál & Gorbatchev, 1987; Lahtinen et al., 2005). These Archean cratons mostly formed during the Saamian (3.1-2.9 Ga) and Lopian (2.9-2.6 Ga) orogenies (Gaál & Gorbatschev, 1987).

The Archean-Paleoproterozoic boundary is (the Luleå-Jokkmokk Zone) is, in its Sweden portion, delineated using Sm-Nd isotopic data and geophysical data (Figure 2.1). It is marked by a steep gradient from negative ε_{Nd} values in the north to positive values in the Skellefte district (Öhlander et al., 1987; Skiold et al., 1988; Öhlander et al., 1993) and by a north-dipping reflector overlying the Skellefte district that is interpreted as a Paleoproterozoic subduction zone (BABEL working Group, 1990).

The 2.5-2.1 Ga period, also called the Karelian stage, was marked by alternating periods of relative quiescence and rifting (Gorbunov et al., 1985 in Gaál, 1990; Lahtinen et al., 2005). Intracontinental extension has led to the continental break up (2.06 Ga) forming a passive margin of the Archean craton. This major event generated rift-related mafic-ultramafic volcanism which is responsible to the Ni-Cu deposits of Pechenga in NW Russia and Kevitsa in Finland, as well as Fe and stratiform Cu deposits (Weihed et al., 2005).

Subsequent convergence led to the 1.9-1.8 Ga Svecofennian/Svecokarelian orogeny (both names occur in the literature). This orogeny occurred within the period 1.9-1.7 Ga and is characterized by intense crust production and related magmatism (Patchett & Arndt, 1986). The complex orogeny (Lundberg, 1980) involved several crustal blocks, various tectonic regimes (i.e. extension, compression, strike slip motion) and environments (e.g. arc, rift). It also gave rise to the formation of numerous ore deposits, including volcanic massive sulfide (VMS) deposits in intra-arc in extension (1.89-1.90 Ga), iron oxide-copper-gold deposits during extension of the Archean crust (1.87 Ga), orogenic gold deposits during the collision stage (e.g. 1.82 Ga), and Ni-Cu deposits between the Archean craton and a microcontinent (i.e. Kotalahti) or between two microcontinents (i.e. Vammala; Weihed et al., 2005). The Älgliden Ni-Cu-Au deposit is in the Skellefte mining district, which contains the majority most deposits in the Fennoscandian shield (Weihed et al., 2005; Figure 2.1).

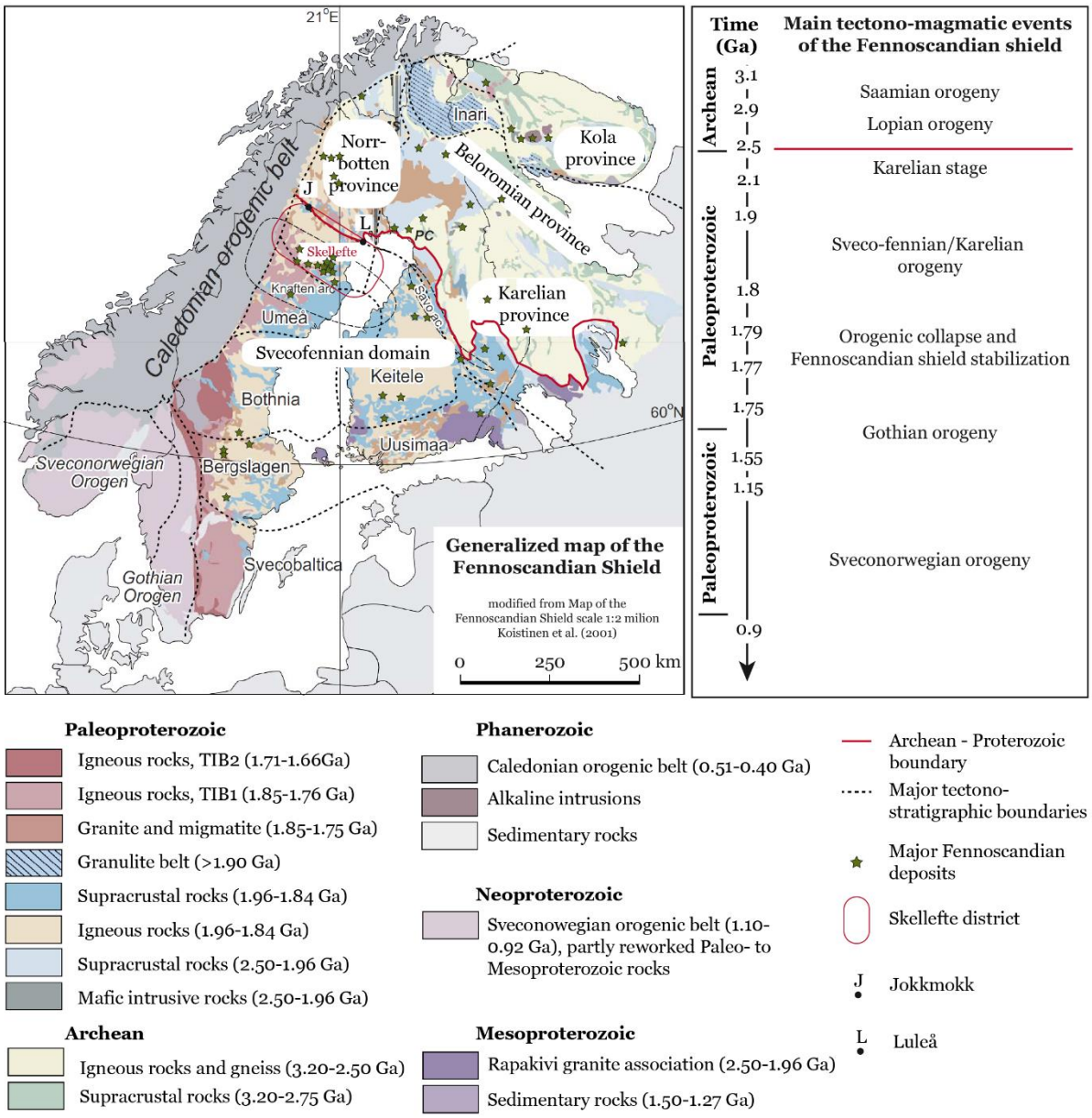

Figure 2.1 Simplified geological map of the Fennoscandian Shield with major tectono-stratigraphic units discussed in the text and the associated chronology of main tectono-magmatic events (Lahtinen et al., 2005). Map adapted from Koistinen et al. (2001), and modified from Weihed et al. (2005) and Rutland et al. (2001). Abbreviations: (TIB) Trans-Scandinavian igneous belt)

2.2. Chronostratigraphic sequence and magmatic activity of the Skellefte district

The Skellefte district is a 120x30 km belt along the Skellefte River in northern Sweden. It is made up of metamorphosed supracrustal volcano-sedimentary and intrusive rocks (Figure 2.2) that have been dated at 1900-1860 Ma. The belt has been extensively studied because it hosts numerous ore deposits.

The volcano-sedimentary sequence is generally regarded as being deposited as an upward shallowing sequence in a continental environment to the north and a deep-marine basin to the south (Bothnian basin; Lundberg, 1980; Zweifel, 1982). The overall sequence is commonly subdivided into four lithostratigraphic units (Figure 2.2).

The Bothnian Super-group

The Bothnian Super-group, located south of the central Skellefte district, consists of greywacke with minor volcanic intercalations that are considered to have emplaced in a deep marine sedimentary environment. Dated at 1960-1860 Ga (Lundqvist et al., 1998), the oldest rocks are suggested to be the basement for the Skellefte Group (Rutland et al., 2001a; Skyttä et al., 2012).

The Skellefte Group

The Skellefte Group, the lower stratigraphic unit, contains volcanogenic rocks and intercalated sediments (Figure 2.2a). Volcanic to subvolcanic rocks are, by order of abundance, rhyolitic, dacitic, andesitic and basaltic in composition (Allen et al., 1996). Rocks of this group have been dated from 1900 to 1840 Ma with most between 1900 to 1880 Ma (Billström & Weihed, 1996; Montelius, 2005; González-Roldán, 2010; Figure 2.2b).

The Vargfors Group

The Vargfors Group overlies the Skellefte group with conformable, unconformable or faulted relationships (Allen et al., 1996; Figure 2.2a) and occurs in the Vargfors sedimentary sub-basin to the south of the Jörn intrusive complex (Dumas, 1986; Kathol and Weihed, 2005; Figure 2.2). This group comprises siliciclastic to subordinate carbonaceous sediments, intercalated with basaltic lava flows, mafic-ultramafic sills and basaltic to andesitic rocks (Bergström, 2001). The basaltic to andesitic volcanic rocks englobe and might be cogenetic to the mafic-intermediate Gallejaur plutonic complex (described below, Kathol and Weihed, 2005). A rare felsic ignimbrite has been dated at 1875±4 Ma (Billström and Weihed, 1996).

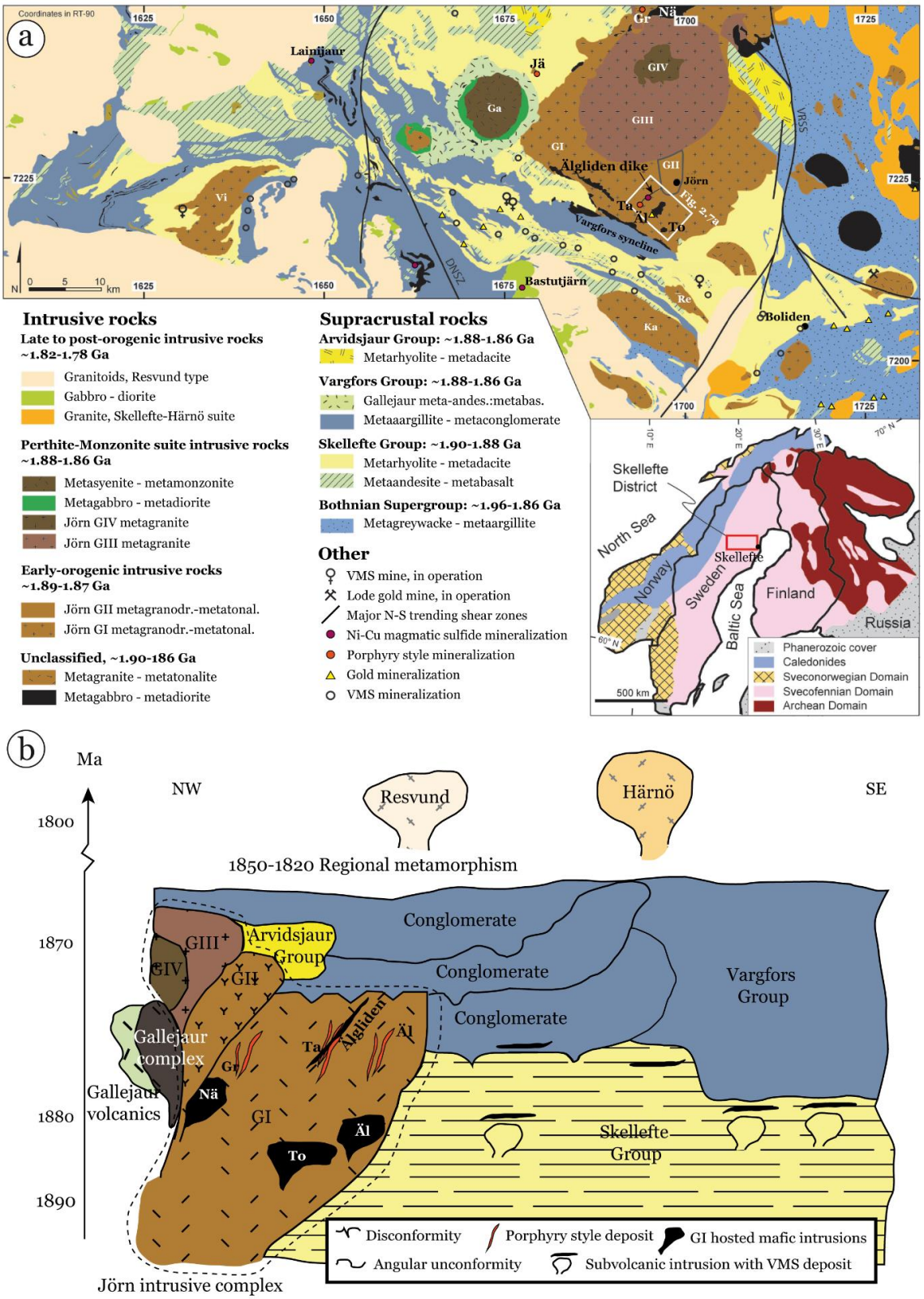

Figure 2.2 a) Geological map of the Skellefte district. Geological information from Kathol et al. (2005) and ore deposits from (Bergman Weihed, 2001) and Weihed et al. (1992). Inset: Global Fennoscandian Shield geology (from Figure 2.1). b) Simplified schematic stratigraphy in the Skellefte district (Modified after Allen et al. 1996, Billström and Weihed, 1996 and Bejgarn et al. 2011). Colors are same as a). Abbreviations: Äl: Älgträsk; Gr: Grangberg; Nä: Näsberg; Ta: Tallberg; To: Torsspiggen.

The Arvidsjaur Group

The Arvidsjaur Group, in contrast to the two previous described groups, comprises subaerial, felsic to intermediate volcanic rocks and volcanoclastic sediments (Lilljequist and Svenson, 1974). Being dated at 1876±3 and 1878±2 Ma (Skiöld et al., 1993), the rocks of the Arvidsjaur Group are suggested to represent the subaerial equivalent of the Vargfors Group (Allen et al., 1996; Weihed et al., 1992).

In the central Skellefte district, the intrusive rocks are mainly early to syn-orogenic. They include the large Jörn intrusive complex juxtaposed to the Gallejaur complex, together with satellite intrusions, from west to east, the Vinterliden, Karsträsk and Rengärd intrusions. Minor intrusive rocks in the western and eastern parts of the Skellefte district are dominated by the late to post orogenic granites of the Resvund and Skellefte Härno suites (Figure 2.2).

The Jörn intrusive complex

The early- to syn-orogenic Jörn intrusive complex (JIC) forms a large batholith that intrudes the volcanosedimentary sequence of the Skellefte district (Figure 2.2). The intrusive rocks, dated at 1890-1860 Ma (U-Pb zircon method), range from gabbro to granite, mostly tonalite and granodiorite (Wilson et al., 1987; González-Roldán, 2010, Bejgarn et al., 2013). The batholith comprises 4 magmatic phases (GI-GIV) based on geological, geochemical, geochronological and geophysical criteria (Wilson et al., 1987; González-Roldán, 2010).

The GI phase is the oldest phase and forms the outer shell of the intrusion (Figure 2.2). It comprises granodiorite and tonalite, together with minor, quartz-feldspar porphyry (QFP) dikes and mafic intrusions (Bejgarn et al., 2011; Bejgarn et al., 2013; González-Roldán, 2010; Wilson et al., 1987). Other coeval GI-type satellite intrusions (e.g. Viterliden, Rengärd intrusion) are distributed farther south (Figure 2.2). The granodiorite and tonalite are dated from 1880.0±3.9 to 1887±3 Ma (Bejgarn et al., 2013; González-Roldán, 2010). Porphyry dikes and mafic intrusions are located on the northern, southern and western external parts of the batholith (Figure 2.2). The Torsspiggen, Älgträsk and Näsberg mafic intrusions are coeval with the granodiorites and the tonalites, while the younger late GI Älgliden dike, dated at 1876±1 Ma, was contemporaneous with QFP dikes (Figure 2.2b).

Younger phases, from GII to GIV, became progressively more felsic and evolved (Wilson et al., 1987; González-Roldán, 2010) and generally postdate the Skellefte Group volcanic rocks. The GII phase is a relatively small intrusion dated from 1874.0±6 to 1871.0±4 Ma (González-Roldán, 2010) that crosscuts the Älgliden dike. GIII, dated at 1862.8±4.7 Ma (González-Roldán, 2010), and GIV, not dated, are concentrically disposed and crosscut GI and GII (Wilson et al., 1987; Figure 2.2).

Gallejaur complex

The Gallejaur complex, west of the JIC, is a concentrically organized pluton with a monzonitic core and a gabbroic rim dated, respectively, at 1873±10 Ma and 1876±4 (Skiöld, 1988; Skiöld et al., 1993). It is surrounded by cogenetic basaltic and andesitic rocks of the Vargfors Group (Kathol and Weihed, 2005). It is coeval with the sedimentary rocks of the Vargfors and Arvidsjaur Group together with the QFP dikes and the Älgliden dike (Figure 2.2).

2.3. Geochemical characteristics of the Skellefte rocks

The Skellefte district, located immediately south of the Swedish Archean-Paleoproterozoic boundary (i.e. Luleå-Jokkmokk Zone), has been interpreted as a volcanic arc (Rickard & Zweifel, 1975; Claesson, 1985; Vivallo & Claesson, 1987; Wilson et al., 1987; Gaál, 1990; Weihed et al., 1992; Öhlander et al., 1993; Allen et al., 1996; Billstrom & Weihed, 1996; Juhlin et al., 2002). In the following section we report some of the geochemical characteristics of the district. They will be discussed in Section 2.6. Geophysical evidence in favor of a volcanic arc includes the NE-dipping reflectors penetrating into the mantle and the 10 km Moho offset interpreted as a fossil subduction zone (Babel Working Group, 1990, 1993).

Rock types and affinities

Volcanic rocks of the Skellefte Group of the Skellefte district have been intensively studied. Their compositions range from basaltic and ultramafic to rhyolitic (Figure 2.3), with significance abundance of intermediate rocks, as in some modern arcs (Allen et al., 1996; Figure 2.3a). Most tectonic environment discriminant diagrams (e.g. Rb vs. Y+Nb diagram, Pearce et al. 1984; Ti-Zr-Y, Pearce & Cann, 1973) of volcanic and intrusive rocks of the Skellefte district favor a subduction setting (Claesson, 1985; Wilson et al, 1987; Weihed et al., 1992; Kahthol and Weihed, 2005; González-Roldán, 2010). Most of the volcanic and intrusive rocks of the Skellefte district are thought to belong to calc-alkaline series with low contents of Nb-Ta and Y (Rickard & Zweifel, 1975; Wilson et al., 1985; Wilson et al. 1987; Weihed et al., 1992). A few mafic volcanic rocks of the Bothnian and Skellefte Group appear to have tholeiitic character (Claesson, 1985; Kahthol and Weihed, 2005). A compilation of mafic to felsic volcanic and intrusive rocks is reported in Figure 2.3b. It shows that rocks of various stratigraphic units, nature and composition, all have similar patterns, with negative Th and Nb-Ta anomalies and positive Pb anomalies, which are characteristics of magmas formed in subduction settings (Perfit et al., 1980; Tatsumi et al., 1986).

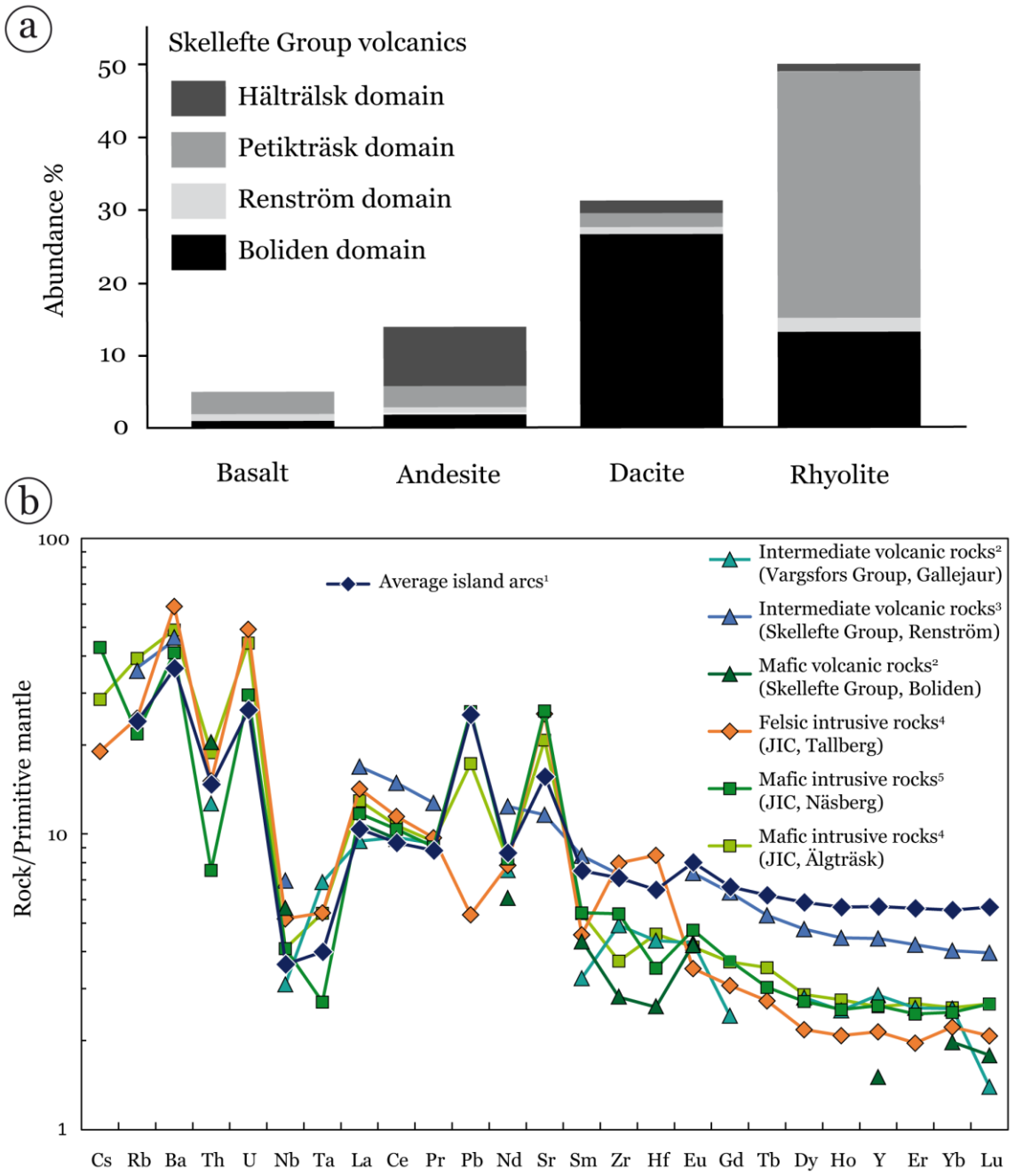

Figure 2.3 Some geochemical features of rocks of the Skellefte district. a) Relative abundance of basalt, andesite, dacite and rhyolite for volcanic rocks of the Skellefte Group (from Allen et al., 1996). b) Mantle-normalized multi-element diagram of the Skellefte and island arc rocks. Data from 1: Gazel et al., 2015; 2: Berge, 2013; 3: Allen & Svenson, 2004; 4: Bejgarn et al., 2011; 5: González-Roldán, 2010.

Isotopic data

Isotopic compositions have been measured only in the felsic rocks of the Skellefte district. The Skellefte granitoids have $\varepsilon_{Nd(t)}$ values ($\varepsilon_{Nd(t)} = [(^{143}Nd/^{144}Nd)_{sample\ (t)} / (^{143}Nd/^{144}Nd)_{CHUR\ (t)} - 1]*1000$) ranging from +1.2 to +3.2 (Wilson et al., 1985, 1987). The mantle at this time is

assumed to have an $\varepsilon_{Nd(t)}$ value about +4, while the 1900 Ma Archean granitic gneiss would have an $\varepsilon_{Nd(t)}$ value of about -11 (Wilson et al., 1987).
Rocks of the Skellefte district mostly yield oxygen isotopic values i.e. $\delta^{18}O$ mostly between +6 and +9‰ and indicate different source for the granitoids (Wilson et al., 1985).
Lead isotope studies on massive sulfides hosted in volcanic rocks of the Skellefte Group showed two distinct isotopic ratios (average μ-values of 9.34 ± 0.10 and 8.96 ± 0.23, 2σ, N= 13 and 82, respectively; Billström & Vivallo, 1994).
Felsic rocks of the Skellefte district (e.g. Vargsfor ignimbrite and Kristineberg granitoid) and rocks of their presumed basement (i.e. the 1.96 Ga Barsele dacite and 1.94 Ga Knaften granite) have highly positive $\varepsilon_{Hf(t)}$ values, i.e. +7.7 and +8.8 in average (Guitreau et al., 2014; the depleted mantle at this time has $\varepsilon_{Hf(t)}$ of +10).

2.4. Tectono-metamorphic evolution of the Skellefte district

Although the Skellefte district was subject to several deformation events (or by one diachronous prolonged event) most of the deformation occurred between 1860 and 1780 Ma. The deformation was partitioned and concentrated into the supracrustal rocks while the JIC intrusions mostly acted as rigid blocks (Kathol and Weihed, 2005 and references therein). The main structures include the broadly N-S oriented and curved major shear zones and the tight folds in supracrustal rocks.
The oldest tectonic fabric is recognized throughout the district as a S1 foliation that is parallel to bedding in clastic volcanic and sedimentary rocks (Allen et al., 1996). This foliation may have developed during D1 deformation but no related folds are recognized. Skyttä et al. (2012) proposed that the earliest deformation occurred at about 1890-1880 Ma synchronously with deposition of the Skellefte Group volcanic rocks (Figure 2.4. The development of a fault pattern of SE-NW-striking normal faults and interlinked SW-NE-striking transfer faults is attributed to regional SE-NW transtension or SW-NE transpression that also opened pull-apart basins (Bauer et al., 2011; Skyttä et al., 2012).
The D2 major tectonic phase is a SW-NE shortening that developed semi-ductile to brittle deformation, with reverse oblique slip movement and upright tight folding (Bergman Weihed, 2001). Older deformation zones were reactivated and inverted with a reverse component during basin inversion which may tentatively be related to a SW-NE transpression (Bauer et al., 2011; Skyttä et al., 2012). The compressional D2 deformation is constrained between 1879 and 1867 Ga (Skyttä et al., 2012; Figure 2.4b).

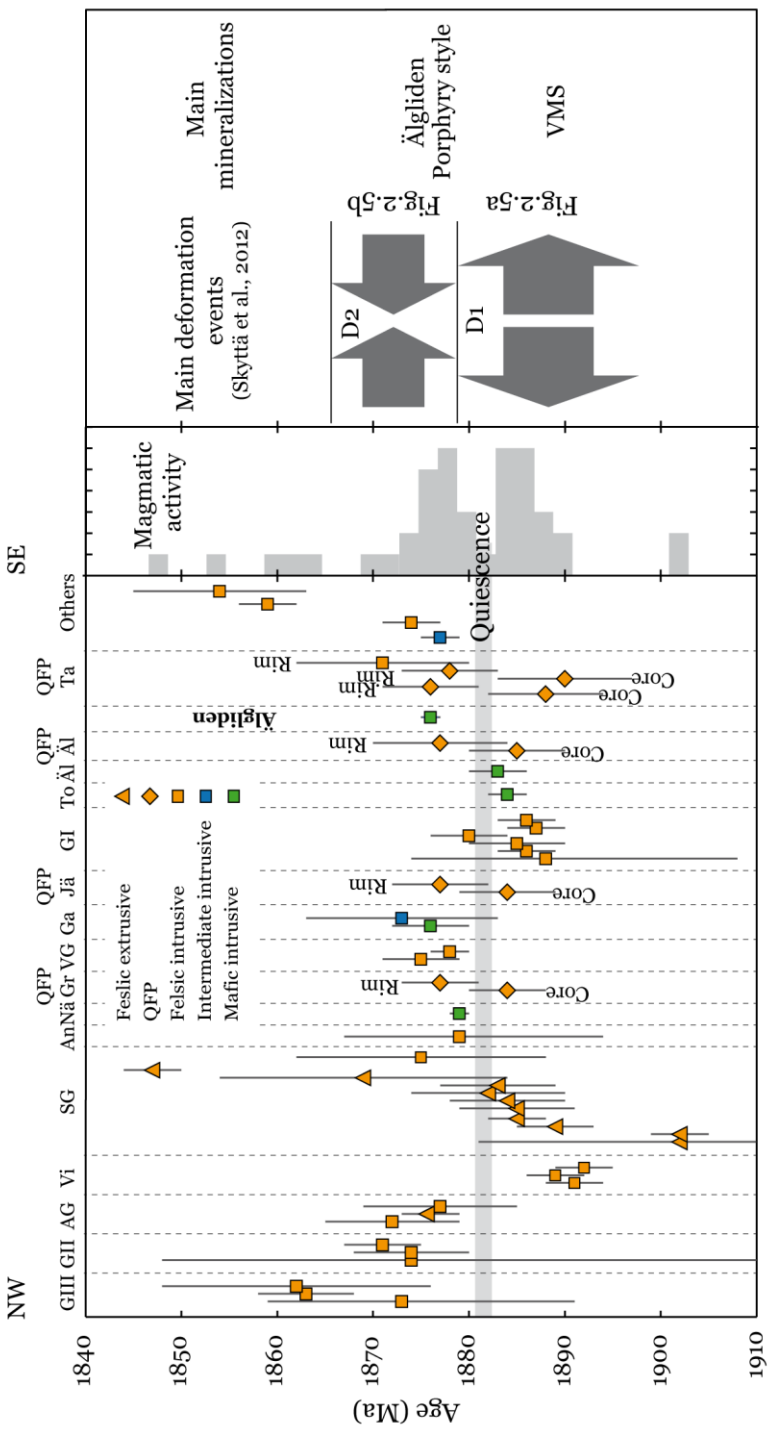

Figure 2.4 Geochronological data of the main geological units of Skellefte district denoting the magmatic activity, and related tectonic regimes and ore deposit formation. Geochronological data are reported in Appendix 9. Abbreviations: (AG) Arvidsjaur Group; (Vi) Viterliden; (SG) Skellefte Group; (An): Antak; (Nä) Näsberg; (QFP) Quartz feldspar porphyry; (Gr) Granberg; (VG) Vargfors Group; (Ga) Gallejaur; (Jä) Järvträsk; (To) Torrspiggen; (Äl) Älgträsk; (Ta) Tallberg. Core and rim from QFP rocks refer to zircons.

The youngest orogenic D3 deformation in the Skellefte district is constrained at approximately 1820-1800 Ma (Weihed et al., 2002). This event, attributed to E-W compression, has resulted in reverse shearing along steeply dipping N-S striking major shear zones, D3 open folds with steep N-NE striking axial surfaces, and crenulation of the main foliation in the central district (Bergman Weihed, 2001; Weihed et al., 2002).

In general the metamorphic grade in the central Skellefte district increases from green schist facies in the north to amphibolite facies in the south (Bergman Weihed, 2001). The peak metamorphism is reached at 1820 Ma and most of the deformation and metamorphism occurred in the interval 1860-1780 Ma (Weihed, 1992a; Bergman Weihed, 2001; Billström & Weihed, 1996; Weihed et al., 2002; Kathol & Weihed 2005; Figure 2.4). However, field evidence records an earlier metamorphic and deformation event with a minimum age of c.a. 1880 Ma (Kathol and Weihed, 2005 and references therein); Kathol et al. (2002) suggest that the early deformation and metamorphism must have occurred within a period spanning from 1910 to 1860 Ma.

2.5. Mineralization of the Skellefte mining district

Skellefte is the most important mining district in Sweden. This is mostly due to its 85 volcanogenic massive sulfide (VMS) deposits, but also its porphyry-type deposits, orogenic gold deposits, Ni-Cu mineralization and minor W, U, Mo and Li mineralization (Weihed et al., 1992). The VMS deposits are mostly found in the Skellefte Group and include Au, Ag, As, Cu, Zn and Pb in variable proportions. Among them the Kristineberg, Boliden and Renström are the most important. They are regarded as syngenetic exhalative sulfides as well as replacement mineralization, mostly emplaced below the sea level (Allen et al., 1996). The Cu-Au porphyries are mainly confined to the Jörn intrusive complex (Weihed, 1992a). These include the Tallberg, Älgträsk, Granberg and Järvträsk deposits located at the southern, northern and western part of the complex (Figure 2.2a). They are spatially associated with (quartz-) feldspar-porphyry dikes and related hydrothermal alteration. Orogenic gold deposits may have formed during syn- to post peak metamorphism (Weihed et al., 2005) whereas Li and Sn-W mineralization occurred within post orogenic granites (Weihed et al., 1992; Kathol and Weihed, 2005). The Ni-Cu mineralization is described separately as follows.

Ni-Cu mineralization related to mafic and ultramafic rocks

No major Ni-Cu-(Co) deposits have been found and in the Skellefte district but the small Lainijaur deposit was mined during World War II (Table 2.1). The magmatic sulfide deposits in the Skellefte area are divided into two types: 1) those with high Ni:Cu ratios (2.2-16) and ultramafic hosts, and 2) those with low Ni:Cu ratios (0.3-3.8) and younger mafic hosts (Nilsson, 1985). The gabbro-related deposits have high copper contents (mostly >3000 ppm), and can include some PGE mineralization. These include the Lainijaur, Älgliden and Bastutjärn deposits (Figure 2.2a). Ultramafic-related deposits are minor; they have a Ni:Cu ratio around 5 and the Ni content is correlated to the MgO content of the rocks (Nilsson, 1985; Kathol and Weihed, 2005). Overall, Co is found as trace metal in most of the deposits. The Älgliden deposit is unusual in that it is hosted by gabbroic rocks but has a very high Cu:Ni ratio (Cu/Ni = 3) compared to the other Ni-Cu deposits (Cu/Ni<1; Weihed et al., 1992) and also significant Au content (0.3 ppm).

The ultramafic-hosted Ni-rich ores are concentrated within a 20 km-wide and WSE-ENE striking tectonic zone south of the Skellefte district, referred to as the Ni zone or the Ni belt (Nilsson 1985, Weihed et al. 1992). Komatiitic to tholeiitic ultramafic volcanic rocks and intrusions occur within metasedimentary rocks and are emplaced along NE-SW striking faults (Nilsson 1985, Weihed et al. 1992). The metamorphic grade in the area is middle to upper amphibolite facies. Ni-Cu sulfides occur as disseminations or veins within the ultramafic bodies or is remobilized as fragmental or breccia ores in the wall rocks (Kathol and Weihed, 2005; Nilsson, 1985). The Mjövattnet deposit is the only one to host massive ore and has the highest Ni grade (1.4 %; Åkerman, 1987; Kathol and Weihed, 2005). The ultramafic-hosted deposits also include the Rörmyrberget deposit which intrudes a graphite- and sulfide-bearing paragneiss, suggesting mineralization could be related to country rock assimilation (Nilsson, 1985). The combined resources from all nine deposits, including Ni and Cu, are lower than those of the Älgliden deposit alone, due largely to the higher Cu grade for Älgliden (Åkerman, 1987).

The gabbro-related Ni deposits form a heterogeneous group, with unclear stratigraphic position (Kathol and Weihed, 2005). Two examples are described below.

The Lainijaur deposit is a lopolithic, layered mafic gabbroic-dioritic intrusion hosted by greywackes of the Vargfors Group (Grip 1961; Martinsson 1987a, 1996; Kathol and Weihed, 2005). Igneous layering seems to be parallel to the bedding of the host sediments, suggesting emplacement is prior to deformation (Kathol and Weihed, 2005). The gabbro grades into diorite, then granodiorite from the base of the intrusion to the top: a dike in the lower central part is thought to be a feeder. The different lithologies show a continuous tholeiitic fractionation trend and are interpreted to crystallize in three distinctive pulses from a common magma source (Martinsson, 1987a quoted in Kahtol and Weihed, 2005). Two massive sulfide

Table 2.1 Grade and tonnage of most Ni-Cu mineralizations in and around the Skellefte district (after Kahtol and Weihed, 2005)

Name	Type[a]	Status	Tonnage	Au	Ag	PGE	Cu	Ni	S	Co	Ni:Cu	Commodity
			kt	ppm	ppm	ppm	%	%	%	%		
Brännorna	1	Prospect	350				0.0	0.6	1.1	0	16	Ni-Cu-(Co)
Byske	1	Mineralization										Ni-Cu-(Co)
Gårkälen	1	Prospect	35				0.2	0.4	3.9	0	2.2	Ni-Cu-(Co)
Holmsvattnet	1	Mineralization										Ni-Cu-(Co)
Källmyrberget	1	Prospect						0.5				Ni-Cu-(Co)
Lappbäcken	1	Mineralization										Ni-Cu-(Co)
Lappvattnet	1	closed mine	1000				0.2	1	4.4	0	4.8	Ni-Cu-(Co)
Mjödvattnet östra	1	Mineralizatior	37				0.1	0.3			6.8	Ni-Cu-(Co)
Mjövattnet	1	Prospect	169				0.2	1.4	4.9	0	7.4	Ni-Cu-(Co)
Munkviken	1	Mineralization										Ni-Cu-(Co)
Njuggträskliden	1	Prospect	106			0.5	0.2	0.7	7.9	0.1	4.1	Ni-Cu-(Co)
Njuggträskliden b	1	Mineralization										Ni-Cu-(Co)
Njuggträskliden c	1	Prospect	190				0.1	0.7	1.5	0	5.4	Ni-Cu-(Co)
Njuggträskliden d	1	Prospect	261	1.2	4.9		0.1	0.7	6.6	0.1	6.4	Ni-Cu-(Co)
Rörmyrberget	1	Prospect	4239				0.1	0.8	1.4		13	Ni-Cu-(Co)
Uttersjön	1	Mineralization										Ni-Cu-(Co)
Vallen	1	Prospect	25				0.1	0.5			4.5	Ni-Cu-(Co)
Öretorp	1	Mineralization										Ni-Cu-(Co)
Bastutjärn	2	Prospect	2400				0.1	0.2			1.3	Ni-Cu-(Co)
Gissträsk	2	Prospect										PGE
Kalvtjärnen	2	Prospect										PGE
Lainijaur	2	Closed mine	119				1	2.2	23		2.2	Ni-Cu-(Co)
Storbodsund	2	Prospect	60				0.6	2.3	21	0.1	3.8	Ni-Cu-(Co)
Älgliden	**2**	**Prospect**	**570**	**0.3**			**0.7**	**0.3**	**6.1**	**0**	**0.4**	**Ni-Cu-(Co)**

(a) 1: Ultramafic-related mineralization; 2: mafic-related mineralization

lenses at the bottom of the lopolith are overlaid by disseminated sulfide, and Ni-As-Cu veins are radially distributed from the massive ore (Grip, 1961).

The Bastutjärn Ni-Cu-Co mineralization is related to a post orogenic gabbroic intrusion (Figure 2.2a). The mineralization is at the contact between the intrusion and the graphite- and sulfide-rich metasedimentary rocks of the Vargfors Group (Zettergren, 2013). The ore occurs as disseminated sulfides, semi-massive sulfides and semi-massive sulfides including graphite and sedimentary fragments (Zettergren, 2013). This together with the occurrence of xenoliths and

hybrid rocks close the contact of the intrusion suggest the assimilation of the S-bearing wall rocks (Zettegren, 2013).

2.6. Tectono-magmatic evolution and related mineralization in the Skellefte district during the Svecofennian orogeny.

The Svecofennian orogeny (1.9-1.8 Ga) is regarded as a complex collage of island arcs and microcontinents (Lahtinen et al., 2005 Weihed et al., 2005; Korja et al., 2006). Lahtinen et al. (2005) proposed that several terranes successively accreted from the SW direction to the growing craton such as during the collisions between a) the Karelian and the Norbotten craton, b) the Keitele and Bothnia microcontinents (i.e. Lapland-Savo orogeny) or c) the newly formed Archean-Paleoproterozoic complex and the Bergslagen microcontinent (i.e. Fenian orogeny; Figure 2.1). The Skellefte district is interpreted as a volcanic arc accreted to the Archean craton (Rickard & Zweifel, 1975; Claesson, 1985; Vivallo & Claesson, 1987; Wilson et al., 1987; Gaál, 1990; Weihed et al., 1992; Öhlander et al., 1993; Allen et al. 1996; Billstrom & Weihed, 1996; Juhlin et al., 2002). The Luleå-Jokkmokk Zone, located in between the Archean craton and the Skellefte district, is interpreted as the Archean paleo-boundary (Öhlander er al., 1993).
NE-dipping reflectors that penetrate into the mantle together with the Moho offset are interpreted as a NE-dipping fossil subduction zone. Juhlin et al. (2002) interpret the bi-vergent crustal structure as resulting from the successive accretion of a continental arc to the Archean craton followed by underthrusting of the Skellefte arc. From the positive $\varepsilon_{Nd(t)}$ values, and $\delta^{18}O$ values of the Skellefte granitoids, Wilson et al. (1985, 1987) suggest that the felsic rocks originate from a mantle-derived magma with minor contribution of sediment derived from the Archean craton. Wilson et al. (1987) also used major and trace elements, particularly the low contents of HFS elements, to propose that the JIC granitoids partly resulted from partial melting of the mantle under hydrous conditions above a subduction zone. The crustal contribution is thus either induced by slab dehydration/melting or by contamination of magma by the Skellefte arc basement. Billström & Vivallo (1994) presented out indirect evidence of a basement to the Skellefte arc at 1890 Ma. This evidence includes: xenoliths in the 1.89 Ga early orogenic igneous complex (Wilson et al., 1987); Nd isotopic data giving a model age of 2.0 Ga for volcanic rocks (Rickard, 1986); an age of ≈ 1.95 Ga for a zircon in Knaften granite about 50 km south of the Skellefte district; and importantly the dominant felsic nature of the magmatism (Vivallo, 1987). Billström & Vivallo (1994) interpret differences in Pb isotope ratios of massive sulfides to indicate that mafic and felsic Skellefte Group volcanic rocks reflect the melting of two different source regions. In their model, melting of the metasomatized mantle created by subduction and recycling of Archean sediments generated the mafic magmas and heat from this magma caused melting of the basement generating the felsic magmas.

Moreover, oxygen isotope compositions of the granitoids indicate they are originated from two different crustal source materials (Wilson et al., 1985). Recent studies of felsic rocks using Hf isotopic data converged toward a similar conclusion. Guitreau et al. (2014), on the basis of Hf isotopic data suggest that the felsic Skellefte rocks originate from (1) the partial melting of the Knafte-Barsele juvenile arc and/or (2) the melting of the subducted oceanic crust younger than that from which the basement was previously formed.

Based on the compilation of ages of most of the Skellefte rocks and the tectonic regimes reported on Figure 2.4, we identified two steps of major magmatic activity, deformation and mineralization during the Svecofennian evolution of the Skellefte district: 1) from 1890 to 1880 Ma, and 2) from 1880 to 1870 Ma. A short period around c.a. 1880 Ma is marked by magmatic quiescence and a basin inversion.

The 1890-1880 Ma period

This period is marked by magmatism dominated by felsic rocks emplaced during extension (Figure 2.4). The magmatism includes the deposition of the volcanic rocks of the Skellefte group and their intrusion by the Jörn intrusive complex and satellite intrusions (Figure 2.2.b and Figure 2.4). The 1890 Ma tholeiitic mafic and calc-alkaline felsic volcanic rocks are thought not to be co-genetic and result in a long period of extension during incipient rifting of a volcanic arc (Claesson, 1985; Vivallo, 1987). Billström & Vivallo (1994) proposed that mafic and felsic magmatism is due to melting of two different regions, i.e. metasomatized mantle and the crust during magma ascent. Emplacement of Skellefte Group volcanic rocks was accompanied by the formation of volcanic massive sulfide (VMS) deposits, in an extensional volcanic arc (Allen et al., 1996; Figure 2.5). Syn-extensional faults in a pull-apart basin controlled the deposition of the volcanic rocks with their VMS deposits as well as the location of the intrusive rocks (Skyttä et al., 2012; Bauer, 2013; Figure 2.5).

Bauer et al. (2013) pointed out that the transition from extension to crustal shortening coincides with the accretion of the Skellefte volcanic arc to the Archaean craton, as also suggested by Weihed et al. (2002) and Bauer et al. (2011). As illustrated in Figure 2.4, the basin inversion seems to be preceded by a short period of magmatic quiescence.

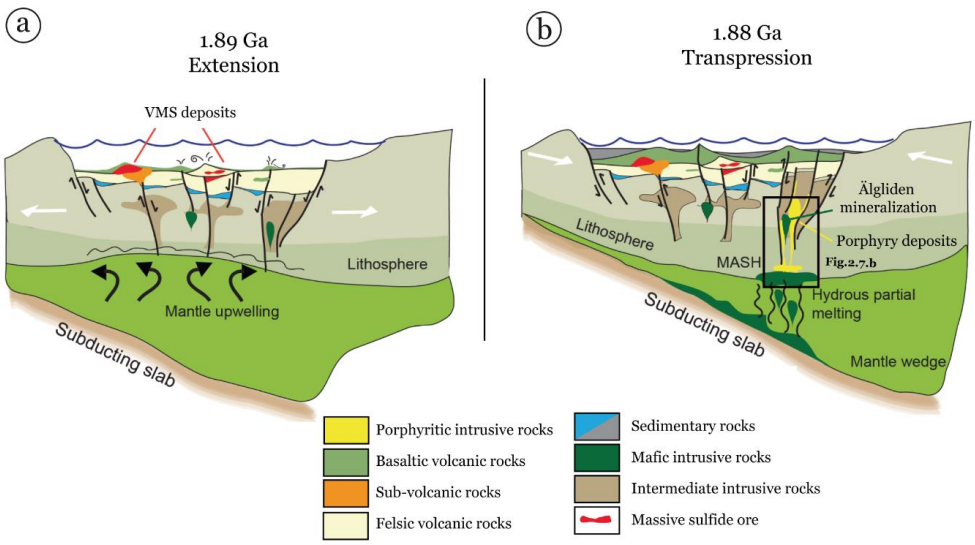

Figure 2.5 Schematic cross section illustrating the tectonic evolution of the Skellefte district at 1.89 and 1.88 Ga. Modified after Allen et al. (2002), Richards (2009) and Bejgarn (2012).

The 1870-1870 Ma period

The syn-tectonic sedimentation of the Vargfors basin contains interesting clues regarding the basin inversion (Bauer et al., 2013). Several clasts of GI granitoid were found in conglomerates of the Vargfors basin which border the JIC to the South (Bauer et al. 2011; Billström and Weihed, 1994). They indicate that in a few Ma only the early GI phase of the JIC is emplaced and subsequently uplift and eroded thanks to inverted normal faults, transfer faults and break-back fault (Bauer et al., 2011; Kathol and Weihed, 2005). Bauer et al. (2013) showed that these same SE-NW-striking inverted normal faults and the SW-NE transfer faults controlled the emplacement of the mafic intrusive and extrusive rocks which include those of the Gallejaur complex, lavas of the Vargfors group and the Älgliden dike (Figure 2.4b). The period of inversion is also marked by the emplacement of the GII-GIV phase of the JIC and the QFP dikes (Figure 2.4). Porphyry style deposits (Tallberg, Järvträsk, Granberg and Älgträsk) together with the Älgliden Ni-Cu-Au deposit formed in this context (Figure 2.4 and Figure 2.5). Bejgarn et al. (2013) showed that zircon in QFP rocks have cores dated between 1890 and 1880 Ma and overgrowth rims dated between 1880 and 1870 Ma. The authors interpreted the cores as xenocrysts that derive from melting of the GI unit (or the related supracrustal rocks) and the rims as overgrowth that crystallized from the QFP magma. On this basis, Bejgarn et al. (2013) suggest that the QFP dike magmatism was produced by a process referred to as melting-assimilation-storage-homogenization, i.e. MASH (Hildreth & Moorbath, 1988; Richards, 2003; Annen et al., 2006; Richards, 2009), in response to the heat produced by the coeval mafic magmatism.

Weihed et al. (1992) argued that the VMS deposits formed in a rifted volcanic arc with the porphyry deposits on the continent side of the arc and the Ni deposits in fore-arc environment.

2.7. Geology of the Ni-Cu-Au hosted Älgliden dike and its surroundings

Älgliden is a small gabbroic intrusion located in the central Skellefte district, in southern part of the Jörn intrusive complex (Figure 2.2). The prominence given to this intrusion stems from its Ni-Cu-Au mineralization, Älgliden being the largest nickel sulfide deposit in Sweden (Nilsson, 1985). It is described as containing disseminated and partly massive copper and nickel with the highest Cu:Ni ratio of Ni deposits in the Skellefte district (Weihed et al., 1992). The intrusion is poorly endowed with platinum group elements (total PGE <0.1 ppm), however (internal report, Boliden). The mineralization was discovered in the 1940's thanks to sulfide-rich boulders. Until now, exploration has been carried out by Boliden and described in company reports. Academic research is confined to the Master thesis of Filoche (2009) and the study of Bejgarn et al. (2013). The following paragraphs summarize the state of knowledge of the Älgliden dike and its mineralization from the literature and internal exploration reports from Boliden.

The geometry of the intrusion is mainly inferred from drilling conducted during several exploration programs from 1964 to 2011, and accounting for a total of 62 drill cores mainly located in the southern half of the intrusion (Figure 2.6). Geophysical surveys also provide indirect access to its extent. The intrusion is 3 km long with a variable width ranging from approximately 20 to 100 m. The dike tends to be thinner at greater depths in some sections (Figure 2.6b). It strikes SW-NE and its dip is near vertical. The dike is slightly offset by faults. Taking into account only the drilled portions of the dike, the different parts are named as shown in Figure 2.6 all along the manuscript. The 1 km-long north-eastern part of the intrusion has only been drilled twice and constitutes the unexplored potential of the Älgliden dike (Figure 2.6).

Bejgarn et al. (2013) described the dominant rock type as coarse-grained olivine gabbro containing olivine, pyroxene and plagioclase with accessory apatite, magnetite, pyrrhotite, chalcopyrite and pentlandite. A more precise description is given by Filoche (2009) who distinguished a mafic suite and leucogabbros.

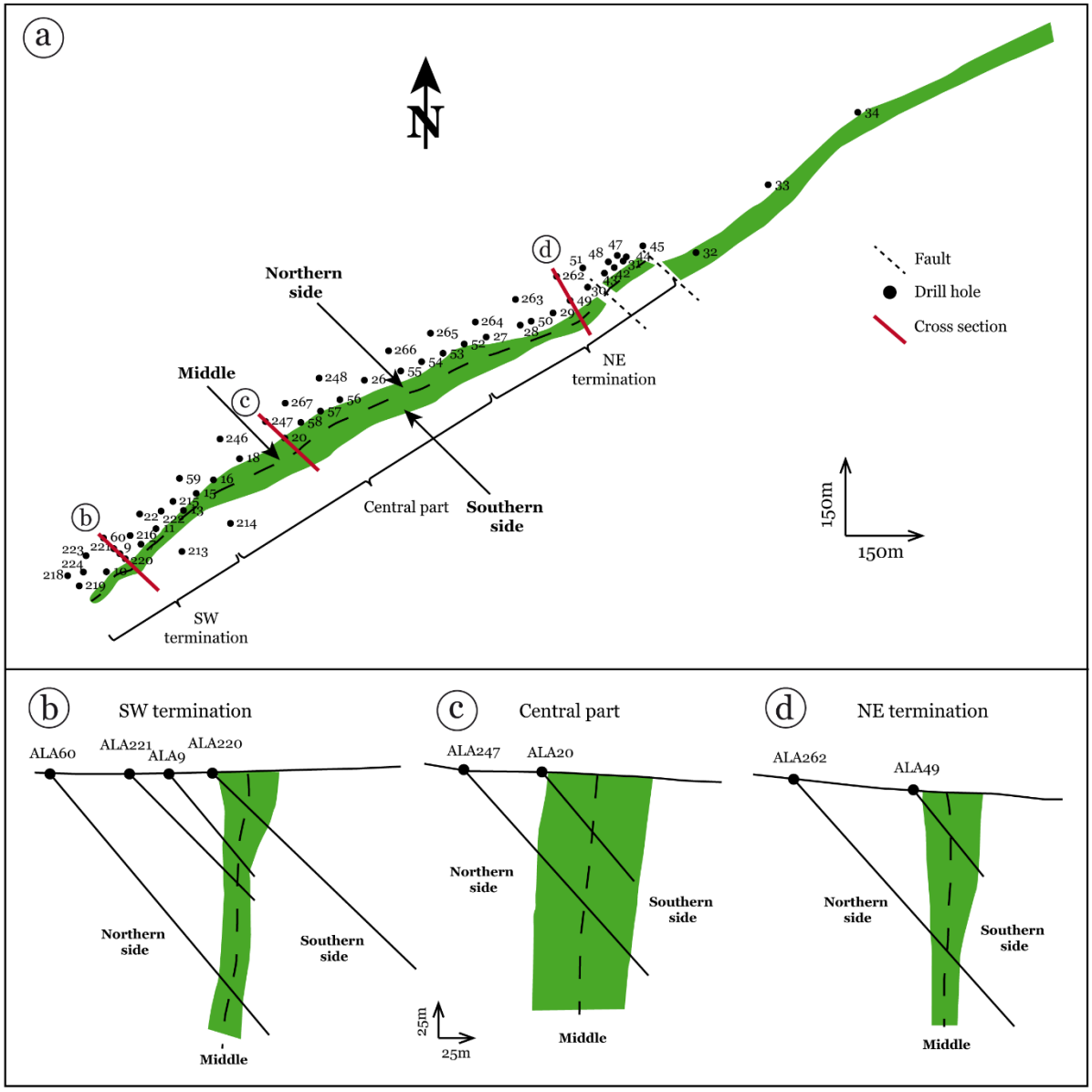

Figure 2.6 Älgliden dike delineation and nomenclature. (a) Map and (b-d) associated cross sections. Data from Boliden.

In the mafic suite, the proportion of olivine plus orthopyroxene is inversely correlated to that of plagioclase, clinopyroxene and hornblende. This gives rise to olivine gabbroic rocks in the middle of the dike and gabbro-norites close to the margins:

- Olivine gabbros are composed of olivine (3 to 20 vol.%), surrounded by orthopyroxene, hornblende and clinopyroxene. Plagioclase is present as small anhedral crystals accounting for less than 30 vol.%.
- Gabbro-norites and norites consist of coarse-grained euhedral to subhedral plagioclase laths (20-50 vol.%), together with orthopyroxene, clinopyroxene and hornblende in variable amount (1 to 10 vol.%). Minor biotite (5 vol.%) with accessory minerals such as apatite, zircon and opaque minerals are found in both lithologies.

- Leucogabbros, in the form of patches up to several decimeters wide (referred to as feldspar-rich patches or anorthosite enclaves by Boliden geologists), contain coarse-grained euhedral to subhedral plagioclase phenocrysts and variable amounts (5-20 vol.%) of medium grained mafic phases and quartz. They are more abundant toward the margins of the dike.

Moderate to strong alteration affects the primary minerals: pyroxene and hornblende are altered to chlorite and secondary biotite, plagioclase to epidote, calcite and sericite, and olivine to serpentine, magnetite and talc.

According to Filoche (2009) and Boliden geologists, the mineralization includes disseminated sulfide bleb or small stringers, "net-textured" ore, and massive sulfide lenses. Massive sulfide lenses are surrounded by dense net-textured mineralization. The sulfide minerals are pyrite, pyrrhotite, pentlandite and chalcopyrite. The sulfide mineralization is disseminated throughout the bulk of the dike or concentrated, as massive sulfide lenses, at the SW and NE terminations in the middle of the dike or on both northern and southern sides (refer to terminology of Figure 2.6).

The mineralization investigated by Boliden is between 5 and 20 Mt in size and the Ni content of the mineralization varies between 0.01 to 0.37% (internal Boliden report: Paulick et al., 2012).

The Älgliden intrusion has been dated at 1876±1 Ma using the U-Pb method on baddeleyite (Bejgarn et al., 2013). It is intruded by some rocks of the 1878-1871 Ma GII phase of the Jörn intrusive complex (Wilson et al., 1987; González-Roldán, 2010). Importantly, it crosscuts the Tallberg Cu-Au porphyry deposit which contains disseminated and stockwork style mineralization, within propylitic and sericitic alteration halos related to QFP dacitic dikes dated between 1876±5 and 1878±5 Ma (Figure 2.7). The Cu-Au porphyry mineralization consists of disseminated and quartz vein stockwork including pyrite, chalcopyrite and molybdenite with minor electrum (Weihed, 1992*b*). The QFP dikes have steeply dipping SW-NE striking orientation similar to the Älgliden dike. These regional SW-NE structures, interpreted as reactivated transfer faults, belong to structures that Bauer et al. (2011) interpret as controlling the emplacement of the felsic and mafic intrusions of the JIC and Gallejaur complex. In support of this idea, Bejgarn et al. (2013) have reported mafic enclaves in the QFP dike of Älgträsk suggesting mafic and felsic magmas follow the same structure. Using fluid inclusions Bejgarn (2012) estimated the depth of formation of the Tallberg deposit to 3-4 km in hydrostatic conditions or <1.5 km in lithostatic conditions. If no vertical motion occurred between the emplacement of the Tallberg intrusions and the Älgliden magma, the Älgliden dike would emplaced at similar depths.

Several observations suggest that the Älgliden dike could have assimilated its Cu-Au-mineralized wall rocks: (i) the Älgliden intrusion contains xenoliths of mineralized country rocks; (ii) the Älgliden ore has high Au content and has the highest Cu:Ni ratio among all deposits in the region; (iii) apart from the Älgliden dike, the mafic intrusions that are spatially associated with the mineralized QFP dikes are all barren (the barren mafic intrusions could predate the mineralized QFP dikes or assimilation was not an important ore-forming process).

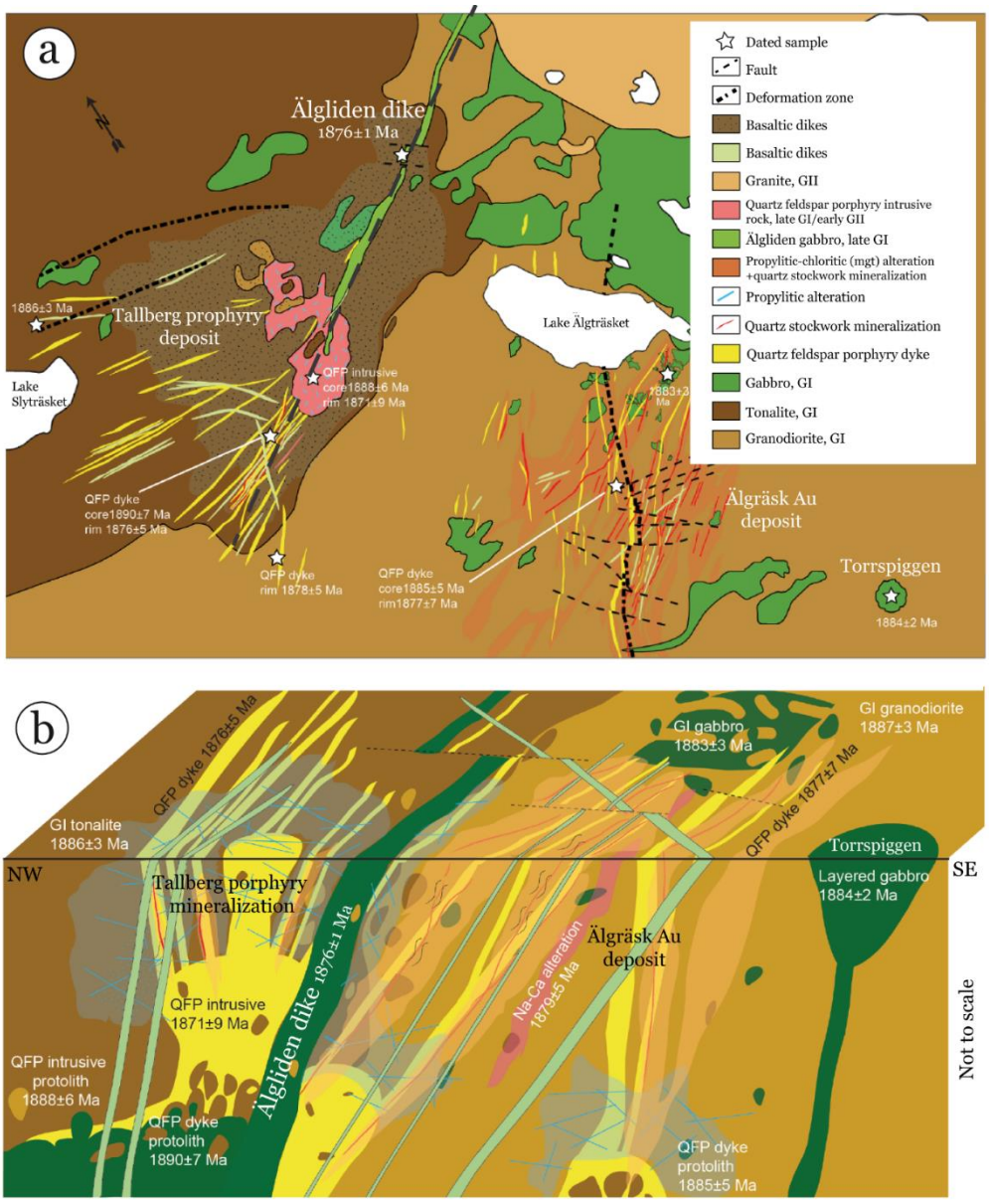

Figure 2.7 Geological map (a) and cross section (b) over the Älgliden-Tallberg-Älgträsk area. Note that the Älgliden dike is aligned along the same SW-NE oriented structure (highlighted by the grey dashed-line) as most of QGP dikes and it intrudes the Tallberg porphyry mineralization. Legend is the same for a) and b). After Bejgarn et al. (2012).

3. Methods

3.1. Sampling and available data

Sampling and core logging focused on two drill cores. ALA264 is located near the thin NE termination and ALA 246 is at the center of the dike. They have contrasting mineralization and petrological features. Because ALA264 is highly altered, most bulk rock analyzes and petrographic observations of silicates were performed on samples of ALA246, whereas ALA64 was used for ore observations. Forty core samples, each 5-10 cm-long, were collected for major and trace element and S isotopic analyses, and variable sized samples (N=75) were used for petrological observation and measurements (Table 3.1). With few exceptions, the samples for bulk rock analyses are accompanied by a thin section.

The lithological logging by Boliden geologists was available for all the drill cores and for 17 drill cores, photos were also provided. The Boliden dataset includes rock descriptions, chemical bulk rocks analyses and assays of elements of economic interest. Whole rock analyses for major and trace elements include two methods of sampling and analysis: 1) 0.2 to 0.7 m-long samples were analyzed at ACME analytical laboratories in Vancouver (http://acmelab.com/) using LiBO2 fusion/dilute nitric digestion and ICP-ES for major elements and ICP-MS for trace elements. 2) 3m-long samples of core ALA246 were analyzed at ALS (https://www.alsglobal.com/) using the same methods as at ACME analytical laboratories.

The length of core samples analyzed by Boliden is commonly larger than the lithological heterogeneities, and problematic samples were rejected based on examination of the texture and mineralogy in cores or thin sections (when available). The dataset was also filtered to avoid analyses of mixtures of norite with xenoliths or leucogabbro and late dikes.

Assays were performed at Labtium laboratory (http://www.labtium.fi/en/) on aliquots for ground and homogenized 3 m-long drill cores from the entire length of the dike. The following elements – Ag, Cd, Co, Cr, Cu, Fe, Mn, Mo, Ni, Sb, Zn, Pb, As and S – were analyzed using the 510P Labtium method (aqua regia leach with ICP-OES). A classical lead-fusion fire assay method with a 25 g or 50 g subsample was used for Au, Pd, and Pt, followed by ICP-OES measurement (705P Labtium method, http://www.labtium.fi/en/). For high grade (>2000 ppb) Au-bearing samples, analyses were performed by gravimetric determination and ICP-OES.

Copper, Ni and Co were analyzed in the sulfide fraction only on 7 drill cores, among them ALA246 and-264, using the 240P Labtium method which employs ammonium citrate leaching and H_2O_2 treatment.

Table 3.1 List of studied samples

Sample #[a]	Unit	Rock type[b]	Bulk major element	Bulk trace element	S isotope	Electron microprobe	Thin section	Mapping
11.73.0	late dike	undefined					X	
246.196.3	wallrock	QFP[c]	X	X	X		X	
246.197.3	wallrock	QFP[c]					X	
246.198.3	Älgliden dike	olivine norite					X	
246.199.0	Älgliden dike	leucogabbro	X	X			X	
246.204.6	Älgliden dike	olivine norite^{2N}	X	X			X	
246.209.0	Älgliden dike	leucogabbro				X	X	
246.209.8	Älgliden dike	olivine norite^{1N}					X	
246.212.3	Älgliden dike	leucogabbro				X	X	
246.212.5	Älgliden dike	olivine norite^{1N}	X	X			X	
246.212.6	Älgliden dike	leucogabbro	X	X		X	X	
246.219.0	Älgliden dike	olivine norite^{1N}	X	X		X	X	
246.223.3	Älgliden dike	leucogabbro	X	X				
246.224.6	Älgliden dike	olivine norite^{1N}	X	X				
246.230.2	Älgliden dike	leucogabbro	X	X		X	X	
246.232.5	Älgliden dike	leucogabbro				X	X	
246.233.2	Älgliden dike	leucogabbro					X	X
246.233.4	Älgliden dike	olivine norite^{2N}					X	
246.233.5	Älgliden dike	olivine norite^{2N}				X	X	
246.239.1	Älgliden dike	olivine norite^{2N}	X	X			X	
246.239.1	Älgliden dike	olivine norite^{2N}				X	X	
246.239.7	Älgliden dike	leucogabbro					X	
246.240.8	Älgliden dike	leucogabbro	X	X	X	X	X	
246.242.5	Älgliden dike	leucogabbro	X	X			X	
246.249.6	late dike	andesite	X	X		X	X	
246.252.5	Älgliden dike	olivine norite^{S}	X	X			X	
246.280.8	Älgliden dike	olivine norite^{1S}	X	X	X	X	X	
246.290.7	Älgliden dike	olivine norite^{1S}	X	X		X	X	X
246.293.1	Älgliden dike	olivine norite^{1S}	X	X	X	X	X	
246.300.9	Älgliden dike	olivine norite^{1S}	X	X		X	X	

(a) sample are named as follows: drillcore number.downhole depth (m)

(b) 1, 2 refer to olivine norites of type-1 and type-2 and N, S to olivine norites from northern and southern sides.

(c) Quartz feldspar porphyry

Table 3.1 (cont.)

Sample #[a]	Unit	Rock type[b]	Bulk major element	Bulk trace element	S isotope	Electron microprobe	Thin section	Mapping
246.302.0	Älgliden dike	olivine norite[1S]					X	
246.308.0	Älgliden dike	olivine norite[1S]	X	X		X	X	
246.319.6	Älgliden dike	olivine norite[1S]	X	X			X	
246.334.0	Älgliden dike	olivine norite[1S]	X	X			X	
246.340.8	Älgliden dike	olivine norite[S]	X	X			X	
246.353.6	Älgliden dike	olivine norite[S]			X			
246.362.8	wallrock	tonalite	X	X			X	
248.213.2	Älgliden dike	leucogabbro	X	X		X	X	
248.230.4	Älgliden dike	leucogabbro	X	X				
248.233.9	Älgliden dike	leucogabbro				X	X	
248.259.1	Älgliden dike	leucogabbro	X	X				
248.262.0	Älgliden dike	leucogabbro				X	X	
248.262.9	Älgliden dike	leucogabbro				X	X	
248.265.0	Älgliden dike	leucogabbro	X	X				
248.265.1	Älgliden dike	leucogabbro				X	X	
248.265.2	Älgliden dike	leucogabbro					X	
248.269.7	Älgliden dike	leucogabbro					X	
264.156.5	wallrock	tonalite	X	X		X	X	
264.161.8	wallrock	quartz vein			X			
264.162.4	wallrock	tonalite	X	X		X	X	
264.169.2	Älgliden dike	olivine norite	X	X			X	
264.170.5	wallrock	wallrock xenolith				X	X	
264.172.0	Älgliden dike	olivine norite					X	
264.172.8	Älgliden dike	olivine norite	X	X				
264.176.5	Älgliden dike	olivine norite					X	
264.180.5	Älgliden dike	olivine norite	X	X				
264.181.6	Älgliden dike	olivine norite					X	
264.181.7	Älgliden dike	massive sulfides				X	X	
264.183.2	wallrock	wallrock xenolith					X	
264.183.5	Älgliden dike	massive sulfides				X	X	
264.185.6	Älgliden dike	olivine norite	X	X				

(a) sample are named as follows: drillcore number.downhole depth (m)

(b) 1, 2 refer to olivine norites of type-1 and type-2 and N, S to olivine norites from northern and southern sides.

Table 3.1 (cont.)

Sample #[a]	Unit	Rock type[b]	Bulk major element	Bulk trace element	S isotope	Electron microprobe	Thin section	Mapping
264.187.4	wallrock	wallrock xenolith					X	
264.187.6	wallrock	wallrock xenolith					X	
264.189.8	wallrock	wallrock xenolith					X	
264.190.0	wallrock	wallrock xenolith			X			
264.190.1	wallrock	wallrock xenolith				X	X	X
264.190.2	Älgliden dike	olivine norite	X	X				
264.191.2	Älgliden dike	olivine norite					X	
264.191.5	Älgliden dike	olivine norite					X	
264.194.7	Älgliden dike	massive sulfides			X		X	
264.195.4	wallrock	wallrock xenolith					X	
264.195.9	late dike contact	-					X	
264.196.8	latye dike	undefined				X	X	
264.200.4	Älgliden dike	olivine norite	X	X				
264.203.5	Älgliden dike	olivine norite					X	
264.203.8	wallrock	wallrock xenolith					X	
264.205.8	Älgliden dike	olivine norite	X	X			X	
264.211.3	Älgliden dike	olivine norite			X			
264.212.5	Älgliden dike	olivine norite	X	X				
264.212.7	wallrock	wallrock xenolith					X	
264.217.3	wallrock	wallrock xenolith					X	
264.217.5	Älgliden dike	olivine norite	X	X				
264.223.8	wallrock	granodiorite	X	X			X	
264.232.6	Älgliden dike	leucogabbro			X			

(a) sample are named as follows: drillcore number.downhole depth (m)

(b) 1, 2 refer to olivine norites of type-1 and type-2 and N, S to olivine norites from northern and southern sides.

3.2. Petrological analyses and measurements

3.2.1. Optical microscopy

Seventy-five thin sections were used for petrological observations and/or measurements. Petrological observations (i.e. mineralogy, texture, and modal abundances estimation) were performed by transmitted light for silicates and reflected light for oxides and sulfides (ISTerre). A micro-imaging program (i.e. Olympus Stream Essentials) was used to measure 2D interfacial olivine-sulfide dihedral angles, crystal lengths and mineral phase areas. Slightly more than 100 2D interfacial olivine-sulfide dihedral angles were measured on 6 samples, 1664 apparent lengths of plagioclase crystal were measured in 10 samples, and areas of sulfide phases were estimated on 5 samples for modal sulfide abundance using a polygon tool.

3.2.2. Electron probe microanalysis

A JEOL JXA-8230 electron microprobe (ISTerre) was used for *in-situ* analysis, back-scattered electron imaging and chemical mapping.

Quantitative microanalyses were performed on feldspar (N=912), pyroxene (N=120), olivine (N=83), biotite (N=86) and amphibole (N=33) grains, on samples of olivine norites (N=11), leucogabbros (N=12), wall rocks (N=2), late dike (N=2) and xenoliths (N=3). *In-situ* analyses include isolated points or profiles. Routine running conditions used for silicates; i.e. 15 kV accelerating voltage, a beam current of 12 nA and ZAF correction. For high-precision analyses of olivine, another protocol was used with accelerating voltage of 15 kV and a beam current of 300 nA (Batanova et al., 2015). The standards were Cr-augite (Ti, Fe, Mn, Mg, Ca, Cr) and/or orthoclase (Si, Al, Na, K) and/or olivine (Si, Ti, Al, Fe, Mn, Mg, Ca, Cr, Ni) and/or hornblende (Si, Ti, Fe, Mg, Ca) (Appendix 1). Standards were analyzed as unknowns every 50 analyses of samples in order to evaluate the instrumental drift and the accuracy of analyses. The accuracy and precision are evaluated as follows:

$$\text{Relative Accuracy (\%)} = 100 * |C_{mes\ avg} - C_{ref}| / C_{ref}$$

$$\text{Relative standard deviation (\%)} = 100 * 2\sigma / C_{mes\ avg}$$

where $C_{mes\ avg}$ is the average value of the standard measured as unknown (%), C_{ref} is the reference value of the considered standard (%), and σ the standard deviation.

Measured concentration were also corrected by standard bracketing when accuracy or precision were bad. Detection limits and relative accuracy and precision are given in Appendix 1. Structural formulae were calculated for each analysis and if the difference between the calculated and theoretical cationic sum is above 5% and/or the sum of the measured elements in different from 100±2 wt.%, the analysis was rejected.

Two semi-quantitative chemical maps were acquired to image the relationship between silicate and sulfide phases. The first map covers an area of 1030 x 500 µm where X-ray intensities were measured by wave dispersive spectrometers (WDS) for Na, S, K, Fe and Ni and by an energy dispersive spectrometer (EDS) for Mg, Al, Si, Ca, Ti and P. EDS is a silicon-drift detector used for quick qualitative analysis, whereas WDSs used analyzing crystals with various inter-reticular distances allowing high spectral resolution and low detections limits for a wide range of X-ray wavelengths. Mapping conditions were 15 kV accelerating voltage, 100nA beam current, beam diameter smaller than 1 µm, 200ms dwell time and 2 µm step size (i.e. the pixel size). The second map was over an area of 550 x 550 µm using the same analytical conditions except that Si, S Na, Fe and Ni were measured by WDS and Mg, Al, P, K, Ca, Ti, Cr and Cu by EDS.

3.2.3.Micro-X-ray fluorescence mapping

Semi-quantitative micro-X-ray fluorescence mapping was performed using an EDAX Eagle III instrument. Three samples were mapped: an olivine norite, a leucogabbro and at the contact between norite and a wallrock xenolith. Measured elements were Si, Al, Fe, Mg, Mn, Ca, K, P, Ti, Cr, Zr, Sr, Cu, Ni, Zn and S. The analytical conditions are listed in Table 3.1. List of studied samples

Table 3.2Semi-quantitative estimations of element abundances were acquired using EDAX Vision software. XMapTool software (Lanari et al., 2014) was used to convert the chemical maps into mineral phase distribution maps using specific regions of interest.

Table 3.2 Analytical conditions for Micro-X-Ray fluorescence mapping

Sample	Map size (mm)	Step size (µm)	Beam diameter (µm)	Beam current (µA)	Accelerating voltage (kV)	Dwell time (ms)
264.190.1	35.82 x 28	70	100	300	30	500
246.233.2	13.45 x 9.87	27	30	300	30	500
256.290.7	13.78 x 10.10	27	30	300	30	500

3.3. Bulk-rock geochemical analyses

To avoid contamination of the core samples by the saw or the drill bit, the outer surfaces of core samples were removed. Then the samples were cleaned into an ultrasonic bath with Milli-Q® water, crushed to 2 mm-sized fragments and then finely ground in an agate ball mill. A complete description of the analytical procedure is given by Chauvel et al. (2011).

3.3.1. Major element concentrations

Rock powders (about 50 mg) were weighed and dissolved in closed Savillex™ beakers using a mixture of 0.3 ml 24N HF and 0.85 ml 14N HNO_3, at 90°C for 4 days. Then, solutions are diluted with 20 ml of H_3BO_3 (20g/l) (to neutralize excess HF) and 250 ml of Milli-Q® water and stored in a fridge.

Solutions, together with standards, blanks and duplicates, were analyzed using a Varian 720-ES inductively coupled plasma atomic emission spectrometer (ICP-AES) at ISTerre. Results were provided in count per second (cps) and calibrated using the BCR-2 international standard. The calibration was made using diluted and non-diluted solution of BCR-2, and with or without a dope solution (1000 ppm of X element) for elements in low concentration in BCR-2 with regard to analyzed samples. Concentrations are expressed as wt.% of oxide, except for S which is expressed as wt.% element.

Quality of the analyses were checked by measuring as unknowns several international rock standards (e.g. BR 24, BE-N, BHVO-2, AGV-1, BCR-2, G-2), blanks, duplicates (i.e. the same sample, from weighing to measurement), "bis" (i.e. the sample solution measured twice) and one in-house standard for S (Appendix 2 and Appendix 3). The accuracy and precision of the in-house standard was checked comparing analyses of the same sample at ISTerre and at the Service d'Analyse des Roches at des Minéraux (SARM, Nancy - known to analyses S) and being measured several times as unknown, respectively (Appendix). For other elements, the precision can be evaluated in Appendix 4, with a reproducibility within <1% relative error, when the concentration is twice higher than the detection limit. The accuracy on the analyzes is about <15% for P_2O_5 and <5% relative error for other major oxides, but it can increases if the measured concentration is 3 times lower than the detection limit (Appendix 5).

The content of volatile components (H_2O, CO_2 and SO_2) was determined by measuring the mass loss of 1 g of powder after heating at 1000°C for 1 h (loss of ignition - LOI). To calculate the bulk composition in silicates only, the contribution of S and Fe in sulfides was subtracted Appendix 6). Concentrations were then normalized without volatiles and sulfides.

3.3.2. Trace element concentrations

Because refractory minerals can host almost the entire inventory of some trace elements (e.g. Zr or Hf in zircon, Cr in chromite), the rock powders (i.e. ≈100 mg) were dissolved at high temperature (150°C) in a mixture of HF and HNO_3 in steel PAAR® bombs for two weeks. Fluorides were neutralized by evaporation/dissolution cycles using 14N HNO_3. Samples were diluted in 40 ml 7N HNO_3. An aliquot of this "mother" solution corresponding to about 8 mg of the initial powder was mixed with a spike (^{9}Be, ^{72}Ge, ^{115}In, ^{169}Tm, ^{209}Bi). The solution was diluted by a factor 5000 using a mixture of 2% v/v HNO_3 with a trace of HF.
Trace elements in the diluted "daughter" solutions were measured on a Thermo X series 2 inductively coupled plasma mass spectrometer (ICP-MS), together with blanks, duplicates, replicates (i.e. daughter solutions from the same mother solution), "bis", and international standards with compositions similar to those of the samples (e.g. BE-N, BHVO-2, AGV-1, G-2).
Data were corrected for isobaric interferences and instrumental drift, and calibrated using the standard BR24.
Results were validated from their accuracy and precision. The precision is estimated by the relative error between duplicate, replicate and "bis" (Appendix 7). The relative error is generally <5% for most of elements. With regard to accuracy, the relative error is estimated from the comparison of measured values on standards with published data (Jochum et al., 2016). It is <5% for most elements and the detection limit values are 3 time those of the blanks (Appendix 8). Concentrations of some elements of the G-2 standard are systematically different when compared to published data, suggesting the powder of the rock is heterogeneous.

3.3.3.S isotope composition

Bulk rock sulfur isotope analyses were performed at the Institut de Physique du Globe de Paris (IPGP) in collaboration with Pierre Cartigny and Nelly Assayag. Ten samples were selected as representative of the different mineralization styles. Three samples are from the country rocks. Among them, one sample (264.161.8) comes from an interval in which high gold concentration (9 g/t) has been measured by Boliden; this sample consists in a sulfide-rich quartz-vein containing pyrite and chalcopyrite. Four samples consist of disseminated sulfide hosted in norites located close to or far from the dike contact, two leucogabbros containing disseminated and network sulfides, and one xenolith with network sulfides.

Sulfur is extracted from bulk rock powder as described by Canfield et al. (1986) and Labidi et al. (2012). The two-step extraction procedure allows for (i) the extraction of monosulfides (i.e. pyrrhotite and chalcopyrite) as acid volatile sulfide (AVS), and (ii) the extraction of disulfides (i.e. pyrite). According to their S content, a few milligrams of rock powder (i.e. 8 μmol S) were transferred into a boiling flask containing 20 ml of 6N HCl. Hydrogen sulfide (H_2S) produced by the reaction between monosulfides and hydrochloric acid solution was separated from acid vapor in a water-cooled condenser and trapped as silver sulfide (Ag_2S) in a solution with excess silver nitrate (i.e. 3 ml of $AgNO_3$ plus 7 ml Milli-Q water). An acidic chromium solution composed of 104 g of chromic chloride ($CrCl_3$), 60 g of solid zinc and 200 ml of 0.6N HCl was introduced in the boiling flask to react with the disulfide, which was then trapped as silver sulfide in a new trapping solution. The two trapping solutions (containing mono- and disulfides) were centrifuged and the silver sulfide precipitates were washed and dried. The precipitates were weighted, wrapped in Al-foil boats, and placed into Ni-reaction bombs with excess of pure fluorine (F_2) for fluorination at 250°C overnight. The sulfur hexafluoride (SF_6) was purified by cryogenic separation at -155°C and gas chromatography.

Sulfur isotope abundances were analyzed by a dual inlet and double collector mass spectrometer (Mat 253 Thermo Finnigan) monitoring m/z=127, 128, 129 and 131 ($^{32}SF_5^+$, $^{33}SF_5^+$, $^{34}SF_5^+$ and $^{36}SF_5^+$) relative to a standard of known isotopic composition. Results were then expressed relative to the international Canon Diablo Troilite (CDT) standard.

4. Lithology and geochemistry of the Älgliden dike and associated rocks, and Älgliden rock petrogenesis

4.1. Rock types: classification, mineralogy, texture, and alteration

4.1.1. Logging

Drillcores ALA246 and -264 were logged in detail and 15 other drillcores were inspected. Olivine norite, the most common lithology of the Älgliden dike, forms more than 95% of the observed drill cores. Leucogabbro is a minor rock type, locally observed in some drillcores, especially ALA246. Figure 4.1a-b are the logs of ALA246 and -264, respectively. Because of significant alteration in ALA264, the petrographic study of olivine norite and leucogabbro was restricted to ALA246, one of the best preserved of all the cores. The modal mineral proportions and the mineral compositions in the olivine norite and the leucogabbro, together with the distribution of leucogabbro, are illustrated in Figure 4.1a. Wall rocks, xenoliths and leucogabbros were studied in cores ALA246, -248 and -264. Figure 4.1b illustrates the abundance of xenoliths in ALA264. Their abundance near the dike margins create zones over a few meters made of a mixture of olivine norites and rocks of the wall rocks. We qualified these margins as diffuse. In others places, as illustrated in ALA246 (Figure 4.1a), contacts are sharp, and virtually no xenolith is observed in the olivine norite.

4.1.2. Olivine norite

Macroscopically the olivine norites are dark colored and fine- to medium-grained. They are composed of olivine (10-40%), orthopyroxene (20-50%), plagioclase (15-25 %), hornblende (10-15%) and biotite (5%), with minor clinopyroxene and Ti-Cr-Fe oxides (i.e. magnetite, ilmenite and chromite; Table 4.1). These rocks contain more than 70% of mafic minerals and correspond to olivine norites in the IUGS classification (Streckeisen, 1976).

The proportions of olivine and orthopyroxene are reversely correlated at the sample scale and across the dike (Figure 4.1a). However, the bulk proportion of olivine and orthopyroxene remains relatively constant. There are two varieties of olivine norite, defined on the basis of the proportions and textures of olivine and orthopyroxene (Figure 4.2). Type-1 norite is olivine-rich (25-45% olivine and 20-35% orthopyroxene; Figure 4.2c-d) while Type-2 norite is olivine-poor (10-20% olivine and 40-50% orthopyroxene; Figure 4.2a-b). Type-2 is locally observed where leucogabbro is abundant whereas Type-1 is observed in the entire dyke (Figure 4.1a).

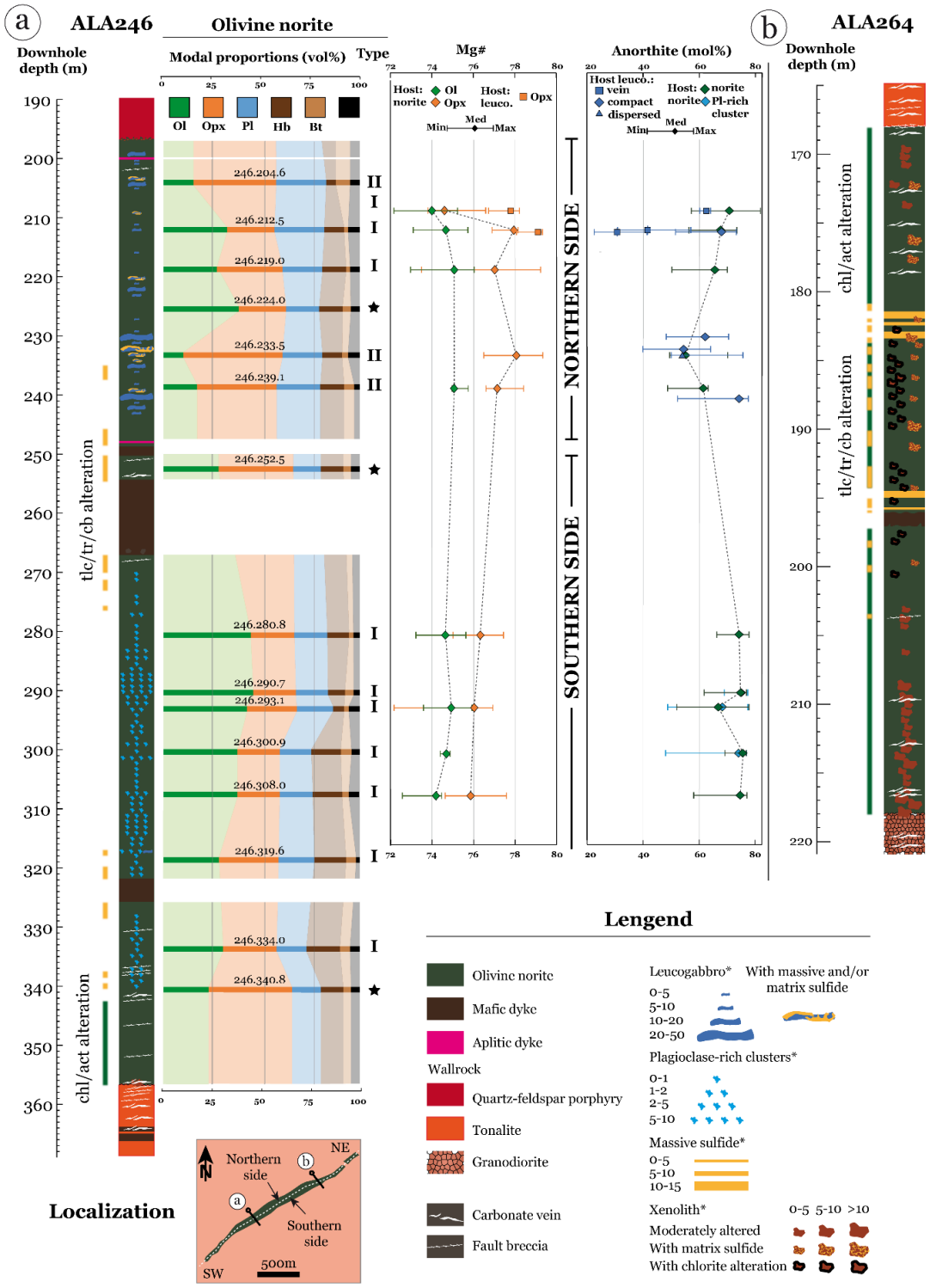

Figure 4.1 Logging of the studied drillcores (a) ALA246: mineral proportions of olivine norite samples as well as mineral chemistry are discontinuously reported. Links between samples are interpretative and merely indicative. Stars indicate sample whose mineral proportions are inferred from CIPW norm and converted to vol% for olivine, orthopyroxene and plagioclase and from the average value of other samples for hornblende, biotite and oxides. (b) ALA264: note the strong alteration and the abundance of xenoliths. Legend: (*) values from 0 to 50 are in vol.% of 1 m-long core or in cm/100 cm. The box on the bottom locates the drillcores and shows the terminology used in the text: the NE and SW terminations, and the northern and southern sides shown separated by the white dashed line. Mineral abbreviations: Ol: olivine; Opx: orthopyroxene; Pl: plagioclase; Hb: hornblende; Bt: biotite; Fe-ox: iron oxide.

Table 4.1 Petrographic data of the olivine norites

Sample[a]	246. 204.6	246. 209.0	246. 212.5 - 212.3	246. 219.0	246. 224.6[b]	246. 233.5	246. 239.1	246. 252.5[b]	246. 280.8	246. 290.7	246. 293.1	246. 300.9	246. 308.0	246. 319.6	246. 334.0	246. 340.8[b]
Type	type-2	type-1	type-1	type-1	n.t.s.	type-2	type-2	n.as.	type-1	type-1	type-1	type-1	type-1	type-1	type-2	n.as.
Olivine	15	n.as.	32	27	35	10	17	27	40	42	37	35	35	28	30	22
Fo (N)[c]	n.a.	$Fo_{74.2}$ (5)	$Fo_{74.9}$ (4)	$Fo_{75.2}$	n.t.s.	n.a.	$Fo_{75.4}$ (6)	n.as.	$Fo_{74.8}$	n.a.	$Fo_{75.1}$ (7)	$Fo_{75.0}$ (8)	$Fo_{74.3}$	n.a.	n.a.	n.as.
Opx	42	n.as.	24	33	22	50	40	36	20	20	22	20	20	30	27	41
Mg# (N)[c]	n.a.	74.8 (7)	77.7 (7)	76.7 (7)	n.t.s.	77.9 (12)	77.5 (7)	n.as.	76.2 (11)	n.a.	75.8 (12)	n.a.	75.7 (14)	n.a.	n.a.	n.as.
Plagioclase	25	n.as.	25	20	16	20	22	13	15	15	16	15	16	18	15	14
An (N)[c]	n.a.	An_{71} (4)	An_{68} (4)	An_{63} (11)	n.t.s.	An_{56} (12)	An_{62} (4)	n.as.	An_{74} (12)	An_{74}	An_{67} (13)	An_{73}	An_{75} (11)	n.a.	n.a.	n.as.
Hornblende	5	n.as.	10	12	11	10	12	11	10	8	5	14	14	16	17	11
Biotite	7	n.as.	2	2	4	3	5	4	2	4	2	5	3	5	5	4
Iron oxides	5	n.as.	6	5	4	6	3	4	3	3	5	4	5	2	5	4
Sulfides	1	n.as.	1	1	2	1	1	3	10	8	13	7	7	1	1	5

n.t.s.: no thin section

n.as.: non assesssable

n.a.: not analyzed

(a) samples are named as follows: drillhole.depth (in m).

(b) Mineral modal proportions of samples 246.224.6, -252.5 and -340.8 are approximated: hydrated phase proportions are the average proportion of all other samples, and anhydre phases are the CIPW normative proportions

(c) Fo and An contents in mol.%. N is the number of analyzed grains; Mg# = 100*Mg /(Mg +Fe)

Olivine crystals have different shapes according to their size and textural relationships with other phases. They range in size from 100 μm to 3 mm with most about 1.5 mm. In Type-1 samples, the olivine grains are usually idiomorphic, contiguous and they are partially to fully enclosed in oikocrystic orthopyroxene, hornblende, biotite or sulfide. Olivine grains that are adjacent to orthopyroxene are sub- to anhedral. (Figure 4.2). Rare olivine grain includes small plagioclase grain. Their abundance and shape suggest they are cumulus (this is confirmed by whole rock and mineral chemistry, see Sections 4.2 and 4.3). Conversely, in Type-2 samples, orthopyroxene forms mantles around each olivine grains and the olivine is anhedral and has irregular shapes. In both types, olivine grains are fractured and partially to completely serpentinized. Parts of some freshest grains are altered into chlorite, especially close to cracks. In Type-1 samples, orthopyroxene forms large (1-3 mm) anhedral oikocrysts that partially or completely encloses smaller olivine and/or plagioclase crystals, as well as thin (< 0.2 mm) overgrowths rimming olivine grains. In Type-2 samples, orthopyroxene is sub- to euhedral, and mostly mantles olivine either as small separate grains (0.5 mm; Figure 4.2c-d) or as larger single grain (1.5 mm).

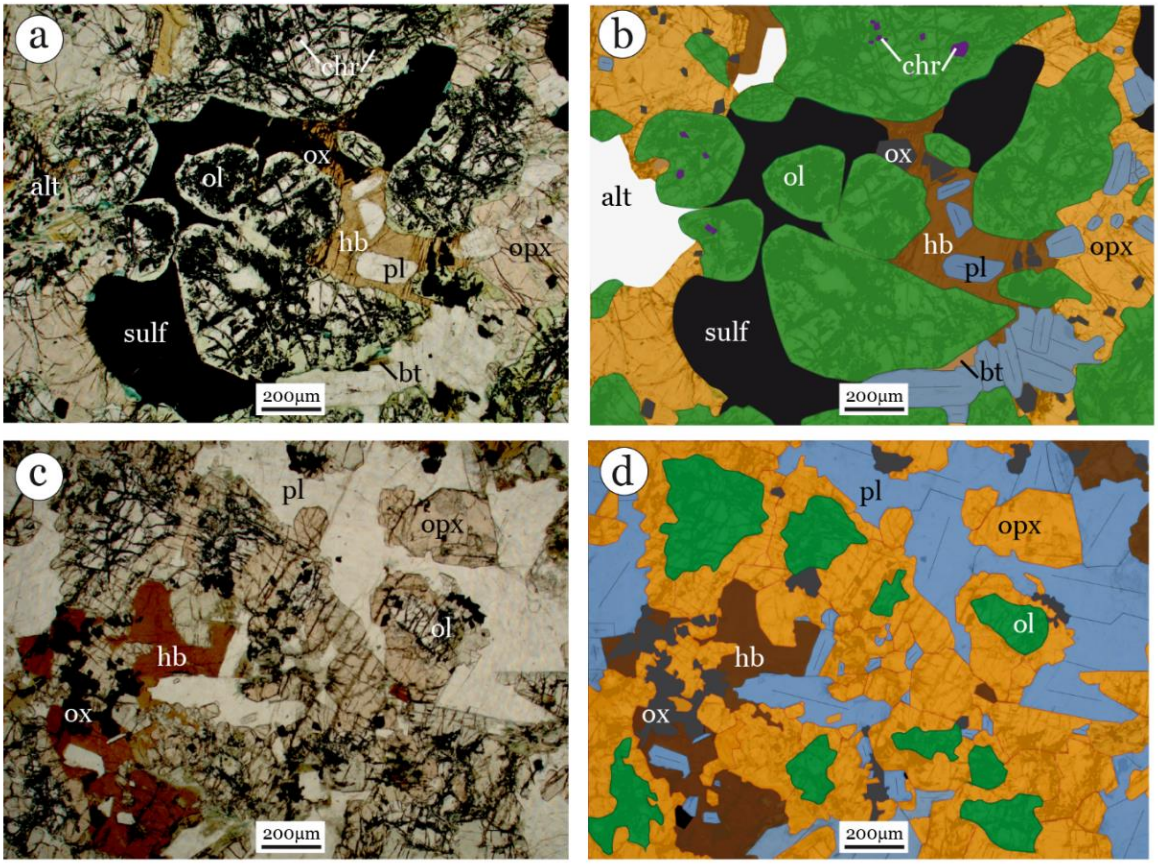

Figure 4.2 Photomicrographs and sketches of the two types of olivine norite (a-b) Type-1: olivine-rich norite, sample 246.290.7, and (c-d) Type-2: olivine-poor norite, sample 246.239.1. Mineral abbreviations: Ol: olivine, Opx: orthopyroxene; Pl: plagioclase; Hb: hornblende; Bt: biotite; ox: iron oxide; Alt: alteration phases.

Figure 4.3 illustrates the peritectic reaction between orthopyroxene and olivine. Orthopyroxene occurs as overgrowths around olivine and as oikocryst that includes one or several anhedral olivine grains. The extinction of the olivine crystals in Figure 4.3 indicates that they were initially a single grain that has been partially replaced by orthopyroxene and which occurs now as separate grains. Similar textures resulting from peritectic reaction are described by Barnes et al. (2016). In type-2 olivine norites, orthopyroxene generally imposes its shape to the plagioclase. The rare clinopyroxene grains in olivine norites occupy textural positions identical to orthopyroxene (i.e. oikocrystic). Orthopyroxene is partially altered to talc.

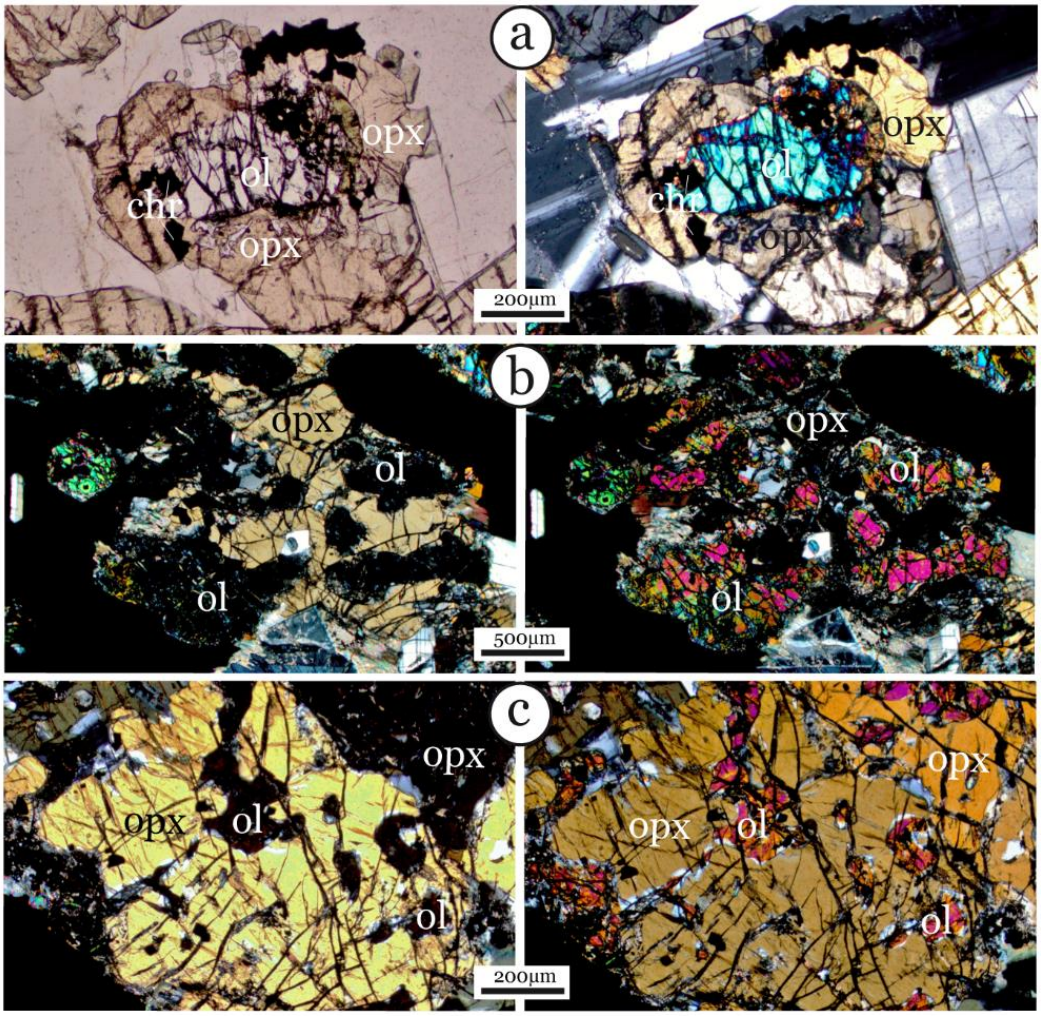

Figure 4.3 Photomicrographs illustrating the peritectic texture between olivine and orthopyroxene. (a) Two orthopyroxene grains form overgrowths rimming the olivine grain. 246.239.1 type-2 olivine norite sample. (b) An orthopyroxene crystal mimics an olivine crystal and an oikocrystic texture. The different grains of olivine actually belong to a single initial crystal (same orientation of extinction), indicating that the orthopyroxene crystal is not an oikocrystic orthopyroxene enclosing different olivine crystals but an anhedral grain having partially replaced a single olivine grain. 246.212.3 type-1 olivine norite sample. (c) As previously, but at a more advanced stage of peritectic reaction: an initial olivine grain (same orientation of extinction) consists now to several anhedral grains due to partial but efficient peritectic reaction. 246.212.3 type-1 olivine norite sample.

The proportion of plagioclase varies only slightly within the dike, except locally where plagioclase-rich clusters occur (Figure 4.1a). Apart from the clusters, in Type-1 olivine norite, plagioclase laths are generally sub- to euhedral, fine grained (0.5-1 mm) and juxtaposed together and/or enclosed within orthopyroxene or hornblende oikocrysts. Some are included in olivine crystals. In Type-2 olivine norite, plagioclase is mainly an- to subhedral. Rare euhedral grains occur adjacent to or within hornblende oikocrysts. In the lower part of two drill cores (i.e. ALA-246 and -247), large prismatic plagioclase grain or large plagioclase-rich clusters (0.5-3 cm in size) of varying grain size are dispersed within the olivine norite. Their occurrences are restricted to the lower part of two drillcores 150 m apart suggesting they may be continuously dispersed within the olivine norite over this distance. In the clusters, the plagioclase is in association with minor anhedral small olivine, oikocrystic hornblende, iron oxides and sulfides. The plagioclase grains are prismatic and coarse (up to 4 mm) or granular and very fine grained (10-100 μm) showing a mosaic-like pattern. Both types can occur in the same cluster. Generally, plagioclase is altered to sericite, but locally, plagioclase is altered to quartz-albite intergrowth (see description in 4.1.3).

Brown hornblende and biotite grains are anhedral and occupy interstitial spaces between other mineral phases. When large enough (up to 3 mm), they may be oikocrystic and enclose olivine and/or plagioclase grains (Figure 4.2). Hornblende may notably be formed by epitaxial growth as it commonly has the same crystallographic orientation and oikocrystic position as the adjacent orthopyroxene or more rarely clinopyroxene.

Iron-titanium oxides vary in shape from perfectly spherical to euhedral and they are mainly enclosed in orthopyroxene, biotite and hornblende, whereas chromite is mainly contained in olivine. The textural relationships between silicate phases of the two types of norite are interpreted to indicate two different crystallization sequences, as shown in Figure 4.4.

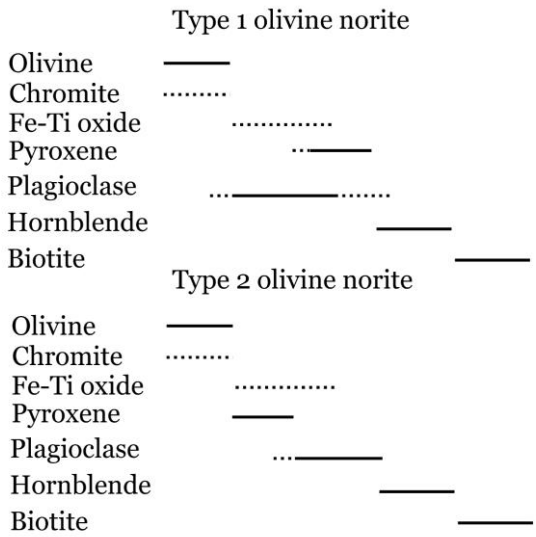

Figure 4.4 Diagram showing the crystallization sequences of the mineral of both types of olivine norite.

Filoche (personal communication) reported 15 samples that she reported as gabbro-norite, a rock type that is not recognized in this study. Generally, Filoche (2009) describes them as containing coarse-grained euhedral to subhedral cumulus plagioclase laths surrounded by minor amount of orthopyroxene, clinopyroxene and hornblende. All of these samples occur in the SW and NE terminations of the dike or close to late dikes where the alteration is pronounced. Filoche (personal communication) described a greyish rock in which plagioclase forms white dots whereas the olivine bearing gabbro-norites are characterized by a dark color. This lithology could have been misinterpreted. We initially described coarse-grained plagioclase bearing rocks close to late dikes (Figure 4.5a), but these rocks are strongly altered and primary silicates are partially to fully replaced by calcite and sericite (Figure 4.5b): this type of alteration highlights white pseudomorphs that can be easily misinterpreted as cumulus plagioclase. Also, in some thin sections of samples that Filoche (personal communication) described as gabbro-norite, minor relicts of olivine (a few percent) are distinguishable but have not been reported. Their aspect and the overall texture are similar to what is observed in type-2 olivine norites (Figure 4.5c-d). For these reasons we think that the gabbro-norites she reported, are strongly altered type-2 olivine norites.

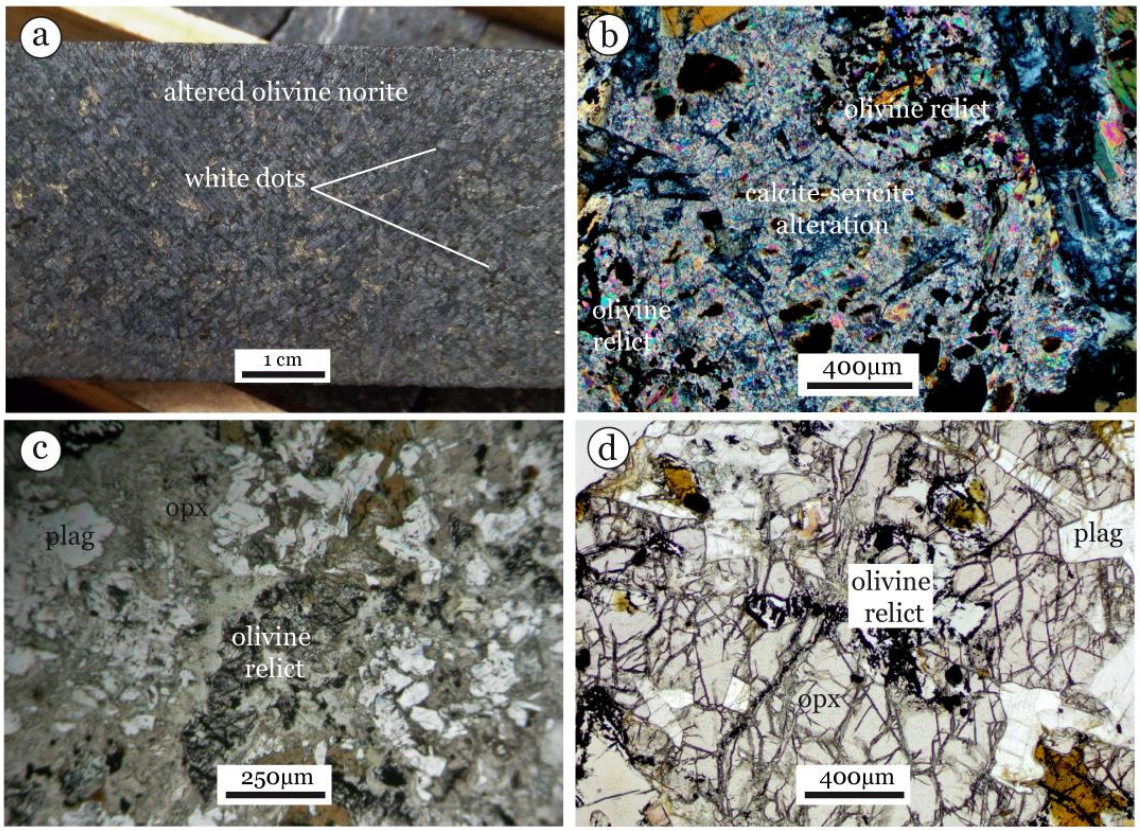

Figure 4.5 Photographs of altered olivine norite at a late dike contact under (natural) light (a) and crossed Nicols (b) illustrating white dots highlighted by the calcite sericite alteration. Microphotographs under polarized light of the gabbro norite (c: Filoche, personal communication) and the type-2 olivine norite (d: this study). Note their similarity.

4.1.3. Leucogabbro

This rock type is found in only some drill cores (e.g. ALA18 -246 -247 -248 -265 -266). It occurs as small bodies, among them veins, that are sporadically disseminated within the olivine norite and represents no more than 5% of the drillcores. Locally, zones with abundant leucogabbros can be traced from one core to another suggesting that they are vertically and laterally continuous. For example, in the drill cores ALA246 and -247, the leucogabbro bodies are distributed in the upper side of the dike whereas the lower side is almost devoid of leucogabbro (Figure 4.1a).

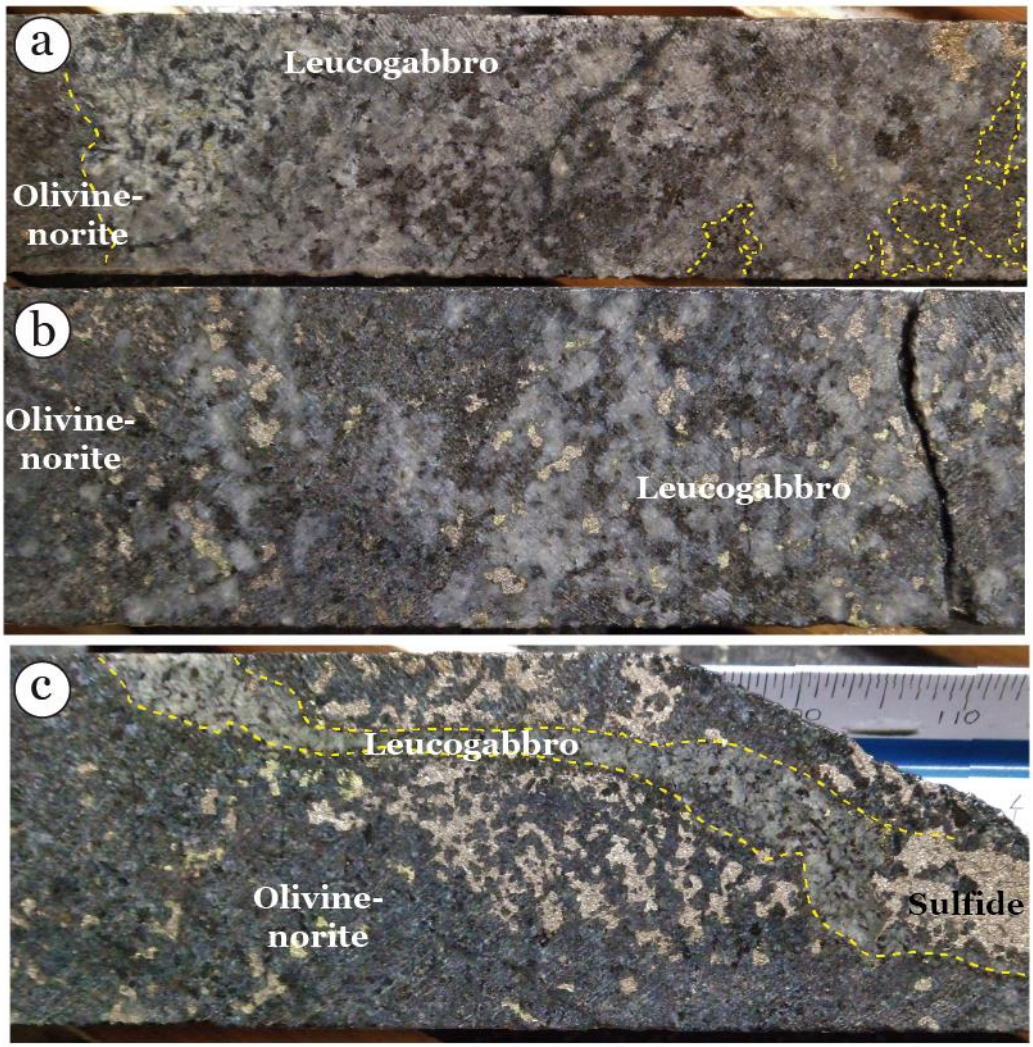

Figure 4.6 Photos of core samples showing the morphologies of the leucogabbro. The dashed lines depict the contact between the leucogabbro bodies and the hosting olivine norite. (a) Relatively compact body with respectively sharp and diffuse contacts on the right and left, sample 246.242.5. (b) Patch of leucogabbro scattered within the olivine norite. Contacts are not shown because of interlocking between the two rocks, sample 246.240.4. (c) Vein with pinch and swell shape, rimmed by amphibole at its contact with the olivine norite, sample 246.212.3.

The leucogabbro contains 0-15% mafic minerals and its grain size varies from very fine to coarse. It is composed of abundant plagioclase (70-85%), biotite (5-15%) and hornblende (0-10%) and its pale color makes it conspicuous within the dark olivine norite. Orthopyroxene, or rarely clinopyroxene, make up less than 10% or may be absent. Accessory minerals are apatite, magnetite and ilmenite. Sulfides can make up a major proportion, up to 30-70%, of these rocks (Section 5). According to the IUGS classification (Streckeisen, 1976), notably taking into account the plagioclase composition (Section 4.2), the rock type is a leucogabbro.

We classify the leucogabbro into different types depending on their geometry:

- *Compact bodies* have relatively sharp contact with the olivine norite (left contact of Figure 4.6a)
- *Dispersed bodies* are small bodies that have diffuse boundaries and are scattered into the host olivine norite (Figure 4.6b)
- *Veins* are more or less sinuous elongated bodies, 5 mm to ≥ 4cm thick (Figure 4.6c)

This classification is rudimentary because the core observations only give a limited picture of the geometry of the leucogabbro, and some bodies show a gradation from one type to an other (e.g. Figure 4.6a-b). Measurements (N=14) of the orientation of the vein-like leucogabbros from non-oriented cores but known dips allow us to propose two possible average apparent dips: 73° or 17°.

The grain size of plagioclase in leucogabbro is highly variable, from 20 µm to 5 mm. The largest size ranges are observed within some large and compact bodies, whereas veins have the smallest variation (Table 4.2). Plagioclase laths are juxtaposed and make up the framework of the leucogabbro. In the coarser-grained areas, plagioclase grains tend to be euhedral while in finer-grained area they are anhedral because of their imbrication (Figure 4.7). Biotite and hornblende are sub- to euhedral and sometimes slightly oikocrystic, especially in fined-grained areas. Their distribution may be related to the plagioclase grain size: in fined-grained areas, they are aggregated into cluster while they form single grain in coarser areas. Rare orthopyroxene grains are subhedral. Euhedral apatite grains are enclosed in one or several plagioclase crystals. In sparse leucogabbros the presence of apatite distinguishes the leucogabbro from the norite. Plagioclase is altered to sericite+albite±calcite±quartz. Quartz-feldspar intergrowths (i.e. myrmekite) exhibit embayments within part of the plagioclase rim and/or core. They are composed of similar proportions of quartz-feldspar rectilinear to curved vermicular rods. The quartz rods may be in continuity with pure quartz. The ferromagnesian phases are altered to chlorite±magnetite.

Some leucogabbro veins are rimmed by euhedral grains of brown amphibole on one or both contacts. In cases where the leucogabbro have diffuse contact with the norite, the adjacent norite is locally made of plagioclase plus orthopyroxene which exhibits characteristic texture. Orthopyroxene forms small (0.1 mm) euhedral grains enclosed in oikocrystic plagioclase.

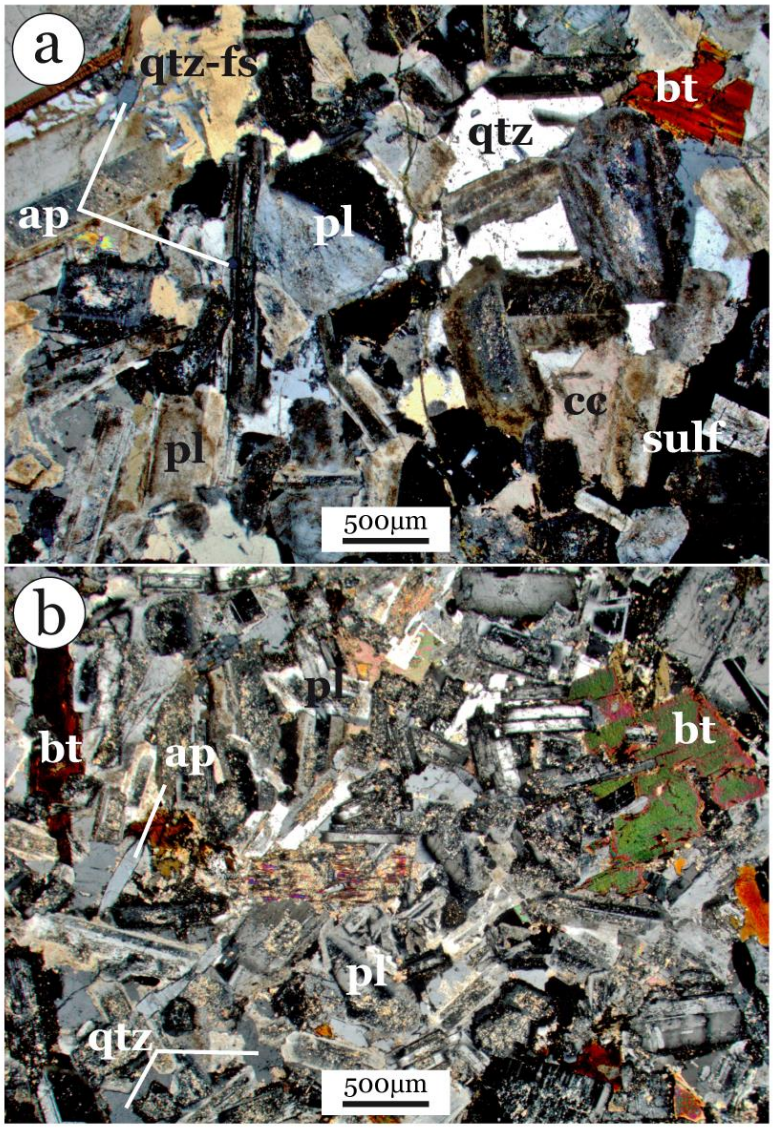

Figure 4.7 Photomicrographs under crossed Nicols of representative leucogabbros. (a) Medium-grained leucogabbro, sample 246.233.2. (b) Fine-grained leucogabbro, sample 246.232.5. Pl: plagioclase; Hb: hornblende; Bt: biotite; Ap: apatite; Qtz: quartz; Fs: feldspar.

Table 4.2 Plagioclase grain size in some leucogabbro samples.

Sample[a]	246. 242.5	246. 232.5	246. 199.0	248. 213.2	246. 230.2	246. 240.8	248. 265.1	246. 212.6	246. 212.6	246. 233.2
Type[b]	2	2	1	1	1	1	2	2	3	3
N	107	265	224	99	112	59	48	304	121	305
MIN	129	112	17	343	217	259	631	138	492	86
Quartil 1[c]	607	246	112	924	534	591	1290	310	813	272
MED	1124	327	335	1281	792	977	2208	467	1074	371
Quartil 3[c]	2027	452	591	1573	1086	1286	3775	659	1300	535
MAX	5480	1080	1737	4010	2284	3384	5446	1742	2725	1091
MAX/MIN	42	10	103	12	11	13	9	13	6	13

(a) sample are named as follows: drillhole.depth (in m)
(b) Types: 1: Compact; 2: Compact and dipersed; 3: Vein
(c) Quartile 1 and 3 comprise 25% of the values from the minimum and maximum, respectively

4.1.4. Late dikes

Numerous late dikes crosscut the wall rocks and the Älgliden dike (Figure 4.1). Their width varies from decimeters to a few tens of meters. Some of them can be followed vertically and laterally from one drill core to another indicating they extend over hundreds of meters. Most contacts are sharp and rectilinear, but one is undulating and marked by a reaction rim of oxide mineral. Late dikes are unmineralized and some contain angular xenoliths of mineralized olivine norite. Most are porphyritic dark-green andesite composed of phenocrysts of plagioclase and green hornblende grains (max. 2 mm sized) within a groundmass of plagioclase and biotite (200-300 µm; Figure 4.8), with secondary quartz. Oscillatory zoning is only observed in phenocrysts of plagioclase while only a few plagioclase of the groundmass show normal zoning. Biotite of the groundmass is partially altered into chlorite, and the borders of plagioclase grains are more albiltic and associated with intergranular quartz (Figure 4.8). Other minor aplitic dikes are composed of very fined-grained quartz, feldspar (>90%) and biotite (<10%).

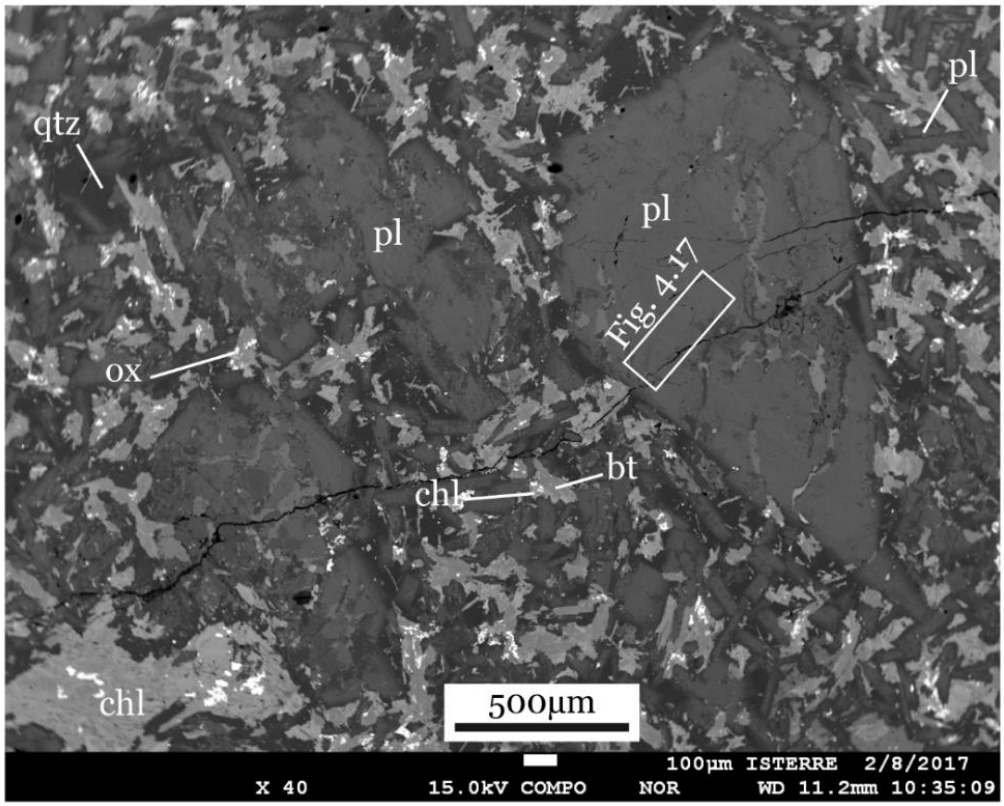

Figure 4.8 Back scattered electron image illustrating the mineralogy and texture of a late dike, sample 246.249.6. Abbreviation: pl: plagioclase, bt: biotite, chl: chlorite, qtz: quartz, ox: iron oxide.

4.1.5. Xenoliths

Numerous xenoliths (2 cm to 2 m) are observed within the dike. Xenoliths have mostly sharp contacts with the host olivine norite but some show more or less diffuse contacts and are even disaggregated into the olivine norite where fragments of the xenolith and feldspar and quartz xenocrysts are dispersed into the olivine norite (Figure 4.9). Most are in the narrower SW and NE parts of the dike but some quartz xenocrysts and xenoliths are also present in the wider central part. In some cases the contact between the intrusion and the wall rocks is a mixed zone where the amount of wall rock can dominate that of the olivine norite and can rather be considered as injection of the noritic magma into the wall rock. Otherwise, xenoliths from the immediate wall rocks are observed close to the margins of the dike (e.g. ALA-264, -248, -222 and -215; Figure 4.9b). As an example, xenoliths account for 20% in volume proportion over 10 m of the core ALA264.

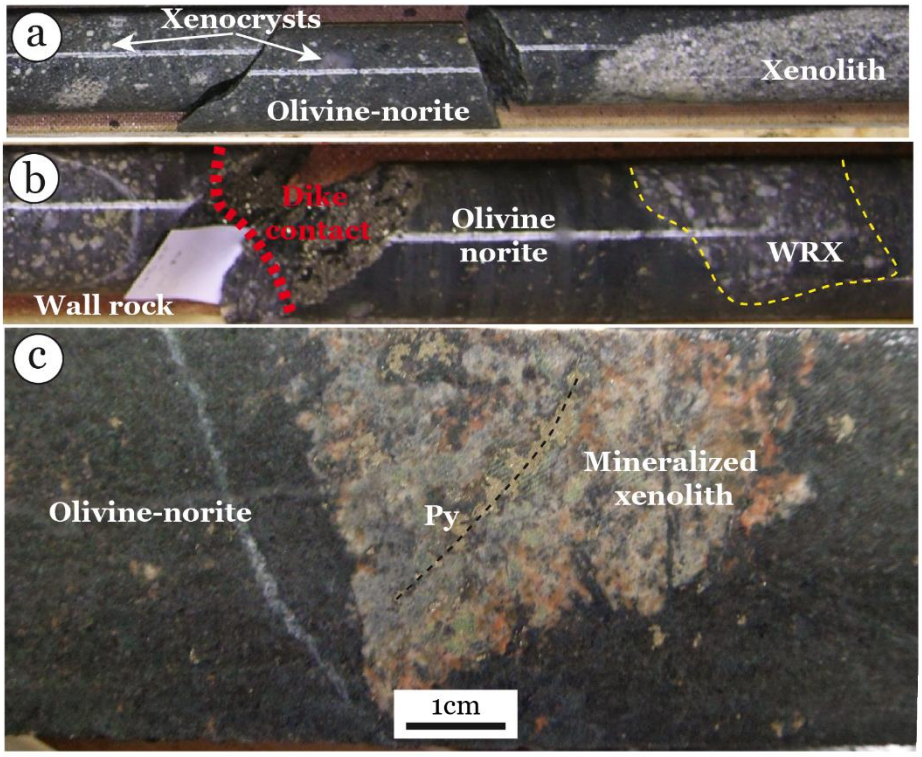

Figure 4.9 Core photos illustrating the variety of xenoliths. (a) Granodiorite xenoliths and xenocrysts within the olivine norite, ALA218. The left part of the core is rich in xenocrysts (b) Quartz-feldspar porphyry wall rock and wall rock xenolith (WRX) close to the margin of the dike, ALA215. The red and yellow dashed lines highlight respectively the dike contact and the WRX border. (c) Granodioritic xenolith hosting a pyrite grain alignment, 264.213.0.

Xenoliths of monzodioritic to granodioritic composition were observed in thin section. For those of monzodioritic composition quartz is absent but the mineralogy is probably uncomplete since some silicate minerals seems to be replaced by sulfides. They are composed of 70% feldspar (mainly plagioclase), 10-30% biotite and 0-20% quartz with minor apatite. Some wall rock xenoliths contain sulfides (i.e. pyrite and chalcopyrite) of probable hydrothermal origin (Figure 4.9c). The biotite grains are very small (10-50 μm) and aggregate together as clusters or are distributed around large plagioclase grains (1-4 mm). Rare K-feldspar occurs as small single grains or as exsolution lamellae or patches within large plagioclase grain. Cores of large feldspars are commonly altered into sericite±epidote or chlorite. The chlorite-alteration can affect the entire feldspar grain, and is more pronounced at the margin of the xenolith. The chlorite alteration affects the entire small xenoliths and is limited to the margin of the biggest xenoliths. Secondary albite occurs at the rim of large feldspar grains or replaces entire small grains.

4.1.6. Wall rocks

Three distinct lithologies are observed in the wall rocks. The rock types and the contacts between them are hard to define because of progressive changes in color and grain size due to strong and heterogeneous alteration.

Granodiorite

The granodiorite is the most widespread lithology of the wall rocks. A representative core sample of granodiorite is illustrated in Figure 4.10a. The texture is equant and the rock consists in coarse-grained feldspar (60%), quartz (35%) and biotite (25%). Feldspar is slightly altered to sericite and is commonly red stained. Biotite is altered to chlorite.

Tonalite

The tonalite is a fine-grained granular rock (Figure 4.10b-c) composed of plagioclase (50%), quartz (25%) and biotite (25%) with minor apatite, magnetite and zircon. Most plagioclase and quartz crystals are fine grained (0.5-1 mm) but some macrocrysts of feldspar reach 1 cm. Plagioclase is altered to sericite±epidote. Biotite grains are very small (10-100 μm) and aggregated together as clusters or distributed along quartz or plagioclase grain boundaries where they are associated with minor small plagioclase (10-20 μm) and magnetite grains (Fig. 4.10c). Alteration of biotite to chlorite is common.

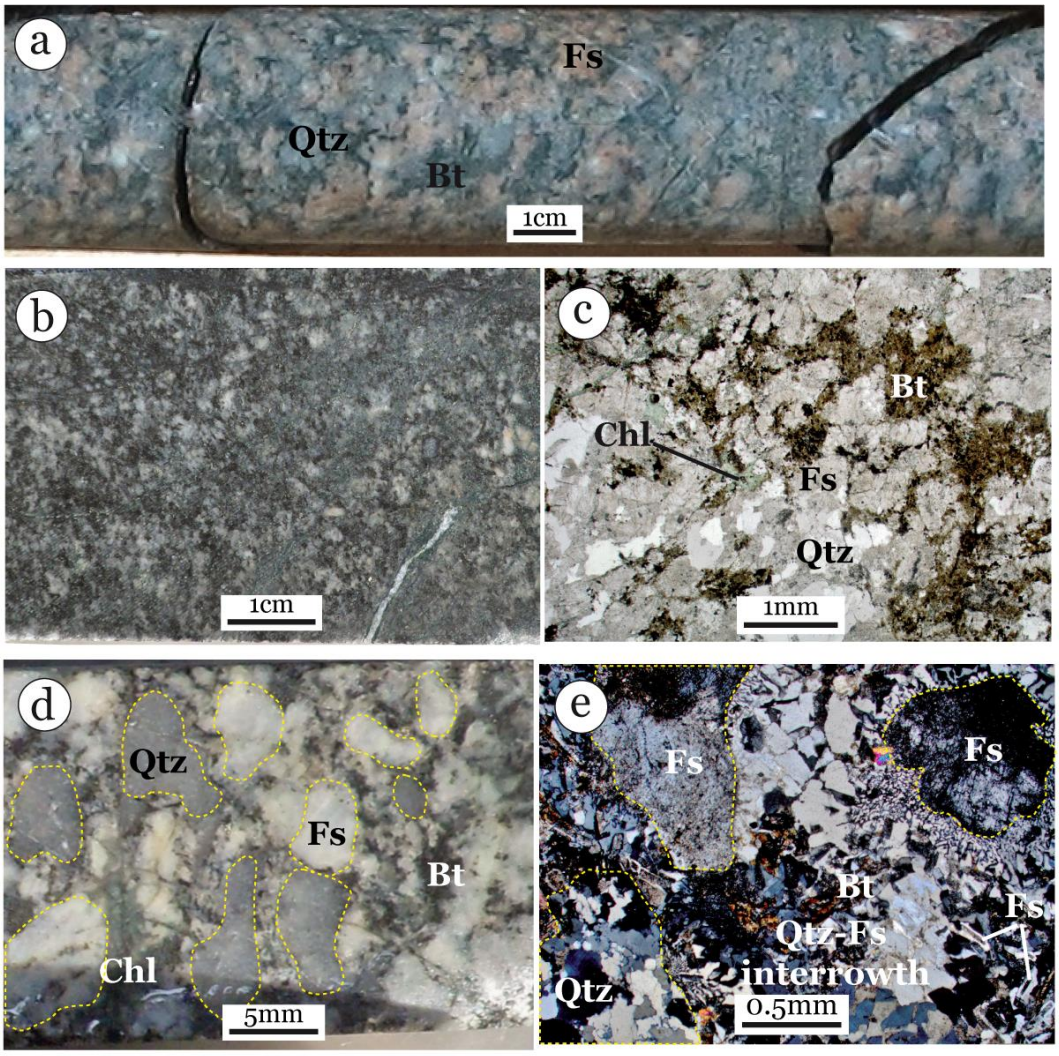

Figure 4.10 Photo(micro)graphs of the wall rocks. (a) Core photo of granodiorite. (b) Core photo and (c) photomicrograph of the tonalite, sample 264.162.4. (d) Core photo and (e) photomicrograph under crossed Nicols of the quartz-feldspar porphyry rock, 246.196.3. Mineral abbreviations: Fs: feldspar; Qtz: quartz; Bt: biotite; Chl: chlorite.

Quartz-feldspar porphyry

This rock type contains macrocrysts of quartz and feldspar within a finer-grained matrix. It comprises 60% feldspar, 25% quartz, 10% biotite, 5% hornblende, and zircon and apatite as accessory minerals. Quartz and feldspar form rounded large macrocrysts (0.5-1 mm; Fig. 4.10d) and intergrowths within the groundmass (Figure 4.10e). The intergrowths consist of angular to cuneiform interdigitated rods of quartz (50%) and feldspar (50%) that entirely surround the feldspar macrocryst. The crystallographic orientation of the feldspar rods is identical to the adjacent macrocryst and perpendicular to that of quartz. Feldspar is dusted by sericite alteration. Within the groundmass, feldspar occurs as small laths (100-300 μm) and biotite is mainly subhedral and small (<300 μm; Figure 4.10d). Biotite and hornblende may also show intergrowths with quartz.

4.1.7. Alteration

Alteration is not uniformly distributed through the dike. A pervasive chlorite±actinolite alteration is distributed over the whole width of the dike in its thinner parts (i.e. at its NE and SW extremities), or is restricted to the margins where the dike is wider. This is illustrated in Figure 4.1. In ALA264, the chlorite-alteration of xenoliths forms dark green aureoles around the biggest xenoliths or small dark green patches when it affects the entire xenoliths (Figure 4.1b). A second type of alteration is a local and channeled (i.e. at lithology contact) alteration composed of talc±tremolite±carbonate (Figure 4.1). Others secondary minerals commonly observed in all the lithologies are quartz, albite, sericite, calcite and epidote. Altogether, this indicates a greenschist regional metamorphic grade.

4.2. Composition of silicate minerals

We measured the compositions of minerals in fresh olivine norite and leucogabbro in drill core ALA246, in wall rocks and xenoliths in core ALA264, and leucogabbro in core ALA248

4.2.1. Olivine

The composition of cores and rims of olivine have been measured in several samples across the dike (Table 4.3). Forsterite contents range from 72.5 to 76.3. In this narrow range, 50% are distributed at ±0.5 mol% around the median value of $Fo_{74.9}$. Olivine grains exhibit a normal zoning with a decrease in Fo, NiO and CaO contents from core to rim (Figure 4.11). CaO and Fo variations are decoupled across the grain with a near constant decrease in Fo from core to rim whereas the CaO content is constant in the core (except for analyzing points close to fractures) and drops drastically close to the rim. Figure 4.1a illustrates the slight increase in olivine Mg# from the outer to inner part of the dike. These variations do not exceed that of zoning within single grains.

4.2.2.Pyroxene

Orthopyroxene in the olivine norite is enstatite with a uniform composition ranging from $En_{70.3}$-$Wo_{1.3}$ to $En_{77.5}$-$Wo_{3.8}$ (Table 4.4). As for olivine, the range of composition is narrow, with 50% of the orthopyroxene having composition in the ±0.7 mol% interval around the median value of $En_{74.6}$. Orthopyroxene of the leucogabbro has similar composition, whose relative variation through the dike seems to follow that of orthopyroxene in the olivine norites, but it

represents the Mg-richest part of the range. This is illustrated in Figure 4.1.a and Figure 4.12. In olivine norites, the orthopyroxene composition seems to depend on several factors: the nature of the host rock, the textural position and the position through the dike. Figure 4.12 shows that the sub- to euhedral orthopyroxene grains have the highest Mg# values while the orthopyroxene that rims olivine grains has the lowest Mg# values. Relatively to other textural types, orthopyroxene overgrowth rims have also the lowest TiO_2 contents. In Figure 4.13 we show the chemical variations in an oikocrystic orthopyroxene which exhibits a slight zoning with an increase of Mg# and decrease of TiO_2 from rim to core.

Despite the chemical variation related to sample texture, a broad trend can be observed through the dike, with an increase of the orthopyroxene Mg# in the northern part of the dike in core ALA246 (Figure 4.1a).

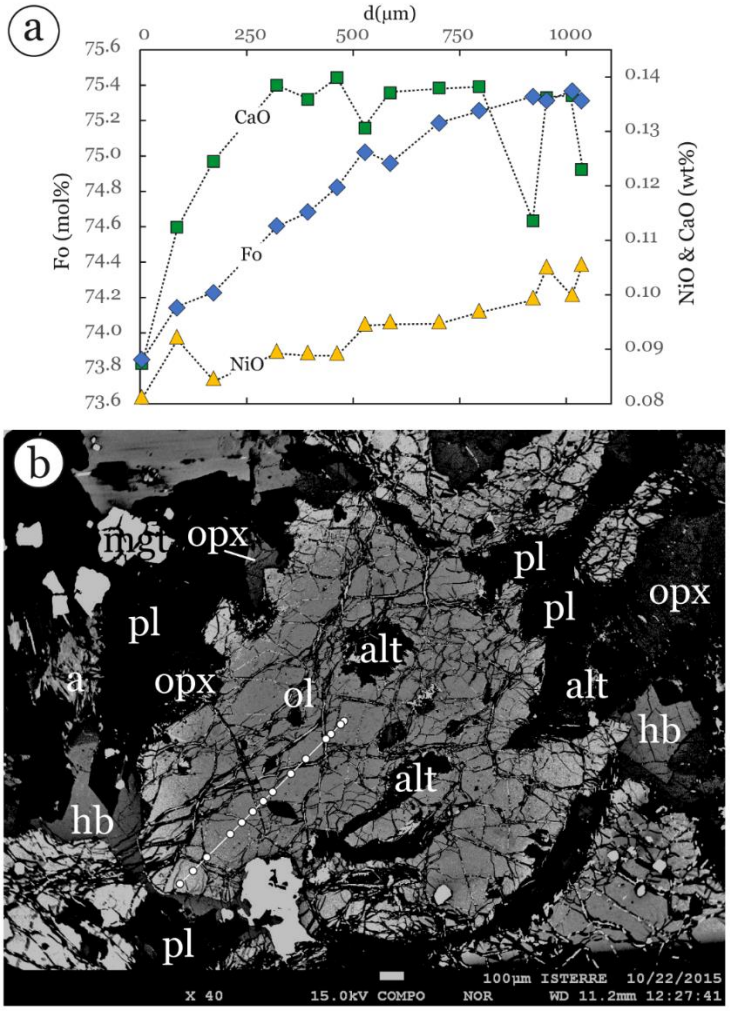

Figure 4.11 Zoning of olivine illustrated by (a) Variation diagram of forsterite, NiO and CaO over distance, and (b) back scattered electron image, sample 246.2090. Irregularities in point spacing come from bad analyzes. Abbreviation: Fo: forsterite, Ol: olivine; Opx: orthopyroxene; Pl: plagioclase; Hb: hornblende; Alt: altered phases; mgt: magnetite. Fo = 100*(Mg/Mg+Fe).

Table 4.3 Electron microprobe analyses of selected olivine grains.

Sample no.[a]	246. 219.0[1]	246. 219.0[1]	246. 239.1[2]	246. 212.3[1]	246. 209.0[1]	246. 209.0[1]	246. 308.0[1]	246. 308.0[1]	246. 300.9[1]	246. 300.9[1]
wt.%										
SiO_2	38.44	38.08	38.36	38.39	38.44	38.49	38.72	38.41	38.42	38.37
TiO_2	0.01	0.02	0.01	0.01	n.a.	n.a.	n.a.	n.a.	0.03	0.02
Al_2O_3	0.02	0.01	0.01	0.02	n.a.	n.a.	n.a.	n.a.	0.03	0.03
FeO	22.56	23.89	22.75	23.07	22.41	23.25	23.13	23.69	22.84	23.18
MnO	0.32	0.35	0.32	0.40	0.34	0.35	0.35	0.36	0.34	0.36
MgO	39.28	38.15	38.85	38.55	38.81	38.13	38.46	38.19	38.64	38.35
CaO	0.11	0.08	0.13	0.14	0.14	0.13	0.13	0.07	0.11	0.13
Cr_2O_3	0.003	0.008	0.008	0.003	n.a.	n.a.	n.a.	n.a.	<0.008	<0.008
NiO	0.11	0.12	0.12	0.06	0.09	0.08	0.07	0.07	0.05	0.05
Total	100.86	100.70	100.56	100.64	100.91	101.11	101.45	101.44	100.48	100.49
Cation numbers based on 4 oxygens										
mol.%										
Si	0.993	0.992	0.995	0.996	0.998	1.001	1.002	0.998	0.997	0.997
Ti	0.0002	0.0005	0.0003	0.0002	0.0000	n.a.	n.a.	n.a.	n.a.	0.0005
Al	0.0005	0.0004	0.0004	0.0006	0.0000	n.a.	n.a.	n.a.	n.a.	0.0008
Fe^{2+}	0.487	0.520	0.494	0.501	0.487	0.506	0.500	0.515	0.496	0.504
Mn	0.007	0.008	0.007	0.009	0.008	0.008	0.008	0.008	0.008	0.008
Mg	1.513	1.482	1.502	1.491	1.503	1.479	1.483	1.479	1.495	1.486
Ca	0.003	0.002	0.004	0.004	0.004	0.004	0.004	0.002	0.003	0.004
Cr	0.0001	0.0002	0.0002	0.0001	n.a.	n.a.	n.a.	n.a.	<D.L.	<D.L.
Ni	0.002	0.002	0.002	0.001	0.002	0.002	0.001	0.001	0.001	0.001
∑ cations	3.006	3.007	3.005	3.003	3.002	2.999	2.998	3.002	3.002	3.002
Fo	75.6	74.0	75.3	74.9	75.5	74.5	74.8	74.2	75.1	74.7
MgO/FeO_{liq}[b]	0.52	0.48	0.51	0.50	0.52	0.49	0.50	0.48	0.51	0.50

Abbreviations: Fo: forsterite (mol.%); <D.L.: below detection limit; n.a.: not analyzed.

(a) 1 and 2 refer to olivine norites of type-1 and type-2, respectively.

(b) calculated from $KD_{Fe-Mg} = 0.3$ according to Roeder & Emslie (1970)

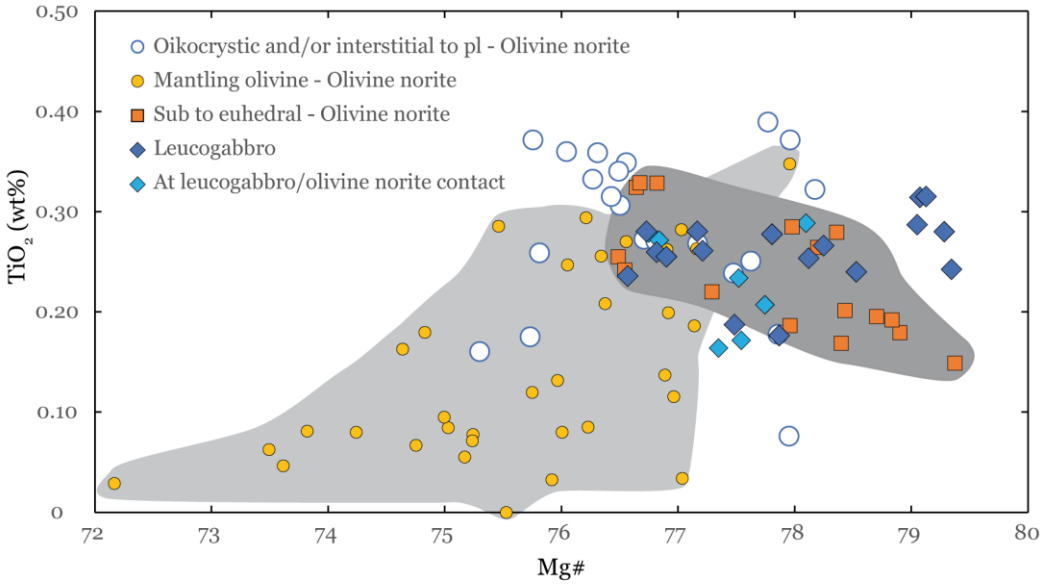

Figure 4.12 Variation diagrams of TiO_2 as function of the Mg# of orthopyroxene. (a) The grey area highlight the distinctive range of composition of the overgrowths and sub- to euhedral pyroxene grains. Abbreviation: Ol: olivine; Opx: orthopyroxene; Pl: plagioclase.

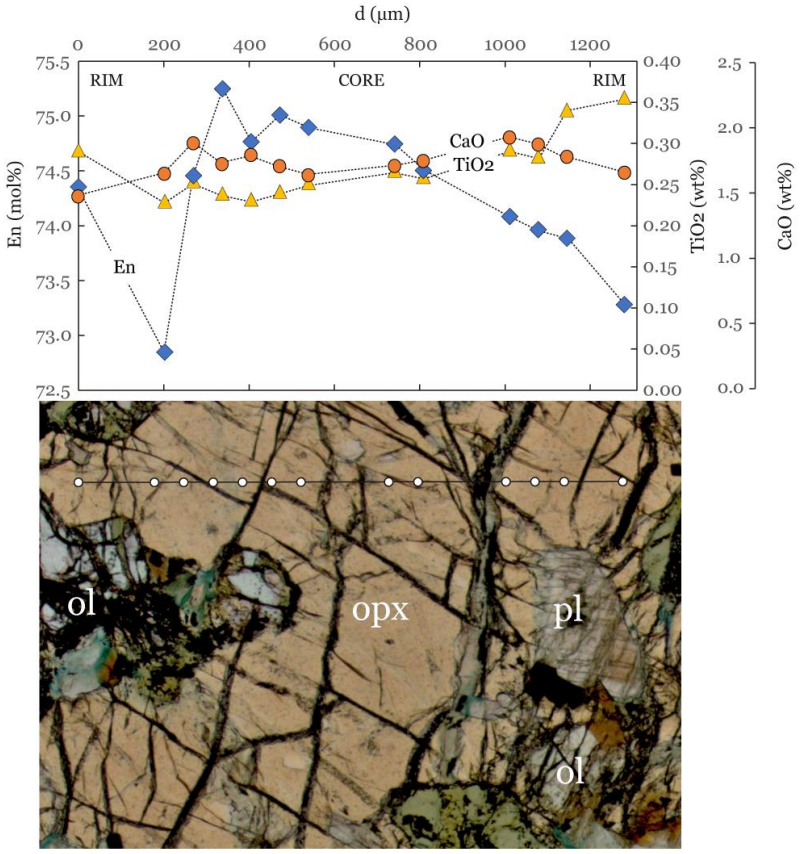

Figure 4.13 Zoning of orthopyroxene illustrated by a variation diagram of enstatite and TiO_2 over distance, sample 246.3080. Note the negative correlation between enstatite and TiO_2. Irregularities in point spacing come from bad analyzes. Abbreviation: En: enstatite; Ol: olivine; Opx: orthopyroxene; Pl: plagioclase.

Table 4.4 Electron microprobe analyses of selected representative pyroxene grains.

Sample no.[a]	246. 233.5[2]	246. 209.0[1]	246. 239.1[2]	246. 280.8[1]	246. 212.3[1]	246. 219.0[1]	246. 212.6[1]	248. 265.1	248. 265.1	248. 262.0	246. 212.3[1]
Host rock	O. nor.	O. nor.	O. nor.	O. nor.	O. nor.	O. nor.	Leuco.	Leuco.	Leuco.	Contact	Contact
wt.%											
SiO_2	54.90	53.65	53.96	54.41	53.40	51.25	54.23	53.53	53.68	54.09	54.45
TiO_2	0.15	0.06	0.28	0.35	0.32	0.67	0.28	0.26	0.26	0.17	0.29
Al_2O_3	1.44	1.64	1.95	1.39	1.88	3.13	1.99	2.45	2.59	1.84	1.34
FeO	13.14	16.70	14.03	14.97	13.55	7.33	13.03	14.59	14.24	14.27	13.73
MnO	0.27	0.35	0.26	0.31	0.28	0.16	0.22	0.24	0.23	0.25	0.30
MgO	28.96	26.86	28.39	27.99	27.80	16.36	28.44	27.57	27.50	28.13	28.08
CaO	1.20	0.90	1.59	1.46	1.77	19.76	1.61	1.36	1.27	1.30	1.76
Na_2O	0.03	0.03	0.05	0.05	0.03	0.34	0.04	<D.L.	<D.L.	0.05	0.03
Cr_2O_3	0.23	0.04	0.27	0.09	0.27	0.62	0.32	0.19	0.26	0.17	0.21
Total	100.33	100.30	100.81	101.03	99.41	99.65	100.33	100.46	100.28	100.28	100.26
Cation numbers based on 6 oxygens											
mol.%											
Si	1.95	1.94	1.93	1.94	1.93	1.90	1.94	1.92	1.93	1.94	1.95
Ti	0.004	0.002	0.008	0.009	0.009	0.019	0.007	0.007	0.007	0.005	0.008
Al	0.06	0.07	0.08	0.06	0.08	0.14	0.08	0.10	0.11	0.08	0.06
Fe^{2+}	0.39	0.51	0.42	0.45	0.41	0.23	0.39	0.44	0.43	0.43	0.41
Mn	0.008	0.011	0.008	0.009	0.009	0.005	0.007	0.007	0.007	0.008	0.009
Mg	1.54	1.45	1.51	1.49	1.50	0.90	1.51	1.48	1.47	1.50	1.50
Ca	0.05	0.04	0.06	0.06	0.07	0.78	0.06	0.05	0.05	0.05	0.07
Na	0.002	0.002	0.004	0.003	0.002	0.024	0.003	<D.L.	<D.L.	0.003	0.002
Cr	0.006	0.001	0.008	0.002	0.008	0.018	0.009	0.005	0.007	0.005	0.006
∑ cations	4.01	4.02	4.02	4.02	4.02	4.02	4.01	4.01	4.01	4.02	4.01
En	77.5	72.4	75.6	74.4	75.5	47.1	76.8	74.8	75.3	75.6	75.4
Wo	2.3	1.7	3.0	2.8	3.5	40.9	3.1	2.6	2.5	2.5	3.4
Fs	20.1	25.8	21.4	22.8	21.1	12.1	20.1	22.6	22.2	21.9	21.2
Mg#	79.4	73.7	78.0	76.6	78.2	79.6	79.3	76.8	77.2	77.5	78.1
MgO/FeO_{liq}	0.60	0.43	0.55	0.50	0.55	0.60	0.59	0.51	0.52	0.53	0.55

Abbreviations: O. nor.: Olivine norite; Leuco: Leucogabbro; <D.L.: below detection limit; En: enstatite (mol.%); Wo: wollastonite (mol.%); Fs: ferrosilite (mol.%)

(a) 1 and 2 refer to olivine norites of type-1 and type-2, respectively.

(b) calculated from $KD_{Fe\text{-}Mg} = 0.27$ according to Gerlach & Grove (1982)

4.2.3.Plagioclase

Compositions have been determined on cores and on unaltered rims (Figure 4.14 and Table 4.5).

Plagioclase of the olivine norite has a labradorite-bytownite composition with anorthite ranging from An_{48} to An_{82} (Figure 4.14). The plagioclase composition is constant in the southern part of the core ALA246, and olivine norite and plagioclase-clusters show the same range of composition with a strict correlation whereby variations occur through the dike (Figure 4.1a). The plagioclase grains of the Type-2 olivine norite have the lowest anorthite contents (around An_{60}). Plagioclase crystals in olivine norite mostly show normal and progressive zoning, but some crystals show oscillatory zoning (Figure 4.15). Plagioclase crystals that are enclosed in oikocrystic orthopyroxene are mainly not zoned.

Within compact and dispersed leucogabbro bodies, the An content of plagioclase is similar to that hosted in the olivine norite, ranging from to An_{39} to An_{78} (mostly labradorite-bytownite composition; Figure 4.14). Across the dike, the composition of plagioclase of the leucogabbro correlates with that of the olivine norite (Figure 4.1a), except in veins where the An content may be far lower compared to the adjacent olivine norites (Figure 4.1a). In the leucogabbro veins, An contents are as high as in olivine norite but extend to significantly lower An values (An_{22}-An_{70}; Figure 4.14). Normal zoning is common within plagioclase of the leucogabbro. This primary zoning is disturbed toward the grain edges where albitization results in strong decrease of An and Or content (Figure 4.16).

The plagioclase grains of the wall rocks have relatively evolved composition, consisting in andesine (i.e. An_{31}-An_{51}) with distinctive low Or content compared to plagioclase of the dike with similar An content (Figure 4.14). Some plagioclase grains of the xenoliths share such compositions but most are similar to plagioclase of the leucogabbro veins with An contents ranging from An_{24} to An_{67} (Figure 4.14).

In a coeval dike which has undulating contacts with the olivine norite, the plagioclase has andesine composition ranging from An_{34} to An_{47}, which is lower than most of plagioclase of the Älgliden rocks (Figure 4.14). However, in a late mafic-intermediate porphyritic dike, the plagioclase compositional range is similar to that of Älgliden rocks (i.e. An_{53}-An_{77}, labradorite-bytownite composition; Figure 4.14). Plagioclase of the groundmass has an average value of An_{64} (N=18) against An_{72} (N=6) in plagioclase phenocrysts. Some plagioclase phenocrysts show oscillatory zoning (Figure 4.17).

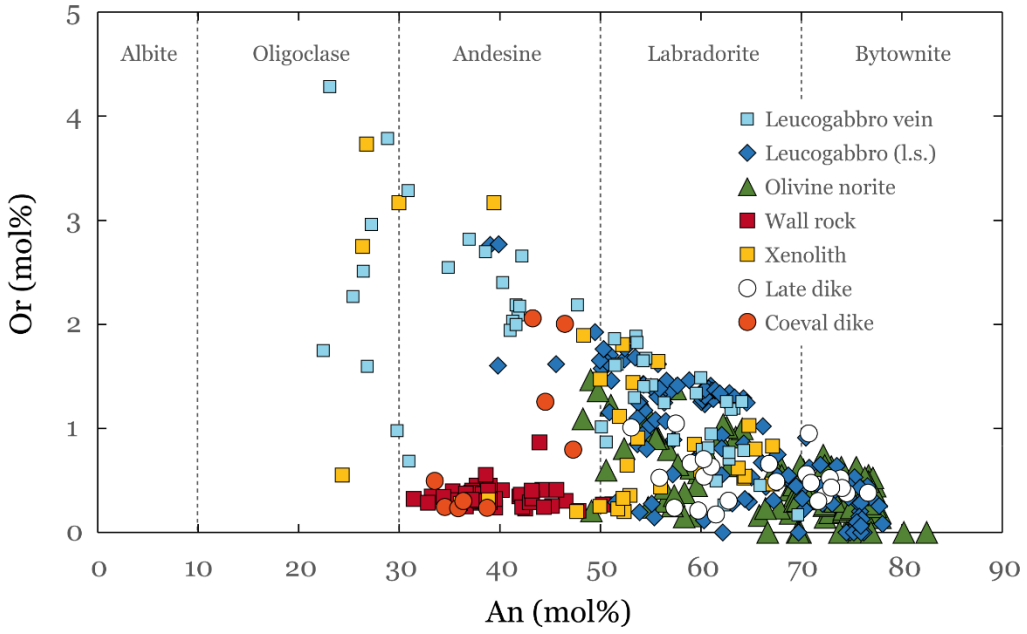

Figure 4.14 Compositional variation of anorthite and orthoclase in plagioclase of the different rocks. Abbreviation: An: anorthite; Or: orthoclase.

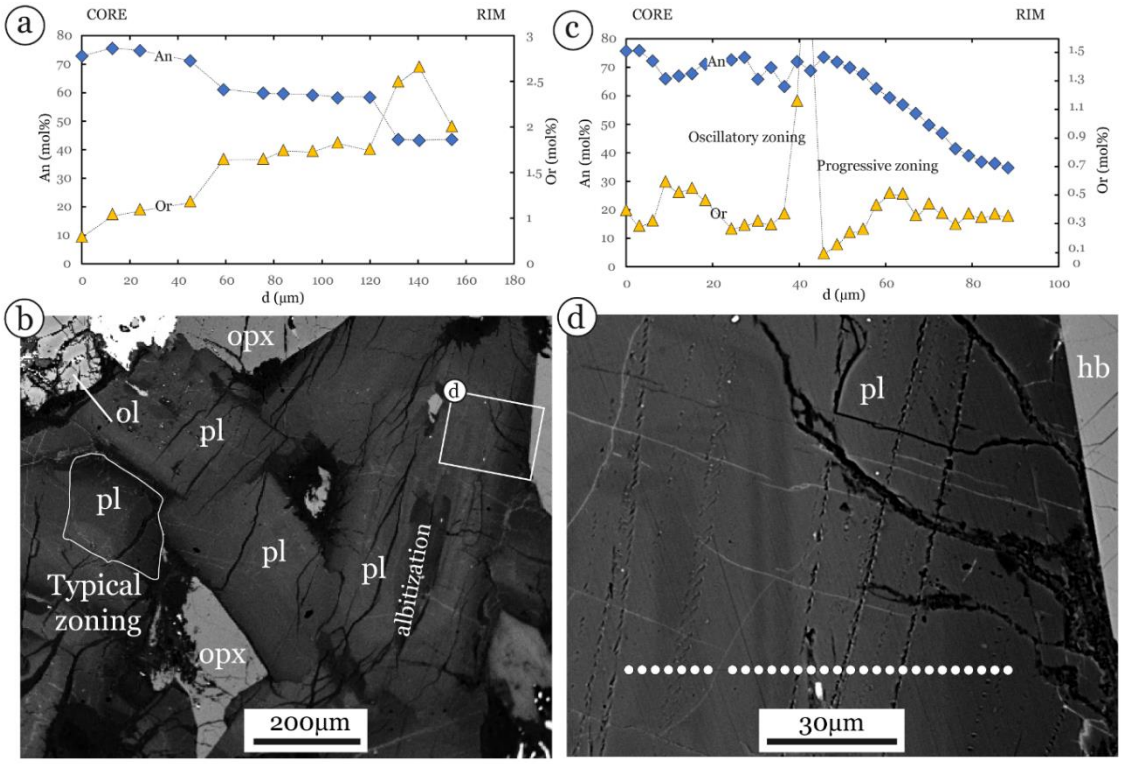

Figure 4.15 Zoning of plagioclase of the olivine norite. (a) Compositional variation of anorthite and orthoclase from core to rim of a representative zoned plagioclase, sample 246.308.0. BSE associated image is not shown. (b) Back scattered electron image illustrating typical zoning in plagioclase, sample 246.308.0 (c) Compositional variation of anorthite and orthoclase from core to rim of a plagioclase showing complex and oscillatory zoning, sample 246.3080. (d) Back scattered electron image illustrating the oscillatory zoning of (c). Irregularities in point spacing come from bad analyzes. Abbreviation: An: anorthite; Or: orthoclase; Pl: plagioclase; Ol: olivine; Opx: orthopyroxene; Hb: hornblende.

Table 4.5 Electron microprobe analyses of selected representative plagioclase.

Sample no.[a]	246. 219.0[1]	246 .219.0[1]	246. 308.0[1]	246. 308.0[1]	246. 232.5[2]	246. 232.5[2]	248. 262.0	248. 262.0	264. 162.4	264. 190.1	246. 249.6
Host rock	O. nor.	O. nor.	O. nor.	O. nor.	Leuco.	Leuco.	Leuco.	Leuco.	Tonalite	Xenolith	Late dike
Crystal position	core	rim	core	rim	core	rim	core	rim	core	core	core
wt.%											
SiO_2	49.86	55.42	48.77	53.59	51.68	67.37	55.19	66.21	56.93	51.55	49.14
TiO_2	<D.L.	0.04	0.03	0.04	0.04	<D.L.	0.04	0.03	0.01	0.03	0.03
Al_2O_3	31.18	27.64	32.49	29.04	30.29	20.32	27.64	20.80	27.35	29.62	31.45
FeO	0.74	0.50	0.88	0.68	0.72	0.15	0.56	0.29	0.40	0.97	0.56
MgO	n.a.	n.a.	n.a.	n.a.	n.a.	n.a.	n.a.	n.a.	<D.L.	0.02	0.08
CaO	14.04	9.49	16.03	11.99	13.26	0.86	9.95	1.66	9.29	12.76	15.18
Na_2O	3.49	6.20	2.61	5.05	3.98	11.60	5.78	11.17	6.46	3.84	2.92
K_2O	0.03	0.12	0.04	0.07	0.15	0.02	0.38	0.07	0.15	0.09	0.09
Total	99.34	99.42	100.86	100.45	100.11	100.32	99.54	100.22	100.59	98.88	99.45
Cation numbers based on 8 oxygens											
mol.%											
Si	2.29	2.51	2.22	2.42	2.35	2.95	2.50	2.91	2.55	2.37	2.26
Ti	<D.L.	0.002	0.001	0.001	0.001	<D.L.	0.001	0.001	0.000	0.001	0.001
Al	1.69	1.48	1.75	1.55	1.63	1.05	1.48	1.08	1.44	1.61	1.71
Fe^{2+}	0.029	0.019	0.033	0.026	0.027	0.005	0.021	0.011	0.015	0.037	0.021
Mg	n.a.	n.a.	n.a.	n.a.	n.a.	n.a.	n.a.	n.a.	<D.L.	0.002	0.006
Ca	0.69	0.46	0.78	0.58	0.65	0.04	0.48	0.08	0.45	0.63	0.75
Na	0.31	0.54	0.23	0.44	0.35	0.98	0.51	0.95	0.56	0.34	0.26
K	0.002	0.007	0.002	0.004	0.009	0.001	0.022	0.004	0.009	0.005	0.005
∑ cations	5.02	5.02	5.02	5.03	5.01	5.02	5.02	5.03	5.02	5.00	5.01
An	68.9	45.5	77.1	56.5	64.3	3.9	47.7	7.6	43.9	64.4	73.9
Ab	30.9	53.8	22.7	43.1	34.9	95.9	50.1	92.0	55.2	35.1	25.6
Or	0.2	0.7	0.2	0.4	0.9	0.1	2.2	0.4	0.9	0.5	0.5

Abbreviations: O. nor.: Olivine norite; Leuco: Leucogabbro; An: anorthite (mol.%); Ab: albite (mol.%); Or: orthose (mol.%); <D.L.: below detection limit.

(a) 1 and 2 refer to olivine norites of type-1 and type-2, respectively.

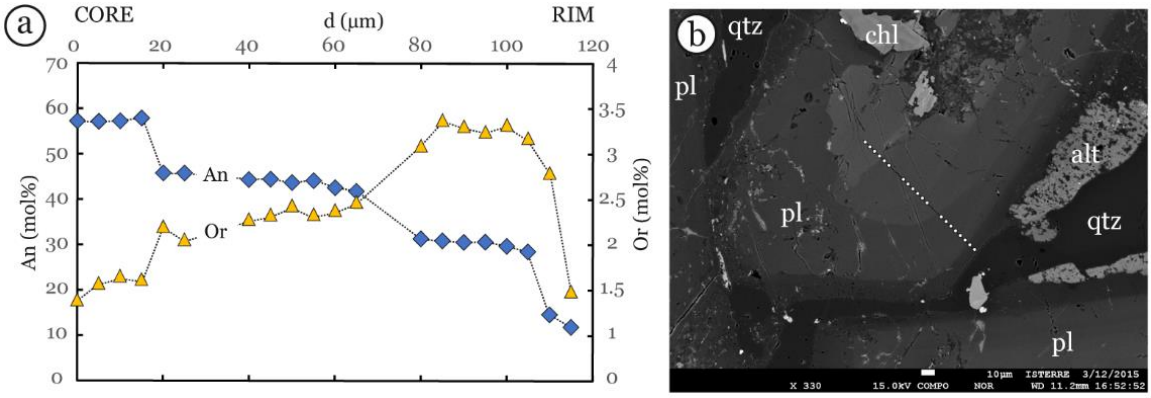

Figure 4.16 Zoning of plagioclase hosted in the leucogabbro illustrated by (a) compositional variations of anorthite and orthoclase from core to rim and (b) its associated back scattered electron image, sample 246.212.3. Note the decoupling between anorthite and orthoclase close to the rim. Irregularities in point spacing come from bad analyzes. Abbreviation: An: anorthite; Or: orthoclase; Pl: plagioclase; Qtz: quartz; Hb: hornblende; Alt: secondary phase.

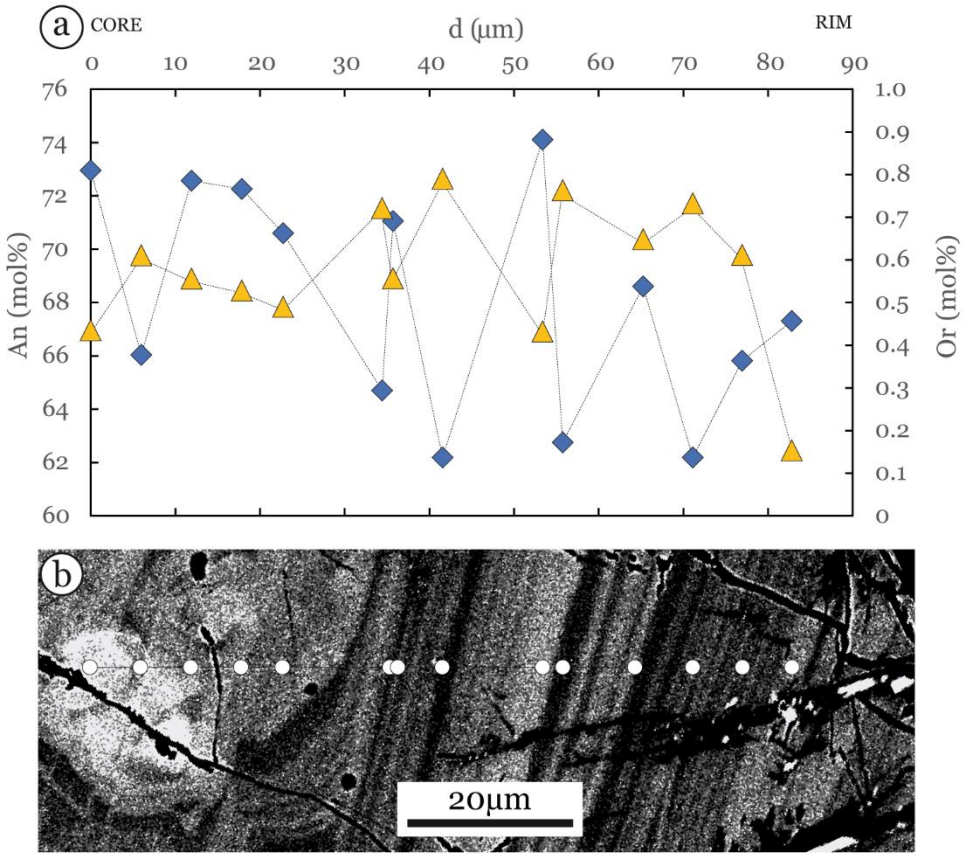

Figure 4.17 Zoning of a plagioclase phenocryst hosted in a late dike illustrated by (a) compositional variations of anorthite and orthoclase from core to rim and (b) its associated back scattered electron image, sample 246.249.6. Abbreviation: An: anorthite; Or: orthoclase.

4.2.4.Biotite

The biotite composition is distinct within the Älgliden dike rocks, the adjacent tonalite, xenoliths and a late dike, but mostly falls in the phlogopite field (Figure 4.18 and Table 4.6). The biotite grains of the olivine norite and the leucogabbro have similar Al content (2.2-2.4 a.p.f.u.), but the Mg# is higher in biotite of the olivine norite (60 compared to 68 in average). The biotite of the wall rocks have higher Al and lower Mg# and extends toward the eastonite composition. In the xenoliths, the biotite composition is intermediate between those of the wall rock and leucogabbro, and it is more the magnesian than in the late dike.

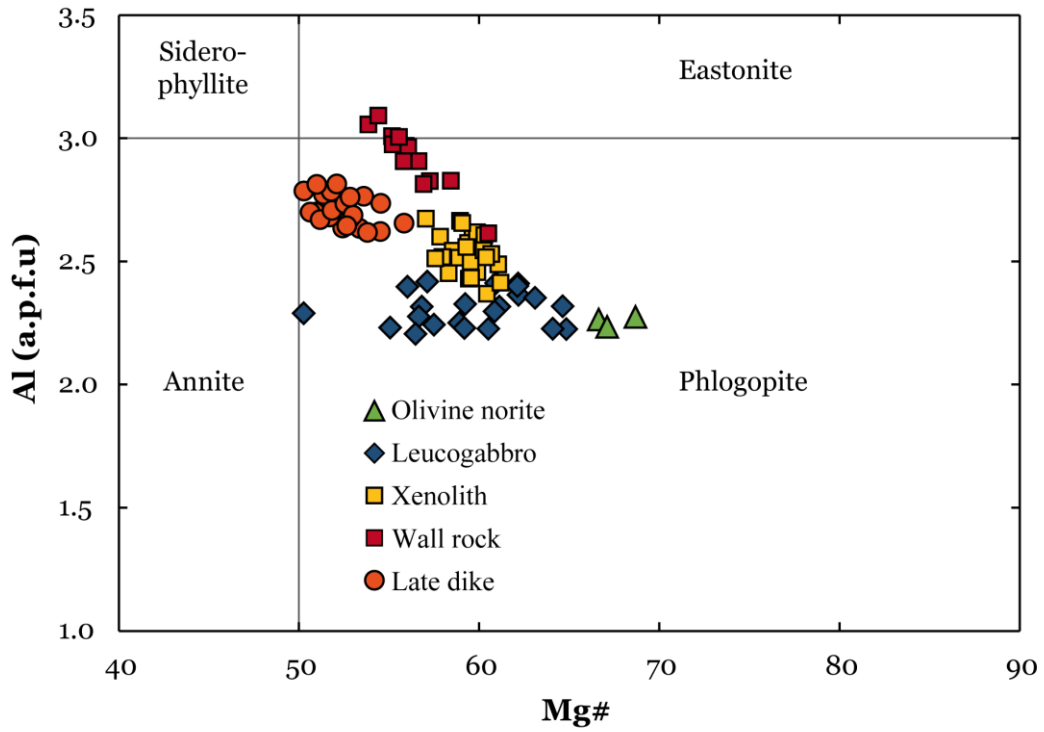

Figure 4.18 Compositional variation of Al (a.p.f.u.) and Mg# in biotite of the Älgliden dike rocks, the adjacent tonalite, xenoliths and a late dike. Abbreviation: (a.p.f.u.) atom per formula unit.

4.2.5.Amphibole

Amphibole occurs as primary (brown amphibole) and secondary phases in replacement of brown amphibole, pyroxene or biotite (green amphibole: i.e. actinolite-tremolite). The two types can be discriminated in the Al_2O_3 versus SiO_2 diagram (Figure 4.18), which shows that the green amphiboles have strong Al depletion and Si enrichment relative to primary amphibole. Brown primary amphibole of the leucogabbro does not significantly differ from that of the olivine norite but tends to have lower Al_2O_3 and higher SiO_2.

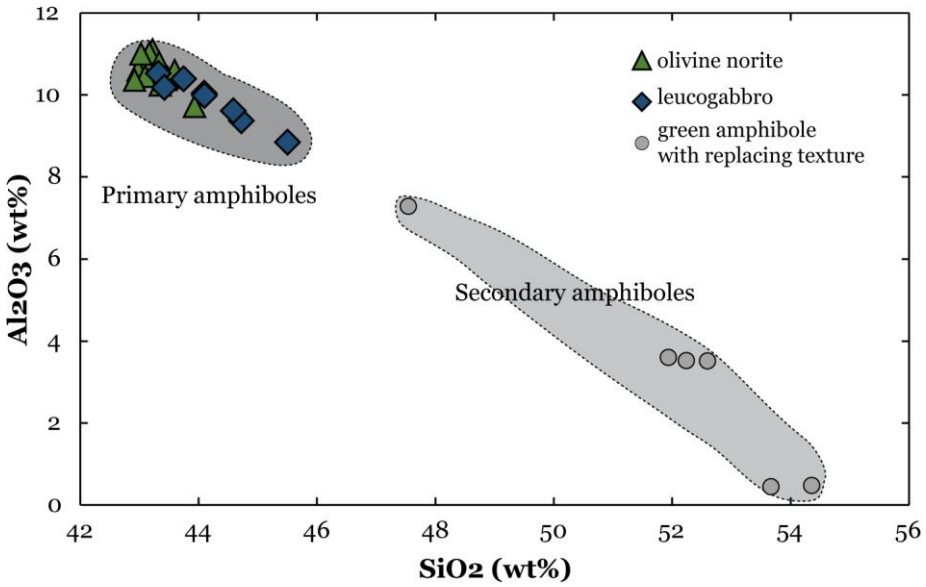

Figure 4.19 Variation diagram of Al_2O_3 and SiO_2 in amphibole of the olivine norite and the leucogabbro. Note the primary and secondary fields.

Table 4.6 Electron microprobe analyses of selected representative biotite and amphibole grains.

Sample no.[a]	Amphibole	[2]246.	[2]246.	[2]246.	[1]246.	[1]246.	Biotite	[2]246.	[2]246.	[2]246.	[2]246.	246.	264.	264.
		233.5	232.5	233.5	219.0	219.0		239.1	239.1	233.5	233.5	249.6	162.4	190.1
Host rock		Leuco.	Leuco.	O. nor.	O. nor.	O. nor.		O. nor.	O. nor.	Leuco.	Leuco.	L. dike	Tonalite	Xenolith
wt.%														
SiO_2		43.32	44.09	43.15	43.24	42.92		38.22	38.78	38.48	37.28	36.67	37.93	37.55
TiO_2		3.97	3.53	4.11	3.05	3.73		3.96	4.85	4.80	5.49	1.32	1.70	1.01
Al_2O_3		10.52	10.04	10.53	10.87	10.36		13.05	13.28	12.92	13.77	15.75	17.07	15.11
FeO		10.76	10.45	10.49	9.76	10.71		15.18	13.77	17.49	15.96	20.72	17.84	19.19
MnO		0.14	0.14	0.13	0.12	0.10		0.07	0.05	0.08	0.10	0.08	0.22	0.21
MgO		14.57	15.21	14.88	15.59	14.93		17.01	16.93	14.06	14.68	12.12	12.70	14.29
CaO		11.32	11.33	11.23	11.19	11.19		<D.L.	0.05	0.01	0.01	0.03	0.14	<D.L.
Na_2O		2.73	2.68	2.77	2.93	2.71		0.49	0.51	0.51	0.67	0.15	0.29	0.04
K_2O		0.83	0.87	0.73	0.72	0.83		8.20	8.40	8.76	8.58	9.24	9.37	8.86
Cr_2O_3		0.08	0.06	0.02	0.38	0.14		0.13	0.27	0.05	0.11	0.25	0.02	<D.L.
Cl		n.a.	0.03	n.a.	0.01	0.02		0.08	0.12	n.a.	n.a.	1.08	n.a.	n.a.
(OH)		1.77	1.65	1.96	1.34	1.73		3.11	2.49	2.84	3.36	2.57	2.73	3.73
Total		100.0	100.1	100.0	99.28	99.36		99.49	99.56	100.0	100.0	100.0	100.0	100.0
Cation numbers based on 23 or 22 oxygens for amphibole or for biotite, respectively.														
mol.%														
Si		6.28	6.36	6.25	6.24	6.25		5.63	5.64	5.69	5.51	5.56	5.60	5.64
Ti		0.43	0.38	0.45	0.33	0.41		0.44	0.53	0.53	0.61	0.15	0.19	0.11
Al		1.80	1.71	1.80	1.85	1.78		2.26	2.27	2.25	2.40	2.82	2.97	2.67
Fe^{3+}		0.32	0.40	0.40	0.55	0.49								
Fe^{2+}		0.99	0.86	0.87	0.63	0.81		1.87	1.67	2.16	1.97	2.63	2.20	2.41
Mn		0.02	0.02	0.02	0.01	0.01		0.01	0.01	0.01	0.01	0.01	0.03	0.03
Mg		3.15	3.27	3.21	3.35	3.24		3.73	3.67	3.10	3.24	2.74	2.79	3.20
Ca		1.76	1.75	1.74	1.73	1.74		<D.L.	0.01	0.00	0.00	0.00	0.02	<D.L.
Na		0.77	0.75	0.78	0.82	0.76		0.14	0.14	0.15	0.19	0.04	0.08	0.01
K		0.15	0.16	0.14	0.13	0.15		1.54	1.56	1.65	1.62	1.79	1.76	1.70
Cr		0.01	0.01	0.00	0.04	0.02		0.01	0.03	0.01	0.01	0.03	0.00	<D.L.
Cl		n.a.	0.01	n.a.	0.00	0.01		0.02	0.03	n.a.	n.a.	0.28	n.a.	n.a.
OH		1.77	1.65	1.96	1.34	1.73		3.11	2.49	2.84	3.36	2.57	2.73	3.73
∑ cations		15.68	15.66	15.66	15.69	15.66		15.64	15.53	15.55	15.57	15.78	15.65	15.77
Mg#		76.1	79.1	78.7	84.2	80.0		66.6	68.7	58.9	62.1	51.0	55.9	57.0

Abbreviations: O. nor.: Olivine norite; Leuco: Leucogabbro; L.dike: Late dike; <D.L.: below detection limit.

(a) 1 and 2 refer to olivine norites of type-1 and type-2, respectively.

4.3. Bulk rock major and trace elements

The major and trace element compositions presented in this section mainly come from this study (Table 4.7) and unpublished data provided by Boliden (see Section 3.1). Most samples come from core ALA246 and some others come from cores ALA264 and -248. Unpublished data include samples from ALA30, -31, -47, -49 and -246. Unpublished data from ALA246 consist in 3m-long half core samples implying that some analyses represent mixtures of different lithologies. Such analyses have not been plotted in variation diagrams. All the data have been normalized to 100% excluding (i) the loss of ignition and sulfides for the Älgliden dike rocks and (ii) the loss of ignition for the wall rocks and the late dike rocks which do not contain significant sulfides. Explanation for the sulfide correction is given in Appendix 6.
Seven samples have been disregarded. Three of them (246.223.3, 248.259.1 and 264.217.5) actually consist of mixtures of lithologies and the 4 others (264.196.7, 264.180.5, 264.185.6 and 264.190.2) show high loss of ignition and/or remobilization of mobile elements such as Rb, Ba, K (Appendix 10).

4.3.1. Olivine norite

Olivine norites are basic-ultrabasic rocks (42.6-52.2% SiO_2) characterized by high MgO (16.6-26.7%) and $Fe_2O_{3\,tot}$ (15.3-20.8%) and low TiO_2 (0.41-0.94%) contents.
Overall, SiO_2, Al_2O_3, CaO and incompatible trace element contents decrease with increasing MgO while Cr_2O_3 and $Fe_2O_{3\,tot}$ increases (Figure 4.20 and Table 4.7). Except for Cr_2O_3 and mobile elements (e.g. Na_2O, K_2O, Sr), the olivine norites define trends that intercept the olivine composition, within the error of the regression. This observation, together with their high MgO contents, support the petrographic observations showing that these samples are cumulates formed by accumulation of olivine. Alternatively, they could have represented residual liquids, as discussed in Section 4.4.1. The two analyzed samples of Type-2 olivine norite are slightly shifted from the trend toward the orthopyroxene composition in SiO_2 and Al_2O_3 *vs.* MgO diagrams: they have higher SiO_2 and lower Al_2O_3 and MgO than the type-1 olivine norites of the same core. Olivine norites from core ALA264, the most altered samples from the dataset, have lower Na_2O contents than the norites from ALA246 (Table 4.7).
In core ALA246, the olivine norites from the southern and northern part of the dike define two distinct trends in the Cr_2O_3 *vs.* MgO diagram, the northern samples being enriched in Cr_2O_3. These two trends can be explained by different amount of cumulus chromite, 0.8% for the northern trend and 0.4% for the southern trend. Olivine norites from core ALA264, as well as from 4 other cores located in the NE termination (Boliden data: ALA30, -31, -47 and -49), plot in between these two trends.

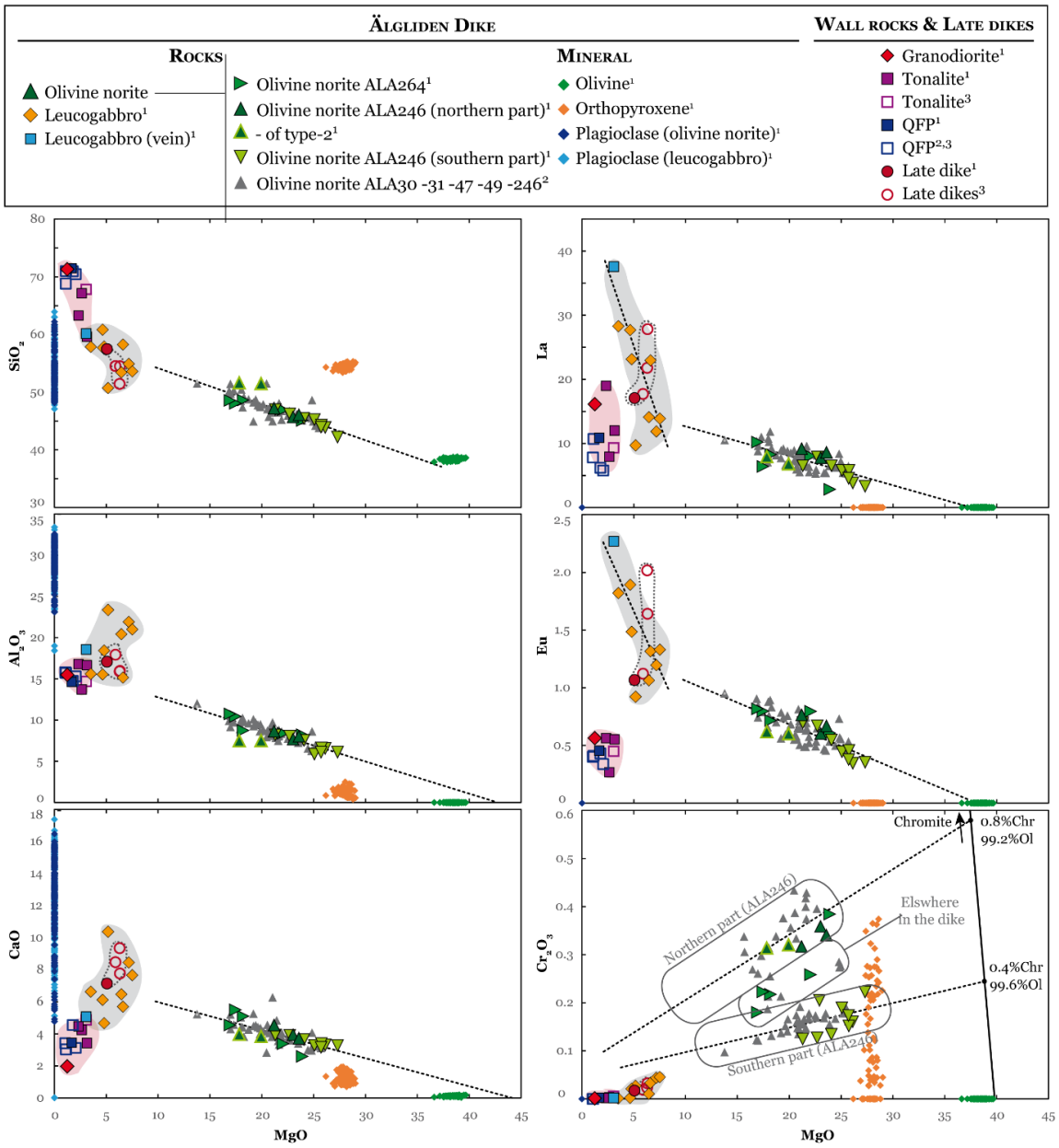

Figure 4.20 Variation diagrams of major and trace element versus MgO contents (wt.%) showing olivine norite, leucogabbro, wall rock, xenolith, late dike and mineral compositions. The dashed lines are the regression lines of all olivine norites and/or leucogabbros. In the Cr_2O_3-MgO diagram the dashed lines are the regression lines of the olivine norites of the northern and southern part of the dike. 1: This study; 2: Unpublished data from Boliden; 3: Data from Bejgarn et al. (2011).

Table 4.7 Major and trace element contents in representative samples from Älgliden dike and wallrocks.

	Sample number	246.204.6	246.212.5	246.219.0	246.224.6	246.239.1	246.252.5
	Unit	Älgliden dike	Älgliden dike	Älgliden dike	Älgliden dike	Älgliden dike	Älgliden dike
	Rock type[a]	olivine norite[2N]	olivine norite[1N]	olivine norite[1N]	olivine norite[1N]	olivine norite[2N]	olivine norite[S]
Major elements (wt%)[b]	SiO_2	50.75	46.48	44.92	45.32	50.69	45.18
	Al_2O_3	7.38	8.53	7.56	7.90	7.42	8.01
	Fe_2O_{3TOT}	17.09	16.25	17.84	16.58	15.29	18.45
	MgO	17.52	20.84	22.62	23.18	19.63	22.47
	CaO	3.91	4.48	3.88	3.66	3.78	3.39
	Na_2O	1.19	1.35	1.27	1.36	1.29	0.53
	K_2O	0.63	0.73	0.59	0.76	0.60	0.82
	TiO_2	0.87	0.66	0.60	0.54	0.77	0.68
	P_2O_5	0.16	0.15	0.15	0.14	0.00	0.14
	MnO	0.20	0.20	0.22	0.21	0.22	0.14
	Cr_2O_3	0.31	0.31	0.35	0.34	0.32	0.20
	SUM	100.0	100.0	100.0	100.0	100.0	100.0
	LOI	2.2	2.2	4.1	3.0	1.7	6.4
	S	0.24	0.14	2.42	0.30	0.42	0.44
Trace elements (ppm)[c]	Li	6.03	9.01	9.06	9.13	7.68	10.12
	Sc	22.4	16.7	11.8	14.6	23.3	11.3
	Ti	4819	3508	2979	2857	3859	3449
	V	169	113	101	94	128	97
	Cr	2038	2069	2180	2196	2089	1277
	Co	91.2	86.7	164.7	104.0	51.9	115.9
	Ni	551	363	1055	473	461	515
	Cu	266	167	3107	511	595	412
	Zn	136	140	159	141	135	136
	Ga	12.1	11.1	10.0	10.2	10.8	10.1
	Rb	11.2	13.3	10.5	13.5	11.0	13.2
	Sr	178	228	187	202	184	74
	Y	10.5	11.2	8.9	10.3	10.9	9.4
	Zr	34.5	48.8	39.8	52.0	38.9	32.8
	Nb	2.62	3.19	2.63	2.89	2.76	2.73
	Cs	1.00	1.23	0.63	0.62	0.73	0.92
	Ba	188	259	205	244	215	231
	La	7.94	9.18	7.79	8.61	6.82	6.78
	Ce	17.2	20.2	17.0	18.9	15.2	15.4
	Pr	2.27	2.68	2.24	2.52	2.09	2.14
	Nd	9.45	11.15	9.32	10.59	9.04	9.30
	Sm	2.08	2.43	1.97	2.26	2.10	2.09
	Eu	0.620	0.765	0.604	0.669	0.602	0.571
	Gd	1.94	2.17	1.79	2.05	1.98	1.96
	Tb	0.294	0.328	0.264	0.306	0.302	0.287
	Dy	1.85	2.00	1.60	1.88	1.91	1.75
	Ho	0.382	0.406	0.320	0.366	0.393	0.344
	Er	1.12	1.14	0.91	1.06	1.16	0.98
	Yb	1.1	1.1	0.8	1.0	1.1	0.9
	Lu	0.16	0.16	0.13	0.14	0.17	0.13
	Hf	1.10	1.33	1.20	1.37	1.19	1.05
	Ta	0.158	0.191	0.160	0.180	0.162	0.158
	Tl	0.761	0.351	0.285	0.257	0.258	0.310
	Pb	4.07	14.59	37.68	16.13	10.93	7.15
	Th	1.05	1.13	1.06	1.33	1.01	0.80
	U	0.854	0.901	1.115	1.205	0.769	0.639

(a) 1, 2 refer to olivine norites of type-1 and type-2 and N, S to olivine norites from northern and southern sides.

(b) Normalized to 100% without LOI and S for Algliden rocks, and without LOI for others, as described in Section 3.3

(c) Normalized to 100% without LOI

Table 4.7 (cont.)

Sample no.	246.280.8	246.290.7	246.293.1	246.300.9	246.308.0	246.319.6
Unit	Älgliden dike	Älgliden dike	Älgliden dike	Älgliden dike	Älgliden dike	Älgliden dike
Rock type[a]	olivine norite[1S]	olivine norite[1S]	olivine norite[1S]	olivine norite[1S]	olivine norite[1S]	olivine norite[1S]
SiO_2	43.09	41.48	44.37	43.47	43.09	45.41
Al_2O_3	6.44	6.01	5.77	6.51	5.98	7.90
Fe_2O_{3TOT}	19.33	20.49	19.73	19.02	20.46	17.70
MgO	25.65	26.84	24.57	25.27	25.21	22.29
CaO	3.24	3.21	3.21	3.33	3.09	3.84
Na_2O	0.93	0.64	0.85	0.96	0.78	1.14
K2O	0.39	0.26	0.38	0.44	0.41	0.58
TiO_2	0.40	0.53	0.48	0.43	0.55	0.61
P_2O_5	0.13	0.09	0.21	0.20	0.00	0.19
MnO	0.24	0.23	0.25	0.23	0.25	0.22
Cr_2O_3	0.16	0.22	0.19	0.15	0.17	0.12
SUM	100.0	100.0	100.0	100.0	100.0	100.0
LOI	6.7	6.1	7.1	6.7	6.3	4.5
S	2.23	2.71	3.31	2.43	2.78	0.27
Li	8.19	4.98	6.30	7.99	7.40	10.83
Sc	13.1	11.6	11.6	10.2	12.7	12.0
Ti	1780	2562	2309	2066	2647	3044
V	58	87	76	65	90	83
Cr	956	1319	1088	897	1019	808
Co	140.1	170.1	204.2	163.4	206.5	113.2
Ni	727	929	1170	932	1267	447
Cu	2215	1807	4505	2969	3169	272
Zn	140	160	187	148	185	132
Ga	6.6	7.0	6.8	6.8	7.5	8.8
Rb	5.2	4.3	6.3	7.4	7.1	11.4
Sr	165	147	113	161	135	210
Y	4.7	4.9	6.5	6.3	5.4	9.2
Zr	18.6	18.2	23.3	24.1	27.9	35.9
Nb	1.24	1.26	1.66	1.75	1.65	2.59
Cs	0.21	0.20	0.29	0.48	0.88	1.62
Ba	124	96	140	156	148	228
La	3.83	3.31	5.79	5.79	4.56	7.89
Ce	8.2	7.5	12.7	12.6	9.8	17.2
Pr	1.09	1.04	1.67	1.66	1.30	2.29
Nd	4.57	4.49	7.10	7.00	5.46	9.62
Sm	0.99	1.01	1.48	1.46	1.17	2.07
Eu	0.346	0.355	0.445	0.457	0.378	0.670
Gd	0.91	0.93	1.34	1.33	1.07	1.86
Tb	0.138	0.141	0.194	0.187	0.157	0.274
Dy	0.85	0.88	1.17	1.14	0.96	1.64
Ho	0.172	0.176	0.241	0.225	0.196	0.333
Er	0.50	0.51	0.67	0.63	0.57	0.93
Yb	0.5	0.5	0.6	0.6	0.5	0.8
Lu	0.08	0.07	0.09	0.09	0.08	0.12
Hf	0.55	0.49	0.71	0.73	0.74	1.08
Ta	0.072	0.067	0.097	0.101	0.103	0.150
Tl	0.175	0.159	0.205	0.323	0.506	0.340
Pb	13.73	13.38	17.14	12.40	13.70	6.74
Th	0.46	0.32	0.56	0.61	0.65	0.93
U	0.353	0.248	0.432	0.443	0.502	0.702

(a) 1, 2 refer to olivine norites of type-1 and type-2 and N, S to olivine norites from northern and southern sides.
(b) Normalized to 100% without LOI and S for Älgliden rocks, and without LOI for others, as described in Section 3.3
(c) Normalized to 100% without LOI

Table 4.7 (cont.)

Sample no.	246.334.0	246.340.8	264.169.2	264.172.8	264.200.4	264.205.8
Unit	Älgliden dike	Älgliden dike	Älgliden dike	Älgliden dike	Älgliden dike	Älgliden dike
Rock type[a]	olivine norite[1S]	olivine norite[S]	olivine norite	olivine norite	olivine norite	olivine norite
SiO_2	44.65	46.12	47.82	47.07	44.36	46.13
Al_2O_3	7.42	8.04	8.60	10.23	8.08	8.25
Fe_2O_{3TOT}	18.14	18.62	17.45	18.04	19.64	17.92
MgO	23.62	20.89	17.89	17.08	23.49	21.66
CaO	3.58	3.85	5.02	5.38	2.55	3.33
Na_2O	1.08	0.70	0.31	0.31	0.29	0.43
K2O	0.48	0.65	1.46	0.34	0.24	1.00
TiO_2	0.51	0.70	0.92	0.92	0.58	0.65
P_2O_5	0.17	0.14	0.13	0.18	0.15	0.17
MnO	0.23	0.17	0.19	0.22	0.24	0.21
Cr_2O_3	0.13	0.12	0.21	0.22	0.38	0.25
SUM	100.0	100.0	100.0	100.0	100.0	100.0
LOI	5.7	6.2	5.9	7.5	6.8	6.0
S	0.28	0.66	0.42	1.40	1.91	0.32
Li	11.14	6.72	10.64	3.53	3.44	8.16
Sc	11.2	16.2	23.8	19.1	14.3	14.2
Ti	2511	3376	4735	4480	2621	3066
V	73	98	163	131	104	105
Cr	842	770	1357	1324	2305	1615
Co	117.2	91.0	26.0	45.0	99.5	54.9
Ni	496	563	567	665	1004	656
Cu	342	855	84	3788	706	129
Zn	129	182	158	191	140	144
Ga	8.0	9.3	10.9	11.9	8.9	10.2
Rb	9.1	11.4	46.5	6.7	3.2	19.0
Sr	213	102	32	61	37	57
Y	7.2	12.5	12.8	12.0	7.7	12.3
Zr	29.8	31.7	48.7	51.9	36.1	48.9
Nb	2.21	2.59	2.81	3.36	2.17	3.08
Cs	1.11	0.84	3.94	0.83	0.47	1.85
Ba	199	250	225	91	51	274
La	6.51	6.51	8.27	6.41	2.85	8.05
Ce	14.0	15.9	18.7	15.9	7.9	18.6
Pr	1.82	2.35	2.52	2.23	1.20	2.56
Nd	7.63	10.87	10.54	10.03	5.55	11.25
Sm	1.60	2.63	2.30	2.53	1.48	2.61
Eu	0.546	0.698	0.716	0.797	0.607	0.795
Gd	1.48	2.49	2.28	2.42	1.49	2.43
Tb	0.212	0.375	0.347	0.372	0.237	0.365
Dy	1.29	2.30	2.19	2.28	1.46	2.25
Ho	0.255	0.457	0.457	0.468	0.297	0.461
Er	0.72	1.26	1.30	1.32	0.85	1.30
Yb	0.7	1.1	1.2	1.2	0.8	1.2
Lu	0.10	0.16	0.18	0.19	0.11	0.17
Hf	0.88	1.08	1.25	1.45	0.99	1.35
Ta	0.130	0.142	0.158	0.200	0.134	0.187
Tl	0.328	0.472	1.318	0.533	0.275	0.730
Pb	7.73	13.29	1.49	2.04	4.17	4.15
Th	0.79	0.70	1.05	1.07	0.91	1.24
U	0.593	0.489	0.876	0.962	0.687	1.086

(a) 1, 2 refer to olivine norites of type-1 and type-2 and N, S to olivine norites from northern and southern sides.
(b) Normalized to 100% without LOI and S for Algliden rocks, and without LOI for others, as described in Section 3.3
(c) Normalized to 100% without LOI

Table 4.7 (cont.)

Sample no.	264.212.5	246.212.6	248.213.2	246.230.2	246.240.8	248.265.0
Unit	Älgliden dike	Älgliden dike	Älgliden dike	Älgliden dike	Älgliden dike	Älgliden dike
Rock type[a]	olivine norite	leucogabbro	leucogabbro	leucogabbro	leucogabbro	leucogabbro
SiO_2	47.77	59.92	57.28	57.83	54.83	60.45
Al_2O_3	10.57	18.51	15.45	15.05	21.90	15.45
Fe_2O_{3TOT}	17.27	3.95	9.72	7.10	1.35	6.29
MgO	16.65	3.05	3.47	6.56	7.16	4.62
CaO	4.48	5.05	6.57	5.65	8.44	6.08
Na_2O	0.87	6.09	4.83	5.06	4.20	5.14
K2O	1.21	1.85	0.96	1.37	1.12	0.35
TiO_2	0.63	0.92	1.10	0.60	0.60	0.84
P_2O_5	0.18	0.57	0.42	0.61	0.22	0.62
MnO	0.20	0.09	0.20	0.14	0.15	0.15
Cr_2O_3	0.18	0.00	0.00	0.03	0.04	0.00
SUM	100.0	100.0	100.0	100.0	100.0	100.0
LOI	5.4	3.5	5.8	4.4	5.0	7.3
S	0.60	0.02	0.04	1.38	3.30	0.50
Li	10.12	10.85	13.95	17.71	11.86	21.23
Sc	16.1	4.0	15.3	10.3	13.7	11.3
Ti	3035	5093	5835	3067	2503	4314
V	105	95	127	64	49	87
Cr	1127	14	8	209	249	13
Co	54.5	12.5	11.2	55.5	92.0	37.3
Ni	710	24	13	250	732	48
Cu	205	227	151	1306	19333	264
Zn	159	56	1048	69	167	123
Ga	12.1	19.3	18.9	16.3	15.2	16.4
Rb	24.7	37.1	18.0	30.2	18.8	4.9
Sr	65	579	387	349	566	298
Y	15.3	23.6	32.0	20.5	14.5	32.6
Zr	57.1	120.5	144.4	183.0	55.8	179.5
Nb	3.81	7.06	8.50	7.48	4.02	10.13
Cs	1.94	1.93	1.62	1.83	1.59	0.34
Ba	363	1396	489	525	466	356
La	10.21	37.57	28.29	22.96	11.86	27.70
Ce	23.6	76.8	62.0	49.6	26.2	61.1
Pr	3.21	9.38	7.95	6.30	3.56	7.91
Nd	13.58	36.67	32.93	25.23	15.22	32.91
Sm	3.10	6.74	7.09	5.02	3.42	7.18
Eu	0.817	2.270	1.820	1.316	1.195	1.892
Gd	2.95	5.73	6.30	4.30	3.04	6.50
Tb	0.438	0.758	0.936	0.625	0.449	0.953
Dy	2.72	4.27	5.69	3.70	2.74	5.74
Ho	0.555	0.806	1.127	0.724	0.543	1.178
Er	1.61	2.16	3.19	2.04	1.49	3.18
Yb	1.5	1.7	2.8	1.8	1.2	2.7
Lu	0.22	0.24	0.41	0.27	0.18	0.39
Hf	1.58	3.01	3.70	4.20	1.58	4.61
Ta	0.231	0.458	0.531	0.503	0.220	0.674
Tl	0.535	0.487	0.256	0.580	0.314	0.076
Pb	4.99	30.24	18.40	31.56	44.55	139.95
Th	1.49	4.52	3.90	4.26	1.16	4.96
U	1.291	3.325	4.391	3.315	0.902	4.865

(a) 1, 2 refer to olivine norites of type-1 and type-2 and N, S to olivine norites from northern and southern sides.
(b) Normalized to 100% without LOI and S for Algliden rocks, and without LOI for others, as described in Section 3.3
(c) Normalized to 100% without LOI

Table 4.7 (cont.)

Sample no.	246.199.0	246.242.5	248.230.4	246.249.6	264.223.8	246.362.8
Unit	Älgliden dike	Älgliden dike	Älgliden dike	late dike	wallrock	wallrock
Rock type[a]	leucogabbro	leucogabbro	leucogabbro	andesite	Granodiorite	tonalite
SiO_2	57.27	53.36	53.05	56.27	70.85	66.00
Al_2O_3	18.30	20.91	20.28	16.73	15.40	13.47
Fe_2O_{3TOT}	7.24	4.25	6.90	7.52	4.79	8.59
MgO	4.75	7.48	6.43	4.96	1.23	2.60
CaO	4.64	7.63	6.42	6.99	1.96	4.17
Na_2O	5.59	4.38	3.86	4.61	3.84	2.63
K2O	0.91	1.01	2.37	1.22	1.60	1.63
TiO_2	0.79	0.64	0.41	0.79	0.25	0.34
P_2O_5	0.36	0.18	0.16	4.00	0.00	0.22
MnO	0.12	0.12	0.11	0.12	0.03	0.07
Cr_2O_3	0.02	0.05	0.01	0.02	0.00	0.00
SUM	100.0	100.0	100.0	103.2	100.0	99.7
LOI	3.1	3.7	4.2	3.4	2.4	2.9
S	0.23	0.77	0.10	0.54	0.05	0.28
Li	9.77	14.91	13.40	16.11	9.53	12.39
Sc	13.6	12.9	11.3	18.3	15.7	19.9
Ti	4268	3048	2106	4066	1283	1239
V	100	48	51	114	51	89
Cr	137	293	66	114	4	14
Co	23.4	19.1	23.0	18.1	4.0	6.4
Ni	82	80	69	48	3	4
Cu	1162	283	93	31	11	600
Zn	153	42	55	104	20	42
Ga	20.2	17.6	17.0	17.8	13.1	10.5
Rb	19.3	19.6	45.0	29.8	27.2	27.7
Sr	644	623	720	607	253	145
Y	19.5	16.6	14.5	13.5	19.2	15.2
Zr	60.8	71.7	71.4	86.5	125.4	43.9
Nb	7.21	5.42	4.00	5.39	4.62	3.03
Cs	1.23	1.41	1.52	1.79	0.99	1.52
Ba	466	556	837	620	378	216
La	23.15	13.86	14.07	17.08	16.11	7.92
Ce	49.3	30.5	29.9	36.4	32.3	16.5
Pr	6.10	4.09	3.85	4.56	3.96	1.95
Nd	24.42	17.38	15.60	17.86	14.96	7.61
Sm	4.97	3.80	3.25	3.50	3.08	1.72
Eu	1.485	1.330	1.063	1.067	0.563	0.267
Gd	4.26	3.41	2.80	2.83	2.82	1.76
Tb	0.620	0.507	0.420	0.408	0.478	0.319
Dy	3.61	3.05	2.56	2.45	3.16	2.24
Ho	0.705	0.600	0.504	0.480	0.683	0.518
Er	1.91	1.66	1.44	1.35	2.05	1.65
Yb	1.6	1.4	1.3	1.2	1.9	1.8
Lu	0.23	0.20	0.19	0.18	0.27	0.27
Hf	1.98	2.21	1.85	2.48	3.51	1.34
Ta	0.414	0.304	0.256	0.314	0.345	0.314
Tl	0.203	0.218	0.659	0.380	0.283	0.388
Pb	45.71	43.49	34.56	15.33	3.22	1.62
Th	2.73	1.56	1.97	2.95	5.61	1.10
U	2.413	1.282	2.125	1.795	2.624	4.247

(a) 1, 2 refer to olivine norites of type-1 and type-2 and N, S to olivine norites from northern and southern sides.
(b) Normalized to 100% without LOI and S for Algliden rocks, and without LOI for others, as described in Section 3.3
(c) Normalized to 100% without LOI

Table 4.7 (cont.)

Sample no.	246.196.3	264.156.5	264.162.4
Unit	wallrock	wallrock	wallrock
Rock type[a]	QFP	tonalite	tonalite
SiO_2	70.39	62.36	58.67
Al_2O_3	14.42	16.55	16.40
Fe_2O_{3TOT}	4.72	8.79	12.49
MgO	1.65	2.30	3.08
CaO	3.39	4.40	3.36
Na_2O	3.89	3.18	3.24
K2O	0.80	1.74	2.13
TiO_2	0.28	0.42	0.45
P_2O_5	0.00	0.00	0.00
MnO	0.06	0.05	0.06
Cr_2O_3	0.00	0.00	0.00
SUM	99.6	99.8	99.9
LOI	2.7	3.1	2.5
S	0.38	0.21	0.11
Li	11.54	13.23	17.86
Sc	13.3	24.8	32.1
Ti	1448	2110	2273
V	86	146	180
Cr	11	9	10
Co	7.9	13.9	8.4
Ni	4	5	6
Cu	381	75	84
Zn	61	47	60
Ga	16.3	14.6	14.9
Rb	16.8	51.2	74.8
Sr	235	285	301
Y	18.1	27.1	26.1
Zr	77.2	46.8	39.0
Nb	4.09	7.18	6.12
Cs	1.79	2.24	4.44
Ba	239	244	232
La	10.86	18.96	12.00
Ce	30.4	41.8	31.1
Pr	2.80	5.22	4.24
Nd	11.05	20.13	16.78
Sm	2.47	4.10	3.50
Eu	0.454	0.562	0.552
Gd	2.43	3.59	3.06
Tb	0.411	0.599	0.545
Dy	2.75	4.02	3.76
Ho	0.614	0.886	0.859
Er	1.85	2.86	2.81
Yb	1.9	3.1	3.2
Lu	0.28	0.45	0.47
Hf	2.21	1.87	1.65
Ta	0.318	0.497	0.407
Tl	0.221	0.842	1.464
Pb	4.88	4.80	3.63
Th	3.10	3.65	1.37
U	2.905	2.227	1.629

(a) 1, 2 refer to olivine norites of type-1 and type-2 and N, S to olivine norites from northern and southern sides.
(b) Normalized to 100% without LOI and S for Algliden rocks, and without LOI for others, as described in Section 3.3
(c) Normalized to 100% without LOI

In the mantle-normalized multi-element diagram of Figure 4.21, the olivine norites show remarkably parallel patterns. The concentrations in incompatible elements increase as the MgO content, and therefore the amount of cumulus olivine, decrease (Figure 4.20). Olivine norites from ALA264 tend to be the more enriched in incompatible elements, consistent with their relatively low MgO contents. In core ALA246, olivine norites of the northern part are globally more enriched than those of the southern part. The fractionation between Light Rare Earth Elements (LREE) and Middle Rare Earth Elements (MREE) is relatively well expressed (i.e. $La_N/Sm_N \approx 2.2$; Figure 4.22a and Figure 4.21). The fractionation of MREE relative to the Heavy Rare Earth Elements (HREE) is of similar magnitude (i.e. $Gd_N/Yb_N \approx 1.7$; Figure 4.22b and Figure 4.21). These fractionations remain constant and independent of the enrichment in incompatible elements (Figure 4.22).

In Figure 4.21 the incompatible trace element patterns of olivine norites are marked by positive anomalies of large-ion-lithophile elements (Pb, Cs, Ba) and U and negative anomalies in most high-field-strength elements (Nb, Ta, Zr, Hf, not Y) and Th. The positive Pb anomaly is the most pronounced but is sensitive to alteration since the most altered samples, from ALA264, have the smallest Pb anomalies (Figure 4.23). This figure also shows that the magnitude of Nb and Pb anomalies are not correlated. The olivine norites from ALA246 show a positive anomaly in Sr while more altered olivine norites from ALA264 show a negative anomaly. Europium anomalies, either slightly positive (max value is $Eu/Eu^*=1.25$, with $Eu^*=\sqrt{(Sm.Gd)}$) or slightly negative (min value is $Eu/Eu^*=0.83$), are observed the olivine norites.

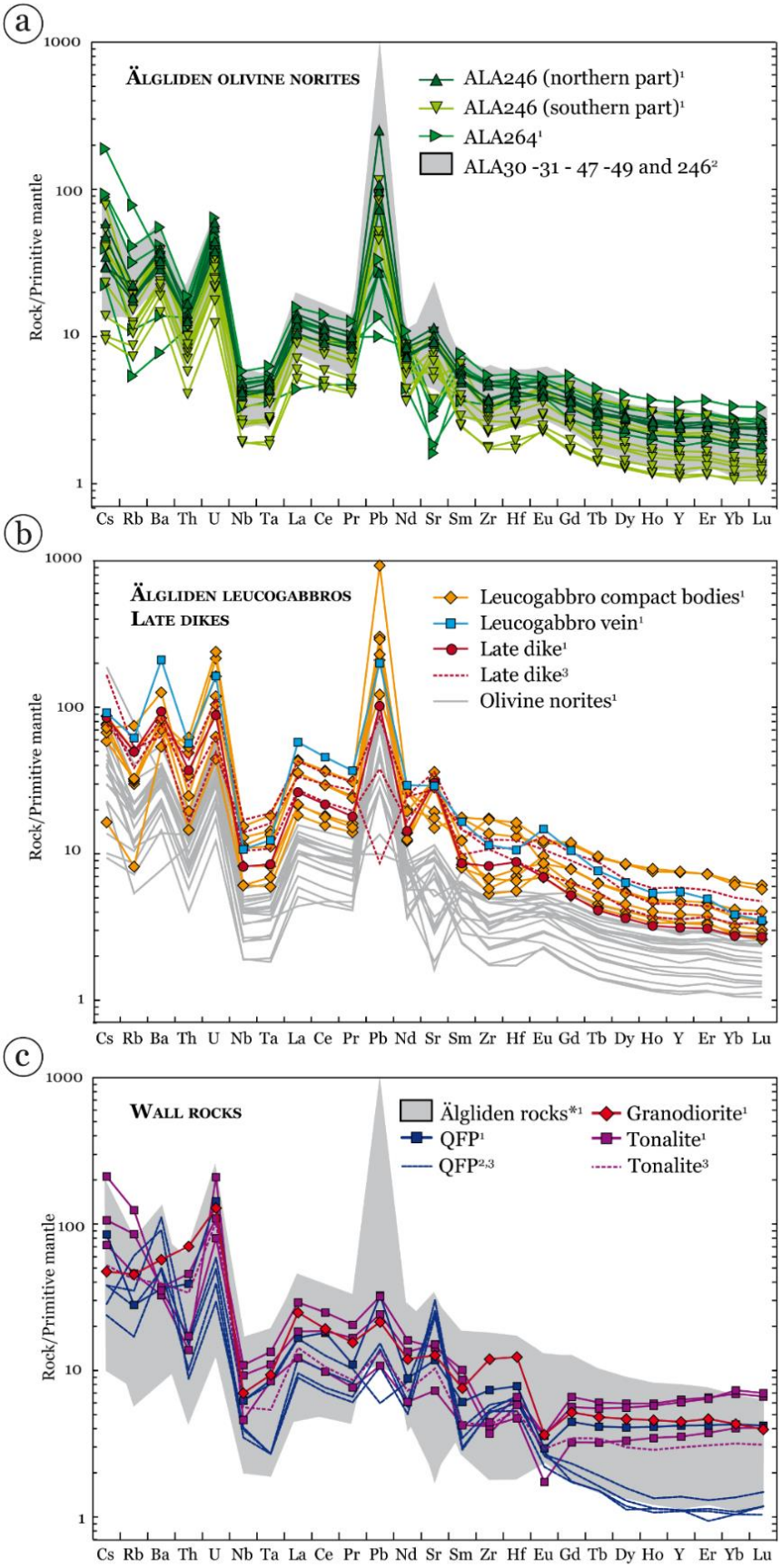

Figure 4.21 Mantle normalized multi-element diagram (Mc-Donough & Sun, 1995) of (a) the olivine norites, (b) the leucogabbros and the late dikes and (c) the country rocks. 1: this study; 2: Unpublished data from Boliden; 3: Bejgarn et al., 2011; *: All Älgliden rocks except the leucogabbro vein, whose REE fractionation is not re-presentative of all other Älgliden rocks.

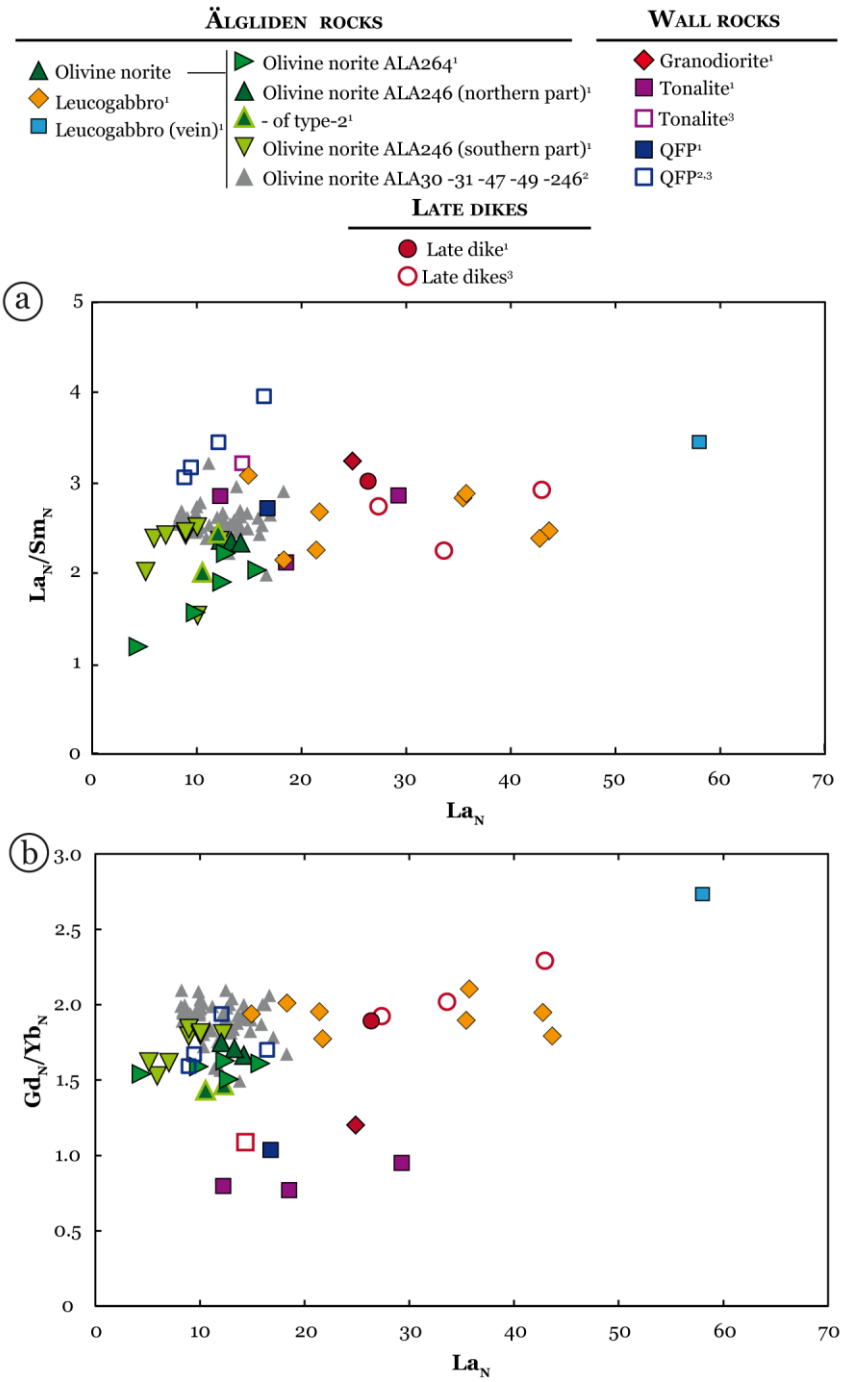

Figure 4.22 Variation diagram of (a) La_N/Sm_N (LREE/MREE) and (b) Gd_N/Yb_N (MREE/HREE) ratios versus La_N contents. Mantle normalization is done according to (McDonough & Sun, 1995). 1: This study; 2: Unpublished data from Boliden; 3: Bejgarn et al. (2011).

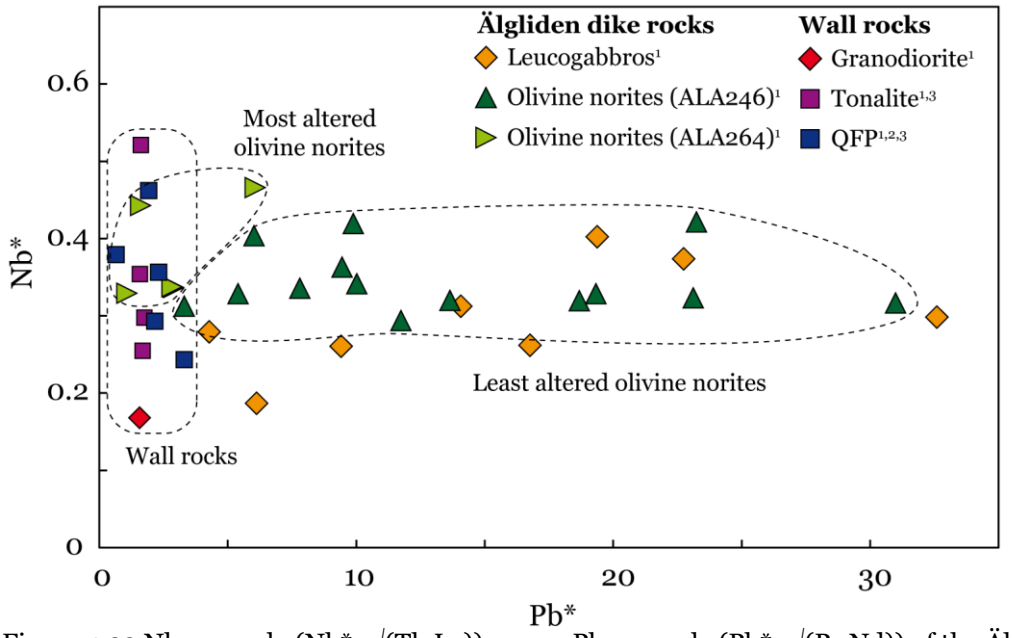

Figure 4.23 Nb anomaly (Nb*=√(Th.La)) versus Pb anomaly (Pb*=√(Pr.Nd)) of the Älgliden dike rocks and the wall rock. 1: This study; 2: Unpublished data from Boliden; 3: Bejgarn et al. (2011).

Figure 4.24 shows compositional profiles observed along the core ALA246 for a selection of major and trace element concentrations. Major and trace elements vary according to 1) the amount of olivine and 2) the polarity of the dike (i.e. northern versus southern parts).

Overall, the chemical composition is directly correlated to the amount of modal olivine: the cross-dike profiles of MgO contents have parabolic shapes similar to those of olivine modal proportions and mirroring those of incompatible elements such as TiO_2 or La. The core of the dike (highlighted by part horizontal dashed lines in Figure 4.24) shows elevated modal olivine proportions and MgO contents together with low incompatible element contents, whereas each margins of the dike shows the reverse relationship with low amounts of modal olivine and MgO and high incompatible element contents.

The dike can be divided into two unequal length sections with slightly different compositions, separated by a late dike of basaltic andesite. The southern half (downhole part of the core) tends to have lower incompatible element and higher MgO contents than the northern part. The average content of Cr_2O_3 and MgO are decoupled in the northern and southern part of the dike: the northern part has low MgO and high Cr_2O_3 average contents relatively to the southern part (Figure 4.24), while Cr_2O_3 and MgO contents are positively correlated in both parts (Figure 4.20).

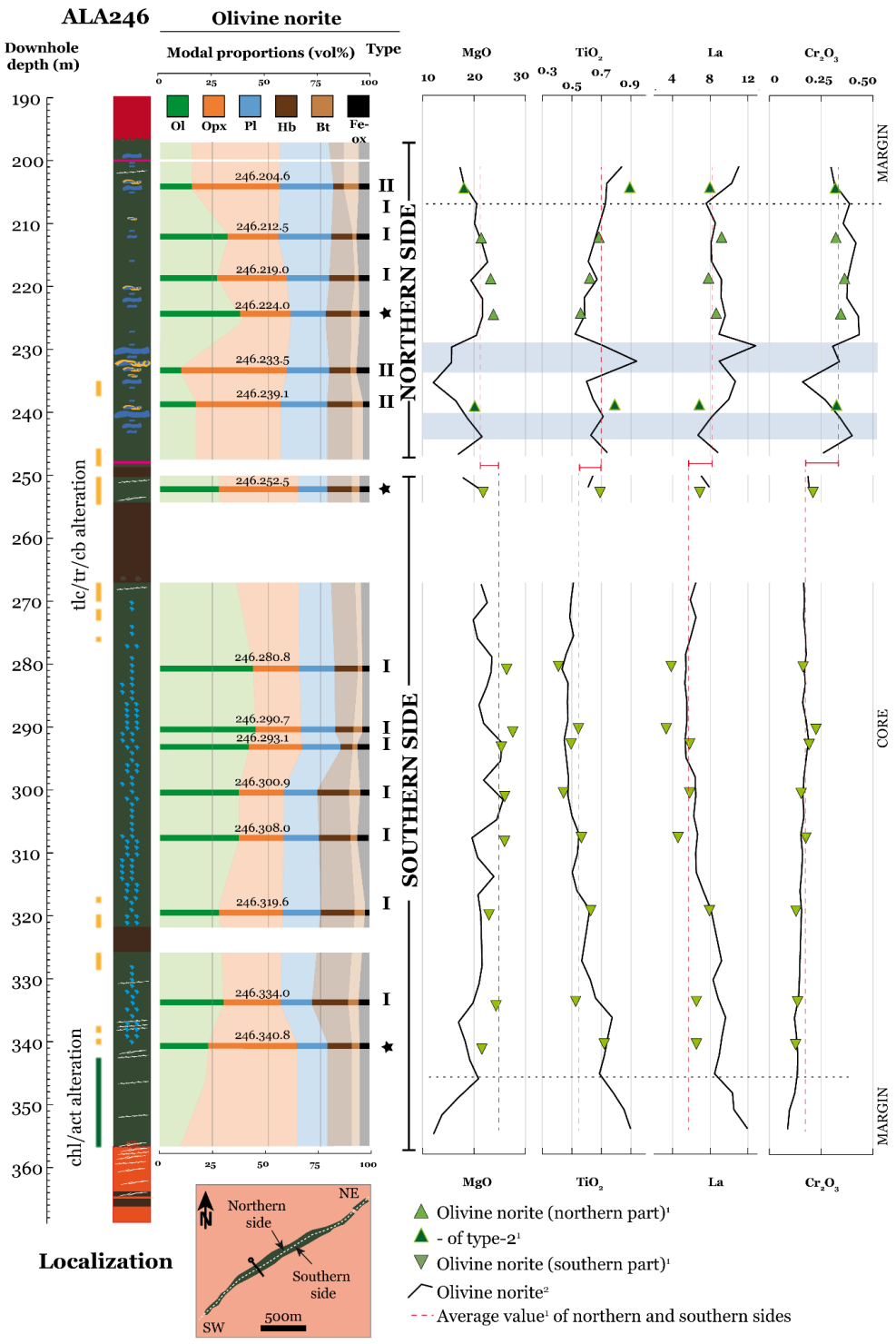

Figure 4.24 Logging of the drillcore ALA246 associated with bulk rock concentration (in wt.%) of some major and trace elements. Symbols show the composition of sample analyzed in this work and line is for unpublished data from Boliden. Blue fields show 3 m-long samples that consist in olivine norite with a significant proportion of leucogabbro. Modal mineral proportions (in vol.%) of the olivine norite samples are reported. Stars indicate sample whose mineral proportions are inferred from CIPW norm and converted to vol.% for olivine, orthopyroxene and plagioclase and from the average value of other samples for hornblende, biotite and oxides. The red dashed lines in profiles show the average value of the northern and southern part of each profile. Mineral abbreviations: Ol: olivine; Opx: orthopyroxene; Pl: plagioclase; Hb: hornblende; Bt: biotite; Fe-ox: iron oxide.

Locally, in the northern part, from its central part to their extremities the MgO and modal olivine amounts, and in a lesser extent the Cr_2O_3 content, decrease while the incompatible elements increase. The type-2 olivine norites are located at the extremities of the northern part.

4.3.2. Leucogabbro

Because dispersed leucogabbro cannot be separated from the olivine norite, we analyzed leucogabbro from compact bodies (6 samples) and one vein. Leucogabbros are intermediate rocks (53.1-60.5% SiO_2) characterized by significantly lower MgO and FeO_{tot} contents than olivine-norites and higher contents of Al_2O_3 (15.1-21.9%), Na_2O, in a lesser extent CaO, and incompatible elements (Figure 4.20). Four samples have high Al_2O_3 contents and plot well above the regression line through the olivine norites whereas the other samples plot near this line.

In the La- and Eu *vs.* MgO diagram (Figure 4.20), the leucogabbros define a linear trend where La and Eu increase with decreasing MgO. Samples with high Al_2O_3 plot on the norite regression line whereas the others define the trend to higher La or Eu contents.

The multi-element diagram of Figure 4.33 confirms that the leucogabbros are more enriched in incompatible trace elements than the olivine norites and it is clear in this figure that both lithologies show near parallel patterns (Figure 4.21). Fractionation of REE in compact leucogabbros is constant and similar to that of the olivine norites whatever the degree of incompatible element enrichment (Figure 4.21 and Figure 4.22). An exception is the leucogabbro vein that has the highest La_N/Sm_N (3.5 against 2.3 in average) and Gd_N/Yb_N ratios (2.7 against 1.8 in average; Figure 4.22). Positive and negative anomalies are of the same magnitude as those of olivine norites except for Zr and Hf which can be positive as well as negative. The parallel patterns suggest a co-genetic relationship between the olivine norites and leucogabbros.

4.3.3. Wall rocks

The wall rocks are intermediate to felsic rocks (58.7-70.9% SiO_2; Table 4.7). The tonalite samples can be distinguished from the granodiorite and the quartz-feldspar porphyry rocks (QFPs) by their relatively high Fe_2O_{3tot} (8.6-12.5%), MgO (2.3-3.1%) and TiO_2 (0.35-0.45%) contents and low SiO_2 (58.7-66.0%) content. The QFP and the granodiorite have similar high SiO_2 contents (~ 71%) and can be discriminated by their CaO contents which are lower in the granodiorite (~ 2 compared to 3-4.5%).

The granodiorite and tonalite REE patterns of this study are very close to those reported for the GI granitoid by González-Roldán (2010) and Weihed et al. (1992) and for quartz-

porphyritic granodiorite of Älgträsk by Bejgarn et al. (2013) (not shown in Figure 4.21). Bejgarn et al. (2013) also showed that all QFPs of the Jörn Intrusive Complex and the Tallberg and Älgträsk tonalites have more fractionated MREE and HREE than the quartz-porphyritic granodiorite.

The multi-element patterns of the wallrocks share some similarities with the Älgliden rocks: they both have negative Nb-Ta anomalies and positive U and Pb anomalies.

There are, however, some significant differences (Figure 4.21 and Figure 4.22). The granitoids (and a single QFP), have distinctly different HREE patterns being flat to relatively enriched in the heaviest REE, in contrast to all samples from Älgliden dike in which these elements are depleted. The Pb anomalies in the wall rocks are less pronounced than those of the dike (Figure 4.23). The QFPs show pronounced positive Sr anomalies, a steeper slope than the Älgliden rocks from Sm to Ho and a relatively flat slope from Ho to Lu. Also, the wall rocks have slightly higher fractionation of LREE over MREE than the Älgliden dike rocks.

4.3.4. Late dikes

We analyzed only one late dike but supplementary unpublished analyses were provided by Boliden (Figure 4.20). The dikes are mafic to intermediate rocks (51.4-57.5% SiO_2) with variable FeO_{tot} (8.4-12.9%) and Na_2O (1.7-4.7%) contents and clustered TiO_2 content (high TiO_2 1.40-1.84% *vs.* low TiO_2 0.81-0.86). Their major and trace element composition is essentially identical to that of the leucogabbros, except for the high TiO_2 in TiO_2-rich samples and for the negative or modestly positive anomaly in Pb.

4.4. Petrogenesis of the Älgliden rocks

In Section 4.4.1, we will make the case that the olivine norites and the leucogabbros derived from a single magma. This is discussed in Section 4.4.2. The formation of these two lithologies is discussed keeping in mind that the olivine norites host the low-grade ore while the minor leucogabbros mostly host the high-grade ore. Finally we will discuss the origin of these mineralized rocks and their parental magma in a subduction setting.

4.4.1. Crystallization of the olivine norite

In binary diagrams *vs.* MgO content, the olivine norites define linear trends (Figure 4.20). In most diagrams these trends intersect the olivine composition (within the limit of error of the regression lines), which indicates that the olivine norites formed by accumulation or

fractionation of olivine. In Figure 4.25, the two alternatives are considered. In the first, a parental liquid of ultramafic composition with 30% MgO content is supposed and the olivine norites are assumed to form by fractional crystallization of this liquid. Liquids with such MgO contents would crystallize olivine with at least ≈Fo_{83}-Fo_{90} content according to partition coefficient for FeO and MgO between olivine and the liquid in equilibrium (Roeder & Emslie, 1970; Figure 4.26), which is different from the relatively evolved olivine composition in the olivine norites ($Fo_{72.5}$ to $Fo_{76.4}$). Alternatively, the olivine norites may have formed by accumulation of olivine in varying proportions in an intercumulus melt having <15% MgO, which is more realistic.

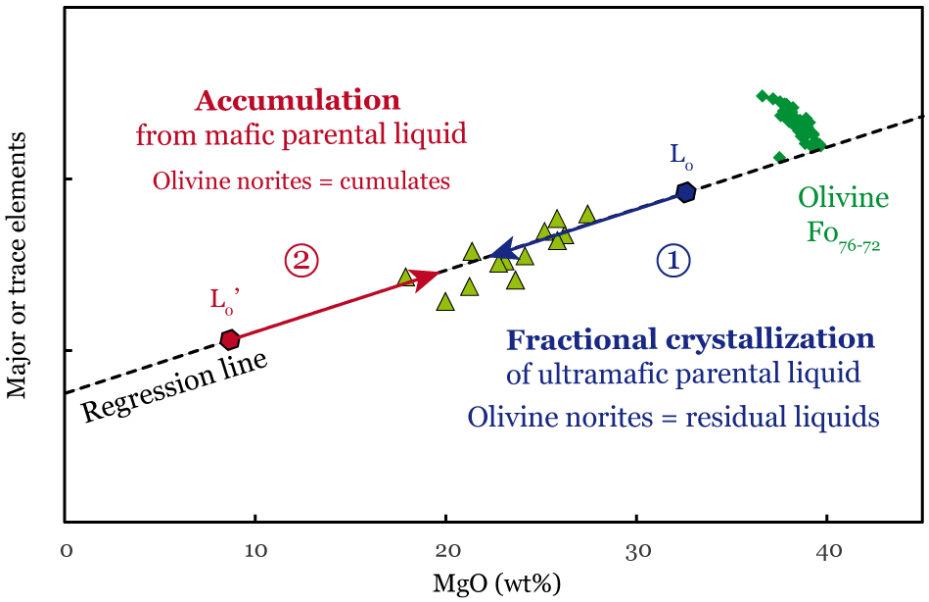

Figure 4.25 Plot of major or trace elements vs. MgO of olivine and olivine norites. Two alternatives are tested: (1) olivine norites correspond to residual liquids formed by fractional crystallization of olivine from an ultramafic parental melt (L_o), or (2) correspond to cumulates formed by accumulation of olivine in a mafic parental melt (L_o'). The dashed line is the regression line of the olivine norites.

In Figure 4.26, the curves represent the MgO contents of liquids containing 8 and 12% FeO in equilibrium with olivine with various Fo contents. In the Älgliden dike, Fo content range from about 72 to 77, and this olivine should have crystallized from liquids with MgO contents between 4 and 13%. The olivine norites and MgO contents between 17 and 27% and plot below the curved indicating that they contain excess olivine. The olivine norites are therefore olivine cumulates, consistent with the petrographic observations.

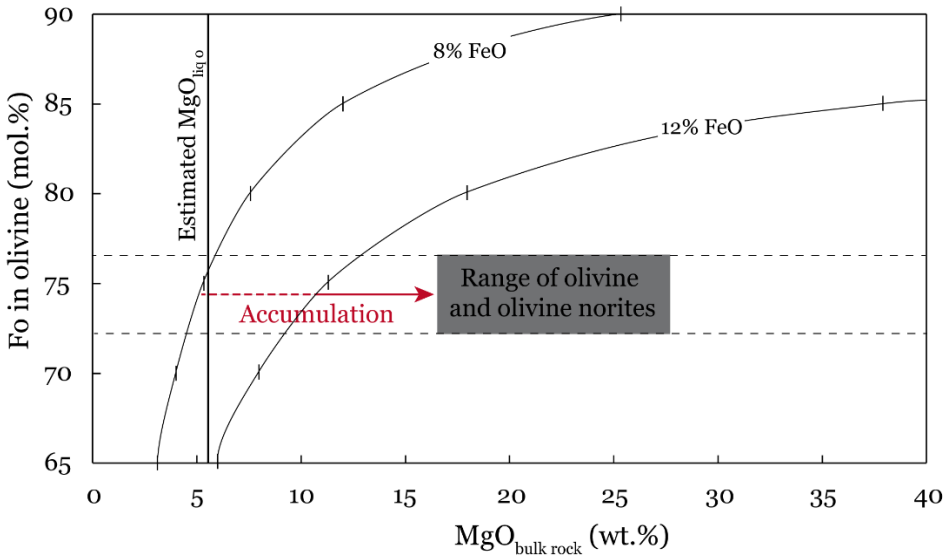

Figure 4.26 Forsterite content of olivine versus MgO of the associated whole rocks or liquids. The curves represent the liquid MgO content calculated from the Fo content of olivine in equilibrium with liquids containing between 8 and 10 wt.% FeO. They have been calculated using partition coefficient of Fe-Mg between olivine and melt of 0.3 (Roeder & Emslie, 1970).

Parental melt composition, fractional crystallization and accumulation

Unlike most volcanic rocks, cumulates do not represent liquid compositions (Cox et al., 1979). Instead they can be considered as melts containing excess crystals. This means that cumulates do not provide any information about the differentiation of the melt. It is possible, however, to estimate the parental melt composition which can be used directly or indirectly to estimate the amount of accumulated olivine and to model the crystallization sequence.

The MgO_{liq} of the parental melt can be estimated using the Fe-Mg partition coefficient between the parental melt and the olivine in equilibrium with this melt, and the linear trend defined by the olivine norites in the FeO *vs.* MgO diagram, as illustrated in Figure 4.27. This calculation assumes that the intercumulus melt lies on the regression line defined by olivine norites.
We use the following relationship to estimate the FeO/MgO ratio of the parental melt:

$$K_{D\,(Fe-Mg)} = \frac{\left(\frac{FeO}{MgO}\right)_{olivine}}{\left(\frac{FeO}{MgO}\right)_{liquid}} = 0.3 \text{ (Roeder \& Emslie, 1970)}$$

where $(FeO/MgO)_{liquid}$ is the ratio in the parental melt, and $(FeO/MgO)_{olivine}$ is ratio in the most primitive olivine. The highest Fo content among the measured olivine grains is 76.4 mol.% but

some orthopyroxene grains crystallized from more primitive liquid, suggesting we missed the most magnesian olivine. Figure 4.28 shows that the melt in equilibrium with the most magnesian orthopyroxene (with $K_{D\ (Fe\text{-}Mg)}$ (opx) = 0.27; Gerlach & Grove, 1982) has an MgO/FeO ratio of 0.6, compared to 0.55 for the liquid in equilibrium with the most primitive olivine grain. Using an MgO/FeO ratio of 0.6 we estimate the most primitive olivine composition to $Fo_{78.6}$.

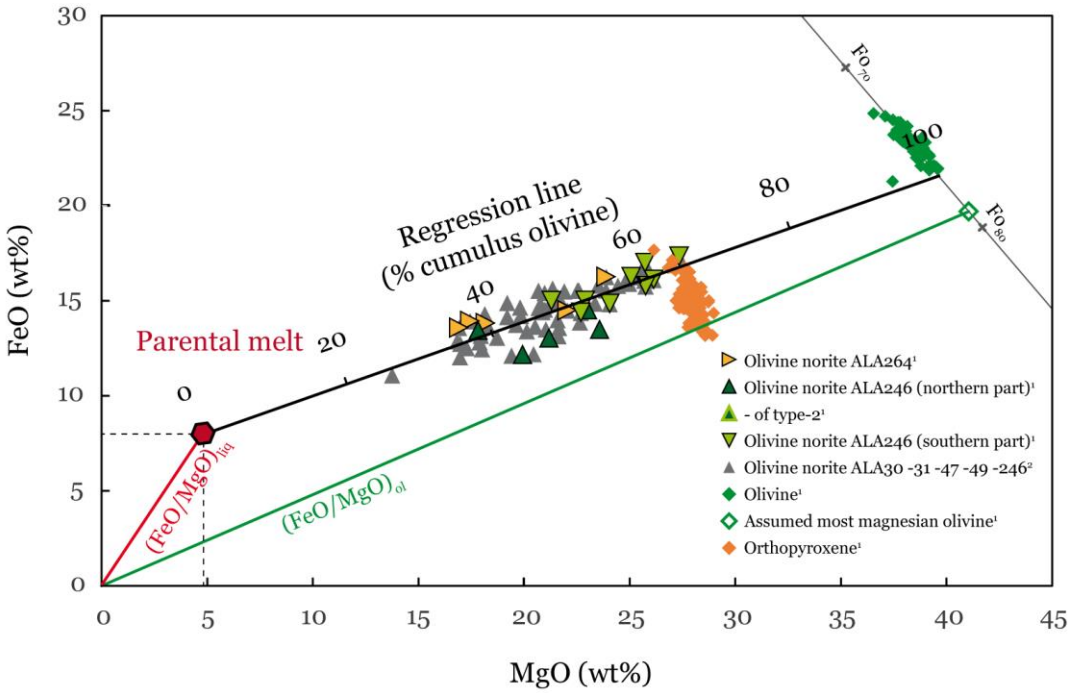

Figure 4.27 Variation diagram of FeO vs. MgO of olivine norites, orthopyroxene and olivine. The FeO/MgO ratio of the olivine is used to calculate that of the liquid according to Roeder & Emslie (1970). The linear trend (dashed line), defined by the olivine norites, together with the $(FeO/MgO)_{liq}$, allow to find the parental melt composition. Proportions of olivine accumulated in the parental melt are found by mass balance calculations.

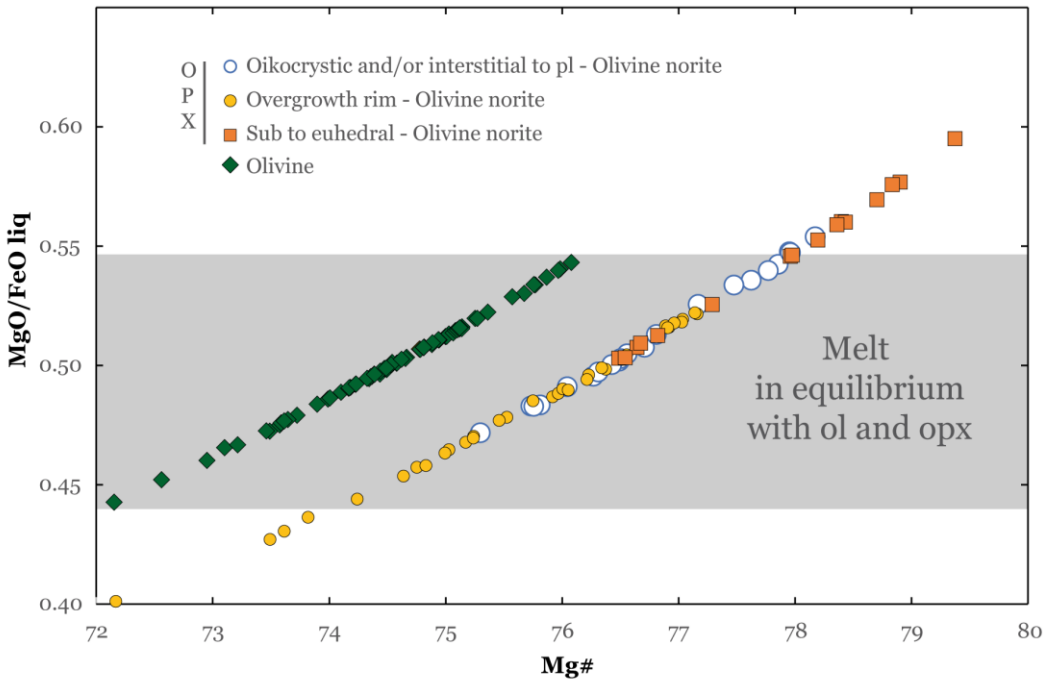

Figure 4.28 Variation diagram of the MgO/FeO ratio of the melt in equilibrium with olivine and orthopyroxene ($K_{D\ Fe\text{-}Mg}$ values are from Roeder and Emslie, 1970 and Gerlach & Grove, 1982) according to their Mg#.

Working with the FeO *vs.* MgO diagram requires that we estimate the relative proportions of ferrous and ferric iron in the olivine norites. The latter is lower in olivine cumulates than in basaltic melt because olivine contains only ferrous iron. Barnes (personal communication) proposed to introduce a ramp function into the $Fe_2O_3/(FeO+Fe_2O_3)$ ratio calculation of cumulate rocks. In the $Fe_2O_3/(FeO+Fe_2O_3)$ *vs.* MgO diagram (Figure 4.29), this function is a line that links the melt and the olivine, on which the MgO content of each norite is a cursor that fixes $Fe_2O_3/(FeO+Fe_2O_3)$. We must also assume values for the $Fe_2O_3/(FeO+Fe_2O_3)$ ratio of the liquid and its MgO content, which are both unknown, as well as the MgO content of the most primitive olivine considered to be $Fo_{78.6}$. We thus calculated iteratively the ramp function for a range of realistic parameters: $Fe_2O_3/(FeO+Fe_2O_3)$ ranging from 0.2 to 0.3 in parental melt, as typical for arc magma (Kelley & Cottrell, 2009) and MgO_{liq} ranging from 5 to 10 wt.%. We show in Appendix 11 that the influence of these parameters on the calculation of the parental melt is not significant and we will assume an MgO_{liq} = 5% and a $Fe_2O_3/(FeO+Fe_2O_3)$ = 0.2 (Figure 4.29). In turn, the $Fe_2O_3/(FeO+Fe_2O_3)$ ratios of the olivine norites range from 0.08 to 0.14. These ratios are used to calculate the FeO contents of the olivine norites, as shown in Table 4.8.

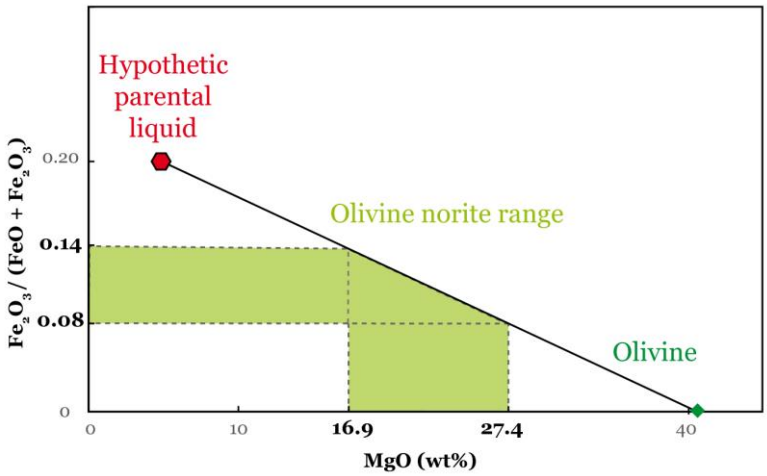

Figure 4.29 Plot of $Fe_2O_3/(FeO+Fe_2O_3)$ vs. MgO showing the ramp function used to estimate the $Fe_2O_3/(FeO+Fe_2O_3)$ of cumulative rocks (modified after Barnes, personal communication).

Table 4.8 Estimations of the Fe2O3/(FeO+Fe2O3) ratio of the olivine norites and calculated modal olivine proportions.

Sample	Type	$Fe_2O_3/(FeO+Fe_2O_3)$	FeO[a]	Fe_2O_3[a]	MgO[a]	Calculated ol prop.	Observed ol prop.[b]	Overestimation factor of ol prop.
264.169.2	n.t.s.	0.13	13.96	2.29	18.15	37	n.t.s.	n.t.s.
264.172.8	n.t.s.	0.13	14.09	2.39	17.41	35	n.t.s.	n.t.s.
264.200.4	n.t.s.	0.10	16.47	1.98	23.84	52	n.t.s.	n.t.s.
264.205.8	n.t.s.	0.11	14.66	1.96	22.00	47	n.t.s.	n.t.s.
264.212.5	n.t.s.	0.14	13.71	2.39	16.89	33	n.t.s.	n.t.s.
246.204.6	type-2	0.13	13.58	2.26	17.78	36	16	2.2
246.212.5	type-1	0.11	13.18	1.85	21.15	45	35	1.3
246.219.0	type-1	0.10	14.69	1.86	22.97	50	29	1.7
246.224.6	n.t.s.	0.10	13.64	1.66	23.54	52	n.t.s.	n.t.s.
246.239.1	type-2	0.12	12.29	1.84	19.89	42	18	2.3
246.252.5	n.t.s.	0.10	15.17	1.94	22.84	50	n.t.s.	n.t.s.
246.280.8	type-1	0.09	16.30	1.69	26.07	59	48	1.3
246.290.7	type-1	0.08	17.55	1.68	27.26	62	49	1.3
246.293.1	type-1	0.09	16.45	1.84	25.01	56	46	1.2
246.300.9	type-1	0.09	15.95	1.70	25.70	58	40	1.5
246.308.0	type-1	0.09	17.21	1.84	25.65	57	40	1.5
246.319.6	type-1	0.10	14.52	1.87	22.64	49	30	1.7
246.334.0	type-1	0.10	15.00	1.78	24.01	53	32	1.7
246.340.8	n.t.s.	0.11	15.14	2.12	21.24	45	n.t.s.	n.t.s.

(a) Elemental contents are in wt.% and recalculated to 100%

(b) Modal proportions have been converted from vol.% to wt.% using density of 3.3 for olivine and orthopyroxene, 2.7 for plagioclase, 5 for sulfides and 5.2 for iron oxides

n.t.s.: no thin section or unusefull thin section

Then, in the FeO *vs.* MgO diagram of Figure 4.27, the composition of the most magnesian olivine (i.e. $Fo_{78.6}$) and its $K_{D\,(Fe\text{-}Mg)}$ are used to estimate the FeO/MgO ratio of the parental melt. The intersection between this FeO/MgO line and the regression line of the rocks gives the MgO_{liq} and FeO_{liq}, under the hypothesis that the intercumulus melt is the parental melt. This leads to MgO_{liq}= 4.8 wt.% and FeO_{liq}= 8.0 wt.%.

For major elements that show a good correlation with MgO (i.e. SiO_2, TiO_2, Al_2O_3, CaO, P_2O_5 and MnO), we estimate their contents in the parental melt from the calculated MgO_{liq}. For other elements, which either are sensitive to alteration and therefore do not show linear trends, such as Na_2O and K_2O, or which show trends that depend on the crystallization of a phase other than olivine, i.e. Cr_2O_3, their contents are approximated using a mass balance calculation (equation (1) considering the average composition of olivine norites and amount of accumulated olivine (see the following subsection; Table 4.8 and Table 4.9). These elements, except for Na_2O, are not determinant in the crystallization modelling of the considered phases since they are present in negligible amount within fractionating mineral phases. An estimation of the parental melt composition is reported in Table 4.9.

Table 4.9 Composition of the calculated parental melt and of the olivine and average olivine norite used for the calculation.

Major oxides	SiO_2	TiO_2	Al_2O_3	FeO_{tot}	MnO	MgO	CaO	Na_2O	K_2O	Cr_2O_3	P_2O_5
Olivine with highest Fo	38.62	0.01	0.02	21.91	0.32	39.67	0.18	n.a.	n.a.	0.01	n.a.
Average olivine norite	47.13	0.62	8.48	15.59	0.23	21.08	4.05	1.06	0.60	0.22	0.16
Parental melt											
Graphical method[a]	56.3	1.1	15.8	8.0	0.2	4.8	7.4	2.0	1.3	0.1	0.3
R^2 (regression line)	0.65	0.50	0.79	0.42	0.15		0.61	0.19	0.36	0.00	0.20
Numerical method[a]	55.7	1.2	17.0	7.7	0.1	2.3	8.0	2.1	1.2	0.4	0.3
Prefered composition	56.3	1.2	15.8	8.0	0.2	4.8	7.4	2.1	1.2	0.4	0.3

(a) see Section 4.4.1 in the text

n.a.: not analyzed

In order to test our estimate of the parental melt composition, fractional crystallization of this melt was modeled and the observed and modelled olivine compositions were compared. Simulations were performed using the Petrolog3 (Danyushevsky & Plechov, 2011) computer program which models fractional crystallization of selected mineral solutions (olivine: Beattie, 1993; orthopyroxene: Ariskin et al., 1993; plagioclase: Danyushevsky, 2001; magnetite: Ariskin & Barmina, 1999) from the estimated parental melt. Amphibole and biotite are not available in the software and ilmenite is voluntarily not taken into consideration since its crystallization

rapidly aborts the simulation, but these mineral phase are not important for the following discussion.

If the intercumulus melt is the parental melt, the MgO content is 4.8 wt.%. The crystallization of olivine is dependent on physico-chemical conditions. The fO_2 modelled by Kelley & Cottrell (2012) in arc magmas corresponds to oxidizing conditions with fO_2 of QFM+1 to +1.6 (Quartz-Fayalite-Magnetite buffer), and an $Fe_2O_3/(FeO+Fe_2O_3)$ ratio of 0.2. The Älgliden dike is suggested to emplace at depths shallower than 4 km (see Section 2.7).

Under these conditions, the Petrolog modelling predicts that the amount of fractionated olivine is very low (i.e. 1 wt.%) and that the range of Fo contents is too low ($Fo_{78.0}$-$Fo_{77.3}$ cf. $Fo_{78.6}$-$Fo_{72.5}$; Figure 4.30a and Table 4.10). At atmospheric pressure, the amount of fractionated olivine reach 2% (Figure 4.30b) but this low pressure is very unlikely. Changing oxidizing conditions also changes the composition of the parental melt since it is determined by $Fe^{2+}O$ vs. MgO diagram.

In order to crystallize more olivine and a wider range of composition the parental melt must have more MgO (Figure 4.30d). Consequently, the hypothesis where the intercumulus melt is the parental melt is not reliable: the parental melt cannot lie at the intersection between the $(FeO/MgO)_{liq}$ line and the regression line through the olivine norite but instead on the $(FeO/MgO)_{liq}$ line with an higher MgO value.

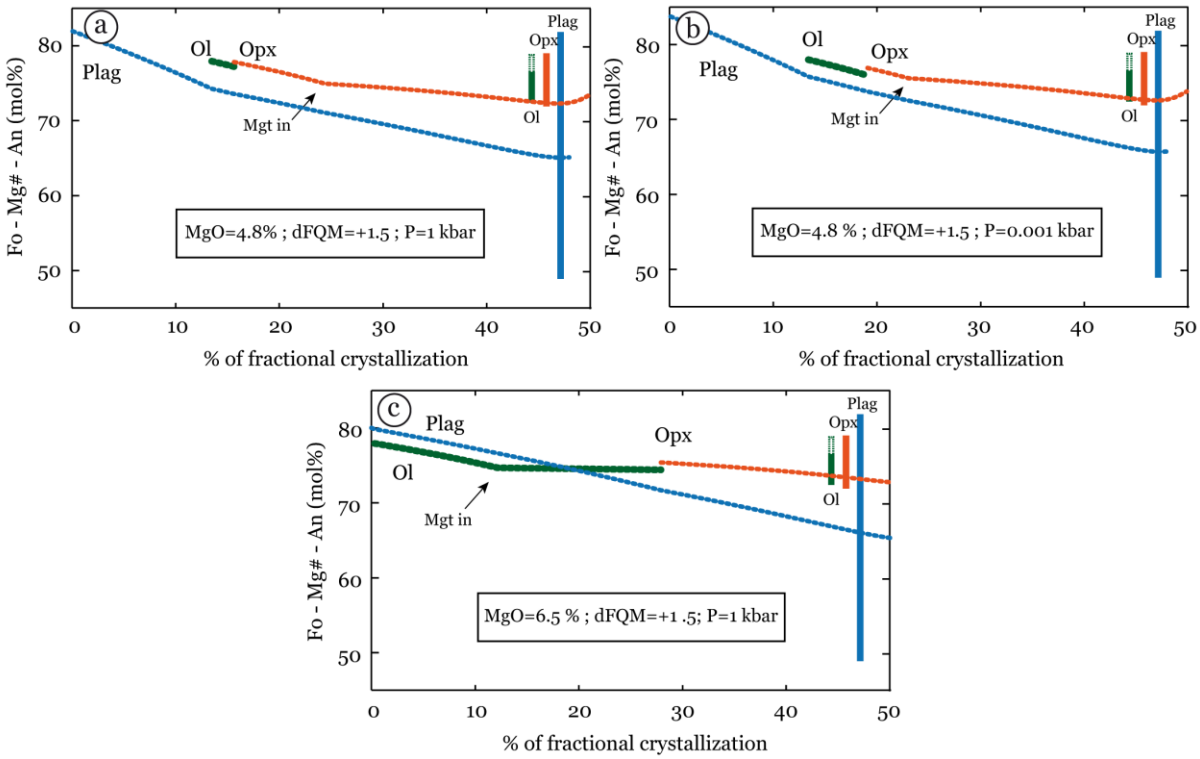

Figure 4.30 Summary of three simulations of fractional crystallization of the parental melt. Simulations are performed using Petrolog3 computer program at different oxygen fugacities, different parental melt compositions, and pressures (given on each graph). The vertical rectangles show the range of mineral compositions observed in olivine norites. Composition of pyroxene and magnetite are given as Mg#. Abbreviation: Ol: olivine; Plag: plagioclase; Opx: Orthopyroxene; Mgt: Magnetite.

Table 4.10 Summary of three simulations of fractional crystallization performed on Petrolog3 software at different oxygen fugacity and different parental melt composition.

Mineral [a]	FC% begin[b]	FC% end [b]	wt.% of crystallized mineral	Mineral composition during FC		
					First crystal	Last crystal
MgO=4.8% [c] ; dFQM=+1.5 [d] ; P=1 kbar						
Olivine	13	16	1	Fo	78.0	77.3
Orthopyroxene	16	50	13	Mg# opx	77.9	73.5
Plagioclase	0	50	29	An	82.0	65.2
Magnetite	24	50	7	Mg# mgt	27.8	17.4
MgO=4.8% [c] ; dFQM=+1.5 [d] ; P=0.001 kbar						
Olivine	13	19	2	Fo	78.0	75.9
Orthopyroxene	19	50	11	Mg# opx	76.9	73.7
Plagioclase	0	50	30	An	83.7	65.7
Magnetite	23	50	7	Mg# mgt	28.0	17.3
MgO=6.5% [c] ; dFQM=+1.5 [d] ; P=1kbar						
Olivine	0	28	7	Fo	78.1	74.5
Orthopyroxene	28	50	8	Mg# opx	75.5	65.4
Plagioclase	0	50	26	An	80.2	72.9
Magnetite	12	50	9	Mg# mgt	30.5	20.7

(a) References for fractionated minerals: olivine (Beatie, 1993), orthopyroxene (Ariskin et al., 1993), plagioclase (Danyushevsky, 2001) and magnetite (Ariskin and Barmina, 1999).

(b) % of fractional crystallization at which the mineral begins and stops to crystallize or when the simulation is stoped, respectively

(c) MgO content of the parental melt in wt.%

(d) Oxygen fugacity modeled after Borisov and Shapkin (1990). dQFM=0 corresponds to fO_2 values on the QFM buffer

Abbreviations: FC: fractional crystallization; FQM: forsterite-quartz-magnetite buffer; Opx: orthopyroxene; Fo: forsterite; An: anorthite; Mgt: magnetite.

A revised estimate of the MgO content of the parental melt is shown in Figure 4.31a. The crystallization of olivine alone in amount enough to produce the observed range of composition requires to consider a melt (labeled L_0) with 5.7 wt.% MgO and FeO content of 9.5 wt.%.

A possible composition for the interstitial melt, which must lie on the line passing through the olivine compositions and the rock compositions, is shown as L_2 in Figure 4.31a, with an MgO content of approximately 4 wt.%. It is seen that the MgO and FeO contents of the interstitial melt are both lower than in the parental melt. Olivine crystallization reduces the MgO content but also increases the FeO content given a composition like L_1, which lies well above the composition of the interstitial melt. This implies that the residual melt must have undergone a FeO loss during or after the olivine crystallization and before the olivine accumulation (Figure 4.31a).

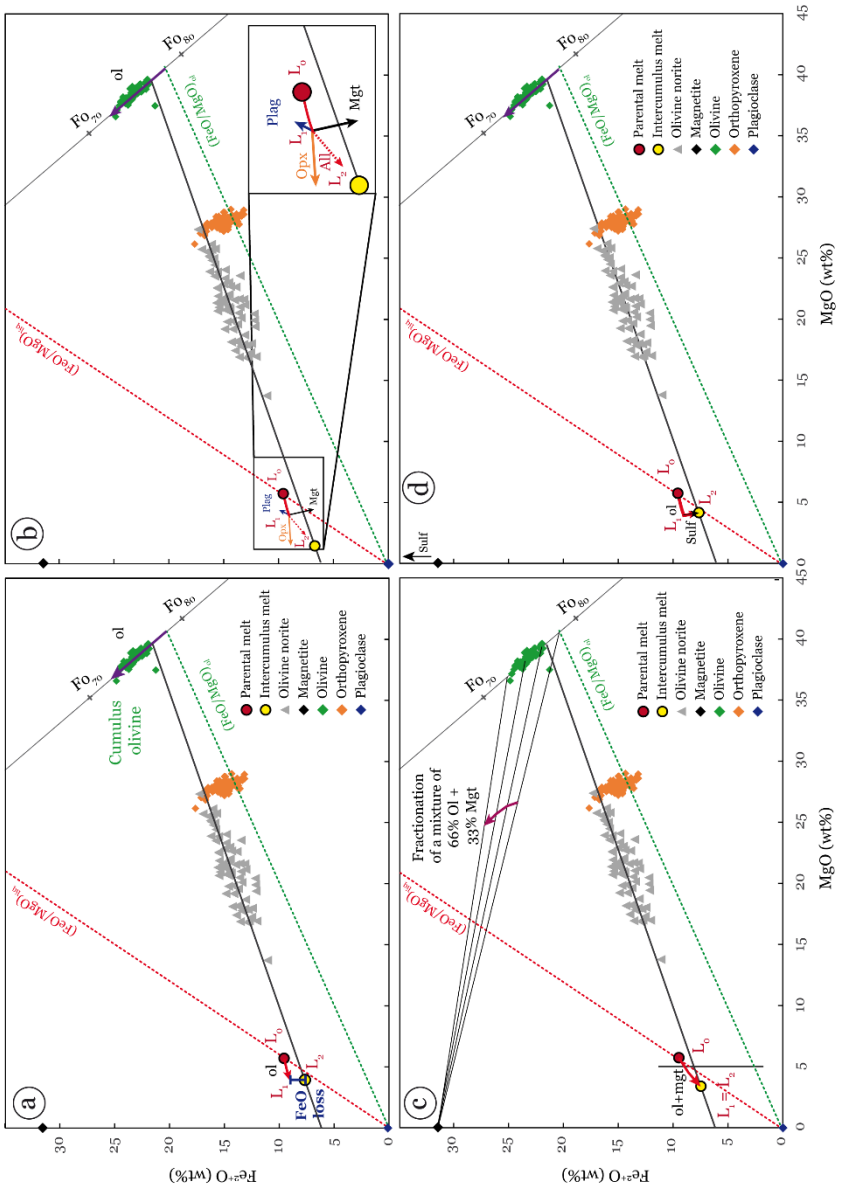

Figure 4.31 FeO versus MgO diagram of the parental melt (L_0), the residual melt after olivine fractionation (L_1) and the intercumulus melt (L_2), considering (a) olivine fractionation ($MgOL_0$=5.7 wt.% and % crystallization=5.2), (b) co-crystallization of olivine and magnetite, (c) the crystallization of 10% orthopyroxene, 10% plagioclase and 10% magnetite following that of olivine and (d) the evolution of the residual melt (after olivine fractionation) toward the intercumulus melt by interaction with a sulfide liquid. The arrows illustrate the evolving composition of residual melt in response to fractional crystallization or the crystallizing phase(s) compositions. Abbreviation: L: liquid; Plag: Plagioclase; Opx: Orthopyroxene; Mgt: Magnetite; Fo: Forsterite; All: all minerals phases.

One way to lose some iron is through the crystallization of Fe-rich minerals such as chromite or magnetite. The crystallization of chromite is excluded because it would rapidly extract all the Cr from the liquid so that only a tiny amount of chromite would have crystallized (<1 wt.% according to Petrolog modelling).

Magnetite crystallization cannot explain the FeO loss because according to the Petrolog modeling and the petrography of the rocks, magnetite crystallizes relatively late and always together with plagioclase and/or orthopyroxene. The crystallization of these Fe-poor phases counters the effect of magnetite crystallization so that, to reach the composition of the intercumulus melt (L_2; Figure 4.31b) an implausible amount of magnetite must crystallize.

Another alternative is the crystallization of a mixture of 66 wt.% olivine and 33 wt.% magnetite (Figure 4.31b). This would imply that a large volume of magnetite accumulates elsewhere.

A final alternative is that the iron was removed from the silicate melt by the segregation of a sulfide liquid (Figure 4.31c). Immiscible magmatic sulfide liquid contains about 60% Fe and the extraction of about 2.5 wt.% of this phase reduces the FeO content of the silicate liquid from 9 to 7.6 %, as shown in Figure 4.31c. Implications regarding the ore forming process are discussed in Section 5.2.

Proportions of accumulated olivine

The proportions of cumulus olivine in each olivine norite can be estimated using a mass balance calculation:

(1) $$C_{bulk} = C_{ol}.X_{ol} + C_{liq}.(1 - X_{ol})$$

with C_{ol}, the concentration of a major oxide in olivine provided by electron microprobe analyses, C_{bulk}, the major oxide concentration of the cumulate provided by bulk rock analyses, C_{liq}, the major oxide concentration in the intercumulus liquid and X_{ol} the proportion of cumulus olivine.

From the MgO content, we can estimate the proportions of cumulus olivine as follows:

(2) $$X_{ol} = \frac{MgO_{bulk} - MgO_{liq}}{MgO_{ol} - MgO_{liq}}$$

The MgO content of the intercumulus melt was taken as 4±2 wt.% using the procedure described earlier. The amounts of cumulus olivine in each olivine norite are reported in Table 4.8. They range from 13 to 62 wt.% for the least and most magnesian samples. These values are higher by an average factor of 1.6 when compared to modal estimates (16-49 wt.%). The difference is probably explained by consummation of olivine the during peritectic reaction. Figure 4.3 illustrates the extent to which orthopyroxene has developed at the expense of olivine by peritectic reaction. Dissolution of olivine and reaction with the intercumulus melt to produce orthopyroxene evolves progressively from Figure 4.3a to Figure 4.3c. It shows that the reaction can convert most of the initial olivine grain into orthopyroxene (Figure 4.3b-c). Barnes

et al. (2016) decribed a similar model in which orthopyroxene oikocrysts grow from olivine during migration of intercumulus melt in the olivine cumulate. This did not appear to occur at Älgliden since the regression line of the olivine norites crosscuts the olivine rather than a mixture of olivine and orthopyroxene. We thus propose that a substantial amount of olivine was consumed by peritectic reaction during post accumulation processes, leading to a ≈40% decrease in the amount of cumulus olivine. It is therefore likely that some currently olivine-free norites, as reported by Filoche (2009), have initially contained small amounts of olivine grains that were subsequently entirely consumed by orthopyroxene.
The relatively small amount of olivine that crystallizes from the parental melt implies that the 15 to 60% olivine in the norites crystallized elsewhere from the site of accumulation (i.e. the dike) and become concentrated via an efficient accumulation process or by the removing a significant volume of interstitial melt. After transportation and injection of cumulus olivine, the intercumulus melt crystallized plagioclase and reacted with olivine to form orthopyroxene. The leucogabbro may have formed in this context.

4.4.2.Origin of leucogabbros

In this section we discuss the relationship between leucogabbro and olivine norite and the formation of leucogabbros in a system dominated by the olivine norites. Figure 4.21 shows that the multi-element patterns of the leucogabbros and the olivine norites are parallel, indicating that these rocks are genetically linked and formed by similar processes; namely accumulation and/or fractional crystallization of minerals that have similar trace-element partition coefficients.

The least-enriched leucogabbro has almost the same composition than the most-enriched olivine norites suggesting that they derive from the same parental melt and are related by different degrees of accumulation and/or fractional crystallization. Mineral compositions support this idea because: (i) the most primitive compositions of orthopyroxene, plagioclase and hornblende in both lithologies are identical or nearly identical; and (ii) the leucogabbros also contain more evolved plagioclase and hornblende (Figure 4.12, Figure 4.14, Figure 4.18 and Figure 4.19). This suggests that the leucogabbros evolved from the intercumulus melt of the olivine norite. Consistently, petrographic observations also show that in numerous cases the contacts between olivine norites and leucogabbros are gradational. Compact bodies of leucogabbro, as shown in Figure 4.6b, often have both sharp and diffuse contacts with the olivine norites. At diffuse contacts plagioclase becomes less and less abundant toward the olivine norite and may locally be described as dispersed leucogabbro (Figure 4.6b). Also, the

occurrence of fine-grained leucogabbros (Figure 4.7b) showing abundant interlocking relationships between plagioclase crystals may reflect quickly solidified melts.

In most diagrams of Figure 4.32, three leucogabbro samples plot as a mixtures of 70% of plagioclase, 30% orthopyroxene and an intercumulus melt whose composition must lie on the regression line through the olivine norites. Of all the leucogabbros, these three samples have the largest positive Sr and Eu anomalies, the highest Al_2O_3 contents, high MgO contents (Table 4.11), suggesting that they formed by accumulation of plagioclase and orthopyroxene. The proportion of cumulus mineral is difficult to estimate because of uncertainties concerning the compositions of the minerals and interstitial melt; estimates vary from <20 to 60%.

Table 4.11 Main petrologic features of selected leucogabbros. Eu*=√(Sm.Gd), Sr*= √(Nd.Sm) and ΔAl_2O_{3i}=Al2O3$_i$ -Al2O$_{avg}$, where i is the considered sample and avg is the average of all samples.

Sample	246. 240.8	246. 242.5	248. 230.4	246. 230.2	246. 199.0	248. 265.0	248. 213.2	246. 212.6
	opx+ plag accumulation							
Type	1	2	1	1	1	2	1	3
La (ppm)	12	14	14	23	23	28	28	38
MgO (wt.%)	7.16	7.51	6.47	6.60	4.79	4.65	3.50	3.06
Sr/Sr*	2.81	2.74	3.62	1.11	2.09	0.69	0.91	1.32
Eu/Eu*	1.13	1.13	1.07	0.86	0.98	0.85	0.83	1.12
ΔAl_2O_3 (wt.%)	3.60	2.67	2.09	-3.18	0.10	-2.79	-2.73	0.25
Plag. compo.	An_{74}	n.a.	n.t.s.	An_{62}	n.a.	An_{60}	An_{55}	An_{31}
modal opx (vol.%)	5	7	n.t.s.	0	0	10	0	0

n.a.: not analyzed ; n.t.s: no thin section

1: Compact; 2: Compact and dipersed; 3:Vein

Several lines of evidence indicate that the other five leucogabbros represent residual liquids: (i) unlike the leucogabbros that are interpreted to have formed by plagioclase and orthopyroxene accumulation, these leucogabbros have lower CaO and higher SiO_2 contents than the intercumulus melt, (ii) they have high contents of La and other incompatible trace elements (not shown) which increase with decreasing MgO; (iii) the average anorthite content of plagioclase of these leucogabbros decreases with decreasing MgO and increasing La contents (Figure 4.32d). These leucogabbros probably were produced by fractional crystallization of plagioclase and orthopyroxene from the intercumulus melt.

In most incompatible trace element *vs.* MgO diagrams, the intersection between the fractionation trends formed by these leucogabbros and the line through the olivine norite lies around 7.5 wt.% MgO suggesting that the intercumulus melt from which the leucogabbros fractionated had this composition. However, the MgO content of the intercumulus melt, calculated from FeO/MgO relationship between olivine and the parental melt and fractional crystallization, is around 4 wt.%. This indicates that the leucogabbros formed from a melt that was less evolved than the interstitial melt whose presence is inferred in the olivine norites.

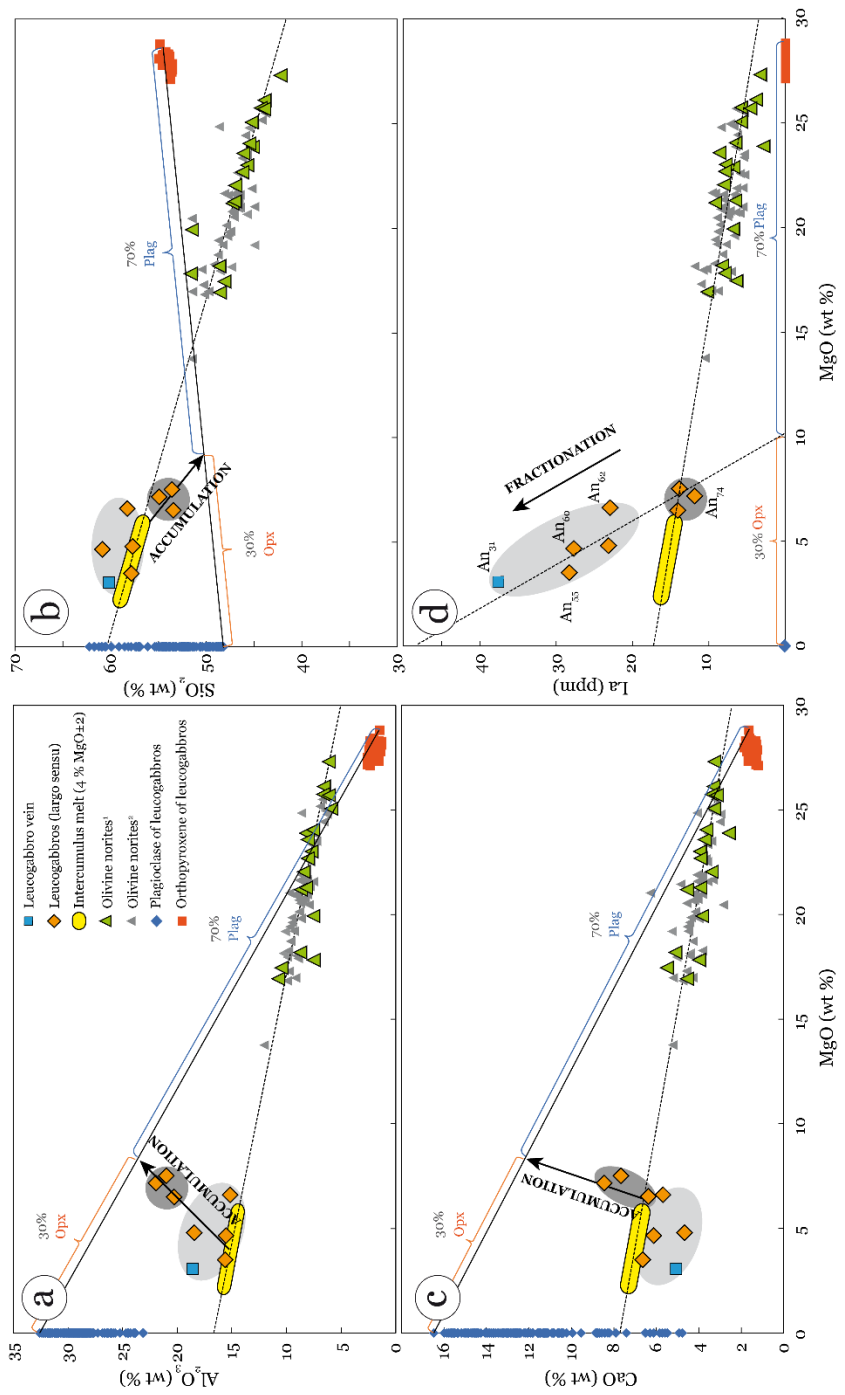

Figure 4.32 Variation diagrams of leucogabbros, olivine norites and the intercumulus melt. (a) La vs. MgO and (b) Al_2O_3, (c) CaO and (d) SiO_2 vs. MgO. The intercumulus melt lies on the regression line of the olivine norites, the uncertainty on its position is explain further in the text. The black line represents the plagioclase-orthopyroxene tie line and the dashed lines are the regression lines of the leucogabbros or olivine norites. Abbreviation: Plag: plagioclase; Opx: orthopyroxene.

The trace element patterns of the leucogabbros are compared with modelled melts produced by Rayleigh fractional crystallization in the estimated intercumulus melt of 40 % plagioclase and 60 % orthopyroxene, i.e. the modal proportions in the olivine norites (Figure 4.33). The trace element contents of the interstitial melt was calculated by mass balance, subtracting the average cumulus olivine proportions from average olivine norite compositions, considering the intercumulus melt with MgO of 4 to 7.5 wt.% (Table 4.12). The leucogabbros with cumulus plagioclase and orthopyroxene have similar trace element contents to modelled residual liquids formed by 0 to 10 % fractional crystallization, except for Sr and Eu, which are more enriched, consistent with the compatibility of these elements in the cumulus phases. The trace-element contents of the leucogabbros are interpreted as evolved liquids like those of modelled melts produced by 20 to 60 % fractionation.

The low An content of plagioclase in the leucogabbro vein (An_{31}) and the low MgO of this sample indicate that it has the highest degree of evolution. According to the LREE of Figure 4.33, it is produced by 70 % of fractional crystallization but this is not enough to reach such evolved anorthite composition. Consistent with the fact that it has also a steeper slope in trace element pattern (Figure 4.22 and Figure 4.33) than the other leucogabbros, the leucogabbro vein was probably generated by a different fractionation process than the other leucogabbros, perhaps involving minor mineral phases with decreasing REE partition coefficients from La to Yb (e.g. apatite, monazite).

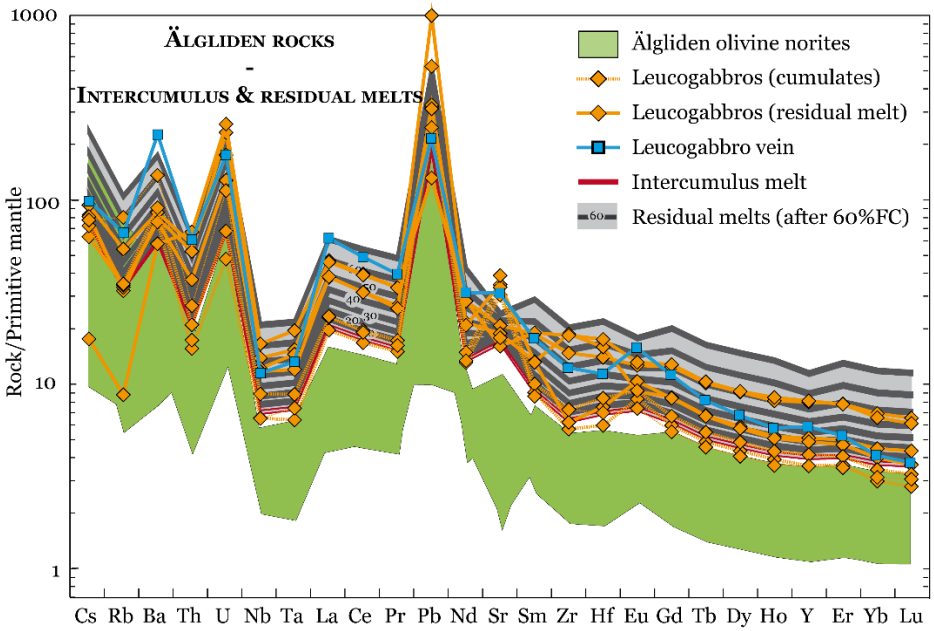

Figure 4.33 Multi-element diagram showing the range for the olivine norites, the leucogabbros and the calculated intercumulus and residual melts. Residuals melt are reported at each 10% of Rayleigh fractional crystallization (FC) of orthopyroxene (60%) and plagioclase (40%). Uncertainty are given by the thickness of the lines.

Table 4.12 Modelling of the trace element composition of the residual melts produced by fractional crystallization of 60% orthopyroxene and 40% plagioclase from the intercumulus melt[a], using Rayleigh fractionation equation[b].

		Cs	Rb	Ba	Th	U	Nb	Ta	La	Ce	Pr	Pb	Nd	Sr	Sm	Zr	Hf	Eu	Gd	Tb	Dy	Ho	Y	Er	Yb	Lu
	Opx	0.010	0.003	0.002	0.130	0.035	0.150	0.150	0.002	0.003	0.005	0.001	0.005	0.007	0.010	0.030	0.055	0.013	0.016	0.019	0.022	0.026	0.200	0.030	0.049	0.060
	Ref.*	4	2	2	2	2	2	2	1	1	1	1	1	2	1	2	2	1	1	1	1	1	2	1	1	1
K_D	Plag	0.130	0.100	0.300	0.010	0.010	0.010	0.040	0.270	0.200	0.170	0.360	0.140	2.000	0.110	0.048	0.051	0.730	0.066	0.060	0.055	0.048	0.030	0.041	0.031	0.025
	Ref.*	5	1	6	3	3	3	5	1	1	1	1	1	1	1	3	3	1	1	1	1	1	3	1	1	1
	D^b	0.052	0.037	0.106	0.084	0.027	0.094	0.104	0.096	0.072	0.062	0.127	0.052	0.704	0.045	0.035	0.051	0.263	0.033	0.032	0.033	0.032	0.131	0.032	0.040	0.045
	100	76.18	33.39	60.42	21.32	67.67	7.17	7.52	20.94	17.90	15.89	186.90	13.75	17.17	9.28	6.46	7.09	7.46	6.37	5.19	4.68	4.26	4.08	4.12	3.79	3.71
	90	68.57	30.06	54.39	19.28	61.20	6.46	6.77	18.85	16.11	14.30	168.21	12.37	15.45	8.35	5.82	6.39	6.71	5.73	4.67	4.21	3.83	3.67	3.71	3.41	3.34
	80	60.95	26.73	48.36	17.23	54.74	5.74	6.01	16.76	14.32	12.71	149.53	11.00	13.74	7.42	5.17	5.68	5.97	5.10	4.16	3.75	3.41	3.27	3.30	3.03	2.97
	70	53.34	23.39	42.33	15.18	48.28	5.03	5.26	14.66	12.54	11.13	130.84	9.63	12.03	6.50	4.53	4.97	5.22	4.46	3.64	3.28	2.98	2.86	2.89	2.65	2.60
F^b	60	45.72	20.06	36.30	13.14	41.82	4.31	4.51	12.57	10.75	9.54	112.15	8.25	10.32	5.57	3.89	4.27	4.48	3.82	3.12	2.81	2.56	2.45	2.48	2.27	2.23
(%)	50	38.11	16.73	30.27	11.09	35.36	3.59	3.76	10.48	8.96	7.95	93.46	6.88	8.60	4.65	3.24	3.56	3.73	3.19	2.60	2.34	2.13	2.05	2.06	1.90	1.86
	40	30.49	13.40	24.24	9.04	28.89	2.88	3.01	8.38	7.17	6.36	74.77	5.51	6.89	3.72	2.60	2.85	2.99	2.55	2.08	1.88	1.71	1.64	1.65	1.52	1.49
	30	22.88	10.06	18.21	6.99	22.43	2.16	2.26	6.29	5.38	4.78	56.08	4.13	5.18	2.79	1.96	2.15	2.24	1.92	1.56	1.41	1.28	1.23	1.24	1.14	1.12
	20	15.26	6.73	12.18	4.95	15.97	1.44	1.50	4.20	3.59	3.19	37.40	2.76	3.46	1.87	1.31	1.44	1.50	1.28	1.04	0.94	0.86	0.83	0.83	0.76	0.75
	10	7.65	3.40	6.15	2.90	9.51	0.73	0.75	2.11	1.80	1.60	18.71	1.39	1.75	0.94	0.67	0.73	0.76	0.65	0.53	0.48	0.43	0.42	0.42	0.38	0.38

(a) The MgO content is assumed to be 4 wt.% (see text).

(b) Rayleigh fractionation equation: $C_L = C_{Lo}F^{(D-1)}$ where C_L is the concentration of an element in the residual melt, C_{Lo} is the concentration in the parental melt, F is the fraction of remaining melt and D is the bulk partition coefficient

*: 1: McKenzie and O'Nions, 1991; 2: Fujimaki et al., 1984; 3: Nielsen et al., 1992; 4: Bacon & Druitt, 1988; 5: Villemant, 1988; 6: Matsui et al., 1977

Abbreviations: Opx: Orthopyroxene; Plag: Plagioclase

4.4.3.Modalities of emplacement of the olivine norites and leucogabbros

The high and relatively homogeneous modal olivine contents, together with the homogeneous olivine composition across the dike, suggest that the olivine norites were emplaced as an olivine-rich crystal mush.

The manner of injection can be inferred from the modal olivine and compositional profiles in Figure 4.24 which show: (i) the average composition in major and trace elements of the northern and southern parts are different and (ii) the profiles show D-shaped pattern for MgO and modal olivine and C-shaped patterns for TiO_2 and La (Figure 4.24).

The difference in average MgO, TiO_2 and La contents between the northern and southern parts is a reflection of the amount of cumulus olivine, which is higher in the southern part. However, the average content of Cr_2O_3 is higher in the northern than in the southern part and, in this respect, does not correlate with MgO content and olivine (Figure 4.24): within each part, Cr_2O_3 and MgO are positively correlated (Figure 4.20). Consistently, in the Cr_2O_3 *vs.* MgO diagram (Figure 4.20), olivine norites from the northern and southern parts form two distinctive trends. This is interpreted as resulting in different proportions of cumulus chromite. Roeder et al. (2006) have shown that the cotectic olivine to spinel ratio is 100:1 and that a higher ratio requires accumulation of olivine without chromite. These ratios are consistent with those inferred for the cumulus assemblage of olivine norites from the northern and southern parts which respectively correspond to cumulus chromite amounts of 0.8 wt.% (i.e. olivine to spinel ratio of 124:1) and 0.4 wt.% (i.e. olivine to spinel ratio of 249:1), as shown in Figure 4.20. This suggests that olivine without chromite accumulated in the southern part of the dike, and a mixture of olivine and chromite in close to cotectic proportions accumulated in the northern part. Other lines of evidence also discriminate the northern from the southern parts. The northern part is marked by the occurrence of leucogabbro together with relatively variable plagioclase and orthopyroxene composition. Inversely, the southern part is characterized by plagioclase rich-clusters and homogenous mineral compositions (Figure 4.1). The contrasting characteristics suggest the two parts were emplaced as separate injections. This could also explain why the two parts are separated by a late dike, which could have intruded along a weak zone.

Filoche (2009) reported parabolic major element profiles across the dike at its NE termination, consistent with concentration of olivine in the center of the dike. In Figure 4.24, we show a similar pattern in the thicker central portion of the dike. Filoche (2009) attributed these compositional profiles to the chemical differences in assimilated country rock and/or prevention of olivine or orthopyroxene crystallization by the contamination.

In Figure 4.24 the modal olivine and MgO contents of the dike are slightly D-shaped at first inspection, with relatively high values in the center of the dike and lower contents at about 10 m from the margins: the profiles have a central plateau with abrupt drops on both extremities. Elements incompatible in olivine (e.g. TiO_2 and La) show the reverse pattern with higher contents at the margins (i.e. C-shape). These compositional profiles reflect the amount of olivine across the dike. They are analogues of the D-shaped sills introduced by (Gibb & Henderson, 1992) where the vertical distribution in modal abundances and/or composition varies symmetrically: the MgO content and olivine mode increase inward from the upper and lower margins of the sills studied by these authors. In the Älgliden dike, the D- or C-shaped variations are oriented differently, with lateral rather than vertical gradients (C-shaped profiles are actually U-shaped profiles) due to the dike-like geometry of the intrusion, but we keep this terminology in order to be consistent with Figure 4.24 and to refer to patterns described in the literature.

Latypov (2003) proposed that D-shaped profiles result from *in situ* crystallization by Soret fractionation in response to temperature gradient imposed by the cold country rocks. Sills with such profiles are thought to have formed from a single pulse of phenocryst-poor parental magma. This explanation for the Älgliden dike is not in agreement with the idea that the olivine norite was injected as an olivine-rich crystal mush whose accumulation occurred before the intrusion. Gibb and Henderson (1992) suggested that the D-shape is neither due to gravity nor thermal convection but is an original feature of the filling process which occurred in a series of pulses. Komar (1972) has shown that the Bagnold effect, described as resulting from grain-dispersive pressure due to the shear of the suspension during a flowing Newtonian suspension, concentrates phenocrysts in the center of sills or dikes, as long as the crystal concentration is higher than 8%. Studying the limits of the Bagnold effect, Barrière (1976) argued that the process is only effective in intrusions narrower than 100 m, which is the case for the Älgliden dike. The fact remains that the olivine crystals are preferentially distributed in the center of the intrusion and with amounts that exceed 15% all across the dike. As mentioned by (Barnes et al., 2015), if the proportion of suspended olivine is greater than 15 wt.%, the density of the suspension exceeds that of normal crustal rocks. Since the amount of modal olivine varies from 15 to about 45% the olivine-rich crystal could have flowed downward, unless driven by overpressure. As suggested by Filoche (2009) who ascribed the mineral distribution across the dike as resulting in flow differentiation, we suggest that the Bagnold effect initially played a role in the distribution of olivine crystal but we propose that another mechanism subsequently acted: from homogeneously distributed crystals across most of the dike, the Bagnold effect could have been reinforced by the fact that the densely packed central mush acted as a plug while the crystal-poor marginal zones acted as a lubricant along the walls of the dike (Figure 4.34a).

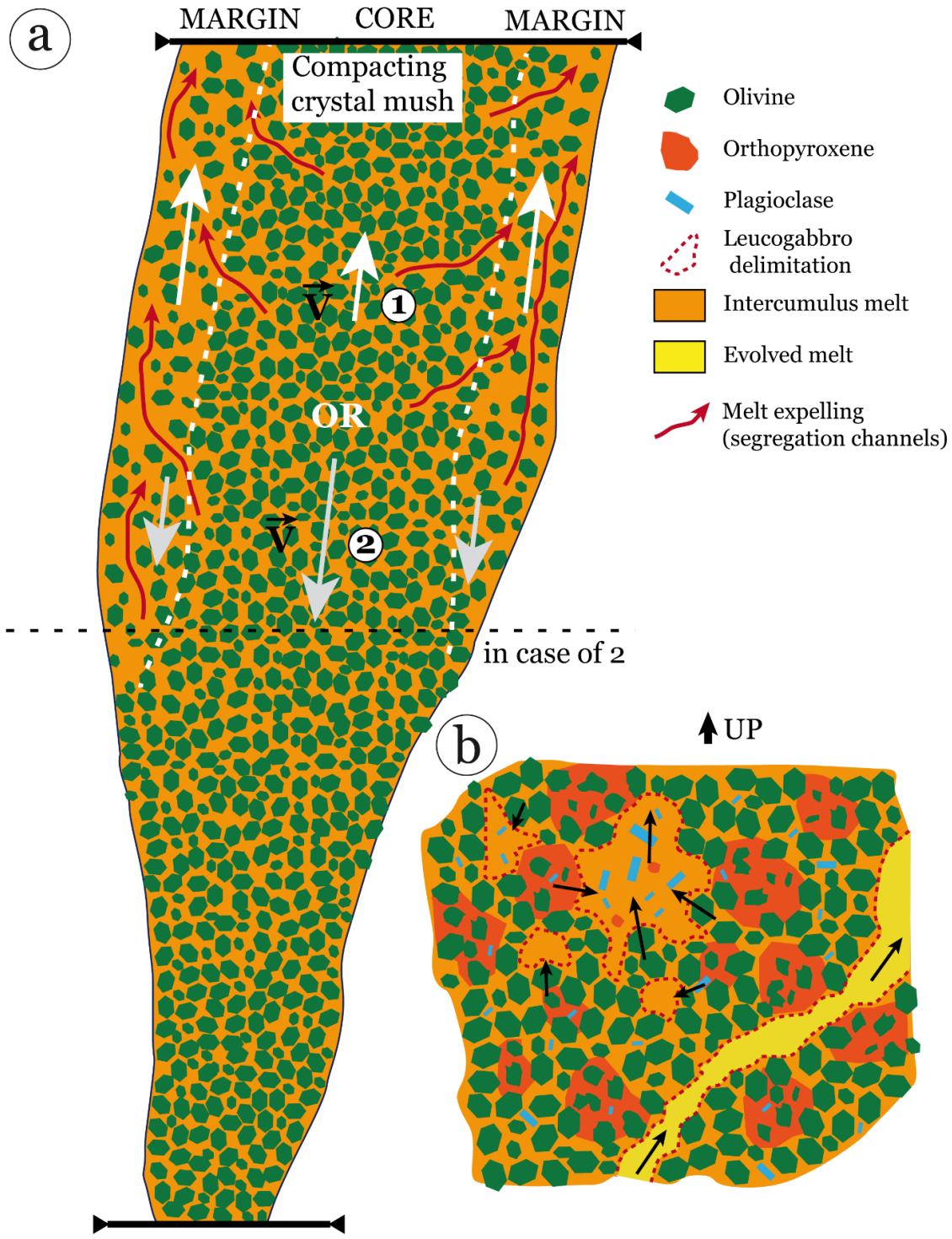

Figure 4.34 Schematic diagram illustrating the emplacement of rocks of the Älgliden dike. a) Injection of the crystal mush, made of cumulus olivine and intercumulus melt, that further gives rise to the formation of the olivine norites and locally the leucogabbros with subsequent crystallization. The distribution of the olivine grains is explained in two scenari: (1) up and (2) down motions with differential velocities between the crystal-rich mush in the center and the crystal-poor mushes at the margins. b) Illustration of the formation of vein, compact and dispersed body of leucogabbro by segregation of melt with or without plagioclase (and minor orthopyroxene) because of compaction and crystallization of the surrounding olivine norite. Straight arrows illustrate a) mush and b) melt displacements.

The northern part has D-shaped patterns for MgO and modal olivine and C-shaped patterns for TiO_2 and La (Figure 4.24). Consistent with the modal olivine distribution, type-2 olivine norites, which are olivine-poor relative to type-1 norites, are located near both margins of this northern part. This supports the idea that this portion of the dike, sampled by the core ALA246, was filled by two distinct and successive injections of olivine-rich crystal mushes. The relative timing of emplacement can be inferred from the fact that the D-shaped pattern of the northern part is preserved while that of the southern part is not, suggesting that the northern portion intruded into the southern portion. If the Filoche's (2009) parabolic compositional profiles in the NE portion of the dike suggest that the D-shaped patterns extend all along the dike. It follows that the wider central part of the dike could be explained by two injections whereas in the thinner NE extremities of the dike were filled by a single injection. It is not possible to refine this interpretation using information from core ALA264 because of pervasive alteration; nonetheless, the southern part shows increases in MgO and normative olivine contents inward from both margin (Figure 4.35). We think that type-1 and type-2 olivine norites are formed in response to the varying amount of cumulus olivine. This could explain why type-2 olivine norites are distributed close to margins where the amount of cumulus olivine is relatively low.

Numerous authors have investigated the origin of plagioclase-rich rocks in mafic intrusions. Wager et al. (1960) proposed a model in which rhythmic pulses of crystallization were followed by gravity-controlled settling and sorting. Such a model is still accepted in the formation of plagioclase cumulates of the Skaergaard intrusion (Nielsen et al., 2015). Other authors proposed that plagioclase cumulates formed by segregation of plagioclase together with removal of dense FeO-rich melt (Scoates et al., 2010; Arndt, 2013; Arai & Maruyama, 2016). The plagioclase segregated because it is buoyant relative to the melt in which it resides. Namur et al. (2011) evaluated the density of plagioclase and that of evolving melts at the Sept Iles layered intrusion and tried to explain why anorthositic rocks occur at both the top and the base of the intrusion. They proposed that plagioclase was initially positively buoyant and accumulated at the roof of the magma chamber, but with further differentiation and evolution of the residual melt, the plagioclase became negatively relatively buoyant and settled downward to form another type of anorthosite in the basal cumulate pile.
Bédard et al. (2007) ascribed similar leucogabbros and anorthosites in channels, layers or pods in the cumulate-textured Basement sill (McMurdo Dry Valleys, Antarctica) to the expulsion and concentration of buoyant melt and plagioclase in low pressure zones in response to suction forces. Bouilhol et al. (2015) proposed a similar model whereby minor plagioclase- and hornblende bearing leucocratic patches in the pyroxenitic feeder pipes of Sapat (Kohistan, Pakistan) are interpreted to represent melt and plagioclase-rich rising pathways accompanying the cumulate formation.

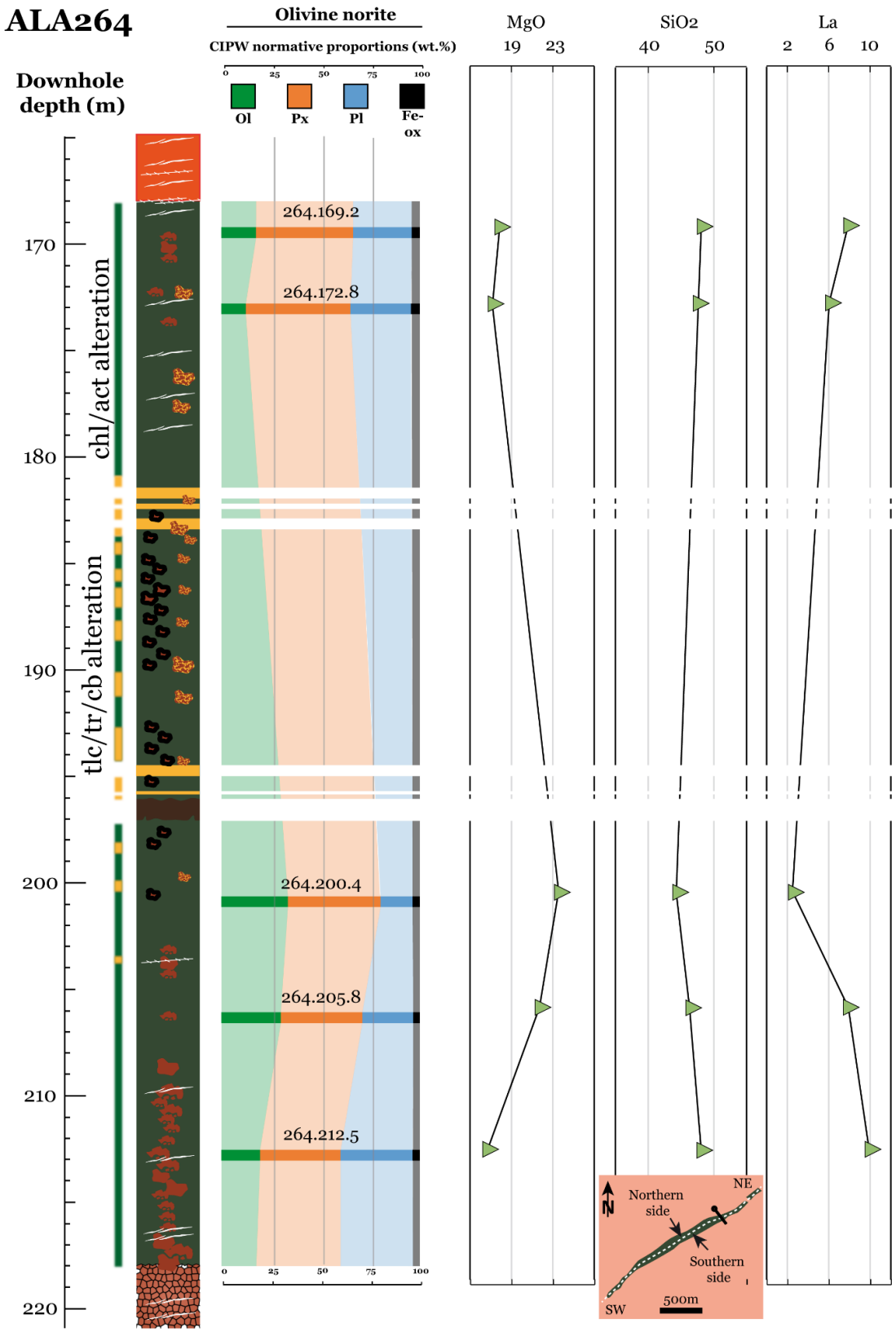

Figure 4.35 Logging of the drillcore ALA264 associated with bulk rock concentration of MgO and SiO_2 (in wt.%) and La (ppm). CIPW normative proportions (in wt.%) of the least altered olivine norite samples are reported. Links between samples are interpretative and merely indicative. Mineral abbreviations: Ol: olivine; Opx: orthopyroxene; Pl: plagioclase; Fe-ox: iron oxide.

In the Älgliden dike, crystal redistribution occurred during the crystal mush flowing, concentrating olivine in the center of the dike. We therefore infer crystals such as plagioclase may also be redistributed before the magma was totally solidified. Simura & Ozawa (2006) modelled crystal redistribution in a sheet-like magma body of similar size to the Älgliden intrusion. They considered that plagioclase concentration occurred as a result of the density contrast between melt and plagioclase, and crystal-crystal and crystal-melt interactions. They concluded that due to the small contrast between the density of plagioclase and melt, as well as its crystal shape, plagioclase is easily affected by melt flow. Plagioclase is enriched by process of return flow of interstitial liquid induced by sinking of heavy particles (i.e. pyroxene crystals). Having in mind these considerations, the plagioclase crystals may have flowed jointly with the melt. This is consistent with the fact that (i) some leucogabbros are interpreted to consist in mixtures of residual melt and cumulus plagioclase; and that (ii) leucogabbros are preferentially distributed close to type-2 norites which represent portions of the crystal mush with a high proportion of melt. In this respect, during the mush injection the interstitial melt might have been expelled from the compacting olivine-rich crystal mush, forming segregation channels and patches where plagioclase crystals and/or melts are concentrated to generate the leucogabbros (Figure 4.34). The dispersed leucogabbros are therefore inferred to represent trapped melt within the mush of olivine, whereas more compact bodies of leucogabbro might result from the segregation and amalgamation of interstitial melt and plagioclase (Figure 4.34b).

4.4.4.Origin of the Älgliden magma

Major and trace element compositions indicate that the Älgliden rocks, especially the olivine norites, are mafic rocks generated from magmas derived from a mantle source. We found that the parental melt of these rocks has an evolved basaltic composition (i.e. $MgO_0 \approx 6$ wt.%; Fo_{78}). In the context of a volcanic arc, partial melting of the mantle produces more primitive melts. Perfit et al. (1980) reported island arc basalts with 10 to 15 wt.% MgO but these authors suggest that most of the basalts have already undergone differentiation. Primitive arc magmas generated in the mantle wedge above subduction zones are in equilibrium with olivine with Fo contents well above that of Älgliden (e.g. Fo_{90-93}; Gavrilenko et al., 2016). The primary melt therefore underwent considerable differentiation before generate the parental melt of the Älgliden magma. Olivine, plagioclase and orthopyroxene, the three cumulus phases in olivine norites and leucogabbros, contain negligible amounts of trace elements (except for Sr and Eu), and therefore the multi-element patterns of Älgliden rocks are parallel to that of the primary melt. All these patterns show relative enrichment of the more incompatible elements, Nb-Ta anomalies and a positive Pb anomaly. Magmas generated in intra-oceanic subduction zones

have a characteristic trace element patterns showing enrichment of the more incompatible elements, relative depletion in HFS elements (i.e. Nb, Ta, Zr, Hf; Perfit et al., 1980) and enrichment in LIL elements (i.e. Rb, Cs, Ba, Sr, Pb, U; Tatsumi et al., 1986) . Similarly, rocks of the continental crust have trace element patterns including depletion in Nb-Ta and the enrichment in Pb relative to other trace elements (Hofmann, 1988). Evolved rocks that share these geochemical characteristics therefore either derive from a source marked by slab-fluxing processes (i.e. slab melting and/or dehydration) or from a magma that underwent crustal contamination. The possibility of crustal contamination is important because this is a key ore forming process in magmatic sulfide deposits (Naldrett, 1992; Naldrett, 2004).

In the following, the possibility that the Älgliden magma have been contaminated by its wallrocks is investigated. The granodiorite and the tonalite which are the most widespread wallrocks, contain porphyry style sulfides, and coeval quartz-feldspar porphyries (QFP) are discontinuously distributed in dikes that follow the same structure than that of Älgliden. Bejgarn et al. (2013) used a small dataset of Älgliden rocks (N=6) and one sample with a highly fractionated REE pattern to propose that the Älgliden rocks underwent contamination. However, the enriched sample was logged as a late dike by Boliden geologists and cannot be used to constrain the contamination process.

In Figure 4.21 we show that multi-element patterns of the Älgliden rocks and their wallrocks are distinct. Differences include the fractionation of MREE relative to the HREE and, to a lesser extent, of the LREE relative to the MREE, and the Pb positive anomaly. Even though the Pb is sensitive to the alteration since its content decreases drastically in altered samples, the anomalies in the Älgliden rocks are much larger than in the wall rocks. The REE of the Älgliden rocks, its wallrocks and other regional mafic intrusives are illustrated in Figure 4.36a. The granitoids, the QFPs and mafic intrusives, including the Älgliden rocks, plot in different fields which, in first approximation, rules out the hypothesis that the Älgliden rocks were contaminated by the felsic wallrocks. If one of the mafic intrusives were contaminated by the felsic wallrock or other deeper rocks this would have modified its REE concentrations instead all mafic intrusive rocks have similar REE relative concentrations. As an illustration, the 1869±7Ma (Billström et al., 2002) ultramafic intrusion of Hemberget, located at ≈100km SW from Älgliden in the southern part of the Skellefte district, and the nearby 1884±2 Ma (Bejgarn et al., 2013) layered intrusion of Torsspiggen, are emplaced after and before the Älgliden intrusion and have parallel multi-element patterns (Figure 4.36b). The temporal and spatial discrepancies between these rocks and the Älgliden dike rocks are not consistent with the fact that they could have been generated from a similar contaminated magma in one single magmatic plumbing.

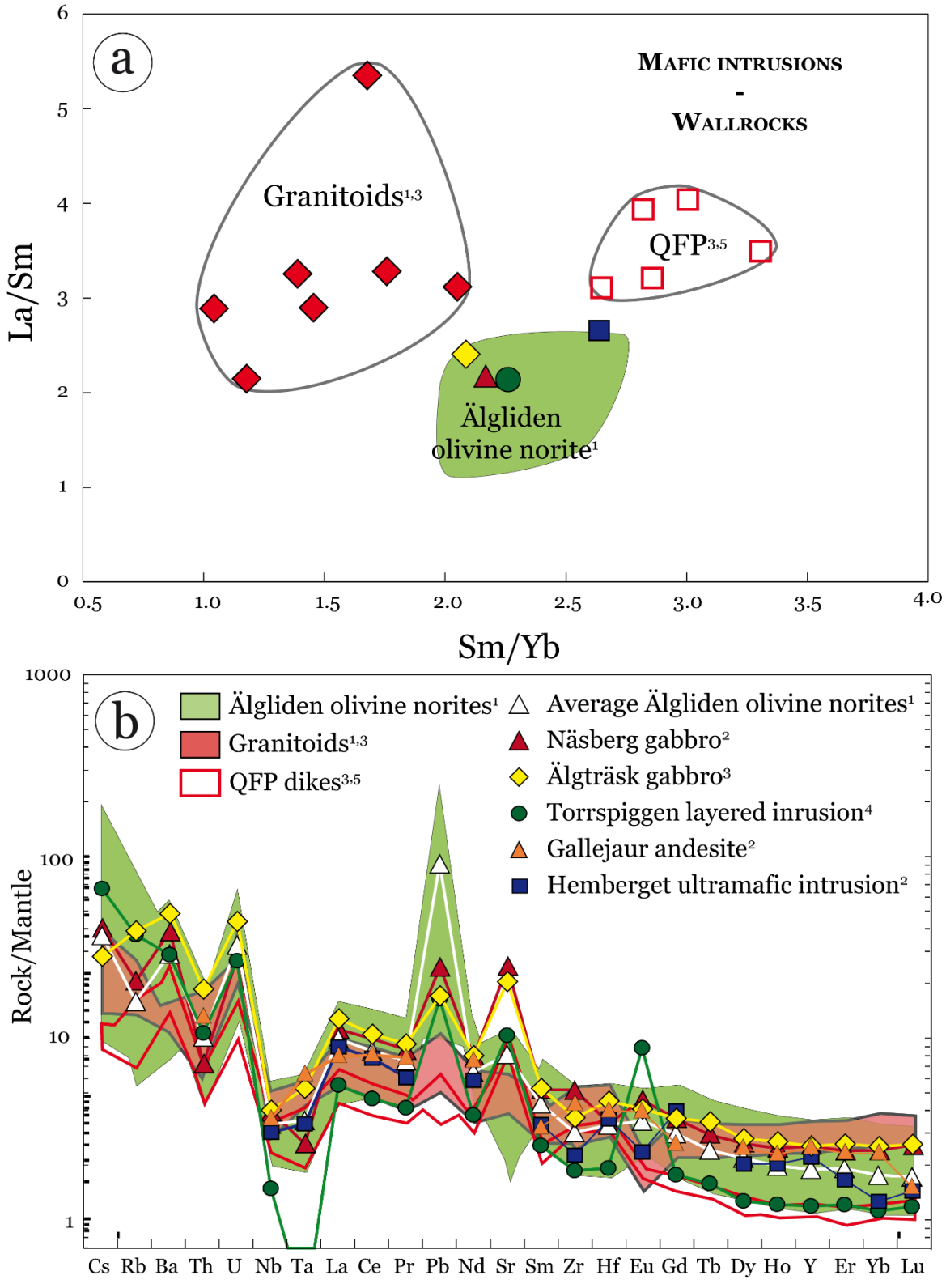

Figure 4.36 (a) La/Sm vs. Sm/Yb diagram of mafic intrusions and felsic wallrocks. (b) Mantle normalized multi-element diagram of the Älgliden dike, its wall rocks and other regional mafic intrusions. References 1: this study, 2: Berge, 2013 and references therein, 3: Bejgarn et al., 2011; 4: Bejgarn et al., 2013; 5: Unpublished data from Boliden.

A more robust and quantitative way to test the hypothesis of the contamination of the Älgliden magma by its wall rock is to consider an assimilation fractional-crystallization (AFC) model (DePaolo, 1981). In this model, the latent heat provided by crystallization triggers assimilation of wall rocks. We considered a scenario in which an arc basalt has been contaminated by either the QFPs or the granitoids during olivine fractionation. Results are illlustrated in Figure 4.37, where the distinctive features of the Älgliden rocks compared to wall rocks are used (i.e. Ce/Pb and Sm/Yb). Even considering drastic assimilation (r= 0.5, see Table 4.13) and 90% of olivine fractionation, the process of AFC does not allow to reproduce the composition of the Älgliden rocks, in particular their low Ce/Pb.

Overall, for all the reasons exposed above, we ascribe the multi-element patterns of all the Skellefte rocks to a regional signature that reflects slab-fluxing processes in a subduction zone rather than crustal contamination.

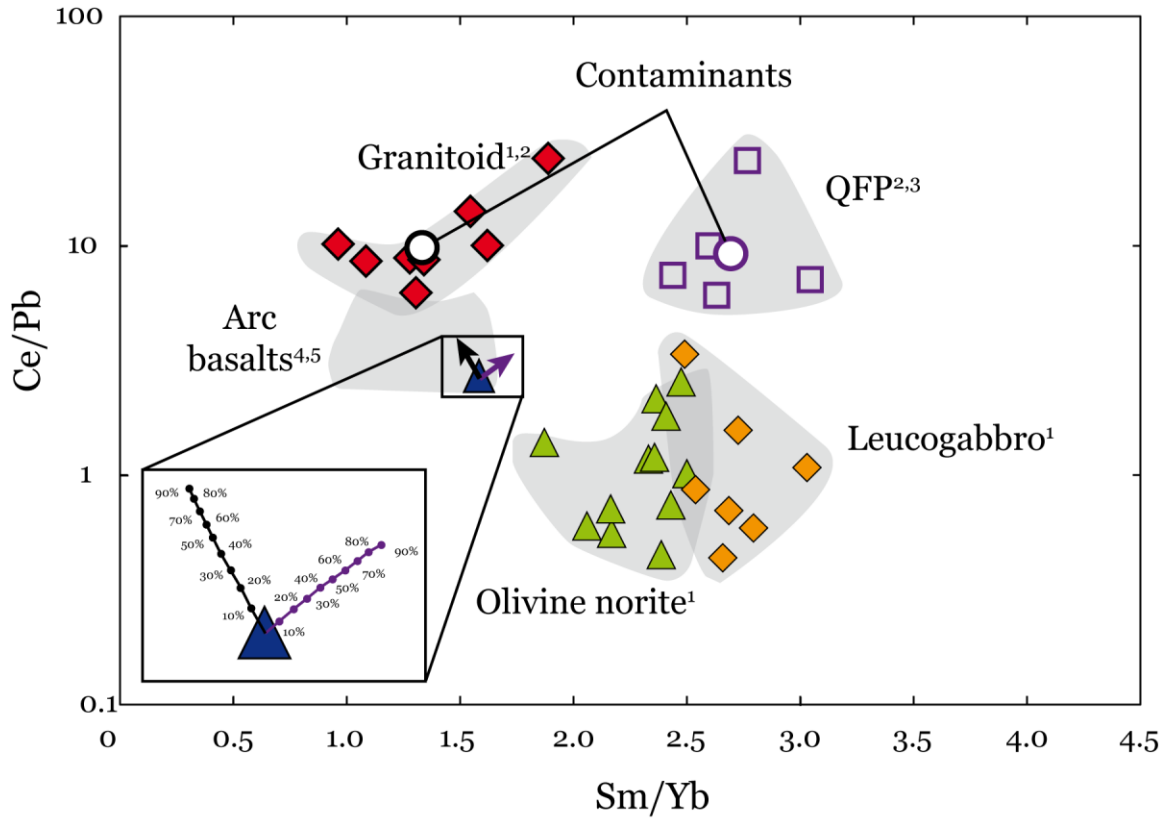

Figure 4.37 Ce/Pb *vs.* Sm/Yb diagram showing the composition of an arc basalt contaminated by QFP or granitoids during olivine fractionation. Percents in the inset are the amounts of fractionated olivine. Parameters used for AFC modeling are listed in Table 4.13. References 1: this study; 2: Bejgarn et al., 2011; 3: Unpublished data from Boliden; 4: Gazel et al., 2015. 5: Sunda Arc, average of lavas with 5 to 7 wt.% MgO obtained from the GEOROC database.

Table 4.13 Modelling of the trace element composition in Ce, Pb, Sm and Yb (wt.%) of the melts produced by assimilation-fractional-crystallization[a] of an arc basalt crystallizing olivine and assimilating the Älgliden wall rocks.

			Ce	Pb	Sm	Yb
Partition coefficient[b]		D^a	0.0005	0.0001	0.0013	0.0015
Sunda arc basalt		$C_{Lo}{}^a$	32.7	12.3	4.56	2.88
Average granitoid		$C_a{}^a$	30.33	3.09	2.74	2.06
Fraction of remaining magma (F^a)	0.9	$C_L{}^a$	39.70	14.01	5.37	3.43
	0.8		48.45	16.15	6.38	4.11
	0.7		59.70	18.90	7.68	4.99
	0.6		74.69	22.56	9.42	6.16
	0.5		95.68	27.69	11.84	7.81
	0.4		127.15	35.38	15.48	10.26
	0.3		179.60	48.21	21.54	14.36
	0.2		284.45	73.85	33.65	22.54
	0.1		598.84	150.78	69.91	47.05
Sunda arc basalt		$C_{Lo}{}^a$	32.70	12.30	4.56	2.88
Average QFP		$C_a{}^a$	16.26	1.76	1.38	0.51
Fraction of remaining magma (F^a)	0.9	$C_L{}^a$	38.14	13.86	5.22	3.26
	0.8		44.93	15.81	6.04	3.73
	0.7		53.66	18.32	7.10	4.33
	0.6		65.31	21.67	8.51	5.13
	0.5		81.61	26.36	10.49	6.26
	0.4		106.05	33.38	13.45	7.95
	0.3		146.77	45.10	18.37	10.76
	0.2		228.20	68.52	28.22	16.38
	0.1		472.33	138.77	57.73	33.20

(a) Equation of DePaolo (1981): $C_L = C_{L0}[F^{-z}+(\frac{r}{r-1})(1-F^{-z})\frac{C_a}{zC_{L0}}]$

where C_L, C_{Lo}, C_a, are the elemental concentration in the contaminated melt, the parental melt and the contaminant, respectively.

$z=\frac{r-1+D}{r-1}$ and $r=\frac{M_a}{M_c}$

where M_a and M_c are the assmilation and crysallization rates, r is fixed to 0.5 to test an efficient contamination scenario

(b) data from McKenzie and O'Nions (1991)

Oxygen, Nd, Pb and Hf isotopic data indicate that the Skellefte rocks mostly originated from a depleted source including oceanic crust recycling processes (Wilson et al., 1985, 1987; Billström and Vivallo, 1994; Guitreau et al., 2014). The slight differences in Pb and $\varepsilon_{Hf(t)}$ values between the felsic Skellefte rocks and their felsic juvenile basement is interpreted to reflect the partial melting of the juvenile arc, previously formed from the subducting oceanic crust, and/or by the melting of younger subducting oceanic crust (Billström and Vivallo, 1994; Guitreau et al., 2014). Hafnium and Nd isotopic signature also rule out significant contamination by older continental crust (Wilson et al., 1985, 1987; Guitreau et al., 2014). Mafic rocks have not been directly subject to isotopic studies but Pb isotope studies of massive sulfide that involve mafic and felsic reservoirs indicate the mafic rocks derived from the metasomatized mantle (Billström and Vivallo, 1994).

Gazel et al. (2015) used incompatible trace elements (e.g. Th, U and Nb) to discriminate between rocks of island arcs and of the continental crust (Figure 4.38a). Thus they gradually classified the intra-oceanic island arcs as transitional island arcs, with continental index close to that of continental crust and depleted island arcs, with continental index far from that of the continental crust. Figure 4.38b shows that mafic intrusive rocks of the Skellefte district overlap that of island arcs, especially of depleted island arcs, and lie far from the continental crust. In this respect, it indicates that they originated in an oceanic island arc, probably a depleted island arc where the magmas mostly derived from the mantle wedge fluid-assisted melting. The fluid influx in the mantle wedge was responsible for the oxidized state of the magma because $Fe^{3+}/\sum Fe$ ratios, H_2O content and slab-derived fluid mobile elements are positively correlated (Kelley and Cottrell, 2009). Another evidence to this at Älgliden is the substantial amounts of hydrated mineral phases in the Älgliden rocks.

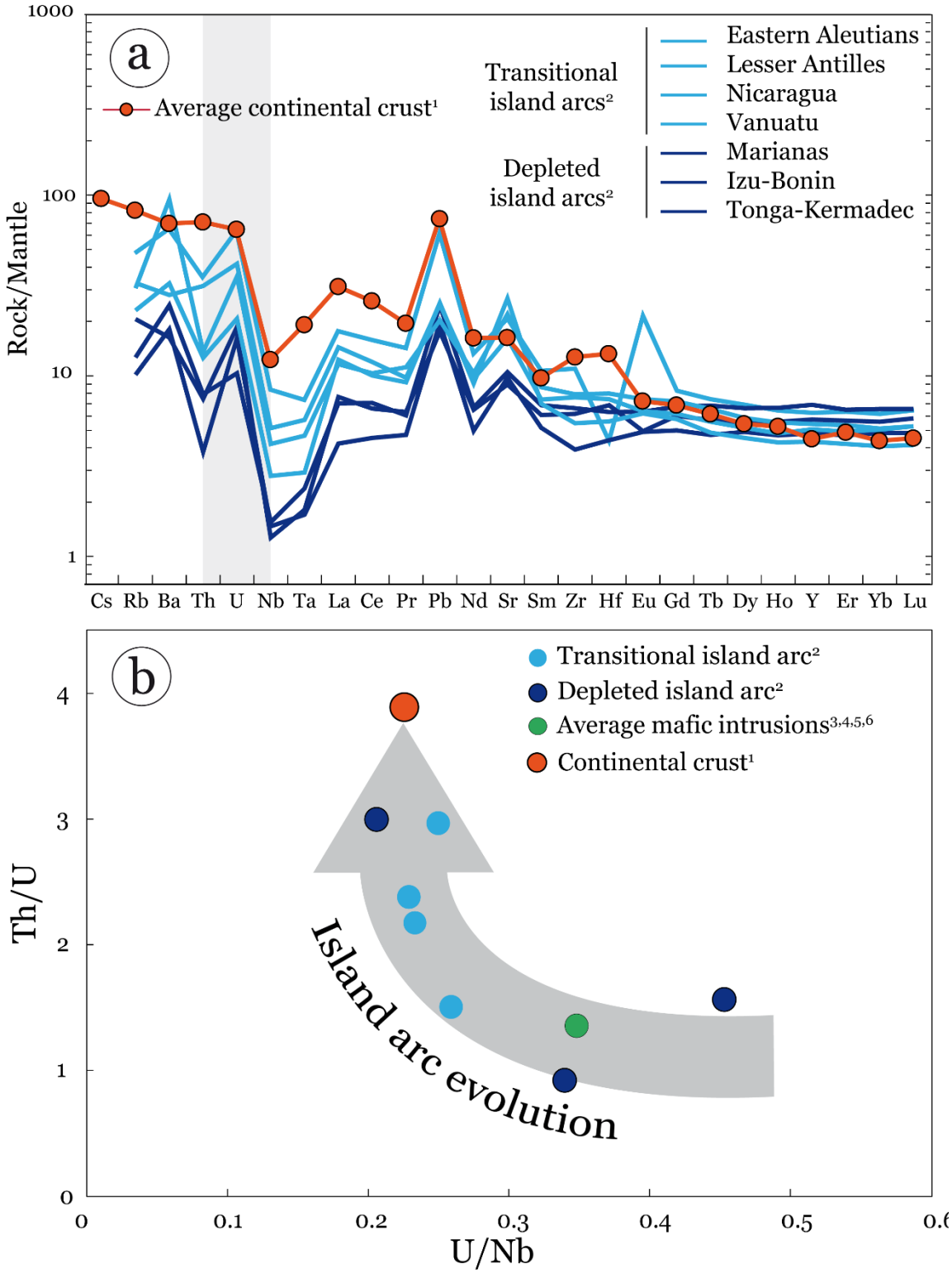

Figure 4.38 (a) Mantle normalized multi-element diagrams of the continental crust and island arcs (b) Th/U vs. U/Nb diagram of Skellefte mafic intrusions, island arc and the average continental crust. Normalization after McDonough & Sun (1995). References 1: Rudnick & Gao, 2003; 2: Gazel et al., 2015; 3: this study, 4: Berge, 2013 and references therein, 5: Bejgarn et al., 2011; 6: Bejgarn et al., 2013.

5. Mineralization and ore formation

5.1. Mineralization styles

When describing sulfide textures, we use the terminology of Barnes et al. (2017). In Sections 5.1.1 and 5.1.2 we do not systematically distinguish the individual sulfide phases and instead refer to sulfide as a single phase that segregated during cooling into minerals such as pyrrhotite, chalcopyrite and pentlandite. The mineralogy and texture of the sulfides that compose the sulfide aggregates are described in Section 5.1.3. Even though magnetite is not a sulfide, it is described in this section because of it spatial and textural association with the sulfides.

The Älgliden ores display a wide variety of textural types that appear to be related to the modal proportions of sulfide in the host rock, the textural relations between sulfides and silicates, and the connectivity of sulfide. With increasing modal abundance and connectivity of sulfides, the texture change from disseminated sulfides (<10%), network sulfides (15 to 70%) to massive sulfides (>80%). These mineralization styles are distinguished using the criteria summarized in Table 5.1 and each mineralization style is described in more detail below. In the descriptions, we emphasize the difference between sulfides that are cusp shaped (i.e. V-terminations with concave contours) and those with bulbous or globular shapes. The exception is for pyrite which almost always has a euhedral habit, independent of whether it is disseminated or massive.

Hydrothermal pyrite and chalcopyrite occur along fractures or shear planes and within quartz-carbonate veins or are pervasively distributed through hydrothermally-altered rock.

Table 5.1 Summary of sulfide mineralization styles at Älgliden

Mineralization style	Sulfide abundance[a]	Host rock	Adjacent silicate phases	Characteristic shape	Size or extension
Disseminated (to patchy network)	0 - 8	Olivine-norite	ol±pl	cusp-shaped	0 - 1mm (<20mm)
Disseminated	0 - 1	Olivine-norite	opx+hb+bt	globular	0.1 - 2mm
Disseminated	0 - 3	Leucogabbro	pl±bt	coarse globular	1 - 15mm
Network	15 - 70	Leucogabbro	pl±bt	worm-gallerie to vein	up to 25cm[b]
Network	15 - 50	Wallrock xenolith	pl+bt	from common net-texture to breccia	up to 25cm[b]
Massive	80 - 100	Leucogabbro and at the dike contacts	n.a.	irregular	up to 20cm

[a]: in vol.%

[b]:dependent of the host rock size

n.a.: not adapted

5.1.1. General aspects

Disseminated sulfides (largo sensu)

This term is used when the sulfide content is low (0.5 to 8%) and when the sulfides are distributed as small (width<3 mm) isolated grains through the rock (Figure 5.1a and Figure 5.2a). This type of sulfide is mainly hosted in the olivine norite and is less common or absent in the leucogabbro. The shape of the sulfide masses is variable, from almost spherical to cusp-shaped, as illustrated in Figure 5.2a. This variation in shape appears related to the nature of adjacent silicate minerals, as discussed below.

Connection between isolated disseminated grains leads to small sulfide networks that we refer to as patchy net-textured sulfides (Figure 5.2c). These networks rarely extend over more than 2 cm. We describe them together with disseminated sulfides because of the similarities they share in terms of texture and sulfide content.

In the leucogabbro, disseminated sulfides are rare and mainly form coarse irregular and globular sulfides (up to 1 cm). They occur within the leucogabbro, at the contact with norite (

Figure 5.1b and Figure 5.2b), or close to network and massive sulfides (Figure 5.1c).

Network sulfides

The term *network* applies to texture that occurs either in the leucogabbro or in the wall rock xenoliths. We use this term to distinguish the textures of the Älgliden dyke from *net-textured* sulfides defined in the literature by the presence of a continuous matrix of sulfide enclosing cumulus crystals such as olivine (Naldrett, 1973; Barnes et al., 2008; Godel et al., 2013; Barnes et al., 2017). In the Älgliden dyke, network sulfides form the matrix enclosing silicate phases other than olivine.

The sulfide networks range in maximum dimension from 5 to 20 cm in the drillcores. The modal proportion of sulfide varies between 15% to 70% for those hosted in the leucogabbro and 15-50% for those observed in the xenoliths. The upper limit of the sulfide content is not well defined because the networks progressively grade into massive sulfides.

Within the leucogabbros, sulfide bodies are linked together to form elongated pores or tube-like channels that merge to form a semi-continuous matrix between the silicate mineral grains. The geometry of the texture depends on the relative proportion of sulfide to silicate minerals. Tube-like forms appear when the proportion of sulfide is greater than 30%, as shown in Figure 5.1c and Figure 5.2d, and form an irregular, semi-continuous network of tubes or channels with increasing proportion of sulfide. The networks are confined in leucogabbro bodies and occupies part of, or the entire, body. The network resembles a worm gallery whose shape seems to be independent of the plagioclase framework that defines the structure of the leucogabbro.

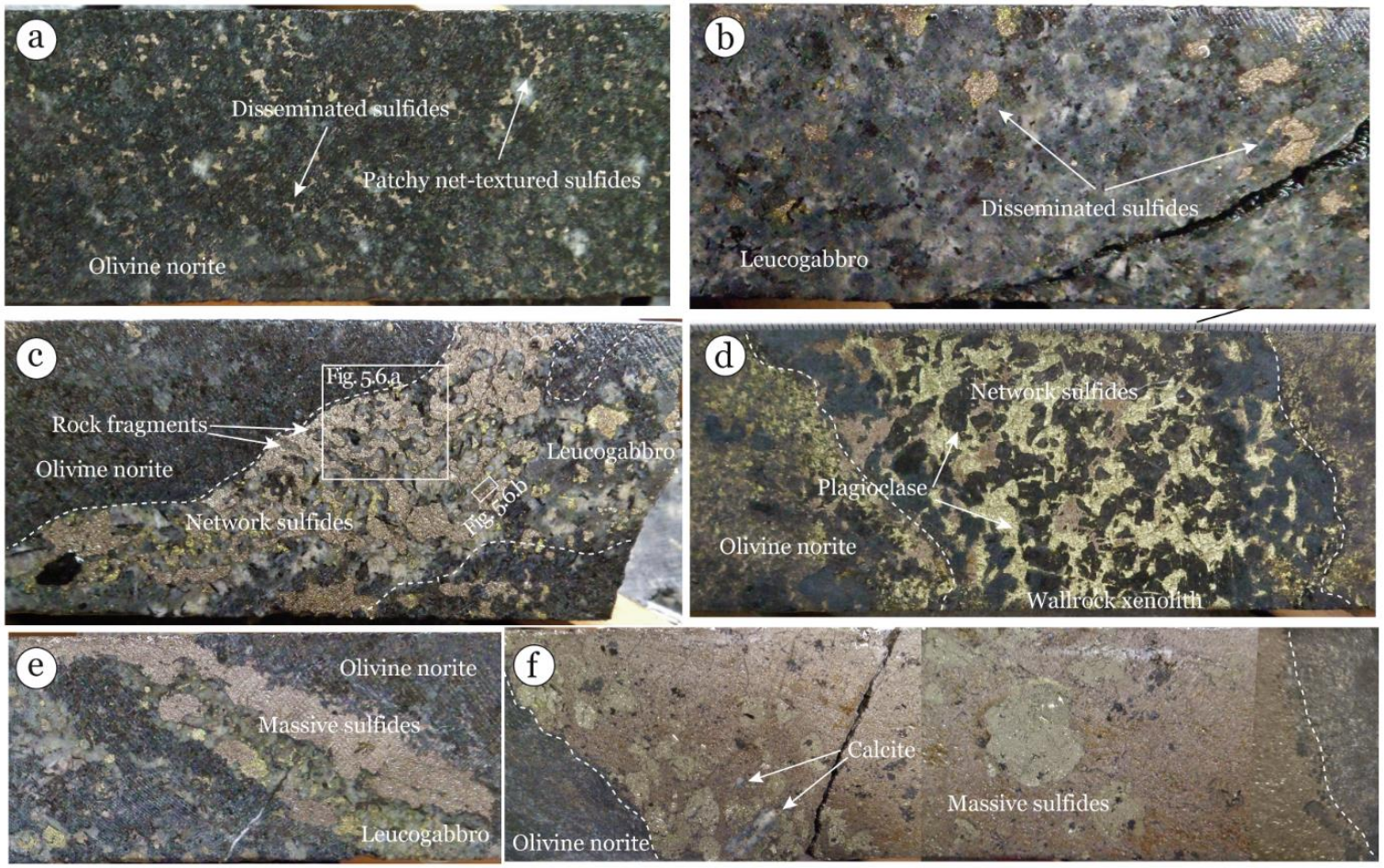

Figure 5.1 Photos of core samples illustrating the sulfide mineralization styles (core diameter is 42 mm). a) Disseminated sulfides hosted in the olivine norite, sample 246.284.5. b) Disseminated sulfides hosted in the leucogabbro, sample 246.230.5. c) Network sulfides hosted in a leucogabbro vein, sample 246.233.2. d) Network sulfides hosted in a wallrock xenolith, sample 246.183.5. e) Massive sulfides hosted in and at the contact of a leucogabbro vein, sample 246.239.7. f) Massive sulfides, sample 264.181.6.

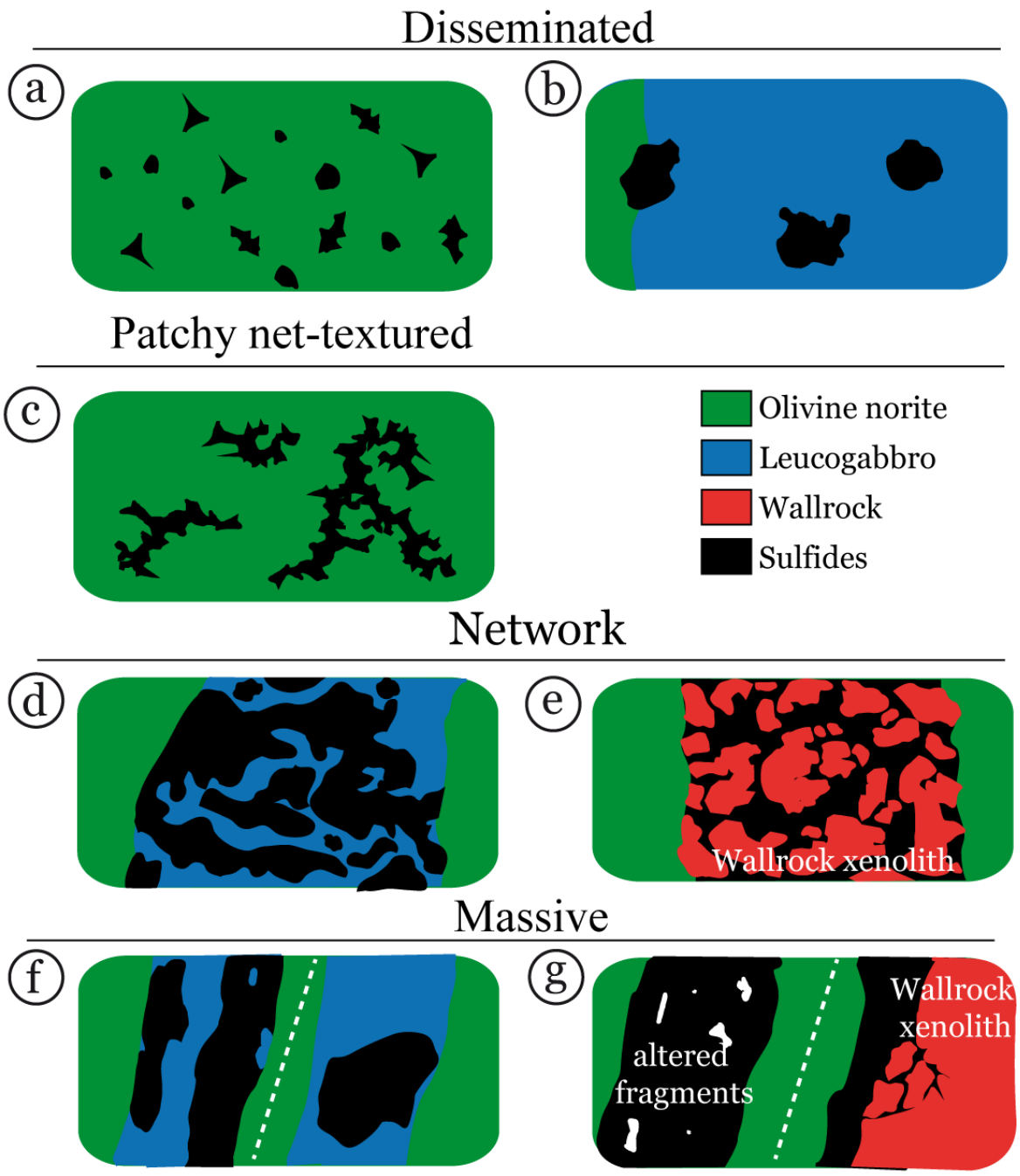

Figure 5.2 Diagrams illustrating the different mineralization styles. a) Disseminated sulfide hosted in the olivine norite. b) Coarse globular sulfides hosted within and at the contact of the leucogabbro. c) Patchy net-textured sulfide in the olivine norite. d) Network sulfide hosted in the leucogabbro. e) Network sulfides hosted in the wall rock xenolith. f) Massive sulfides hosted in the leucogabbro. g) Massive sulfides hosted in the olivine norite and at the wallrock contact. Order of magnitude is given in the text. Some diagrams are inspired from Figure 5.1, (e) is inspired from the Figure 5.9, and right part of (g) is inspired from Figure 5.3.a

Two distinctive characteristics of this type of network are (i) the width of the network channels, which are larger than silicate grains and locally form near massive patches of sulfide and (ii) the mostly lobate contacts between sulfides and silicates. Isolated bulbous sulfides are likely artefact of 2D sections and probably consist of cross sections of channels.

In areas of the network where sulfide proportion exceeds that of silicates, the sulfide network contains domains of leucogabbro as shown in Figure 5.1c. Most of domains are lobate and rounded, but others show straight borders that correspond to silicate crystal faces. Increasing sulfide proportion can lead to massive sulfides containing fragments of silicate minerals or rocks. Within wall rock xenoliths, the networks form a matrix consisting of channels, 200 μm to 1 mm wide, which link near-massive patches of sulfide (3 mm). Aggregates of silicate grains or individual grains are enclosed within the sulfide matrix as shown in Figure 5.1d and Figure 5.2e. Depending on the proportion of sulfide to silicates, the networks are more or less continuous. Like the networks hosted in the leucogabbro, these matrix networks are confined to the wall rock xenoliths, or into the adjacent wall rocks.

The geometry of the networks are defined by the shape and size of the individual crystal or crystal aggregates that are enclosed by the network (Figure 5.1d and Figure 5.1e). Most wall rock xenoliths are composed of large feldspar grains. In some, intergranular quartz or aggregates of plagioclase and biotite are preferentially developed at the contacts of large feldspar grains. As illustrated in the macroscopic sample shown in Figure 5.1d the sulfide networks develop at the interfaces of large plagioclase crystals or aggregates and, in places, include small anhedral plagioclase and biotite grains.

Massive sulfides

This term applies to aggregates of >90% sulfide with areas of >2 cm^2. The remaining 10% consists of individual mineral grains or rock fragments. The largest massive sulfide bodies extent to more than 100 cm along the core but most to few decimeters. Their overall shape is hard to define because of the small size of the core compared to the sulfide bodies, but generally they have non-parallel and irregular borders. Massive sulfides preferentially occur at the contacts of xenoliths or leucogabbro bodies (Figure 5.2f-g and Figure 5.3) and some penetrate nearby into the wall rocks. Rare examples occur in the norite, in areas of strong alteration that make petrographic observations difficult.

There is a continuum between network sulfides and massive sulfides which depends on the relative proportions of sulfide and silicates. The transition between the two is observed at the sample scale where the sulfide network forms large connecting channels or branches, which, in the leucogabbro, can grade into veins of sulfides. Similarly, against the wallrock xenolith the massive sulfide can grade to network sulfides that appears to penetrate into the wallrock xenolith (Figure 5.3a-b).

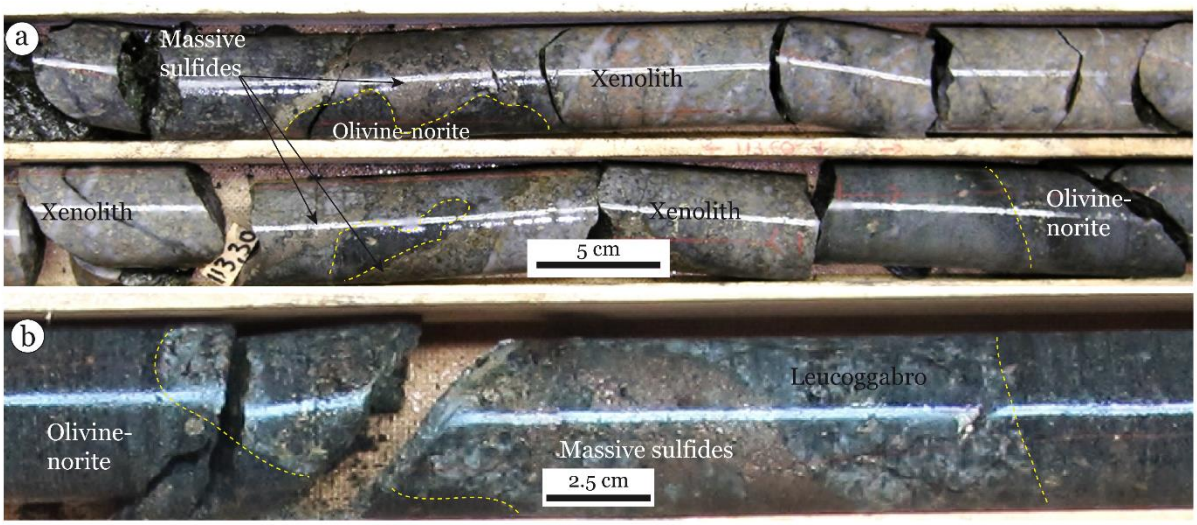

Figure 5.3 Photos of core samples illustrating massive sulfide mineralization. For (a) and (b) massive sulfides occur at the contact between the olivine norite and wall rock xenolith and appears to penetrate into xenoliths, ALA222, from 1122.5 to 113.5 m. refer to right part of Figure 5.2g. c) Massive sulfide vein inside a leucogabbro body ALA247, at 115.5 m.

5.1.2. Morphologies of sulfides and their textural relations with silicate phases

Two types of contacts between sulfide and silicate grains are observed in mineralized domains. Either the silicate crystals impose their shape on the sulfide, and the silicate/sulfide contacts are defined by the crystal faces of silicate grains, or the contacts of the sulfides are rounded or lobate and appear to penetrate into or replace the silicate grains.

Disseminated sulfides

The distribution of disseminated to patchy net-textured sulfides is related to the types of silicate phases; i.e. whether they are cumulus (olivine) or oikocrystic (orthopyroxene, hornblende, biotite). The sulfides preferentially occur in contact with, and interstitial to, sub- to euhedral olivine grains (Figure 5.4). As illustrated in Figure 5.4, in the norites there is a reverse relationship between the abundance of sulfide and the abundance of oikocrystic or interstitial phases: areas with abundant orthopyroxene, hornblende and plagioclase are almost devoid of sulfide.

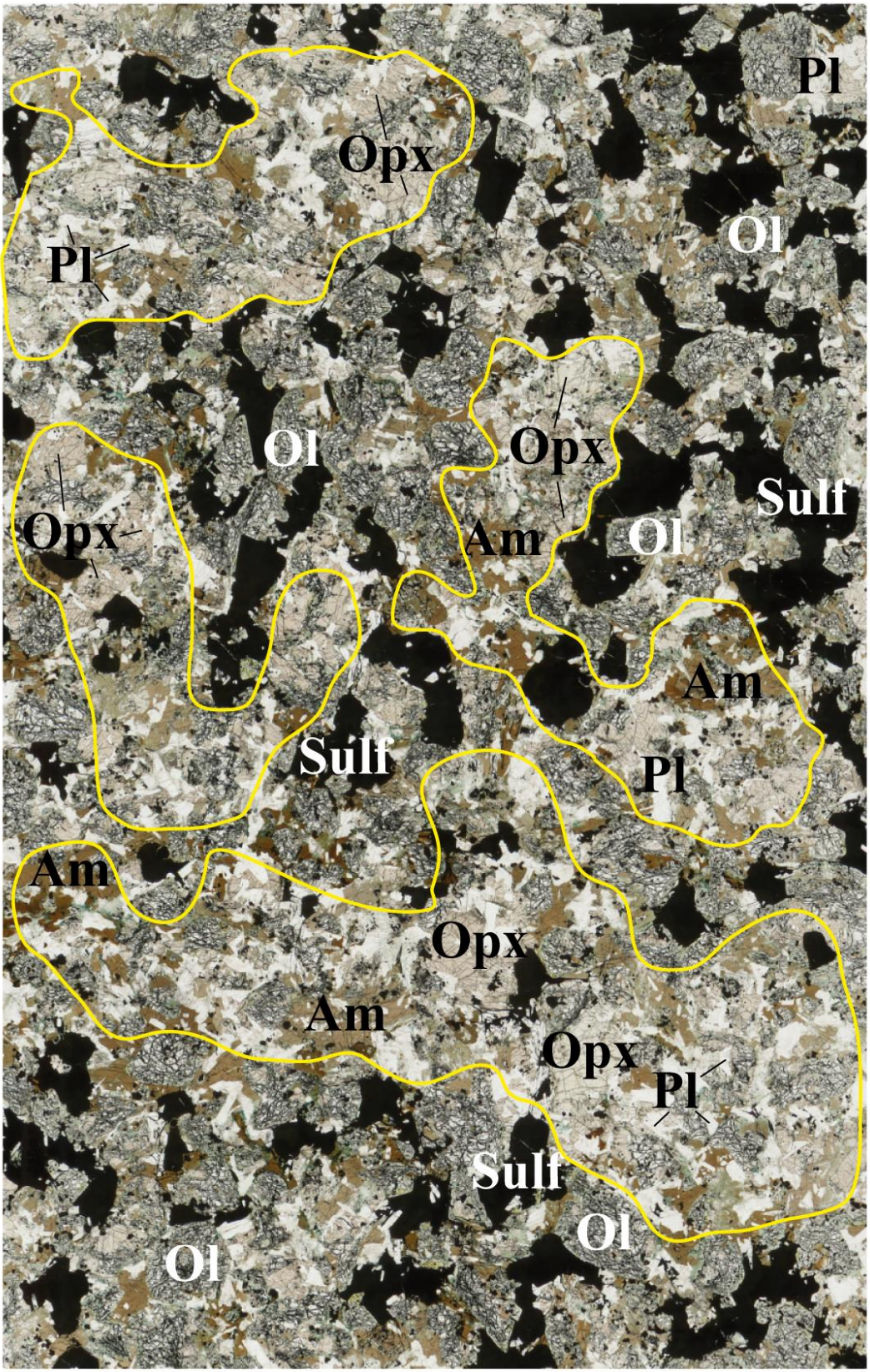

Figure 5.4 Scan of thin section showing the distribution of disseminated sulfides within the olivine norite, sample 246.209.8. The areas outlined in yellow are rich in orthopyroxene, amphibole and plagioclase relative to other areas where olivine and sulfide predominate. Abbreviations: Ol: Olivine; Opx: Orthopyroxene; Pl: Plagioclase; Am: Amphibole; Sulf: Sulfide.

The shape of the disseminated sulfides is directly governed by the type of silicate mineral with which they are in contact. As shown in Figure 5.5a-b, olivine and plagioclase crystals, whether they are sub- or euhedral, impose their habit on the sulfides and define the contacts. In some cases, however, the sulfide forms irregular contacts with plagioclase crystals, with embayments that can crosscut their twinning. More generally, the sulfide adjacent to olivine±plagioclase molds them and is therefore cusp-shaped. Cusps systematically occur at triple junctions between the sulfides and two olivine grains (highlighted by arrows in these figures).

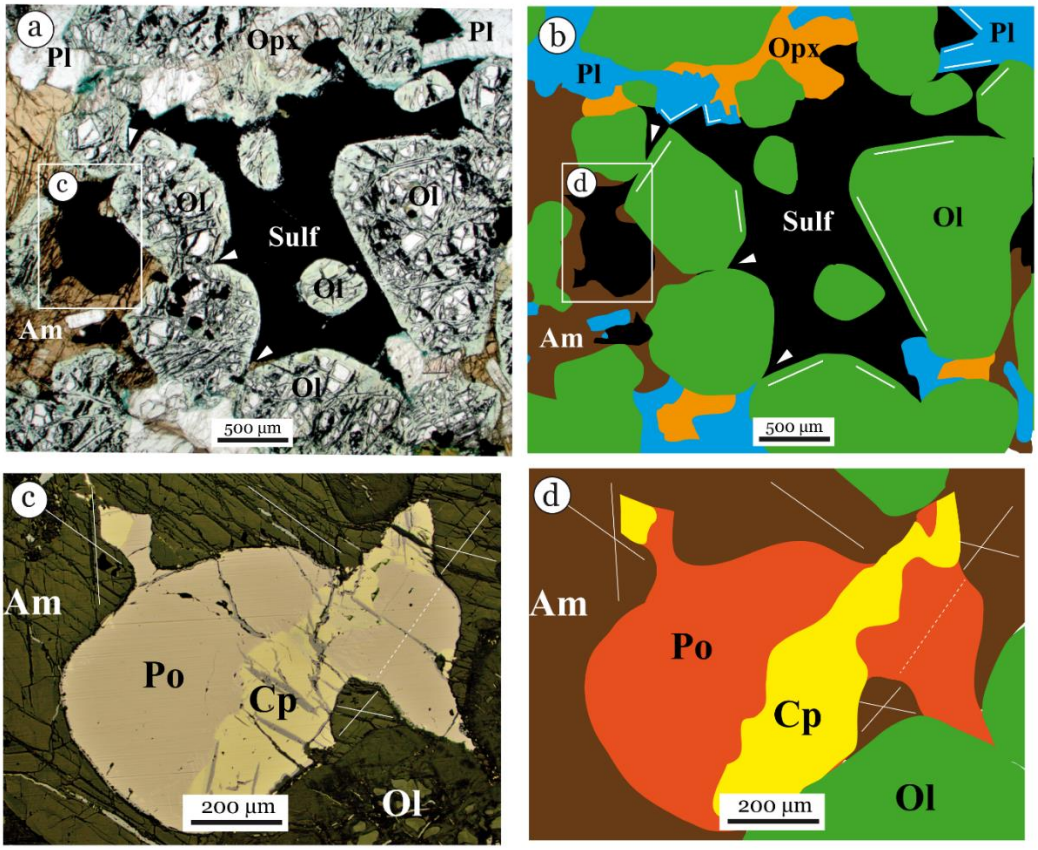

Figure 5.5 a) Photomicrograph and b) sketch illustrating disseminated sulfides in contact with the different silicate phases within the olivine norite, sample 246.280.8. The white thick lines and arrow heads highlight the preserved crystal faces of olivine and plagioclase and the low dihedral angles between sulfide and olivine. c) Photomicrograph and d) sketch depicting a bulbous sulfide in contact with hornblende phases. The white lines indicating the hornblende cleavage allow the identification of the different hornblende crystals. The dashed line links the cleavage of a hornblende interdigitated with the sulfide. Abbreviations: Ol: Olivine; Opx: Orthopyroxene; Pl: Plagioclase; Am: Amphibole; Sulf: Sulfide; Po: Pyrrhotite; Cp: Chalcopyrite.

Dihedral angles at sulfide-olivine contacts were measured in six samples giving average values between 44 and 51° (N=108; Table 5.2). The majority of these angles (76%) are less than 60° indicating that sulfide wets the olivine crystals (Rose & Brenan, 2001). Dihedral angles involving sulfides and plagioclase are too rare to be measured accurately.
Disseminated sulfides in contact with oikocrystic or interstitial phases (i.e. orthopyroxene, hornblende and biotite) generally have globular forms (Figure 5.5c-d), and the sulfide appears to impose its shape on the silicate mineral grains. The sulfide blob of Figure 5.5c-d, has a sinuous lobate contact with hornblende and appears to cut across cleavage traces of the two adjacent hornblende grains.

Table 5.2 Dihedral angles between sulfides and two olivine crystals

Sample no.	Number	Min	Max	Average	Median
246.280.8	16	27	71	44	41
246.290.7	25	13	109	44	40
246.293.1	20	10	114	51	49
246.300.9	13	13	79	49	51
246.302.0	26	15	101	45	42
246.308.0	8	13	109	46	41

Network sulfides
The contours of net-textured sulfides are also controlled by the form and nature of rock or silicate minerals. At Älgliden, we observed two distinctive types of sulfide networks, those in leucogabbros and those in wallrock xenoliths.

In the leucogabbros, both sharp and gradual contacts can be observed between the sulfides and silicate host rock (Figure 5.6a). Sharp contacts are more common when sulfide is more abundant and occurs at large scale (i.e. at the leucogabbro body scale) and gradual contacts where sulfide is sparse and at a smaller scale (a few millimeters; Figure 5.6).
Small networks with irregular contacts occur locally, at small scale: (i) within larger network that have sharp contacts with the host rock or (ii) at the margins of relatively large globular sulfide or massive sulfides hosted in leucogabbros. In these occurrences, sulfides appear to resorb some phases and/or specific parts of silicate minerals: they replace or resorb parts of the albitic plagioclase rims while the cores are well preserved, and apatite grains are partially resorbed when they are entirely hosted in sulfide or are better preserved where they are in

contact with plagioclase (Figure 5.7). This leads to the formation of complex small-scaled networks with jagged contacts between sulfides and the silicate or phosphate minerals.

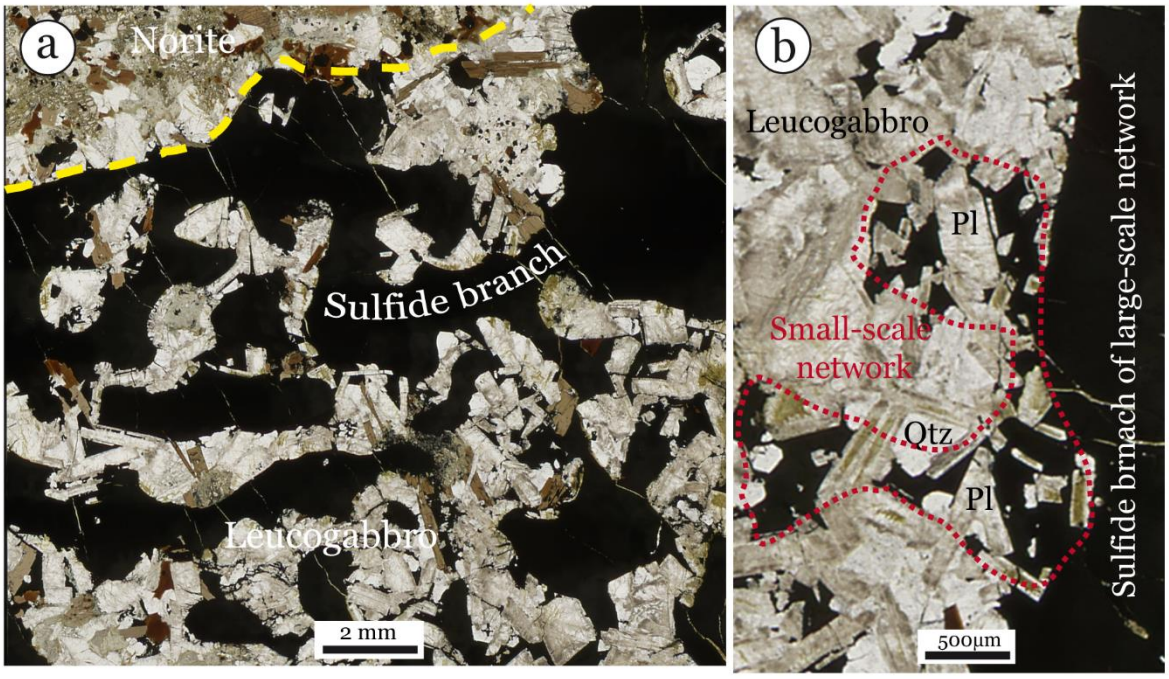

Figure 5.6 Network sulfides hosted in the leucogabbro. a) Scan of thin section showing the "worm-gallery"-shaped network hosted in a leucogabbro vein, sample 246.233.2. b) Scan of thin section illustrating the two types of contact and network between a sulfide gallery branch and the leucogabbro: irregular in the small-scale network and frank and sharp on the upper part of the sulfide branch, sample 246.233.2. Abbreviations: Pl: Plagioclase; Qtz: quartz.

Larger sulfide networks or veins commonly have sharp, lobate contacts with leucogabbro (Figure 5.6a-b and Figure 5.8). In this case, the sulfide imposes its shape and seems to cut indiscriminately across crystal boundaries. This type of contact is well developed where sulfides predominate. In Figure 5.8, a rounded domain of leucogabbro is in both sharp and lobate contact with the sulfides. The twin planes of plagioclase laths are sharply transected by the sulfide. The sulfides also crosscuts secondary (i.e. likely deuteric) phases. For example in Figure 5.8 the sulfides cut across quartz-feldspar intergrowths and the chloritic cores of plagioclase, and they truncate boundaries between silicate grains. On the bottom right of Figure 5.8, sulfide-filled embayments penetrate deeply into a plagioclase crystal. Just above, rounded quartz grains are enclosed within the sulfides. However, sulfide network also contains numerous plagioclase crystals that exhibit preserved faces and retain their overall magmatic habit (Figure 5.8a-b).

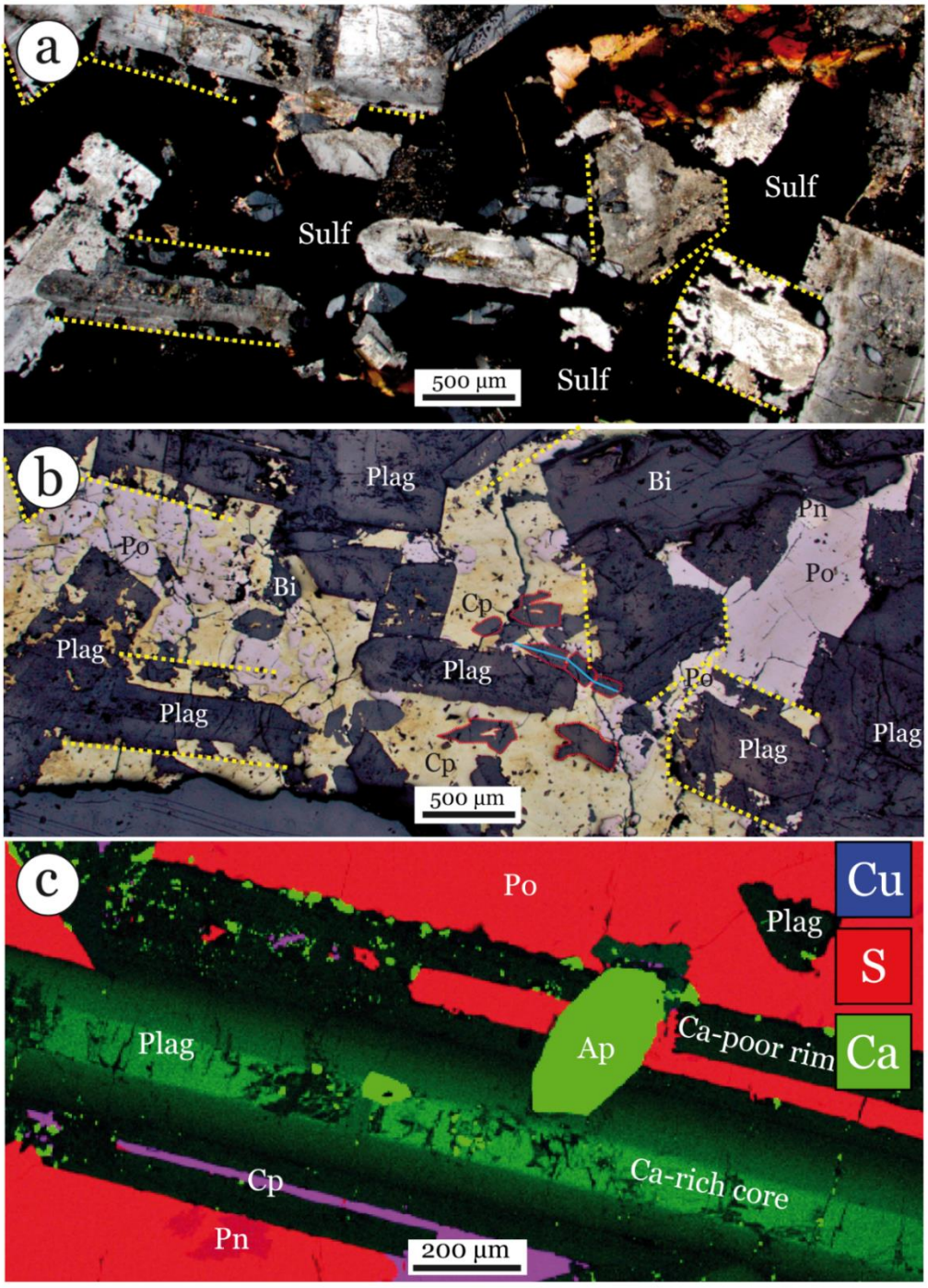

Figure 5.7 Small-scale network of sulfides in the leucogabbro. a) Photomicrograph in transmitted light and b) in reflected light illustrating the contacts between the sulfides and the plagioclases of the leucogabbro at the margin of a relatively large disseminated globule of sulfide, sample 246.233.5. The dashed yellow lines represent the faces of plagioclase crystals if they were euhedral. Note that the cores of zoned plagioclases often show straight contacts with the sulfide, contrary to the plagioclase rims. Some resorbed apatite grains are outlined in red, and one shows relatively preserved habit in contact with plagioclase grains. c) Chemical map of Cu, S and Ca illustrating resorption of plagioclase rims by the sulfides. Note the well-preserved apatite grain partially included in the plagioclase lath, sample 246.233.2. Abbreviations: Plag: Plagioclase; Bi: Biotite; Sulf: Sulfide; Po: Pyrrhotite; Pn; Pentlandite; Cp: Chalcopyrite.

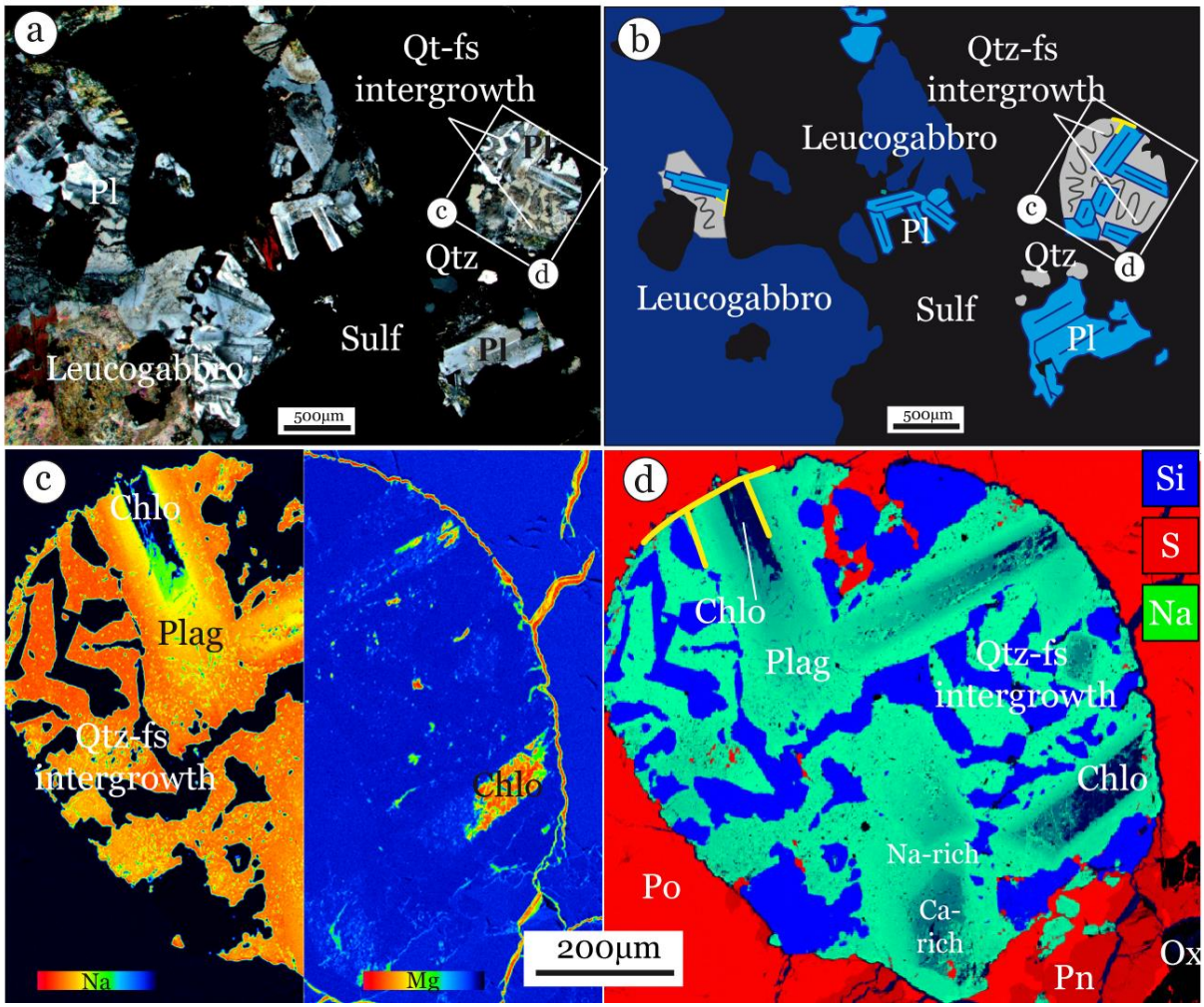

Figure 5.8 Rounded fragment of leucogabbro within the sulfide network, sample 246.232.5. Photomicrograph in a) transmitted light and b) sketch of the leucogabbro fragment. Note the plagioclase with idiomorphic shape and preserved faces and the truncated and lobate outlines of the quartz-feldspar intergrowth and plagioclase. Chemical maps of (c) Na on the left part and Mg on the right part, and (d) Si, S and Na. The yellow lines highlight the truncated silicate grain joints. Abbreviations: Pl: Plagioclase; Qtz: quartz; Qtz-fs: Quartz-feldspar; Chlo: Chlorite; Ox: iron oxide; Sulf: Sulfide; Po: Pyrrhotite; Pn; Pentlandite.

In places where the plagioclase grains are partially to fully chlorite-altered, i.e. in wallrock xenoliths, the large chlorite crystal developed near the sulfide contact have grown into the sulfides and hide the primary contact but the overall shape of the plagioclase is preserved (e.g. left of Figure 5.9a-b). Plagioclase as well as biotite grains are not always completely preserved especially when they occur as small grains within the sulfides. For example, in Figure 5.9c-d the outlined plagioclase shows embayments and has disaggregated in several pieces. Most biotite crystals are anhedral, with jagged contacts, and sulfides penetrate along their cleavage planes.

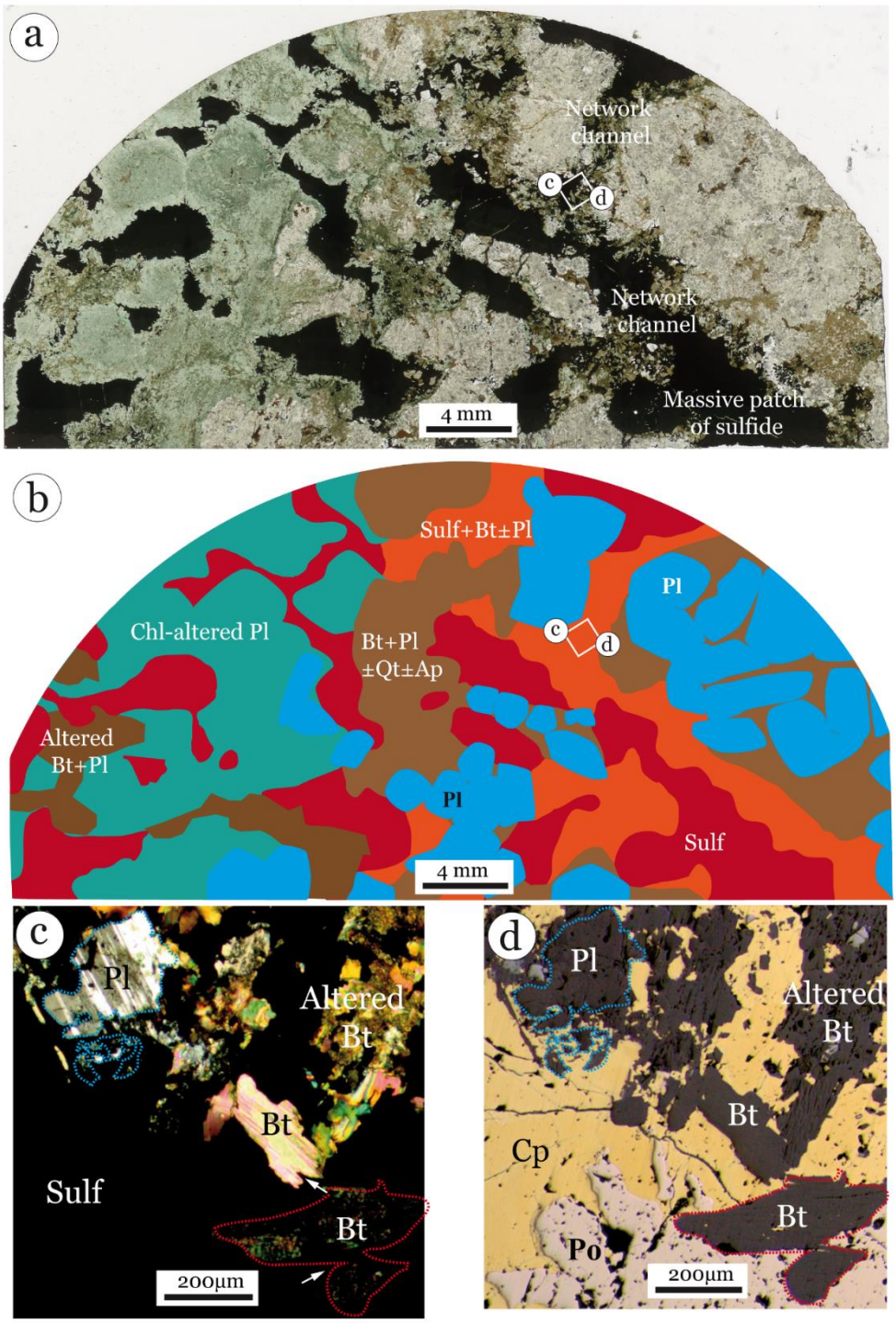

Figure 5.9 Network sulfides in wallrock xenolith, sample 264.190.1. a) Scan of thin section and b) sketch illustrating the semi-continuous sulfide network around large plagioclase crystals or silicate aggregates, and showing the channels of the network as being a mixture of sulfides, biotite and plagioclase. c) Transmitted and d) reflected light showing silicates crystals with resorbed faces. The dashed blue and red lines highlight the portions of a plagioclase crystal and an indented biotite crystal. Note that indentations (some are shown by arrow heads) occurred preferentially at biotite cleavages. Abbreviations: Pl: Plagioclase; Qtz: quartz; Fs: Feldspar; Bt: Biotite; Chl: Chlorite; Ap: Apatite; Sulf: Sulfide; Po: Pyrrhotite; Pn; Pentlandite; Cp: Chalcopyrite.

Massive sulfides

Within leucogabbros, the massive sulfides show two different relationships with the silicate crystals. Figure 5.10a illustrates an example of massive sulfides hosted within and at the margin of a leucogabbro vein. At the contact between the leucogabbro vein and the olivine norite, silicate grains from the olivine norite that are included into massive sulfides show rounded and corroded morphologies (Figure 5.10a-b). The boundary between silicate grains are cut by the sulfides in a leucogabbro fragment hosted in the massive sulfides (Figure 5.10c).

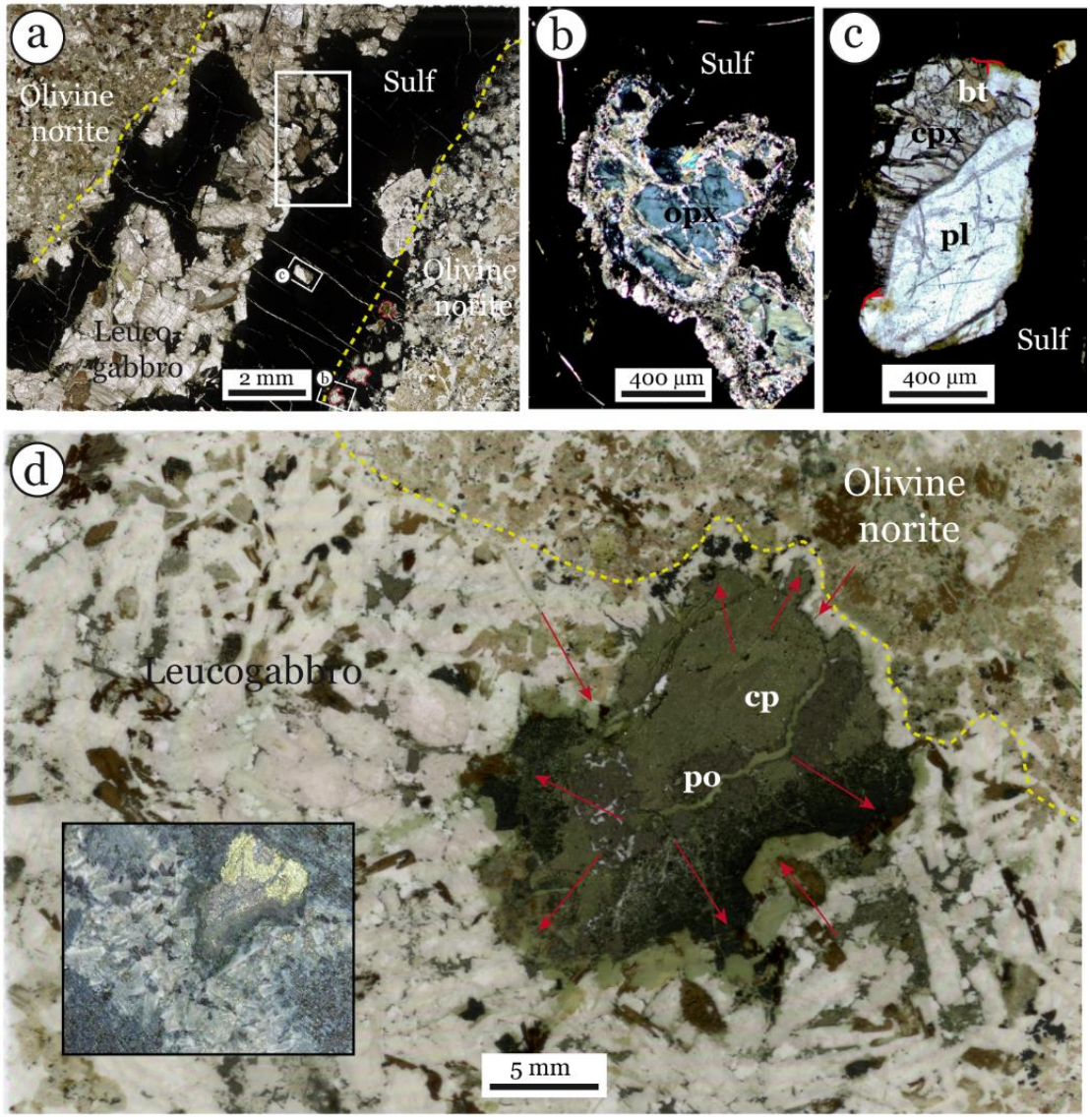

Figure 5.10 Massive sulfides associated with leucogabbro. a) Massive sulfides hosted in a leucogabbro vein, along its contact with the olivine norite, sample 248.233.9. Sulfides locally grade into small-scale network sulfides at the contact with the leucogabbro. Note the different texture in the rectangle, with (b) corroded silicate grains and (c) the close up which shows a truncated silicate grain joint. d) Globule of massive sulfides hosted in leucogabbro. Both silicate and sulfide grains impose their shape to each other with equilibrium texture (straight and clear contacts). Red arrows illustrate spatial competition where the sulfide globule forms bulges and embayments. Inset: Photomicrograph of the hand-specimen. Abbreviations: Opx: Orthopyroxene; Cpx: Clinopyroxene; Bt: Biotite; Chl: Chlorite; Ap: Apatite; Sulf: Sulfide; Po: Pyrrhotite; Cp: Chalcopyrite.

However, leucogabbros can also host massive sulfides without crosscutting or resorbing textures. Instead they show embayments and bulges where both silicate and sulfide grains are in equilibrium. In these cases, the sulfide masses has a globular shape similar to that of globular disseminated sulfides hosted in leucogabbros (Figure 5.10d).

Massive sulfides are observed in places where the norite is strongly altered into talc+tr±cb±mgt and the relationships between sulfide and silicate are difficult to describe. We however report some microscopic evidences of ubiquitous relationships. As described previously, plagioclase crystals within xenoliths have undergone partial to full chlorite-alteration. When in contact with the sulfides, chlorite crystals that have replaced the plagioclase are far larger at the margin of the altered grain and have grown into the sulfides. Primary contacts are therefore overprinted. However, locally, when not fully altered to chlorite, plagioclase crystals within xenolith can show primary contacts as illustrated in Figure 5.11 where an albitized plagioclase at the margin of the massive sulfides contains an embayment filled with sulfides.

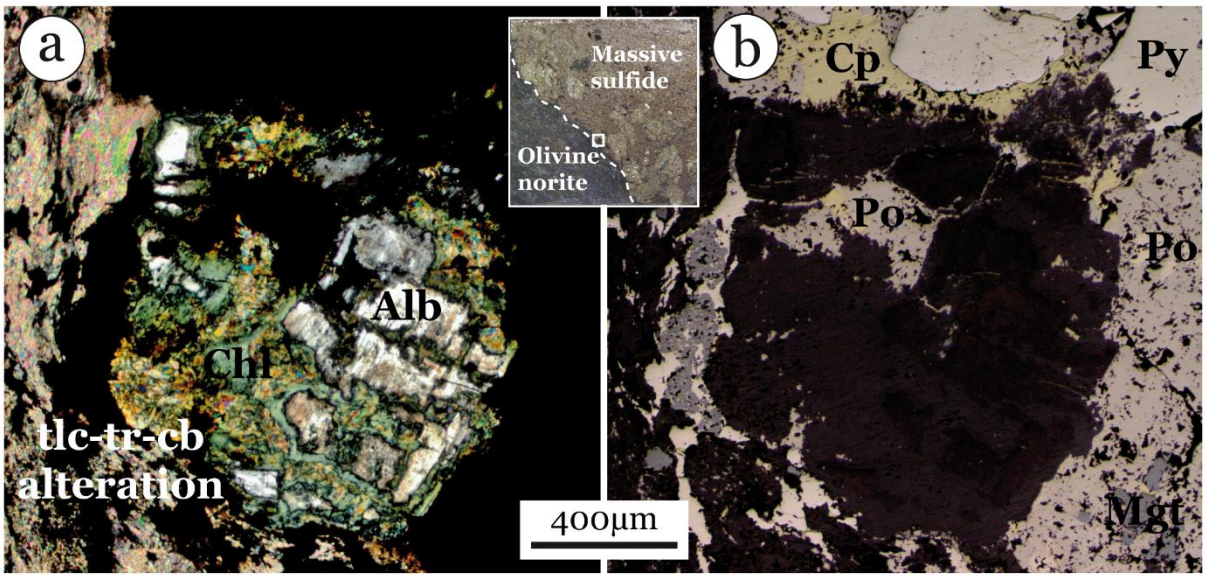

Figure 5.11 Crosscutting relationship between massive sulfides and a feldspar grain of xenocrystic origin located at the margin between massive sulfides and the olivine norite. a) Transmitted light in cross Nicols. b) Reflected light. Abbreviations: Chl: Chlorite; Alb: Albite; tlc: Talc; tr: tremolite; cb: Carbonate; Po: Pyrrhotite; Cp: Chalcopyrite; Py: Pyrite; Pn: Pentlandite.

5.1.3. Sulfide phases: texture, abundance and distribution

The sulfide phases are pyrrhotite, chalcopyrite and pentlandite, with or without pyrite and commonly associated with magnetite (Figure 5.12, Table 5.3).

Table 5.3 Sulfides phase proportions among disseminated sulfides.

Sample no.	pyrrhotite	chalcopyrite	pentlandite	magnetite
		vol.%		
246.280.8	76.6	17.0	3.1	3.3
246.293.1	91.1	4.8	1.9	2.1
246.302.0	85.8	12.0	0.9	1.3
246.209.8	79.7	14.2	3.5	2.6
246.233.5	84.6	12.7	0.6	2.1

Pyrrhotite is the most widespread sulfide and accounts for approximately 80% of the overall sulfide phases (Figure 5.1, Figure 5.12 and Figure 5.13b-d); in network sulfides and massive sulfides it can reach more than 95%. Grains are exclusively anhedral showing (i) lobate interdigitation with chalcopyrite, (ii) small to large exsolution lamellae of pentlandite, and (iii) mostly rectilinear contacts with the magnetite or pyrite (Figure 5.13). In some disseminated sulfides, pyrrhotite shows wavy exsolution lamellae of hexagonal and monoclinic pyrrhotite.
Chalcopyrite generally accounts for 5 to 17 vol.% of the sulfides. It is scarce in large massive sulfide bodies and also rare in large-scale sulfide networks hosted in the leucogabbro. However, chalcopyrite is locally the predominant sulfide in some sulfide networks such as in small-scale networks in leucogabbros and networks in wall rock xenoliths (Figure 5.1d and Figure 5.12a-b). In Figure 5.1d, the sulfide network is composed of approximately 80 vol.% chalcopyrite. Overall, it occurs as areas of pure chalcopyrite with more or less interdigitated contact with pyrrhotite (Figure 5.6d and Figure 5.13c), or occur as isolated exsolution lamellae or bulbous shapes within the pyrrhotite.

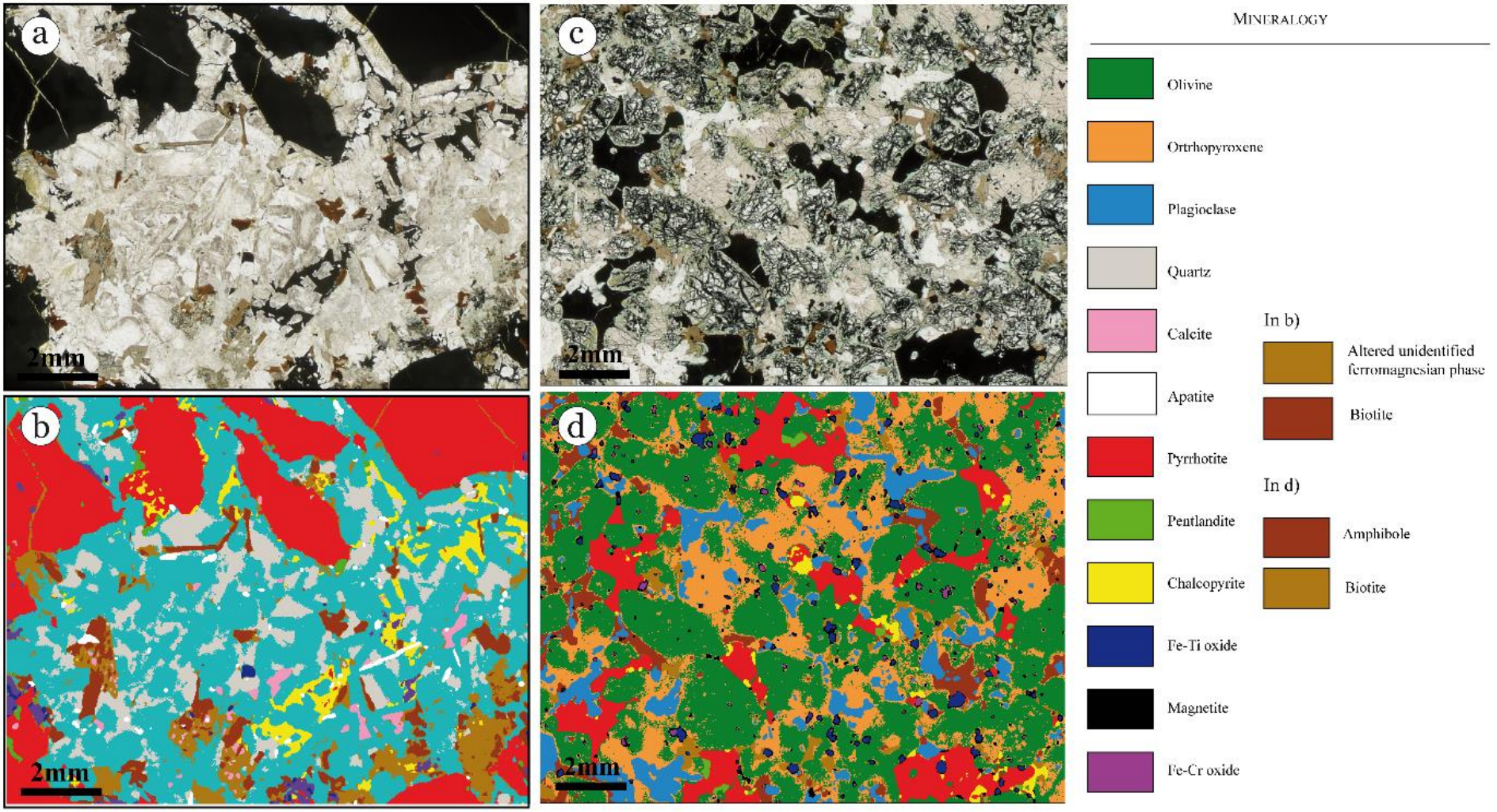

Figure 5.12 Thin section scans and X-ray micro fluorescence derived maps of (a-b) Network sulfides in the leucogabbro and (c-b) disseminated sulfides in the olivine norite. Note the sulfide phase proportions and the large- and small-scale networks of sulfide dominated by pyrrhotite and chalcopyrite, respectively.

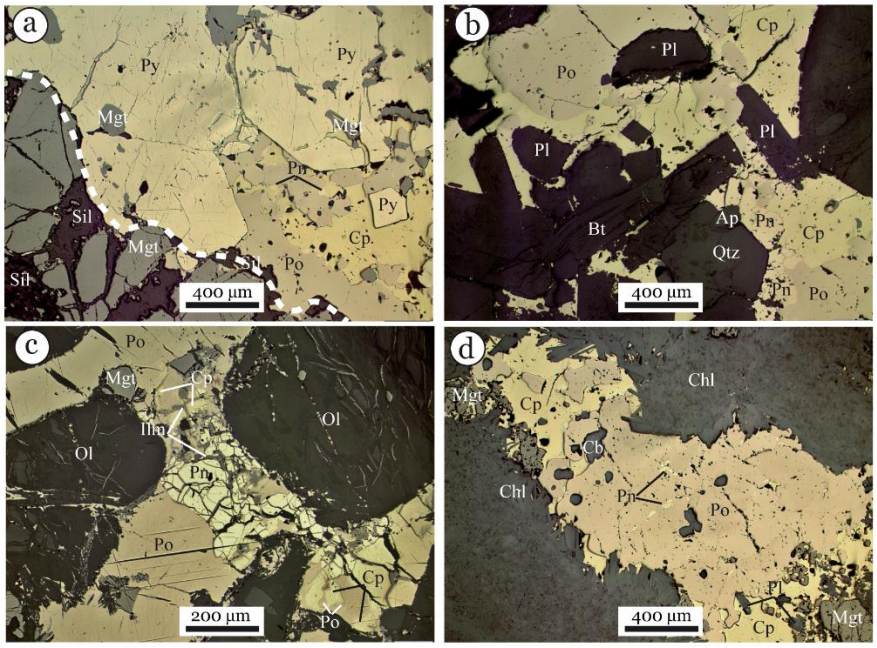

Figure 5.13 Microphotographs illustrating sulfide phase texture in reflected light. (a) Massive sulfide body edge with a rim of subhedral magnetite grain. (b) Network sulfide hosted in the leucogabbro, made of pyrrhotite, chalcopyrite and pentlandite. Note the granular pentlandite grain. (c) Disseminated sulfides. Note the large granular pentlandite grain and the pyrrhotite/chalcopyrite exsolutions. Ilmenite is located at sulfide grain boundary. (d) Network sulfide hosted in a wallrock xenolith. The sulfide channel consists in pyrrhotite, chalcopyrite and small flames of pentlandite. Abbreviations: Sil: Silicate; Chl: Chlorite; Alb: Albite; tlc: Talc; tr: tremolite; cb: Carbonate; Po: Pyrrhotite; Cp: Chalcopyrite; Py: Pyrite, Mgt: Magnetite.

Pentlandite is a minor sulfide phase (1-3.5 vol.%). It occurs as exsolution lamellae located at irregularities (grain joint, cracks, pore…) as small oriented flames (tens of microns) or as relatively massive granular crystals (> 100 µm; Figure 5.13b-d) in pyrrhotite.

The pyrite is abnormally abundant for magmatic ore (from 1 to 10 vol.% of sulfides) and is preferentially distributed at margins of the dike, especially when the dike width is small and in spatial association with chlorite/actinolite alteration (Figure 5.14). Close to the margins, pyrite can be the most abundant sulfide phase or even be the sole sulfide phase (Figure 5.14). Disseminated pyrite occurs as single euhedral crystals or subhedral aggregates with or without other sulfide crystals. Otherwise, the pyrite occurs in massive sulfides as sub- to euhedral crystals within a massive pyrrhotite/chalcopyrite groundmass (Figure 5.13a). The grain boundaries with other sulfides and with magnetite are sharp and regular.

Magnetite frequently occurs as a minor phase (1-3 %) in the sulfides. Grains are quite large, especially in massive sulfides (>300 µm), relative to those in the host rocks (<200 µm). They occur mainly along the margins of the sulfide assemblages. Most are sub- to euhedral but some are rounded (Figure 5.13a and c). Magnetite also forms rims between massive sulfide bodies and their silicate host rock.

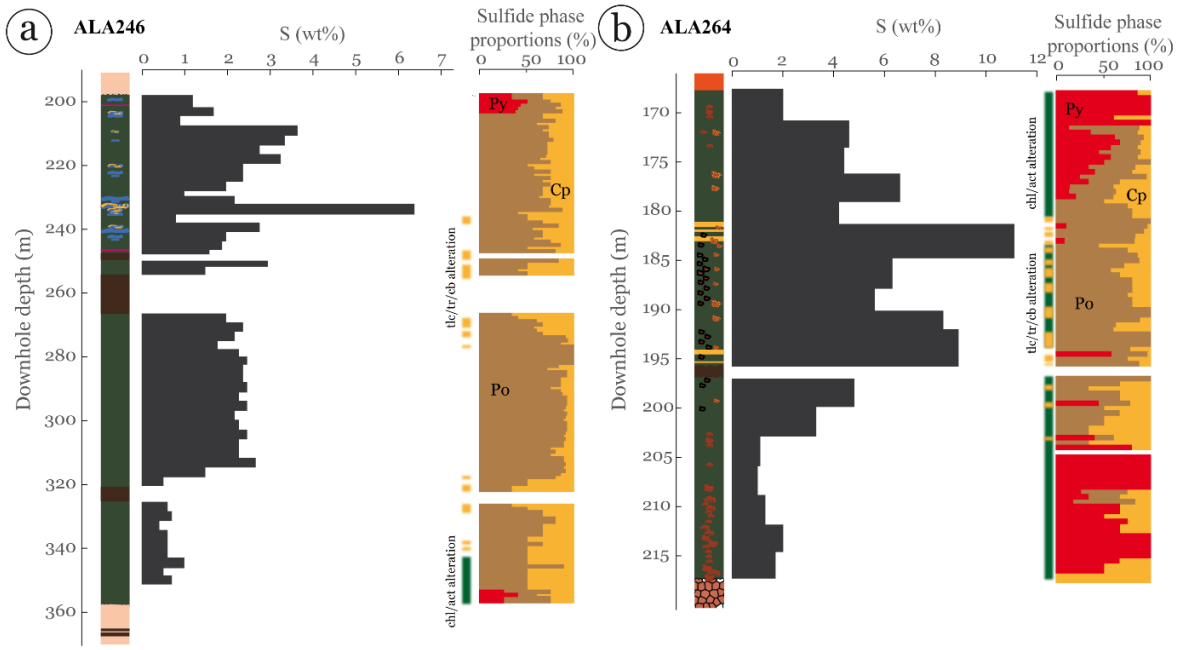

Figure 5.14 Log indicating S contents and sulfide phase proportions through (a) drillcore 264 and (b) drillcore 246. Because chalcopyrite is minor and more eye-catcher its estimation is probably overestimated. Abbreviations: Chl: Chlorite; tlc: Talc; tr: tremolite; cb: Carbonate; Po: Pyrrhotite; Cp: Chalcopyrite; Py: Pyrite; Pn: Pentlandite; Cb: Carbonate.

5.1.4. Ore distribution

Vertically, the sulfide distribution is quite continuous whatever the position along the strike of the dike (Figure 5.15). Figure 5.15 shows two cross sections, one located in the wide central part and the other at a thin termination of the dike. Along each cross section, the sulfide distribution pattern, as well as the mineralization style are similar for the two drillcores. Relative variations and absolute S contents can be vertically transposed from core to core, over 150 m depth.

Along strike, the sulfide distribution is not always continuous, and can vary significantly from one core to another one (e.g. ALA263 and -264; Figure 5.16), but a persistent tendency appears. The highest sulfide concentrations are preferentially distributed in thin NE and SW terminations (Figure 5.16). They mostly consist of massive sulfides and network sulfides associated with xenoliths or located at dike margins in some cases penetrating into the adjacent wallrock. In the wide central part of the dike, the highest sulfide concentrations are observed as network to massive sulfides in association with the leucogabbro (e.g. ALA246, -247, 266), but locally can also penetrate into the adjacent wallrock as illustrated in Figure 5.15b. In this wide central portion, sulfur concentrations are overall moderate (Figure 5.16) and sulfides are mostly disseminated in the olivine norite. As an example, ALA246, one of the most prospective cores in terms of sulfide tonnage, contains 52 m at 2.3 wt.% S (from 267 m to 319 m) composed exclusively of disseminated sulfides in the olivine norite.

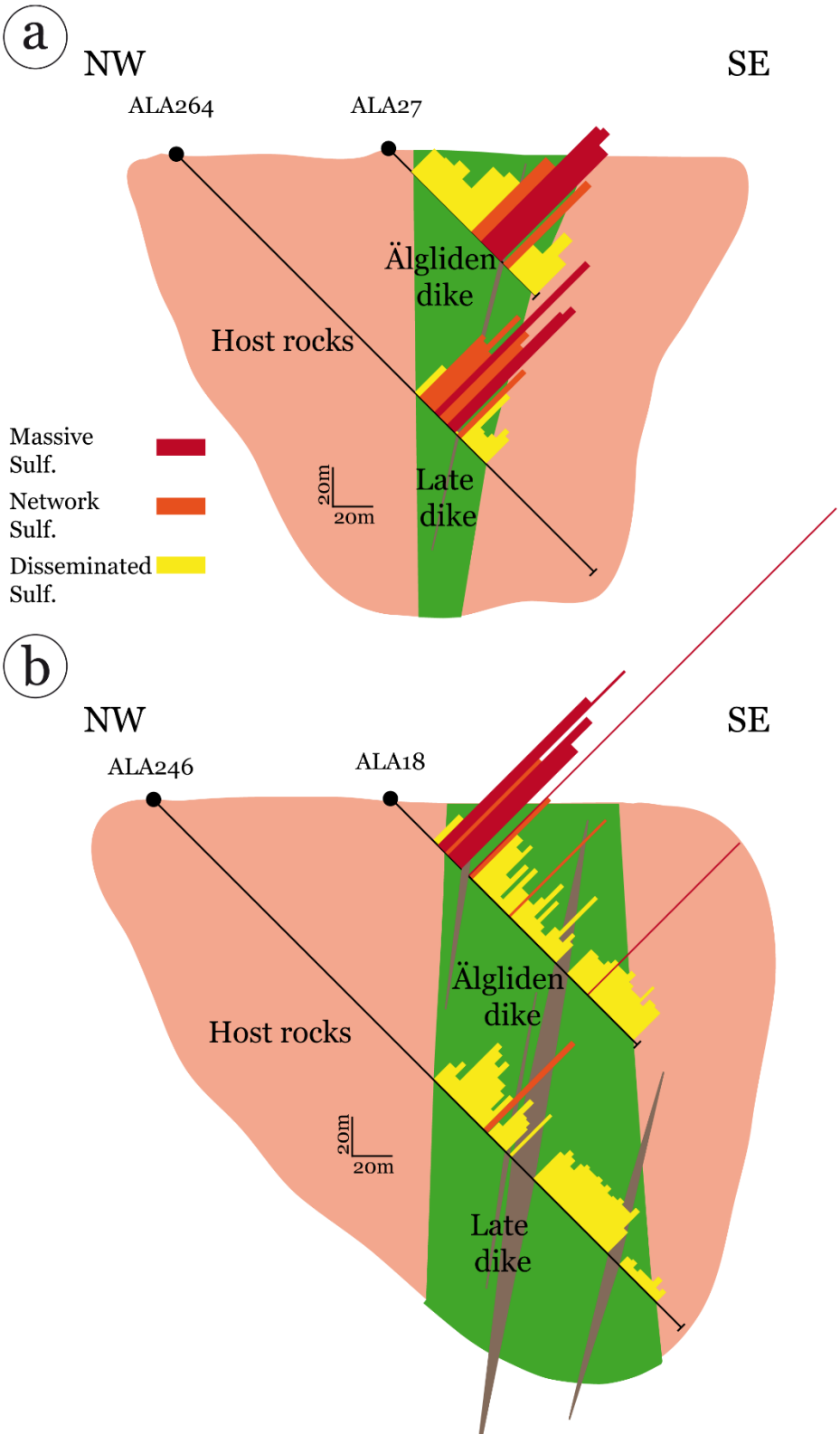

Figure 5.15 Cross sections of the dike showing the vertical distribution of the S content and the sulfide mineralization styles (a) in a thinner part of the dike (ALA264 and ALA27) and (b) in the wide central part of the dike (ALA246 and ALA18). S contents (Boliden unpuplished data) are at the same scale in all drillcores. Abbreviations: Sulf: Sulfides.

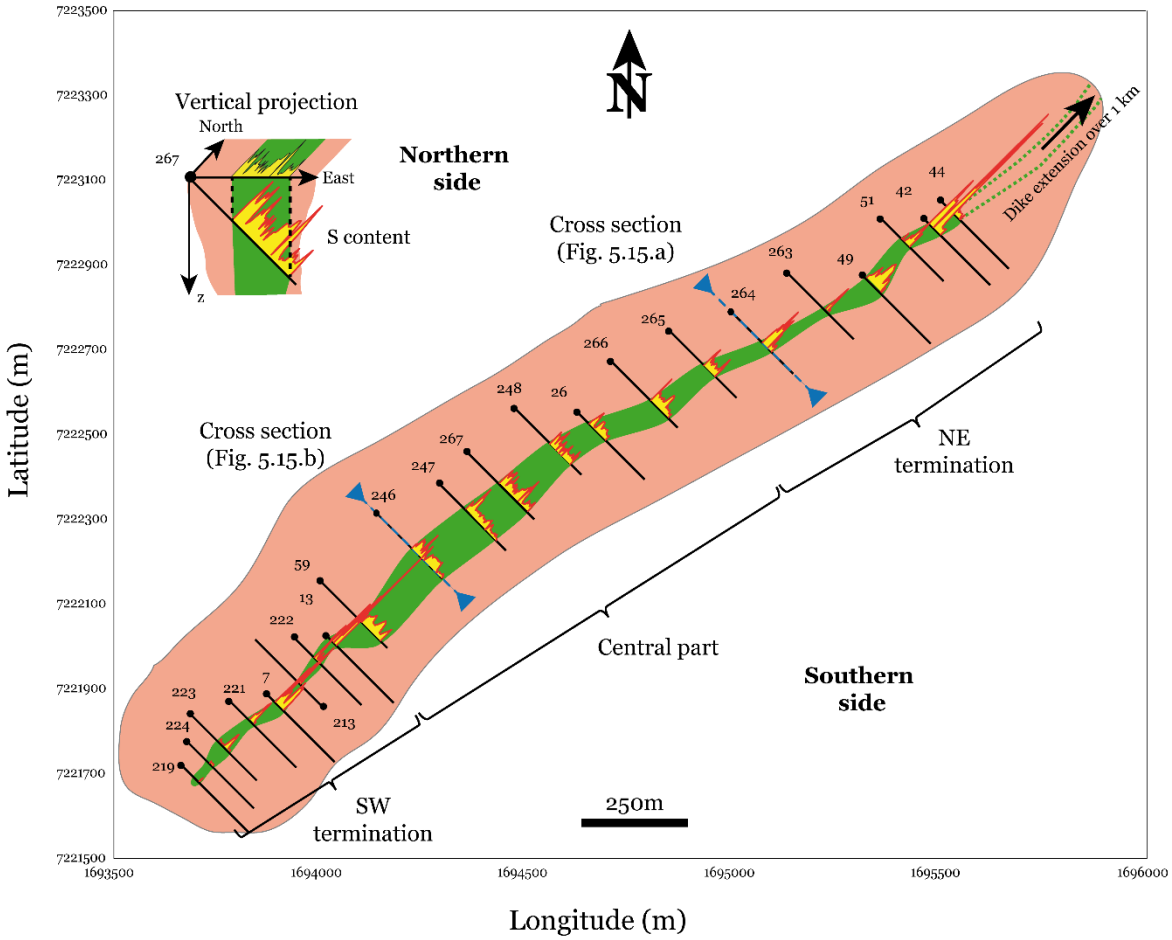

Figure 5.16 Distribution of S content (wt.%; i.e. sulfide proxy; from Boliden unpublished data) along the dike. The apparent outline of the dike as well as the sulfide distribution are made by vertical projections from different depths. Drill cores 7 to 59 intercept the middle of the dike at approximately 100 m and drill cores 213 to 267 at 200 m.

5.2. Sulfur isotope composition

Sulfur isotope compositions of sulfides of the different lithologies are reported in Figure 5.17 and Table 5.4. In the olivine norites the sulfides have a moderate range of positive $\delta^{34}S$ value, ranging from 3.8 to 4.6‰. Sulfides hosted in leucogabbros fall in this range. One sample of xenolith with magmatic sulfides have a relatively high $\delta^{34}S$, i.e. at the upper limit of the range of the Älgliden rocks. The porphyry-style sulfides of the wall rocks have a moderate range of $\delta^{34}S$ whose lower limit is close to that of the Älgliden range but that extents to higher values, up to 6.2 ‰ $\delta^{34}S$. Both magmatic and hydrothermal sulfides have $\delta^{34}S$ values higher than in the mantle of mid-ocean ridge or oceanic island basalts (i.e. $\delta^{34}S \approx 0 \pm 0.5$‰; Sakai et al., 1982, 1984). However, the S isotopic composition of magmas from subduction zones range from 1.5 to 6.5 ‰ and overlaps those in dike and wall rocks.

Table 5.4 Sulfur isotope composition of suflide of the Älgliden rocks and the wall rocks

Sample no.	Host rock	monosulfide[a]		disulfide[a]		Bulk	$\Delta^{33}S$
		$\delta^{34}S_{V\text{-}CDT}$	wt.%	$\delta^{34}S_{V\text{-}CDT}$	wt.%	$\delta^{34}S_{V\text{-}CDT}$	
264.161.8	Wallrock	4.79	42	7.23	58	6.21	-0.025
246.194.7	Wallrock	none	0	5.03	100	5.03	-0.026
246.196.3	Wallrock	none	0	5.03	100	5.03	-0.014
264.190.0	Xenolith	3.23	27	5.16	73	4.64	-0.028
246.232.6	Leuco.	3.68	74	5.29	26	4.10	-0.025
246.240.8	Leuco.	3.06	64	5.81	36	4.05	-0.023
264.280.8	O. nor.	3.01	25	5.06	75	4.55	-0.019
264.293.1	O. nor.	4.05	62	3.35	38	3.78	-0.005
246.353.6	O. nor.	3.62	50	4.78	50	4.20	-0.023
264.211.3	O. nor.	none	0	4.35	100	4.35	-0.007

(a): monosulfides refer to chalcopyrite, pyrrhotite and pentlandite whereas disulfides refer to pyrite

Abbreviations: Leuco: Leucogabbro; O. nor.: Olivine norite; V-CDT: Vienna Canyon Diablo Troilite

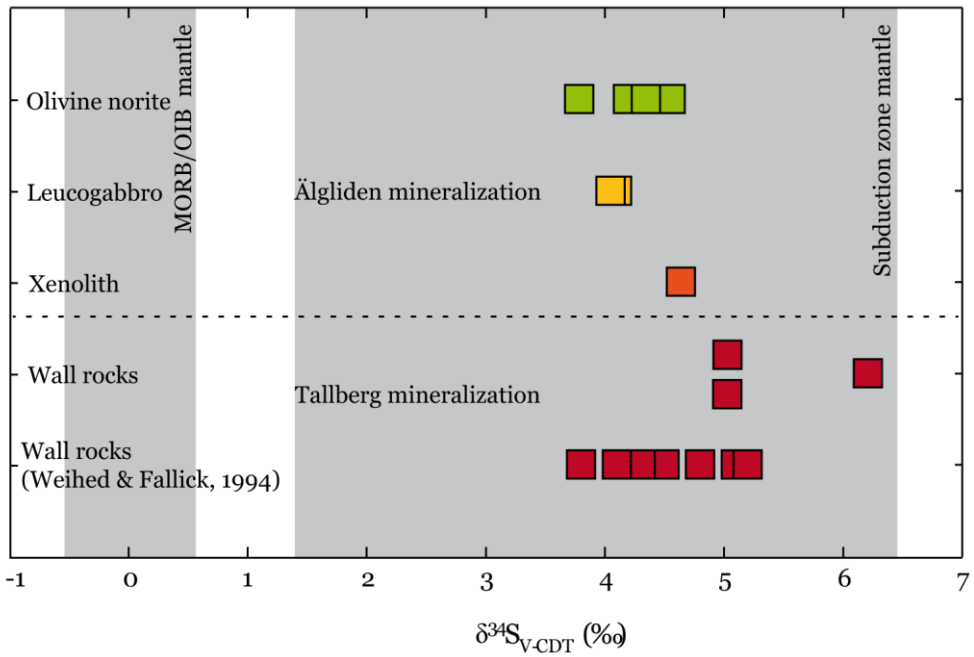

Figure 5.17 Sulfur isotopic composition of sulfides from the Älgliden dyke and the Tallberg porphyry wall rocks. The grey field represents a range of $\delta^{34}S$ compositions from subduction settings: Marianas arc (1.4–5.5‰; Alt et al., 1993); Indonesian arc (4.7 ± 1.4‰, 1σ; de Hoog et al., 2001); Mexican arc (2.7–6.4; Luhr and Logan, 2002); Japanese arc (4.4 ± 2.1‰, 1σ; Ueda and Sakai, 1984); and Sierra Nevada batholith (1.6–4.0‰; Ishihara and Sasaki, 1989). Some wall rock data are from Weihed & Fallick (1994). Abbreviation: V-CDT: Vienna Canyon Diablo Troilite.

5.3. Ore-forming processes

According to accepted models the contamination of mafic to ultramafic magmas by their country rock is a key process in the formation of magmatic sulfide deposits (e.g. Naldrett, 1992; Ripley & Li, 2003; Keays and Lightfoot, 2010). The background of this hypothesis is as follows. Because the solubility of sulfide varies inversely with pressure (Wendlandt, 1982; Keays, 1995; Mavrogenes & O'Neil, 1999) when magmas generated deep in the mantle arrive near the surface, they are undersaturated in sulfide. Two main processes can trigger the segregation of sulfides; either the sulfide solubility can be lowered (e.g. by adding siliceous material) or S can be added directly to the magma (e.g. Naldrett, 1992; Naldrett, 1999; Lightfoot & Keays, 2005; Ripley & Li, 2013). In many ore deposits there is abundant evidence of one or both processes; e.g. at Kambalda pyrite-bearing cherts were assimilated and at Norils'k the contaminant is anhydrite-bearing evaporates.

Sulfides that segregate directly from mafic or ultramafic magmas normally have relatively low contents of ore metals like Ni or Cu. To upgrade these levels to those encountered in the richer ore deposits, it is postulated (Naldrett et al., 1995; 1996) that the sulfide interacted with the silicate melt, a process that extracts the chalcophile ore metals and concentrates them in the sulfide phase. This process is quantified by R- or N-factors. The first corresponds to the magma/sulfide ratio, considering the equilibration between the two liquid phases. The second is similar but supposes that volumes of sulfide liquid are continuously exposed to fresh silicate melt.

To form an economic deposit it is required that the large amount of sulfide have to concentrate without the concomitant crystallization of abundant silicate. According to Naldrett (2004), accumulation of massive sulfides is achieved in several deposits, including e.g. Kambalda, Noril'sk, Jinchuan, thanks to hydrodynamic forces; at Sudbury, however, the sulfide concentrated at the base of a magma chamber without dynamic control. The weakly disseminated sulfides along the northwestern margin of the Duluth Complex, considered to be uneconomic, are thought to be emplaced without of hydrodynamic forces, thus preventing in concentrating sulfide during magma flowing.

The formation of an ore deposit is therefore thought to require several steps; those involving interaction of the host magma with its wall rocks and interaction of the sulfide with the host silicate liquid.

These ideas were developed, however, for the formation of the tholeiitic or komatiitic magmas that host most major Ni-sulfide deposits. These magmas form in mantle plumes, either those that generate large igneous provinces or those that are the source of Archean ultramafic lavas. As described in previous sections, the Älgliden deposit formed in a different type of geodynamic setting, one associated with subduction zones. The parental magmas are calk-

alkaline and they probably behaved very differently from tholeiitic or komatiitic magmas during their ascent through the crust. In the following section we develop a model for the formation of Ni-sulfide mineralization in such a setting.

5.3.1. Origin of the Ni-Cu-Au mineralization in Älgliden

Previous authors (Maier, personal communication, Bejgarn et al., 2013) have suggested that the Älgliden mineralization was the result of the contamination of the parental gabbroic magma with the country rocks. Evidence in support of this model is found in the nature of the country rocks, which are felsic and contain Au, Cu and sulfide mineralization. The assimilation of the Älgliden wall rocks would therefore have added Si to reduce S solubility, and would have added S in addition to metals such as Cu and Au. A way to test these hypotheses would be to investigate trace elements and S isotopes. The trace element data presented in the earlier sections (4.3 and 4.4.4) indicate, however, that contamination of the Älgliden magma by its wall rocks did not occur, or was not a major process. Wallrock xenolith melting is recognized as the most efficient process for adding crustal S in other deposits (e.g. Kambalda; Robertson et al., 2015). Even if other processes might occur in the case of Älgliden, the S isotope signatures of sulfides of Älgliden and its wallrock cannot unequivocally support the hypothesis of assimilation since both signatures are included in the range of the subduction zone mantle (Figure 5.17).

S, and Ni, Cu and Au in subductions zones

Subduction zones are important sites of recycling of volatiles such as H and S from volatile-rich subducted sediments and altered oceanic crust. Wallace (2005) estimated that in subduction zones ~15-30% of the amount of subducted S is cycled from the mantle to the surface while the remainder is transferred into the mantle wedge. As a consequence the S content in basaltic arc magmas are greater than in mid-ocean ridge basalts (MORB; Wallace, 2005).

It is accepted that arc magmas are generally more oxidized than MORB (e.g. Ballhaus, 1993). A consequence of these oxidizing conditions is the speciation of S and its solubility in the magma. Carroll and Rutherford (1985, 1987), Luhr (1990) and Jugo et al. (2005) experimentally showed that silicate melts are able to carry more S when S^{6+} is the dominant species, i.e. in oxidizing conditions. Modelling of S speciation and solubility showed that the sulfur content at sulfide saturation (SCSS; i.e. the maximum dissolved S in the magma), increases with increasing oxygen fugacities and reaches a maximum from ~FQM+2 to +2.5 (Jugo, 2009). The authors predicted SCSS of 1300-1500 ppm S at FQM -1 to +0.5 for MORB,

7500 ppm S with FQM +2 for back arc basalts and OIB and 14 000 ppm S (i.e. 1.4 wt.% S) at FQM +2.3 in arc magmas.
On this basis, arc magmas are initially S-enriched and able to dissolve more S than magmas in other geological contexts. This gives them an interesting potential with respect to the formation of magmatic sulfide deposits. In the following, the behavior and concentration of Au, Cu and Ni during melting and magma differentiation in subduction zones are investigated. Because these metals are not mobile during slab deshydratation and mantle wedge metasomatism (Jenner, 2017), they are not expected to be enriched in the mantle wedge compared to other mantle regions.

Ni concentration in the mantle is mostly buffered by olivine (Barnes & Lightfoot, 2005) which make up close to 100 % of the mantle whereas the average sulfide content is 0.054 wt.% (Lorand, 1993). As a consequence, high degrees of partial melting of the mantle allow to melt more olivine and sulfide thus incorporate more Ni in the magma (Arndt et al., 2005; Barnes & Lightfoot, 2005). Based on modelling, Barnes and Lightfoot (2005) estimated the Ni content in melts at 328 ppm with 15% of partial melting and at 833 ppm at 30%. Komatiitic magmas, supposed to formed at high degree of partial melting (Arndt, 1977) are Ni-rich and are good examples illustrating this process. Li & Audétat (2012) showed that the partition coefficient of Ni between the sulfide phase, i.e. the sulfide liquid (SL) or the monosulfide solid solution (MSS), and the silicate melt (SM) decreases slightly from ≈800 to ≈300 as fO_2 increases. The silicate melt would therefore be more Ni-enriched in oxidizing conditions than in more reducing conditions during partial melting of the mantle because it is less partitioned in the sulfide phase of the melting mantle source. The Ni content in arc magmas, however, are not higher than in other geological environments (Barnes & Arndt, in press) suggesting other parameters influence the Ni content in silicate melts during mantle melting, such as lithology of the mantle source (Sobolev et al., 2005; 2007) or temperature and pressure (e.g. Matzen et al., 2013).
The Cu contents in MORB/OIB vary from 70 to 110 ppm, and are similar to those in primitive arc magmas (Jenner et al., 2010, Lee et al., 2012). Modeling of the Cu content in the silicate melt at different degrees of partial melting showed that it increases until 15% partial melting when the sulfide entirely melts, reaching 116 ppm, then decreases to 67 ppm at 30% partial melting (Barnes & Lightfoot, 2005). The variable partial melting degrees thus could account for the variability of Cu observed in melt in different geological settings.
The gold content in silicate primary melt slightly varies during partial melting, i.e. from at least 1.8 ppb at 1% partial melting to at most 5.3 ppb at 15% partial melting (Barnes & Lightfoot, 2005), but other parameters/processes can change it to greater orders of magnitude. Botcharnikov et al. (2011) showed that the Au solubility is highest in redox conditions where

sulfide is transformed into sulfate species in the magma (i.e. ~ FQM+1). However, Jégo & Pichavant (2012) argued that even if the maximum Au content is reached in oxidizing conditions, highly oxidizing conditions are not necessarily required since the Au enrichment occur over a wide range of $f O_2$. Instead, experiments showed that the critical factor controlling the gold solubility and enrichment is the abundance of S in the silicate melt. More recently, Li & Audétat (2013) proposed that the main factor controlling the enrichment of Au in the silicate melt resides in the difference of the partition coefficient between the sulfide liquid (SL) and silicate melt (SM), and SL and MSS. This interpretation is based on the facts that 1) at mantle wedge P-T conditions the sulfide phase is dominated by MSS rather than SL, reversely to MORB, and 2) the partition coefficient of gold between the sulfide liquid and the silicate melt is far greater than that between the MSS and the silicate melt ($D_{Au\ SL/SM}$=8000 and $D_{Au\ MSS/SM}$=180; Li & Audétat, 2013). As a result, during partial melting of an MSS-bearing mantle the Au content in the silicate melt is higher than if the sulfide phase of the melting mantle source was dominated by sulfide liquid. Thus, the oxidizing conditions, the abundance of S and the MSS-dominated melting mantle make primary arc magmas Au-enriched compared to other types of magma.

During magma differentiation, the behavior of the Au, Cu and Ni in the silicate and in sulfide liquids is controlled by their compatibility with the crystallizing phases and the timing of crystallization of these phases.

All three metals are chalcophile elements, which are therefore partitioned into sulfides from the moment that a sulfide phase occur within the silicate magma. None of them are compatible with silicate phases except for Ni which is compatible with olivine. Consequently, during early stage of differentiation and olivine fractionation, the Ni is subtracted from the silicate melt and its content decreases, as shown in Figure 11.18. Reversely, the Au and Cu contents increase as long as the silicate melt remains sulfide-undersaturated, i.e. no any sulfide phase occurs in the magma (Figure 5.18).

The later the sulfide saturation occurs during magma differentiation, the more Cu- and Au-enriched the silicate magma would be.

Data from glass from different arc localities of Jenner et al. (2010), Labidi et al. (2015) and Park et al. (2015) suggest that sulfide saturation occurs between ~3 and ~6 wt.% MgO during arc magma differentiation. This late sulfide saturation thus allows the silicate magma to be enriched in Cu and Au but depleted in Ni. To illustrate this point, Park et al. (2015) pointed out the role of late sulfide saturation in the formation of Cu-and Au-rich magmas: magma which experienced early or late sulfide liquid segregation are not or are fertile with respect to Cu and Au, respectively. These considerations suggest that a late sulfide saturation implies that the

magma is Ni-poor and Cu- and Au-rich, as well as the sulfide liquid which will further scavenged the chalcophile element from the silicate melt.

The relative proportions of Ni, Cu and Au in the Älgliden mineralization and the evolved composition (i.e. <6 wt.%) of the Älgliden magma suggests the late sulfide saturation during the differentiation of an oxidized magma.

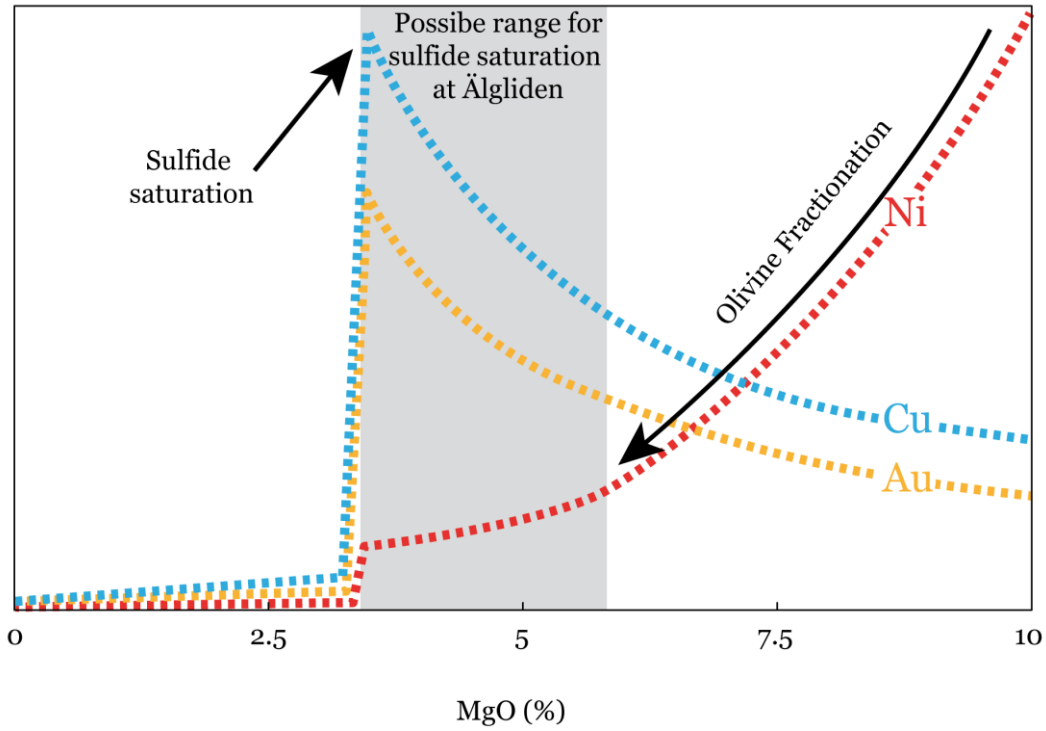

Figure 5.18 Evolution of the Ni, Cu and Au contents during arc magma differentiation marked by sulfide saturation. Note the Ni, Cu and Au relative contents in the window in which sulfide saturation may have occurred at Älgliden (grey field), considering that can even have occurred at lower MgO contents. Modified after Jenner et al. (2010), Labidi et al. (2015), Park et al. (2015) and Keith et al. (2017).

The timing of the sulfide liquid segregation cannot be precisely determined. However, the Ni content in olivine (Figure 5.19) suggests that the segregation of the immiscible sulfide melt occurred after the olivine fractionation because olivine grains are not Ni-poor relative to normal arc olivine. Indeed if the sulfide segregation occurred prior to olivine fractionation, the sulfide melt would have extracted the Ni from the silicate melt and the olivine that subsequently fractionated would have been Ni-poor. Olivine grains in the southern part of the dike show Ni-depletion that could result from the Ni-exchange between the olivine grains and the liquid or solid sulfides. In contrast olivine in the northern part is not depleted. This suggest separate injection in the two parts. Ni sulfides are present in both parts, suggesting that the Ni depleted olivine has interacted with sulfide before injection.

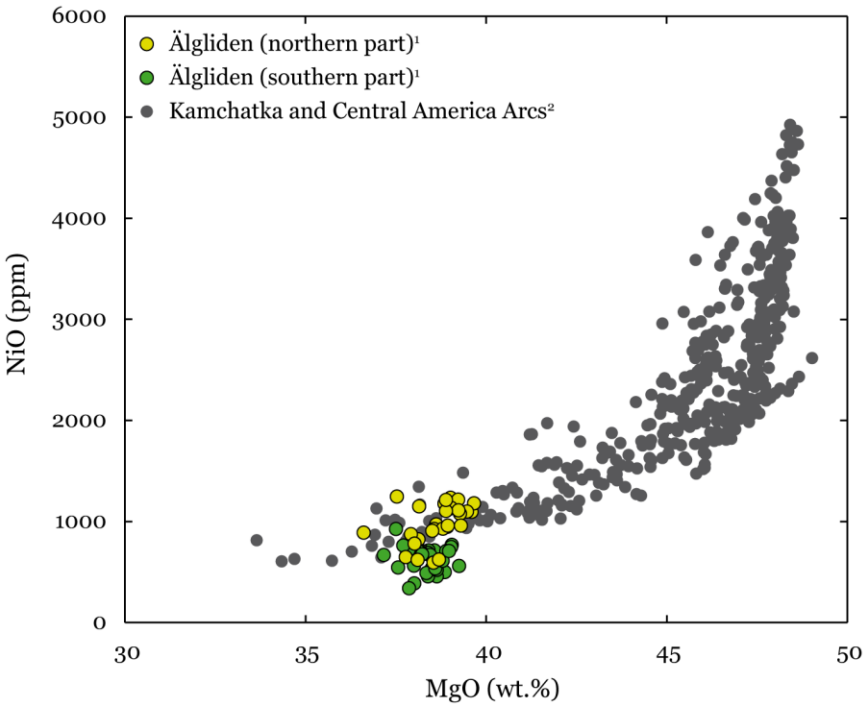

Figure 5.19 NiO *vs.* MgO diagram of olivine from Älgliden and arcs. The Älgliden olivine from the northern part of ALA246 follows the trend defined by arcs of Kamchatka and Central America whereas those of the southern part are slightly NiO-depleted. References: 1: This study; 2: Gavrilenko et al. (2016).

Sulfide saturation and sulfide liquid segregation

The triggering of sulfide saturation is a key process in the formation magmatic sulfide deposits. It occurs by increasing the S content in the silicate magma to reach the SCSS threshold or by lowering the sulfide solubility by addition of siliceous material (Naldrett, 2004). Since assimilation of the mineralized felsic rocks is not supported by trace element and S isotope data, neither S nor SiO_2 addition is favored. Another process for lowering the sulfide solubility is to lower the FeO content of the magma (Li and Naldrett, 1993). Li and Naldrett (1993) showed that mixing of a mafic magma whose S content is 2/3 of the SCSS together with 20-80% of a S-free felsic magma can cause the segregation of an immiscible sulfide liquid. However, no evidence of magma mixing is reported at Älgliden: instead the rocks and minerals have relatively homogeneous composition.

An alternative way for an oxidized silicate melt to reach sulfide saturation is to lower its sulfide solubility by reduction. During differentiation of arc magmas, Jenner et al. (2010) pointed out the concomitant drops in chalcophile elements (e.g. Cu, Au, Pt; Figure 5.18) and in V, TiO_2, FeO_{tot} at ~3 wt.% MgO. The authors attributed these drastic drops to result from magnetite and sulfide saturation and interpreted the sulfide saturation to be induced by the magnetite

crystallization. The magnetite is suggested to reduce the silicate melt by the following redox equilibrium:

$$SO_4^{2-} + 8\ Fe^{2+}O = S^{2-} + 8\ Fe^{3+}O_{1.5}$$

The crystallization of magnetite (*largo sensu*) consumes about twice more Fe^{3+} than Fe^{2+} so that it tends to reduce the silicate melt (Jenner et al., 2010). It is proposed that the crystallization of a few percent of magnetite (e.g. 2.6 wt.%) in closed-system triggers the conversion of significant amount of SO_4^{2-} to S^{2-} and the saturation of a sulfide phase. Similarly, the associated drop of P_2O_5 is attributed to apatite saturation via the same process of decreasing the Fe^{3+} content that lowers the solubility of P and triggers apatite fractionation.

In the Älgliden dike, Ti-bearing magnetite grains commonly occur within the post-cumulus phases, i.e. oikocrystic orthopyroxene and hornblende, of the olivine norites and in a lesser extent within the leucogabbros (Figure 5.12). Consistently, drops in V and TiO_2 contents are observed during the evolution from the estimated intercumulus melt of the olivine norites to the melt that generate the leucogabbro (Figure 5.20), suggesting the fractionation of Ti-bearing magnetite occurred before the generation of the leucogabbros.

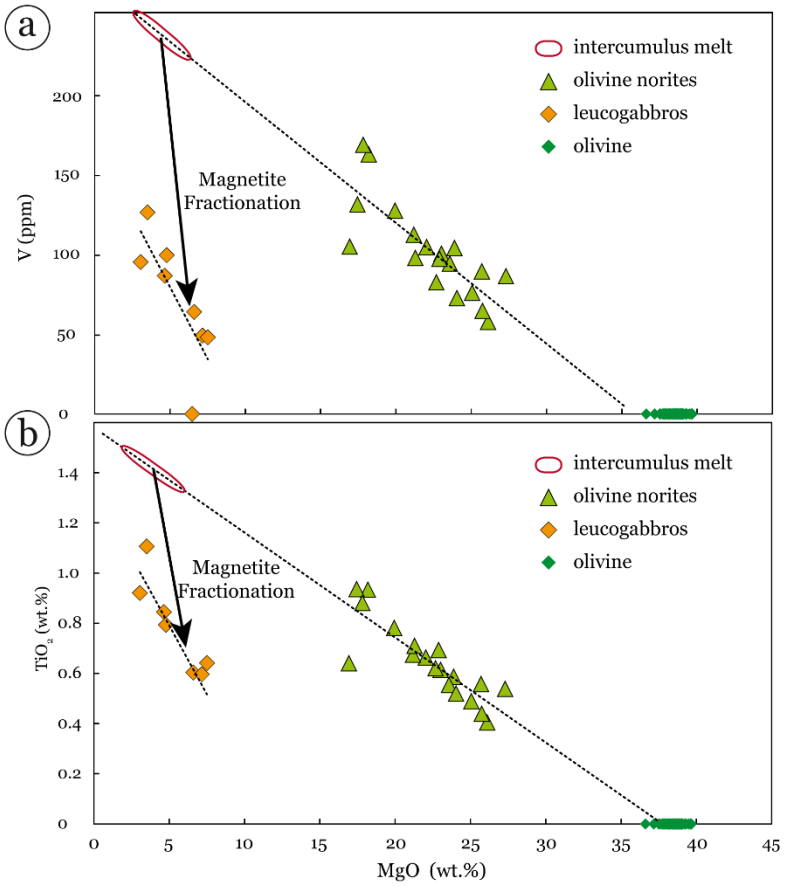

Figure 5.20 Binary diagram of a) V and b) TiO_2 vs. MgO illustrating the magnetite crystallization between the intercumulus melt that forms the olivine norites and the residual melt that fractionates to produce the leucogabbros.

Moreover, apatite is absent or rare in the olivine norites while it occurs in substantial amounts in the leucogabbros. We report one sample of magnetite-rich leucogabbro where magnetite form amoeboidal grains (Figure 5.21a-b) similarly to chromite described by Vukmanovic et al. (2012) at the base of the Merensky Reef.

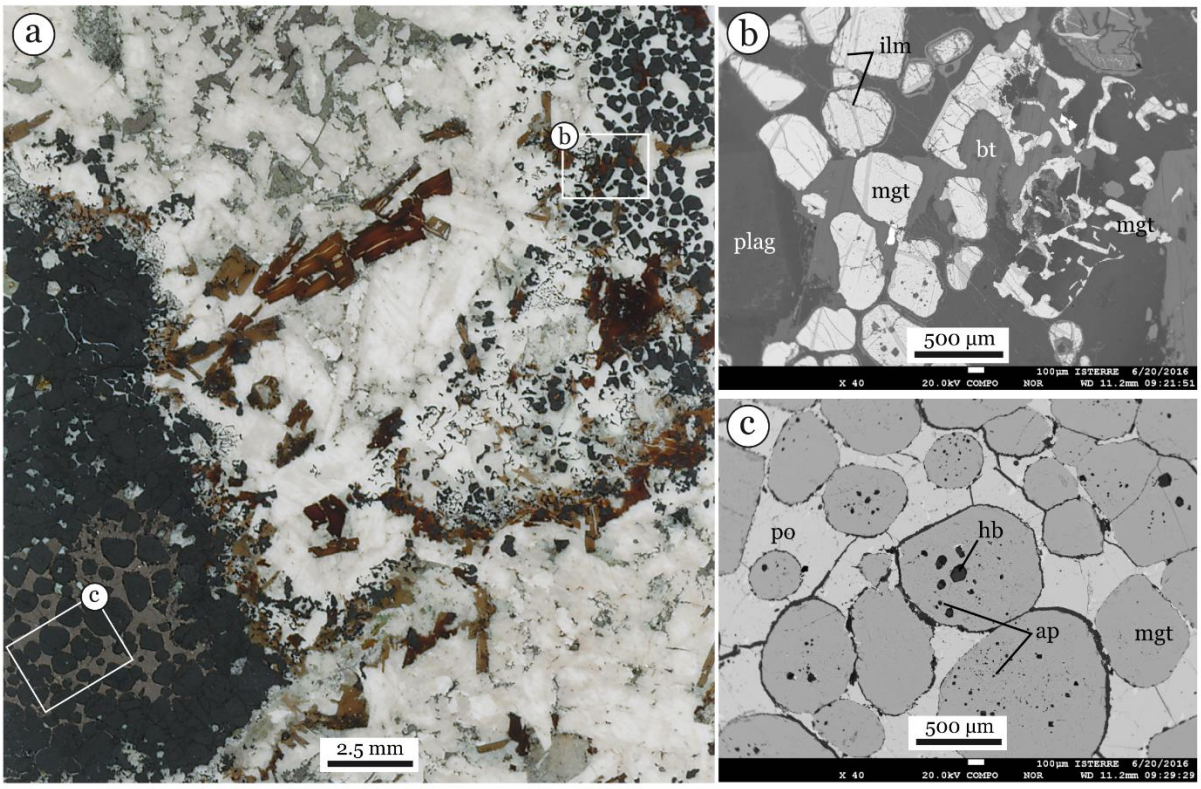

Figure 5.21 Magnetite-rich leucogabbro sample, 246.250.4. (a) Scan of thin section. (b) Back scattered electron (BSE) image showing the amoeboidal to rounded shape of magnetite grains. (c) BSE image of magnetite grains that are enclosed in a sulfide matrix and that host numerous apatite and hornblende inclusions. Abbreviations: Plag: Plagioclase; Hb: Hornblende; Ap: Apatite; Mgt: magnetite; Ilm: Ilmenite; Po: Pyrrhotite.

Inclusions of apatite and hornblende are abundant in these magnetite grains (Figure 5.21b) and some magnetite grains are included in net-textured sulfides (Figure 5.21c). In these words, and because of these mineralogical associations, the Älgliden magma could have experienced concomitant magnetite and apatite saturation during its differentiation after olivine accumulation. These, however, do not necessarily share causal relationships with the reduction of the silicate melt and the sulfide saturation. In the model proposed by Jenner et al. (2010) the reduction of the silicate melt is induced by the crystallization of magnetite alone. However, the co-crystallization of Fe^{2+}-bearing phase such as orthopyroxene would counter the subtraction of Fe^{3+} from the silicate melt. Petrolog3 modeling indicates that the fractionation of magnetite or Ti-bearing magnetite with $Fe_2O_3/(Fe_2O_3+FeO)$ ratios of 0.69 and 0.64,

respectively, only slightly decreases the $Fe_2O_3/(Fe_2O_3+FeO)$ of the melt, due to co-crystallization of olivine, orthopyroxene, or plagioclase, and that it significantly reduces the melt at the late stage of crystallization (>40% crystallization), when the relative proportion of fractionating magnetite with respect to other phases increases (Figure 5.22).

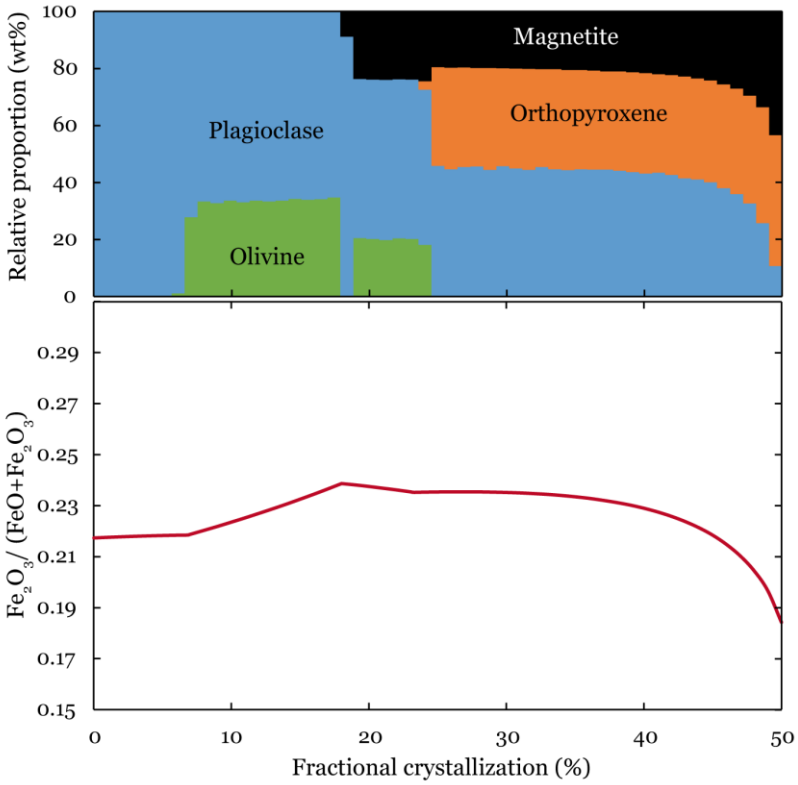

Figure 5.22 Modelled evolution of the $Fe_2O_3/(FeO+Fe_2O_3)$ ratio during fractional crystallization of magnetite and silicate phases in varying relative proportions, using Petrolog3 computer program. References as in Table 4.10

Taking into account the fractionation of hornblende with $Fe_2O_3/(Fe_2O_3+FeO)$ ranging from 0.26 to 0.56 (Table 4.6), the co-crystallization of magnetite and hornblende could efficiently reduce the silicate melt, but this appears unlikely because the textural position of hornblende suggests it fractionates at the latest stages of crystallization of the intercumulus melt. Kelley & Cottrell (2012) showed that during the magma differentiation of the Marianas arc, where both magnetite crystallization and degassing occurred, the $Fe_2O_3/(Fe_2O_3+FeO)$ is only slightly decreased, from 0.28 to 0.27, in response to magnetite crystallization and the authors argued that it cannot be responsible for the overall reduction recorded by the melt inclusions. Because of the positive and good correlation between S and $Fe_2O_3/(Fe_2O_3+FeO)$ in melt inclusions, they showed that 50% of degassing may reduce the $Fe_2O_3/(Fe_2O_3+FeO)$ from 0.30 to 0.24, and they concluded that S degassing may play a major role in reducing the melt during differentiation.

It is possible that the fractionation of Fe-rich mineral(s) i.e. magnetite±orthopyroxene decreases the sulfide solubility and triggers sulfide saturation not because of reduction of the melt but rather by reducing the FeO activity (Haughton et al.,1974; Li et al., 2001), as it is suggested in PGE-reefs formation (Maier et al. 2003, 2005). Both effects can operate for reducing the S solubility: the decrease in FeO activity combined with the slight reduction induced by magnetite fractionation.

The model of sulfide saturation induced by degassing has been proposed by Longpré et al. (2017). They studied an oxidized volatile-rich magma (i.e. CO_2, H_2O and S) which experienced concurrent H_2O and S degassing. The correlations between S contents, S speciation and H_2O contents indicate a strong reduction of the magma, causing the sulfide saturation (Longpré et al., 2017). The redox change induced by SO_2 degassing is described as follows:

$$S^{2-}_{melt} + 3Fe_2O_{3melt} \rightarrow SO_{2\ gas} + 6FeO_{melt} + O^{2-}_{melt}$$

where 1 mole of S reduces 6 moles of Fe. Even if the process of degassing also involves S loss, the data showed that the S loss is overcome by the reduction of S so that the SCSS threshold can be reached at high SCSS (Longpré et al., 2017).

The Älgliden magma is favorable for undergoing H_2O and S degassing because it intruded a coeval porphyry style mineralization which is estimated to emplace at 4 km or <1.5 km in hydrostatic or lithostatic conditions, respectively (Filoche, 2012). According to the solubility data of Dixon (1997), all CO_2 exsolves at >25 MPa while H_2O begins to exsolve later, at <25 MPa but recent studies of Longpré et al. (2017) showed that S and H_2O can degas deeper, at <300 MPa. Whatever the depth, CO_2 should exsolve deeper than H_2O and S, and loss of CO_2 tends to oxidize the magma (Mathez, 1984) whereas the latter tends to reduce it (Kelley & Cottrell, 2012; Longpré et al., 2017). This process should be significant because arc magmas are particularly volatile-rich (Wallace, 2005). However, we do not have direct evidences that support the hypothesis of degassing as we did not analyze the melt inclusions. Possible illustrations could be the sieve texture in some plagioclase cores or the microcrystalline (i.e. <100 μm) plagioclase-rich clusters observed in the olivine norites (Figure 5.23; see Section 4.1.2) since degassing may induce rapid and extensive crystallization (e.g. Métrich et al., 2001; Blundy et al., 2006). Similar patchy zoned sieve texture in plagioclase grains are described by Landi et al. (2004), which attributed the texture to result from undercooling conditions caused by degassing.

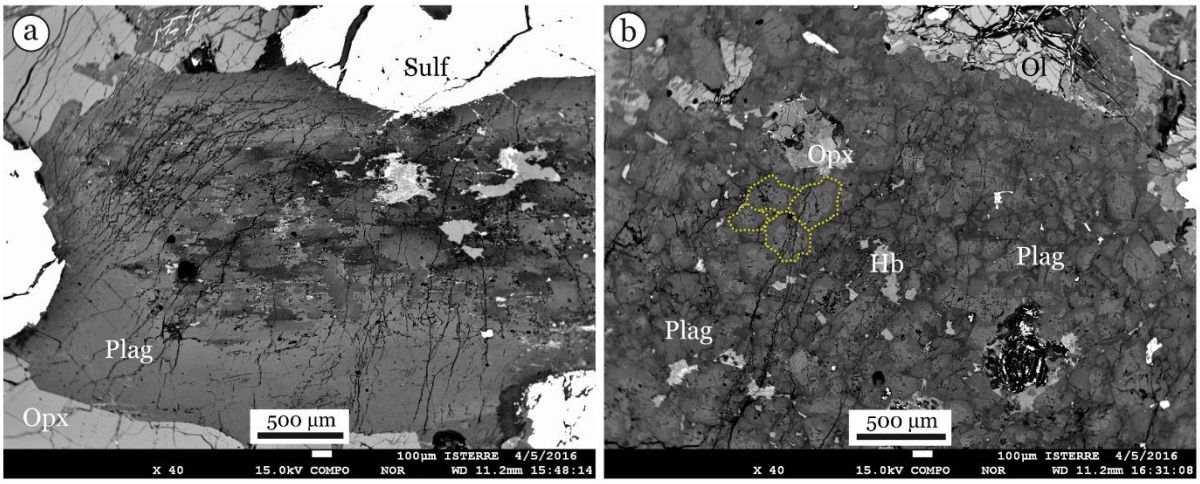

Figure 5.23 BSE images illustrating (a) a sieve texture with patchy zoning in a large plagioclase crystal and (b) microcrystalline grains in a plagioclase-rich cluster, sample 246.300.9. The dashed yellow lines delineate some plagioclase grains. Abbreviations: Plag: Plagioclase; Opx: Orthopyroxene; HB: Hornblende; Sulf: Sulfide.

The sulfide saturation is likely reached in response to magnetite crystallization and/or degassing. In both cases, it possibly occurs in situations where the magma has experienced significant crystallization since it happened either after magnetite crystallization, or within a crystal-rich mush whose crystallinity in susceptible to rapidly increase due to degassing.

5.3.2. Ore composition and distribution

Distribution of metals between sulfides and silicates

Bulk rock Ni, Cu, Au and Co contents correlate positively with S contents suggesting these metals are hosted in or in spatial association with sulfides (Figure 5.24). However correlations are not always very well defined.

Ni shows a well-defined linear trend with S with a restricted dispersion, but this trend intercepts the Ni axis at ~300 ppm (Figure 5.24a) indicating that Ni is homogeneously distributed within sulfide and that a small fraction (i.e. 300 ppm) is hosted elsewhere in the rock, no doubt in olivine. In Figure 5.24b the Ni contents in both bulk rock (i.e. in silicate and sulfide phases) and in the leachable fraction (i.e. in sulfides only) are reported. The data plot on a linear trend that is almost parallel to the 1:1 line but with a near constant offset that corresponds to the Ni in olivine. This mineral contains ~ 600 ppm Ni in average and makes up between 30 to 50% of the rock. Based on the difference in Ni contents between the bulk rock and the sulfides (from leaching analyzes), nickel in olivine accounts for ~20% of the total Ni in the dike, the rest being in sulfides. In the sulfides, Ni is mostly in pentlandite, which makes up 10% of the total sulfides (Figure 5.24a).

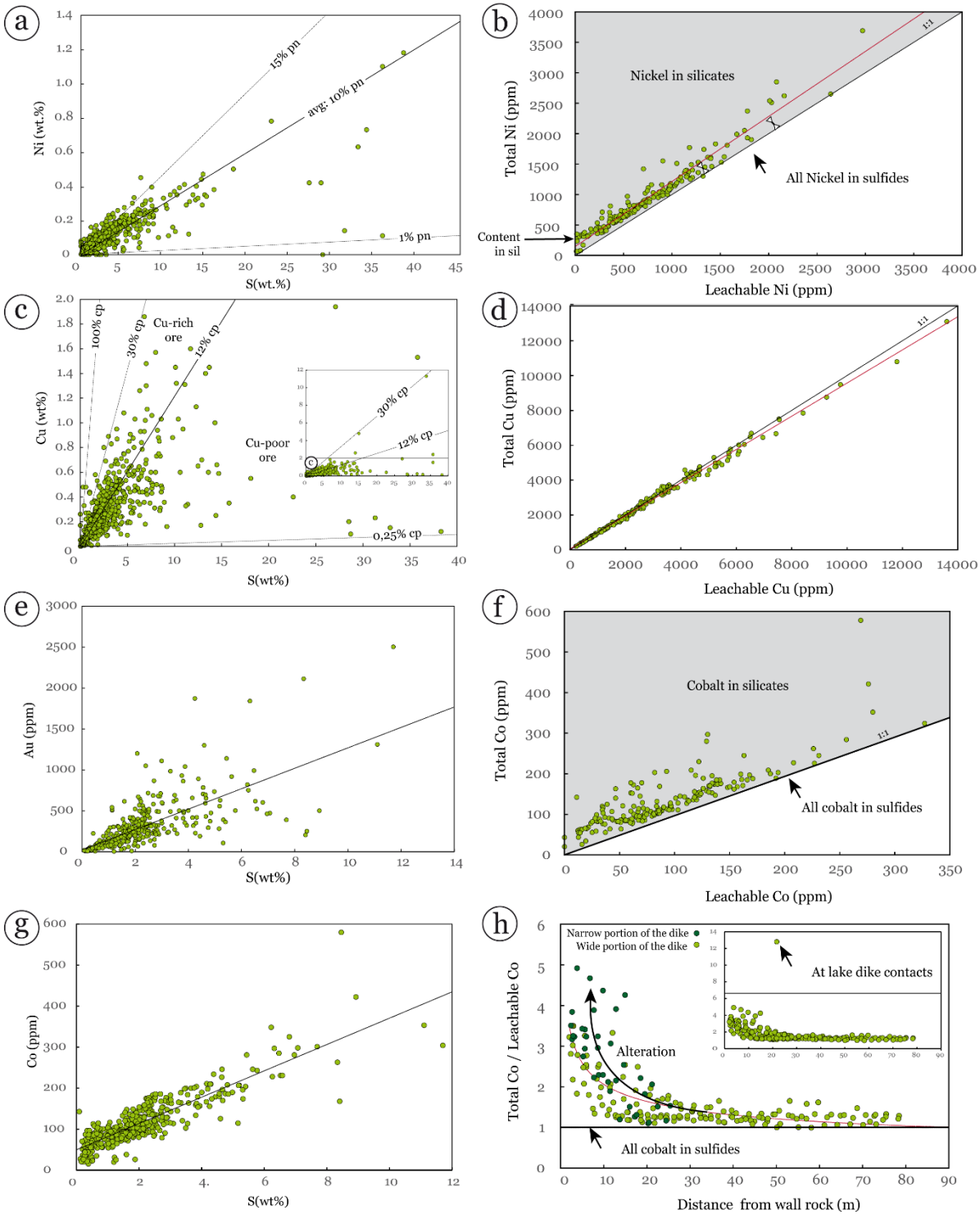

Figure 5.24 Metal distribution in sulfides and silicates. Right panels: Ni, Cu Au, and Co vs. S contents. Left panels (except h): Total vs. Leachable Ni, Cu and Co. The leachable fraction corresponds to the sulfide fraction only whereas the total contents include silicates. For (a) and (b), the pentlandite (pn) is $Fe_{4.5}Ni_{4.5}S_8$ and the chalcopyrite (cp) is $CuFeS_2$. (h) Total/Leachable Co ratio as function of the distance from the wall rocks. The latter is a proxy for the alteration degree since alteration is developed at the margin of the dike or in thin portions of the dike.

The correlation between Cu and S contents is not as well defined as for Ni, indicating Cu is not homogeneously distributed within sulfides, in accord with the uneven distribution of chalcopyrite in the dike. This heterogeneity results in Cu-rich and Cu-poor ores (Figure 5.24c). In Figure 5.24d the trend defined by total Cu vs leachable Cu is very close to line 1:1 indicating all Cu is contained in sulfide. Assuming that Cu is hosted in chalcopyrite only, the Cu-rich ore contains up to 30% chalcopyrite while the Cu-poor ore contain less than ~12% chalcopyrite.
Like Cu, the Au *vs.* S diagram shows a positive correlation with some scatter (Figure 5.24e). This suggests that the Au is heterogeneously distributed within sulfides (explained further on).

Co also correlates positively with S but the trend intercept the Co axis at 50 ppm. This show that small amount of Co is not hosted within sulfides (Figure 5.24g), an information that was already reported by geologists of the Boliden Company. In the total Co *vs.* leachable Co diagram of Figure 5.24f, the data define a linear trend slightly above line 1:1 but with numerous samples well above this line. This indicates that Co is mostly contained in sulfide but, in some cases, a significant amount is hosted in significant amount in silicate phases. In particular, in the altered samples closed to the walls of the dike, the Co content can be up to 5 times higher in silicates than in sulfides, with enrichment up to 12 times in a strongly altered sample at the contact of a late dike (Figure 5.24h). This suggests that Co is partially hosted in secondary silicate phases close to the dike contacts or in the narrow terminations of the dike. Close to the walls of the dike (<20 m), Co is distributed in similar proportions between sulfides and silicate phases whereas in samples located far (>20 m) from the wallrock and protected from alteration about 80% is contained in sulfides (Figure 5.24h).

The Cu/S ratio, a proxy for the proportion of chalcopyrite relative to the overall sulfides, is particularly variable for samples with high S contents, and discriminate between Cu-rich and Cu-poor ores. Consistently, we have observed that chalcopyrite is rare in massive sulfides but can constitutes the dominant phase in some network sulfides (Figure 5.1.c-d and Figure 5.12b). This variability in Cu-sulfide distribution may reflect zoning at the sample scale. In support of this interpretation, some parts of large sulfide globules consist only of chalcopyrite while other parts are made up of pyrrhotite+pentlandite (inset of Figure 5.10d). This ore zoning is commonly attributed to fractional crystallization of the sulfide liquid whereby a Cu-poor monosulfide solid solution (MSS) fractionates early (1150-1120°C; Naldrett, 1969) and subsequently crystallizes pyrrhotite and pentlandite whereas the Cu-rich residual liquid crystallizes later (950-800°C; Dare et al.,2014) as intermediate solid solution (ISS) which crystallizes as chalcopyrite (e.g. Naldrett, 1969; Czamanske & Moore, 1977; Barnes et al., 1997; Mungall et al., 2005; Dare et al., 2014). This process could have worked at a larger scale in the dike and which would explain why some samples, especially those with high sulfide amounts,

are Cu-rich or Cu-poor. A consequence to this is the distribution of Au. Barnes et al. (2006; 2008) and Dare et al. (2014) found that Au is concentrated in the ISS during the fractional crystallization of the sulfide liquid, but further crystallizes as tellurides, bismithides and alloys in spatial association with the sulfides. In this respect, the dispersion in the Au *vs.* S diagram (Figure 5.24e) likely results from the sulfide liquid fractionation, whereby Au is locally and heterogeneously concentrated. Furthermore Au positively correlates with Pd and Pt (not shown; internal Boliden report), further investigations of platinum group elements could provide information on the process of sulfide fractionation.

Sulfides distribution

Most major Ni-Cu sulfide deposits occur in the lower parts of horizontal flows (e.g. Kambalda) or sills (e.g Norilsk-Talnakh). In this situation, the concentration of sulfides, which separate from the host magma as droplets of immiscible sulfide liquid, accumulate in the lower part of the units through gravitative settling. The common zoning from a basal layer of massive sulfide upward through net-textured and disseminated sulfide is attributed to sorting related to the different densities of the accumulating phases (sulfide > olivine > silicate melt). This type of model cannot apply, however, to the accumulation of sulfides in steeply dipping conduits like the Älgliden dike.

Conduit-style mineralizations has been studied by many authors, including Seat et al. (2007), Mungall et al. (2010), and Manor et al. (2016). In many conduit-hosted Ni-Cu-PGE deposits, including the Eagle deposit (Ripley & Li, 2011), the Eagle's Nest deposit (Mungall et al., 2010), Reid Brook zone of Voisey's Bay (Lightfoot et al., 2012), the Nebo-Babel deposit (Seat et al., 2007) and the Brunswick #1 and 1900 orebodies of Giant Mascot (Manor et al., 2016), the ores are concentrated in the center of the vertical intrusion or close to the footwall of gently dipping intrusions in association with cumulates. In some example, concentrically zoned lenses of massive sulfides are surrounded by disseminated to semi massive sulfides. The emplacement of these mineralized intrusions is thought to occur by several pulses of crystal-rich and sulfide-laden magma through the same channelway, with period of solidification between each pulse (Ripley & Li, 2011; Seat et al., 2007; Manor et al., 2016). These models of emplacement imply that cumulus crystals and sulfide were concentrated, likely by hydrodynamic and gravity forces, before being injected as a mush.

At Älgliden the distribution of the ore is different: only 10 vol% of the dyke is not mineralized, about 75 vol.% is composed of disseminated sulfides, and 15 vol.% the dyke accounts for network and massive sulfides associated with the leucogabbro bodies and xenoliths. The scenario proposed for sulfide concentration must account for this variation in mineralization styles.

The ore body, defined by S>0.5 wt.%, consists mainly of disseminated sulfide hosted by olivine norites. Disseminated sulfides are preferentially located in olivine-rich areas, where they partially to fully enclose olivine grains, whereas inclusions of sulfide are scarce in areas rich in oikocrystic phases (i.e. orthopyroxene ± hornblende ± biotite), as described in the Kevitsa or Raglan deposits (Barnes, 2017). In sulfide-rich samples, the sulfides tend to form discontinuous networks described as patchy net-texture sulfides. We pointed out in Section 11.1 that the dihedral angles between olivine and sulfides were <60°, suggesting wetting properties that cause molten sulfide to be distributed along olivine crystal faces. It has been proposed that the fO_2 strongly controls the wetting properties between olivine and sulfide (Rose & Brenan, 2001); i.e. reducing conditions lower the surface tension between the two phases. In section 5.3.1 we argued that the silicate melt was reduced when it was in presence of sulfide liquid due to the degassing and/or the crystallization of magnetite.
In conditions where sulfide wet olivine grains, Rose & Brenan (2001) argued that the sulfide liquid can migrate by compaction of the crystal-rich mush. Mungall & Su (2005), however, found that the sulfide melt cannot migrate through crystal-mush by capillary forces alone, without the aid of the simultaneously flowing silicate melt. Chung & Mungall (2009) suggested that the coalescence of small sulfide droplets into pre-existing standed droplets can give rise to connected net-textured domains. The co-migration of sulfide and silicate melts through the interstitial pore space might produce patchy textures as proposed by Barnes et al. (2017). If the connected sulfide network exceeds a given height (0.5-1.5 m with 1 mm-sized olivine). Chung & Mungall (2009) argued that the sulfide is able to move downward to further form massive or net-textured ore.

At Älgliden, however, most of patchy net-textured sulfides do not extend over 2 cm and true net-textured sulfides do not occur suggesting that the migration of the interstitial sulfide and silicate melt has been limited. Relatively high concentrations of sulfides occurs as networks, veins or large globules which generally do not exceed decimeters and are confined in the leucogabbro bodies or as massive sulfides along and within leucogabbros and xenoliths. The association of sulfide concentrations with wallrock xenoliths, either as networks within the xenoliths or as massive accumulations at their contacts with olivine norite, may result from local assimilation of siliceous and/or S-bearing xenolith that could locally decrease the sulfide solubility and/or increase th S content, hence triggering sulfide saturation.

The sulfide globules are rare in olivine norites, where they are systematically included in relatively late crystallizing phases (i.e. oikocrystic orthopyroxene, hornblende) and they are widespread in leucogabbros. We propose that the sulfide segregated from the interstitial mafic melt that experienced either magnetite fractionation and/or degassing. In liquid-rich domains

the sulfide droplets should be relatively free to agglomerate. Chung & Mungall showed that sulfide droplets similar in size to the crystal of the mush cannot percolate through the mush. As soon as the size of the sulfide droplets floating in silicate channels or pockets of late crystallizing melts are similar to the grainsize of crystal mush, the sulfide droplet may be trapped. We propose that this could explain why the sulfides concentrations occur in olivine-poor domains and together with the leucogabbro (Figure 5.25).

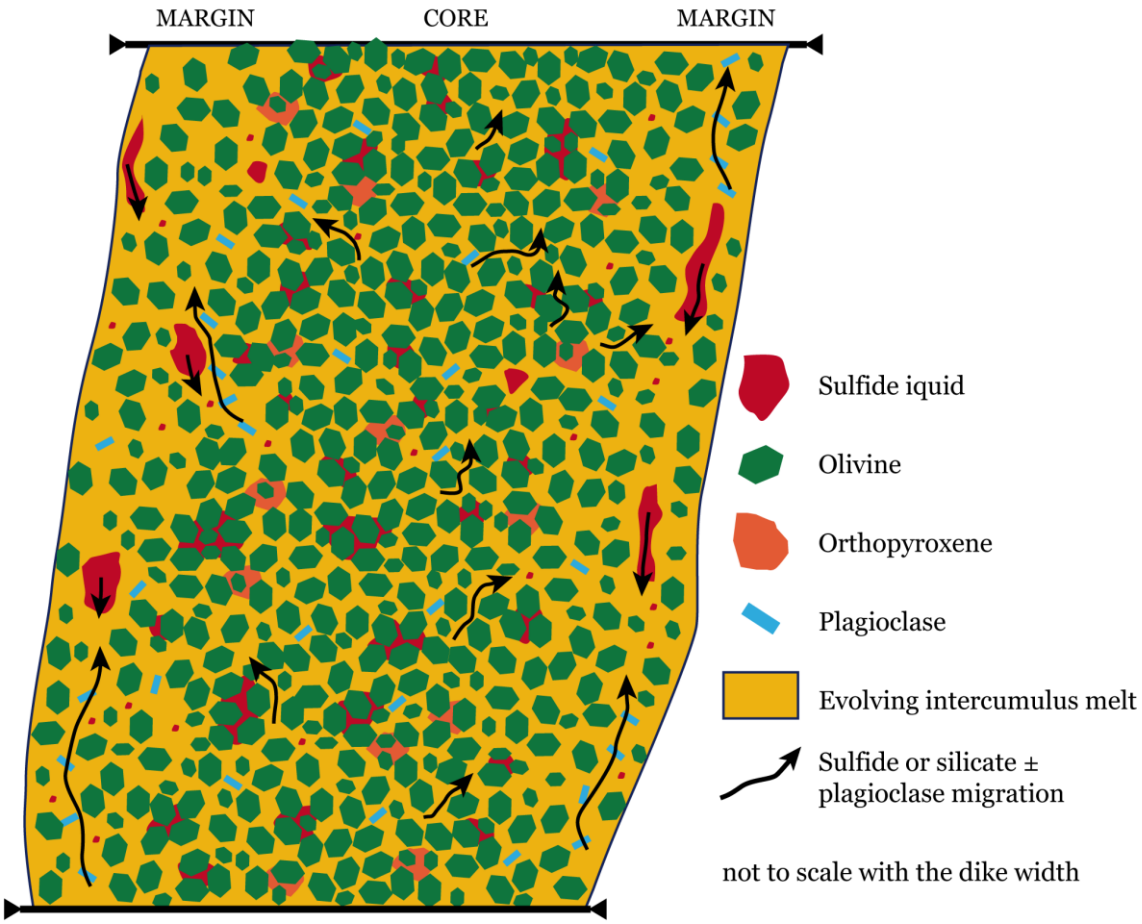

Figure 5.25 Schematic illustration showing the distribution of the sulfide liquid in the crystal-rich mush from which olivine norite and leucogabbros were formed. Note the disseminated sulfide in the crystal-rich domains and the relatively small sulfide concentration in the liquid-rich domains. Arrows illustrate the flowing of the silicate melt and the sulfide liquids relative to olivine. The migration of small sulfide volumes through the crystal much is governed by that of the silicate melt, that of large enough sulfide volume is indicated with arrows.

Based on the following observations: 1) the close spatial association of sulfides and leucogabbros, 2) sulfide segregation occurred at a relatively advanced stage of crystallization and 3) the absence of significant massive accumulation, we propose that the sulfide liquid did not strongly interact with the silicate liquid. Figure 5.26 illustrates the low Ni and Cu contents in the sulfides of Älgliden relative to other deposits of comparable Ni/Cu ratios, i.e. degree of differentiation. This suggests that the R-factor (the effective ratio of sulfide to silicate melt) was low, and that the metal contents of sulfide were only slightly upgraded through interaction between the sulfide liquid and the silicate melt.

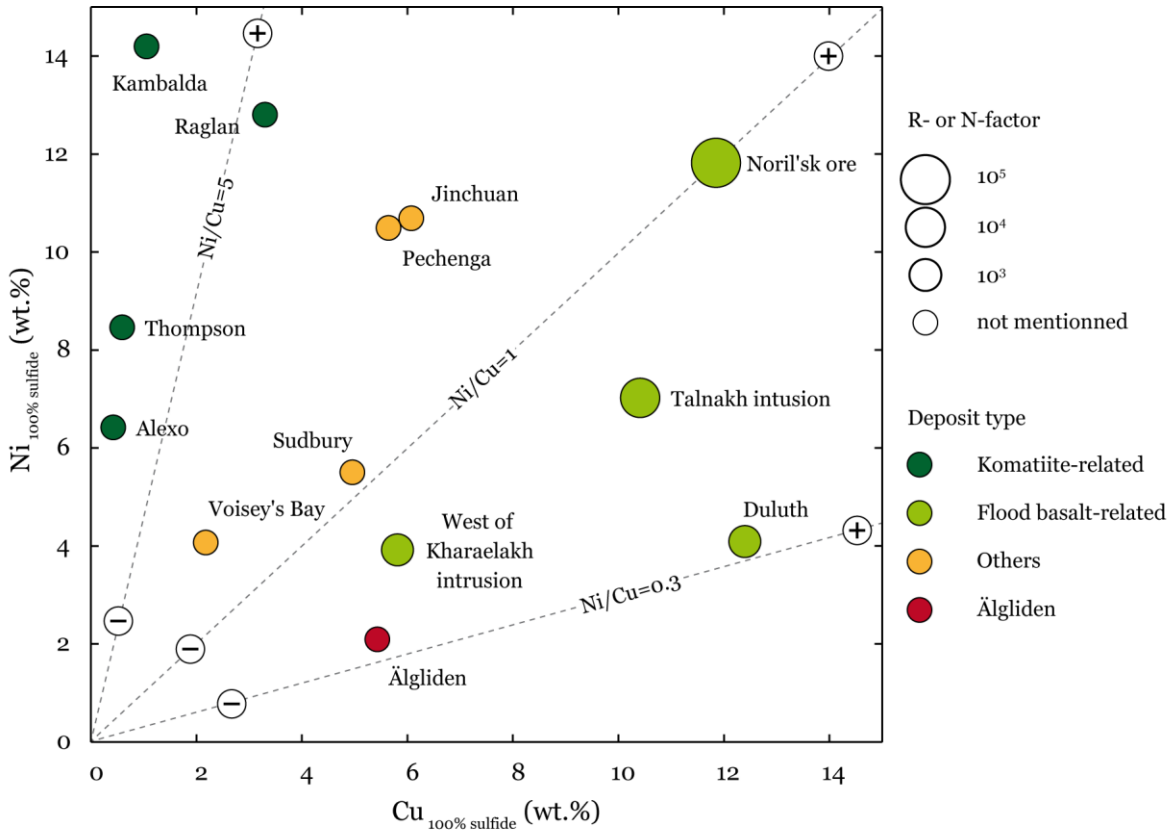

Figure 5.26 Ni vs. Cu contents calculated to 100% sulfides of some Ni-Cu deposits. N-factor of Duluth is from Thériault et al. (2000). Maximum R-factors of Noril'sk region are from Naldrett (2004). Note the probably low R- or N-factor of Älgliden compared to deposits of similar Ni/Cu ratios. Plus and minus signs are qualitative indications of R factor values.

The manner in which the intrusion was emplaced, and the timing of the sulfide liquid segregation, are of critical importance for the Älgliden mineralization. It was proposed above that the sulfide liquid segregated from the intercumulus melt, after the olivine fractionation,

due to magnetite fractionation or degassing. However, olivine with Fo_{78} composition crystallized at relatively low temperature (~1200°C according to Petrolog3 modelling), and even lower if we take into account the presence of volatiles (H_2O and CO_2) which lower the liquidus temperature. In these conditions, the temperature interval for sulfide segregation and concentration is very limited since the sulfide liquid begins to crystallize from 1150 to 1120°C depending on its composition (Naldrett, 1969). Ballhaus et al. (2001) showed that if sulfide liquids with low metal/S ratios coexist with oxidized silicate melts, like those suggested for Älgliden, these sulfides solidify in the stability field of ISS at temperatures as low as 950-800°C when the amount of remaining silicate melt is very low. At these temperatures, the silicate melt has largely crystallized and the sulfide droplets are likely to be trapped between mineral grains and have limited chance to upgrade and concentrate. For example, the crystallization of intercumulus orthopyroxene starts at 1170°C, and this allows only 20 to 50°C for the sulfide melt to interact with the silicate melt and concentrate. As a result, only small sulfide volumes became concentrated during interstitial melt migration (Figure 5.25).

The late sulfide segregation implies that the Älgliden orebody occupies the entire dike. It consists of disseminated sulfides plus minor concentrations associated with leucogabbros and xenoliths close to the dike margins or terminations. This differs from what was previously suggested by Filoche (2009) who proposed that the massive sulfide were surrounded by net-texture sulfides and preferentially located in the center of the dike in response to flow differentiation. Massive sulfides located near the margin are thought to emplace when the dike was slightly dipping. It also differs from what is commonly observed in larger ore deposits in magma conduits where net-textured and massive sulfides occur together with the cumulate rocks.

Late concentration and remobilization of sulfides

The sulfide networks hosted in leucogabbro provides evidence for relatively late incorporation of sulfide into the silicate mush. As illustrated in Figure 5.7 and Figure 5.8, the sulfides appear to resorb or replace both primary and secondary phases of the leucogabbro. The primary phases include plagioclase, pyroxene and amphibole. The secondary phases include albitic rims of plagioclase, quartz-albite intergrowth and minor chlorite. In their studies of sub-solidus reactions, Yuguchi & Nishiyama (2007; 2008) interpreted myrmekite development, as well as albitization of plagioclase, as late magmatic or deuteric processes (<500°C). On this basis, it is likely that sulfide remobilization occurred after deuteric alteration when the rock has largely or completely solidified. However, the coexistence of leucogabbro and sulfide is thought to have occurred while both phases were still molten. The late remobilization of sulfide appears to be confined in leucogabbro bodies suggesting limited re-concentration of the sulfides elsewhere.

6. Genetic model for the Älgliden deposit

6.1. Tectonic context and origin of the Älgliden magma

In the following section, we summarize our work on the petrogenesis of the Älgliden magma and the processes that formed the Ni-Cu-Au mineralization. We then identify the processes that explain the unusual characteristics of the Älgliden Ni-Cu deposit and we propose some key characteristics for this new type of magmatic sulfide deposits which occurs in subduction zone settings.

Several lines of evidence indicate that the Älgliden dike was emplaced in a subduction zone. These include Nd, Pb, Hf and S isotopes, as well as major and trace element compositions. Billström and Vivallo (1994) and Guitreau et al. (2014) used the radiogenic isotope compositions of the felsic rocks of the Skellefte district to suggest these rocks were generated by melting of a pre-existing island arc basement and/or by melting of the oceanic slab. The mafic magmas, such as those in the Älgliden intrusion, may derive from the melting in the mantle wedge above the subduction zone (Figure 6.1; Billström and Vivallo, 1994). The influx of subduction-related fluids enriched the source in fluid-mobile elements including S and volatiles, and conferred an oxidized state to the source (Wallace, 2005; Kelley & Cottrell, 2012). Under the P-T conditions of the mantle wedge, the sulfide phase consists mainly of solid MSS for which the Au partition coefficient is far less than for sulfide liquid (Li & Audétat, 2013). Copper and Ni, on the other hand are as much compatible with monosulfide solid solution (MSS) than with sulfide liquid. The mantle wedge is also oxidized and this increases the solubility of sulfur (Carroll and Rutherford, 1985, 1987; Luhr, 1990; Jugo et al. 2005, 2009). Consequently, melting in the mantle wedge forms magmas that are hydrous and oxidized, strongly under-saturated in sulfur, and relatively enriched in Au compared to the other chalcophile elements (Wallace, 2005; Kelley & Cottrell, 2009; Plank et al., 2013; Labidi et al., 2015).

The presence of mafic volcanic rocks (e.g. up to Mg#=69; Allen and Svenson, 2004) in the Skellefte district, together with the fact that primitive arc magmas generated in the mantle wedge usually crystallize Fo_{90} olivine (e.g. Gavrilenko et al., 2016), indicate that the primitive melt of the Älgliden rocks was probably highly mafic in composition and that it underwent significant differentiation, mainly olivine fractionation in a deep magma chamber, before reaching the shallow level in the crust where it intruded (Figure 6.1). The trace element compositions of olivine-norites and leucogabbros show that the melt did not undergo significant crustal contamination.

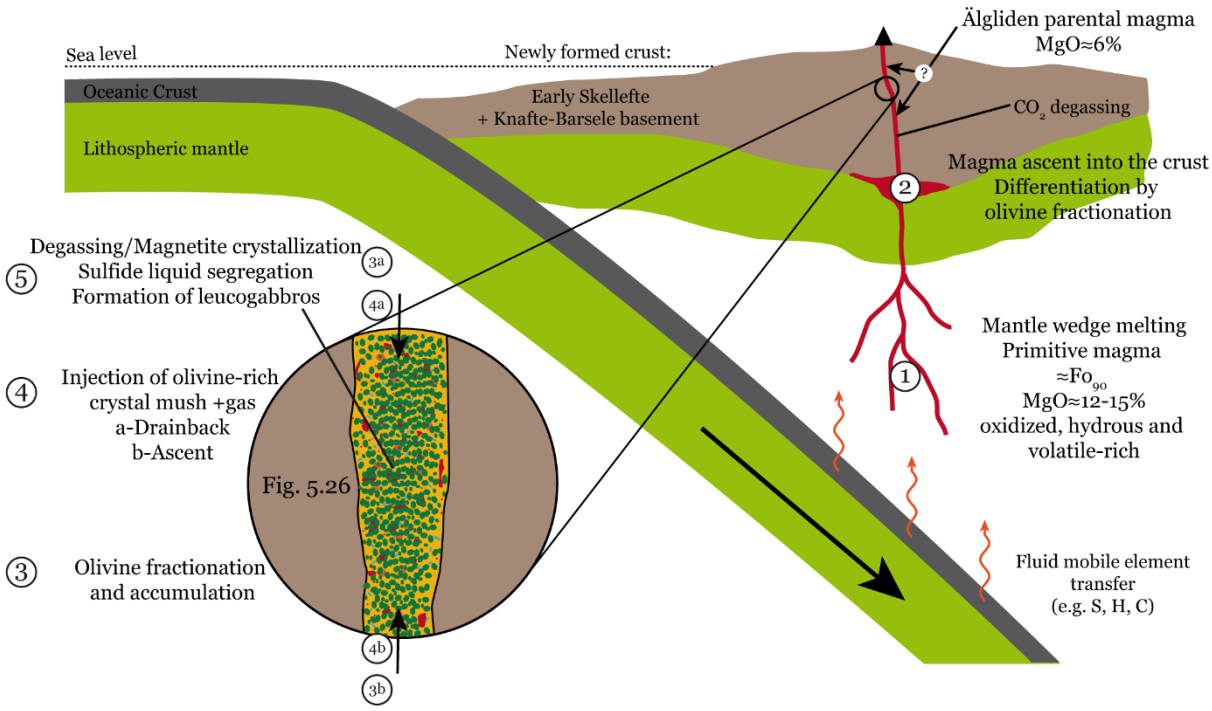

Figure 6.1 Schematic representation of the tectonic context and the origin and evolution of the Älgliden magma.

Before arriving at its final level of emplacement the Älgliden magma crystallized olivine (Fo_{78} to Fo_{72}) and these crystals accumulated in the magma. The uniform distribution and composition of olivine within the dike suggest that an olivine-rich crystal mush was introduced as a single injection, with a possible second pulse in the wider central part of the dike. It is possible that these injections were emplaced as upward flow, driven by overpressure or gas-supported buoyancy, or as back flow from shallower levels in the magma conduit in response to the high density of the olivine crystal mush (Figure 6.1). We estimated that after emplacement the intercumulus melt crystallized an additional 60% of orthopyroxene and plagioclase with minor magnetite, amphibole and biotite to produce the Älgliden leucogabbros. We suggest that dynamic sorting between the different crystals and between melts was responsible for the small-scale lithological variations. Due to the Bagnold effect, olivine crystals were concentrated toward the center of the dike generating the olivine-rich norites while the silicate melt was more abundant close to the margins of the dike where olivine-poor norites are observed (Fig. 6.1). The segregation of residual melts with or without plagioclase and orthopyroxene, led to the formation of buoyant segregation channels or pockets that facilitated the formation of leucogabbro. Before and/or during its emplacement, the Älgliden volatile-rich magma probably experienced CO_2, S and H_2O degassing even if we do not have direct evidence for this process.

Several features suggest that the sulfide liquid phase segregated relatively late during the crystallization of the magma: (i) the olivine has relatively high (undepleted) Ni contents (ii) the sulfides are concentrated with leucogabbros and have low metal grades likely due to weak interaction and exchange between sulfide and silicate liquids, (iii) the sulfides have low Ni/Cu ratios consistent with segregation from evolved liquid. The sulfide liquid segregation was probably triggered by the reduction of the melt, in response to magnetite crystallization or to degassing.

6.2. The Älgliden mineralization: a new type a magmatic sulfide deposit

Here we develop a model in which certain unusual features of the Älgliden mineralization are governed by the geological setting in which it formed. These features are:

- the association with calk-alkaline magmas that were generated in a subduction setting
- an absence of clear evidence of contamination with wall rocks
- the low Ni/Cu and high Au contents of the sulfide mineralization
- the disseminated nature of the mineralization and the apparent absence of massive sulfide
- the presence of mineralization in a near-vertical dike

The main features of the new model are compared with the classical model of formation of Ni-Cu deposits in Table 6.1.

Table 6.1 Main features and key factors in the formation of Ni-Cu magmatic sulfide deposits in ultramafic and mafic igneous rocks according to the accepted model and to the new model applied in subduction zones and to the Älgliden mineralization.

Standard model	New model
Plume-related reduced magma	Oxidized arc magmas
Mafic-ultramafic host rocks	Relatively evolved mafic host rocks
S immiscibility triggered by contamination	S immiscibility triggered by magma reduction
Early segregation	Late segregation
Ni-rich Cu- and Au-poor	Au- & Cu-rich and Ni-poor
Upgrading by significant interaction with silicate melt	Limited upgrading by weak interaction with silicate melt
Basal accumulation	Dissemination and limited accumulation

Most Ni-Cu deposits are associated with tholeiitic or komatiitic magmas. These magmas are reduced, in contrast to oxidized arc magmas. Oxidizing conditions tend to increase the sulfur solubility in silicate magmas and thus to allow the magma to carry a large amount of S (Carroll and Rutherford, 1985, 1987; Luhr, 1990; Jugo et al., 2005). Arc primary melts are therefore S-rich (Wallace, 2005) giving them the potential to form a magmatic sulfide deposit if sulfide saturation is achieved. However, because of the high S solubility, most oxidized magmas are strongly undersaturated in the sulfur-bearing species (usually sulfate). The amount of dissolved S (Jégo & Pichavant, 2012), the oxidizing conditions (Botcharnikov et al., 2011) and a sulfide phase dominated by solid MSS in their source (Li & Audétat, 2013), lead to high Au contents in these magmas.

En route to the surface, pressure decreases and this increases sulfur solubility (Mavrogenes & O'Neil, 1999). The magmas become more S-undersaturated as long as they remain oxidized (Jugo et al., 2009). As shown in Figure 6.2, a typical arc lava might contain ≈ 1000-3000 ppm S (references in Wallace, 2005) whereas the S solubility range from 2000 to 14000 ppm (Jugo, 2009). This compares with typical plume-derived magmas, which contain 500-1250 ppm (Ruscitto, et al., 2010) for a sulfur solubility of 1000 to 7500 ppm (Jugo, 2009). Because of the high S solubility, an efficient process is needed to induce sulfide segregation.

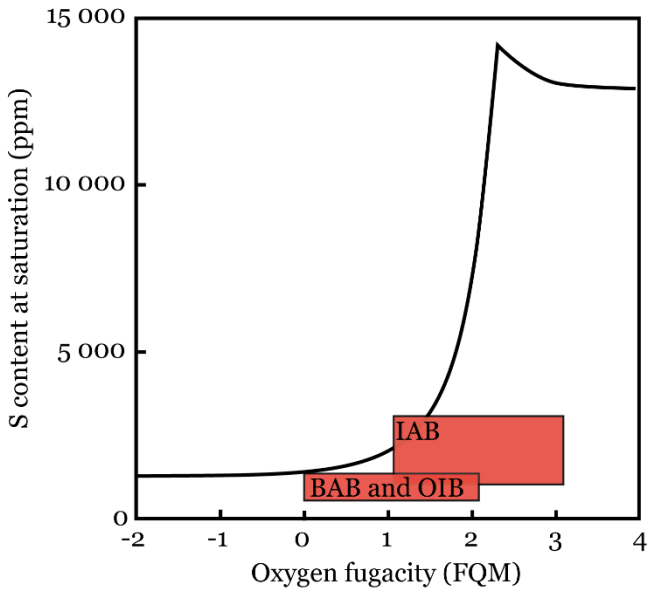

Figure 6.2 S content at sulfide and sulfate saturation from island arc basalts (IAB), back-arc basalts (BAB) and oceanic-island basalts (OIB) and mid-ocean ridge basalts (MORB). After Jugo (2009).

As explained above, in most Ni-Cu deposits, sulfide saturation is reached by assimilation of crustal siliceous and/or S-bearing rocks. In the Älgliden case, the magma does not appear to

have assimilated abundant wall rock, except possibly locally. The reduction of the S-rich undersaturated and oxidized magma hence appears to have been caused by another process. Kelley & Cottrell (2012) and Jenner et al. (2010) have shown that reduction of arc magmas occurs during differentiation, but this is commonly achieved relatively late during the differentiation. Arndt et al. (2005) pointed out the critical importance of the timing of segregation on the processes of metal-upgrading and concentration of the sulfide liquid. The timing of sulfide liquid segregation first controls the relative content of Ni, Cu and Au in the sulfide liquid because, during differentiation, the contents in incompatible chalcophile elements, such as Cu and Au, tend to increase in the silicate melt whereas the contents in compatible chalcophile elements, such as Ni and Co, decrease. These chalcophile elements are subsequently partitioned similarly in the sulfide liquid as they have comparable partition coefficients between the sulfide liquid and silicate melt (except for Au which can be much higher, Li & Audétat, 2013). Early sulfide segregation will therefore result in Ni-rich and Cu- and Au-poor mineralization whereas late sulfide segregation produces Au- and Cu-rich, Ni-poor mineralization. The Ni/Cu ratios of the ore deposits are hence related to the MgO content of the magma from which they derived. This is illustrated in Figure 6.3, where the Älgliden Ni-Cu mineralization forms the low Ni/Cu and low MgO endmember of the trend defined by worldwide Ni sulfide deposits.

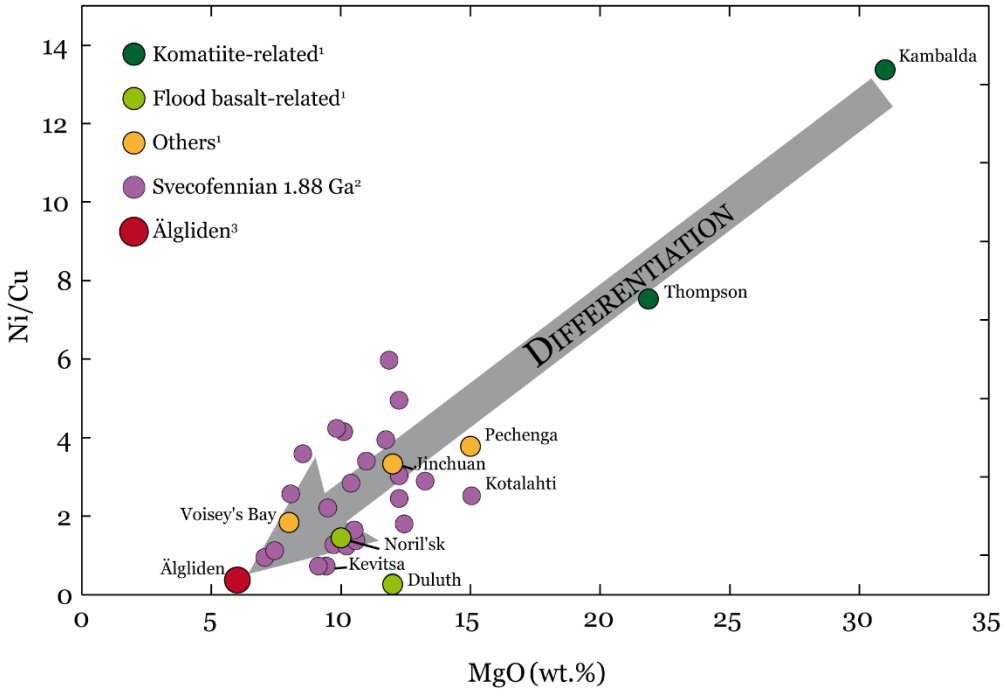

Figure 6.3 Ni/Cu ratios vs. estimated MgO content of the parental magma of some deposit types. References: 1: Naldrett (2004) and references therein for Ni/Cu ratios and Arndt et al. (2008) for MgO; 2: Makkonen et al. (2017) and references therein; 3: This study.

Metal upgrading in the ore requires the transfer of chalcophile elements (e.g. Ni, Cu and Au) from the silicate melt. This process is effective when the sulfide liquid interacts with a large amount of silicate melt, as occurs in deposits recognized to have high R-factors; e.g. in channelized flow of komatiite such as Kambalda (Lesher and Arndt, 1995) or in feeder channels of large igneous provinces such as Noril'sk (Naldrett, 2004 and references therein). In this type of Ni-Cu deposits, sulfide segregates during the early magmatic stages, prior or during emplacement of the host rock (Arndt et al., 2005). Magmatic conduits are privileged locations where high magma fluxes allow efficient upgrading. In the vertical intrusion of Älgliden, however, the sulfide liquid was not substantially upgraded, probably due to its late segregation. The accumulation of sulfide is commonly thought to occur by settling and hydrodynamic flowage, aided by the low viscosity and high density of the sulfide liquid (Dobrovinski et al., 1969; Dobson et al., 2000; Naldrett, 2004; Mungall & Su, 2005). During their transport, sulfide liquids tend to be concentrated at the base of intrusions, in depressions or at places where the conduits widen and where the flow rate suddenly drops (Barnes et al., 2015). The mechanism of gravitational backflow of the sulfide liquid has been recently advocated as a critical process in forming large concentrations of sulfide ore (e.g. Eagle Nest; Arndt et al., 2013; Barnes et al., 2015; Saumur et al., 2015). In this way, massive sulfides accumulate in intrusions of various geometries, even in vertical conduits (Eagle's Nest deposit - Mungall et al., 2010; Reid Brook zone of Voisey's Bay - Lightfoot et al., 2012). However, efficient process of accumulation requires the early segregation of the sulfide, whereas in other deposits, the sulfide ores are disseminated through the whole host intrusion (e.g. Duluth, Katiniq). This is the case at Älgliden.

The temperature windows in which both sulfide and silicate liquid coexist might play a significant role in the ore forming processes of Ni-Cu deposits. Figure 6.4 illustrates the temperature windows, defined by the difference between the silicate and sulfide liquidus (ΔT). To form an ore-deposit, the sulfide liquid has to segregate, upgrade and accumulate in these temperature windows. If it is assumed that silicate magmas rarely exist above their liquidus temperature (i.e. in a superheated state), then the interval in which hydrous magma coexists with completely molten sulfide liquid is small. In subduction zones, where the water content is 4 wt.% in average (Plank et al., 2013), the sulfide ore has, therefore, a restricted range of temperatures to form. This is particularly true for evolved melts such as those at Älgliden in which sulfide liquid segregated from an evolved mafic melts, at relatively low temperature. Hence the evolved and hydrous character of the Älgliden magmas is not favorable for the genesis of sulfide ore. Segregation of the sulfide liquid occurred late, following crystallization of most of the magma limiting the processes of upgrading and accumulation.

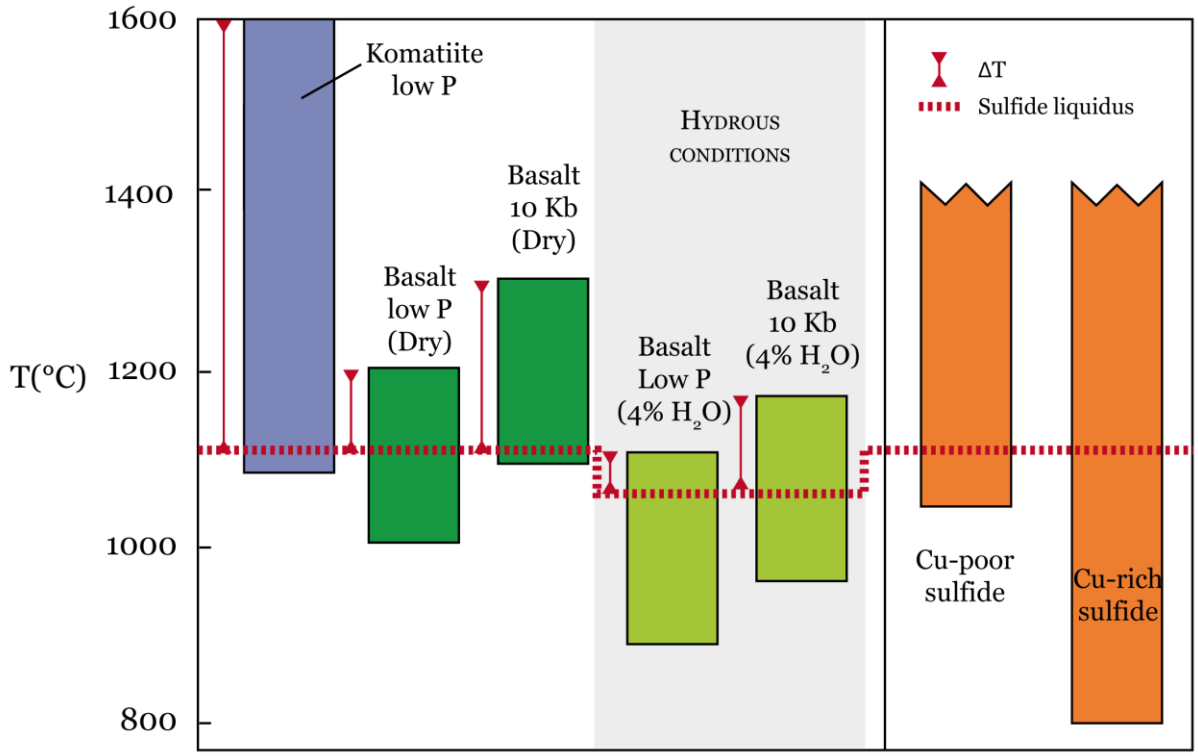

Figure 6.4 Temperature ranges between liquidus and solidus for silicate and sulfide melts at various pressure and water contents. ΔT is the temperature window in which the sulfide or silicate phases are partially or fully melted, respectively. The red line is the sulfide liquidus, with hydrous conditions according to Wykes & Mavrogenes (2005). After Barnes et al. (2015).

Other deposits in subduction settings

Other Ni-Cu deposits have been recognized in convergent margins, including Aguablanca (Spain; Casquet et al., 2001; Tornos et al., 2001), Giant Mascot (British Columbia; Manor et al., 2014), and the Huangshangdong, Kalatongkte or Xiangshan deposits in China (e.g Mao et al., 2008).). These deposits share certain characteristics of the Älgliden deposit which distinguish them from other Ni-Cu deposits: e.g. evolved hornblende±biotite-bearing mafic host; low Ni/Cu ratios; low grade and/or weak sulfide accumulation (Table 6.2). These distinctive characteristics, which are not found all together in each deposit, appear to be related to the geological environment in which they formed. For example, Keith et al. (2017) studied sulfide globules hosted in glasses from different environments and concluded that monosulfide solid solutions in subduction-related magmas occur preferentially in evolved melts and have low Ni and low Ni/Cu ratios, such as discussed above. In addition, the differentiated character of the host rocks may also influence the grade and the concentration of the ore, as proposed for Älgliden. As an illustration, noted that disseminated sulfides of the Kalatongke Ni-Cu deposit in the Tianshan-Altai belt are hosted in rocks with relatively low-Fo olivine (i.e. ≈Fo_{70-85}; Table 6.2), suggesting the sulfide liquid segregation occurred at an advanced stage of differentiation.

Thus, Ni-Cu sulfide deposits associated with mafic magmas in subduction zones have special features compared to deposits in other environments. The particularities of Ni-Cu deposits in arcs include the relatively Ni-poor and Cu- and Au-rich mineralization. The oxidizing conditions of arc magmas allow them to carry high amount of dissolved sulfide making them propitious for the formation of magmatic sulfides. However, it also makes them highly sulfide undersaturated implying that these magmas are not predisposed to form Ni-Cu deposits if no efficient process allows them to reach the sulfide saturation. This emphasizes the critical importance of the timing of the sulfide saturation and the way it is reached. In the case of the Älgliden mineralization, the late sulfide saturation is thought to be responsible for the low ore grade and the low tenor of the sulfide. However, in other places, such as in the Finnish belts that are tectonically equivalent of the Skellefte belt, or at Giant Mascot in Canada, contamination and early sulfide saturation have been invoked (Weihed et al., 2005; Makkonen & Huhma, 2007; Manor et al., 2016) suggesting that the sulfides had time to upgrade and concentrate as massive sulfides. This factor appears critical in the formation of economic Ni-Cu deposits in subduction zones. In addition, in arc settings, the active deformation may concentrate sulfides (e.g. breccia-textured vein sulfides) and be associated with their emplacement, such as it is observed at Vammala (Peltonen, 1995) or at Aguablanca (Tornos et al., 2001) where sulfides breccias appear to have been injected into their present site during compressive deformation.

Despite the strongly sulfide-undersaturated character of oxidized magmas in subduction zones, the latter are prospective for Ni-Cu deposits, as observed in the Skellefte, Kotalahti or Vammala belts. The Älgliden mineralization appears as an endmember among Ni-Cu deposits because of its low Ni and high Cu and Au contents, which may be related to the evolved nature of the parental magma, and because of its low sulfide grade and concentrations, due to late sulfide segregation. Other mafic intrusions in arc settings clearly host more substantial Ni-Cu sulfide deposits.

Table 6.2 Characteristics of mineralization and host rock for some arc-related deposits.

Deposit	Country	Ni (wt.%)	Cu (wt.%)	Ni/Cu	Ni+ Cu	Host rocks	Fo (mol.%)	Ore type
Kalatongke ore I	China	0.88	1.4	0.6	2.3	Biotite-hornblende norite and hornblende pyroxenite	71.6-78[1]	Dominantly disseminated and massive and subordinately colloidal and vein
Kalatongke ore II	China	0.6	1.1	0.5	1.7	Biotite-hornblende norite and biotite-hornblende gabbro	71.6-78[1]	Dominantly disseminated and subordinately cumulophyric and massive
Kalatongke ore III	China	0.6	1.1	0.5	1.7	Hornblende gabbro and hornblende norite	71.6-78[1]	Disseminated and cumulophyric
Huangshandong	China	0.52	0.3	1.7	0.8	Gabbro norite and hornblende lherzolite	75-84[2]	Dominantly disseminated and subordinately massive and stockwork
Huangshan	China	0.49	0.3	1.6	0.8	Hornblende gabbro and hornblende lherzolite	70.7-85.8[3]	Dominantly disseminated and subordinately massive and stockwork
Tudun	China	0.3	0.2	1.5	0.5	Hornblende peridotite, hornblende gabbro and norite	85[4]	Disseminated
Xiangshan	China	0.5	0.3	1.7	0.8	Hornblende wehrlite, pyroxenite and hornblende gabbro	82.5-85.9[5]	Disseminated and massive
Tula'ergen	China	0.24-0.42	0.27	0.88-1.55	0.51-0.69	Gabbro and hornblende olivine gabbro	73-85.7[6]	Disseminated
Erthongwa	China	0.2	0.2	1.0	0.4	Lherzolite, gabbro norite and olivine gabbro	-	Disseminated
Aguablanca	Spain	0.6	0.4	1.5	1.0	Biotite-bearing hornblende norite and gabbro-norites and clinopyroxene-bearing biotite-amphibole diorites and quartz diorites	-	Dominantly disseminated and massive, breccia and vein
Kotalahti	Finland	0.72	0.27	2.7	1.0	Differentiated peridotite-gabbro±diorite	-	Disseminated and breccia
Giant Mascot	B.C.	0.77	0.34	2.3	1.1	Hornblende-bearing dunite, peridotite and pyroxenite	80-89	Disseminated, net-textured and massive
Älgliden	Sweden	0.11	0.31	0.4	0.4	Horblende- and biotite-bearing olivine-gabbro and leucogabbro	72.3-78.6	Dominantly disseminated, network to vein and massive

B.C.: British Columbia

References: Ni and Cu contents in mineralizations in Chinese deposits from Mao et al. (2008) and references therein; Aguablanca from Ortega et al., (2004) and Piña et al. (2013); Kotalahti from Weihed et al. (2005); Giant Mascot from Manor et al. (2016) ; Älgliden from this study; 1: Gao et al. (2012); 2: Gao & Zou (2013); 3: Deng et al. (2017); 4: Wang et al. (2015) and references therein; 5: Xiao et al. (2010); 6: Sun (2009).

7. Conclusions and perspectives

Conclusions

The main objectives of this PhD thesis were to understand the origin of the Älgliden Ni-Cu-Au mineralization and to study the formation of Ni-Cu deposit in subduction zones. Detailed petrological studies, including mineral and bulk rock composition as well as texture description and S isotope analyzes provided answers to these issues. The main results and conclusions are as follow:

- The Älgliden intrusion is composed mainly of olivine norites with minor leucogabbros. The olivine norite represents cumulate made of 15 to 60% olivine, whereas the leucogabbro is interpreted as 0-60% fractionated interstitial melt together with 0-30% plagioclase and orthopyroxene. The Älgliden magma was injected into a vertical structure as a crystal mush following the accumulation of abundant olivine. During the emplacement of the olivine-rich mush, concentration of olivine crystals in the center of the intrusion resulted in the formation of olivine-rich norite while sparser amounts of olivine crystals in the margins produced olivine-poor norite. Locally, dynamic sorting between crystals and melts during compaction and crystallization of the intercumulus liquid led to the segregation of interstitial melt±crystals which formed minor amounts of leucogabbros.

- The parental magma of the Älgliden intrusion was a hydrous evolved basalt with ≈ 6 wt.% MgO. Its distinctive trace element composition indicates that it formed in a subduction zone. Although the intrusion crosscuts the Tallberg Cu-Au porphyry deposit, assimilation of this material is ruled out by differences in trace-element ratios, particularly the ratios between middle and heavy rare earth elements, and contrasting concentrations of elements, such as Pb. Assimilation of wall rocks is therefore not considered instrumental in the formation of the Ni-Cu-Au sulfide mineralization. Instead, the distinctive proportions of Ni, Cu and Au in the ore – low Ni/Cu and high Au — thought to result from the evolved and oxidized character of the parental magma which resulted from its generation in a subduction setting.

- The sulfide ore is mainly disseminated within the olivine norite that dominates the intrusion, but some moderate concentrations occurred as networks, veins and massive sulfides in spatial association with leucogabbros and wallrock xenoliths. Whereas sulfides are commonly associated with mafic/ultramafic cumulates in most Ni-Cu deposits, at Älgliden they occur together with evolved leucogabbros that represent residual liquids.

- The low amount of sulfide and the low ore tenors at Älgliden are attributed to late sulfide liquid segregation from an evolved silicate melt which inhibited both the concentration of sulfide liquid and interaction between sulfide and silicate melt. Sulfide saturation is thought to have been achieved by reduction of the oxidized magma which lowered the sulfide solubility. The reduction probably resulted from magnetite crystallization and/or degassing.

- Larger and richer Ni-Cu-Au deposits may form in a subduction-related geodynamic setting, if significant wall-rock assimilation or magma reduction occurs at an early stage of magma differentiation or if sulfides are concentrated by tectonic processes.

- The study of the Älgliden mineralization provided an opportunity to investigate exploration strategies for the targeting of Ni-Cu deposits in subduction-related geodynamic settings. In plume-related Ni-Cu deposits where assimilation of crustal material is invoked, sulfur isotope composition is an efficient tool to assess this process because the $\delta^{34}S$ values of the mantle-derived magma and of the crustal S are clearly distinct. This cannot systematically be applied to subduction zone environment where the $\delta^{34}S$ values of subduction-related magmas and crustal S commonly overlap. In the case of non-contaminated arc magmas, the forsterite content of olivine is a good proxy to estimate the differentiation degree of the host rock the late segregation of sulfide liquid. This may help to identify Ni-Cu deposits that share similarities with the Älgliden mineralization: i.e. relatively low grade Cu- and Au-rich and Ni-poor sulfide ores.

Perspectives

Before extrapolating to other Ni-Cu deposits in subduction zone environments, additional and more information is required from the Älgliden regarding the extent of assimilation of wall rocks and the process by which the sulfide liquid segregated.

Possible future investigations regarding contamination include additional $\delta^{34}S$ analyses, in order to establish the extent of $\delta^{34}S$ of magmatic and hydrothermal sulfides. It may be possible to use the more range in the Älgliden sulfides compared with the Tallberg sulfides. Otherwise, a combination of radiogenic isotopes (including Pb, Sr, Nd) on bulk rocks, and stable isotopes (e.g. O, H, Fe, Ni *etc.*) on bulk rocks and the *in-situ* determination of Pb and Re-Os isotope composition by secondary ion mass spectrometry on sulfide grains would be useful to identify and/or quantify the extent of assimilation. Care must be taken when using radiogenic isotope systems because of possible effects of later metamorphism and alteration, which may perturb parent-daughter ratios and/or isotopic compositions.

To test the assumption that the reduction could be responsible for reaching sulfide saturation, the oxidation state of magma has to be investigated. One possible approach would be to estimate the oxygen fugacity at early stage of crystallization of the Älgliden magma, when the silicate melt is supposed to be sulfide undersaturated, using V/V(Cr+Al) systematics (Papike et al., 2004) on chromite inclusions in Ni-undepleted olivine grains. Later in the crystallization sequence, to verify if the magnetite crystallization plays a role in the reduction of the magma, the oxygen fugacity can be estimated using Fe-Ti oxides (ilmenite-ulvöspinel oxygen barometer; Ghiorso & Sack, 1991) in both olivine norite and leucogabbro. After the sulfide segregation, the oxygen fugacity can also be estimated using Fe-Ni exchange between olivine and sulfides (Brenan & Caciagli, 2000). If any magma reduction can be identified, it must then be related to magnetite crystallization and/or degassing.
Tracing the process of degassing could be achieved directly, using fluid inclusions in olivine in hornblende, or in a roundabout way by estimating the pressure of emplacement using an oxygen barometer such as Fe-Ti oxides. This offers the opportunity to study degassing in mafic magmas. The latter is considered as an important process in the formation of porphyry deposit in subduction zones (Hattori and Keith, 2001; Wallace, 2005). Experimental studies of degassing in mafic hence could be undertaken to better understand how it also acts on Ni-Cu mineralization.

Bulk rock or *in situ* platinum group element (PGE) concentrations could be determined using fire assay on bulk rocks or laser ablation on sulfide grains. They would be useful for the estimation of the R-factor using Cu-Pd systematics (e.g. Barnes & Ripley, 2016), as well as to investigate how the sulfide liquid crystallized, hence allowing a better understanding of how Au and PGE are distributed. Comparison of PGE concentrations in different types of mineralization, i.e. disseminated, network, vein and massive sulfides, could provide information on the processes that concentrated the sulfides.

Because of lack of time, the interpretation of the replacement and resorption textures between sulfide and silicate, especially in the leucogabbros, is incomplete. Further work should be undertaken to better understand how these processes might have contributed to the concentration of sulfides. Because secondary silicate phases are involved in such texture, this work could be done jointly with study of the alteration and its potential for remobilizing metals, as carried out by Le Vaillant et al. (2016) at Kevista, or Holwell et al. (2017) in the Bushveld Complex.

References

Åkerman, C. (1987). Summary of results from nickel prospecting. A consulting report. *Sveriges Geologiska AB, prospekterings rapport, prap 87007*, 70.

Allen, R. L., Weihed, P., & Svenson, S.-A. (1996). Setting of Zn-Cu-Au-Ag massive sulfide deposits in the evolution and facies architecture of a 1.9 Ga marine volcanic arc, Skellefte District, Sweden. *Economic Geology, 91,* 1022–1053.

Allen, R. J., Weihed, P., the Global VHMS Research Project team (2002). Global comparison of volcanic-associated massive sulphide districts. In: Blundell, D. J., Neubauer, F., von Quadt, A. (Eds.), The Timing and Location of Major Ore Deposits in an Evolving Orogen: *Geological Society, London, Special Publications, 204*, 13–37.

Allen, R. L. and Svenson, S-Å. (2004). 1.9 Ga Volcanic Stratigraphy, Structure, and Zn-Pb-Cu-Au-Ag Massive Sulphide deposits of the Renström area, Skellefte District, Sweden. *In:* Allen, R.L., Martinsson, O. and Weihed, P. (editors), Svecofennian Ore-Forming Environments: Volcanic-Associated Zn-Cu-Au-Ag, Intrusion-Associated Cu-Au, Sediment-Hosted Pb-Zn, and Magnetite-Apatite Deposits of Northern Sweden. *Society of Economic Geologists Guidebook Series, 33*, 65-88.

Alt, J. C., Shanks, W. C., & Jackson, M. C. (1993). Cycling of sulfur in subduction zones: The geochemistry of sulfur in the Mariana Island Arc and back-arc trough. *Earth and Planetary Science Letters, 119,* 477–494.

Annen, C., Blundy, J. D., Sparks, R. S. J. (2006). The genesis of intermediate and silicic magmas in deep crustal hot zones. *Journal of Petrology, 47,* 505–539

Arai, T., & Maruyama, S. (2017). Formation of anorthosite on the Moon through magma ocean fractional crystallization. *Geoscience Frontiers, 8,* 299-308.

Ariskin, A. A., Frenkel, M. Y., Barmina, G. S., & Nielsen, R. L. (1993). Comagmat: a Fortran program to model magma differentiation processes. *Computers & Geosciences, 19*, 1155–1170.

Ariskin, A. A., & Barmina, G. S. (1999). An empirical model for the calculation of spinel-melt equilibria in mafic igneous systems at atmospheric pressure: 2. Fe-Ti oxides. *Contributions to Mineralogy and Petrology, 134*, 251–263.

Arndt, N. T. (1977). Ultrabasic magmas and high-degree melting of the mantle. *Contributions to Mineralogy and Petrology, 64*, 205–221.

Arndt, N. T., Lesher, C. M., Czamanske, G. K. (2005). Mantle-derived magmas and magmatic Ni-Cu-(PGE) deposits. *Economic Geology, 100th Anniversary Volume,* 5–24.

Arndt, N. T., Lesher, C. M., Barnes, S. J., (2008). Komatiite. *Cambridge University Press, Cambridge*. 467 pp.

Arndt, N. T. (2013). The formation of massif anorthosite: Petrology in reverse. Geoscience *Frontiers, 4*, 195–198.

Arndt, N. T., Sobolev, S., Barnes, S. J. & Robertson, J. (2013). Magma dynamics and the formation of magmatic sulfide deposits. *In:* Jonsson, E., Aghazadeh, M. Allen, R., et al. (eds) *Proceedings of the 12th Biennial SGA Meeting*, 12–15 August 2013, Uppsala, Sweden, 930–932.

Babel Working Group. (1990). Evidence for early Proterozoic plate tectonics from seismic reflection profiles in the Baltic shield. *Nature*, 348.

Babel Working Group. (1993). Integrated Seismic Studies of the Baltic Shield Using Data in the Gulf of Bothnia Region. *Geophysical Journal International, 112*, 305–324.

Bacon, C. R. and Druitt, T. H. (1988) Compositional Evolution of the Zoned Calcalkaline Magma Chamber of Mount Mazama, Crater Lake, Oregon. *Contributions to Mineralogy and Petrology, 98,* 224-256.

Baeur, T. (2012). The Älgträsk intrusion-related Au (Cu, Zn) deposit, Skellefte district, northern Sweden (Doctoral Thesis) (p. 142). Luleå: Luleå University of Technology.

Ballhaus, C. (1993). Redox states of lithospheric and asthenospheric upper mantle. *Contributions to Mineralogy and Petrology, 114*, 331–348.

Ballhaus, C., Tredoux, M., & Späth, A. (2001). Phase Relations in the Fe–Ni–Cu–PGE–S System at Magmatic Temperature and Application to Massive Sulphide Ores of the Sudbury Igneous Complex. *Journal of Petrology, 42*, 1911–1926.

Barnes, S. J., Fiorentini, M. L., Austin, P., Gessner, K., Hough, R. M., & Squelch, A. P. (2008). Three-dimensional morphology of magmatic sulfides sheds light on ore formation and sulfide melt migration. *Geology, 36*, 655–658.

Barnes, S. J., Cruden, A. R., Arndt, N., & Saumur, B. M. (2016). The mineral system approach applied to magmatic Ni-Cu-PGE sulphide deposits. *Ore Geology Reviews, 76,* 296-316.

Barnes, S. J., Mole, D. R., Vaillant, M. L., Campbell, M. J., Verrall, M. R., Roberts, M. P., & Evans, N. J. (2016). Poikilitic Textures, Heteradcumulates and Zoned Orthopyroxenes in the Ntaka Ultramafic Complex, Tanzania: Implications for Crystallization Mechanisms of Oikocrysts. Journal of Petrology, 57, 1171–1198.

Barnes, S. J., Mungall, J. E., Le Vaillant, M., Godel, B., Lesher, C. M., Holwell, D. A., Lightfoot, P. C., Krivolutskaya, N. A., and Wei, B. (2017). Sulfide-silicate textures in magmatic Ni-Cu-PGE sulfide ore deposits: Disseminated and net-textured ores. *American Mineralogist, 102*, 473-206.

Barnes, S.-J., Makovicky, E., Karup-Moller, S., Makovicky, M., and Rose-Hanson, J. (1997). Partition coefficients for Ni, Cu, Pd, Pt, Rh and Ir between monosulfide solid solution and sulfide liquid and the implications for the formation of compositionally zoned Ni-Cu sulfide bodies by fractional crystallization of sulfide liquid. *Canadian Journal of Earth Sciences, 34*, 366–374.

Barnes, S-J. and Lightfoot, P. C. (2005). Formation of magmatic nickel-sulfide ore deposits and processses affecting their copper and platinum-group element contents. *In* Hedenquist, J. W., Thompson, J. F. H., Goldfarb, R. J. and Richards, J.P. (eds.) *Economic Geology 100th Anniversary Volume*, 179-213.

Barnes, S.-J., Cox, R. A., Zientek, M. (2006). Platinum-group element, gold, silver and base metal distribution in compositionally zoned sulfide droplets from the Medvezky Creek Mine, Noril'sk, Russia. *Contributions to Mineralogy and Petrology, 152*, 187–200.

Barnes, S.-J., Prichard, H. M., Cox, R. A., Fisher, P. C., & Godel, B. (2008). The location of the chalcophile and siderophile elements in platinum-group element ore deposits (a textural, microbeam and whole rock geochemical study): Implications for the formation of the deposits. Chemical Geology, 248, 295–317.

Barnes, S.-J., & Ripley, E. M. (2016). Highly Siderophile and Strongly Chalcophile Elements in Magmatic Ore Deposits. *Reviews in Mineralogy and Geochemistry, 81*, 725–774.

Barrière, M. (1976). Flowage differentiation: Limitation of the “Bagnold effect” to the narrow intrusions. *Contributions to Mineralogy and Petrology, 55*, 139–145.

Batanova, V. G., Sobolev, A. V., & Kuzmin, D. V. (2015). Trace element analysis of olivine: High precision analytical method for JEOL JXA-8230 electron probe microanalyser. Chemical *Geology, 419*, 149–157.

Bauer, T. E., Skyttä, P., Allen, R. L., & Weihed, P. (2011). Syn-extensional faulting controlling structural inversion – Insights from the Palaeoproterozoic Vargfors syncline, Skellefte mining district, Sweden. *Precambrian Research, 191*, 166–183.

Bauer, T. E., Skyttä, P., Allen, R. L., & Weihed, P. (2013). Fault-controlled sedimentation in a progressively opening extensional basin: the Palaeoproterozoic Vargfors basin, Skellefte mining district, Sweden. *International Journal of Earth Sciences, 102*, 385–400.

Bauer, T. E. (2013). The crustal architecture of the Central Skellefte district, Sweden (Doctoral Thesis) (p. 142). Luleå: Luleå University of Technology.

Beattie, P. (1993). Olivine-melt and orthopyroxene-melt equilibria. *Contributions to Mineralogy and Petrology, 115*, 103–111.

Bédard, J. H. J., Marsh, B. D., Hersum, T. G., Naslund, H. R., & Mukasa, S. B. (2007). Large-scale Mechanical Redistribution of Orthopyroxene and Plagioclase in the Basement Sill, Ferrar Dolerites, McMurdo Dry Valleys, Antarctica: Petrological, Mineral-chemical and

Field Evidence for Channelized Movement of Crystals and Melt. *Journal of Petrology, 48*, 2289–2326.

Bejgarn, T., Årebäck, H., Weihed, P., & Nylander, J. (2011). Geology, petrology and alteration geochemistry of the Palaeoproterozoic intrusive hosted Älgträsk Au deposit, Northern Sweden. *Geological Society, London, Special Publications, 350*, 105–132.

Bejgarn, T. (2012). The Älgträsk intrusion-related Au (Cu, Zn) deposit, Skellefte district, Northern Sweden (Doctoral Thesis) (p. 142). Luleå: Luleå University of Technology.

Bejgarn, T., Söderlund, U., Weihed, P., Årebäck, H., & Ernst, R. E. (2013). Palaeoproterozoic porphyry Cu–Au, intrusion-hosted Au and ultramafic Cu–Ni deposits in the Fennoscandian Shield: Temporal constraints using U–Pb geochronology. *Lithos, 174,* 236–254.

Berge, J. (2013). Likely “mantle plume” activity in the Skellefte district, Northern Sweden. A reexamination of mafic/ultramafic magmatic activity: Its possible association with VMS and gold mineralization. *Ore Geology Reviews, 55,* 64–79.

Bergman Weihed, J. B., Bergstrom, U., Billstrom, K., & Weihed, P. (1996). Geology, tectonic setting, and origin of the Paleoproterozoic Boliden Au-Cu-As deposit, Skellefte District, northern Sweden. *Economic Geology, 91*, 1073–1097.

Bergman Weihed, J. (2001). Paeleoproterozoic deformation zones in the Skellefte and Ardvidsjaur areas, northern Sweden. *In* Weihed, P. (ed.): *Economic geology research*. Vol. 1, 1999-2000. *Swedish Geological Survey, Uppsala*, 46-68. 1.

Bergström, U. (2001).Geochemistry and tectonic setting of volcanic units in the northern Västerbotten county, northern Sweden. *In:* Weihed,P. (Ed.), *SGU Economic Geology Research, 1999–2000. Uppsala,* 69–92.

Billström, K., & Vivallo, W. (1994). Synvolcanic mixing of ore lead and the development of lead isotopic provinces in the Skellefte district, Sweden. *Mineralium Deposita, 29*, 111–119.

Billstrom, K., & Weihed, P. (1996). Age and provenance of host rocks and ores in the Paleoproterozoic Skellefte District, northern Sweden. *Economic Geology, 91*, 1054–1072.

Billström, K.,Wasström, A.,Bergström,U.,Stigh,J. (2002). Age, geochemistry and crustal contamination of the Hemberget mafic–ultramafic layered intrusion in the Knaften area, northern Sweden. *In:* Bergman, S. (Ed.), Radiometric dating results 5. Uppsala: *Sveriges geologiska undersökning, C834. ISBN: 91-7158-668-7,* 18–30.

Blundy, J., Cashman, K., & Humphreys, M. (2006). Magma heating by decompression-driven crystallization beneath andesite volcanoes. *Nature, 443*, 76–80.

Borisov, A. A., & Shapkin, A. I. (1990). New empirical equation rating Fe^{3+}/Fe^{2+} in magmas to their composition, oxygen fugacity, and temperature. *Geochemistry International, 27,* 111–116.

Botcharnikov, R. E., Linnen, R. L., Wilke, M., Holtz, F., Jugo, P. J., & Berndt, J. (2011). High gold concentrations in sulphide-bearing magma under oxidizing conditions. *Nature Geoscience, 4*, 112–115.

Bouilhol, P., Schmidt, M. W., & Burg, J.-P. (2015). Magma Transfer and Evolution in Channels within the Arc Crust: the Pyroxenitic Feeder Pipes of Sapat (Kohistan, Pakistan). *Journal of Petrology, 56*, 1309–1342.

Brenan J. M., Caciagli N. C. (2000). Fe-Ni exchange between olivine and sulfide liquid: Implications for oxygen barometry in sulfide-saturated magmas. *Geochimica et Cosmochimica Acta, 64*, 307-320.

Canfield, D. E., Raiswell, R., Westrich, J. T., Reaves, C. M., & Berner, R. A. (1986). The use of chromium reduction in the analysis of reduced inorganic sulfur in sediments and shales. *Chemical Geology, 54*, 149–155.

Carroll, M. R., and Rutherford, M. J., (1985). Sulfide and sulfate saturation in hydrous silicate melts. *Journal of Geophysical Research, 90*, C601–C612.

Carroll, M. R., and Rutherford, M. J. (1987). The stability of igneous anhydrite - Experimental results and implications for sulfur behavior in the 1982 El Chichon trachyandesite and other evolved magmas. *Journal of Petrology, 28*, 781–801.

Casquet, C., Galindo, C., Tornos, F., Velasco, F., & Canales, A. (2001). The Aguablanca Cu–Ni ore deposit (Extremadura, Spain), a case of synorogenic orthomagmatic mineralization: age and isotope composition of magmas (Sr, Nd) and ore (S). *Ore Geology Reviews, 18*, 237–250.

Chauvel, C., Bureau, S., & Poggi, C. (2011). Comprehensive Chemical and Isotopic Analyses of Basalt and Sediment Reference Materials. *Geostandards and Geoanalytical Research, 35*, 125–143.

Chung, H.-Y., & Mungall, J. E. (2009). Physical constraints on the migration of immiscible fluids through partially molten silicates, with special reference to magmatic sulfide ores. *Earth and Planetary Science Letters, 286*, 14–22.

Claesson, L. Å. (1985). The geochemistry of early Proterozoic metavolcanic rocks hosting massive sulphide deposits in the Skellefte district, northern Sweden. *Journal of the Geological Society, 142*, 899–909.

Cox, K. G., Bell, J. D., & Pankhurst, R. J. (1979). The interpretation of igneous rocks. *Springer Netherlands.*

Czamanske, G. K., & Moore, J. G. (1977). Composition and phase chemistry of sulfide globules in basalt from the Mid-Atlantic Ridge rift valley near 37°N lat. *GSA Bulletin, 88*, 587–599.

Czamanske, G. K., Zen'ko, T. E., Fedorenko, V. A., Calk, L. C., Budahn, J. R., Bullock, J. H., Jr., Fries, T. L., King, B. S. & Siems, D. F. (1995). Petrography and geochemical characterization of ore-bearing intrusions of the Noril'sk type, Siberia; with discussion of their origin. *Resource Geology Special Issue 18*, 1-48.

Danyushevsky, L. V. (2001). The effect of small amounts of H2O on crystallisation of mid-ocean ridge and backarc basin magmas. *Journal of Volcanology and Geothermal Research, 110*, 265–280.

Danyushevsky, L. V., & Plechov, P. (2011). Petrolog3: Integrated software for modeling crystallization processes. *Geochemistry, Geophysics, Geosystems, 12*, Q07021.

Dare, S. A. S., Barnes, S.-J., Prichard, H. M., & Fisher, P. C. (2014). Mineralogy and Geochemistry of Cu-Rich Ores from the McCreedy East Ni-Cu-PGE Deposit (Sudbury, Canada): Implications for the Behavior of Platinum Group and Chalcophile Elements at the End of Crystallization of a Sulfide Liquid. *Economic Geology, 109*, 343–366.

De Hoog, J. C. M., Taylor, B. E., & van Bergen, M. J. (2001). Sulfur isotope systematics of basaltic lavas from Indonesia: implications for the sulfur cycle in subduction zones. *Earth and Planetary Science Letters, 189*, 237–252.

Deng, Y.-F., Song, X.-Y., Hollings, P., Chen, L.-M., Zhou, T., Yuan, F., … Zhao, B. (2017). Lithological and geochemical constraints on the magma conduit systems of the Huangshan Ni-Cu sulfide deposit, NW China. *Mineralium Deposita, 52*, 845–862.

DePaolo, D. J. (1981). A neodymium and strontium isotopic study of the Mesozoic calc-alkaline granitic batholiths of the Sierra Nevada and Peninsula Ranges, California. *Journal of Geophysical Research, 86*, 10470–10488.

Dixon, J. E. (1997). Degassing of alkalic basalts. *American Mineralogist, 82*, 368–378.

Dobrovinski, I. E., Esin, O. A., Barmin, L. N. & Chuchmarev, S. K. (1969). Physicochemical properties of sulfide melts. *Russian Journal of Physical Chemistry, 43*, 1769–1771.

Dobson D. P., Crichton W. A., Vocadlo L., Jones A. P., Wang Y., Uchida T., Rivers M., Sutton S., Brodholt J. P. (2000). In situ measurement of viscosity of liquids in the Fe-FeS system at high pressures and temperatures. *American Mineralogist, 85*, 1838-42.

Dumas, H. (1986). Litho-facies of the Metasedimentary Formations in the Central Part of the Skellefte district (Licentiate Thesis) (p. 72). Luleå: Luleå University of Technology.

Eilu, P. (2012). Mineral deposits and metallogeny of Fennoscandia. *Geological Survey of Finland, Special Paper, 53*, 401

Filoche, C. (2009). Geology of the Älgliden Cu-Ni-Au mineralization, northern Sweden (Master's Thesis) (p. 56). Luleå: Luleå University of Technology.

Frietsch, R., Billström, K., & Perdahl, J. A. (1995). Sulphur isotopes in Lower Proterozoic iron and sulphide ores in northern Sweden. *Mineralium Deposita, 30*, 275–284.

Fujimaki, H., Tatsumoto, M., & Aoki, K. (1984). Partition coefficients of Hf, Zr, and ree between phenocrysts and groundmasses. *Journal of Geophysical Research: Solid Earth, 89,* B662–B672.

Gaál, G., & Gorbatschev, R. (1987). An Outline of the precambrian evolution of the baltic shield. *Precambrian Research, 35*, 15–52.

Gaál, G. (1990). Tectonic styles of Early Proterozoic ore deposition in the Fennoscandian Shield. *Precambrian Research, 46*, 83–114.

Gao, J.-F., Zhou, M.-F., Lightfoot, P. C., Wang, C. Y., & Qi, L. (2012). Origin of PGE-Poor and Cu-Rich Magmatic Sulfides from the Kalatongke Deposit, Xinjiang, Northwest China. *Economic Geology, 107*, 481–506.

Gao, J.-F., & Zhou, M.-F. (2013). Generation and evolution of siliceous high magnesium basaltic magmas in the formation of the Permian Huangshandong intrusion (Xinjiang, NW China). *Lithos, 162*, 128–139.

Gavrilenko, M., Herzberg, C., Vidito, C., Carr, M. J., Tenner, T., & Ozerov, A. (2016). A Calcium-in-Olivine Geohygrometer and its Application to Subduction Zone Magmatism. *Journal of Petrology, 57*, 1811–1832.

Gazel, E., Hayes, J. L., Hoernle, K., Kelemen, P., Everson, E., Holbrook, W. S.,...Yogodzinski, G. M. (2015). Continental crust generated in oceanic arcs. *Nature Geoscience, 8*, 321–327.

Gerlach, D. C., & Grove, T. L. (1982). Petrology of Medicine Lake Highland volcanics: Characterization of endmembers of magma mixing. *Contributions to Mineralogy and Petrology, 80*, 147–159.

Ghiorso M. S., Sack R. O. (1991). Fe-Ti oxide geothermometry: thermodynamic formulation and the estimation of intensive variables in silicic magmas. *Contributions to Mineralogy and Petrology,* 108:485–510.

Gibb, F. G. F., & Henderson, C. M. B. (1992). Convection and crystal settling in sills. *Contributions to Mineralogy and Petrology, 109*, 538–545.

Godel, B. M., Barnes, S. J., & Barnes, S.-J. (2013). Deposition Mechanisms of Magmatic Sulphide Liquids: Evidence from High-Resolution X-Ray Computed Tomography and Trace Element Chemistry of Komatiite-hosted Disseminated Sulphides. *Journal of Petrology, 54*, 1455–1481.

González-Roldán, M. (2010). Mineralogy, petrology and geochemistry of syn-volcanic intrusions in the Skellefte mining district, Northern Sweden (PhD thesis) (p.237), University of Huelva.

Gorbunov, G. I., Zagorodny, V. G. and Robonen, W. I. (1985). Main features of the geological history of the Baltic Shield and the epochs of ore formation. *Geological Survey of Finland, Bulletin 333,* 2-41.

Grip, E. (1961). Geology of the Nickel-Deposit at Lainijaur in northern Sweden. *Sveriges geologiska undersökning, C 577*, 1-79.

Guitreau, M., Blichert-Toft, J., & Billström, K. (2014). Hafnium isotope evidence for early-Proterozoic volcanic arc reworking in the Skellefte district (northern Sweden) and implications for the Svecofennian orogen. *Precambrian Research, 252*, 39–52.

Hattori, K. H. & Keith, J. D. (2001). Contribution of mafic melt to porphyry copper mineralization: Evidence from Mount Pinatubo, Philippines, and Bingham Canyon, Utah, USA. *Mineralium Deposita 36*, 799–806.

Haughton, D. R., Roeder, P. L., & Skinner, B. J. (1974). Solubility of Sulfur in Mafic Magmas. *Economic Geology, 69*, 451–467.

Hildreth, W., & Moorbath, S. (1988). Crustal contributions to arc magmatism in the Andes of Central Chile. *Contributions to Mineralogy and Petrology, 98*, 455–489.

Hofmann, A. W. (1988). Chemical differentiation of the Earth: the relationship between mantle, continental crust, and oceanic crust. *Earth and Planetary Science Letters, 90*, 297–314.

Ishihara, S., & Sasaki, A. (1989). Sulfur isotopic ratios of the magnetite-series and ilmenite-series granitoids of the Sierra Nevada batholith—A reconnaissance study. *Geology, 17*, 788–791.

Jégo, S., & Pichavant, M. (2012). Gold solubility in arc magmas: Experimental determination of the effect of sulfur at 1000 °C and 0.4 GPa. *Geochimica et Cosmochimica Acta, 84*, 560–592.

Jenner, F. E., O'Neill, H. S. C., Arculus, R. J., & Mavrogenes, J. A. (2010). The Magnetite Crisis in the Evolution of Arc-related Magmas and the Initial Concentration of Au, Ag and Cu. *Journal of Petrology, 51*, 2445–2464.

Jenner, F. E. (2017). Cumulate causes for the low contents of sulfide-loving elements in the continental crust. *Nature Geoscience, 10*, 524-529.

Jochum, K. P., Weis, U., Schwager, B., Stoll, B., Wilson, S. A., Haug, G. H., … Enzweiler, J. (2016). Reference Values Following ISO Guidelines for Frequently Requested Rock Reference Materials. *Geostandards and Geoanalytical Research, 40*, 333–350.

Jugo, P., Luth, R., and Richards, J., (2005a). An experimental study of the sulfur content in basaltic melts saturated with immiscible sulfide or sulfate liquids at 1300 °C and 1.0 GPa. *Journal of Petrology, 46*, 783–798.

Jugo, P. J. (2009). Sulfur content at sulfide saturation in oxidized magmas. *Geology, 37*, 415–418.

Juhlin, C., Elming, S.-Å., Mellqvist, C., Öhlander, B., Weihed, P., & Wikström, A. (2002). Crustal reflectivity near the Archaean-Proterozoic boundary in northern Sweden and implications for the tectonic evolution of the area. *Geophysical Journal International, 150*, 180–197.

Kathol, B., Persson, P.O. (1997). U–Pb zircon dating of the Antak granite, northeastern Västerbotten County, northern Sweden. In: Lundqvist, T. (Ed.), Radiometric Dating Results 3: *Sveriges geologiska undersökning, C830*, 6–13.

Kathol, B., Bergman, S. & Persson, P.-O. (2002). Early Svecokarelian deformation and metamorphism in the Skellefte District and surrounding areas. *Sveriges geologiska undersökning, Rapport 2002, 29*, 10–11.

Kathol, B., Weihed, P., (2005). Description of regional geological and geophysical maps of the Skellefte District and surrounding areas. *Sveriges geologiska undersökning: Geological Survey of Sweden, Ba 57*, 1-202.

Kathol, B., Weihed, P., Antal Lundin, I., Bark, G., Bergman Weihed, J., Bergström, U., Billström, K., Björk, L., Claesson, L., Daniels, J., Eliasson, T., Frumerie, M., Kero, L., Kumpulainen, R.A., Lundström, H., Lundström, I., Mellqvist, C., Petersson, J., Skiöld, T., Sträng, T., Stølen, L.-K., Söderman, J., Triumf, C.-A., Wikström, A., Wikström, T., Årebäck, H. (2005). Regional geological and geophysical maps of the Skellefte district and surrounding areas. Bedrock Map, *Sveriges Geologiska Undersökning, Ba 57,* 1-202

Keays, R. R. (1995). The role of komatiite and picritic magmatism and S-saturation in the formation of ore deposits. *Lithos 34*, 1-18.

Keays, R. R., and Lightfoot, P. C., 2010, Crustal sulfur is required to form magmatic Ni-Cu sulfide deposits: Evidence form chalcophile element signatures of Siberian and Deccan Trap basalts. *Mineralium Deposita, 45*, 241–257.

Keith, M., Haase, K. M., Klemd, R., Schwarz-Schampera, U., & Franke, H. (2017). Systematic variations in magmatic sulphide chemistry from mid-ocean ridges, back-arc basins and island arcs. *Chemical Geology, 451*, 67–77.

Kelley, K. A., & Cottrell, E. (2009). Water and the Oxidation State of Subduction Zone Magmas. *Science, 325*, 605–607.

Kelley, K. A., & Cottrell, E. (2012). The influence of magmatic differentiation on the oxidation state of Fe in a basaltic arc magma. *Earth and Planetary Science Letters, 329–330,* 109–121.

Koistinen, T., Stephens, M. B., Bogatchev, V., Nordgulen, Ø., Wennerström, M. , Korhonen, J. (2001). Geological map of the Fennoscandian Shield, scale 1:2 000 000. Espoo: Trondheim: Uppsala: R. Lahtinen et al. / *Lithos 262* (2016) 507–525 523 Moscow: Geological Survey of Finland: Geological Survey of Norway: Geological Survey of Sweden: Ministry of Natural Resources of Russia.

Komar, P. D. (1972). Flow Differentiation in Igneous Dikes and Sills: Profiles of Velocity and Phenocryst Concentration. *Geological Society of America Bulletin, 83*, 3443–3448.

Korja, A., Lahtinen, R., & Nironen, M. (2006). The Svecofennian orogen: a collage of microcontinents and island arcs. *Geological Society, London, Memoirs, 32*, 561–578.

Labidi, J., Cartigny, P., Birck, J. L., Assayag, N., & Bourrand, J. J. (2012). Determination of multiple sulfur isotopes in glasses: A reappraisal of the MORB $\delta^{34}S$. *Chemical Geology, 334*, 189–198.

Labidi, J., Cartigny, P., & Jackson, M. G. (2015). Multiple sulfur isotope composition of oxidized Samoan melts and the implications of a sulfur isotope 'mantle array' in chemical geodynamics. *Earth and Planetary Science Letters, 417*, 28–39.

Lahtinen, R., Korja, A., Nironen, M. (2005). Paleoproterozoic tectonic evolution. *In:* Lehtinen, M., Nurmi, P.A., Rämö, O.T. (Eds.), Precambrian Geology of Finland—Key to the Evolution of the Fennoscandian Shield. *Elsevier Science*, *B.V., Amsterdam*, 481– 532.

Lanari, P., Vidal, O., De Andrade, V., Dubacq, B., Lewin, E., Grosch, E. G., & Schwartz, S. (2014). XMapTools: A MATLAB©-based program for electron microprobe X-ray image processing and geothermobarometry. *Computers & Geosciences, 62*, 227–240.

Landi, P., Métrich, N., Bertagnini, A., & Rosi, M. (2004). Dynamics of magma mixing and degassing recorded in plagioclase at Stromboli (Aeolian Archipelago, Italy). *Contributions to Mineralogy and Petrology, 147*, 213–227.

Latypov, R. M. (2003). The Origin of Basic–Ultrabasic Sills with S-, D-, and I-shaped Compositional Profiles by in Situ Crystallization of a Single Input of Phenocryst-poor Parental Magma. *Journal of Petrology, 44*, 1619–1656.

Lee, C.-T. A., Luffi, P., Chin, E. J., Bouchet, R., Dasgupta, R., Morton, D. M., Le Roux, V., Yin, Q.-Z., Jin, D. (2012). Copper systematics in arc magmas and implications for Crust-Mantle differentiation. *Science, 336*, 64–68.

Le Vaillant, M., Barnes, S. J., Fiorentini, M. L., Santaguida, F., & Törmänen, T. (2016). Effects of hydrous alteration on the distribution of base metals and platinum group elements within the Kevitsa magmatic nickel sulphide deposit. *Ore Geology Reviews*, *72*, 128–148.

Lesher, C. M., and Groves, D. I. (1986). Controls on the formation of komatiite-associated Nickel-copper sulfide deposits, *in* Friedrich, G. H., ed., *Geology and metallogeny of copper deposits: Berlin, Springer-Verlag*, 43–62.

Lesher, C. M., Arndt, N. T. (1995). REE and Nd isotope geochemistry, petrogenesis and volcanic evolution of contaminated komatiites at Kambalda, Western Austrlalia. *Lithos 34*, 127–158.

Lesher, C. M. & Keays, R. R. (2002). Komatiite-associated Ni-Cu-PGE deposits. Canadian Inst. Mining, *Metallurgy Petroleum, Spec. Vol. 54*, 579–617.

Li C., Naldrett A. J. (1993). Sulfide capacity of magma: a quantitative model and its application to the formation of sulfide ores at Sudbury Ontario. *Economic Geology, 88,* 1253-1260

Li, C., Maier, W. D., & Waal, S. A. de. (2001). The Role of Magma Mixing in the Genesis of PGE Mineralization in the Bushveld Complex: Thermodynamic Calculations and New Interpretations. *Economic Geology, 96*, 653–662.

Li, C., Ripley, E. M. (2005). Empirical equations to predict the sulfur content of mafic magmas at sulfide saturation and applications to magmatic sulfide deposits. *Mineralium Deposita, 40,* 218-230.

Li, C., Ripley, E. M. & Naldrett, A. J. (2009). A new genetic model for the giant Ni-Cu-PGE sulfide deposits associated with the Siberian flood basalts. *Economic Geology 104*, 291-301.

Li, Y., & Audétat, A. (2012). Partitioning of V, Mn, Co, Ni, Cu, Zn, As, Mo, Ag, Sn, Sb, W, Au, Pb, and Bi between sulfide phases and hydrous basanite melt at upper mantle conditions. *Earth and Planetary Science Letters, 355–356*, 327–340.

Li, Y., & Audétat, A. (2013). Gold solubility and partitioning between sulfide liquid, monosulfide solid solution and hydrous mantle melts: Implications for the formation of Au-rich magmas and crust–mantle differentiation. *Geochimica & Cosmochimica Acta, 118*, 247–262.

Lightfoot, P. C., & Keays, R. R. (2005). Siderophile and Chalcophile Metal Variations in Flood Basalts from the Siberian Trap, Noril'sk Region: Implications for the Origin of the Ni-Cu-PGE Sulfide Ores. *Economic Geology, 100*, 439–462.

Lightfoot, P. C., Keays, R. R., Evans-Lamswood, D., & Wheeler, R. (2012). S saturation history of Nain Plutonic Suite mafic intrusions: origin of the Voisey's Bay Ni–Cu–Co sulfide deposit, Labrador, Canada. *Mineralium Deposita, 47*, 23–50.

Lilljequist, R., and Svenson, S-Å (1974). Exceptionally well preserved Precambrian ignimbrites and basic lavas in N. Sweden. *Geologiska Föreningens i Stockholm Förhandlingar. 96,* 221-229.

Longpré, M.-A., Stix, J., Klügel, A., & Shimizu, N. (2017). Mantle to surface degassing of carbon- and sulphur-rich alkaline magma at El Hierro, Canary Islands. *Earth and Planetary Science Letters, 460,* 268–280.

Lorand, J. P., (1993). Comment on "Content and isotopic composition of Sulphur in ultramafic xenoliths from central Asia" by D. A. Ionov, J. Hoefs, K. H. Wedepohl and U. Wiechert. Discussion: *Earth and Planetary Science Letters*, *119*, 627–634.

Luhr, J. F., (1990). Experimental phase relations of water-saturated and sulfur-saturated arc magmas and the 1982 eruptions of El Chichon volcano. *Journal of Petrology, 31*, 1071–1114.

Luhr, J. F., & Logan, M. A. V. (2002). Sulfur isotope systematics of the 1982 El Chichón trachyandesite: an ion microprobe study. *Geochimica et Cosmochimica Acta, 66*, 3303–3316.

Lundberg, B. (1980). Aspects of the geology of the Skellefte field, northern Sweden. *Geologiska Föreningens i Stockholm Förhandlingar, 102,* 156–166.

Lundqvist, T., Vaasjoki, M., & Persson, P.-O. (1998). U-Pb ages of plutonic and volcanic rocks in the Svecofennian Bothnian Basin, central Sweden, and their implications for the Palaeoproterozoic evolution of the Basin. *GFF, 120*, 357–363.

Lundström, I., Vaasjoki, M.,Bergström, U., Antal, I., Strandman, F., Lundström, I., Vaasjoki, M., Bergström,U., Antal, I., Strandman, F. (1997). Radiometric age determinations of plutonic rocks in the Boliden area: the Hobergsliden granite and the Stavaträsk diorite. *In:* Lundqvist, T. (Ed.), Radiometric Dating Results 3: *Sveriges geologiska undersökning, C830*, 20–30.

Lundström, I., Persson, P.-O., Bergström, U. (1999). Indications of early deformational events in the northeast part of the Skellefte field. Indirect evidence from geologic and radiometric data from the Stavaträsk-Klintån area, Boliden map-sheet. *In:* Bergman, S. (Ed.), Radiometric Dating Results 4: *Sveriges geologiska undersökning, C831*, 52–69.

Maier, W. D., Li, C., & Waal, S. A. D. (2001). Why are there no major Ni-Cu sulfide deposits in large layered intrusions? *The Canadian Mineralogist, 39*, 547–556.

Maier, W. D., Barnes, S.-J., Gartz, V., & Andrews, G. (2003). Pt-Pd reefs in magnetitites of the Stella layered intrusion, South Africa: A world of new exploration opportunities for platinum group elements. *Geology, 31*, 885–888.

Maier, W. D. (2005). Platinum-group element (PGE) deposits and occurrences: Mineralization styles, genetic concepts, and exploration criteria. *Journal of African Earth Sciences, 41*, 165–191.

Makkonen, H. V., Huhma, H. (2007). Sm–Nd data for mafic-ultramafic intrusions in the Svecofennian (1.88 Ga) Kotalahti Nickel Belt, Finland—implications for crustal contamination at the Archaean/Proterozoic boundary. *Geological Survey of Finland Bulletin*, *79*, 175–201.

Makkonen, H. V., Halkoaho, T., Konnunaho, J., Rasilainen, K., Kontinen, A., & Eilu, P. (2017). Ni-(Cu-PGE) deposits in Finland – geology and exploration potential. *Ore Geology Reviews*. (In press)

Mao, J. W., Pirajno, F., Zhang, Z. H., Chai, F. M., Wu, H., Chen, S. P., … Zhang, C. Q. (2008). A review of the Cu–Ni sulphide deposits in the Chinese Tianshan and Altay orogens (Xinjiang Autonomous Region, NW China): Principal characteristics and ore-forming processes. *Journal of Asian Earth Sciences*, *32*, 184–203.

Martinsson, E. (1996). Geochemistry and petrogenesis of the Palaeoproterozoic, nickel–copper bearing Lainijaur intrusion, northern Sweden. *GFF* 118, 97-109.

Martinsson, E. (1987*a).* Lainijaur intrusionens geokemi. *Licentiate uppsats 1987:05L, Luleå University, Sweden*, 80.

Mathez, E. A. (1976). Sulfur solubility and magmatic sulfides in submarine basalt glass. *Journal of Geophysical Research, 81*, 4269–4276.

Mathez, E. A. (1984). Influence of degassing on oxidation states of basaltic magmas, *Nature, 310*, 371-375.

Matsui, Y., Onuma, N., Nagasawa, H., Higuchi, H. and Banno, S. (1977). Crystal structure control in trace element partition between crystal and magma. *Tectonics 100*, 315-324.

Matzen, A. K., Baker, M. B., Beckett, J. R., & Stolper, E. M. (2013). The Temperature and Pressure Dependence of Nickel Partitioning between Olivine and Silicate Melt. *Journal of Petrology, 54*, 2521–2545.

Mavrogenes, J. A., O'Neill, H. S. C. (1999). The relative effects of pressure temperature and oxygen fugacity on the solubility of sulfide in mafic magmas. *Geochimica et Cosmochimica Acta, 63*, 1173-1180

McDonough, W. F., & Sun, S. -s. (1995). The composition of the Earth. *Chemical Geology, 120*, 223–253.

McKenzie, D. and O'Nions, R. K. (1991). Partial melt distributions from inversion of rare Earth element concentrations. *Journal of Petrology, 32*, 1021-1091.

Métrich, N., Bertagnini, A., Landi, P., & Rosi, M. (2001). Crystallization Driven by Decompression and Water Loss at Stromboli Volcano (Aeolian Islands, Italy). *Journal of Petrology, 42*, 1471–1490.

Montelius, C. (2005). The genetic relationship between rhyolitic volcanism and Zn-Cu-Au deposits in the Maurliden volcanic centre, Skellefte district, Sweden : volcanic facies, lithogeochemistry and geochronology (Doctoral Thesis) (p. 135). Luleå: Luleå University of Technology.

Mungall, J., & Su, S. (2005). Interfacial tension between magmatic sulfide and silicate liquids: Constraints on kinetics of sulfide liquation and sulfide migration through silicate rocks. *Earth and Planetary Science Letters, 234*, 135–149.

Mungall, J. E., Harvey, J. D., Balch, S. J., Azar, B., Atkinson, J., and Hamilton, M. A., (2010). Eagle's Nest: A magmatic Ni-sulfide deposit in the James Bay Lowlands, Ontario, Canada. *Society of Economic Geologists Special Publication, 15*, 539–557.

Naldrett, A. J., (1969). A portion of the system Fe-S-O between 900 and 1080°C and its application to sulfide ore magmas. *Journal of Petrology, 10*, 171–201.

Naldrett, A. J. (1973). Nickel sulphide deposits: their classification and genesis, with special emphasis on deposits of volcanic association. *Canadian Institute of Mining and Metallurgy Bulletin, 66,* 45-63.

Naldrett, A. J. (1992). A model for the Ni-Cu-PGE ores of the Noril'sk region and its application to other areas of flood basalt. *Economic Geology, 87*, 1945–1962.

Naldrett A. J., Fedorenko V. A., Lightfoot P. C., Kunilov V.E., Gorbachev N.S., Doherty W., Johan J. (1995). Ni-Cu-PGE deposits of the Noril'sk region Siberia: Their formation in conduits for flood basalt volcanism. *Trans. lost Min. Met., 104*, B18-B36.

Naldrett, A. J. (1996). Ni-Cu-PGE deposits of the Noril'sk region and other world-class nickel sulfide deposits. Trans. Inst. Mining Metall.

Naldrett, A. J., Fedorenko, V. A., Asif, M., Lin, S., Kunilov, V. E., Stekhin, A. I., ... Gorbachev, N. S. (1996). Controls on the composition of Ni-Cu sulfide deposits as illustrated by those at Noril9sk, Siberia. *Economic Geology, 91*, 751–773.

Naldrett, A. J. (2004). Magmatic Sulfide Deposits: Geology, Geochemistry and Exploration. *Heidelberg, Berlin: Springer Verlag. 723 pp.*

Namur, O., Charlier, B., Pirard, C., Hermann, J., Liégeois, J.-P., & Auwera, J. V. (2011). Anorthosite formation by plagioclase flotation in ferrobasalt and implications for the lunar crust. *Geochimica et Cosmochimica Acta, 75*, 4998–5018.

Nielsen, R. L., Gallahan, W. E., & Newberger, F. (1992). Experimentally determined mineral-melt partition coefficients for Sc, Y and REE for olivine, orthopyroxene, pigeonite, magnetite and ilmenite. *Contributions to Mineralogy and Petrology, 110*, 488–499.

Nielsen, T. F. D., Andersen, J. C. Ø., Holness, M. B., Keiding, J. K., Rudashevsky, N. S., Rudashevsky, V. N., ... Veksler, I. V. (2015). The Skaergaard PGE and Gold Deposit: the Result of in situ Fractionation, Sulphide Saturation, and Magma Chamber-scale Precious Metal Redistribution by Immiscible Fe-rich Melt. *Journal of Petrology, 56*, 1643–1676.

Nilsson, G. (1985). Nickel-copper deposits in Sweden. *Geological Survey of Finland, Bulletin 333*, 316-362.

Nironen, M. (1997). The Svecofennian Orogen: a tectonic model. *Precambrian Research, 86*, 21-44.

Öhlander, B., Skiöld, T., Hamilton, P. J., & Claesson, L.-Å. (1987). The western border of the Archaean province of the Baltic shield: evidence from northern Sweden. *Contributions to Mineralogy and Petrology, 95*, 437–450.

Öhlander, B., Skiöld, T., Elming, S.-Å., Claesson, S., & Nisca, D. H. (1993). Delineation and character of the Archaean-Proterozoic boundary in northern Sweden. *Precambrian Research, 64*, 67–84.

O'Neill, H. S. C. & Mavrogenes, J. A. (2002). The sulfide capacity and sulfur content at sulfide saturation of silicate melts at 1400°C and 1 bar*. Journal of Petrology, 43*, 1049–1087.

Ortega, L., Lunar, R., García-Palomero, F., Moreno, T., Martín-Estévez, J. R., Prichard, H. M., & Fisher, P. C. (2004). The aguablanca Ni–Cu–PGE deposit, southwestern iberia: magmatic ore-forming processes and retrograde evolution. *The Canadian Mineralogist, 42*, 325–350.

Papike, J. J., Karner, J. M., Shearer, C., K. (2004). Comparative planetary mineralogy: V/(Cr+Al) systematics in chromite as an indicator of relative oxygen fugacity. *American Mineralogist, 89*, 1557-1560.

Papunen, H., Gorbunov G.I. (eds) (1985). Nickel-copper deposits of the Baltic Shield and Scandinavian Caledonides. *Geological Survey of Finland Bulletin,* 333-394.

Park, J.-W., Campbell, I. H., Kim, J., & Moon, J.-W. (2015). The Role of Late Sulfide Saturation in the Formation of a Cu- and Au-rich Magma: Insights from the Platinum Group Element Geochemistry of Niuatahi–Motutahi Lavas, Tonga Rear Arc. *Journal of Petrology, 56*, 59–81.

Patchett, P., & Arndt, N. T. (1986). Nd isotopes and tectonics of 1.9-1.7 Ga crustal genesis. *Earth and Planetary Science Letters, 78*, 329–338.

Paulick, H., Nylander, J., (2010). Cu-Ni-Au mineralization in the Älgliden Gabbro Dike – results of the 2009 drilling campaign. *Exploration report, GP 2010-17,* 32.

Paulick, H., Nordfeldt, E., Mattson, B. (2012). Cu-Ni-Au mineralization in the Älgliden Gabbro Dike –results of the 2010/2011 drilling campaign. *Exploration report, GP 2012-18,* 30.

Pearce, J. A., & Cann, J. R. (1973). Tectonic setting of basic volcanic rocks determined using trace element analyses. *Earth and Planetary Science Letters, 19*, 290–300.

Pearce, J. A., Harris, N. B. W., & Tindle, A. G. (1984). Trace Element Discrimination Diagrams for the Tectonic Interpretation of Granitic Rocks. *Journal of Petrology, 25*, 956–983.

Peltonen P. (1995). Mafma-country rock interaction and the genesis of Ni-Cu deposits in the Vammala Nickel Belt, SW Finland. *Mineralogy and Petrology, 52,* 1—24.

Perfit, M. R., Gust, D. A., Bence, A. E., Arculus, R. J., & Taylor, S. R. (1980). Chemical characteristics of island-arc basalts: Implications for mantle sources. *Chemical Geology, 30*, 227–256.

Piña, R., Gervilla, F., Barnes, S.-J., Ortega, L., & Lunar, R. (2013). Platinum-group elements-bearing pyrite from the Aguablanca Ni-Cu sulphide deposit (SW Spain): a LA-ICP-MS study. *European Journal of Mineralogy, 25*, 241–252.

Plank, T., Kelley, K. A., Zimmer, M. M., Hauri, E. H., & Wallace, P. J. (2013). Why do mafic arc magmas contain ~4 wt% water on average? *Earth and Planetary Science Letters, 364*, 168–179.

Rasmussen, T. M., Roberts, R. G., & Pedersen, L. B. (1987). Magnetotellurics along the Fennoscandian Long Range profile. *Geophysical Journal International, 89*, 799–820.

Richards, J. P. (2003). Tectono-Magmatic Precursors for Porphyry Cu-(Mo-Au) Deposit Formation. *Economic Geology, 98*, 1515–1533.

Richards, J. P. (2009). Postsubduction porphyry Cu-Au and epithermal Au deposits: Products of remelting of subduction-modified lithosphere. *Geology, 37*, 247–250.

Rickard, D. T., & Zweifel, H. (1975). Genesis of Precambrian sulfide ores, Skellefte District, Sweden. *Economic Geology, 70*, 255–274.

Rickard, D. T., Zweifel, H., & Donnelly, T. H. (1979). Sulfur isotope systematics in the Aasen pyrite-barite deposits, Skellefte District, Sweden. *Economic Geology, 74*, 1060–1068.

Rickard, D. T. (1986). The Skellefte field. *Sveriges Geolgiska Underskning, Series Ca, 62,* 1-54

Ripley, E. M., & Li, C. (2003). Sulfur isotope exchange and metal enrichment in the formation of magmatic Cu-Ni-(PGE) deposits. *Economic Geology, 98*, 635–641.

Ripley, M. E., & Li, C. (2011). A Review of Conduit-Related Ni-Cu-(PGE) Sulfide Mineralization at the Voisey's Bay Deposit, Labrador, and the Eagle Deposit, Northern Michigan. *Society of Economic Geologists, 17,* 181–197.

Ripley, E. M., & Li, C. (2013). Sulfide Saturation in Mafic Magmas: Is External Sulfur Required for Magmatic Ni-Cu-(PGE) Ore Genesis? *Economic Geology, 108,* 45–58.

Robertson, J., Ripley, E. M., Barnes, S. J., & Li, C. (2015). Sulfur Liberation from Country Rocks and Incorporation in Mafic Magmas. *Economic Geology, 110*, 1111–1123.

Roeder, P. L., & Emslie, R. F. (1970). Olivine-liquid equilibrium. *Contributions to Mineralogy and Petrology, 29*, 275–289.

Roeder, P., Gofton, E., & Thornber, C. (2006). Cotectic Proportions of Olivine and Spinel in Olivine-Tholeiitic Basalt and Evaluation of Pre-Eruptive Processes. *Journal of Petrology, 47,* 883–900.

Rose, L. A., & Brenan, J. M. (2001). Wetting Properties of Fe-Ni-Co-Cu-O-S Melts against Olivine: Implications for Sulfide Melt Mobility. *Economic Geology, 96*, 145–157.

Rudnick, R. L., & Gao, S. (2003). 3.01 - Composition of the Continental Crust. In H. D. H. K. Turekian (Ed.), Treatise on Geochemistry (pp. 1–64). *Oxford: Pergamon*.

Ruscitto, D. M., Wallace, P. J., Johnson, E. R., Kent, A. J. R., & Bindeman, I. N. (2010). Volatile contents of mafic magmas from cinder cones in the Central Oregon High Cascades: Implications for magma formation and mantle conditions in a hot arc. *Earth and Planetary Science Letters*, *298*, 153–161.

Rutland, R. W. R., Kero, L., Nilsson, G., & Stølen, L. K. (2001). Nature of a major tectonic discontinuity in the Svecofennian province of northern Sweden. *Precambrian Research, 112*, 211–237.

Sakai, H., Casadevall, T. J., & Moore, J. G. (1982). Chemistry and isotope ratios of sulfur in basalts and volcanic gases at Kilauea volcano, Hawaii. *Geochimica et Cosmochimica Acta, 46*, 729–738.

Sakai, H., Marais, D. J. D., Ueda, A., & Moore, J. G. (1984). Concentrations and isotope ratios of carbon, nitrogen and sulfur in ocean-floor basalts. *Geochimica et Cosmochimica Acta, 48*, 2433–2441.

Saumur, B. M., Cruden, A. R., & Boutelier, D. (2015). Sulfide Liquid Entrainment by Silicate Magma: Implications for the Dynamics and Petrogenesis of Magmatic Sulfide Deposits. *Journal of Petrology, 56*, 2473–2490.

Saumur, B. M., & Cruden, A. R. (2017). Ingress Of Magmatic Ni-Cu Sulphide Liquid Into Surrounding Brittle Rocks: Physical & Structural Controls. *Ore Geology Reviews.*

Schulz, K. J., Chandler, V. W., Nicholson, S. W., Piatak, Nadine, Seall, II, R. R., Woodruff, L. G., and Zientek, M. L. (2010), Magmatic sulfide-rich nickel-copper deposits related to picrite and (or) tholeiitic basalt dike-sill complexes—A preliminary deposit model. *U.S. Geological Survey Open-File Report 2010*, 1179, 25.

Scoates, J. S., Lindsley, D. H., & Frost, B. R. (2010). Magmatic and Structural Evolution of an Anorthositic Magma Chamber: The Poe Mountain Intrusion, Laramie Anorthosite Complex, Wyoming. *The Canadian Mineralogist, 48*, 851–885.

Seat, Z., Beresford, S. W., Grguric, B. A., Waugh, R. S., Hronsky, J. M. A., Gee, M. A. M., … Mathison, C. I. (2007). Architecture and emplacement of the Nebo–Babel gabbronorite-hosted magmatic Ni–Cu–PGE sulphide deposit, West Musgrave, Western Australia. *Mineralium Deposita, 42*, 551–581.

Shima, H. & Naldrett, A. J. (1975). Solubility of sulfur in an ultramafic melt and the relevance of the system Fe–S–O. *Economic Geology, 70*, 960–967.

Simura, R., & Ozawa, K. (2006). Mechanism of Crystal Redistribution in a Sheet-like Magma Body: Constraints from the Nosappumisaki and Other Shoshonite Intrusions in the Nemuro Peninsula, Northern Japan. *Journal of Petrology, 47*, 1809–1851.

Skiöld, T. (1988). Implications of new U□Pb zircon chronology to early proterozoic crustal accretion in northern Sweden. *Precambrian Research, 38*, 147–164.

Skiöld, T., Öhlander, B., Markkula, H., Widenfalk, L., & Claesson, L.-Å. (1993). Chronology of Proterozoic orogenic processes at the Archaean continental margin in northern Sweden. *Precambrian Research, 64*, 225–238.

Skyttä, P., Hermansson, T., Andersson, J., Whitehouse, M., & Weihed, P. (2011). New zircon data supporting models of short-lived igneous activity at 1.89 Ga in the western Skellefte District, central Fennoscandian Shield. *Solid Earth, 2*, 205–217.

Skyttä, P., Bauer, T. E., Tavakoli, S., Hermansson, T., Andersson, J., & Weihed, P. (2012). Pre-1.87Ga development of crustal domains overprinted by 1.87Ga transpression in the Palaeoproterozoic Skellefte district, Sweden. *Precambrian Research*, *206–207*, 109–136.

Sobolev, A. V., Hofmann, A. W., Sobolev, S. V., & Nikogosian, I. K. (2005). An olivine-free mantle source of Hawaiian shield basalts. *Nature, 434*, 590–597.

Sobolev, A. V., Hofmann, A. W., Kuzmin, D. V., Yaxley, G. M., Arndt, N. T., Chung, S.-L., … others. (2007). The amount of recycled crust in sources of mantle-derived melts. *Science, 316*, 412–417.

Staude, S., Barnes, S. J., & Vaillant, M. L. (2016). Evidence of lateral thermomechanical erosion of basalt by Fe-Ni-Cu sulfide melt at Kambalda, Western Australia. *Geology, 44*, 1047–1050.

Staude, S., Barnes, S. J., & Le Vaillant, M. (2017). Thermomechanical erosion of ore-hosting embayments beneath komatiite lava channels: Textural evidence from Kambalda, Western Australia. *Ore Geology Reviews.*

Streckeisen, A. (1976). To each plutonic rock its proper name. *Earth-Science Reviews, 12*, 1–33.

Sun, H. (2009). Ore-Forming Mechanism in Conduit System and Ore-Bearing Property Evaluation for Mafic-Ultramafic Complex in Eastern Tianshan, Xinjiang: [Dissertation]. Institute of Geology and Geophysics, Chinese Academy of Sciences, Beijing (in Chinese with English Abstract).

Tatsumi, Y., Hamilton, D. L., & Nesbitt, R. W. (1986). Chemical characteristics of fluid phase released from a subducted lithosphere and origin of arc magmas: Evidence from high-pressure experiments and natural rocks. *Journal of Volcanology and Geothermal Research, 29*, 293–309.

Thériault, R. D., Barnes, S.-J., & Severson, M. J. (2000). Origin of Cu-Ni-PGE Sulfide Mineralization in the Partridge River Intrusion, Duluth Complex, Minnesota. Economic *Geology, 95*, 929–943.

Tornos, F., Casquet, C., Galindo, C., Velasco, F. & Canales, A. (2001). A new style of Ni–Cu mineralization related to magmatic breccia pipes in a transpressional magmatic arc, Aguablanca, Spain. *Mineralium Deposita 36*, 700-706.

Ueda, A., & Sakai, H. (1984). Sulfur isotope study of Quaternary volcanic rocks from the Japanese Islands Arc. *Geochimica et Cosmochimica Acta, 48*, 1837–1848.

Villemant, B. (1988). Trace element evolution in the Phlegrean Fields (Central Italy): fractional crystallization and selective enrichment. *Contributions to Mineralogy and Petrology, 98*, 169–183.

Vivallo, W. (1987). Early Proterozoic bimodal volcanism, hydrothermal activity, and massive sulfide deposition in the Boliden-Langdal area, Skellefte District, Sweden. *Economic Geology, 82*, 440–456.

Vivallo, W., & Claesson, L.-Å. (1987). Intra-Arc Rifting and Massive Sulphide Mineralization in an Early Proterozoic Volcanic Arc, Skellefte District, Northern Sweden. *Geological Society, London, Special Publications, 33*, 69–79.

Vukmanovic, Z., Barnes, S. J., Reddy, S. M., Godel, B., & Fiorentini, M. L. (2012). Morphology and microstructure of chromite crystals in chromitites from the Merensky Reef (Bushveld Complex, South Africa). *Contributions to Mineralogy and Petrology, 165*, 1031–1050.

Wager, L. R., Brown, G. M., & Wadsworth, W. J. (1960). Types of Igneous Cumulates. *Journal of Petrology, 1*, 73–85.

Wallace, P. J. (2005). Volatiles in subduction zone magmas: concentrations and fluxes based on melt inclusion and volcanic gas data. *Journal of Volcanology and Geothermal Research, 140*, 217–240.

Wang, M., Guo, X., Michalak, P. P., Xia, Q., Xiao, F., Wang, W., & Liu, K. (2015). Origin of the Tudun Cu–Ni sulfide deposit in the eastern Tianshan, NW China: Constraints on the geochemistry of platinum group elements. *Ore Geology Reviews, 64,* 445–454.

Weihed, P. (1992a). Geology and genesis of the Early Proterozoic Tallberg porphyry-type deposit, Skellefte district, northern Sweden. PhD thesis, University of Gothenburg.

Weihed, P. (1992b). Lithogeochemistry, Metal and Alteration Zoning in the Proterozoic Tallberg Porphyry-Type Deposit, Northern Sweden. *Journal of Geochemical Exploration 42*, 301-325.

Weihed, P., Bergman, J., & Bergström, U. (1992). Metallogeny and tectonic evolution of the Early Proterozoic Skellefte district, northern Sweden. *Precambrian Research, 58*, 143–167.

Weihed, P., Vaasjoki, M. (1993). Regional implications of an age determination of a gneissose granitoid south of the Skellefte district, northern Sweden. *Geologiska Föreningens i Stockholm Förhandlingar, 115*, 189–191.

Weihed, P., & Fallick, A. E. (1994). A stable isotope study of the Palaeoproterozoic Tallberg porphyry-type deposit, northern Sweden. *Mineralium Deposita, 29*, 128–138.

Weihed, P., Billström, K., Persson, P.-O., Bergman Weihed, J. (2002). Relationship between 1.90–1.85 Ga accretionary processes and 1. 82–1.80 Ga oblique subduction at the Karelian craton margin, Fennoscandian Shield. *GFF 124,* 163–180.

Weihed, P., Arndt, N., Billström, K., Duchesne, J.-C., Eilu, P., Martinsson, O., … Lahtinen, R. (2005). 8: Precambrian geodynamics and ore formation: The Fennoscandian Shield. *Ore Geology Reviews, 27*, 273–322.

Welin, E. (1987). The depositional evolution of the Svecofennian supracrustal sequence in Finland and Sweden. *Precambrian Research, 35*, 95–113.

Wendlandt, R. F. (1982). Sulfide saturation of basalt and andesite melts at high pressures and temperatures, *American Mineralogist, 67*, 877-885.

Wilson, M. R., Hamilton, P. J., Fallick, A. E., Aftalion, M., & Michard, A. (1985). Granites and early Proterozoic crustal evolution in Sweden: evidence from SmNd, UPb and O isotope systematics. *Earth and Planetary Science Letters, 72*, 376–388.

Wilson, M. R., Sehlstedt, S., Claesson, L.-Å., Smellie, J. A., Aftalion, M., Joseph Hamilton, P., & Fallick, A. E. (1987). Jörn: an early Proterozoic intrusive complex in a volcanic-arc environment, north Sweden. *Precambrian Research, 36*, 201–225.

Wykes, J. L., & Mavrogenes J. A. (2005). Hydrous sulfide melting: experimental evidence for the solubility of H_2O in sulfide melts. *Society of Economic Geologists, 100,* 157-164.

Wykes, J. L., O'Neill, H. C., Mavrogenes, J. A. (2105). The effect of FeO on the sulfur content at sulfide saturation (SCSS) and the selenium content at selenide saturation of silicate melts. *Journal of Petrology, 56*, 1407-1424.

Xiao, Q. H., Qin, K. Z., Tang, D. M., et al. (2010). Xiangshanxi Composite Cu-Ni-Ti-Fe Deposit belongs to Comagmatic Evolution Product: Evidences from Ore Microscopy, Zircon U-Pb Chronology and Petrological Geochemistry, Hami, Xinjiang, NW China. *Acta Petrologica Sinica, 26,* 502–522 (in Chinese with English Abstract).

Yuguchi, T., & Nishiyama, T. (2007). Cooling process of a granitic body deduced from the extents of exsolution and deuteric sub-solidus reactions: Case study of the Okueyama granitic body, Kyushu, Japan. *Lithos, 97*, 395–421.

Yuguchi, T., & Nishiyama, T. (2008). The mechanism of myrmekite formation deduced from steady-diffusion modeling based on petrography: Case study of the Okueyama granitic body, Kyushu, Japan. *Lithos, 106*, 237–260.

Zettergren, A. (2013). Bastutjärn Ni-Cu-Co mineralization (Master's Thesis) (p. 62). Luleå: Luleå University of Technology.

Zweifel, H. (1982). Ore deposition in the Skelleftfe field volcanic activity and depositional environment. *Geologiska Föreningens i Stockholm Förhandlingar, 104,* 369.

Appendix 1 Standard reproducibility and accuracy of electron probe microanalyses

Cr-Augite	Reference values (%)	D.L. (%)	Serie 1 average (N=12)	1 σ	R.A. (%)	R.S.D.	Serie 2 average (N=12)	1 σ	R.A. (%)	R.S.D.	Serie 5 average (N=15)	1 σ	R.A. (%)	R.S.D.	Serie 6 average (N=18)	1 σ	R.A. (%)	R.S.D.	Serie 7 average (N=12)	1 σ	R.A. (%)	R.S.D.
SiO_2	50.94	0.043	50.75	0.20	0.37	0.8	51.05	0.10	0.22	0.4	50.82	0.15	0.24	0.6	50.87	0.14	0.14	0.6	50.85	0.18	0.17	0.7
TiO_2	**0.50**	0.030	0.48	0.02	3.59	8.2	0.49	0.01	1.87	5.7	0.49	0.02	1.31	7.8	0.48	0.02	3.10	6.6	0.49	0.01	1.48	4.3
Al_2O_3	7.43	0.045	7.61	0.06	2.40	1.5	7.67	0.04	3.17	1.1	7.59	0.05	2.21	1.4	7.61	0.06	2.40	1.5	7.63	0.06	2.70	1.5
FeO	**4.70**	0.032	4.55	0.07	3.27	3.1	4.67	0.07	0.65	3.0	4.63	0.04	1.41	1.8	4.62	0.03	1.63	1.5	4.65	0.04	1.06	1.6
MnO	**0.11**	0.040	0.11	0.03	1.74	50.1	0.12	0.02	7.13	38.5	0.13	0.01	19.79	15.1	0.12	0.01	10.17	22.8	0.12	0.02	12.87	30.3
MgO	**17.29**	0.036	17.51	0.06	1.26	0.7	17.48	0.06	1.13	0.6	17.34	0.06	0.30	0.7	17.26	0.08	0.19	0.9	17.29	0.07	0.01	0.8
CaO	**17.33**	0.021	17.05	0.12	1.60	1.4	17.29	0.06	0.23	0.8	17.32	0.07	0.05	0.8	17.29	0.08	0.22	0.9	17.25	0.05	0.45	0.6
Na_2O	0.83	0.041	0.89	0.02	7.54	5.5	0.90	0.02	8.44	4.9	0.88	0.02	6.46	4.9	0.90	0.03	8.64	5.8	0.88	0.03	6.54	7.5
K_2O	0.01	0.022	0.00	0.00	70.83	314.0	0.01	0.01	38.50	240.2	0.00	0.00	61.40	255.3	0.00	0.00	68.17	276.0	0.00	0.00	62.92	217.3
Cr_2O_3	**0.87**	0.040	0.87	0.02	0.07	5.6	0.89	0.02	2.07	4.3	0.87	0.02	0.38	5.2	0.88	0.02	1.24	5.1	0.88	0.01	0.86	3.2

Orthoclase	Reference values (%)	D.L. (%)	Serie 3 average (N=12)	1 σ	R.A. (%)	R.S.D.	Serie 4 average (N=12)	1 σ	R.A. (%)	R.S.D.	Serie 5 average (N=15)	1 σ	R.A. (%)	R.S.D.	Serie 6 average (N=18)	1 σ	R.A. (%)	R.S.D.	Serie 7 average (N=12)	1 σ	R.A. (%)	R.S.D.
SiO_2	**65.04**	0.043	65.44	0.19	0.62	0.6	65.51	0.16	0.72	0.5	64.98	0.18	0.10	0.6	65.11	0.11	0.11	0.4	64.95	0.19	0.14	0.6
Al_2O_3	**18.53**	0.045	18.53	0.08	0.02	0.8	18.57	0.06	0.24	0.7	18.40	0.12	0.68	1.3	18.37	0.09	0.85	1.0	18.38	0.11	0.83	1.2
Na_2O	**1.36**	0.041	1.42	0.03	4.33	4.6	1.42	0.02	4.27	3.4	1.38	0.04	1.43	6.2	1.41	0.05	3.78	7.1	1.40	0.03	3.30	4.8
K_2O	**14.67**	0.022	14.70	0.06	0.23	0.8	14.64	0.06	0.20	0.9	14.74	0.05	0.49	0.7	14.68	0.07	0.09	1.0	14.77	0.05	0.65	0.7

σ: standard deviation; R.A.: relative accuracy (also defined as relative error) R.A. = 100 * $|C_{mes\ avg} - C_{ref}| / C_{ref}$; R.S.D.: relative standard deviation R.S.D= 100 * 2σ / $C_{mes\ avg}$;

D.L.: detection limit; n.a.: not analyzed; n.c.: not calculated

Appendix 1 (cont.)

Olivine	Reference values (%)	D.L. (%)	Serie 1 average (N=6)	1 σ	R.A. (%)	R.S.D.	Serie 2 average (N=6)	1 σ	R.A. (%)	R.S.D.	Serie 4 average (N=9)	1 σ	R.A. (%)	R.S.D.	Serie 5 average (N=6)	1 σ	R.A. (%)	R.S.D.
SiO_2	**40.81**	0.009	41.16	0.07	0.85	0.3	41.07	0.09	0.63	0.4	40.81	0.14	0.01	0.7	40.90	0.02	0.22	0.1
TiO_2	**0.004**	0.002	0.003	0.001	18.75	73.9	0.01	0.01	80.83	209.9	n.a.	n.a.	n.c.	n.c.	0.00	0.00	1.67	103.6
Al_2O_3	**0.033**	0.001	0.033	0.001	0.66	7.0	0.04	0.02	18.74	86.5	n.a.	n.a.	n.c.	n.c.	0.04	0.00	13.23	16.2
FeO	**9.55**	0.003	9.55	0.01	0.02	0.2	9.55	0.08	0.00	1.7	9.59	0.02	0.44	0.4	9.58	0.01	0.35	0.3
MnO	**0.1425**	0.001	0.1442	0.0010	1.17	1.3	0.16	0.02	9.53	23.2	0.14	0.00	0.13	3.2	0.14	0.00	2.39	3.0
MgO	**49.42**	0.006	48.75	0.22	1.36	0.9	49.38	0.06	0.07	0.2	49.17	0.15	0.50	0.6	48.96	0.03	0.92	0.1
CaO	**0.093**	0.001	0.094	0.001	0.75	1.4	0.09	0.01	1.34	18.0	0.08	0.00	15.52	2.5	0.10	0.00	5.13	2.8
Cr_2O_3	**0.0152**	0.002	0.0139	0.0016	8.77	23.7	0.01	0.01	46.16	179.0	n.a.	n.a.	n.c.	n.c.	0.01	0.00	10.64	29.5
NiO	**0.374**	0.002	0.383	0.002	2.38	1.3	0.36	0.03	4.09	17.1	0.37	0.00	0.10	2.0	0.35	0.00	5.63	1.6

Hornblende	Reference values (%)	D.L. (%)	Serie 3 average (N=12)	1 σ	R.A. (%)	R.S.D.	Serie 4 average (N=15)	1 σ	R.A. (%)	R.S.D.
SiO_2	**40.37**	0.043	40.54	0.16	0.42	0.8	40.45	0.21	0.20	1.0
TiO_2	**4.72**	0.03	4.77	0.04	1.12	1.6	4.79	0.06	1.42	2.3
Al_2O_3	14.9	0.045	14.40	0.08	3.37	1.2	14.39	0.11	3.45	1.5
FeO	**10.92**	0.032	10.47	0.15	4.09	2.9	10.42	0.09	4.58	1.7
MnO	0.09	0.04	0.09	0.01	2.75	34.2	0.09	0.02	4.24	45.2
MgO	**12.8**	0.036	12.71	0.21	0.70	3.3	12.88	0.13	0.62	2.0
CaO	**10.3**	0.021	9.93	0.06	3.60	1.2	9.93	0.07	3.64	1.3
Na_2O	2.6	0.041	2.74	0.07	5.45	5.4	2.76	0.05	6.28	3.3
K_2O	2.05	0.022	2.04	0.03	0.41	2.6	2.03	0.03	0.97	2.6

σ: standard deviation; R.A.: relative accuracy (also defined as relative error) R.A. = 100 * $|C_{mes\ avg} - C_{ref}| / C_{ref}$; R.S.D.: relative standard deviation R.S.D= 100 * 2σ / $C_{mes\ avg}$;

D.L.: detection limit; n.a.: not analyzed; n.c.: not calculated

Appendix 1 (cont.)

Cr-Augite	Reference values (%)	Sv8 average (N=9)	1 σ	R.A. (%)	R.S.D.	Serie 9 average (N=6)	1 σ	R.A. (%)	R.S.D.	Serie 10 average (N=12)	1 σ	R.A. (%)	R.S.D.
SiO_2	50.94	50.89	0.12	0.10	0.5	50.73	0.13	0.42	0.5	51.12	0.19	0.35	0.7
TiO_2	**0.50**	0.51	0.01	1.69	5.8	0.49	0.01	1.23	3.9	0.52	0.01	3.35	4.7
Al_2O_3	7.43	7.61	0.08	2.37	2.1	7.62	0.05	2.52	1.2	7.56	0.05	1.78	1.4
FeO	**4.70**	4.66	0.04	0.95	1.9	4.65	0.05	1.15	2.1	4.66	0.05	0.77	2.1
MnO	**0.11**	0.12	0.02	6.55	32.6	0.14	0.01	30.41	16.2	0.12	0.02	13.60	30.2
MgO	**17.29**	17.53	0.08	1.40	0.9	17.54	0.10	1.42	1.1	17.54	0.06	1.42	0.7
CaO	**17.33**	17.26	0.04	0.41	0.4	17.25	0.07	0.48	0.8	17.27	0.05	0.32	0.6
Na_2O	0.83	0.89	0.01	7.81	3.3	0.88	0.03	5.53	7.1	0.90	0.03	8.67	5.8
K_2O	0.01	0.00	0.00	67.22	205.8	0.00	0.00	78.67	222.3	0.00	0.01	56.00	257.4
Cr_2O_3	**0.87**	0.89	0.01	1.96	3.0	0.89	0.02	1.85	4.9	0.89	0.02	2.26	4.3

Orthoclase	Reference values (%)	Serie 8 average (N=9)	1 σ	R.A. (%)	R.S.D.	Serie 9 average (N=6)	1 σ	R.A. (%)	R.S.D.	Serie 10 average (N=10)	1 σ	R.A. (%)	R.S.D.
SiO_2	**65.04**	64.77	0.15	0.41	0.5	65.14	0.20	0.15	0.6	65.53	0.11	0.75	0.3
Al_2O_3	**18.53**	18.24	0.10	1.57	1.1	18.45	0.06	0.45	0.7	18.21	0.10	1.70	1.1
Na_2O	**1.36**	1.40	0.03	2.80	3.7	1.41	0.05	3.66	7.2	1.40	0.03	3.04	4.6
K_2O	**14.67**	14.70	0.06	0.24	0.9	14.74	0.08	0.49	1.1	14.73	0.05	0.43	0.7

σ: standard deviation; R.A.: relative accuracy (also defined as relative error) R.A. = 100 * $|C_{mes\ avg} - C_{ref}| / C_{ref}$; R.S.D.: relative standard deviation R.S.D= 100 * 2σ / $C_{mes\ avg}$; D.L.: detection limit; n.a.: not analyzed; n.c.: not calculated

Appendix 2 Sulfur reproducibility of the S in-house standard.

Sessions		1	2	3	4	5	6	7	8	9	10	11	12	13	14	15	16	17
Reference value	wt.%	2.37	2.36	2.38	2.39	2.35	2.38	2.38	2.42	2.42	2.42	2.42	2.37	2.49	2.51	2.44	2.45	2.48
2.33	% diff	1.62	1.49	2.35	2.42	0.98	2.26	2.31	3.65	4.07	3.85	3.81	1.89	6.79	7.55	4.88	5.02	6.42

in wt%; % diff: relative error

Appendix 3 Sulfur in-house standard analyses performed at SARM (Nancy) and ISTerre (Grenoble) laboratories for accuracy estimation.

Sample name	SARM Nancy (wt.%)	ISTerre Grenoble (wt.%)	% diff
90-M-022-01	2.31	2.38	3.14
90-M-022-02	2.32	2.38	2.79
90-M-022-03	2.32	2.39	2.86
90-M-022-04	2.35	2.38	1.44
90-M-022-05	2.34	2.35	0.55

SARM: Service d'Analyse des Roches at des Minéraux; ISTerre: Institut des Sciences de la Terre; % diff: relative error

Appendix 4 Major element concentrations of duplicates

wt.% oxide	264.196.7	dup	% diff	246.224.6	dup	% diff	246.230.2	dup	% diff
SiO_2	26.91	27.00	0.35	43.95	44.12	0.38	53.38	52.48	1.72
TiO_2	1.03	1.00	2.99	0.53	0.53	0.47	0.55	0.54	1.72
Al_2O_3	24.39	24.53	0.55	7.66	7.64	0.34	13.89	13.81	0.63
Fe_2O_3t	14.84	14.82	0.10	16.67	16.60	0.42	9.07	8.99	0.89
MnO	0.24	0.24	0.43	0.20	0.20	0.22	0.13	0.12	0.47
MgO	21.93	21.82	0.48	22.48	22.36	0.56	6.05	6.02	0.54
CaO	<D.L.	<D.L.	n.c.	3.55	3.51	1.08	5.22	5.18	0.70
Na_2O	0.15	0.16	7.49	1.32	1.31	0.84	4.68	4.68	0.10
K_2O	0.55	0.54	2.15	0.73	0.73	0.37	1.26	1.25	0.97
P_2O_5	0.12	0.12	0.43	0.14	0.13	5.33	0.56	0.56	0.65

D.L.: detection limit; n.c. not calculated; % diff: relative error

Appendix 5 Major element concentrations of standards measured as unknown

wt.% oxide	D.L. (wt.%)	Accuracy (%)	BE-N	BE-N (n=3)	% diff	BHVO-2	BHVO-2 (n=2)	% diff	BR24	BR24 (n=1)	% diff	JSd-1	JSd-1 (n=1)	% diff
SiO_2	1.30	1	38.20	38.28	0.2	49.90	49.93	0.1	46.20	44.88	2.9	66.60	67.71	1.6
TiO_2	0.003	1	2.61	2.63	0.8	2.73	2.72	0.3	2.96	2.93	1.0	0.64	0.67	4.2
Al_2O_3	0.02	1	10.07	10.03	0.4	13.50	13.67	1.2	13.60	13.35	1.9	14.70	14.62	0.5
Fe_2O_3t	0.07	1	12.84	12.91	0.6	12.30	12.40	0.8	12.50	12.43	0.6	5.06	4.99	1.5
MnO	0.001	2	0.20	0.20	0.1	0.17	0.17	0.2	0.16	0.16	2.4	0.09	0.09	5.1
MgO	0.005	2	13.15	13.44	2.2	7.23	7.45	3.0	9.60	10.08	4.8	1.81	1.81	0.1
CaO	0.03	1	13.87	13.93	0.4	11.40	11.61	1.8	9.40	9.53	1.4	3.03	3.09	2.0
Na_2O	0.05	1	3.18	3.22	1.4	2.22	2.22	0.2	3.06	3.02	1.4	2.73	2.62	4.2
K_2O	0.03	3	1.39	1.45	4.6	0.52	0.55	4.8	0.76	0.79	4.3	2.18	2.11	3.5
P_2O_5	0.01	10	1.05	1.09	3.5	0.27	0.27	1.5	0.45	n.a.	n.c.	0.12	0.12	0.0

D.L.: detection limit; n.a.: not analyzed; n.c. not calculated; % diff: relative error

Appendix 5 (cont.)

wt.% oxide	D.L. (wt.%)	Accuracy (%)	AGV-1	AGV-1 (n=3)	% diff	BCR-2	BCR-2 (n=2)	% diff	G-2	G-2 (n=1)	% diff	BIR	BIR (n=1)	% diff
SiO_2	1.30	0	58.84	59.39	0.9	54.1	53.94	0.3	69.14	69.55	0.6	47.7	47.5	0.3
TiO_2	0.003	1	1.05	1.04	1.2	2.26	2.27	0.6	0.48	0.47	3.1	0.97	0.96	1.5
Al_2O_3	0.02	1	17.15	17.00	0.9	13.5	13.74	1.8	15.39	15.55	1.0	15.4	16	4.0
Fe_2O_3t	0.07	2	6.77	6.67	1.5	13.8	14.13	2.4	2.66	2.58	3.2	11.3	11.7	3.0
MnO	0.001	2	0.10	0.10	3.5	0.2	0.20	0.4	0.03	0.03	5.7	0.18	0.18	0.4
MgO	0.005	2	1.53	1.49	2.4	3.59	3.65	1.8	0.75	0.70	6.9	9.7	9.86	1.6
CaO	0.03	1	4.94	4.93	0.2	7.12	7.14	0.3	1.96	1.89	3.8	13.4	12.8	4.4
Na_2O	0.05	1	4.26	4.21	1.3	3.16	3.13	1.0	4.08	4.05	0.7	1.81	1.85	2.4
K_2O	0.03	2	2.92	2.82	3.5	1.79	1.79	0.0	4.48	4.27	5.0	<L.D.	0.04	n.c.
P_2O_5	0.01	15	0.49	0.50	2.0	0.35	0.36	2.3	0.14	0.13	7.1	0.03	0.02	77.6

D.L.: detection limit; n.a.: not analyzed; n.c. not calculated; % diff: relative error

Appendix 6 Iron correction for sulfide-free major element analyses.

This iron correction aims to remove the iron contained in sulfides and recalculate the bulk major oxide composition, the steps used to achieve are described below.

1- In order to perform calculations that use mole numbers, major oxide concentrations (in wt.%) are first converted into element concentrations (in ppm):
$C(Al) = 10000*C(Al_2O_3)*[M(Al)/M(Al_2O_3)]$
where C is the elemental or major oxide concentration (in ppm or wt.%, respectively), M the molar weight ($kg.mol^{-1}$) and n the mole number (mol).

2- Calculation of the Fe content contained in the chalcopyrite according to the bulk Cu content, assuming that all the Cu is hosted by the chalcopyrite (cp).
This calculation is applied only if the S content is present in sufficient quantities according to the stoichiometric proportions between Cu and S in the chalcopyrite. If $C(S)/(2*M(S)) < C(Cu)/M(Cu)$ no correction will be applied.
For 1 mole of Cu the cp ($CuFeS_2$) contains 1 mole of Fe. This leads to : $C(Fe_{cp}) = C(Cu_{cp})*[M(Fe)/M(Cu)]$

3- Calculation of the S content involved in the chalcopyrite.
For 1 mole of Fe the cp contains 2 moles of S: $C(S_{cp}) = 2*C(Fe_{cp})*[M(S)/M(Fe)]$

4- Calculation of the remaining S (S_r) contained in the bulk rock :
$S_r=S_{tot} - S_{cp}$

5- Calculation of Fe content contained in the pyrrhotite (po: $Fe_{(1-x)}S$ with $0<x<0.25$) according to the remaining S in the bulk rock, and approximating the Fe_{po} mole number to 0.875 (in the middle between the two poles that formed the pyrrhotite solid solution):
$C(Fe_{po}) = [C(S_r)/0.875]*[M(Fe)/M(S)]$

6- Calculation of the total Fe content hosted by sulfides :
$C(Fe_{sulf}) = C(Fe_{cp}) + C(Fe_{po})$

7- Calculation of the new Fe content hosted by silicates (Fe_{sil}), by removing the Fe hosted in sulfides (sulf).
$C(Fe_{sil}) = C(Fe_{tot}) - C(Fe_{sulf})$

8- Element concentration (ppm) are converted into major oxide concentrations (in wt.%):
$C(Al_2O_3) = [C(Al)/10000]*[M(Al_2O_3)*M(Al)]$

Appendix 7: Traces element concentration of duplicates, replicates and bis.

	Duplicates									Replicate		
ppm	246.334.0	dup	% diff	246.223.8	dup	% diff	246.180.5	dup	% diff	246.199.0	rep	% diff
Li	11.4	11.4	0.0	9.88	8.97	-9.2	3.29	3.53	7.3	10	9.94	-0.6
Sc	11.5	12.9	12.2	16.3	18.8	15.3	17.3	15.7	-9.2	13.9	13.8	-0.7
Ti	2570	2770	7.8	1330	1380	3.8	2840	2810	-1.1	4370	4350	-0.5
V	74.5	80.4	7.9	53.3	62.6	17.4	130	124	-4.6	102	101	-1.0
Cr	862	933	8.2	4.27	4.98	16.6	2010	1900	-5.5	140	134	-4.3
Co	120	127	5.8	4.13	4.85	17.4	160	152	-5.0	24	23	-4.2
Ni	508	545	7.3	3.41	4.04	18.5	1320	1260	-4.5	84	81.2	-3.3
Cu	350	373	6.6	11.5	13.7	19.1	1370	1310	-4.4	1190	1140	-4.2
Zn	132	141	6.8	20.6	24.2	17.5	144	132	-8.3	157	154	-1.9
Ga	8.15	8.79	7.9	13.6	15.6	14.7	9.24	8.42	-8.9	20.7	20.3	-1.9
Rb	9.29	9.26	-0.3	28.2	27.2	-3.5	0.836	0.988	18.2	19.8	19.6	-1.0
Sr	218	214	-1.8	262	246	-6.1	20.9	21.8	4.3	659	658	-0.2
Y	7.36	7.33	-0.4	19.9	19.2	-3.5	7.09	7.51	5.9	20	20	0.0
Zr	30.5	30	-1.6	130	127	-2.3	29.6	32.5	9.8	62.2	62.4	0.3
Nb	2.26	2.26	0.0	4.79	4.73	-1.3	2.07	2.12	2.4	7.38	7.35	-0.4
Cs	1.14	1.18	3.5	1.03	1.06	2.9	0.191	0.177	-7.3	1.26	1.25	-0.8
Ba	204	211	3.4	392	399	1.8	8.94	8.78	-1.8	477	474	-0.6
La	6.66	6.91	3.8	16.7	17.6	5.4	2.52	2.5	-0.8	23.7	23.7	0.0
Ce	14.3	14.7	2.8	33.5	35.4	5.7	6.74	6.52	-3.3	50.5	49.8	-1.4
Pr	1.86	1.91	2.7	4.1	4.24	3.4	0.992	0.978	-1.4	6.25	6.19	-1.0
Nd	7.81	8.04	2.9	15.5	16	3.2	4.7	4.62	-1.7	25	24.8	-0.8
Sm	1.64	1.7	3.7	3.19	3.31	3.8	1.3	1.31	0.8	5.09	5.02	-1.4
Eu	0.559	0.574	2.7	0.583	0.606	3.9	0.459	0.449	-2.2	1.52	1.52	0.0
Gd	1.51	1.54	2.0	2.92	3.08	5.5	1.39	1.37	-1.4	4.36	4.29	-1.6
Tb	0.217	0.224	3.2	0.495	0.493	-0.4	0.221	0.216	-2.3	0.635	0.624	-1.7
Dy	1.32	1.32	0.0	3.27	3.31	1.2	1.42	1.38	-2.8	3.7	3.66	-1.1
Ho	0.261	0.272	4.2	0.708	0.717	1.3	0.288	0.283	-1.7	0.722	0.713	-1.2
Er	0.738	0.756	2.4	2.12	2.16	1.9	0.797	0.803	0.8	1.96	1.99	1.5
Yb	0.681	0.697	2.3	1.97	1.97	0.0	0.743	0.734	-1.2	1.68	1.71	1.8
Lu	0.102	0.104	2.0	0.277	0.272	-1.8	0.108	0.105	-2.8	0.236	0.235	-0.4
Hf	0.898	0.908	1.1	3.64	3.61	-0.8	0.83	0.872	5.1	2.03	2.05	1.0
Ta	0.133	0.136	2.3	0.358	0.358	0.0	0.126	0.121	-4.0	0.424	0.416	-1.9
Pb	7.91	7.71	-2.5	3.34	3.35	0.3	4.97	5.09	2.4	46.8	46.4	-0.9
Th	0.81	0.839	3.6	5.81	5.78	-0.5	0.649	0.625	-3.7	2.8	2.81	0.4
U	0.607	0.61	0.5	2.72	2.63	-3.3	0.698	0.705	1.0	2.47	2.45	-0.8

% diff: relative error

Appendix 7 (continued)

Replicate											
246.219.0	rep	% diff	246.213.2	rep	% diff	246.224.6	rep	% diff	246.212.5	bis	% diff
9.19	9.02	-1.8	14.1	14.1	0.0	10	9.59	-4.1	10.5	11.5	9.5
12	12.6	5.0	15.6	15.6	0.0	14.3	15.4	7.7	16.7	15.5	-7.2
3020	3030	0.3	5950	6000	0.8	2930	2960	1.0	3150	3080	-2.2
102	103	1.0	131	129	-1.5	96.3	102	5.9	109	101	-7.3
2210	2250	1.8	7.73	7.55	-2.3	2220	2350	5.9	1170	1080	-7.7
167	169	1.2	11.5	11.4	-0.9	106	111	4.7	56.6	51.8	-8.5
1070	1080	0.9	13.3	12.9	-3.0	489	514	5.1	737	669	-9.2
3150	3190	1.3	160	157	-1.9	527	553	4.9	213	193	-9.4
161	159	-1.2	30.8	32.3	4.9	139	143	2.9	165	151	-8.5
10.1	9.66	-4.4	19.3	19.1	-1.0	10.1	10.5	4.0	12.6	11.6	-7.9
10.6	10.8	1.9	17.8	17.9	0.6	13.9	13.4	-3.6	25.6	26.6	3.9
190	193	1.6	386	393	1.8	210	205	-2.4	67	70.3	4.9
9.07	9.03	-0.4	31.9	31.6	-0.9	10.7	10.3	-3.7	15.9	16.1	1.3
40.4	40.2	-0.5	134	133	-0.7	50.6	48.7	-3.8	59.3	60	1.2
2.67	2.66	-0.4	8.46	8.42	-0.5	3.04	2.95	-3.0	3.96	4.03	1.8
0.64	0.656	2.5	1.62	1.61	-0.6	0.625	0.62	-0.8	2.01	2.03	1.0
208	210	1.0	491	484	-1.4	247	247	0.0	377	381	1.1
7.9	7.93	0.4	28.1	27.7	-1.4	8.84	8.85	0.1	10.6	10.6	0.0
17.2	17.2	0.0	61.8	60.9	-1.5	19.1	19.1	0.0	24.5	24.6	0.4
2.27	2.28	0.4	7.95	7.84	-1.4	2.55	2.55	0.0	3.33	3.32	-0.3
9.45	9.49	0.4	32.9	32.4	-1.5	10.8	10.7	-0.9	14.1	14	-0.7
2	2.02	1.0	7.08	6.89	-2.7	2.33	2.32	-0.4	3.22	3.24	0.6
0.612	0.614	0.3	1.82	1.79	-1.6	0.681	0.675	-0.9	0.848	0.844	-0.5
1.81	1.82	0.6	6.34	6.16	-2.8	2.12	2.1	-0.9	3.06	3.04	-0.7
0.268	0.269	0.4	0.947	0.919	-3.0	0.316	0.312	-1.3	0.455	0.462	1.5
1.62	1.61	-0.6	5.69	5.59	-1.8	1.92	1.89	-1.6	2.82	2.89	2.5
0.324	0.32	-1.2	1.14	1.11	-2.6	0.388	0.379	-2.3	0.576	0.592	2.8
0.918	0.912	-0.7	3.2	3.12	-2.5	1.09	1.08	-0.9	1.67	1.69	1.2
0.838	0.828	-1.2	2.84	2.81	-1.1	0.988	0.974	-1.4	1.54	1.57	1.9
0.127	0.126	-0.8	0.42	0.407	-3.1	0.146	0.144	-1.4	0.232	0.232	0.0
1.22	1.21	-0.8	3.72	3.64	-2.2	1.43	1.39	-2.8	1.64	1.67	1.8
0.162	0.156	-3.7	0.539	0.528	-2.0	0.188	0.187	-0.5	0.24	0.248	3.3
38.2	37.8	-1.0	17.7	17.4	-1.7	16.2	16.1	-0.6	5.18	5.11	-1.4
1.07	1.05	-1.9	3.97	3.84	-3.3	1.4	1.38	-1.4	1.55	1.54	-0.6
1.13	1.12	-0.9	4.45	4.39	-1.3	1.26	1.24	-1.6	1.34	1.38	3.0

% diff: relative error

Appendix 7 (continued)

BIS														
246.240.8	bis	% diff	246.340.8	bis	% diff	246.249.6	bis	% diff	246.290.7	bis	% diff	246.212.5	bis	% diff
12.7	13.4	5.5	6.93	6.69	-3.5	16.6	16.9	1.8	4.9	5.15	5.1	10	10.1	1.0
14.7	14.2	-3.4	16.7	17.7	6.0	18.9	20.1	6.3	12.6	11.9	-5.6	16.7	16.4	-1.8
2680	2640	-1.5	3480	3710	6.6	4190	4430	5.7	2490	2400	-3.6	3660	3640	-0.5
52.7	50.2	-4.7	101	107	5.9	117	123	5.1	95.5	91.3	-4.4	117	117	0.0
267	256	-4.1	794	833	4.9	117	122	4.3	1440	1380	-4.2	2150	2140	-0.5
98.5	93.8	-4.8	93.8	97.1	3.5	18.7	19.3	3.2	186	175	-5.9	90.4	89.9	-0.6
784	739	-5.7	580	609	5.0	49.7	51.7	4.0	1030	968	-6.0	388	382	-1.5
20700	19600	-5.3	881	910	3.3	31.9	32.9	3.1	1990	1880	-5.5	178	175	-1.7
179	175	-2.2	188	191	1.6	107	109	1.9	169	163	-3.6	142	141	-0.7
16.3	16.1	-1.2	9.56	9.87	3.2	18.3	18.4	0.5	7.6	7.23	-4.9	11.4	11.3	-0.9
20.1	20.3	1.0	11.7	11.5	-1.7	30.7	30.2	-1.6	4.32	4.39	1.6	13.9	13.8	-0.7
606	620	2.3	105	113	7.6	626	623	-0.5	148	154	4.1	240	244	1.7
15.5	15.6	0.6	12.9	12.5	-3.1	13.9	13.4	-3.6	4.98	5.01	0.6	11.8	11.6	-1.7
59.7	59.5	-0.3	32.7	31.7	-3.1	89.1	85.7	-3.8	17.2	17.2	0.0	48	46.8	-2.5
4.3	4.28	-0.5	2.67	2.61	-2.2	5.55	5.39	-2.9	1.28	1.28	0.0	3.45	3.36	-2.6
1.7	1.67	-1.8	0.863	0.864	0.1	1.84	1.85	0.5	0.2	0.195	-2.5	1.29	1.26	-2.3
499	502	0.6	258	257	-0.4	639	637	-0.3	98.7	96.4	-2.3	271	264	-2.6
12.7	12.6	-0.8	6.71	6.76	0.7	17.6	17.6	0.0	3.37	3.28	-2.7	9.58	9.36	-2.3
28.1	27.8	-1.1	16.4	16.4	0.0	37.5	37.3	-0.5	7.6	7.39	-2.8	20.8	20.3	-2.4
3.81	3.8	-0.3	2.42	2.4	-0.8	4.7	4.65	-1.1	1.07	1.03	-3.7	2.8	2.71	-3.2
16.3	16.5	1.2	11.2	11	-1.8	18.4	18.2	-1.1	4.69	4.55	-3.0	11.7	11.4	-2.6
3.66	3.69	0.8	2.71	2.66	-1.8	3.61	3.55	-1.7	1.05	1.04	-1.0	2.53	2.5	-1.2
1.28	1.31	2.3	0.719	0.715	-0.6	1.1	1.09	-0.9	0.366	0.354	-3.3	0.784	0.761	-2.9
3.25	3.36	3.4	2.57	2.56	-0.4	2.92	2.89	-1.0	0.978	0.939	-4.0	2.32	2.25	-3.0
0.481	0.494	2.7	0.386	0.381	-1.3	0.42	0.416	-1.0	0.15	0.143	-4.7	0.343	0.336	-2.0
2.93	3	2.4	2.37	2.35	-0.8	2.52	2.46	-2.4	0.923	0.885	-4.1	2.11	2.04	-3.3
0.581	0.598	2.9	0.471	0.464	-1.5	0.495	0.477	-3.6	0.184	0.179	-2.7	0.425	0.409	-3.8
1.59	1.64	3.1	1.3	1.3	0.0	1.39	1.35	-2.9	0.527	0.505	-4.2	1.19	1.17	-1.7
1.31	1.32	0.8	1.15	1.12	-2.6	1.25	1.24	-0.8	0.5	0.486	-2.8	1.11	1.08	-2.7
0.188	0.187	-0.5	0.163	0.165	1.2	0.189	0.182	-3.7	0.078	0.075	-3.5	0.167	0.162	-3.0
1.69	1.7	0.6	1.11	1.08	-2.7	2.56	2.48	-3.1	0.512	0.5	-2.3	1.4	1.35	-3.6
0.236	0.236	0.0	0.146	0.142	-2.7	0.324	0.313	-3.4	0.073	0.072	-1.9	0.2	0.195	-2.5
47.7	47.4	-0.6	13.7	13.6	-0.7	15.8	15.4	-2.5	13.6	13.2	-2.9	14.8	14.5	-2.0
1.24	1.25	0.8	0.718	0.688	-4.2	3.04	2.88	-5.3	0.344	0.333	-3.2	1.18	1.16	-1.7
0.966	0.972	0.6	0.504	0.487	-3.4	1.85	1.74	-5.9	0.259	0.256	-1.2	0.937	0.929	-0.9

% diff: relative error

Appendix 8 Trace element concentrations of standards measured as unknown.

	AGV-1 (n=3)				BHVO-2 (n=2)				BE-N (n=3)				G-2 (n=2)			
ppm	avg	RSD%	Ref	diff %	avg	RSD%	Ref	diff %	avg	RSD%	Ref	diff %	avg	RSD%	Ref	diff %
Li	11.2	0.5	10.7	4.7	4.78	0.3	4.5	6.2	13.3	1.3	12.9	3.1	34.3	0.8	33.6	2.1
Sc	11.8	3.5	12.4	-4.8	31.9	3.1	31.8	0.3	21.9	1.7	22.6	-3.1	3.94	11.7	3.66	7.7
Ti	5800	3.8	6300	-7.9	16000	3.5	16400	-2.4	15000	3.1	15700	-4.5	2610	1.1	2880	-9.4
V	113	0.9	119	-5.0	311	3.0	318	-2.2	219	2.1	232	-5.6	32.5	1.7	35.1	-7.4
Cr	8.12	2.9	9.47	-14.3	276	2.3	287	-3.8	328	1.8	353	-7.1	6.47	1.2	7.88	-17.9
Co	14.7	0.7	15.1	-2.6	44.5	1.4	44.9	-0.9	59	2.2	59	0.0	4.26	1.7	4.48	-4.9
Ni	14.1	3.2	15.4	-8.4	120	0.6	120	0.0	255	2.9	270	-5.6	2.01	4.6	3.46	-41.9
Cu	53.1	1.9	58.4	-9.1	122	5.2	129	-5.4	65.1	1.7	68.8	-5.4	8.74	3.5	11	-20.5
Zn	86.5	1.4	86.8	-0.3	106	8.6	104	1.9	118	1.3	123	-4.1	81.9	4.0	83.5	-1.9
Ga	20.2	0.8	20.4	-1.0	21.1	0.7	21.4	-1.4	18.1	5.3	17.2	5.2	23.6	5.1	23.3	1.3
Rb	63.4	0.6	67.8	-6.5	8.98	2.6	9.26	-3.0	47.1	1.3	47.6	-1.1	167	1.3	169	-1.2
Sr	640	0.7	661	-3.2	391	0.5	394	-0.8	1390	0.8	1390	0.0	464	0.2	475	-2.3
Y	19.5	1.1	19.7	-1.0	26.1	1.9	25.9	0.8	29.8	0.6	29.4	1.4	10	2.2	9.88	1.2
Zr	223	9.1	232	-3.9	153	8.8	171	-10.5	265	8.5	273	-2.9	353	3.2	319	10.7
Nb	14	1.2	14.5	-3.4	17.8	0.4	18.1	-1.7	115	1.5	113	1.8	12.2	2.3	12	1.7
Cs	1.29	1.2	1.25	3.2	0.1	0.7	0.1	2.4	0.75	1.8	0.73	2.7	1.43	4.0	1.36	5.1
Ba	1300	5.5	1220	6.6	130	0.0	131	-0.8	1070	4.3	1040	2.9	2060	1.0	1860	10.8
La	37.3	2.0	38.2	-2.4	15.1	0.9	15.2	-0.7	83.4	4.4	82.6	1.0	89.8	1.7	88.4	1.6
Ce	73.9	17.8	68.6	7.7	37.3	0.9	37.5	-0.5	175	14.5	153	14.4	173	4.5	161	7.5
Pr	8.32	1.5	8.31	0.1	5.36	2.0	5.34	0.4	17.5	2.3	17.4	0.6	16.4	0.9	16.9	-3.0
Nd	31.2	1.9	32.1	-2.8	24.5	2.3	24.3	0.8	66.6	2.5	66.4	0.3	53	1.7	53.8	-1.5
Sm	5.72	2.5	5.76	-0.7	6.11	1.7	6.02	1.5	12.2	2.2	12	1.7	7.17	2.2	7.19	-0.3
Eu	1.56	2.8	1.66	-6.0	2.04	1.7	2.04	0.0	3.63	2.1	3.68	-1.4	1.36	1.6	1.41	-3.5
Gd	4.55	5.7	4.86	-6.4	5.97	0.5	6.21	-3.9	9.73	5.2	10.1	-3.7	4.47	2.1	4.23	5.7
Tb	0.62	3.6	0.67	-7.7	0.91	1.0	0.939	-3.4	1.24	3.3	1.3	-4.6	0.46	0.6	0.5	-6.5
Dy	3.51	2.9	3.58	-2.0	5.29	2.5	5.28	0.2	6.4	3.4	6.48	-1.2	2.19	2.3	2.28	-3.9
Ho	0.67	3.5	0.68	-2.2	0.98	2.2	0.989	-0.7	1.08	3.0	1.08	0.0	0.37	4.2	0.37	0.0
Er	1.83	3.3	1.83	0.0	2.54	3.6	2.51	1.2	2.57	3.9	2.61	-1.5	0.93	1.1	0.93	0.2
Yb	1.63	2.9	1.66	-1.8	2	3.2	1.99	0.5	1.85	3.9	1.82	1.6	0.76	3.6	0.72	5.7
Lu	0.24	3.9	0.25	-4.8	0.27	4.6	0.275	-0.4	0.25	4.1	0.25	0.8	0.1	1.4	0.1	2.0
Hf	5.05	3.2	5.09	-0.8	4.35	3.6	4.47	-2.7	5.73	3.9	5.72	0.2	8.2	4.2	7.78	5.4
Ta	0.83	3.3	0.87	-4.4	1.1	1.3	1.15	-4.3	5.64	4.1	5.64	0.0	0.79	2.8	0.83	-4.8
Pb	35.7	1.3	36.4	-1.9	1.69	2.1	1.65	2.4	4.14	0.6	4.08	1.5	30.5	1.4	30	1.7
Th	6.31	0.7	6.35	-0.6	1.21	3.5	1.22	-0.8	11	0.9	10.6	3.8	24.2	4.1	24.5	-1.2
U	1.81	1.1	1.9	-4.7	0.4	3.0	0.412	-3.9	2.45	1.9	2.44	0.4	1.89	15.4	1.96	-3.6

Avg: average; RSD: relative standard deviation; Ref: reference value; %diff: relative error

Appendix 9 Geochronological data of rocks of the Skellefte district

Geological unit	Rock information	Age	Precision (+/-)		Methods	Reference
Skellefte Group	Rhyolite	1902	21	21	U-Pb zr	Montelius (2005)
Skellefte Group	Rhyolite	1902	3	3	U-Pb zr	Montelius (2005)
Skellefte Group	Mass flow	1889	4	4	U-Pb zr	Billström & Weihed (1996)
Skellefte Group	Rhyolite	1885	6	3	U-Pb zr	Montelius (2005)
Skellefte Group	Rhyolite	1885	6	6	U-Pb zr	Montelius (2005)
Skellefte Group	Rhyodacite	1884	6	6	U-Pb zr	Billström & Weihed (1996)
Skellefte Group	Rhyolite	1882	8	8	U-Pb zr	Welin (1987)
Skellefte Group	Rhyolite	1883	6	6	U-Pb zr	Skyttä et al. (2011)
Skellefte Group	Dacite	1869	15	15	Pb-Pb zr	Bergman Weihed et al. (1996)
Skellefte Group	Mass flow	1847	3	3	U-Pb zr	Billström & Weihed (1996)
Skellefte Group	Feslic intrusion	1875	13	13	U-Pb zr ttn	Weihed (2002a)
Arvidsjaur Group	Gneissic tonalite	1872	7	7	U-Pb zr, ttn, mnz	Lundström & Persson (1999)
Arvidsjaur Group	Rhyolite	1876	3	3	U-Pb zr	Skiöld et al. (1993)
Arvidsjaur Group	Granite	1877	8	8	U-Pb zr	Skiöld et al. (1993)
Arvidsjaur Gruop	Rhyolite	1878	2	2	U-Pb zr	Skiöld et al. (1993)
Vargfors Group	Felsic ignimbrite	1875	4	4	U-Pb zr	Billström & Weihed (1996)
GI	Granodiorite	1888	20	14	U-Pb zr	Wilson et al. (1987)
GI	Granodiorite	1886	3	3	U-Pb zr	González-Roldán (2010)
GI	Granodiorite	1885	5	5	U-Pb zr	González-Roldán (2010)
GI	Granodiorite	1880	4	4	U-Pb zr	González-Roldán (2010)
GI	QPG	1887	3	3	U-Pb zr	Bejgarn et al. (2013)
GI	Tonalite	1886	3	3	U-Pb zr	Bejgarn et al. (2013)
GII	Granodiorite	1874	48	26	U-Pb zr	Wilson et al. (1987)
GII	Granite	1874	6	6	U-Pb zr	González-Roldán (2010)
GII	Granite	1871	4	4	U-Pb zr	González-Roldán (2010)
GIII	Granite	1873	18	14	U-Pb zr	Wilson et al. (1987)
GIII	Granite	1863	5	5	U-Pb zr	González-Roldán (2010)
GIII	Granite	1862	14	14	Pb-Pb ttn	Lundström et al. (1997)
Viterliden	Tonalite	1891	3	3	U-Pb zr	Skyttä et al. (2011)
Viterliden	Tonalite	1889	3	3	U-Pb zr	Skyttä et al. (2011)
Viterliden	Tonalite	1892	3	3	U-Pb zr	Skyttä et al. (2011)
Granberg	QFP core	1884	4	4	U-Pb zr	Bejgarn et al. (2013)
Granberg	QFP rim	1877	4	4	U-Pb zr	Bejgarn et al. (2013)
Järvträsk	QFP core	1884	5	5	U-Pb zr	Bejgarn et al. (2013)
Järvträsk	QFP rim	1877	5	5	U-Pb zr	Bejgarn et al. (2013)
Älgträsk	QFP core	1885	5	5	U-Pb zr	Bejgarn et al. (2013)
Älgträsk	QFP rim	1877	7	7	U-Pb zr	Bejgarn et al. (2013)
Tallberg	QFP core	1888	6	6	U-Pb zr	Bejgarn et al. (2013)
Tallberg	QFP rim	1871	9	9	U-Pb zr	Bejgarn et al. (2013)
Tallberg	QFP core	1890	7	7	U-Pb zr	Bejgarn et al. (2013)
Tallberg	QFP rim	1878	5	5	U-Pb zr	Bejgarn et al. (2013)
Tallberg	QFP rim	1876	5	5	U-Pb zr	Bejgarn et al. (2013)
Näsberg	Layered gabbro	1879	1	1	U-Pb bdt	Bejgarn et al. (2013)
Torrspiggen	Layered gabbro	1884	2	2	U-Pb bdt	Bejgarn et al. (2013)
Älgräsk	Gabbro	1883	3	3	U-Pb zr	Bejgarn et al. (2013)
Älgliden	Gabbro-norite	1876	1	1	U-Pb bdt	Bejgarn et al. (2013)
Gallejaur	Gabbro	1876	4	4	U-Pb zr	Skiöld et al. (1993)
Gallejaur	Monzonite	1873	10	10	U-Pb zr	Skiöld (1988)
Antak	Granite	1879	15	12	U-Pb zr	Kahtol and Persson (1997)
Stavaträsk	Diorite	1877	2	2	U-Pb zr	Lundström et al. (1997)
Putarliden	Trondhjemite	1874	3	3	U-Pb zr, mnz	Lundström et al. (1999)
Sikträsk	Gneissic granodiorit	1859	3	3	U-Pb zr	Weihed & Vaasjoki (1993)
Sikträsk	Granite	1854	9	9	U-Pb zr	Billtröm & Weihed (1996)

Abbreviations: QPG: Quartz Porphyry Granodiorite; QFP: Quartz Feldspar porphyry; zr: zircon; ttn: titanite; mnz: monazite; bdt: baddeleyite.

Appendix 10: K_2O versus Loss of Ignition (LOI) showing discarded samples.

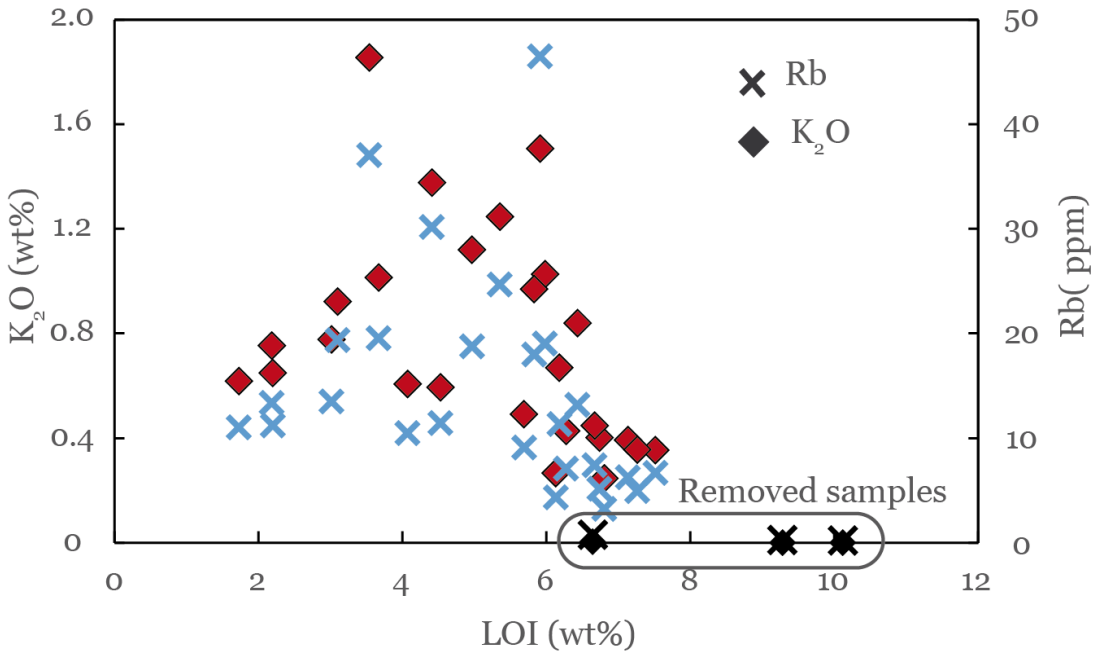

Appendix 11: Ferric and Ferrous proportion in cumulates

This appendix aims to evaluate the implication of the approximation of the relative proportions of ferric and ferrous iron in the olivine norites on the estimation of their parental melt. The varying initial parameters are the $Fe_2O_3/(FeO+Fe_2O_3)$ ratio and MgO content of the melt chosen in the ramp function introduced by Barnes (2007), where the used olivine composition is Fo79 with 41 wt.% MgO. The ramp functions have varying slopes according to their initial parameters, and each slope allows to attribute different $Fe_2O_3/(FeO+Fe_2O_3)$ ratios to the bulk cumulates depending on their MgO content (Figure 9.1). Subsequently, the $Fe_2O_3/(FeO+Fe_2O_3)$ ratio of each cumulate, and therefore their FeO content, are used in a FeO vs. MgO diagram in order to estimate the MgO and FeO contents of the parental melt (Figure 9.2). We tested $Fe_2O_3/(FeO+Fe_2O_3)$ ratios ranging from 0.1 to 0.3 and MgO contents of 5 and 10 wt.% of the melt.

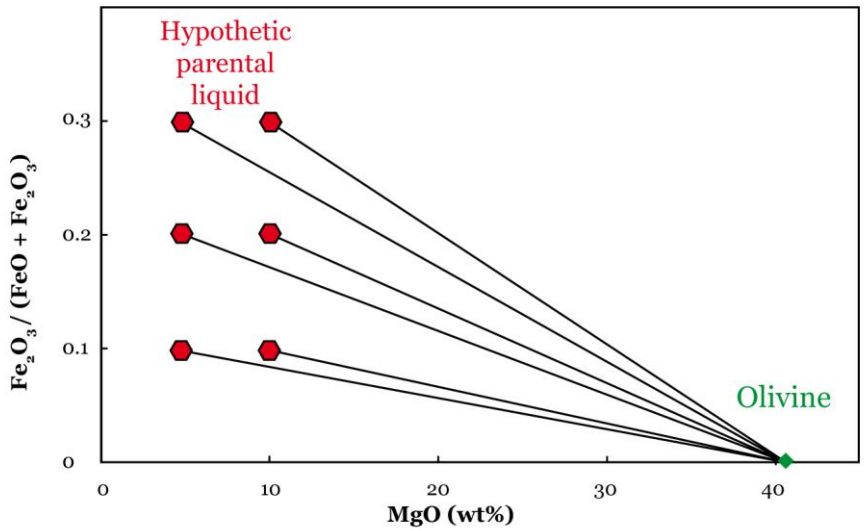

Figure 1 Ramp functions of olivine cumulates with different $Fe_2O_3/(FeO+Fe_2O_3)$ ratios and MgO contents of the parental melt.

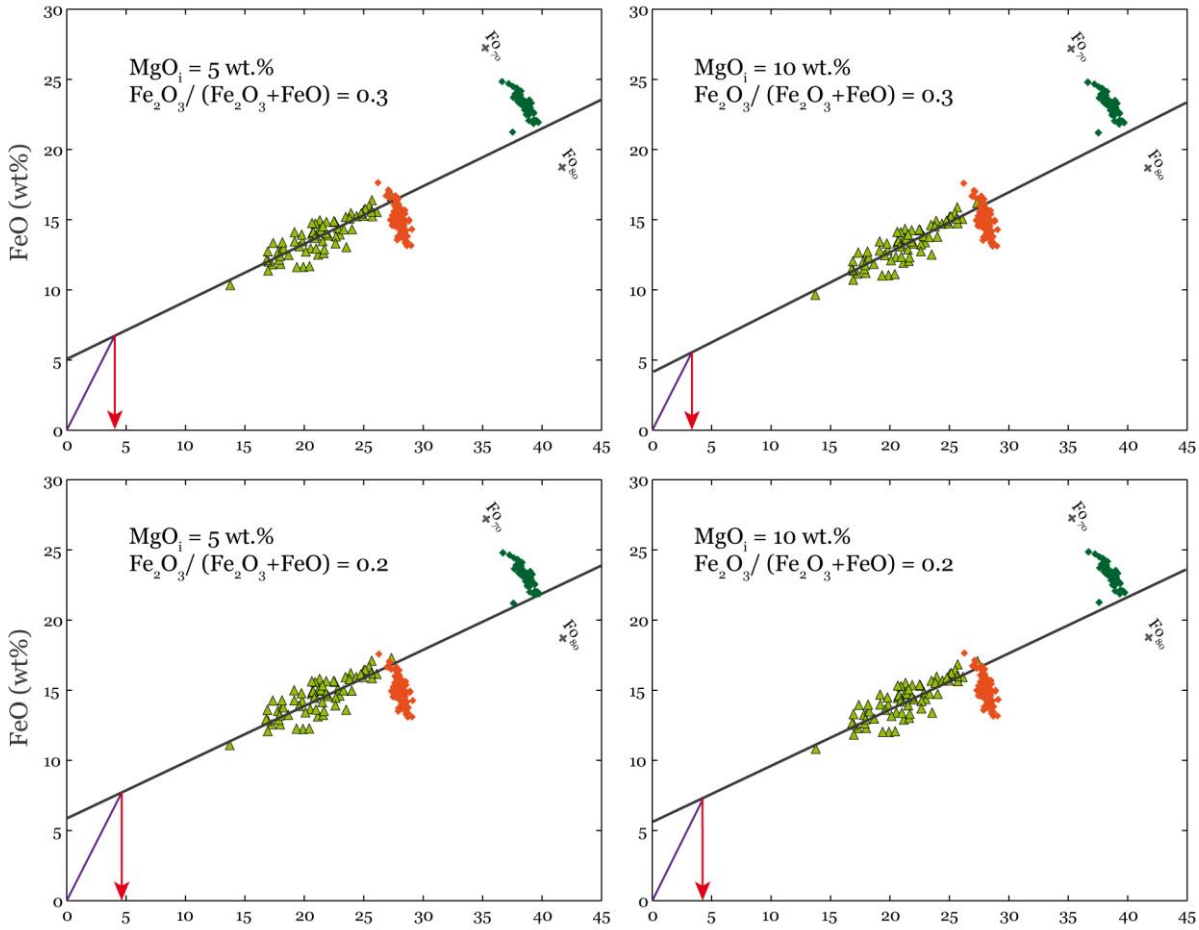

Figure 2 FeO versus MgO diagram with different initial parameters of the parental melt. The purple line is the FeO/MgO ratio of the melt in equilibrium with Fo_{79}. The estimated MgO ranges of the parental melt are highlighted by arrows.

The FeO/MgO slope defined by the regression of the olivine norites in each diagram varies according to the selected initial parameters of the hypothetic parental melt (Figure 9.2). Increasing the MgO content of the hypothetic parental melt, from 5 to 10 wt.%, has negligible effects (<0.5 wt.% MgO) on the determination of the parental melt. It shows that the estimation of the MgO content of the parental melt ranges around 5 wt.% MgO, and the retained value for the MgO content of the hypothetic parental melt is therefore 5 wt.%. To the contrary, variations on the $Fe_2O_3/(FeO+Fe_2O_3)$ ratio have more effects on the determination of the parental melt. Considering a $Fe_2O_3/(FeO+Fe_2O_3)$) ratio of 0.3 allows to estimate an overall MgO range from 3.2 to 4 wt.% for the parental melt, which is particularly low for a melt that crystallizes Fo79. Moreover a $Fe_2O_3/(FeO+Fe_2O_3)$ ratio of 0.3 represents a highly oxidized magma. A $Fe_2O_3/(FeO+Fe_2O_3)$ ratio of 0.1 is not compatible with those of arc magmas, we therefore choose an intermediate situation with a $Fe_2O_3/(FeO+Fe_2O_3)$ ratio of 0.2.

Appendix 12 Electron microprobe analyses of olivine in olivine norites

Sample no.	SiO_2	TiO_2	Al_2O_3	FeO	MnO	MgO	CaO	Cr_2O_3	NiO	Total	Pos.	Fo
246.209.0	38.44	n.a.	n.a.	22.41	0.341	38.81	0.14	n.a.	0.093	100.91		75.5
246.209.0	38.23	n.a.	n.a.	23.42	0.345	37.92	0.13	n.a.	0.087	100.81		74.3
246.209.0	38.49	n.a.	n.a.	23.25	0.348	38.13	0.13	n.a.	0.082	101.11		74.5
246.209.0	38.45	n.a.	n.a.	23.46	0.348	38.03	0.11	n.a.	0.078	101.17	rim	74.3
246.209.0	37.89	n.a.	n.a.	24.81	0.370	36.61	0.06	n.a.	0.089	100.52		72.5
246.219.0	38.53	0.01	0.02	22.06	0.322	39.48	0.18	0.006	0.110	100.72		76.1
246.219.0	38.57	0.01	0.02	21.99	0.320	39.60	0.17	0.007	0.110	100.80	core	76.3
246.219.0	38.56	0.01	0.02	22.65	0.322	39.24	0.12	0.012	0.111	101.04	rim	75.5
246.219.0	38.44	0.01	0.02	22.56	0.323	39.28	0.11	0.003	0.108	100.86		75.6
246.219.0	38.08	0.02	0.01	23.89	0.347	38.15	0.08	0.008	0.115	100.70		74.0
246.219.0	37.99	0.02	0.01	24.47	0.333	37.53	0.06	0.003	0.125	100.55		73.2
246.219.0	38.62	0.01	0.02	21.91	0.316	39.67	0.18	0.014	0.118	100.86	core	76.3
246.219.0	38.55	0.01	0.02	22.74	0.330	38.89	0.08	0.006	0.110	100.73	rim	75.3
246.219.0	38.44	0.02	0.02	22.62	0.328	38.92	0.17	0.007	0.095	100.61	core	75.4
246.219.0	38.28	0.01	0.02	23.07	0.327	38.52	0.08	0.007	0.091	100.40	rim	74.8
246.219.0	38.43	0.01	0.02	23.13	0.332	38.63	0.15	0.008	0.097	100.80		74.9
246.219.0	38.40	0.01	0.02	23.36	0.337	38.57	0.11	0.005	0.092	100.90		74.6
246.239.1	38.45	0.02	0.01	22.79	0.318	38.90	0.07	<D.L.	0.121	100.69	rim	75.3
246.239.1	38.36	0.01	0.01	22.75	0.317	38.85	0.13	0.008	0.118	100.56	core	75.3
246.239.1	38.43	0.03	0.01	22.05	0.309	39.23	0.03	0.030	0.122	100.26		76.0
246.239.1	38.42	0.01	0.02	22.79	0.310	39.02	0.16	0.008	0.124	100.86	core	75.3
246.239.1	38.53	0.01	0.02	22.72	0.326	38.97	0.12	0.006	0.112	100.82		75.4
246.239.1	38.46	0.02	0.02	22.74	0.324	39.04	0.11	0.007	0.113	100.83		75.4
246.212.3	38.39	0.01	0.02	23.07	0.396	38.55	0.14	0.003	0.059	100.64		74.9
246.212.3	38.38	0.01	0.02	22.89	0.350	38.74	0.15	0.002	0.066	100.62		75.1
246.212.3	38.52	0.01	0.02	22.09	0.327	39.31	0.12	0.010	0.096	100.50	rim	76.0
246.212.3	38.15	0.01	0.01	24.35	0.425	37.78	0.11	<D.L.	0.065	100.91		73.4
246.280.8	38.67	<D.L.	0.03	21.23	0.262	37.51	0.10	<D.L.	0.093	97.93		75.9
246.280.8	38.10	0.03	0.03	23.51	0.298	38.90	0.09	<D.L.	0.071	101.04		74.7
246.280.8	38.25	<D.L.	<D.L.	24.14	0.301	38.02	0.13	<D.L.	0.039	100.92		73.7
246.280.8	38.04	<D.L.	<D.L.	23.47	0.346	38.39	0.16	<D.L.	0.069	100.53	rim	74.5
246.280.8	38.55	<D.L.	<D.L.	23.29	0.340	39.08	0.14	<D.L.	<D.L.	101.47	rim	74.9
246.280.8	38.26	<D.L.	<D.L.	22.74	0.316	39.05	0.19	<D.L.	0.077	100.69		75.4
246.280.8	38.28	<D.L.	0.03	23.24	0.315	38.60	0.13	0.019	<D.L.	100.65		74.8

Abbreviations: Pos: Crystal position; Fo: forsterite.

Appendix 12 (cont.)

Sample no.	SiO_2	TiO_2	Al_2O_3	FeO	MnO	MgO	CaO	Cr_2O_3	NiO	Total	Pos.	Fo
246.280.8	38.04	<D.L.	<D.L.	23.14	0.332	38.80	0.15	<D.L.	0.061	100.56	rim	74.9
246.280.8	38.30	<D.L.	<D.L.	23.40	0.323	38.57	0.14	<D.L.	0.072	100.85		74.6
246.280.8	37.95	<D.L.	<D.L.	24.13	0.325	38.21	0.14	<D.L.	0.070	100.86	rim	73.8
246.280.8	38.08	<D.L.	<D.L.	22.99	0.314	38.98	0.08	<D.L.	0.071	100.53	rim	75.1
246.280.8	38.35	0.03	<D.L.	22.88	0.326	38.94	0.12	<D.L.	0.096	100.78	core	75.2
246.280.8	38.01	<D.L.	<D.L.	22.91	0.360	38.70	0.10	<D.L.	0.062	100.20	rim	75.1
246.280.8	38.32	0.02	<D.L.	22.72	0.298	39.03	0.07	<D.L.	0.075	100.55	core	75.4
246.280.8	37.87	<D.L.	<D.L.	24.34	0.353	37.87	0.10	<D.L.	0.034	100.60	rim	73.5
246.293.1	38.67	n.a.	n.a.	21.82	0.315	39.26	0.10	n.a.	0.056	100.65		76.2
246.293.1	38.38	n.a.	n.a.	23.33	0.343	38.00	0.10	n.a.	0.056	100.67	rim	74.4
246.293.1	38.78	n.a.	n.a.	22.05	0.340	38.86	0.09	n.a.	0.050	100.65		75.9
246.293.1	38.24	n.a.	n.a.	23.68	0.350	37.57	0.11	n.a.	0.054	100.48	rim	73.9
246.293.1	38.67	n.a.	n.a.	22.74	0.338	38.72	0.13	n.a.	0.054	101.16		75.2
246.293.1	38.55	n.a.	n.a.	22.48	0.330	38.64	0.14	n.a.	0.055	100.70		75.4
246.293.1	38.51	n.a.	n.a.	23.31	0.342	38.11	0.12	n.a.	0.062	100.98		74.4
246.300.9	38.29	0.03	0.04	22.80	0.344	38.51	0.12	0.002	0.054	100.19		75.1
246.300.9	38.42	0.03	0.03	22.84	0.344	38.64	0.11	0.003	0.046	100.48		75.1
246.300.9	38.37	0.02	0.03	23.07	0.361	38.47	0.12	0.003	0.052	100.49		74.8
246.300.9	38.44	0.02	0.04	23.10	0.358	38.40	0.13	0.002	0.046	100.52		74.8
246.300.9	38.49	0.02	0.02	23.03	0.353	38.57	0.12	0.003	0.053	100.66		74.9
246.300.9	38.37	0.02	0.03	23.18	0.357	38.35	0.13	0.002	0.049	100.49		74.7
246.300.9	38.50	0.02	0.03	22.76	0.342	38.64	0.14	0.006	0.052	100.49		75.2
246.300.9	38.44	0.02	0.03	22.81	0.350	38.60	0.15	0.003	0.054	100.46		75.1
246.308.0	38.47	n.a.	n.a.	23.34	0.347	38.17	0.14	n.a.	0.070	101.11		74.5
246.308.0	38.53	n.a.	n.a.	23.26	0.346	38.15	0.14	n.a.	0.070	101.06	rim	74.5
246.308.0	38.60	n.a.	n.a.	23.16	0.348	38.41	0.12	n.a.	0.071	101.30		74.7
246.308.0	38.72	n.a.	n.a.	23.13	0.345	38.46	0.13	n.a.	0.067	101.45	rim	74.8
246.308.0	38.38	n.a.	n.a.	24.67	0.386	37.17	0.12	n.a.	0.067	101.38		72.9
246.308.0	38.48	n.a.	n.a.	23.80	0.353	37.87	0.10	n.a.	0.072	101.28	rim	73.9
246.308.0	38.58	n.a.	n.a.	23.94	0.344	37.71	0.13	n.a.	0.076	101.40	rim	73.7
246.308.0	38.57	n.a.	n.a.	23.17	0.340	38.26	0.11	n.a.	0.071	101.16		74.6
246.308.0	38.44	n.a.	n.a.	23.19	0.344	38.23	0.12	n.a.	0.068	101.03	rim	74.6
246.308.0	38.60	n.a.	n.a.	23.24	0.346	38.43	0.15	n.a.	0.067	101.48		74.7
246.308.0	38.41	n.a.	n.a.	23.69	0.356	38.19	0.07	n.a.	0.068	101.44		74.2
246.308.0	38.50	n.a.	n.a.	23.79	0.360	37.80	0.13	n.a.	0.067	101.31		73.9

Abbreviations: Pos: Crystal position; Fo: forsterite.

Appendix 13 Electron microprobe analyses in pyroxene.

Sample no.	SiO_2	TiO_2	Al_2O_3	FeO	MnO	MgO	CaO	Na_2O	Cr_2O_3	Total	Rock	En	Wo	Mg#
246.233.5	54.56	0.19	1.56	13.92	0.26	28.14	1.36	0.03	0.21	100.22	O. nor.	75.9	2.6	78.0
246.233.5	54.22	0.32	1.40	14.58	0.31	27.41	1.61	0.02	0.18	100.04	O. nor.	74.2	3.1	76.6
246.233.5	53.64	0.26	2.50	13.71	0.23	28.05	1.34	0.03	0.37	100.13	O. nor.	76.2	2.6	78.2
246.233.5	54.55	0.18	1.58	13.33	0.24	28.47	1.44	0.01	0.25	100.04	O. nor.	76.7	2.8	78.9
246.233.5	54.79	0.19	1.67	13.42	0.27	28.61	1.43	0.03	0.24	100.66	O. nor.	76.7	2.7	78.8
246.233.5	54.26	0.33	1.49	14.53	0.30	27.59	1.71	0.06	0.14	100.41	O. nor.	74.3	3.3	76.8
246.233.5	54.39	0.17	1.60	13.68	0.26	28.39	1.38	0.02	0.23	100.13	O. nor.	76.3	2.7	78.4
246.233.5	54.30	0.33	1.30	14.62	0.33	27.58	1.55	0.02	0.16	100.19	O. nor.	74.4	3.0	76.7
246.233.5	54.16	0.26	1.65	14.86	0.31	27.69	1.39	0.01	0.25	100.57	O. nor.	74.4	2.7	76.5
246.233.5	54.38	0.22	1.56	14.35	0.28	27.92	1.40	0.02	0.26	100.38	O. nor.	75.2	2.7	77.3
246.233.5	54.85	0.20	1.58	13.50	0.23	28.47	1.39	0.02	0.29	100.53	O. nor.	76.6	2.7	78.7
246.233.5	54.90	0.15	1.44	13.14	0.27	28.96	1.20	0.03	0.23	100.33	O. nor.	77.5	2.3	79.4
246.209.0	53.65	0.06	1.64	16.70	0.35	26.86	0.90	0.03	0.04	100.24	O. nor.	72.4	1.7	73.7
246.239.1	53.96	0.28	1.95	14.03	0.26	28.39	1.59	0.05	0.27	100.79	O. nor.	75.6	3.0	78.0
246.239.1	54.34	0.20	2.19	13.81	0.23	28.64	1.01	0.05	0.27	100.75	O. nor.	76.9	2.0	78.4
246.239.1	53.83	0.28	2.30	13.73	0.26	28.43	1.13	0.03	0.36	100.35	O. nor.	76.6	2.2	78.4
248.254.0	54.78	0.24	1.18	15.09	0.27	28.14	1.38	<0.02	0.04	101.13	O. nor.	74.5	2.6	76.5
246.293.1	54.44	0.20	1.18	15.55	0.30	28.07	1.02	0.02	0.08	100.86	O. nor.	74.5	1.9	75.9
246.308.0	55.02	0.18	0.90	15.66	0.34	28.01	1.15	<0.02	0.04	101.30	O. nor.	74.1	2.2	75.7
246.308.0	53.84	0.26	1.86	15.29	0.28	27.38	1.75	0.03	0.35	101.05	O. nor.	73.3	3.4	75.8
246.308.0	54.49	0.27	1.53	14.86	0.26	27.94	1.73	0.05	0.22	101.36	O. nor.	74.2	3.3	76.7
246.308.0	54.73	0.16	1.14	15.91	0.34	27.80	0.93	0.06	<D.L.	101.08	O. nor.	74.0	1.8	75.3
246.219.0	55.15	0.08	0.57	14.31	0.32	29.03	0.91	0.03	0.05	100.43	O. nor.	76.6	1.7	78.0
246.212.3	54.40	0.27	1.32	14.58	0.39	28.38	0.94	0.02	0.07	100.35	O. nor.	75.8	1.8	77.2
248.254.0	54.67	0.18	1.66	14.20	0.26	28.54	1.48	0.04	0.22	101.25	O. nor.	75.7	2.8	77.9
246.308.0	54.38	0.25	1.78	14.23	0.27	28.23	1.67	0.03	0.31	101.16	O. nor.	75.1	3.2	77.6
246.280.8	54.29	0.33	1.39	15.13	0.27	27.77	1.64	0.03	0.10	100.96	O. nor.	73.9	3.1	76.3
246.280.8	54.41	0.35	1.39	14.97	0.31	27.99	1.46	0.05	0.09	101.02	O. nor.	74.4	2.8	76.6
246.280.8	54.41	0.34	1.46	14.91	0.27	27.71	1.69	0.05	0.11	100.94	O. nor.	74.0	3.2	76.5
246.280.8	54.22	0.24	1.58	14.27	0.35	28.21	1.81	0.05	0.27	101.01	O. nor.	74.8	3.4	77.5
246.308.0	54.40	0.36	1.38	15.34	0.29	28.25	1.21	0.03	<D.L.	101.25	O. nor.	74.6	2.3	76.3
246.308.0	54.67	0.31	1.28	15.14	0.30	28.19	1.14	0.06	<D.L.	101.07	O. nor.	74.8	2.2	76.5
246.308.0	54.16	0.37	1.38	15.46	0.31	27.65	1.53	0.02	0.05	100.93	O. nor.	73.5	2.9	75.8
246.212.3	53.59	0.39	1.50	14.06	0.26	28.10	1.31	0.04	0.13	99.38	O. nor.	75.8	2.5	77.8
246.212.3	54.04	0.37	1.37	14.02	0.30	28.41	1.32	0.06	0.09	99.98	O. nor.	76.0	2.5	78.0
246.212.3	53.40	0.32	1.88	13.55	0.28	27.80	1.77	0.03	0.27	99.30	O. nor.	75.5	3.5	78.2

Abbreviations: En: enstatite; Wo: wollastonite; O. nor.: Olivine norite; Leuco: Leucogabbro; <D.L.: below detection limit

Appendix 13 (cont.)

Sample no.	SiO_2	TiO_2	Al_2O_3	FeO	MnO	MgO	CaO	Na_2O	Cr_2O_3	Total	Rock	En	Wo	Mg#
246.293.1	53.92	0.32	1.21	14.97	0.28	27.75	1.63	0.04	0.08	100.19	O. nor.	74.0	3.1	76.4
246.293.1	54.62	0.27	1.29	14.55	0.33	27.65	1.93	0.04	0.22	100.89	O. nor.	74.0	3.7	76.8
246.293.1	53.96	0.36	1.41	14.97	0.32	27.23	1.75	0.03	0.10	100.14	O. nor.	73.5	3.4	76.0
246.219.0	55.29	0.03	0.40	14.97	0.32	28.79	0.88	0.05	<D.L.	100.74	O. nor.	75.7	1.7	77.0
246.219.0	55.20	0.03	0.65	15.62	0.30	28.16	0.70	0.04	<D.L.	100.71	O. nor.	74.9	1.3	75.9
246.219.0	55.02	<D.L.	0.75	15.83	0.36	28.04	0.80	0.04	<D.L.	100.84	O. nor.	74.4	1.5	75.5
246.219.0	54.33	0.06	0.84	17.10	0.29	27.05	0.73	0.05	<D.L.	100.46	O. nor.	72.5	1.4	73.5
246.239.1	54.21	0.28	1.52	14.49	0.29	27.81	1.64	0.07	0.17	100.48	O. nor.	74.6	3.2	77.0
246.239.1	53.74	0.20	1.63	14.64	0.32	27.99	1.35	0.05	0.22	100.14	O. nor.	74.9	2.6	76.9
246.239.1	54.09	0.26	1.57	14.42	0.28	27.85	1.64	0.04	0.20	100.35	O. nor.	74.7	3.2	77.2
246.212.3	53.57	0.35	2.06	13.77	0.26	27.84	1.94	0.02	0.32	100.14	O. nor.	75.0	3.8	78.0
246.212.3	54.69	0.14	0.82	14.90	0.37	28.51	0.79	0.03	0.08	100.33	O. nor.	75.7	1.5	76.9
246.280.8	55.26	0.19	0.75	14.88	0.31	28.77	1.20	<D.L.	0.03	101.40	O. nor.	75.4	2.3	77.1
246.280.8	54.73	0.06	1.01	16.10	0.32	27.90	0.95	0.02	0.04	101.13	O. nor.	73.8	1.8	75.2
246.280.8	54.44	0.13	1.11	15.61	0.30	28.23	0.91	0.02	<D.L.	100.76	O. nor.	74.7	1.7	76.0
246.280.8	54.65	0.21	1.25	15.41	0.27	28.45	1.07	0.03	0.04	101.39	O. nor.	74.8	2.0	76.4
246.280.8	54.61	0.08	0.98	16.08	0.33	27.67	1.22	0.03	0.03	101.04	O. nor.	73.3	2.3	75.0
246.280.8	54.77	0.12	0.93	15.68	0.39	28.17	0.91	0.03	0.05	101.05	O. nor.	74.4	1.7	75.7
246.280.8	54.44	0.26	1.25	15.26	0.32	28.21	1.19	<D.L.	0.03	100.97	O. nor.	74.6	2.3	76.3
246.293.1	55.29	0.09	0.58	15.38	0.32	28.26	0.98	<D.L.	<D.L.	100.89	O. nor.	74.8	1.9	76.2
246.293.1	54.81	0.08	0.58	15.66	0.33	28.43	0.89	0.08	<D.L.	100.86	O. nor.	74.7	1.7	76.0
246.293.1	54.91	0.12	0.64	14.76	0.34	28.31	1.15	0.04	<D.L.	100.27	O. nor.	75.3	2.2	77.0
246.293.1	54.33	0.03	0.86	17.62	0.37	26.18	1.34	0.07	<D.L.	100.81	O. nor.	70.3	2.6	72.2
246.293.1	54.76	0.08	1.13	15.88	0.34	27.66	0.80	<D.L.	0.03	100.67	O. nor.	74.1	1.5	75.2
246.293.1	54.97	0.07	0.90	15.99	0.32	27.81	0.84	<D.L.	<D.L.	100.90	O. nor.	74.0	1.6	75.2
246.293.1	54.87	0.26	1.05	14.69	0.33	28.07	1.37	0.07	0.04	100.74	O. nor.	74.9	2.6	76.9
246.293.1	54.47	0.25	1.28	15.35	0.27	27.84	1.16	<D.L.	0.04	100.65	O. nor.	74.4	2.2	76.1
246.308.0	54.76	0.05	0.90	17.01	0.32	27.12	0.93	0.04	<D.L.	101.12	O. nor.	72.3	1.8	73.6
246.308.0	54.79	0.09	1.04	16.04	0.31	27.53	1.00	<D.L.	<D.L.	100.82	O. nor.	73.5	1.9	75.0
246.308.0	55.11	0.27	0.90	15.07	0.30	28.15	1.34	0.03	<D.L.	101.16	O. nor.	74.6	2.6	76.6
246.308.0	54.55	0.29	1.45	15.10	0.27	27.63	1.90	0.07	0.19	101.46	O. nor.	73.5	3.6	76.2
246.308.0	54.94	0.07	0.93	16.46	0.32	27.88	0.85	0.05	<D.L.	101.50	O. nor.	73.5	1.6	74.8
246.209.0	54.20	0.08	1.32	16.71	0.36	27.00	0.94	<D.L.	<D.L.	100.61	O. nor.	72.5	1.8	73.8
246.209.0	54.34	0.16	1.34	16.43	0.29	27.61	0.91	0.02	<D.L.	101.11	O. nor.	73.3	1.7	74.6
246.209.0	54.45	0.18	1.35	16.35	0.28	27.74	0.91	0.04	<D.L.	101.30	O. nor.	73.5	1.7	74.8
246.209.0	54.28	0.08	1.28	16.55	0.28	27.21	1.13	0.03	<D.L.	100.83	O. nor.	72.6	2.2	74.2

Abbreviations: En: enstatite; Wo: wollastonite; O. nor.: Olivine norite; Leuco: Leucogabbro; <D.L.: below detection limit

Appendix 13 (cont.)

Sample no.	SiO_2	TiO_2	Al_2O_3	FeO	MnO	MgO	CaO	Na_2O	Cr_2O_3	Total	Rock	En	Wo	Mg#
246.209.0	53.83	0.29	1.53	15.58	0.37	27.51	1.28	0.04	0.28	100.70	O. nor.	73.6	2.5	75.5
246.308.0	54.80	0.11	1.04	16.70	0.37	27.65	1.02	0.03	0.06	101.78	O. nor.	72.8	1.9	74.3
246.219.0	54.52	0.31	1.39	14.12	0.36	28.24	1.56	0.04	0.12	100.65	O. nor.	75.3	3.0	77.7
246.219.0	53.93	0.28	2.25	13.13	0.21	28.62	1.64	0.03	0.37	100.46	O. nor.	76.8	3.2	79.3
246.239.1	53.77	0.26	1.61	14.58	0.31	27.36	1.62	0.06	0.26	99.83	O. nor.	74.2	3.2	76.6
246.209.0	54.83	0.29	1.19	15.09	0.28	28.07	1.47	0.07	<D.L.	101.31	O. nor.	74.4	2.8	76.5
246.219.0	51.24	0.65	3.17	7.88	0.21	16.41	19.50	0.34	0.49	99.89	O. nor.	46.9	40.1	78.3
246.219.0	51.25	0.67	3.13	7.33	0.16	16.36	19.76	0.34	0.62	99.61	O. nor.	47.1	40.9	79.6
248.254.0	52.06	0.53	2.43	9.21	0.24	16.43	19.87	0.40	0.06	101.24	O. nor.	45.6	39.7	75.6
248.254.0	51.90	0.52	2.32	9.07	0.18	16.24	20.11	0.35	0.10	100.81	O. nor.	45.3	40.3	75.8
246.209.0	54.01	0.28	1.80	14.57	0.28	28.16	1.45	0.03	0.15	100.75	Leuco.	75.0	2.8	77.2
246.209.0	53.95	0.27	2.31	13.78	0.24	28.30	1.49	0.05	0.37	100.77	Leuco.	76.0	2.9	78.2
246.209.0	53.96	0.28	2.03	14.12	0.27	28.32	1.55	0.06	0.28	100.86	Leuco.	75.5	3.0	77.8
246.209.0	54.00	0.28	1.68	14.75	0.27	27.80	1.75	0.04	0.25	100.82	Leuco.	74.2	3.4	76.7
246.209.0	54.96	0.18	1.27	13.95	0.29	28.10	1.71	0.03	0.23	100.72	Leuco.	75.3	3.3	77.9
246.212.6	54.22	0.28	1.83	13.09	0.28	28.28	1.75	0.05	0.31	100.09	Leuco.	76.4	3.4	79.0
246.212.6	54.23	0.28	1.99	13.03	0.22	28.44	1.61	0.04	0.32	100.16	Leuco.	76.8	3.1	79.3
246.212.6	54.84	0.24	1.46	13.11	0.26	28.81	1.64	<D.L.	0.19	100.55	Leuco.	76.8	3.1	79.3
246.212.6	54.60	0.24	1.27	13.50	0.28	28.27	1.66	<D.L.	0.15	99.97	Leuco.	76.0	3.2	78.5
246.212.6	54.50	0.25	1.56	13.71	0.27	27.98	1.85	<D.L.	0.26	100.39	Leuco.	75.3	3.6	78.1
246.212.6	53.82	0.31	2.33	13.07	0.24	28.21	1.67	<D.L.	0.45	100.10	Leuco.	76.5	3.2	79.1
246.212.6	54.27	0.31	2.04	13.04	0.27	28.30	1.79	<D.L.	0.36	100.39	Leuco.	76.4	3.5	79.1
248.254.0	50.61	0.77	3.16	8.84	0.15	15.56	20.89	0.42	0.09	100.50	Leuco.	43.7	42.1	75.5
248.254.0	52.49	0.48	1.72	8.21	0.26	16.08	21.05	0.40	<D.L.	100.69	Leuco.	44.7	42.1	77.2
248.265.1	53.53	0.26	2.45	14.59	0.24	27.57	1.36	<D.L.	0.19	100.19	Leuco.	74.8	2.6	76.8
248.265.1	53.68	0.26	2.59	14.24	0.23	27.50	1.27	<D.L.	0.26	100.03	Leuco.	75.3	2.5	77.2
248.265.1	53.73	0.26	2.59	14.35	0.20	27.17	1.31	0.06	0.21	99.87	Leuco.	74.9	2.6	76.9
248.265.1	54.57	0.19	1.36	14.13	0.26	27.79	1.38	0.05	0.10	99.83	Leuco.	75.4	2.7	77.5
248.265.1	53.72	0.24	2.31	14.56	0.23	27.11	1.21	0.05	0.23	99.66	Leuco.	74.7	2.4	76.6
246.212.3	54.45	0.29	1.34	13.73	0.30	28.08	1.76	0.03	0.21	100.20	Contact	75.4	3.4	78.1
248.262.0	54.44	0.21	1.66	14.08	0.28	28.14	1.30	0.04	0.07	100.22	Contact	75.8	2.5	77.7
248.262.0	54.49	0.16	1.56	14.55	0.21	28.28	1.32	0.03	0.12	100.74	Contact	75.4	2.5	77.3
248.262.0	54.09	0.17	1.84	14.27	0.25	28.13	1.30	0.05	0.17	100.26	Contact	75.6	2.5	77.5
248.262.0	53.53	0.23	2.43	14.14	0.26	27.86	1.24	0.02	0.26	99.98	Contact	75.6	2.4	77.5
248.262.0	53.76	0.28	1.56	14.50	0.25	27.33	1.68	0.04	0.15	99.55	Contact	74.2	3.3	76.7
248.262.0	53.60	0.27	2.13	14.53	0.23	27.48	1.44	0.05	0.20	99.93	Contact	74.7	2.8	76.8

Abbreviations: En: enstatite; Wo: wollastonite; O. nor.: Olivine norite; Leuco: Leucogabbro; <D.L.: below detection limit

Appendix 14 Electron microprobe analyses in feldspar.

Sample no.	SiO_2	TiO_2	Al_2O_3	FeO	MgO	CaO	Na_2O	K_2O	Total	Pos.	Host rock	An	Or
246.233.5	53.68	0.07	28.72	0.64	0.01	11.57	4.97	0.16	99.81		Olivine norite	55.7	0.9
246.233.5	53.54	0.06	28.86	0.71	0.02	11.55	5.04	0.17	99.95		Olivine norite	55.4	0.9
246.233.5	54.79	0.05	27.92	0.64	0.04	10.74	5.55	0.22	99.93		Olivine norite	51.0	1.2
246.233.5	53.64	0.07	28.69	0.72	0.01	11.67	4.94	0.05	99.78		Olivine norite	56.4	0.3
246.233.5	53.35	0.07	28.53	0.69	0.06	11.50	4.99	0.16	99.36		Olivine norite	55.5	0.9
246.233.5	52.93	0.05	28.97	0.71	0.02	11.92	4.75	0.11	99.47		Olivine norite	57.7	0.6
246.233.5	53.57	0.06	28.41	0.69	0.04	11.29	5.06	0.20	99.32		Olivine norite	54.6	1.2
246.233.5	53.72	0.08	28.79	0.51	0.00	11.45	5.21	0.04	99.80		Olivine norite	54.7	0.2
246.233.5	52.95	0.07	28.72	0.86	0.27	11.47	4.86	0.07	99.27		Olivine norite	56.4	0.4
246.233.5	54.97	0.05	27.75	0.61	0.04	10.43	5.67	0.24	99.75		Olivine norite	49.8	1.4
246.233.5	53.76	0.07	28.29	0.65	0.03	11.32	5.19	0.19	99.50		Olivine norite	54.0	1.1
246.233.5	50.03	0.03	30.71	0.68	0.03	14.32	3.30	0.07	99.19		Olivine norite	70.3	0.4
246.219.0	49.76	0.05	31.63	0.54	n.a.	14.33	3.34	0.06	99.71	core	Olivine norite	70.1	0.3
246.219.0	58.48	0.03	25.59	0.44	n.a.	7.33	7.53	0.14	99.54		Olivine norite	34.7	0.8
246.219.0	61.59	<D.L.	23.48	0.43	n.a.	4.72	9.04	0.12	99.39	rim	Olivine norite	22.3	0.7
246.219.0	62.21	<D.L.	23.34	0.58	n.a.	4.56	9.32	0.03	100.04	rim	Olivine norite	21.2	0.2
246.219.0	52.43	0.02	30.06	0.42	n.a.	12.24	4.60	0.03	99.82		Olivine norite	59.4	0.2
246.219.0	49.86	<D.L.	31.18	0.74	n.a.	14.04	3.49	0.03	99.34	core	Olivine norite	68.9	0.2
246.219.0	50.94	0.05	30.62	0.73	n.a.	13.36	3.92	0.10	99.73		Olivine norite	64.9	0.6
246.219.0	55.42	0.04	27.64	0.50	n.a.	9.49	6.20	0.12	99.42	rim	Olivine norite	45.5	0.7
246.219.0	62.45	<D.L.	22.94	0.50	n.a.	4.25	9.54	0.07	99.75		Olivine norite	19.7	0.4
246.219.0	54.31	0.07	28.60	0.64	n.a.	10.51	5.61	0.10	99.85		Olivine norite	50.6	0.6
246.219.0	52.39	0.04	29.82	0.65	n.a.	12.22	4.61	0.11	99.83		Olivine norite	59.1	0.6
246.219.0	64.02	<0.02	21.93	0.55	n.a.	2.44	10.11	0.36	99.41	rim	Olivine norite	11.5	2.0
246.219.0	59.28	<0.02	25.27	0.36	n.a.	6.75	7.88	0.22	99.76		Olivine norite	31.7	1.2
246.219.0	52.06	0.05	29.77	0.66	n.a.	12.33	4.52	0.10	99.48	core	Olivine norite	59.8	0.6
246.219.0	62.51	0.04	23.05	0.46	n.a.	4.39	9.38	0.17	99.99	rim	Olivine norite	20.4	0.9
246.219.0	50.11	0.02	31.16	0.52	n.a.	13.91	3.62	0.04	99.37	core	Olivine norite	67.8	0.2
246.219.0	50.04	0.04	31.46	0.81	n.a.	14.03	3.47	0.07	99.92	core	Olivine norite	68.8	0.4
246.219.0	52.10	0.04	29.46	0.73	n.a.	12.22	4.61	0.11	99.26	core	Olivine norite	59.0	0.6
246.219.0	60.43	<D.L.	24.14	0.39	n.a.	5.73	8.44	0.12	99.25	core	Olivine norite	27.1	0.7
246.219.0	67.54	0.02	19.95	0.25	n.a.	0.58	11.81	0.07	100.23		Olivine norite	2.6	0.4
246.219.0	50.76	0.05	30.86	0.47	n.a.	13.54	3.87	0.03	99.58	core	Olivine norite	65.8	0.2
246.219.0	49.07	0.05	31.90	0.53	n.a.	14.94	3.05	<D.L.	99.53		Olivine norite	73.0	0.0

<D.L.: below detection limit; Pos: Crystal position; An: Anorthite; Or: Orthose; n.a.: not analyzed

Appendix 14 (cont.)

Sample no.	SiO_2	TiO_2	Al_2O_3	FeO	MgO	CaO	Na_2O	K_2O	Total	Pos.	Host rock	An	Or
246.219.0	50.98	0.03	30.83	0.39	n.a.	13.25	4.02	<D.L.	99.52	rim	Olivine norite	64.5	0.0
246.219.0	50.67	0.02	30.79	0.66	n.a.	13.62	3.78	0.04	99.58	core	Olivine norite	66.4	0.2
246.219.0	48.75	0.04	31.91	0.68	n.a.	15.00	2.92	0.02	99.31		Olivine norite	73.9	0.1
246.219.0	54.58	0.05	28.39	0.41	n.a.	10.46	5.76	0.05	99.70	rim	Olivine norite	49.9	0.3
246.293.1	51.10	0.06	30.28	0.77	n.a.	13.18	4.09	0.16	99.65	core	Olivine norite	63.4	0.9
246.239.1	56.45	0.04	27.12	0.54	n.a.	9.22	6.35	0.10	99.81	rim	Olivine norite	44.3	0.5
246.239.1	49.74	0.04	31.11	0.81	n.a.	14.24	3.37	0.12	99.43		Olivine norite	69.6	0.7
246.239.1	51.08	0.04	30.23	0.78	n.a.	13.19	3.97	0.17	99.47	core	Olivine norite	64.1	1.0
246.239.1	51.63	0.06	29.74	0.67	n.a.	12.71	4.09	0.17	99.08	core	Olivine norite	62.6	1.0
246.239.1	61.01	<D.L.	23.92	0.30	n.a.	5.39	8.32	0.61	99.56	rim	Olivine norite	25.4	3.4
246.239.1	51.93	0.06	29.54	0.93	n.a.	12.45	4.37	0.13	99.40		Olivine norite	60.7	0.8
246.239.1	54.70	0.05	27.84	0.48	n.a.	10.28	5.73	0.26	99.34		Olivine norite	49.0	1.5
246.212.3	52.76	0.07	29.04	0.71	n.a.	11.70	4.84	0.14	99.24		Olivine norite	56.7	0.8
246.212.3	50.30	0.05	30.79	0.60	n.a.	13.88	3.56	0.11	99.29	core	Olivine norite	67.8	0.6
246.212.3	48.94	0.03	31.44	0.84	n.a.	14.80	2.96	0.11	99.11		Olivine norite	73.0	0.6
246.212.3	50.18	0.04	30.88	0.62	n.a.	13.71	3.60	0.11	99.13	core	Olivine norite	67.4	0.6
246.212.3	48.88	<D.L.	31.86	0.75	n.a.	14.91	2.93	0.08	99.41	core	Olivine norite	73.5	0.5
246.212.3	60.92	<D.L.	24.08	0.36	n.a.	5.56	8.35	0.16	99.44	rim	Olivine norite	26.7	0.9
246.293.1	48.58	0.02	32.39	0.60	n.a.	16.01	2.79	0.03	100.41	core	Olivine norite	75.9	0.2
246.293.1	51.75	0.05	29.85	0.79	n.a.	13.16	4.31	0.15	100.06	rim	Olivine norite	62.3	0.8
246.293.1	48.40	0.05	32.23	0.73	n.a.	16.15	2.64	0.03	100.22	core	Olivine norite	77.1	0.2
246.293.1	52.93	0.07	29.45	0.74	n.a.	12.64	4.69	0.08	100.60	core	Olivine norite	59.6	0.4
246.293.1	49.40	0.05	31.52	0.77	n.a.	15.16	3.07	0.09	100.07	core	Olivine norite	72.8	0.5
246.293.1	53.01	0.03	29.56	0.42	n.a.	12.35	4.86	0.03	100.26	core	Olivine norite	58.3	0.2
246.293.1	55.48	0.05	27.17	0.57	n.a.	9.61	6.33	0.07	99.27	rim	Olivine norite	45.4	0.4
246.293.1	53.04	0.04	28.86	0.76	n.a.	12.15	5.01	0.05	99.90	core	Olivine norite	57.1	0.3
246.293.1	59.83	0.03	24.62	0.47	n.a.	6.32	8.13	0.03	99.43	rim	Olivine norite	30.0	0.2
246.293.1	50.01	0.04	31.33	0.81	n.a.	14.98	3.41	0.08	100.66	core	Olivine norite	70.5	0.5
246.293.1	48.42	0.03	32.58	0.70	n.a.	16.28	2.55	0.03	100.58	core	Olivine norite	77.8	0.1
246.293.1	55.37	0.04	27.87	0.53	n.a.	10.38	5.92	0.04	100.15	core	Olivine norite	49.1	0.2
246.293.1	62.86	<0.02	23.25	0.34	n.a.	4.59	9.31	0.12	100.48	core	Olivine norite	21.3	0.7
246.293.1	48.23	0.04	32.39	0.81	n.a.	16.17	2.57	0.06	100.27	core	Olivine norite	77.4	0.4
246.293.1	51.97	0.06	30.18	0.60	n.a.	13.33	4.29	0.11	100.55	core	Olivine norite	62.8	0.6
246.293.1	49.34	0.05	31.91	0.65	n.a.	15.60	2.96	0.11	100.62		Olivine norite	73.9	0.6

<D.L.: below detection limit; Pos: Crystal position; An: Anorthite; Or: Orthose; n.a.: not analyzed

Appendix 14 (cont.)

Sample no.	SiO_2	TiO_2	Al_2O_3	FeO	MgO	CaO	Na_2O	K_2O	Total	Pos.	Host rock	An	Or
246.293.1	53.53	0.05	29.21	0.55	n.a.	11.99	4.90	0.20	100.44		Olivine norite	56.8	1.1
246.308.0	48.63	0.03	32.29	0.75	n.a.	15.81	2.65	0.08	100.23	core	Olivine norite	76.4	0.4
246.308.0	48.42	0.04	32.24	0.48	n.a.	15.81	2.80	0.02	99.81	rim	Olivine norite	75.6	0.1
246.308.0	48.71	0.04	32.00	0.65	n.a.	15.71	2.93	0.01	100.05	core	Olivine norite	74.7	0.1
246.308.0	48.77	0.03	32.49	0.88	n.a.	16.03	2.61	0.04	100.86	core	Olivine norite	77.1	0.2
246.308.0	53.59	0.04	29.04	0.68	n.a.	11.99	5.05	0.07	100.45	rim	Olivine norite	56.5	0.4
246.308.0	58.89	<D.L.	25.80	0.42	n.a.	7.87	7.38	0.21	100.58	core	Olivine norite	36.6	1.2
246.308.0	48.65	0.04	32.29	0.47	n.a.	16.03	2.67	<D.L.	100.15	core	Olivine norite	76.8	0.0
246.308.0	48.65	0.02	32.28	1.04	n.a.	16.05	2.64	0.10	100.78	core	Olivine norite	76.7	0.5
246.308.0	49.05	0.05	32.30	0.83	n.a.	15.68	2.87	0.07	100.85	core	Olivine norite	74.8	0.4
246.308.0	53.06	0.04	29.52	0.65	n.a.	12.29	4.80	0.07	100.43	core	Olivine norite	58.4	0.4
246.308.0	49.33	0.06	31.83	0.78	n.a.	15.05	3.13	0.02	100.20		Olivine norite	72.6	0.1
246.308.0	55.35	0.05	28.21	0.56	n.a.	10.59	5.99	0.01	100.76	rim	Olivine norite	49.4	0.1
246.308.0	50.63	0.05	31.02	0.89	n.a.	14.27	3.65	0.10	100.61	core	Olivine norite	68.0	0.5
246.209.0	47.78	0.05	33.09	0.75	n.a.	16.68	2.28	<D.L.	100.63	core	Olivine norite	80.2	0.0
246.209.0	47.11	0.05	33.41	0.75	n.a.	17.38	2.05	<D.L.	100.74	core	Olivine norite	82.4	0.0
246.209.0	50.64	0.05	30.62	0.87	n.a.	13.68	3.57	0.39	99.83		Olivine norite	66.4	2.3
246.209.0	51.92	0.05	29.70	0.59	n.a.	13.16	4.30	0.18	99.90	core	Olivine norite	62.2	1.0
246.209.0	56.82	0.05	26.99	0.52	n.a.	9.19	6.49	0.14	100.20	rim	Olivine norite	43.6	0.8
246.209.0	53.43	0.07	29.10	0.56	n.a.	12.03	4.76	0.24	100.18		Olivine norite	57.5	1.4
246.280.8	49.43	0.04	31.33	0.84	n.a.	15.17	3.15	0.13	100.09	core	Olivine norite	72.2	0.7
246.280.8	48.23	0.05	32.11	0.82	n.a.	16.37	2.55	0.03	100.16	core	Olivine norite	77.8	0.2
246.280.8	49.07	0.02	31.94	0.73	n.a.	15.59	2.91	0.04	100.32	core	Olivine norite	74.5	0.3
246.280.8	48.30	0.04	32.01	0.70	n.a.	16.06	2.69	0.03	99.83	core	Olivine norite	76.6	0.2
246.280.8	48.77	0.04	31.90	0.72	n.a.	15.66	2.91	0.06	100.06	core	Olivine norite	74.6	0.3
246.280.8	48.76	0.03	32.47	0.62	n.a.	15.88	2.82	0.03	100.61	core	Olivine norite	75.5	0.2
246.280.8	50.24	0.05	31.05	0.60	n.a.	14.51	3.51	0.06	100.04	core	Olivine norite	69.3	0.4
246.280.8	50.82	0.05	30.78	0.63	n.a.	14.05	3.89	<D.L.	100.22	core	Olivine norite	66.6	0.0
246.280.8	49.54	0.03	31.58	0.65	n.a.	15.32	3.10	0.06	100.27	core	Olivine norite	73.0	0.4
246.280.8	59.02	0.02	23.73	0.94	n.a.	5.93	7.75	0.16	97.55	rim	Olivine norite	29.4	0.9
246.280.8	49.71	0.04	31.65	0.41	n.a.	15.16	3.19	0.03	100.17	core	Olivine norite	72.3	0.1
246.280.8	53.09	0.06	29.39	0.40	n.a.	12.24	4.88	0.06	100.12		Olivine norite	57.9	0.3
246.280.8	57.86	0.02	25.82	1.29	n.a.	7.61	7.15	0.03	99.78	rim	Olivine norite	37.0	0.2
246.280.8	48.42	0.03	32.42	1.04	n.a.	16.10	2.59	0.03	100.64	core	Olivine norite	77.3	0.2

<D.L.: below detection limit; Pos: Crystal position; An: Anorthite; Or: Orthose; n.a.: not analyzed

Appendix 14 (cont.)

Sample no.	SiO_2	TiO_2	Al_2O_3	FeO	MgO	CaO	Na_2O	K_2O	Total	Pos.	Host rock	An	Or
246.280.8	49.21	0.03	31.91	0.80	n.a.	15.60	2.94	0.05	100.55	core	Olivine norite	74.3	0.3
246.290.7	48.36	0.04	31.66	0.61	n.a.	15.76	2.51	0.08	99.02	core	Olivine norite	77.3	0.4
246.290.7	52.78	0.05	29.07	0.59	n.a.	12.27	4.62	0.21	99.59	rim	Olivine norite	58.7	1.2
246.290.7	48.67	0.04	31.79	0.64	n.a.	15.73	2.49	0.06	99.43	core	Olivine norite	77.4	0.3
246.290.7	49.40	0.05	31.22	0.61	n.a.	14.92	2.90	0.10	99.20	core	Olivine norite	73.6	0.6
246.290.7	48.56	0.04	31.24	0.72	n.a.	15.38	2.72	0.10	98.76	core	Olivine norite	75.3	0.6
246.290.7	48.50	0.04	31.49	0.68	n.a.	15.75	2.53	0.09	99.07	core	Olivine norite	77.1	0.5
246.290.7	48.78	0.05	31.46	0.54	n.a.	15.42	2.70	0.11	99.06	core	Olivine norite	75.4	0.6
246.290.7	53.96	0.07	28.16	0.57	n.a.	11.37	4.96	0.27	99.36	rim	Olivine norite	55.0	1.6
246.290.7	49.07	0.04	31.53	0.52	n.a.	15.34	2.82	<D.L.	99.32	core	Olivine norite	75.0	0.0
246.290.7	48.53	<D.L.	31.86	0.69	n.a.	15.65	2.68	0.03	99.44	core	Olivine norite	76.2	0.2
246.290.7	53.58	0.08	28.63	0.64	n.a.	11.72	4.92	0.10	99.66	rim	Olivine norite	56.5	0.6
246.290.7	49.41	<D.L.	31.20	0.61	n.a.	14.83	3.07	0.11	99.23	core	Olivine norite	72.3	0.6
246.290.7	56.20	<D.L.	27.16	0.41	n.a.	9.67	6.16	0.17	99.78	rim	Olivine norite	46.0	0.9
246.290.7	48.27	0.06	31.77	0.59	n.a.	15.80	2.60	0.04	99.13	core	Olivine norite	76.9	0.2
246.290.7	49.30	0.04	30.95	0.62	n.a.	14.95	2.98	0.08	98.92	core	Olivine norite	73.1	0.5
246.290.7	48.77	0.05	31.65	0.75	n.a.	15.57	2.69	<D.L.	99.48	core	Olivine norite	76.2	0.0
246.290.7	53.60	0.10	28.48	0.70	n.a.	11.71	5.00	0.05	99.63	rim	Olivine norite	56.3	0.3
246.290.7	50.25	0.05	30.38	0.54	n.a.	14.37	3.48	0.05	99.13	core	Olivine norite	69.3	0.3
246.290.7	57.89	<D.L.	25.65	0.41	n.a.	8.36	6.60	0.47	99.38	core	Olivine norite	40.1	2.7
246.290.7	48.65	<D.L.	31.49	0.65	n.a.	15.68	2.51	0.04	99.01	core	Olivine norite	77.3	0.2
246.290.7	49.09	<D.L.	31.34	0.75	n.a.	15.27	2.80	0.07	99.32	core	Olivine norite	74.8	0.4
246.290.7	48.62	0.04	31.59	0.61	n.a.	15.66	2.58	0.05	99.15	core	Olivine norite	76.8	0.3
246.290.7	49.00	0.04	31.40	0.58	n.a.	15.22	2.90	0.03	99.17	core	Olivine norite	74.2	0.2
246.290.7	57.53	<D.L.	25.76	0.39	n.a.	8.39	6.78	0.49	99.35		Olivine norite	39.5	2.8
246.290.7	50.30	0.05	30.69	0.84	n.a.	14.43	3.32	0.10	99.73	core	Olivine norite	70.2	0.6
246.290.7	48.86	0.04	31.46	0.71	n.a.	15.38	2.78	0.07	99.30	core	Olivine norite	75.0	0.4
246.290.7	48.39	<D.L.	31.62	0.70	n.a.	15.70	2.61	<D.L.	99.02	core	Olivine norite	76.9	0.0
246.290.7	48.41	<D.L.	31.90	0.71	n.a.	15.84	2.57	0.08	99.50	core	Olivine norite	77.0	0.5
246.290.7	52.46	0.05	29.13	0.58	n.a.	12.62	4.45	0.04	99.33		Olivine norite	60.9	0.3
246.290.7	49.57	<D.L.	30.48	1.01	n.a.	14.21	3.08	0.05	98.40		Olivine norite	71.6	0.3
246.290.7	53.49	0.04	28.21	0.58	n.a.	11.58	4.96	0.16	99.03		Olivine norite	55.8	0.9
246.300.9	53.57	0.09	29.10	0.45	n.a.	11.97	4.88	0.06	100.12		Olivine norite	57.3	0.4
246.300.9	56.55	0.03	26.63	0.55	n.a.	9.42	6.41	0.04	99.64		Olivine norite	44.7	0.3

<D.L.: below detection limit; Pos: Crystal position; An: Anorthite; Or: Orthose; n.a.: not analyzed

Appendix 14 (cont.)

Sample no.	SiO_2	TiO_2	Al_2O_3	FeO	MgO	CaO	Na_2O	K_2O	Total	Pos.	Host rock	An	Or
246.300.9	55.82	0.04	27.37	0.35	n.a.	10.10	5.86	0.19	99.74		Olivine norite	48.3	1.1
246.300.9	62.60	<D.L.	22.98	0.36	n.a.	4.83	8.69	0.67	100.13		Olivine norite	22.6	3.7
246.300.9	48.59	<D.L.	31.47	0.69	n.a.	15.55	2.56	0.08	98.95		Olivine norite	76.6	0.5
246.300.9	48.60	<D.L.	31.72	0.52	n.a.	15.66	2.75	0.06	99.32	core	Olivine norite	75.6	0.4
246.300.9	52.41	0.08	29.05	0.69	n.a.	12.42	4.47	0.10	99.21	rim	Olivine norite	60.2	0.6
246.300.9	50.17	<D.L.	30.82	0.44	n.a.	14.42	3.43	<D.L.	99.28		Olivine norite	69.9	0.0
246.300.9	48.42	<D.L.	31.67	0.67	n.a.	15.59	2.62	0.09	99.06	core	Olivine norite	76.3	0.5
246.300.9	52.87	0.06	29.10	0.64	n.a.	12.35	4.50	0.20	99.72	rim	Olivine norite	59.6	1.1
246.300.9	48.94	<D.L.	31.72	0.69	n.a.	15.32	2.79	0.06	99.52	core	Olivine norite	75.0	0.4
246.300.9	49.13	0.03	31.42	0.55	n.a.	15.34	2.81	0.04	99.32	core	Olivine norite	74.9	0.2
246.300.9	49.23	0.06	31.62	0.56	n.a.	15.08	2.96	<D.L.	99.52	core	Olivine norite	73.8	0.0
246.300.9	58.44	0.05	25.86	0.58	n.a.	8.13	7.25	0.05	100.35	rim	Olivine norite	38.1	0.3
246.300.9	50.08	0.05	30.63	0.66	n.a.	14.23	3.32	0.11	99.08	core	Olivine norite	69.9	0.6
246.300.9	49.56	<D.L.	31.54	0.68	n.a.	14.89	3.13	0.05	99.85	core	Olivine norite	72.2	0.3
246.300.9	49.22	<D.L.	31.52	0.56	n.a.	15.22	2.90	0.04	99.46	core	Olivine norite	74.2	0.2
246.300.9	48.69	0.04	31.53	0.67	n.a.	15.62	2.66	0.07	99.29	core	Olivine norite	76.1	0.4
246.300.9	49.10	0.04	31.67	0.40	n.a.	15.37	2.74	<D.L.	99.31	core	Olivine norite	75.6	0.0
246.300.9	48.95	<D.L.	31.53	0.66	n.a.	15.38	2.70	0.07	99.29	core	Olivine norite	75.6	0.4
246.300.9	49.24	<D.L.	31.51	0.46	n.a.	15.15	2.87	0.07	99.30	core	Olivine norite	74.1	0.4
246.300.9	48.47	0.06	31.67	0.59	n.a.	15.66	2.60	<D.L.	99.04	core	Olivine norite	76.9	0.0
246.300.9	53.60	0.03	28.32	0.56	n.a.	11.77	5.05	0.10	99.43	rim	Olivine norite	56.0	0.5
246.300.9	50.22	0.07	30.73	0.46	n.a.	14.29	3.41	0.05	99.24	core	Olivine norite	69.6	0.3
246.300.9	49.56	0.05	31.35	0.42	n.a.	14.87	3.12	0.05	99.41	core	Olivine norite	72.3	0.3
246.300.9	49.51	0.05	31.32	0.47	n.a.	15.06	3.00	0.05	99.46	core	Olivine norite	73.3	0.3
246.300.9	53.49	0.08	28.50	0.45	n.a.	11.74	4.85	0.11	99.22	rim	Olivine norite	56.9	0.6
246.300.9	49.07	0.06	31.55	0.53	n.a.	15.20	2.78	0.04	99.24	core	Olivine norite	74.9	0.2
246.300.9	54.09	0.04	27.81	0.50	n.a.	10.96	5.31	0.06	98.77	rim	Olivine norite	53.1	0.4
246.300.9	50.49	0.05	30.81	0.38	n.a.	14.28	3.43	<D.L.	99.45	core	Olivine norite	69.7	0.0
246.300.9	53.96	0.06	28.27	0.51	n.a.	11.38	5.10	0.16	99.44	rim	Olivine norite	54.7	0.9
246.300.9	49.13	0.06	31.93	0.54	n.a.	15.53	2.72	<D.L.	99.90	core	Olivine norite	75.9	0.0
246.300.9	48.78	0.04	31.64	0.76	n.a.	15.29	2.77	0.04	99.32	core	Olivine norite	75.1	0.3
246.300.9	48.59	0.03	31.69	0.67	n.a.	15.56	2.70	<D.L.	99.24	core	Olivine norite	76.1	0.0
246.300.9	48.58	0.05	32.10	0.59	n.a.	15.43	2.70	0.08	99.52	core	Olivine norite	75.6	0.5
246.300.9	48.66	0.05	32.02	0.55	n.a.	15.69	2.60	<D.L.	99.57	core	Olivine norite	76.9	0.0

<D.L.: below detection limit; Pos: Crystal position; An: Anorthite; Or: Orthose; n.a.: not analyzed

Appendix 14 (cont.)

Sample no.	SiO_2	TiO_2	Al_2O_3	FeO	MgO	CaO	Na_2O	K_2O	Total	Pos.	Host rock	An	Or
246.300.9	49.69	<D.L.	31.52	0.55	n.a.	14.94	3.06	0.03	99.80	core	Olivine norite	72.8	0.2
246.300.9	48.84	<D.L.	31.82	0.62	n.a.	15.72	2.65	<D.L.	99.65	core	Olivine norite	76.6	0.0
246.300.9	50.44	0.05	30.70	0.40	n.a.	14.23	3.44	<D.L.	99.25	core	Olivine norite	69.6	0.0
246.300.9	48.46	<D.L.	31.84	0.90	n.a.	15.76	2.62	<D.L.	99.58	core	Olivine norite	76.9	0.0
246.300.9	48.60	<D.L.	31.34	0.70	n.a.	15.35	2.76	0.06	98.81	core	Olivine norite	75.2	0.3
248.213.2	53.15	0.04	29.05	0.81	0.04	11.80	4.89	0.16	99.93		Leucogabbro	56.6	0.9
248.213.2	55.71	0.03	27.45	0.59	0.07	9.96	5.96	0.34	100.10		Leucogabbro	47.1	1.9
248.213.2	53.97	0.04	28.34	0.72	0.08	11.29	5.16	0.26	99.84		Leucogabbro	53.9	1.5
248.213.2	53.92	0.05	28.49	0.77	0.07	11.29	5.26	0.24	100.09		Leucogabbro	53.5	1.4
248.213.2	53.66	0.05	28.83	0.80	0.07	11.62	4.99	0.23	100.25		Leucogabbro	55.5	1.3
248.213.2	53.76	0.06	28.68	0.74	0.08	11.40	5.14	0.25	100.12		Leucogabbro	54.3	1.4
248.213.2	53.37	0.05	28.56	0.79	0.08	11.66	4.91	0.24	99.67		Leucogabbro	56.0	1.3
248.213.2	54.86	0.03	28.42	0.66	0.08	10.91	5.44	0.28	100.66		Leucogabbro	51.8	1.6
248.213.2	53.42	0.06	28.64	0.79	0.08	11.68	4.87	0.23	99.75		Leucogabbro	56.3	1.3
248.213.2	53.44	0.04	28.73	0.76	0.07	11.60	5.03	0.25	99.91		Leucogabbro	55.3	1.4
248.213.2	54.24	0.04	28.50	0.67	0.08	11.16	5.24	0.23	100.17		Leucogabbro	53.4	1.3
248.213.2	53.93	0.04	28.26	0.71	0.06	11.27	5.24	0.30	99.80		Leucogabbro	53.4	1.7
248.213.2	53.96	0.04	28.44	0.75	0.07	11.35	5.09	0.26	99.96		Leucogabbro	54.4	1.5
248.213.2	53.75	0.02	28.45	0.71	0.06	11.30	5.11	0.23	99.62		Leucogabbro	54.3	1.3
248.213.2	53.45	0.04	29.06	0.78	0.08	11.90	4.78	0.22	100.31		Leucogabbro	57.2	1.3
248.213.2	53.31	0.05	28.57	0.76	0.09	11.79	4.99	0.21	99.77		Leucogabbro	55.9	1.2
248.213.2	54.13	0.05	28.30	0.71	0.10	11.31	5.11	0.24	99.96		Leucogabbro	54.3	1.4
248.213.2	54.04	0.06	28.37	0.70	0.07	11.13	5.24	0.21	99.84		Leucogabbro	53.3	1.2
248.213.2	54.27	0.05	28.29	0.69	0.07	10.93	5.29	0.26	99.85		Leucogabbro	52.5	1.5
248.213.2	53.65	0.04	28.62	0.74	0.07	11.52	5.00	0.25	99.89		Leucogabbro	55.2	1.4
248.213.2	54.45	0.05	28.27	0.63	0.07	10.99	5.35	0.12	99.94		Leucogabbro	52.8	0.7
248.213.2	53.41	0.02	28.52	0.84	0.06	11.51	5.00	0.27	99.63		Leucogabbro	55.2	1.5
248.213.2	53.15	0.05	28.50	0.81	0.11	11.79	4.82	0.24	99.47		Leucogabbro	56.7	1.4
248.213.2	52.78	0.05	28.80	0.79	0.08	11.86	4.76	0.23	99.35		Leucogabbro	57.2	1.3
248.213.2	53.02	0.05	28.89	0.77	0.09	11.89	4.87	0.18	99.75		Leucogabbro	56.9	1.0
248.213.2	53.35	0.04	28.54	0.79	0.09	11.68	4.85	0.24	99.58		Leucogabbro	56.3	1.4
248.213.2	53.50	0.05	28.48	0.74	0.08	11.37	5.07	0.24	99.53		Leucogabbro	54.6	1.4
248.213.2	54.24	0.04	28.51	0.73	0.07	11.04	5.29	0.26	100.20		Leucogabbro	52.8	1.5
248.213.2	53.82	0.04	28.68	0.77	0.07	11.41	5.13	0.25	100.16		Leucogabbro	54.4	1.4

<D.L.: below detection limit; Pos: Crystal position; An: Anorthite; Or: Orthose; n.a.: not analyzed

Appendix 14 (cont.)

Sample no.	SiO_2	TiO_2	Al_2O_3	FeO	MgO	CaO	Na_2O	K_2O	Total	Pos.	Host rock	An	Or
248.213.2	53.47	0.05	28.62	0.81	0.11	11.53	5.11	0.14	99.84		Leucogabbro	55.1	0.8
248.213.2	53.84	0.03	28.62	0.87	0.12	11.61	4.99	0.18	100.25		Leucogabbro	55.7	1.0
246.230.2	54.39	0.04	28.37	0.55	0.08	10.96	5.32	0.25	99.97		Leucogabbro	52.5	1.4
246.230.2	54.53	0.06	28.55	0.48	0.06	10.76	5.37	0.23	100.04		Leucogabbro	51.9	1.3
246.230.2	54.83	0.06	28.33	0.52	0.08	10.59	5.53	0.29	100.24		Leucogabbro	50.5	1.7
246.230.2	53.33	0.06	28.95	0.57	0.07	11.55	5.04	0.17	99.74		Leucogabbro	55.4	1.0
246.230.2	54.17	0.08	28.40	0.58	0.06	11.00	5.26	0.27	99.81		Leucogabbro	52.8	1.5
246.230.2	54.20	0.06	28.71	0.56	0.07	11.11	5.25	0.24	100.19		Leucogabbro	53.2	1.4
246.230.2	54.24	0.03	28.59	0.49	0.06	10.92	5.36	0.18	99.87		Leucogabbro	52.4	1.0
246.230.2	51.26	0.04	31.02	0.44	0.01	13.55	4.00	0.03	100.35		Leucogabbro	65.1	0.2
246.230.2	53.22	0.05	29.17	0.57	0.03	11.86	4.86	0.14	99.88		Leucogabbro	57.0	0.8
246.230.2	49.79	0.05	31.16	0.72	0.01	14.57	3.25	0.07	99.63		Leucogabbro	70.9	0.4
246.230.2	52.30	0.07	29.52	0.62	0.03	12.31	4.48	0.11	99.45		Leucogabbro	59.9	0.6
246.230.2	50.35	0.05	30.66	0.62	0.05	13.88	3.59	0.12	99.31		Leucogabbro	67.7	0.7
246.230.2	52.94	0.04	29.55	0.61	0.04	12.02	4.78	0.05	100.02		Leucogabbro	58.0	0.3
246.230.2	51.24	0.03	30.49	0.70	0.07	13.32	3.96	0.14	99.94		Leucogabbro	64.5	0.8
246.230.2	51.35	0.06	30.43	0.63	0.06	13.42	3.97	0.14	100.05		Leucogabbro	64.6	0.8
246.230.2	51.24	0.05	30.42	0.73	0.05	13.53	4.00	0.13	100.14		Leucogabbro	64.7	0.7
246.230.2	49.85	0.00	31.94	0.28	0.01	14.73	3.31	0.01	100.13		Leucogabbro	71.0	0.0
246.230.2	51.14	0.06	30.60	0.61	0.06	13.53	3.86	0.07	99.93		Leucogabbro	65.7	0.4
246.230.2	51.38	0.05	30.51	0.59	0.02	13.33	4.02	0.01	99.91		Leucogabbro	64.7	0.1
246.230.2	50.98	0.05	30.87	0.71	0.06	13.81	3.75	0.04	100.28		Leucogabbro	66.9	0.3
246.230.2	52.15	0.05	30.15	0.60	0.05	12.83	4.38	0.08	100.29		Leucogabbro	61.5	0.5
246.230.2	55.17	0.04	27.53	0.50	0.07	10.09	5.90	0.25	99.55		Leucogabbro	47.9	1.4
246.230.2	51.21	0.05	30.21	0.75	0.06	13.35	3.91	0.15	99.71		Leucogabbro	64.8	0.9
246.230.2	52.19	0.05	30.21	0.50	0.02	12.80	4.41	0.05	100.22		Leucogabbro	61.4	0.3
246.230.2	51.77	0.05	30.29	0.55	0.02	13.07	4.18	0.04	99.97		Leucogabbro	63.2	0.2
246.230.2	50.97	0.06	30.60	0.68	0.04	13.65	3.84	0.10	99.94		Leucogabbro	65.9	0.6
246.233.5	53.72	0.07	28.65	0.59	0.07	11.57	4.91	0.23	99.80	core	Leucogabbro	55.8	1.3
246.233.5	54.18	0.04	28.67	0.48	0.02	11.19	5.12	0.16	99.87		Leucogabbro	54.2	0.9
246.233.5	53.81	0.05	28.53	0.69	0.06	11.31	5.11	0.20	99.77		Leucogabbro	54.4	1.2
246.233.5	53.45	0.06	28.60	0.67	0.07	11.57	4.95	0.23	99.59		Leucogabbro	55.7	1.3
246.233.5	48.96	0.02	32.27	0.52	0.02	15.59	2.74	0.03	100.13		Leucogabbro	75.7	0.2
246.233.5	54.68	0.04	27.93	0.59	0.02	10.62	5.53	0.20	99.62		Leucogabbro	50.9	1.2

<D.L.: below detection limit; Pos: Crystal position; An: Anorthite; Or: Orthose; n.a.: not analyzed

Appendix 14 (cont.)

Sample no.	SiO_2	TiO_2	Al_2O_3	FeO	MgO	CaO	Na_2O	K_2O	Total	Pos.	Host rock	An	Or
246.233.5	54.97	0.05	27.73	0.50	0.05	10.41	5.48	0.28	99.46		Leucogabbro	50.4	1.6
246.233.5	54.27	0.06	28.82	0.44	0.02	11.28	5.31	0.03	100.22		Leucogabbro	53.9	0.2
246.233.5	54.07	0.05	28.27	0.54	0.07	11.16	5.18	0.29	99.63		Leucogabbro	53.4	1.7
246.233.5	53.95	0.05	28.43	0.57	0.07	11.33	4.96	0.24	99.60		Leucogabbro	55.0	1.4
246.233.5	54.68	0.04	27.84	0.49	0.04	10.59	5.44	0.25	99.37	core	Leucogabbro	51.1	1.5
246.233.5	54.28	0.03	28.43	0.57	0.05	11.16	5.04	0.25	99.81	core	Leucogabbro	54.2	1.4
246.233.5	54.07	0.06	28.51	0.63	0.06	11.32	5.21	0.22	100.08	core	Leucogabbro	53.9	1.3
246.233.5	54.92	0.03	28.00	0.52	0.07	10.44	5.56	0.28	99.81	core	Leucogabbro	50.1	1.6
246.233.5	53.81	0.07	28.61	0.55	0.04	11.49	5.10	0.18	99.85	core	Leucogabbro	54.9	1.0
246.233.5	53.51	0.06	28.32	0.64	0.05	11.49	4.97	0.19	99.22		Leucogabbro	55.5	1.1
246.233.5	54.11	0.05	28.54	0.68	0.03	11.24	5.20	0.22	100.06		Leucogabbro	53.8	1.2
246.233.5	53.78	0.07	28.33	0.49	0.07	11.16	5.23	0.23	99.34		Leucogabbro	53.4	1.3
246.233.5	53.82	0.06	28.29	0.54	0.06	11.31	5.10	0.25	99.42		Leucogabbro	54.3	1.4
246.233.5	53.41	0.06	28.63	0.54	0.05	11.54	4.88	0.24	99.35		Leucogabbro	55.9	1.4
246.233.5	53.52	0.07	28.66	0.43	0.00	11.46	5.09	0.03	99.25		Leucogabbro	55.4	0.1
246.233.5	53.85	0.07	28.36	0.65	0.02	11.24	5.24	0.19	99.61		Leucogabbro	53.7	1.1
246.232.5	66.39	<0.02	21.67	0.37	n.a.	2.04	10.87	0.02	101.36	rim	Leucogabbro	9.4	0.1
246.232.5	62.39	0.03	23.99	0.38	n.a.	5.27	8.92	0.04	101.02		Leucogabbro	24.5	0.2
246.232.5	53.87	0.05	28.99	0.70	n.a.	11.80	4.90	0.19	100.50	core	Leucogabbro	56.5	1.1
246.232.5	55.41	0.05	28.22	0.54	n.a.	10.57	5.49	0.29	100.55	core	Leucogabbro	50.7	1.6
246.232.5	68.72	0.02	20.10	0.30	n.a.	0.34	11.98	0.02	101.47		Leucogabbro	1.5	0.1
246.232.5	68.92	<0.02	20.18	0.29	n.a.	0.40	12.00	0.02	101.80		Leucogabbro	1.8	0.1
246.232.5	57.42	0.04	26.37	0.39	n.a.	8.44	6.87	0.29	99.81	core	Leucogabbro	39.8	1.6
246.232.5	64.49	<D.L.	22.02	0.22	n.a.	2.99	9.90	0.46	100.06	rim	Leucogabbro	13.9	2.6
246.232.5	53.76	0.04	28.76	0.57	n.a.	11.44	4.99	0.25	99.81		Leucogabbro	55.1	1.4
246.232.5	55.04	0.05	27.99	0.52	n.a.	10.37	5.56	0.29	99.82	core	Leucogabbro	49.9	1.7
246.232.5	66.01	<D.L.	21.43	0.17	n.a.	2.04	10.81	0.03	100.48	rim	Leucogabbro	9.4	0.1
246.232.5	54.88	0.05	27.96	0.53	n.a.	10.48	5.52	0.31	99.74	core	Leucogabbro	50.3	1.8
246.232.5	65.75	0.02	22.01	0.24	n.a.	2.44	10.40	0.13	101.00	rim	Leucogabbro	11.4	0.7
246.232.5	66.57	<D.L.	21.44	0.54	n.a.	1.71	11.01	0.01	101.28	rim	Leucogabbro	7.9	0.1
246.232.5	67.71	<D.L.	20.38	0.26	n.a.	0.57	11.83	0.03	100.78	rim	Leucogabbro	2.6	0.1
246.232.5	53.86	0.05	28.57	0.74	n.a.	11.48	5.19	0.14	100.03	core	Leucogabbro	54.6	0.8
246.232.5	66.93	0.02	20.80	0.24	n.a.	1.26	11.37	0.10	100.73	rim	Leucogabbro	5.7	0.6
246.232.5	51.68	0.04	30.29	0.72	n.a.	13.26	3.98	0.15	100.11	core	Leucogabbro	64.3	0.9

<D.L.: below detection limit; Pos: Crystal position; An: Anorthite; Or: Orthose; n.a.: not analyzed

Appendix 14 (cont.)

Sample no.	SiO_2	TiO_2	Al_2O_3	FeO	MgO	CaO	Na_2O	K_2O	Total	Pos.	Host rock	An	Or
246.232.5	67.37	<D.L.	20.32	0.15	n.a.	0.86	11.60	0.02	100.32	rim	Leucogabbro	3.9	0.1
246.232.5	52.83	0.06	29.66	0.68	n.a.	12.43	4.51	0.02	100.21	core	Leucogabbro	60.3	0.1
248.262.0	54.88	0.05	28.15	0.58	n.a.	10.56	5.60	0.15	99.97	core	Leucogabbro	50.6	0.9
248.262.0	66.32	0.04	21.02	0.27	n.a.	1.67	10.95	0.24	100.52	rim	Leucogabbro	7.7	1.3
248.262.0	57.01	0.08	26.84	0.46	n.a.	8.85	6.51	0.39	100.13	rim	Leucogabbro	42.0	2.2
248.262.0	67.90	<D.L.	20.56	0.17	n.a.	0.41	11.79	0.14	100.98	rim	Leucogabbro	1.9	0.8
248.262.0	55.19	0.04	27.64	0.56	n.a.	9.95	5.78	0.38	99.54	core	Leucogabbro	47.7	2.2
248.262.0	66.21	0.03	20.80	0.29	n.a.	1.66	11.17	0.07	100.22	rim	Leucogabbro	7.6	0.4
248.262.0	52.26	0.04	29.44	0.70	n.a.	12.39	4.40	0.26	99.48	core	Leucogabbro	60.0	1.5
248.262.0	52.21	0.04	29.60	0.76	n.a.	12.54	4.39	0.14	99.69	core	Leucogabbro	60.7	0.8
248.262.0	52.05	0.04	29.89	0.68	n.a.	12.80	4.26	0.05	99.77	core	Leucogabbro	62.3	0.3
248.262.0	52.64	0.04	29.43	0.75	n.a.	12.38	4.50	0.23	99.98	core	Leucogabbro	59.5	1.3
246.212.3	56.89	<D.L.	26.68	0.43	n.a.	8.76	6.50	0.37	99.63	core	Leucogabbro	41.8	2.1
246.212.3	65.25	<D.L.	21.72	0.23	n.a.	2.49	10.49	0.20	100.38	rim	Leucogabbro	11.5	1.1
246.212.3	59.91	0.03	24.67	0.37	n.a.	6.52	7.68	0.58	99.76	core	Leucogabbro	30.9	3.3
246.212.3	63.86	<D.L.	22.26	0.27	n.a.	3.42	9.83	0.31	99.94		Leucogabbro	15.8	1.7
246.212.3	66.06	<D.L.	20.95	0.31	n.a.	1.83	11.16	0.01	100.32	rim	Leucogabbro	8.3	0.1
246.212.3	53.42	0.07	28.52	0.74	n.a.	11.57	4.81	0.22	99.35	core	Leucogabbro	56.3	1.2
246.212.3	57.84	0.04	25.67	0.53	n.a.	7.92	7.08	0.36	99.45		Leucogabbro	37.5	2.0
246.212.3	57.08	0.04	26.63	0.47	n.a.	8.67	6.59	0.36	99.84	core	Leucogabbro	41.2	2.0
246.212.3	62.09	<D.L.	23.06	0.36	n.a.	4.63	8.84	0.60	99.59		Leucogabbro	21.7	3.4
246.212.3	65.63	<D.L.	20.93	0.20	n.a.	2.10	10.77	0.18	99.82	rim	Leucogabbro	9.6	1.0
246.209.0	52.00	0.07	29.79	0.54	n.a.	13.13	4.22	0.12	99.87	core	Leucogabbro	62.8	0.7
246.209.0	56.38	0.02	27.28	0.34	n.a.	9.43	6.53	0.09	100.08	rim	Leucogabbro	44.1	0.5
246.209.0	51.37	0.07	30.56	0.68	n.a.	13.91	3.93	0.08	100.61	core	Leucogabbro	65.9	0.5
246.209.0	51.40	0.06	30.01	0.72	n.a.	13.44	4.04	0.14	99.81	core	Leucogabbro	64.2	0.8
246.209.0	52.09	0.08	30.01	0.69	n.a.	13.19	4.23	0.14	100.43	core	Leucogabbro	62.8	0.8
246.209.0	52.79	0.05	29.37	0.65	n.a.	12.55	4.51	0.14	100.05	core	Leucogabbro	60.1	0.8
246.209.0	59.82	<D.L.	24.64	0.40	n.a.	6.48	7.85	0.39	99.57	rim	Leucogabbro	30.6	2.2
246.209.0	52.30	0.05	29.65	0.47	n.a.	12.76	4.40	0.17	99.80	core	Leucogabbro	61.0	0.9
246.209.0	55.42	0.05	27.95	0.54	n.a.	10.45	5.82	0.07	100.31	rim	Leucogabbro	49.6	0.4
246.209.0	66.18	0.02	21.29	0.19	n.a.	1.85	10.81	0.11	100.47		Leucogabbro	8.6	0.6
246.209.0	65.84	<D.L.	21.09	0.21	n.a.	2.02	10.78	0.13	100.08		Leucogabbro	9.3	0.7
246.209.0	64.13	<D.L.	22.34	0.26	n.a.	3.46	9.63	0.55	100.37		Leucogabbro	16.0	3.1

<D.L.: below detection limit; Pos: Crystal position; An: Anorthite; Or: Orthose; n.a.: not analyzed

Appendix 14 (cont.)

Sample no.	SiO_2	TiO_2	Al_2O_3	FeO	MgO	CaO	Na_2O	K_2O	Total	Pos.	Host rock	An	Or
248.254.0	48.90	0.03	32.15	0.82	n.a.	15.99	2.77	0.02	100.68	core	Leucogabbro	76.0	0.1
248.254.0	48.14	0.04	32.39	0.85	n.a.	16.48	2.55	0.01	100.48	core	Leucogabbro	78.0	0.1
248.254.0	48.97	<D.L.	31.87	0.76	n.a.	15.77	2.82	0.02	100.20	core	Leucogabbro	75.5	0.1
248.254.0	53.07	0.04	28.90	0.73	n.a.	12.16	4.85	0.06	99.82	rim	Leucogabbro	57.9	0.4
248.254.0	51.62	0.03	30.37	0.86	n.a.	13.83	4.05	0.10	100.86	core	Leucogabbro	65.0	0.5
248.254.0	55.66	0.03	27.94	0.94	n.a.	10.42	5.91	0.07	100.98	rim	Leucogabbro	49.1	0.4
248.254.0	53.86	0.06	28.50	0.69	n.a.	11.56	5.13	0.30	100.09	core	Leucogabbro	54.5	1.7
248.254.0	58.56	0.03	25.71	0.60	n.a.	7.63	7.20	0.36	100.10	rim	Leucogabbro	36.2	2.0
248.254.0	54.49	0.05	27.90	0.69	n.a.	10.82	5.44	0.33	99.71	core	Leucogabbro	51.4	1.9
248.254.0	61.85	<D.L.	23.23	0.41	n.a.	4.82	8.51	1.05	99.88	rim	Leucogabbro	22.5	5.8
248.254.0	54.79	0.04	27.87	0.72	n.a.	10.87	5.48	0.29	100.06	core	Leucogabbro	51.5	1.6
248.254.0	63.70	0.03	22.19	0.38	n.a.	3.35	9.51	0.73	99.90	rim	Leucogabbro	15.7	4.1
248.254.0	53.94	0.05	28.43	0.67	n.a.	11.33	5.11	0.25	99.76	core	Leucogabbro	54.3	1.4
248.254.0	63.46	0.03	21.93	0.39	n.a.	3.26	9.30	1.21	99.58	rim	Leucogabbro	15.1	6.7
248.254.0	54.57	0.04	28.31	0.62	n.a.	11.23	5.27	0.23	100.27	core	Leucogabbro	53.4	1.3
248.254.0	60.60	0.03	24.54	0.47	n.a.	6.12	7.91	0.68	100.34	core	Leucogabbro	28.8	3.8
248.254.0	66.24	0.03	21.57	0.49	n.a.	2.06	10.79	0.07	101.25	rim	Leucogabbro	9.5	0.4
248.254.0	57.16	0.06	26.43	0.58	n.a.	8.81	6.36	0.47	99.87	core	Leucogabbro	42.2	2.7
248.254.0	65.80	<D.L.	20.98	0.45	n.a.	1.93	10.60	0.70	100.46	rim	Leucogabbro	8.8	3.8
248.254.0	54.19	0.05	28.38	0.70	n.a.	11.44	5.14	0.29	100.19	core	Leucogabbro	54.3	1.7
248.254.0	63.62	0.03	22.33	0.48	n.a.	3.60	8.96	1.18	100.21		Leucogabbro	17.0	6.6
248.254.0	65.69	0.03	20.89	0.39	n.a.	1.84	10.60	0.49	99.93	rim	Leucogabbro	8.5	2.7
248.254.0	61.67	0.03	24.00	0.37	n.a.	5.48	8.64	0.41	100.60	core	Leucogabbro	25.4	2.3
248.254.0	52.56	0.05	29.54	0.78	n.a.	13.04	4.34	0.10	100.41	core	Leucogabbro	62.1	0.6
248.254.0	53.36	0.04	28.72	0.75	n.a.	12.02	4.91	0.10	99.90	core	Leucogabbro	57.2	0.6
248.254.0	51.69	0.04	30.12	0.70	n.a.	13.65	4.00	0.22	100.42	core	Leucogabbro	64.5	1.2
248.254.0	64.81	<D.L.	21.84	0.36	n.a.	2.77	10.33	0.09	100.19	rim	Leucogabbro	12.9	0.5
248.254.0	51.24	0.05	30.33	0.78	n.a.	13.85	3.80	0.18	100.23	core	Leucogabbro	66.2	1.0
248.254.0	63.69	<D.L.	22.66	0.42	n.a.	3.62	9.46	0.49	100.35	rim	Leucogabbro	17.0	2.7
248.262.0	54.66	0.04	28.10	0.69	n.a.	10.92	5.45	0.29	100.14	core	Leucogabbro	51.7	1.6
248.262.0	62.94	0.02	23.02	0.35	n.a.	3.64	8.93	1.10	100.01	rim	Leucogabbro	17.3	6.2
248.262.0	52.33	0.04	29.42	0.79	n.a.	13.06	4.46	0.09	100.18	core	Leucogabbro	61.5	0.5
248.262.0	64.04	<D.L.	22.46	0.44	n.a.	3.37	9.69	0.30	100.29	rim	Leucogabbro	15.8	1.7
248.262.0	52.01	0.05	29.64	0.77	n.a.	13.37	4.15	0.21	100.19	core	Leucogabbro	63.3	1.2

<D.L.: below detection limit; Pos: Crystal position; An: Anorthite; Or: Orthose; n.a.: not analyzed

Appendix 14 (cont.)

Sample no.	SiO_2	TiO_2	Al_2O_3	FeO	MgO	CaO	Na_2O	K_2O	Total	Pos.	Host rock	An	Or
248.262.0	62.40	0.03	23.09	0.43	n.a.	4.53	8.82	0.85	100.15	rim	Leucogabbro	21.1	4.7
248.262.0	54.93	0.05	27.94	0.60	n.a.	10.59	5.71	0.18	100.00	core	Leucogabbro	50.1	1.0
248.262.0	60.22	0.03	24.45	0.39	n.a.	6.23	7.97	0.43	99.72	rim	Leucogabbro	29.5	2.4
248.262.0	61.43	0.04	23.91	0.44	n.a.	5.41	8.20	0.82	100.26	rim	Leucogabbro	25.5	4.6
248.262.0	54.56	0.05	28.37	0.71	n.a.	11.09	5.10	0.33	100.22	core	Leucogabbro	53.5	1.9
248.262.0	60.83	<D.L.	24.32	0.37	n.a.	5.69	8.07	0.78	100.07	rim	Leucogabbro	26.8	4.4
248.262.0	54.30	0.04	28.37	0.62	n.a.	11.26	5.17	0.32	100.08	core	Leucogabbro	53.6	1.8
248.262.0	60.80	<D.L.	24.40	0.46	n.a.	6.00	8.28	0.29	100.23	rim	Leucogabbro	28.1	1.6
248.262.0	63.10	0.04	22.79	0.41	n.a.	4.16	9.22	0.28	99.99	core	Leucogabbro	19.6	1.6
248.262.0	52.27	0.05	29.89	0.79	n.a.	13.28	4.18	0.21	100.67	core	Leucogabbro	63.0	1.2
248.262.0	52.01	<D.L.	29.64	0.84	n.a.	13.22	4.23	0.22	100.15	core	Leucogabbro	62.5	1.3
248.262.0	51.90	0.03	29.97	0.87	n.a.	13.64	4.08	0.23	100.71	core	Leucogabbro	64.1	1.3
246.240.8	48.71	0.04	31.84	0.68	n.a.	15.53	2.74	0.05	99.59	core	Leucogabbro	75.6	0.3
246.240.8	49.99	0.06	30.98	0.53	n.a.	14.55	3.37	0.04	99.51	core	Leucogabbro	70.3	0.2
246.240.8	48.76	0.06	31.58	0.53	n.a.	15.35	2.85	<D.L.	99.14	core	Leucogabbro	74.8	0.0
246.240.8	48.31	0.05	32.06	0.61	n.a.	15.85	2.48	0.04	99.40	core	Leucogabbro	77.7	0.3
246.240.8	53.20	0.06	28.73	0.51	n.a.	11.91	4.90	0.11	99.41		Leucogabbro	57.0	0.6
246.240.8	60.15	0.04	24.38	0.29	n.a.	6.55	8.12	<D.L.	99.52	rim	Leucogabbro	30.8	0.0
246.240.8	49.90	0.04	30.90	0.54	n.a.	14.45	3.33	0.08	99.23	core	Leucogabbro	70.3	0.4
246.240.8	48.76	0.04	31.71	0.58	n.a.	15.36	2.84	0.06	99.34	core	Leucogabbro	74.7	0.3
246.240.8	49.30	0.04	31.41	0.48	n.a.	15.05	2.98	0.07	99.33	core	Leucogabbro	73.3	0.4
246.240.8	53.89	0.05	28.16	0.46	n.a.	11.35	5.19	0.25	99.35	rim	Leucogabbro	53.9	1.4
246.240.8	49.97	0.06	30.96	0.60	n.a.	14.46	3.37	0.06	99.47	core	Leucogabbro	70.1	0.3
246.240.8	56.19	0.05	26.91	0.47	n.a.	9.52	6.12	0.36	99.62	rim	Leucogabbro	45.3	2.0
246.240.8	49.32	0.05	31.57	0.50	n.a.	15.18	2.95	0.11	99.68	core	Leucogabbro	73.5	0.6
246.240.8	53.33	0.04	28.88	0.45	n.a.	11.95	4.85	0.18	99.69	rim	Leucogabbro	57.1	1.0
246.240.8	53.32	0.07	28.62	0.57	n.a.	11.81	4.82	0.23	99.45	core	Leucogabbro	56.7	1.3
246.240.8	49.74	0.05	31.27	0.63	n.a.	14.96	3.09	0.08	99.82	core	Leucogabbro	72.5	0.5
246.240.8	48.89	0.06	31.78	0.50	n.a.	15.33	2.91	<D.L.	99.46	core	Leucogabbro	74.4	0.0
246.240.8	53.96	0.06	28.16	0.55	n.a.	11.30	5.19	0.23	99.45	rim	Leucogabbro	53.9	1.3
246.240.8	48.52	<D.L.	31.59	0.60	n.a.	15.49	2.69	0.05	98.94	core	Leucogabbro	75.9	0.3
246.240.8	48.68	0.05	32.04	0.57	n.a.	15.60	2.70	<D.L.	99.64	core	Leucogabbro	76.2	0.0
246.240.8	48.80	<D.L.	31.52	0.62	n.a.	15.47	2.75	0.09	99.25	core	Leucogabbro	75.3	0.5
246.240.8	48.36	0.04	31.78	0.55	n.a.	15.76	2.62	0.08	99.18	core	Leucogabbro	76.6	0.4

<D.L.: below detection limit; Pos: Crystal position; An: Anorthite; Or: Orthose; n.a.: not analyzed

Appendix 14 (cont.)

Sample no.	SiO_2	TiO_2	Al_2O_3	FeO	MgO	CaO	Na_2O	K_2O	Total	Pos.	Host rock	An	Or
246.240.8	49.85	0.05	30.82	0.50	n.a.	14.53	3.27	0.16	99.18	core	Leucogabbro	70.4	0.9
246.240.8	54.53	0.04	27.93	0.50	n.a.	11.10	5.38	0.30	99.77	core	Leucogabbro	52.4	1.7
246.240.8	48.79	0.04	31.63	0.46	n.a.	15.35	2.80	<D.L.	99.07	core	Leucogabbro	75.2	0.0
246.240.8	54.04	0.04	27.98	0.47	n.a.	10.96	5.50	0.17	99.16	rim	Leucogabbro	51.9	1.0
246.240.8	48.59	0.04	31.22	0.68	n.a.	14.83	2.74	0.08	98.18	core	Leucogabbro	74.6	0.5
246.240.8	53.17	0.08	28.28	0.59	n.a.	11.84	4.86	0.26	99.08	core	Leucogabbro	56.6	1.5
246.240.8	53.06	0.03	28.48	0.57	n.a.	11.86	4.73	0.25	98.97	rim	Leucogabbro	57.2	1.4
246.240.8	53.45	0.06	28.06	0.55	n.a.	11.60	4.91	0.28	98.90	core	Leucogabbro	55.7	1.6
246.240.8	57.29	0.03	25.93	0.34	n.a.	8.55	6.70	0.38	99.24		Leucogabbro	40.5	2.2
246.240.8	48.69	0.04	31.55	0.56	n.a.	15.64	2.71	0.07	99.27	core	Leucogabbro	75.8	0.4
246.240.8	53.26	0.07	28.35	0.48	n.a.	11.74	4.87	0.23	98.99		Leucogabbro	56.4	1.3
246.240.8	60.50	<D.L.	23.73	0.32	n.a.	5.97	8.23	0.53	99.28	rim	Leucogabbro	27.8	2.9
246.240.8	50.06	0.05	30.96	0.55	n.a.	14.40	3.46	<D.L.	99.48	core	Leucogabbro	69.7	0.0
246.240.8	53.68	0.05	28.54	0.60	n.a.	11.65	4.92	0.14	99.59		Leucogabbro	56.2	0.8
246.240.8	59.64	<D.L.	24.80	0.51	n.a.	7.04	7.82	0.05	99.85	rim	Leucogabbro	33.1	0.3
246.240.8	64.39	<D.L.	22.30	0.55	n.a.	3.55	9.90	<D.L.	100.69	rim	Leucogabbro	16.5	0.0
246.240.8	54.49	0.06	28.33	0.51	n.a.	11.25	5.19	0.16	99.99	core	Leucogabbro	54.0	0.9
246.240.8	48.36	0.04	31.71	0.62	n.a.	15.68	2.75	<D.L.	99.15	core	Leucogabbro	75.9	0.0
246.240.8	53.70	0.08	28.18	0.75	n.a.	11.36	5.14	0.12	99.33	rim	Leucogabbro	54.6	0.7
246.212.6	61.72	<D.L.	23.09	0.31	n.a.	4.92	8.55	0.77	99.36	core	Leucogabbro	23.1	4.3
246.212.6	66.23	<D.L.	20.99	0.14	n.a.	1.86	10.86	0.21	100.28	rim	Leucogabbro	8.5	1.2
246.212.6	62.23	<D.L.	23.15	0.30	n.a.	4.77	8.93	0.31	99.69	core	Leucogabbro	22.4	1.7
246.212.6	66.38	<D.L.	21.03	0.19	n.a.	1.84	10.82	0.08	100.33	rim	Leucogabbro	8.6	0.4
246.212.6	64.78	<D.L.	18.14	0.06	n.a.	0.00	0.65	15.96	99.59	rim	Leucogabbro	0.0	94.2
246.212.6	63.70	<D.L.	17.97	1.00	n.a.	0.31	1.38	14.61	98.97		Leucogabbro	1.5	86.1
246.212.6	59.96	0.05	24.44	0.39	n.a.	6.51	7.95	0.12	99.42	core	Leucogabbro	30.9	0.7
246.212.6	57.05	<D.L.	26.00	0.45	n.a.	8.57	6.74	0.43	99.23	core	Leucogabbro	40.3	2.4
246.212.6	64.87	<D.L.	18.12	0.20	n.a.	0.08	0.70	15.84	99.80		Leucogabbro	0.4	93.3
246.212.6	67.80	<D.L.	20.58	0.19	n.a.	1.05	11.20	0.06	100.87		Leucogabbro	4.9	0.3
246.212.6	64.36	<D.L.	18.23	0.12	n.a.	0.05	0.74	15.66	99.16		Leucogabbro	0.2	93.1
246.212.6	68.05	<D.L.	20.33	0.23	n.a.	0.88	11.11	0.07	100.67		Leucogabbro	4.2	0.4
246.212.6	61.23	<D.L.	23.94	0.31	n.a.	5.58	8.31	0.45	99.83	core	Leucogabbro	26.4	2.5
246.212.6	60.93	<D.L.	23.82	0.36	n.a.	5.72	8.44	0.29	99.55	core	Leucogabbro	26.8	1.6
246.212.6	59.12	0.05	25.22	0.40	n.a.	7.41	7.36	0.45	100.00	core	Leucogabbro	34.8	2.5

<D.L.: below detection limit; Pos: Crystal position; An: Anorthite; Or: Orthose; n.a.: not analyzed

Appendix 14 (cont.)

Sample no.	SiO_2	TiO_2	Al_2O_3	FeO	MgO	CaO	Na_2O	K_2O	Total	Pos.	Host rock	An	Or
246.212.6	60.89	<D.L.	23.91	0.35	n.a.	5.85	8.30	0.53	99.84	core	Leucogabbro	27.2	3.0
246.212.6	57.31	0.04	26.10	0.40	n.a.	8.69	6.68	0.35	99.56	core	Leucogabbro	41.0	1.9
246.212.6	56.97	0.04	26.37	0.43	n.a.	8.79	6.59	0.35	99.54	core	Leucogabbro	41.6	2.0
246.212.6	60.47	0.04	24.27	0.36	n.a.	6.30	8.09	0.17	99.71	core	Leucogabbro	29.8	1.0
246.212.6	57.84	0.05	25.81	0.36	n.a.	8.20	6.91	0.48	99.65	core	Leucogabbro	38.5	2.7
246.212.6	52.37	0.06	29.63	0.44	n.a.	12.85	4.32	<D.L.	99.68	core	Leucogabbro	62.2	0.0
246.212.6	54.69	0.07	27.99	0.45	n.a.	10.84	5.60	0.05	99.69	core	Leucogabbro	51.5	0.3
246.212.6	49.02	<D.L.	31.08	0.72	n.a.	15.17	2.95	0.08	99.03	core	Leucogabbro	73.6	0.5
246.212.6	52.63	0.05	29.21	0.58	n.a.	12.43	4.58	0.13	99.61	core	Leucogabbro	59.6	0.7
246.212.6	50.00	<D.L.	30.68	0.71	n.a.	14.52	3.30	0.10	99.31	core	Leucogabbro	70.4	0.6
246.212.6	51.02	0.06	30.32	0.50	n.a.	13.76	3.79	0.08	99.53	core	Leucogabbro	66.5	0.4
246.212.6	50.38	<D.L.	31.00	0.58	n.a.	14.36	3.49	0.08	99.90	core	Leucogabbro	69.2	0.5
246.212.6	51.79	0.04	29.71	0.49	n.a.	12.98	4.29	0.14	99.45	core	Leucogabbro	62.0	0.8
246.212.6	49.62	<D.L.	31.00	0.65	n.a.	14.66	3.27	0.11	99.32	core	Leucogabbro	70.8	0.6
246.212.6	50.57	0.04	30.44	0.62	n.a.	14.04	3.63	0.13	99.47	core	Leucogabbro	67.6	0.7
246.212.6	50.64	0.04	30.56	0.62	n.a.	14.07	3.66	0.09	99.68	core	Leucogabbro	67.6	0.5
246.212.6	51.23	0.05	30.18	0.57	n.a.	13.55	4.04	0.05	99.66	core	Leucogabbro	64.8	0.3
246.212.6	50.67	0.04	30.44	0.58	n.a.	13.97	3.73	0.05	99.49	core	Leucogabbro	67.2	0.3
246.212.6	51.43	0.04	30.09	0.57	n.a.	13.45	4.08	0.06	99.73	core	Leucogabbro	64.3	0.3
246.212.6	49.56	<D.L.	31.08	0.66	n.a.	14.87	3.15	0.07	99.39	core	Leucogabbro	72.0	0.4
246.212.6	49.71	0.03	31.20	0.68	n.a.	14.94	3.06	0.07	99.69	core	Leucogabbro	72.6	0.4
246.212.6	49.39	0.05	31.05	0.68	n.a.	14.65	3.11	0.07	98.99	core	Leucogabbro	71.9	0.4
246.212.6	49.20	0.07	31.14	0.64	n.a.	15.02	3.03	0.05	99.14	core	Leucogabbro	73.0	0.3
246.212.6	55.26	0.04	27.53	0.46	n.a.	10.38	5.86	0.08	99.59	rim	Leucogabbro	49.3	0.5
246.212.6	50.52	<D.L.	30.86	0.67	n.a.	14.26	3.53	0.10	99.94	core	Leucogabbro	68.7	0.5
246.212.6	55.11	0.04	27.79	0.40	n.a.	10.43	5.77	0.10	99.63	rim	Leucogabbro	49.7	0.6
246.212.6	49.94	<D.L.	30.86	0.62	n.a.	14.40	3.45	0.08	99.35	core	Leucogabbro	69.5	0.4
246.212.6	50.69	0.05	30.47	0.60	n.a.	13.69	3.81	0.12	99.43	core	Leucogabbro	66.0	0.7
246.212.6	49.73	<D.L.	31.13	0.70	n.a.	14.73	3.11	0.11	99.51	core	Leucogabbro	71.9	0.7
248.265.1	54.40	0.06	28.25	0.57	n.a.	11.09	5.35	0.31	100.04	core	Leucogabbro	52.4	1.8
248.265.1	55.36	0.04	27.69	0.54	n.a.	10.22	5.55	0.33	99.73	core	Leucogabbro	49.4	1.9
248.265.1	52.60	0.04	29.22	0.77	n.a.	12.63	4.31	0.25	99.82	core	Leucogabbro	61.0	1.4
248.265.1	52.81	0.04	29.12	0.69	n.a.	12.51	4.40	0.21	99.79	core	Leucogabbro	60.4	1.2
248.265.1	52.50	0.04	29.10	0.78	n.a.	12.46	4.44	0.22	99.54	core	Leucogabbro	60.0	1.3

<D.L.: below detection limit; Pos: Crystal position; An: Anorthite; Or: Orthose; n.a.: not analyzed

Appendix 14 (cont.)

Sample no.	SiO_2	TiO_2	Al_2O_3	FeO	MgO	CaO	Na_2O	K_2O	Total	Pos.	Host rock	An	Or
248.265.1	52.67	0.05	29.08	0.70	n.a.	12.61	4.47	0.22	99.80	core	Leucogabbro	60.1	1.3
248.265.1	52.66	0.03	29.20	0.70	n.a.	12.65	4.28	0.22	99.76	core	Leucogabbro	61.2	1.3
248.265.1	52.54	0.04	29.18	0.72	n.a.	12.67	4.36	0.24	99.75	core	Leucogabbro	60.8	1.4
248.265.1	58.16	0.05	25.99	0.41	n.a.	8.29	6.84	0.49	100.23	core	Leucogabbro	39.0	2.8
248.265.1	52.61	0.05	29.19	0.69	n.a.	12.59	4.27	0.24	99.64	core	Leucogabbro	61.1	1.4
248.265.1	52.40	0.03	29.07	0.69	n.a.	12.56	4.40	0.23	99.38	core	Leucogabbro	60.4	1.3
248.265.1	52.83	0.05	28.96	0.69	n.a.	12.58	4.48	0.24	99.83	core	Leucogabbro	60.0	1.3
248.265.1	52.43	0.05	29.23	0.72	n.a.	12.72	4.26	0.24	99.65	core	Leucogabbro	61.4	1.4
248.265.1	56.57	0.03	26.88	0.48	n.a.	9.61	6.13	0.29	100.00	rim	Leucogabbro	45.6	1.6
248.265.1	52.46	0.06	29.29	0.73	n.a.	12.62	4.41	0.24	99.82	core	Leucogabbro	60.4	1.4
248.265.1	57.84	0.07	26.05	0.45	n.a.	8.41	6.69	0.49	100.00	core	Leucogabbro	39.9	2.8
248.265.1	53.22	0.06	28.67	0.71	n.a.	12.23	4.56	0.26	99.71	core	Leucogabbro	58.8	1.5
248.265.1	52.22	0.06	29.20	0.73	n.a.	12.86	4.24	0.16	99.47	core	Leucogabbro	62.0	0.9
248.265.1	51.82	0.04	29.48	0.66	n.a.	13.28	3.94	0.22	99.46	core	Leucogabbro	64.2	1.3
248.265.1	51.91	0.04	29.30	0.72	n.a.	13.01	4.09	0.23	99.30	core	Leucogabbro	62.9	1.3
248.265.1	52.40	0.05	29.33	0.68	n.a.	13.06	4.12	0.23	99.87	core	Leucogabbro	62.8	1.3
248.265.1	52.78	0.06	29.00	0.72	n.a.	12.68	4.25	0.24	99.72	core	Leucogabbro	61.4	1.4
248.265.1	52.16	<D.L.	29.35	0.73	n.a.	13.03	4.02	0.22	99.53	core	Leucogabbro	63.3	1.3
248.265.1	52.51	0.06	29.16	0.64	n.a.	12.73	4.19	0.23	99.52	core	Leucogabbro	61.9	1.3
248.262.0	52.57	0.05	29.04	0.86	n.a.	12.15	4.53	0.12	99.32		Contact*	59.3	0.7
248.262.0	48.46	0.03	32.59	0.83	n.a.	15.54	2.72	0.01	100.19		Contact*	75.9	0.1
248.262.0	53.90	0.04	28.55	0.56	n.a.	11.11	5.20	0.15	99.52		Contact*	53.7	0.8
248.262.0	66.52	<D.L.	20.56	0.25	n.a.	1.09	11.40	0.05	99.87		Contact*	5.0	0.3
248.262.0	56.09	0.05	27.27	0.52	n.a.	9.55	6.11	0.29	99.88		Contact*	45.6	1.6
248.262.0	53.37	0.06	28.84	0.55	n.a.	11.45	5.12	0.05	99.43		Contact*	55.1	0.3
248.262.0	51.70	0.04	29.80	0.86	n.a.	12.94	4.14	0.05	99.53		Contact*	63.1	0.3
246.196.8	55.77	0.04	27.72	0.25	0.00	9.79	5.98	0.35	99.91		Coeval dyke	46.4	2.0
246.196.8	56.18	0.03	27.26	0.29	0.00	9.14	6.36	0.36	99.63		Coeval dyke	43.2	2.1
246.196.8	55.40	0.04	27.68	0.32	0.02	9.99	6.03	0.14	99.62		Coeval dyke	47.3	0.8
246.196.8	55.84	0.05	27.45	0.20	0.01	9.40	6.30	0.22	99.47		Coeval dyke	44.5	1.3
246.196.8	57.90	0.03	26.63	0.48	0.01	8.21	7.12	0.04	100.42		Coeval dyke	38.7	0.2
246.196.8	58.16	0.04	26.01	0.37	0.04	7.40	7.69	0.05	99.75		Coeval dyke	34.5	0.3
246.196.8	58.50	0.05	26.34	0.37	0.00	7.65	7.50	0.04	100.45		Coeval dyke	35.8	0.2
246.196.8	58.18	0.03	26.54	0.32	0.01	7.80	7.48	0.06	100.41		Coeval dyke	36.3	0.3

<D.L.: below detection limit; Pos: Crystal position; An: Anorthite; Or: Orthose; n.a.: not analyzed

Appendix 14 (cont.)

Sample no.	SiO_2	TiO_2	Al_2O_3	FeO	MgO	CaO	Na_2O	K_2O	Total	Pos.	Host rock	An	Or
246.196.8	58.88	0.07	25.81	0.23	0.01	7.14	7.73	0.09	99.96		Coeval dyke	33.5	0.5
246.249.6	49.14	0.03	31.45	0.56	0.08	15.18	2.92	0.09	99.45	core	Late dike	73.9	0.5
246.249.6	52.70	0.06	29.01	0.64	0.07	12.23	4.59	0.13	99.43	rim	Late dike	59.2	0.8
246.249.6	53.21	0.06	28.69	0.67	0.06	11.87	4.74	0.18	99.47		Late dike	57.5	1.0
246.249.6	53.68	0.04	29.05	0.66	0.07	11.68	5.04	0.09	100.30		Late dike	55.9	0.5
246.249.6	52.02	0.05	29.69	0.63	0.10	12.84	4.43	0.03	99.80		Late dike	61.5	0.2
246.249.6	53.13	0.06	29.10	0.55	0.11	12.23	4.64	0.12	99.95		Late dike	59.0	0.7
246.249.6	52.93	0.04	29.06	0.58	0.05	11.85	4.85	0.04	99.39		Late dike	57.4	0.2
246.249.6	52.09	0.05	29.88	0.51	0.10	12.99	4.24	0.05	99.91		Late dike	62.8	0.3
246.249.6	50.02	0.02	31.10	0.53	0.08	14.54	3.31	0.10	99.71		Late dike	70.5	0.6
246.249.6	49.55	0.03	31.36	0.57	0.10	14.82	3.01	0.09	99.54		Late dike	72.8	0.5
246.249.6	49.24	0.02	31.32	0.53	0.10	14.84	3.11	0.06	99.23	core	Late dike	72.3	0.4
246.249.6	49.19	0.02	31.73	0.58	0.09	15.28	2.86	0.07	99.80	core	Late dike	74.5	0.4
246.249.6	52.44	0.04	29.71	0.52	0.12	12.89	4.26	0.15	100.12	rim	Late dike	62.1	0.9
246.249.6	48.79	0.01	32.37	0.50	0.10	15.81	2.63	0.07	100.28		Late dike	76.6	0.4
246.249.6	49.28	0.03	31.83	0.49	0.08	15.17	2.90	0.07	99.85		Late dike	74.0	0.4
246.249.6	52.47	0.06	29.56	0.64	0.07	12.50	4.49	0.09	99.89		Late dike	60.3	0.5
246.249.6	52.66	0.06	29.63	0.66	0.09	12.80	4.45	0.11	100.46		Late dike	61.1	0.6
246.249.6	51.10	0.03	30.67	0.65	0.12	13.80	3.73	0.12	100.21		Late dike	66.8	0.7
246.249.6	49.57	0.04	31.48	0.75	0.14	14.50	3.22	0.16	99.86		Late dike	70.7	1.0
246.249.6	52.66	0.03	29.54	0.65	0.07	12.40	4.60	0.04	99.99		Late dike	59.8	0.2
246.249.6	52.52	0.04	29.51	0.65	0.07	12.49	4.48	0.12	99.89		Late dike	60.3	0.7
246.249.6	54.34	0.06	27.95	0.68	0.08	11.02	5.27	0.18	99.57		Late dike	53.1	1.0
246.249.6	50.56	0.01	30.76	0.80	0.08	14.07	3.70	0.09	100.05		Late dike	67.5	0.5
246.249.6	49.76	0.02	31.58	0.61	0.10	14.73	3.19	0.05	100.04		Late dike	71.7	0.3
246.249.6	49.92	0.00	31.36	0.53	0.09	14.61	3.26	0.08	99.86		Late dike	71.0	0.5
264.181.7	67.93	0.00	19.76	0.48	0.00	0.20	12.08	0.05	100.51		Massive sulfide	0.9	0.3
264.181.7	68.43	<D.L.	19.61	0.39	0.00	0.14	11.98	0.04	100.59		Massive sulfide	0.6	0.2
264.181.7	68.71	0.01	20.10	0.32	0.00	0.10	12.16	0.07	101.47		Massive sulfide	0.5	0.4
264.162.4	56.93	0.01	27.35	0.40	0.00	9.29	6.46	0.15	100.59	core	Tonalite	43.9	0.9
264.162.4	58.34	0.00	26.77	0.44	0.00	8.30	7.13	0.08	101.05		Tonalite	39.0	0.5
264.162.4	57.82	<D.L.	26.47	0.16	0.01	8.41	7.09	0.04	100.00		Tonalite	39.5	0.2
264.162.4	58.20	<D.L.	26.16	0.13	0.02	8.03	7.28	0.06	99.87		Tonalite	37.7	0.3
264.162.4	57.87	0.01	26.32	0.13	0.00	8.33	7.01	0.06	99.72		Tonalite	39.5	0.3

<D.L.: below detection limit; Pos: Crystal position; An: Anorthite; Or: Orthose; n.a.: not analyzed

Appendix 14 (cont.)

Sample no.	SiO_2	TiO_2	Al_2O_3	FeO	MgO	CaO	Na_2O	K_2O	Total	Pos.	Host rock	An	Or
264.162.4	59.40	<D.L.	25.32	0.11	0.00	7.08	7.83	0.06	99.80		Tonalite	33.2	0.3
264.162.4	58.57	<D.L.	26.17	0.10	0.00	7.86	7.19	0.07	99.96		Tonalite	37.5	0.4
264.162.4	58.66	0.01	26.08	0.12	0.00	7.95	7.40	0.07	100.29		Tonalite	37.1	0.4
264.162.4	58.29	<D.L.	26.21	0.10	0.00	8.12	7.19	0.07	99.98		Tonalite	38.3	0.4
264.162.4	58.02	<D.L.	26.33	0.09	0.00	8.29	7.14	0.05	99.92		Tonalite	39.0	0.3
264.162.4	58.04	<D.L.	26.46	0.16	0.00	8.26	7.11	0.06	100.09		Tonalite	39.0	0.3
264.162.4	58.22	0.00	26.34	0.10	0.01	8.25	7.14	0.07	100.12		Tonalite	38.8	0.4
264.162.4	59.31	<D.L.	25.96	0.09	0.00	7.46	7.51	0.07	100.41		Tonalite	35.3	0.4
264.162.4	59.16	<D.L.	25.69	0.08	0.01	7.52	7.64	0.06	100.15		Tonalite	35.1	0.3
264.162.4	58.11	<D.L.	26.33	0.08	0.00	8.16	7.25	0.05	99.99		Tonalite	38.2	0.3
264.162.4	58.71	0.01	26.03	0.07	0.00	7.78	7.42	0.05	100.06		Tonalite	36.6	0.3
264.162.4	60.25	0.01	25.27	0.10	0.00	6.68	8.03	0.06	100.39		Tonalite	31.4	0.3
264.162.4	56.80	<D.L.	27.50	0.08	0.01	9.49	6.34	0.05	100.26		Tonalite	45.2	0.3
264.162.4	59.23	<D.L.	25.64	0.17	0.00	7.35	7.71	0.06	100.16		Tonalite	34.4	0.3
264.162.4	59.46	0.01	25.40	0.13	0.01	6.89	7.75	0.05	99.70		Tonalite	32.9	0.3
264.162.4	58.35	0.00	26.58	0.12	0.00	8.12	7.08	0.10	100.35		Tonalite	38.6	0.6
264.162.4	57.10	0.00	27.35	0.09	0.00	9.20	6.65	0.07	100.47		Tonalite	43.2	0.4
264.162.4	58.73	0.01	25.95	0.11	0.01	7.78	7.40	0.07	100.05		Tonalite	36.6	0.4
264.162.4	56.75	0.00	27.38	0.10	0.00	9.35	6.44	0.04	100.06		Tonalite	44.4	0.2
264.162.4	56.36	<D.L.	27.54	0.07	0.00	9.60	6.28	0.07	99.92		Tonalite	45.6	0.4
264.162.4	58.46	0.00	26.32	0.12	0.00	8.07	7.25	0.05	100.28		Tonalite	38.0	0.3
264.181.7	58.80	<D.L.	26.16	0.09	0.02	7.94	7.37	0.06	100.43		Tonalite	37.2	0.3
264.156.5	56.34	<D.L.	27.48	0.10	n.a.	9.87	6.23	0.05	100.07	core	Tonalite	46.5	0.3
264.156.5	56.19	<D.L.	28.12	0.08	n.a.	10.03	6.02	0.04	100.47	core	Tonalite	47.8	0.2
264.156.5	58.50	<D.L.	26.04	0.10	n.a.	8.00	7.25	0.07	99.95		Tonalite	37.7	0.4
264.156.5	57.51	<D.L.	27.12	0.04	n.a.	9.08	6.77	0.04	100.57		Tonalite	42.5	0.2
264.156.5	58.45	<D.L.	26.10	0.09	n.a.	8.00	7.24	0.05	99.94		Tonalite	37.8	0.3
264.156.5	57.16	<D.L.	26.73	0.08	n.a.	8.87	6.75	0.06	99.66	core	Tonalite	41.9	0.3
264.156.5	58.67	<D.L.	26.17	0.08	n.a.	7.97	7.22	0.08	100.18		Tonalite	37.7	0.5
264.156.5	57.36	<D.L.	26.69	0.12	n.a.	8.87	6.71	0.06	99.82		Tonalite	42.1	0.4
264.156.5	57.98	<D.L.	26.74	0.14	n.a.	8.55	6.99	0.07	100.48		Tonalite	40.2	0.4
264.156.5	57.26	<D.L.	26.83	0.09	n.a.	8.91	6.71	0.04	99.84	core	Tonalite	42.2	0.2
264.156.5	61.10	<D.L.	24.61	0.09	n.a.	6.14	8.53	0.07	100.53		Tonalite	28.4	0.4
264.156.5	58.48	<D.L.	25.95	0.08	n.a.	7.94	7.39	0.05	99.89	rim	Tonalite	37.2	0.3

<D.L.: below detection limit; Pos: Crystal position; An: Anorthite; Or: Orthose; n.a.: not analyzed

Appendix 14 (cont.)

Sample no.	SiO_2	TiO_2	Al_2O_3	FeO	MgO	CaO	Na_2O	K_2O	Total	Pos.	Host rock	An	Or
264.156.5	58.72	<D.L.	26.13	0.07	n.a.	7.96	7.38	0.07	100.33	core	Tonalite	37.2	0.4
264.156.5	56.90	<D.L.	27.22	0.06	n.a.	9.21	6.73	0.05	100.17	core	Tonalite	42.9	0.3
264.156.5	57.07	<D.L.	27.13	0.10	n.a.	9.33	6.45	0.07	100.16	core	Tonalite	44.2	0.4
264.156.5	59.86	<D.L.	25.31	0.08	n.a.	7.09	8.06	0.06	100.46	rim	Tonalite	32.6	0.3
264.156.5	56.89	<D.L.	26.78	0.05	n.a.	9.13	6.60	0.06	99.50	core	Tonalite	43.2	0.3
264.156.5	60.56	<D.L.	25.10	0.10	n.a.	6.62	8.07	0.06	100.50	rim	Tonalite	31.1	0.3
264.183.5	55.32	0.03	27.51	0.54	0.04	9.94	6.02	0.04	99.44	core	Xenolith	47.6	0.2
264.183.5	54.94	0.02	27.79	0.57	0.03	10.43	5.75	0.04	99.57	core	Xenolith	50.0	0.3
264.183.5	54.58	0.03	27.86	0.66	0.04	10.80	5.41	0.20	99.57	rim	Xenolith	51.9	1.1
264.183.5	53.81	0.03	28.39	0.60	0.03	10.81	5.26	0.31	99.25		Xenolith	52.2	1.8
264.183.5	54.48	0.01	28.13	0.61	0.04	10.95	5.48	0.04	99.73		Xenolith	52.4	0.2
264.183.5	54.17	0.04	28.15	0.56	0.02	10.78	5.53	0.04	99.29		Xenolith	51.7	0.2
264.183.5	53.95	0.05	28.10	0.65	0.03	11.05	5.39	0.06	99.28		Xenolith	52.9	0.4
264.190.1	63.91	0.00	18.44	0.52	0.01	0.00	0.08	16.31	99.28		Xenolith	0.0	99.2
264.190.1	53.45	0.03	28.64	0.91	0.05	11.61	5.00	0.08	99.77		Xenolith	56.0	0.4
264.190.1	54.10	0.06	28.20	0.64	0.07	10.92	5.35	0.11	99.46		Xenolith	52.6	0.6
264.190.1	53.19	0.04	28.31	0.72	0.05	11.58	4.89	0.29	99.07		Xenolith	55.7	1.6
264.190.1	63.00	0.02	18.45	0.12	0.02	0.03	0.17	15.78	97.59		Xenolith	0.1	98.2
264.190.1	63.03	0.00	18.42	0.16	0.00	0.01	0.21	15.85	97.68		Xenolith	0.0	98.0
264.190.1	51.07	0.04	30.06	0.88	0.06	13.51	3.94	0.18	99.74		Xenolith	64.8	1.0
264.190.1	50.46	0.07	30.38	0.97	0.02	13.86	3.71	0.08	99.55		Xenolith	67.1	0.5
264.190.1	61.49	0.03	19.01	0.34	0.02	0.03	0.15	15.04	96.11		Xenolith	0.1	98.3
264.190.1	50.51	0.02	30.44	0.99	0.04	13.92	3.68	0.15	99.74	core	Xenolith	67.1	0.8
264.190.1	51.06	0.05	30.01	1.07	0.03	13.38	3.83	0.14	99.57	core	Xenolith	65.4	0.8
264.190.1	51.65	0.03	30.04	1.18	0.03	13.37	4.05	0.09	100.45	core	Xenolith	64.3	0.5
264.190.1	51.55	0.03	29.62	0.97	0.02	12.76	3.84	0.09	98.88	core	Xenolith	64.4	0.5
264.190.1	52.83	0.06	27.68	1.12	0.13	11.04	5.16	0.16	98.18	core	Xenolith	53.7	0.9
264.190.1	51.46	0.07	29.94	1.09	0.05	13.13	4.06	0.11	99.92	core	Xenolith	63.7	0.6
264.170.5	54.35	0.06	28.22	0.65	0.08	11.02	5.19	0.25	99.81	core	Xenolith	53.2	1.4
264.170.5	55.17	0.04	27.24	0.55	0.07	10.13	5.76	0.33	99.29	core	Xenolith	48.3	1.9
264.170.5	60.50	0.03	23.47	0.47	0.02	5.69	8.18	0.67	99.03	core	Xenolith	26.7	3.7
264.170.5	59.88	0.01	24.37	0.36	0.02	6.35	7.85	0.56	99.41	core	Xenolith	29.9	3.2
264.170.5	54.82	0.08	27.66	1.17	0.44	6.60	5.18	2.33	98.28	core	Xenolith	35.2	14.8
264.170.5	54.78	0.07	27.85	0.66	0.06	10.64	5.71	0.26	100.05	core	Xenolith	50.0	1.5

<D.L.: below detection limit; Pos: Crystal position; An: Anorthite; Or: Orthose; n.a.: not analyzed

Appendix 14 (cont.)

Sample no.	SiO_2	TiO_2	Al_2O_3	FeO	MgO	CaO	Na_2O	K_2O	Total	Pos.	Host rock	An	Or
264.170.5	61.38	0.04	23.40	0.51	0.13	5.13	8.75	0.10	99.44	core	Xenolith	24.3	0.6
264.170.5	60.51	0.04	23.60	0.39	0.02	5.62	8.37	0.49	99.03	core	Xenolith	26.3	2.7
264.170.5	54.28	0.07	27.84	0.70	0.00	10.93	5.49	0.06	99.37		Xenolith	52.2	0.3
264.170.5	57.76	0.04	25.88	0.56	0.02	8.22	7.12	0.06	99.66		Xenolith	38.8	0.3
264.170.5	52.20	0.06	29.21	0.86	0.06	12.30	4.47	0.10	99.25		Xenolith	60.0	0.6
264.170.5	52.75	0.06	29.23	0.93	0.06	12.26	4.54	0.15	99.97		Xenolith	59.3	0.8
264.170.5	58.71	0.08	25.46	0.65	0.04	7.65	7.46	0.05	100.09		Xenolith	36.1	0.3

<D.L.: below detection limit; Pos: Crystal position; An: Anorthite; Or: Orthose; n.a.: not analyzed

Appendix 15 Electron microprobe analyses in amphibole and biotite.

Sample no.	SiO_2	TiO_2	Al_2O_3	FeO	MnO	MgO	CaO	Na_2O	K_2O	Cr_2O_3	Cl	(OH)	Total	Rock	Mg#
Amphibole															
246.233.5	43.32	3.97	10.52	10.76	0.136	14.57	11.32	2.73	0.83	0.077	n.a.	1.77	100.00	Leuco.	76
246.232.5	44.09	3.53	10.04	10.45	0.142	15.21	11.33	2.68	0.87	0.061	0.026	1.65	100.07	Leuco.	79
246.232.5	44.10	3.51	9.99	10.80	0.163	15.15	11.16	2.68	0.78	0.052	0.023	1.37	99.84	Leuco.	80
246.232.5	43.75	3.35	10.40	10.97	0.179	14.72	11.22	2.70	0.88	0.089	0.029	1.49	99.76	Leuco.	78
248.262.0	45.50	2.39	8.85	10.46	0.187	16.10	11.04	2.75	0.75	<D.L.	0.026	1.57	99.67	Leuco.	85
248.262.0	44.72	2.79	9.37	10.53	0.176	15.96	11.22	2.83	0.81	<D.L.	0.045	1.16	99.66	Leuco.	83
248.262.0	43.42	3.10	10.18	10.39	0.182	15.25	11.25	2.98	0.94	<D.L.	0.159	1.82	99.68	Leuco.	80
248.262.0	44.59	2.41	9.61	10.24	0.170	15.86	11.13	2.86	0.81	0.042	0.040	1.88	99.64	Leuco.	84
246.212.3	42.92	3.83	10.92	10.55	0.126	14.79	11.23	2.87	0.71	0.323	0.022	1.27	99.56	Contact	79
246.212.3	48.34	1.99	6.10	12.60	0.248	15.33	10.96	1.94	0.54	0.034	0.041	1.39	99.51	Contact	79
246.232.5	47.54	2.15	7.29	11.39	0.206	15.85	11.03	2.32	0.62	0.084	0.033	1.54	100.05	Leuco.	82
248.262.0	53.67	<D.L.	0.45	26.05	1.066	15.44	0.88	0.12	0.01	<D.L.	0.038	1.80	99.59	Leuco.	51
248.262.0	52.24	0.55	3.52	10.01	0.358	18.18	11.39	1.24	0.30	0.025	0.040	1.77	99.63	Leuco.	91
248.262.0	54.35	0.05	0.48	22.66	0.866	18.29	0.63	0.37	0.09	0.031	0.112	1.66	99.59	Leuco.	59
246.212.3	51.94	0.66	3.60	11.65	0.188	16.49	11.97	0.97	0.30	<D.L.	0.051	1.66	99.52	Leuco.	79
248.262.0	52.60	0.58	3.51	9.73	0.211	18.59	10.77	1.25	0.26	0.031	0.024	1.97	99.59	Contact	97
248.262.0	43.77	2.93	10.22	10.78	0.113	15.45	11.28	2.90	0.83	0.047	0.037	1.28	99.64	Contact	82
248.262.0	43.78	2.97	10.35	10.29	0.134	15.45	11.23	2.81	0.86	0.084	0.021	1.58	99.63	Contact	82
246.233.5	42.98	4.18	10.60	10.51	0.147	14.93	11.25	2.90	0.71	0.001	n.a.	1.79	100.00	O. nor.	79
246.233.5	43.15	4.11	10.53	10.49	0.135	14.88	11.23	2.77	0.73	0.021	n.a.	1.96	100.00	O. nor.	79
246.233.5	43.35	3.96	10.24	10.76	0.150	14.75	11.23	2.80	0.78	0.053	n.a.	1.93	100.00	O. nor.	77
246.233.5	43.45	3.91	10.38	10.78	0.177	14.63	11.28	2.77	0.76	0.085	n.a.	1.79	100.00	O. nor.	77
246.233.5	43.41	3.94	10.42	10.68	0.134	14.91	11.32	2.80	0.70	0.048	n.a.	1.63	100.00	O. nor.	78
246.233.5	43.47	4.04	10.42	10.62	0.167	14.89	11.22	2.83	0.72	0.054	n.a.	1.55	100.00	O. nor.	78
246.219.0	43.24	3.05	10.87	9.76	0.116	15.59	11.19	2.93	0.72	0.376	0.015	1.34	99.28	O. nor.	84
246.219.0	43.22	2.85	11.10	10.21	0.102	15.45	11.05	2.91	0.82	0.180	0.029	1.38	99.30	O. nor.	85
246.219.0	43.16	2.77	11.03	10.00	0.140	15.34	11.17	3.01	0.77	0.337	0.022	1.50	99.31	O. nor.	83
246.219.0	43.33	2.96	10.79	9.85	0.112	15.49	11.16	2.79	0.82	0.171	0.017	1.79	99.34	O. nor.	83
246.219.0	43.10	3.77	10.45	10.27	0.124	15.05	11.27	2.79	0.79	0.179	0.015	1.53	99.32	O. nor.	80
246.219.0	42.92	3.73	10.36	10.71	0.101	14.93	11.19	2.71	0.83	0.142	0.021	1.73	99.36	O. nor.	80
246.212.3	43.03	3.77	11.00	9.68	0.118	15.21	11.15	2.85	0.67	0.205	0.021	1.60	99.36	O. nor.	82
246.239.1	43.93	3.05	9.72	11.48	0.148	14.53	11.09	2.51	0.81	0.209	0.030	1.83	99.37	O. nor.	78
246.239.1	43.59	3.62	10.59	10.70	0.134	14.60	11.20	2.65	0.82	0.076	0.023	1.38	99.38	O. nor.	77
Biotite															
264.162.4	37.50	1.66	17.19	18.14	0.174	12.52	0.03	0.02	9.77	0.012	n.a.	3.00	100.00	Tonalite	55
264.162.4	38.88	1.74	16.31	17.35	0.181	13.04	0.07	0.05	9.72	0.008	n.a.	2.65	100.00	Tonalite	57
264.162.4	37.04	1.76	17.38	18.58	0.177	12.16	0.07	0.04	9.65	0.003	n.a.	3.14	100.00	Tonalite	54
264.162.4	39.55	1.77	15.03	16.14	0.159	13.87	0.02	0.05	10.03	0.003	n.a.	3.39	100.00	Tonalite	60
264.162.4	37.93	1.70	17.07	17.84	0.217	12.70	0.14	0.29	9.37	0.015	n.a.	2.73	100.00	Tonalite	56
264.162.4	37.14	1.68	17.62	18.13	0.159	12.14	0.03	0.03	9.94	<D.L.	n.a.	3.12	100.00	Tonalite	54
264.162.4	37.12	1.76	16.88	18.20	0.145	12.58	0.02	0.05	9.71	0.016	n.a.	3.53	100.00	Tonalite	55
264.162.4	37.74	1.69	16.92	17.68	0.175	12.65	0.05	0.04	9.82	0.006	n.a.	3.25	100.00	Tonalite	56
264.162.4	37.33	1.77	17.14	17.85	0.188	12.51	0.01	0.04	10.11	<D.L.	n.a.	3.05	100.00	Tonalite	56
264.162.4	38.27	1.84	16.11	17.56	0.163	13.02	<D.L.	0.03	10.03	0.003	n.a.	2.97	100.00	Tonalite	57
264.162.4	38.43	1.55	16.18	16.97	0.131	13.38	0.02	0.04	9.95	0.001	n.a.	3.35	100.00	Tonalite	58
264.162.4	37.61	1.80	16.59	17.79	0.162	13.03	0.01	0.07	9.74	0.002	n.a.	3.18	100.00	Tonalite	57
264.162.4	37.36	1.88	16.52	18.00	0.176	12.76	0.00	0.03	9.94	0.025	n.a.	3.31	100.00	Tonalite	56
246.233.5	38.70	3.67	12.77	15.55	0.111	16.09	0.03	0.54	8.75	0.090	n.a.	3.71	100.00	Leuco.	65
246.233.5	38.04	5.04	13.21	16.76	0.078	14.62	0.00	0.62	8.76	0.036	n.a.	2.83	100.00	Leuco.	61
246.233.5	37.66	5.51	13.58	15.82	0.104	14.60	<D.L.	0.60	8.86	0.020	n.a.	3.25	100.00	Leuco.	62
246.233.5	38.48	4.80	12.92	17.49	0.078	14.06	0.01	0.51	8.76	0.048	n.a.	2.84	100.00	Leuco.	59
246.233.5	37.28	5.49	13.77	15.96	0.099	14.68	0.01	0.67	8.58	0.105	n.a.	3.36	100.00	Leuco.	62
246.233.5	37.06	5.51	13.70	16.05	0.094	14.04	0.02	0.67	8.64	0.023	n.a.	4.20	100.00	Leuco.	61
246.233.5	38.66	4.45	12.79	15.49	0.088	15.49	0.05	0.58	8.64	0.025	n.a.	3.75	100.00	Leuco.	64
246.233.5	37.62	5.31	13.51	15.63	0.104	14.99	<D.L.	0.56	8.90	0.046	n.a.	3.33	100.00	Leuco.	63
246.233.5	37.91	5.12	13.33	17.17	0.079	13.98	0.00	0.61	8.83	0.024	n.a.	2.95	100.00	Leuco.	59
246.233.5	38.47	4.51	12.59	18.58	0.093	13.51	0.01	0.60	8.70	0.136	n.a.	2.80	100.00	Leuco.	56
246.233.5	43.30	3.81	10.40	11.05	0.153	14.81	11.22	2.79	0.79	0.079	n.a.	1.61	100.00	Leuco.	70
246.233.5	37.83	4.89	12.66	17.38	0.110	14.14	0.15	0.56	8.51	0.047	n.a.	3.72	100.00	Leuco.	59
264.190.1	38.39	1.29	14.30	18.16	0.201	15.18	<D.L.	0.07	9.32	0.011	n.a.	3.07	100.00	Xenolith	60

Abbreviations: O. nor.: Olivine norite; Leuco: Leucogabbro; <D.L.: below detection limit; n.a.: not analyzed

Appendix 15 (cont.)

Sample no.	SiO_2	TiO_2	Al_2O_3	FeO	MnO	MgO	CaO	Na_2O	K_2O	Cr_2O_3	Cl	(OH)	Total	Rock	Mg#
264.190.1	38.63	0.79	14.21	18.16	0.200	15.97	0.05	0.03	8.29	<D.L.	n.a.	3.66	100.00	Xenolith	61
264.190.1	36.96	0.61	14.69	19.34	0.210	16.02	0.01	0.05	8.44	0.007	n.a.	3.68	100.00	Xenolith	60
264.190.1	39.26	1.01	13.55	18.22	0.193	15.60	0.01	0.01	8.91	0.021	n.a.	3.20	100.00	Xenolith	60
264.190.1	38.58	1.11	13.91	17.87	0.220	14.97	<D.L.	0.06	9.27	0.027	n.a.	3.97	100.00	Xenolith	60
264.190.1	38.66	1.09	13.84	18.50	0.199	15.20	0.00	0.05	9.18	0.013	n.a.	3.27	100.00	Xenolith	59
264.190.1	37.90	1.22	14.75	18.72	0.219	14.40	<D.L.	0.03	9.43	0.019	n.a.	3.31	100.00	Xenolith	58
264.190.1	39.12	1.24	14.04	18.64	0.207	14.62	<D.L.	0.04	9.34	0.006	n.a.	2.76	100.00	Xenolith	58
264.190.1	38.28	1.36	14.46	18.41	0.179	14.58	0.02	0.02	9.29	<D.L.	n.a.	3.41	100.00	Xenolith	59
264.190.1	38.72	0.87	14.35	18.65	0.182	14.97	<D.L.	0.04	9.02	0.025	n.a.	3.19	100.00	Xenolith	59
264.190.1	39.58	0.89	13.83	17.56	0.172	15.52	0.01	0.05	8.82	0.014	n.a.	3.56	100.00	Xenolith	61
264.190.1	37.55	1.01	15.11	19.19	0.209	14.29	<D.L.	0.04	8.86	<D.L.	n.a.	3.73	100.00	Xenolith	57
264.190.1	38.99	1.00	13.85	18.19	0.214	15.02	0.02	0.05	8.98	0.020	n.a.	3.68	100.00	Xenolith	60
264.190.1	34.79	0.80	13.39	18.86	0.169	14.59	0.57	0.93	6.64	0.017	n.a.	9.24	100.00	Xenolith	58
264.190.1	38.43	0.95	14.20	18.46	0.185	15.23	0.02	0.07	8.75	0.020	n.a.	3.68	100.00	Xenolith	60
264.170.5	37.74	2.83	14.29	18.43	0.133	14.03	0.04	0.05	9.22	0.031	n.a.	3.21	100.00	Xenolith	58
264.170.5	37.56	1.84	14.56	18.13	0.107	14.88	0.09	0.09	8.20	0.145	n.a.	4.40	100.00	Xenolith	59
264.170.5	37.58	1.58	14.84	18.13	0.098	15.18	0.05	0.02	8.15	0.061	n.a.	4.31	100.00	Xenolith	60
264.170.5	37.94	1.69	14.50	18.10	0.117	14.77	0.01	0.02	8.81	0.060	n.a.	3.98	100.00	Xenolith	59
264.170.5	36.94	1.71	15.02	18.33	0.129	14.77	0.04	0.05	8.55	0.101	n.a.	4.37	100.00	Xenolith	59
264.170.5	38.65	1.69	14.91	17.12	0.079	14.58	0.03	0.04	9.23	0.068	n.a.	3.60	100.00	Xenolith	60
264.170.5	38.33	1.74	15.19	17.69	0.077	14.31	<D.L.	0.06	9.31	0.054	n.a.	3.22	100.00	Xenolith	59
264.170.5	38.36	1.69	14.47	17.47	0.079	14.84	0.05	0.07	8.72	0.041	n.a.	4.21	100.00	Xenolith	60
264.170.5	38.96	1.65	14.51	17.35	0.107	15.01	0.02	0.10	8.64	0.071	n.a.	3.59	100.00	Xenolith	61
264.170.5	39.12	1.49	14.42	17.32	0.091	14.81	0.04	0.08	9.02	0.087	n.a.	3.52	100.00	Xenolith	60
246.232.5	39.57	2.64	13.48	16.19	0.063	16.60	0.08	0.44	7.84	<D.L.	0.115	2.90	99.93	Leuco.	65
246.232.5	36.64	5.39	13.62	17.71	0.094	13.23	0.08	0.53	8.42	<D.L.	0.102	3.93	99.75	Leuco.	57
246.232.5	36.86	4.26	12.44	18.21	0.080	13.81	0.15	0.39	8.35	<D.L.	0.099	5.15	99.80	Leuco.	57
246.212.3	36.97	4.79	13.54	18.50	0.130	13.22	<D.L.	0.25	9.16	0.046	0.050	3.01	99.66	Leuco.	56
246.212.3	37.88	4.86	12.68	19.11	0.102	13.14	<D.L.	0.49	8.85	0.036	0.088	2.34	99.65	Leuco.	55
246.212.3	37.11	4.64	12.79	20.98	0.088	11.89	0.02	0.40	8.32	<D.L.	0.067	3.31	99.61	Leuco.	50
246.232.5	38.41	3.62	13.24	16.89	0.092	14.89	<D.L.	0.54	8.74	0.025	0.127	3.28	99.85	Leuco.	61
246.232.5	39.04	3.43	12.77	17.42	0.113	14.96	0.03	0.47	8.55	<D.L.	0.113	2.93	99.82	Leuco.	60
248.262.0	38.02	3.99	13.15	18.45	0.089	13.62	0.05	0.60	8.66	<D.L.	0.105	2.94	99.68	Leuco.	57
248.262.0	37.61	3.42	13.73	16.74	0.030	15.42	<D.L.	0.55	8.72	<D.L.	0.048	3.43	99.70	Leuco.	62
246.212.3	37.92	4.44	12.89	18.27	0.091	13.39	0.24	0.31	8.75	0.070	0.098	3.15	99.63	Leuco.	57
246.239.1	38.22	3.96	13.05	15.18	0.066	17.01	<D.L.	0.49	8.20	0.127	0.077	3.11	99.49	O. nor.	67
246.239.1	38.78	4.85	13.28	13.77	0.053	16.93	0.05	0.51	8.40	0.272	0.120	2.49	99.56	O. nor.	69
246.212.3	38.86	3.37	12.93	15.11	0.124	17.28	0.07	0.35	8.24	0.169	0.087	2.96	99.55	O. nor.	67
246.249.6	36.78	1.32	15.49	20.55	0.047	12.20	<D.L.	0.17	9.34	0.191	1.082	2.84	100.00	Late dike	51
246.249.6	36.70	1.24	15.56	20.55	0.065	12.41	0.02	0.13	9.27	0.049	1.005	3.00	100.00	Late dike	52
246.249.6	37.87	1.20	14.78	19.55	0.049	13.15	0.04	0.13	9.07	0.312	0.794	3.06	100.00	Late dike	55
246.249.6	37.18	1.39	15.11	20.75	0.029	12.10	0.03	0.14	9.16	0.232	1.183	2.72	100.00	Late dike	51
246.249.6	37.44	1.32	14.77	20.29	0.053	12.57	<D.L.	0.16	9.18	0.284	1.073	2.86	100.00	Late dike	52
246.249.6	37.74	1.21	14.83	20.00	0.056	12.85	0.02	0.12	9.15	0.313	1.040	2.67	100.00	Late dike	53
246.249.6	37.89	1.26	14.74	19.72	0.058	12.89	0.03	0.12	9.11	0.246	0.890	3.05	100.00	Late dike	54
246.249.6	36.45	1.44	14.93	20.90	0.056	12.04	0.07	0.18	8.90	0.315	1.140	3.57	100.00	Late dike	51
246.249.6	37.05	1.24	14.85	20.03	0.039	12.58	0.02	0.15	9.23	0.208	1.089	3.51	100.00	Late dike	53
246.249.6	36.61	1.20	14.86	20.91	0.056	12.58	0.03	0.08	8.71	0.228	1.132	3.59	100.00	Late dike	52
246.249.6	36.22	1.31	15.42	20.60	0.073	13.37	0.02	0.14	7.89	0.287	0.998	3.67	100.00	Late dike	54
246.249.6	36.95	1.29	14.84	20.81	0.033	12.26	0.00	0.11	9.09	0.230	1.215	3.17	100.00	Late dike	51
246.249.6	37.40	1.04	14.98	19.72	0.058	13.98	0.02	0.10	8.45	0.271	0.746	3.23	100.00	Late dike	56
246.249.6	36.63	1.21	15.52	21.04	0.078	11.96	0.02	0.12	9.18	0.266	1.218	2.78	100.00	Late dike	50
246.249.6	36.78	1.20	14.98	20.26	0.041	12.25	0.01	0.05	9.20	0.200	1.202	3.81	100.00	Late dike	52
246.249.6	36.13	1.32	15.64	20.59	0.069	12.58	0.06	0.15	8.52	0.222	1.036	3.69	100.00	Late dike	52
246.249.6	36.67	1.32	15.75	20.72	0.080	12.12	0.03	0.15	9.24	0.254	1.085	2.57	100.00	Late dike	51
246.249.6	36.44	1.24	15.23	20.85	0.081	12.97	0.05	0.11	8.17	0.269	1.133	3.45	100.00	Late dike	53
246.249.6	37.51	1.27	15.13	20.20	0.044	12.79	0.02	0.10	9.03	0.210	1.138	2.56	100.00	Late dike	53
246.249.6	37.38	1.20	15.54	19.93	0.051	12.55	0.02	0.13	9.40	0.132	0.937	2.72	100.00	Late dike	53
246.249.6	36.97	1.34	14.67	20.09	0.032	12.55	0.02	0.07	9.28	0.171	1.040	3.76	100.00	Late dike	53
246.249.6	37.13	1.26	15.28	19.18	0.040	12.92	0.01	0.09	9.15	0.127	0.729	4.08	100.00	Late dike	55

Abbreviations: O. nor.: Olivine norite; Leuco: Leucogabbro; <D.L.: below detection limit; n.a.: not analyzed

Appendix 16 Electron microprobe profiles in plagioclase.

Sample no.	Rock	d (μm)	SiO_2	TiO_2	Al_2O_3	FeO	CaO	Na_2O	K_2O	Total	An
						wt.%					mol.%
246.293.1	O. nor.	0.0	53.82	0.04	28.11	1.26	10.79	5.34	0.14	99.80	52.3
246.293.1	O. nor.	3.2	55.11	0.02	27.84	0.74	10.20	5.92	0.08	100.14	48.5
246.293.1	O. nor.	6.4	54.83	0.03	27.10	1.27	9.91	5.90	0.07	99.63	47.9
246.293.1	O. nor.	9.5	55.90	0.02	27.29	0.48	9.77	6.35	0.03	99.93	45.9
246.293.1	O. nor.	12.8	56.36	0.04	27.33	0.49	9.65	6.37	0.03	100.33	45.5
246.293.1	O. nor.	16.0	56.55	0.04	27.21	0.46	9.49	6.41	0.03	100.25	44.9
246.308.0	O. nor.	0.0	48.72	0.03	32.53	0.67	15.88	2.78	0.07	100.71	75.6
246.308.0	O. nor.	3.1	48.76	<D.L.	32.16	0.69	15.70	2.73	0.05	100.15	75.9
246.308.0	O. nor.	6.1	50.04	0.05	31.32	0.61	15.11	3.17	0.06	100.45	72.2
246.308.0	O. nor.	9.1	51.29	0.03	30.63	0.67	13.92	3.90	0.11	100.60	66.0
246.308.0	O. nor.	12.2	50.86	<D.L.	30.90	0.71	14.00	3.76	0.09	100.43	66.9
246.308.0	O. nor.	15.2	50.67	0.05	30.79	0.71	14.22	3.68	0.10	100.27	67.8
246.308.0	O. nor.	18.3	50.04	0.04	31.38	0.73	14.80	3.27	0.08	100.43	71.1
246.308.0	O. nor.	24.3	49.68	0.04	31.63	0.68	15.23	3.16	0.05	100.54	72.5
246.308.0	O. nor.	27.4	49.46	0.04	31.89	0.75	15.29	3.01	0.05	100.61	73.5
246.308.0	O. nor.	30.5	51.33	0.04	30.56	0.70	13.77	3.92	0.06	100.46	65.8
246.308.0	O. nor.	33.5	50.36	0.04	31.23	0.66	14.64	3.46	0.05	100.49	69.8
246.308.0	O. nor.	36.6	52.01	0.06	29.96	0.72	13.33	4.23	0.07	100.44	63.3
246.308.0	O. nor.	39.6	49.17	0.06	31.20	0.93	14.70	3.03	0.20	99.49	72.0
246.308.0	O. nor.	42.6	47.63	0.05	31.15	2.54	11.71	2.19	1.14	98.03	68.8
246.308.0	O. nor.	45.7	49.57	0.04	32.07	0.77	15.42	3.06	0.02	100.99	73.5
246.308.0	O. nor.	48.8	49.31	0.06	31.43	0.72	14.97	3.22	0.03	100.10	71.8
246.308.0	O. nor.	51.7	50.38	0.06	31.41	0.65	14.59	3.45	0.04	100.63	69.9
246.308.0	O. nor.	54.8	50.94	0.06	30.94	0.58	14.29	3.75	0.05	100.71	67.6
246.308.0	O. nor.	57.8	52.18	0.07	30.23	0.65	13.12	4.30	0.08	100.71	62.5
246.308.0	O. nor.	60.9	52.87	0.06	29.80	0.52	12.45	4.66	0.09	100.52	59.3
246.308.0	O. nor.	64.0	52.83	0.05	29.00	0.53	11.91	4.94	0.09	99.41	56.8
246.308.0	O. nor.	67.0	54.40	0.05	28.70	0.40	11.36	5.35	0.07	100.36	53.8
246.308.0	O. nor.	70.0	55.39	0.04	28.04	0.39	10.64	5.90	0.08	100.52	49.7
246.308.0	O. nor.	73.1	56.16	0.04	27.60	0.43	10.01	6.22	0.07	100.60	46.9
246.308.0	O. nor.	76.1	57.19	0.02	26.56	0.39	8.78	6.82	0.05	99.87	41.4
246.308.0	O. nor.	79.2	57.97	0.03	26.32	0.39	8.29	7.11	0.07	100.27	39.0
246.308.0	O. nor.	82.2	58.67	0.03	25.93	0.40	7.88	7.43	0.06	100.47	36.8
246.308.0	O. nor.	85.2	58.59	<D.L.	25.66	0.41	7.76	7.51	0.07	100.07	36.2
246.308.0	O. nor.	88.3	59.23	<D.L.	25.84	0.44	7.45	7.69	0.07	100.76	34.7

Abbreviations: O. nor: Olivine norite; An: anorthite

Appendix 16 (cont.)

Sample no.	Rock	d (μm)	SiO_2	TiO_2	Al_2O_3	FeO	CaO	Na_2O	K_2O	Total	An
						wt.%					mol.%
246.308.0	O. nor.	0.0	50.34	0.05	31.46	0.68	14.58	3.53	0.08	100.80	69.2
246.308.0	O. nor.	2.7	49.60	0.06	31.84	0.74	15.24	3.06	0.07	100.72	73.0
246.308.0	O. nor.	5.4	51.41	0.05	30.70	0.77	13.87	3.92	0.13	100.95	65.7
246.308.0	O. nor.	8.1	50.83	0.04	30.74	0.76	14.04	3.68	0.14	100.28	67.3
246.308.0	O. nor.	10.9	50.87	0.04	31.20	0.77	14.40	3.51	0.14	101.01	68.9
246.308.0	O. nor.	13.6	49.77	0.03	31.88	0.85	15.24	3.16	0.10	101.17	72.3
246.308.0	O. nor.	16.2	49.76	0.03	31.83	0.80	15.34	3.08	0.09	100.96	73.0
246.308.0	O. nor.	19.0	49.70	0.03	31.91	0.89	15.16	3.13	0.10	101.02	72.4
246.308.0	O. nor.	21.7	49.84	0.04	31.79	0.85	15.04	3.21	0.08	100.95	71.8
246.308.0	O. nor.	24.4	49.55	0.04	32.15	0.74	15.36	3.02	0.04	100.95	73.6
246.308.0	O. nor.	27.1	54.02	0.06	28.90	0.68	11.68	5.10	0.06	100.58	55.7
246.308.0	O. nor.	29.8	54.67	0.06	28.80	0.76	11.58	5.32	0.04	101.40	54.5
246.308.0	O. nor.	0.0	50.45	0.05	31.37	0.70	14.58	3.37	0.06	100.70	70.3
246.308.0	O. nor.	5.1	50.56	0.03	31.19	0.62	14.53	3.52	<D.L.	100.51	69.5
246.308.0	O. nor.	10.0	49.46	0.04	31.68	0.81	14.92	3.24	0.05	100.28	71.6
246.308.0	O. nor.	20.1	45.62	0.04	26.29	6.67	8.38	2.90	0.09	98.43	61.0
246.308.0	O. nor.	25.0	53.51	0.04	29.55	0.63	12.01	4.82	0.11	100.71	57.6
246.308.0	O. nor.	29.9	52.75	0.06	28.26	1.29	11.14	4.79	0.12	99.74	55.8
246.308.0	O. nor.	39.7	62.81	0.05	23.15	0.41	4.45	9.44	<D.L.	100.36	20.7
246.308.0	O. nor.	44.6	62.71	<D.L.	23.46	0.41	4.66	9.34	0.17	100.86	21.4
246.290.7	O. nor.	0.0	52.22	0.04	29.13	0.71	12.83	4.26	0.16	99.66	61.9
246.290.7	O. nor.	6.1	50.99	0.05	29.98	0.70	13.71	3.81	0.13	99.70	66.1
246.290.7	O. nor.	12.1	51.66	0.06	29.51	0.66	13.14	4.01	0.13	99.45	64.0
246.290.7	O. nor.	18.3	52.53	0.06	28.86	0.69	12.52	4.51	0.13	99.58	60.1
246.290.7	O. nor.	24.3	52.86	<D.L.	28.73	0.62	12.11	4.63	0.16	99.43	58.6
246.290.7	O. nor.	30.3	52.71	0.05	28.45	0.74	12.12	4.60	0.16	99.11	58.8
246.290.7	O. nor.	36.4	52.78	0.04	28.55	0.66	12.17	4.68	0.14	99.32	58.5
246.290.7	O. nor.	51.9	49.55	<D.L.	30.74	0.76	14.77	3.13	0.08	99.36	71.9
246.290.7	O. nor.	49.2	51.65	0.05	29.04	0.74	12.72	4.27	0.13	99.10	61.7
246.290.7	O. nor.	54.5	52.12	0.05	29.10	0.64	12.81	4.42	0.13	99.57	61.1
246.290.7	O. nor.	60.0	49.43	0.04	30.93	0.76	14.81	3.14	0.08	99.51	72.0
246.290.7	O. nor.	64.5	51.46	0.04	29.50	0.65	13.21	4.10	0.11	99.37	63.6
246.290.7	O. nor.	69.1	49.77	0.05	30.37	0.71	14.38	3.31	0.08	98.99	70.2
246.290.7	O. nor.	78.6	48.39	<D.L.	31.39	0.77	15.64	2.55	0.05	99.15	77.0
246.290.7	O. nor.	84.6	48.47	0.05	31.37	0.87	15.66	2.67	0.04	99.46	76.2

Abbreviations: O. nor: Olivine norite; An: anorthite

Appendix 16 (cont.)

Sample no.	Rock	d (μm)	SiO_2	TiO_2	Al_2O_3	FeO	CaO	Na_2O	K_2O	Total	An
						wt.%					mol.%
246.300.9	O. nor.	0.0	49.28	0.04	31.30	0.70	15.05	2.93	0.08	99.70	73.6
246.300.9	O. nor.	19.4	49.39	<D.L.	31.15	0.69	14.92	3.06	0.09	99.68	72.5
246.300.9	O. nor.	53.8	51.08	0.05	29.84	0.81	13.47	3.82	0.12	99.74	65.6
246.300.9	O. nor.	80.7	50.95	0.06	28.49	1.07	12.16	4.02	0.18	98.60	61.9
246.300.9	O. nor.	104.6	52.44	0.08	29.36	0.65	12.66	4.29	0.18	100.00	61.3
246.300.9	O. nor.	116.6	52.40	0.05	29.18	0.71	12.71	4.33	0.18	99.88	61.2
246.300.9	O. nor.	136.2	52.39	0.05	29.19	0.67	12.52	4.31	0.19	99.69	61.0
246.300.9	O. nor.	155.6	52.60	0.05	28.99	0.66	12.45	4.44	0.17	99.66	60.2
246.300.9	O. nor.	175.0	52.54	0.05	29.08	0.77	12.23	4.32	0.30	99.89	59.9
246.300.9	O. nor.	194.5	53.18	0.07	28.84	0.63	11.81	4.76	0.19	99.79	57.2
246.300.9	O. nor.	210.4	53.07	0.07	28.23	0.75	11.17	5.01	0.18	99.11	54.7
246.300.9	O. nor.	241.2	58.81	<D.L.	25.43	0.36	7.54	7.47	0.08	99.95	35.7
246.300.9	O. nor.	251.7	58.78	<D.L.	25.44	0.41	7.77	7.50	0.09	100.23	36.2
246.300.9	O. nor.	272.3	60.12	<D.L.	24.68	0.44	6.71	8.06	0.07	100.29	31.4
246.290.7	O. nor.	0.0	49.45	0.03	31.18	0.65	14.99	3.03	0.10	99.75	72.8
246.290.7	O. nor.	3.6	48.06	<D.L.	31.75	0.93	14.37	2.48	0.67	98.82	73.1
246.290.7	O. nor.	2.1	49.15	0.04	31.09	0.63	15.04	2.95	0.07	99.29	73.5
246.290.7	O. nor.	5.5	52.77	0.06	28.83	0.67	12.11	4.48	0.26	99.50	59.0
246.290.7	O. nor.	4.2	52.94	0.08	28.64	0.61	12.05	4.70	0.16	99.49	58.1
246.290.7	O. nor.	5.3	53.02	0.05	28.56	0.75	11.63	4.82	0.20	99.42	56.5
246.290.7	O. nor.	6.3	53.44	0.08	28.52	0.58	11.68	4.94	0.13	99.69	56.2
246.290.7	O. nor.	6.4	53.38	0.06	28.34	0.63	11.81	4.84	0.25	99.63	56.6
246.290.7	O. nor.	6.7	53.40	0.06	28.35	0.62	11.79	4.76	0.23	99.56	57.0
246.290.7	O. nor.	9.2	53.47	0.04	28.41	0.67	11.72	4.82	0.22	99.69	56.6
246.290.7	O. nor.	10.9	53.37	<D.L.	28.33	0.56	11.70	4.87	0.11	99.26	56.7
246.290.7	O. nor.	11.2	54.46	0.06	27.61	0.58	10.86	5.27	0.26	99.40	52.5
246.290.7	O. nor.	5.8	57.24	0.03	26.20	0.50	8.94	6.48	0.19	99.83	42.8
246.290.7	O. nor.	13.0	57.91	<D.L.	25.86	0.57	8.35	6.87	0.24	100.03	39.7
246.290.7	O. nor.	13.9	58.43	<D.L.	25.57	0.63	8.02	7.08	0.19	100.18	38.1
246.290.7	O. nor.	0.0	49.51	0.05	30.92	0.68	14.94	3.05	0.05	99.51	72.8
246.290.7	O. nor.	12.7	48.84	<D.L.	31.22	0.66	15.33	2.69	0.09	99.19	75.5
246.290.7	O. nor.	24.2	48.82	0.05	31.31	0.67	15.28	2.79	0.10	99.36	74.7
246.290.7	O. nor.	83.5	52.06	0.04	29.07	0.66	12.89	4.25	0.17	99.48	62.0
246.290.7	O. nor.	45.1	49.64	0.06	30.64	0.66	14.57	3.19	0.12	99.23	71.1
246.290.7	O. nor.	59.0	52.20	0.06	29.11	0.66	12.65	4.33	0.20	99.55	61.0

Abbreviations: O. nor: Olivine norite; An: anorthite

Appendix 16 (cont.)

Sample no.	Rock	d (μm)	SiO_2	TiO_2	Al_2O_3	FeO	CaO	Na_2O	K_2O	Total	An
						wt.%					mol.%
246.290.7	O. nor.	75.5	51.77	<D.L.	28.31	1.18	11.97	4.32	0.19	98.48	59.8
246.290.7	O. nor.	83.9	52.75	0.07	28.91	0.62	12.33	4.47	0.22	99.74	59.6
246.290.7	O. nor.	96.1	52.76	0.05	28.85	0.57	12.26	4.55	0.22	99.61	59.1
246.290.7	O. nor.	106.5	53.13	0.07	28.61	0.55	12.04	4.64	0.23	99.59	58.1
246.290.7	O. nor.	119.9	52.87	0.04	28.64	0.58	12.16	4.65	0.22	99.48	58.3
246.290.7	O. nor.	131.7	56.68	<D.L.	26.29	0.38	9.17	6.35	0.35	99.51	43.5
246.290.7	O. nor.	140.4	56.86	<D.L.	26.20	0.44	9.04	6.32	0.38	99.51	43.2
246.290.7	O. nor.	154.0	56.80	0.05	26.39	0.59	9.09	6.34	0.26	99.78	43.5
246.290.7	O. nor.	0.0	49.01	0.06	31.28	0.70	15.09	2.89	0.06	99.41	74.0
246.290.7	O. nor.	2.4	48.81	0.05	31.57	0.65	15.53	2.70	0.05	99.67	75.8
246.290.7	O. nor.	4.8	48.71	0.04	31.43	0.62	15.49	2.65	0.09	99.36	75.9
246.290.7	O. nor.	7.2	50.87	0.09	30.36	0.62	13.82	3.59	0.15	99.80	67.4
246.290.7	O. nor.	9.5	50.65	0.08	30.40	0.58	13.92	3.63	0.14	99.68	67.4
246.290.7	O. nor.	11.9	50.01	0.08	30.59	0.67	14.35	3.37	0.14	99.51	69.6
246.290.7	O. nor.	14.3	49.93	0.08	30.70	0.66	14.43	3.31	0.13	99.60	70.1
246.290.7	O. nor.	16.9	49.96	0.07	30.93	0.64	14.57	3.22	0.11	99.81	71.0
246.290.7	O. nor.	22.7	52.66	0.07	28.91	0.57	12.20	4.65	0.08	99.48	58.9
246.290.7	O. nor.	23.1	53.52	0.05	28.54	0.53	11.66	4.87	0.12	99.60	56.6
246.290.7	O. nor.	24.6	53.82	0.04	28.35	0.58	11.62	4.99	0.11	99.79	55.9
246.290.7	O. nor.	26.0	54.27	0.06	28.42	0.56	11.22	5.21	0.08	100.12	54.1
246.290.7	O. nor.	28.7	54.13	0.03	28.30	0.51	11.35	5.18	0.09	99.88	54.5
246.290.7	O. nor.	31.1	54.26	0.07	28.34	0.49	11.14	5.18	0.07	99.79	54.1
246.290.7	O. nor.	15.0	50.59	0.06	30.42	0.57	14.11	3.68	<D.L.	99.79	67.9
246.300.9	O. nor.	0.0	49.30	<D.L.	31.63	0.43	15.22	2.88	<D.L.	99.76	74.5
246.300.9	O. nor.	3.0	49.47	0.03	31.57	0.49	15.17	2.88	<D.L.	99.92	74.4
246.300.9	O. nor.	6.0	49.43	<D.L.	31.53	0.49	15.03	2.99	<D.L.	99.83	73.5
246.300.9	O. nor.	9.0	51.25	0.04	30.30	0.47	13.70	3.77	<D.L.	99.81	66.8
246.300.9	O. nor.	12.1	50.64	0.04	30.88	0.32	14.12	3.56	<D.L.	99.86	68.6
246.300.9	O. nor.	14.9	54.10	<D.L.	29.22	0.19	11.75	5.10	<D.L.	100.67	56.0
246.300.9	O. nor.	17.9	56.27	<D.L.	27.24	0.39	9.65	6.38	0.04	100.23	45.4
246.300.9	O. nor.	20.9	56.29	0.04	27.14	0.46	9.69	6.15	0.06	100.10	46.4
246.300.9	O. nor.	23.9	56.17	<D.L.	27.14	0.43	9.72	6.10	0.07	99.89	46.6
246.300.9	O. nor.	26.9	56.38	<D.L.	27.09	0.41	9.59	6.26	0.09	100.10	45.6
246.300.9	O. nor.	29.9	61.30	<D.L.	23.95	0.37	5.85	8.38	0.13	100.18	27.6
246.300.9	O. nor.	32.9	62.82	<D.L.	23.25	0.39	4.75	9.32	0.12	100.85	21.8

Abbreviations: O. nor: Olivine norite; An: anorthite

Appendix 16 (cont.)

Sample no.	Rock	d (μm)	SiO_2	TiO_2	Al_2O_3	FeO	CaO	Na_2O	K_2O	Total	An
						wt.%					mol.%
246.300.9	O. nor.	35.9	63.33	<D.L.	22.80	0.33	4.33	9.36	0.12	100.48	20.2
246.300.9	O. nor.	38.9	63.90	<D.L.	22.49	0.35	3.91	9.78	0.11	100.76	18.0
246.300.9	O. nor.	41.9	64.57	<D.L.	22.73	0.34	3.71	9.55	0.09	101.20	17.6
248.254.0	Leuco.	0.0	50.02	0.03	31.03	1.00	14.57	3.49	0.03	100.22	69.6
248.254.0	Leuco.	3.0	50.44	0.04	30.89	0.82	14.43	3.43	0.03	100.12	69.8
248.254.0	Leuco.	6.1	50.79	0.04	30.83	0.89	14.27	3.71	0.02	100.59	67.9
248.254.0	Leuco.	9.1	50.05	0.05	30.89	0.88	14.61	3.49	0.01	100.01	69.8
248.254.0	Leuco.	12.2	53.01	0.03	29.11	0.74	12.13	4.88	0.04	99.97	57.8
248.254.0	Leuco.	15.2	54.42	0.04	28.19	0.83	11.05	5.64	0.03	100.29	51.9
248.254.0	Leuco.	18.3	55.86	0.03	27.23	0.68	9.64	6.43	0.01	99.95	45.3
248.254.0	Leuco.	21.3	60.01	0.05	24.64	0.64	6.77	8.14	<D.L.	100.27	31.5
248.262.9	Leuco.	0.0	58.54	0.05	25.67	0.54	7.90	7.13	0.51	100.39	36.9
248.262.9	Leuco.	2.1	59.13	0.03	25.39	0.49	7.41	7.37	0.53	100.47	34.7
248.262.9	Leuco.	4.1	60.11	0.03	25.06	0.46	6.90	7.56	0.53	100.69	32.5
248.262.9	Leuco.	6.1	60.33	0.04	24.65	0.39	6.39	7.90	0.47	100.25	30.1
248.262.9	Leuco.	8.2	59.03	0.04	22.95	1.16	5.44	8.46	0.24	97.40	25.9
248.262.9	Leuco.	10.3	60.98	0.04	23.32	0.46	4.63	7.96	0.70	98.16	23.3
248.262.9	Leuco.	16.4	62.00	0.03	22.75	1.40	4.52	8.84	0.40	100.16	21.5
248.262.9	Leuco.	18.5	62.94	<D.L.	22.56	0.96	3.55	9.21	0.41	99.82	17.2
248.262.9	Leuco.	20.5	63.98	<D.L.	22.43	0.38	3.68	9.37	0.77	100.63	17.1
248.262.9	Leuco.	22.6	64.15	<D.L.	22.12	0.37	3.47	9.29	0.77	100.26	16.4
248.262.9	Leuco.	24.7	63.20	0.03	21.65	0.73	3.18	9.17	0.74	99.55	15.4
248.262.9	Leuco.	26.6	64.78	<D.L.	22.23	0.31	2.77	9.56	0.62	100.36	13.3
248.262.9	Leuco.	30.8	64.44	<D.L.	21.83	0.98	2.64	9.88	0.19	100.63	12.7
248.262.9	Leuco.	36.9	65.60	<D.L.	21.32	0.39	2.45	10.10	0.64	100.54	11.4
248.262.9	Leuco.	38.9	65.67	0.02	21.49	0.36	2.32	10.56	0.32	100.84	10.6
248.262.9	Leuco.	41.0	65.76	<D.L.	21.46	0.31	2.25	10.64	0.17	100.67	10.4
248.262.9	Leuco.	43.0	65.92	0.03	21.44	0.29	2.10	10.63	0.14	100.56	9.8
248.262.9	Leuco.	45.1	66.13	<D.L.	21.09	0.31	2.02	10.55	0.12	100.25	9.5
248.262.9	Leuco.	47.1	66.17	0.04	21.20	0.38	1.79	10.85	0.16	100.66	8.3
248.262.9	Leuco.	49.1	66.22	0.03	21.55	0.27	1.77	11.10	0.09	101.09	8.1
248.262.9	Leuco.	51.2	66.35	<D.L.	21.14	0.38	1.68	10.82	0.09	100.54	7.9
248.262.9	Leuco.	53.2	68.54	<D.L.	20.24	0.15	0.19	12.14	0.03	101.30	0.8

Abbreviations: O. nor: Olivine norite; LeucoLeucogabbro; An: anorthite

Appendix 16 (cont.)

Sample no.	Rock	d (μm)	SiO_2	TiO_2	Al_2O_3	FeO	CaO	Na_2O	K_2O	Total	An
						wt.%					mol.%
246.212.3	Leuco.	0.0	53.12	0.06	29.02	0.69	11.92	4.82	0.16	99.88	57.2
246.212.3	Leuco.	5.0	53.18	0.07	28.99	0.67	11.87	4.80	0.19	99.85	57.1
246.212.3	Leuco.	10.0	53.30	0.06	29.30	0.63	11.88	4.77	0.20	100.20	57.3
246.212.3	Leuco.	15.0	53.13	0.07	29.07	0.48	11.93	4.67	0.19	99.62	57.9
246.212.3	Leuco.	20.0	56.24	0.05	27.37	0.45	9.56	6.06	0.30	100.04	45.8
246.212.3	Leuco.	25.0	56.07	0.03	27.19	0.45	9.53	6.06	0.27	99.69	45.8
246.212.3	Leuco.	40.0	56.57	0.04	27.06	0.47	9.29	6.24	0.31	100.02	44.3
246.212.3	Leuco.	45.0	56.10	0.05	26.92	0.43	9.22	6.15	0.32	99.22	44.5
246.212.3	Leuco.	50.0	56.50	0.03	26.93	0.44	9.09	6.25	0.34	99.62	43.7
246.212.3	Leuco.	55.0	56.47	0.04	27.03	0.44	9.19	6.22	0.32	99.81	44.1
246.212.3	Leuco.	60.0	56.81	<D.L.	26.81	0.43	8.80	6.34	0.33	99.57	42.6
246.212.3	Leuco.	65.0	57.00	0.06	26.49	0.44	8.69	6.46	0.34	99.53	41.8
246.212.3	Leuco.	80.0	59.97	0.03	24.99	0.33	6.61	7.71	0.46	100.15	31.3
246.212.3	Leuco.	85.0	60.00	0.03	24.86	0.34	6.62	7.82	0.52	100.29	30.9
246.212.3	Leuco.	90.0	59.96	<D.L.	24.92	0.36	6.52	7.85	0.50	100.21	30.6
246.212.3	Leuco.	95.0	59.98	<D.L.	24.76	0.36	6.56	7.87	0.49	100.09	30.7
246.212.3	Leuco.	100.0	60.41	<D.L.	24.65	0.38	6.39	7.99	0.51	100.38	29.8
246.212.3	Leuco.	104.9	60.79	<D.L.	24.39	0.36	6.01	8.00	0.47	100.08	28.5
246.212.3	Leuco.	110.0	64.36	<D.L.	22.36	0.28	3.17	9.91	0.42	100.52	14.7
246.212.3	Leuco.	115.0	65.22	0.02	21.72	0.29	2.59	10.45	0.18	100.56	11.9
248.265.1	Leuco.	0.0	53.23	0.07	28.93	0.68	12.07	4.73	0.25	100.31	57.7
248.265.1	Leuco.	43.8	53.22	0.05	28.77	0.62	11.84	4.89	0.24	99.95	56.4
248.265.1	Leuco.	69.2	53.97	0.06	28.65	0.65	11.61	4.88	0.27	100.42	55.9
248.265.1	Leuco.	103.9	53.82	0.04	28.41	0.59	11.33	5.04	0.28	99.83	54.5
248.265.1	Leuco.	135.4	54.42	0.06	28.24	0.60	11.20	5.10	0.28	100.24	53.9
248.265.1	Leuco.	171.1	54.84	0.04	28.19	0.62	11.10	5.25	0.19	100.58	53.3
248.265.1	Leuco.	207.6	54.38	0.06	28.09	0.61	10.90	5.35	0.23	99.94	52.3
248.265.1	Leuco.	251.7	55.03	0.05	27.60	0.55	10.66	5.61	0.30	100.08	50.4
248.265.1	Leuco.	285.0	55.61	0.06	27.67	0.51	10.31	5.48	0.35	100.26	49.9
248.265.1	Leuco.	311.2	56.88	0.06	26.59	0.45	9.07	6.27	0.42	100.01	43.4
248.265.1	Leuco.	348.3	58.19	0.04	26.04	0.46	8.25	6.82	0.15	100.24	39.7
248.265.1	Leuco.	394.9	58.21	0.05	25.81	0.44	7.97	7.05	0.50	100.26	37.4
248.265.1	Leuco.	420.1	62.03	0.03	23.26	0.37	5.13	9.01	0.16	100.17	23.7
248.265.1	Leuco.	452.8	63.35	<D.L.	22.61	0.36	4.06	9.60	0.21	100.40	18.7
248.265.1	Leuco.	482.4	64.18	<D.L.	22.01	0.41	3.32	10.09	0.11	100.32	15.3

Abbreviations: LeucoLeucogabbro; An: anorthite

Appendix 16 (cont.)

Sample no.	Rock	d (μm)	SiO_2	TiO_2	Al_2O_3	FeO	CaO	Na_2O	K_2O	Total	An
						wt.%					mol.%
248.265.1	Leuco.	0.0	55.05	0.06	27.63	0.61	10.66	5.48	0.30	100.06	50.9
248.265.1	Leuco.	19.4	55.21	<D.L.	27.74	0.61	10.58	5.43	0.28	100.18	51.0
248.265.1	Leuco.	74.7	55.01	0.05	27.80	0.60	10.44	5.53	0.27	100.07	50.2
248.265.1	Leuco.	99.7	54.99	0.07	27.86	0.55	10.70	5.60	0.23	100.32	50.7
248.265.1	Leuco.	126.1	55.06	0.06	28.08	0.60	10.68	5.55	0.12	100.49	51.2
248.265.1	Leuco.	155.9	55.27	0.04	27.85	0.64	10.32	5.67	0.30	100.36	49.3
248.265.1	Leuco.	176.8	55.02	0.06	27.64	0.59	10.65	5.63	0.15	100.02	50.7
248.265.1	Leuco.	207.8	55.28	0.04	27.56	0.57	10.60	5.57	0.25	100.17	50.5
248.265.1	Leuco.	222.8	55.39	0.05	27.44	0.53	10.48	5.76	0.26	100.22	49.4
248.265.1	Leuco.	251.5	61.55	<D.L.	23.98	0.36	5.59	8.39	0.37	100.46	26.3
248.265.1	Leuco.	284.6	62.90	0.04	23.05	0.34	4.49	9.07	0.46	100.53	20.9
248.265.1	Leuco.	302.5	64.60	<D.L.	22.57	0.38	3.28	9.77	0.11	100.94	15.6
248.265.1	Leuco.	337.2	66.34	<D.L.	22.12	0.41	2.68	9.99	0.06	101.80	12.9
248.212.6	Leuco.	0.0	57.34	0.04	26.32	0.45	8.78	6.56	0.39	100.21	41.6
248.212.6	Leuco.	12.0	57.11	0.04	26.10	0.39	8.55	6.70	0.41	99.61	40.4
248.212.6	Leuco.	29.0	56.83	0.04	26.48	0.41	9.06	6.32	0.37	99.79	43.3
248.212.6	Leuco.	44.9	56.68	0.04	26.61	0.40	9.02	6.43	0.25	99.72	43.1
248.212.6	Leuco.	55.1	56.01	0.05	25.96	0.45	8.97	6.24	0.23	98.20	43.7
248.212.6	Leuco.	68.4	57.22	0.04	26.33	0.44	7.94	6.72	0.55	99.70	38.2
248.212.6	Leuco.	86.9	60.81	<D.L.	23.89	0.29	5.95	8.42	0.29	99.96	27.6
248.212.6	Leuco.	101.4	61.47	<D.L.	23.47	0.33	5.16	8.59	0.39	99.66	24.4
248.212.6	Leuco.	115.3	62.54	<D.L.	23.15	0.30	4.92	8.98	0.26	100.43	22.9
248.212.6	Leuco.	132.5	62.60	<D.L.	23.25	0.37	3.77	8.94	0.67	99.95	18.2
248.212.6	Leuco.	144.8	63.80	<D.L.	22.27	0.22	3.65	9.70	0.19	100.10	17.0
248.212.6	Leuco.	159.0	63.56	<D.L.	21.92	0.21	3.40	9.81	0.14	99.32	16.0
248.212.6	Leuco.	170.9	64.86	<D.L.	21.96	0.15	2.10	9.63	1.21	100.16	10.0
248.212.6	Leuco.	191.3	66.14	<D.L.	20.88	0.17	1.71	10.80	0.15	100.09	8.0
248.212.6	Leuco.	204.6	67.42	<D.L.	19.91	0.08	0.45	11.50	0.13	99.76	2.1
248.240.8	Leuco.	0.0	48.19	0.05	31.12	0.75	14.27	2.84	0.32	98.35	72.1
248.240.8	Leuco.	5.1	49.40	<D.L.	31.11	0.56	14.94	3.17	0.05	99.55	72.1
248.240.8	Leuco.	9.3	48.91	0.05	31.55	0.49	15.38	2.85	0.05	99.57	74.7
248.240.8	Leuco.	14.0	53.16	0.07	28.59	0.57	11.81	4.86	0.19	99.54	56.7
248.240.8	Leuco.	18.6	54.68	0.05	27.70	0.49	10.73	5.54	0.29	99.80	50.8
248.240.8	Leuco.	23.2	55.93	0.05	26.88	0.48	9.76	5.97	0.36	99.69	46.5
248.240.8	Leuco.	27.9	57.26	0.06	25.88	0.43	8.53	6.78	0.43	99.65	40.0

Abbreviations: LeucoLeucogabbro; An: anorthite

Appendix 16 (cont.)

Sample no.	Rock	d (μm)	SiO_2	TiO_2	Al_2O_3	FeO	CaO	Na_2O	K_2O	Total	An
						wt.%					mol.%
248.240.8	Leuco.	32.6	58.07	<D.L.	25.70	0.44	8.08	6.86	0.49	99.94	38.3
248.240.8	Leuco.	37.3	58.38	<D.L.	25.43	0.45	8.00	7.04	0.52	100.12	37.5
248.240.8	Leuco.	42.0	58.50	<D.L.	25.27	0.46	7.75	7.11	0.52	99.89	36.5
248.240.8	Leuco.	46.7	58.73	0.05	25.28	0.50	7.51	7.34	0.49	100.19	35.1
248.240.8	Leuco.	51.3	59.39	<D.L.	24.97	0.48	7.24	7.46	0.37	100.18	34.2
248.240.8	Leuco.	55.8	59.32	<D.L.	25.08	0.49	7.13	7.79	0.24	100.36	33.1
248.240.8	Leuco.	60.7	61.41	<D.L.	24.19	0.53	5.82	8.62	0.12	100.95	27.0
248.240.8	Leuco.	65.4	62.66	<D.L.	23.54	0.42	4.27	9.21	0.44	100.77	19.9
248.240.8	Leuco.	0.0	48.66	0.04	31.90	0.51	15.53	2.72	0.03	99.73	75.8
248.240.8	Leuco.	4.1	48.84	0.04	32.05	0.56	15.30	2.79	0.08	100.00	74.8
248.240.8	Leuco.	9.0	48.91	0.04	31.90	0.53	15.33	2.81	0.04	99.83	74.9
248.240.8	Leuco.	12.4	51.19	0.05	30.41	0.47	13.50	3.87	0.05	99.85	65.7
248.240.8	Leuco.	16.4	52.77	0.04	29.47	0.49	12.35	4.70	0.07	100.17	59.0
248.240.8	Leuco.	20.6	52.93	0.06	29.34	0.46	12.17	4.68	0.07	100.02	58.8
248.240.8	Leuco.	24.7	53.01	0.05	29.15	0.49	12.05	4.71	0.07	99.85	58.3
248.240.8	Leuco.	28.9	52.70	0.03	29.24	0.49	12.23	4.78	0.07	99.85	58.3
248.240.8	Leuco.	33.0	52.72	0.06	29.08	0.51	12.00	4.73	0.09	99.54	58.1
248.240.8	Leuco.	37.1	53.48	0.06	28.94	0.51	11.62	5.05	0.07	100.02	55.7
248.240.8	Leuco.	39.7	53.80	0.07	28.49	0.52	10.98	5.25	0.22	99.76	52.9
248.240.8	Leuco.	45.5	55.20	0.07	27.56	0.49	10.20	5.91	0.07	99.79	48.6
248.240.8	Leuco.	49.6	56.13	0.05	26.98	0.46	9.34	6.40	0.10	99.83	44.4
248.240.8	Leuco.	52.8	58.87	<D.L.	25.60	0.41	5.07	7.74	0.96	99.41	25.1
248.240.8	Leuco.	57.9	60.95	<D.L.	23.13	0.71	4.73	8.92	0.07	99.71	22.6
248.240.8	Leuco.	0.0	48.29	<D.L.	32.02	0.60	15.65	2.56	0.06	99.54	76.9
248.240.8	Leuco.	4.1	49.49	0.05	31.56	0.54	14.77	3.03	0.09	99.85	72.5
248.240.8	Leuco.	7.5	53.53	0.06	28.85	0.55	11.68	4.98	0.18	100.12	55.9
248.240.8	Leuco.	13.5	53.78	0.04	28.94	0.45	11.54	5.03	0.20	100.27	55.3
248.240.8	Leuco.	16.5	53.96	<D.L.	28.44	0.43	11.31	5.13	0.24	99.84	54.2
248.240.8	Leuco.	20.7	54.10	0.04	28.30	0.50	11.21	5.25	0.25	99.96	53.4
248.240.8	Leuco.	24.7	54.75	<D.L.	28.11	0.41	10.72	5.49	0.26	100.07	51.1
248.240.8	Leuco.	28.8	57.20	0.04	26.50	0.41	8.85	6.58	0.36	100.19	41.8
248.240.8	Leuco.	33.0	57.58	0.03	26.23	0.38	8.44	6.88	0.35	100.15	39.6
248.240.8	Leuco.	37.1	57.63	0.06	26.48	0.40	8.49	6.77	0.33	100.43	40.2
248.240.8	Leuco.	41.2	57.31	0.04	26.19	0.41	8.49	6.90	0.30	99.91	39.8
248.240.8	Leuco.	45.3	58.02	0.05	26.13	0.40	8.29	6.93	0.26	100.37	39.2

Abbreviations: LeucoLeucogabbro; An: anorthite

Appendix 16 (cont.)

Sample no.	Rock	d (μm)	SiO_2	TiO_2	Al_2O_3	FeO	CaO	Na_2O	K_2O	Total	An
						wt.%					mol.%
248.240.8	Leuco.	49.4	58.27	<D.L.	25.94	0.43	8.01	7.18	0.33	100.48	37.4
248.240.8	Leuco.	53.5	60.08	<D.L.	24.51	0.43	6.44	8.05	0.39	100.18	30.0
248.240.8	Leuco.	57.6	60.86	<D.L.	24.16	0.38	5.77	8.44	0.28	100.16	27.0
248.240.8	Leuco.	61.8	62.46	<D.L.	23.27	0.37	4.91	9.15	0.15	100.55	22.7
248.240.8	Leuco.	65.9	62.31	<D.L.	22.98	0.38	4.60	9.45	0.11	100.12	21.1
248.240.8	Leuco.	70.0	63.03	<D.L.	22.52	0.41	4.06	9.72	0.10	100.08	18.6
248.240.8	Leuco.	74.1	63.04	<D.L.	23.02	0.40	4.26	9.79	0.10	100.86	19.3
248.240.8	Leuco.	78.2	68.54	<D.L.	19.46	0.34	0.04	12.44	<D.L.	101.06	0.2
264.156.5	Tonalite	0.0	55.36	<D.L.	28.54	0.09	10.71	5.61	0.05	100.62	51.2
264.156.5	Tonalite	17.0	56.20	<D.L.	27.67	0.10	9.63	6.07	0.32	100.26	45.8
264.156.5	Tonalite	31.4	55.34	<D.L.	28.14	0.08	10.49	5.86	0.06	100.26	49.6
264.156.5	Tonalite	47.7	56.83	<D.L.	27.26	0.09	9.39	6.51	0.06	100.39	44.2
264.156.5	Tonalite	63.0	57.32	<D.L.	27.03	0.07	8.95	6.67	0.04	100.33	42.5
264.156.5	Tonalite	78.7	57.57	<D.L.	26.86	0.09	8.91	6.70	0.05	100.45	42.3
264.156.5	Tonalite	89.1	57.66	<D.L.	26.88	0.07	8.64	6.95	0.05	100.48	40.6
264.156.5	Tonalite	111.9	59.25	<D.L.	25.57	0.04	7.55	7.53	0.08	100.29	35.5
264.156.5	Tonalite	123.1	59.13	<D.L.	25.68	0.07	7.56	7.54	0.06	100.28	35.5
264.156.5	Tonalite	141.7	58.70	<D.L.	26.21	0.07	7.97	7.40	0.07	100.68	37.2
264.156.5	Tonalite	0.0	55.52	<D.L.	28.75	0.06	10.67	5.82	0.05	101.18	50.2
264.156.5	Tonalite	15.7	56.71	<D.L.	26.93	0.10	7.58	6.40	0.98	99.05	37.3
264.156.5	Tonalite	31.4	55.48	<D.L.	28.13	0.07	10.48	5.77	0.05	100.28	49.9
264.156.5	Tonalite	47.3	56.87	<D.L.	27.23	0.06	9.32	6.50	0.10	100.37	44.0
264.156.5	Tonalite	63.0	57.43	<D.L.	27.13	0.04	8.96	6.57	0.05	100.43	42.8
264.156.5	Tonalite	78.7	57.38	<D.L.	26.88	0.06	8.91	6.62	0.04	100.20	42.6
264.156.5	Tonalite	94.4	58.45	<D.L.	26.42	0.06	8.29	7.17	0.05	100.71	38.9
264.156.5	Tonalite	110.2	59.81	<D.L.	25.51	<D.L.	7.12	7.91	0.09	100.76	33.0
264.156.5	Tonalite	126.0	58.93	<D.L.	25.58	0.08	7.62	7.46	0.06	99.97	36.0
264.156.5	Tonalite	141.7	58.68	<D.L.	26.31	0.07	7.97	7.12	0.07	100.47	38.1
246.249.6	Late dike	0.0	49.63	0.03	31.71	0.51	15.02	3.03	0.08	99.88	73.0
246.249.6	Late dike	6.0	51.15	0.02	30.44	0.51	13.65	3.81	0.11	99.62	66.0
246.249.6	Late dike	11.9	49.44	0.03	31.29	0.58	15.08	3.09	0.10	99.50	72.6
246.249.6	Late dike	17.8	49.53	0.03	31.48	0.54	15.02	3.12	0.09	99.69	72.3
246.249.6	Late dike	22.7	50.03	0.02	31.11	0.53	14.67	3.32	0.09	99.67	70.6
246.249.6	Late dike	34.4	51.30	0.02	30.27	0.52	13.47	3.98	0.13	99.64	64.7
246.249.6	Late dike	35.7	49.53	0.02	31.36	0.56	14.69	3.24	0.10	99.43	71.1

Abbreviations: An: anorthite

Appendix 16 (cont.)

Sample no.	Rock	d (μm)	SiO_2	TiO_2	Al_2O_3	FeO	CaO	Na_2O	K_2O	Total	An
						wt.%					mol.%
246.249.6	Late dike	41.6	52.21	0.05	29.73	0.59	12.99	4.27	0.14	99.95	62.2
246.249.6	Late dike	53.4	49.25	0.03	31.73	0.51	15.16	2.88	0.07	99.52	74.1
246.249.6	Late dike	55.8	51.67	0.05	29.73	0.54	13.05	4.19	0.13	99.32	62.8
246.249.6	Late dike	65.2	50.47	0.04	30.72	0.58	14.14	3.50	0.11	99.45	68.6
246.249.6	Late dike	71.1	52.23	0.03	29.60	0.55	12.88	4.24	0.13	99.66	62.2
246.249.6	Late dike	76.9	51.12	0.03	30.52	0.59	13.73	3.87	0.11	99.92	65.8
246.249.6	Late dike	82.8	50.76	0.03	30.57	0.50	13.93	3.72	0.03	99.44	67.3

Abbreviations: An: anorthite

Appendix 17 Electron microprobe profiles in olivine and orthopyroxene in olivine norite.

Sample no.	d (μm)	SiO_2	TiO_2	Al_2O_3	FeO	MnO	MgO	CaO	NiO	Total	Fo/En	Mg#
Olivine												
246.209.0	0	38.53	0.27	26.49	22.30	0.32	38.73	0.12	0.1056	100.86	75.6	75.3
246.209.0	21	38.61	0.27	26.52	22.32	0.32	38.87	0.14	0.1001	101.11	75.6	75.4
246.209.0	80	38.56	0.27	26.59	22.37	0.32	38.84	0.14	0.1052	101.12	75.6	75.3
246.209.0	111	38.53	0.27	26.63	22.38	0.32	38.91	0.11	0.0995	101.14	75.6	75.3
246.209.0	235	38.48	0.27	26.73	22.35	0.33	38.69	0.14	0.0971	100.89	75.5	75.3
246.209.0	326	38.40	0.27	26.80	22.40	0.33	38.64	0.14	0.0951	100.83	75.5	75.2
246.209.0	438	38.40	0.27	26.86	22.66	0.33	38.62	0.14	0.0951	101.08	75.2	75.0
246.209.0	496	38.48	0.27	26.90	22.60	0.34	38.66	0.13	0.0947	101.16	75.3	75.0
246.209.0	560	38.44	0.27	26.93	22.78	0.34	38.56	0.14	0.0893	101.21	75.1	74.8
246.209.0	627	38.47	0.27	26.97	22.89	0.35	38.46	0.14	0.0894	101.25	75.0	74.7
246.209.0	698	38.41	0.27	27.00	22.96	0.35	38.41	0.14	0.0897	101.22	74.9	74.6
246.209.0	843	38.25	0.27	27.07	23.27	0.34	38.16	0.12	0.0847	101.12	74.5	74.2
246.209.0	927	38.33	0.27	27.10	23.35	0.34	38.12	0.11	0.0923	101.25	74.4	74.1
246.209.0	1007	38.17	0.27	27.14	23.55	0.35	37.88	0.09	0.0813	101.03	74.1	73.9
Orthopyroxene												
246.308.0	0	54.83	0.29	1.19	15.09	0.28	28.07	1.47	n.a.	101.36	74.4	76.5
246.308.0	202	54.05	0.23	1.40	15.63	0.47	27.42	1.65	n.a.	101.80	72.8	75.2
246.308.0	270	54.61	0.25	1.35	14.49	0.28	28.11	1.88	n.a.	101.33	74.5	77.2
246.308.0	337	56.07	0.24	1.41	14.09	0.28	28.27	1.72	n.a.	102.40	75.3	77.8
246.308.0	405	54.94	0.23	1.32	14.30	0.31	28.10	1.79	n.a.	101.34	74.8	77.4
246.308.0	472	54.47	0.24	1.75	14.30	0.28	28.23	1.71	n.a.	101.32	75.0	77.5
246.308.0	539	54.36	0.25	1.87	14.33	0.31	28.02	1.63	n.a.	101.20	74.9	77.3
246.308.0	742	54.26	0.27	1.94	14.39	0.30	28.02	1.71	n.a.	101.30	74.7	77.3
246.308.0	809	54.22	0.26	1.87	14.59	0.31	28.10	1.75	n.a.	101.49	74.5	77.1
246.308.0	1011	54.35	0.29	1.61	14.79	0.27	28.11	1.93	n.a.	101.69	74.1	76.9
246.308.0	1078	54.20	0.28	1.56	14.80	0.32	27.92	1.87	n.a.	101.19	74.0	76.7
246.308.0	1146	54.31	0.34	1.49	14.90	0.29	27.73	1.78	n.a.	101.09	73.9	76.5
246.308.0	1280	54.33	0.36	1.41	15.59	0.28	27.70	1.66	n.a.	101.50	73.3	75.7

Abbreviations: Fo: forsterite; En: enstatite.

Appendix 18 Raw major and trace element composition of samples from Älgliden dike and wallrock

	Sample number	246.204.6	246.212.5	246.219.0	246.224.6	246.239.1	246.252.5
	Unit	Älgliden dike	Älgliden dike	Älgliden dike	Älgliden dike	Älgliden dike	Älgliden dike
	Rock type[a]	olivine norite^{2N}	olivine norite^{1N}	olivine norite^{1N}	olivine norite^{1N}	olivine norite^{2N}	olivine norite^{S}
Major elements (wt%)	SiO_2	49.78	46.09	40.35	43.95	49.74	41.93
	Al_2O_3	7.23	8.45	6.79	7.66	7.28	7.43
	Fe_2O_{3TOT}	17.22	16.38	20.62	16.67	15.82	17.92
	MgO	17.19	20.67	20.31	22.48	19.26	20.85
	CaO	3.84	4.44	3.48	3.55	3.71	3.14
	Na_2O	1.17	1.34	1.14	1.32	1.27	0.50
	K2O	0.62	0.73	0.53	0.73	0.59	0.76
	TiO_2	0.85	0.66	0.54	0.53	0.75	0.63
	P_2O_5	0.16	0.15	0.14	0.14	0.00	0.13
	MnO	0.20	0.20	0.19	0.20	0.21	0.13
	Cr_2O_3	0.30	0.31	0.32	0.33	0.31	0.19
	S	0.24	0.14	2.34	0.30	0.42	0.41
	LOI	2.2	2.2	4.1	3.0	1.7	6.4
	SUM	101.0	101.7	100.8	100.9	101.1	100.4
Trace elements (ppm)	Li	6.24	9.45	9.19	9.40	7.94	10.30
	Sc	23.2	17.5	12.0	15.0	24.1	11.5
	Ti	4990	3680	3020	2940	3990	3510
	V	175	118	102	97	132	99
	Cr	2110	2170	2210	2260	2160	1300
	Co	94.4	90.9	167.0	107.0	53.7	118.0
	Ni	571	381	1070	487	477	524
	Cu	275	175	3150	526	615	419
	Zn	141	147	161	145	140	138
	Ga	12.5	11.6	10.1	10.5	11.2	10.3
	Rb	11.6	14.0	10.6	13.9	11.4	13.4
	Sr	184	239	190	208	190	75
	Y	10.9	11.7	9.1	10.6	11.3	9.6
	Zr	35.7	51.2	40.4	53.5	40.2	33.4
	Nb	2.71	3.35	2.67	2.97	2.85	2.78
	Cs	1.04	1.29	0.64	0.64	0.76	0.94
	Ba	195	272	208	251	222	235
	La	8.22	9.63	7.90	8.86	7.05	6.90
	Ce	17.8	21.2	17.2	19.5	15.7	15.7
	Pr	2.35	2.81	2.27	2.59	2.16	2.18
	Nd	9.79	11.70	9.45	10.90	9.35	9.47
	Sm	2.15	2.55	2.00	2.33	2.17	2.13
	Eu	0.642	0.802	0.612	0.689	0.622	0.581
	Gd	2.01	2.28	1.81	2.11	2.05	1.99
	Tb	0.304	0.344	0.268	0.315	0.312	0.292
	Dy	1.92	2.10	1.62	1.93	1.98	1.78
	Ho	0.396	0.426	0.324	0.377	0.406	0.350
	Er	1.16	1.20	0.92	1.09	1.20	0.99
	Yb	1.1	1.1	0.8	1.0	1.2	0.9
	Lu	0.17	0.17	0.13	0.15	0.18	0.13
	Hf	1.14	1.40	1.22	1.41	1.23	1.07
	Ta	0.164	0.200	0.162	0.185	0.168	0.161
	Tl	0.788	0.368	0.289	0.265	0.267	0.316
	Pb	4.21	15.30	38.20	16.60	11.30	7.28
	Th	1.09	1.19	1.07	1.37	1.04	0.82
	U	0.884	0.945	1.130	1.240	0.795	0.650

(a) 1, 2 refer to olivine norites of type-1 and type-2 and N, S to olivine norites from northern and southern sides.

Appendix 18 (cont.)

Sample	246.280.8	246.290.7	246.293.1	246.300.9	246.308.0	246.319.6
Unit	Älgliden dike	Älgliden dike	Älgliden dike	Älgliden dike	Älgliden dike	Älgliden dike
Rock type[a]	olivine norite[1S]	olivine norite[1S]	olivine norite[1S]	olivine norite[1S]	olivine norite[1S]	olivine norite[1S]
SiO_2	38.84	36.94	36.87	38.62	36.81	43.38
Al_2O_3	5.81	5.35	4.79	5.78	5.11	7.54
Fe_2O_{3TOT}	21.59	23.29	22.39	21.46	22.53	17.41
MgO	23.12	23.90	20.42	22.45	21.53	21.29
CaO	2.92	2.86	2.67	2.96	2.64	3.67
Na_2O	0.84	0.57	0.70	0.85	0.67	1.09
K2O	0.35	0.23	0.32	0.39	0.35	0.55
TiO_2	0.36	0.47	0.40	0.38	0.47	0.58
P_2O_5	0.12	0.08	0.17	0.17	0.00	0.18
MnO	0.22	0.20	0.21	0.21	0.22	0.21
Cr_2O_3	0.14	0.19	0.15	0.13	0.15	0.12
S	2.15	2.62	3.05	2.33	2.59	0.26
LOI	6.7	6.1	7.1	6.7	6.3	4.5
SUM	103.2	102.8	99.3	102.4	99.3	100.8
Li	8.65	5.21	6.14	8.32	7.24	11.10
Sc	13.8	12.1	11.3	10.6	12.4	12.3
Ti	1880	2680	2250	2150	2590	3120
V	61	91	74	67	88	85
Cr	1010	1380	1060	934	997	828
Co	148.0	178.0	199.0	170.0	202.0	116.0
Ni	768	972	1140	970	1240	458
Cu	2340	1890	4390	3090	3100	279
Zn	148	167	182	154	181	135
Ga	7.0	7.3	6.6	7.1	7.4	9.0
Rb	5.5	4.5	6.1	7.7	6.9	11.7
Sr	174	154	110	168	132	215
Y	5.0	5.2	6.4	6.6	5.3	9.4
Zr	19.6	19.0	22.7	25.1	27.3	36.8
Nb	1.31	1.32	1.62	1.82	1.61	2.65
Cs	0.22	0.21	0.28	0.50	0.86	1.66
Ba	131	100	136	162	145	234
La	4.05	3.46	5.64	6.03	4.46	8.09
Ce	8.7	7.8	12.4	13.1	9.6	17.6
Pr	1.15	1.09	1.63	1.73	1.27	2.35
Nd	4.83	4.70	6.92	7.29	5.34	9.86
Sm	1.05	1.06	1.44	1.52	1.14	2.12
Eu	0.365	0.371	0.434	0.476	0.370	0.687
Gd	0.96	0.98	1.31	1.38	1.05	1.91
Tb	0.146	0.147	0.189	0.195	0.154	0.281
Dy	0.90	0.92	1.14	1.19	0.94	1.68
Ho	0.182	0.184	0.235	0.234	0.192	0.341
Er	0.53	0.53	0.65	0.66	0.56	0.95
Yb	0.5	0.5	0.6	0.6	0.5	0.9
Lu	0.08	0.07	0.09	0.09	0.08	0.13
Hf	0.58	0.51	0.69	0.76	0.73	1.11
Ta	0.076	0.071	0.095	0.105	0.101	0.154
Tl	0.185	0.166	0.200	0.336	0.495	0.348
Pb	14.50	14.00	16.70	12.90	13.40	6.91
Th	0.48	0.34	0.54	0.64	0.64	0.96
U	0.373	0.259	0.421	0.461	0.491	0.719

(a) 1, 2 refer to olivine norites of type-1 and type-2 and N, S to olivine norites from northern and southern sides.

Appendix 18 (cont.)

Sample	246.334.0	246.340.8	264.169.2	264.172.8	264.200.4	264.205.8
Unit	Älgliden dike	Älgliden dike	Älgliden dike	Älgliden dike	Älgliden dike	Älgliden dike
Rock type[a]	olivine norite[1S]	olivine norite[S]	olivine norite	olivine norite	olivine norite	olivine norite
SiO_2	42.11	42.96	44.75	42.06	40.07	43.66
Al_2O_3	7.00	7.49	8.04	9.14	7.29	7.81
Fe_2O_{3TOT}	17.64	18.58	17.08	18.82	21.22	17.53
MgO	22.27	19.46	16.74	15.26	21.22	20.50
CaO	3.38	3.59	4.69	4.81	2.30	3.15
Na_2O	1.02	0.65	0.29	0.28	0.26	0.41
K2O	0.45	0.61	1.37	0.31	0.22	0.94
TiO_2	0.48	0.65	0.86	0.82	0.52	0.62
P_2O_5	0.16	0.13	0.12	0.16	0.14	0.16
MnO	0.22	0.15	0.18	0.19	0.22	0.20
Cr_2O_3	0.12	0.11	0.20	0.19	0.34	0.24
S	0.27	0.63	0.40	1.31	1.83	0.30
LOI	5.7	6.2	5.9	7.5	6.8	6.0
SUM	100.8	101.2	100.6	100.9	102.4	101.5
Li	11.40	6.93	10.90	3.62	3.60	8.49
Sc	11.5	16.7	24.4	19.6	14.9	14.8
Ti	2570	3480	4850	4600	2740	3190
V	75	101	167	135	109	109
Cr	862	794	1390	1360	2410	1680
Co	120.0	93.8	26.6	46.2	104.0	57.1
Ni	508	580	581	683	1050	682
Cu	350	881	86	3890	738	134
Zn	132	188	162	196	146	150
Ga	8.2	9.6	11.2	12.2	9.3	10.6
Rb	9.3	11.7	47.6	6.8	3.4	19.8
Sr	218	105	33	63	38	59
Y	7.4	12.9	13.1	12.3	8.1	12.8
Zr	30.5	32.7	49.9	53.3	37.7	50.9
Nb	2.26	2.67	2.88	3.45	2.27	3.20
Cs	1.14	0.86	4.04	0.85	0.49	1.92
Ba	204	258	230	94	54	285
La	6.66	6.71	8.47	6.58	2.98	8.37
Ce	14.3	16.4	19.2	16.3	8.3	19.4
Pr	1.86	2.42	2.58	2.29	1.25	2.66
Nd	7.81	11.20	10.80	10.30	5.80	11.70
Sm	1.64	2.71	2.36	2.60	1.55	2.72
Eu	0.559	0.719	0.733	0.818	0.635	0.827
Gd	1.51	2.57	2.34	2.49	1.56	2.53
Tb	0.217	0.386	0.355	0.382	0.248	0.380
Dy	1.32	2.37	2.24	2.34	1.53	2.34
Ho	0.261	0.471	0.468	0.481	0.310	0.480
Er	0.74	1.30	1.33	1.36	0.89	1.35
Yb	0.7	1.2	1.3	1.3	0.8	1.3
Lu	0.10	0.16	0.19	0.19	0.12	0.18
Hf	0.90	1.11	1.28	1.49	1.04	1.40
Ta	0.133	0.146	0.162	0.205	0.140	0.195
Tl	0.336	0.486	1.350	0.547	0.288	0.759
Pb	7.91	13.70	1.53	2.09	4.36	4.32
Th	0.81	0.72	1.08	1.10	0.95	1.29
U	0.607	0.504	0.897	0.988	0.718	1.130

(a) 1, 2 refer to olivine norites of type-1 and type-2 and N, S to olivine norites from northern and southern sides.

Appendix 18 (cont.)

Sample	264.212.5	264.180.5	264.185.6	264.190.2	264.217.5	246.212.6
Unit	Älgliden dike	Älgliden dike	Älgliden dike	Älgliden dike	Älgliden dike	Älgliden dike
Rock type[a]	olivine norite	olivine norite	olivine norite	olivine norite	olivine norite	leucogabbro
SiO_2	45.15	37.63	28.49	26.66	48.17	57.13
Al_2O_3	9.99	6.77	3.34	2.96	13.70	17.65
Fe_2O_{3TOT}	17.43	27.73	34.04	34.58	10.43	3.85
MgO	15.74	20.04	18.74	17.07	9.09	2.90
CaO	4.23	1.26	3.87	5.60	8.85	4.82
Na_2O	0.82	0.20	0.11	0.11	2.06	5.81
K2O	1.14	0.07	0.00	0.00	2.51	1.76
TiO_2	0.60	0.54	0.30	0.31	0.74	0.87
P_2O_5	0.17	0.13	0.07	0.06	0.33	0.54
MnO	0.19	0.16	0.18	0.18	0.17	0.08
Cr_2O_3	0.17	0.16	0.16	0.17	0.07	0.00
S	0.58	3.28	7.27	7.98	0.04	0.01
LOI	5.4	6.6	10.1	9.3	3.7	3.5
SUM	101.6	104.6	106.7	105.0	99.9	99.0
Li	10.50	3.29	1.67	1.77	14.80	10.80
Sc	16.7	17.3	9.6	9.9	26.3	4.0
Ti	3150	2840	1590	1650	4230	5070
V	109	130	98	99	159	95
Cr	1170	2010	2170	2340	725	14
Co	56.6	160.0	369.0	343.0	20.1	12.4
Ni	737	1320	3290	3430	104	24
Cu	213	1370	462	258	44	226
Zn	165	144	83	87	94	56
Ga	12.6	9.2	6.2	5.9	16.1	19.2
Rb	25.6	0.8	0.2	0.2	68.7	36.9
Sr	67	21	100	86	601	576
Y	15.9	7.1	4.4	3.1	14.5	23.5
Zr	59.3	29.6	16.8	14.1	85.0	120.0
Nb	3.96	2.07	1.07	0.92	6.08	7.03
Cs	2.01	0.19	0.04	0.03	5.21	1.92
Ba	377	9	3	2	581	1390
La	10.60	2.52	3.13	4.47	21.10	37.40
Ce	24.5	6.7	6.3	8.4	47.0	76.5
Pr	3.33	0.99	0.84	1.03	6.29	9.34
Nd	14.10	4.70	3.71	4.11	26.60	36.50
Sm	3.22	1.30	0.83	0.71	5.56	6.71
Eu	0.848	0.459	0.211	0.311	1.510	2.260
Gd	3.06	1.39	0.84	0.66	4.31	5.70
Tb	0.455	0.221	0.128	0.091	0.538	0.755
Dy	2.82	1.42	0.80	0.57	2.87	4.25
Ho	0.576	0.288	0.168	0.123	0.524	0.802
Er	1.67	0.80	0.49	0.35	1.40	2.15
Yb	1.5	0.7	0.5	0.3	1.2	1.7
Lu	0.23	0.11	0.07	0.05	0.18	0.24
Hf	1.64	0.83	0.49	0.40	2.11	3.00
Ta	0.240	0.126	0.067	0.058	0.305	0.456
Tl	0.555	0.177	0.240	0.141	1.010	0.485
Pb	5.18	4.97	11.50	7.52	2.74	30.10
Th	1.55	0.65	0.43	0.36	2.95	4.50
U	1.340	0.698	0.369	0.321	2.110	3.310

(a) 1, 2 refer to olivine norites of type-1 and type-2 and N, S to olivine norites from northern and southern sides.

Appendix 18 (cont.)

Sample	248.213.2	246.230.2	246.240.8	248.265.0	246.199.0	246.242.5
Unit	Älgliden dike	Älgliden dike	Älgliden dike	Älgliden dike	Älgliden dike	Älgliden dike
Rock type[a]	leucogabbro	leucogabbro	leucogabbro	leucogabbro	leucogabbro	leucogabbro
SiO_2	53.68	53.38	46.36	56.11	55.32	51.60
Al_2O_3	14.48	13.89	18.52	14.34	17.68	20.23
Fe_2O_{3TOT}	9.22	9.07	10.94	6.68	7.62	5.42
MgO	3.25	6.05	6.05	4.29	4.59	7.23
CaO	6.16	5.22	7.14	5.65	4.48	7.38
Na_2O	4.53	4.68	3.55	4.77	5.40	4.23
K2O	0.90	1.26	0.95	0.33	0.88	0.98
TiO_2	1.03	0.55	0.50	0.78	0.76	0.62
P_2O_5	0.39	0.56	0.19	0.58	0.35	0.17
MnO	0.19	0.13	0.12	0.14	0.12	0.11
Cr_2O_3	0.00	0.03	0.04	0.00	0.02	0.04
S	0.04	1.33	3.22	0.47	0.23	0.76
LOI	5.8	4.4	5.0	7.3	3.1	3.7
SUM	99.7	100.6	102.5	101.4	100.5	102.4
Li	14.10	17.90	12.70	22.00	10.00	15.70
Sc	15.5	10.4	14.7	11.7	13.9	13.6
Ti	5900	3100	2680	4470	4370	3210
V	128	65	53	90	102	51
Cr	8	211	267	13	140	309
Co	11.3	56.1	98.5	38.6	24.0	20.1
Ni	13	253	784	50	84	85
Cu	153	1320	20700	274	1190	298
Zn	1060	70	179	127	157	44
Ga	19.1	16.5	16.3	17.0	20.7	18.5
Rb	18.2	30.5	20.1	5.1	19.8	20.6
Sr	391	353	606	309	659	656
Y	32.4	20.7	15.5	33.8	20.0	17.5
Zr	146.0	185.0	59.7	186.0	62.2	75.5
Nb	8.59	7.56	4.30	10.50	7.38	5.71
Cs	1.64	1.85	1.70	0.36	1.26	1.49
Ba	494	531	499	369	477	586
La	28.60	23.20	12.70	28.70	23.70	14.60
Ce	62.7	50.1	28.1	63.3	50.5	32.1
Pr	8.04	6.37	3.81	8.19	6.25	4.31
Nd	33.30	25.50	16.30	34.10	25.00	18.30
Sm	7.17	5.07	3.66	7.44	5.09	4.00
Eu	1.840	1.330	1.280	1.960	1.520	1.400
Gd	6.37	4.35	3.25	6.73	4.36	3.59
Tb	0.946	0.632	0.481	0.987	0.635	0.534
Dy	5.75	3.74	2.93	5.95	3.70	3.21
Ho	1.140	0.732	0.581	1.220	0.722	0.632
Er	3.23	2.06	1.59	3.29	1.96	1.75
Yb	2.9	1.9	1.3	2.8	1.7	1.5
Lu	0.42	0.28	0.19	0.40	0.24	0.22
Hf	3.74	4.24	1.69	4.78	2.03	2.33
Ta	0.537	0.508	0.236	0.698	0.424	0.320
Tl	0.259	0.586	0.336	0.079	0.208	0.230
Pb	18.60	31.90	47.70	145.00	46.80	45.80
Th	3.94	4.31	1.24	5.14	2.80	1.64
U	4.440	3.350	0.966	5.040	2.470	1.350

(a) 1, 2 refer to olivine norites of type-1 and type-2 and N, S to olivine norites from northern and southern sides.

Appendix 18 (cont.)

Sample	248.230.4	246.223.3	248.259.1	246.249.6	246.249.6	264.223.8
Unit	Älgliden dike	Älgliden dike	Älgliden dike	late dike	late dike	wallrock
Rock type[a]	leucogabbro	leucogabbro	leucogabbro	andesite	andesite	Granodiorite
SiO_2	50.44	44.56	45.26	55.03	27.16	70.26
Al_2O_3	19.28	17.95	20.85	16.36	24.29	15.27
Fe_2O_{3TOT}	6.73	10.64	7.80	7.35	14.82	4.75
MgO	6.11	8.95	4.63	4.85	21.48	1.22
CaO	6.10	6.16	9.26	6.84	0.00	1.94
Na_2O	3.67	3.46	2.21	4.51	0.17	3.81
K2O	2.26	0.90	1.58	1.19	0.55	1.58
TiO_2	0.39	0.30	0.32	0.78	1.03	0.25
P_2O_5	0.15	0.00	0.13	0.22	0.12	0.00
MnO	0.11	0.11	0.19	0.12	0.24	0.03
Cr_2O_3	0.01	0.15	0.02	0.02	0.00	0.00
S	0.09	1.48	1.25	0.53	0.00	0.05
LOI	4.2	5.4	5.8	3.4	11.1	2.4
SUM	99.6	100.0	99.3	101.2	101.0	101.6
Li	14.00	18.30	18.20	118.68	121.00	9.88
Sc	11.8	6.1	6.5	46.8	47.7	16.3
Ti	2200	1690	1820	6160	6280	1330
V	53	59	46	144	147	53
Cr	69	1030	171	0	0	4
Co	24.0	63.4	57.8	25.2	25.7	4.1
Ni	72	348	540	2	2	3
Cu	98	7760	1820	1	1	12
Zn	58	111	72	168	171	21
Ga	17.8	16.2	18.5	21.1	21.5	13.6
Rb	47.0	18.2	29.1	4.3	4.4	28.2
Sr	752	578	357	142	145	262
Y	15.1	5.5	8.8	17.5	17.8	19.9
Zr	74.6	60.1	47.1	54.9	56.0	130.0
Nb	4.18	1.97	2.56	4.86	4.95	4.79
Cs	1.59	0.84	0.91	0.37	0.38	1.03
Ba	874	514	418	2472	2520	392
La	14.70	12.50	10.40	8.35	8.51	16.70
Ce	31.2	22.3	21.1	17.5	17.8	33.5
Pr	4.02	2.45	2.66	2.10	2.14	4.10
Nd	16.30	8.79	10.60	8.19	8.35	15.50
Sm	3.40	1.52	2.09	1.87	1.91	3.19
Eu	1.110	0.801	0.991	0.641	0.654	0.583
Gd	2.93	1.34	1.85	2.17	2.21	2.92
Tb	0.439	0.175	0.263	0.373	0.380	0.495
Dy	2.67	0.99	1.56	2.71	2.76	3.27
Ho	0.526	0.192	0.308	0.628	0.640	0.708
Er	1.50	0.53	0.88	2.00	2.04	2.12
Yb	1.3	0.5	0.8	2.2	2.3	2.0
Lu	0.20	0.07	0.12	0.36	0.36	0.28
Hf	1.93	1.35	1.23	1.73	1.76	3.64
Ta	0.267	0.149	0.172	0.354	0.361	0.358
Tl	0.688	0.361	0.526	0.090	0.092	0.293
Pb	36.10	101.00	79.70	1.06	1.08	3.34
Th	2.06	2.06	1.38	3.77	3.84	5.81
U	2.220	1.540	1.480	2.276	2.320	2.720

(a) 1, 2 refer to olivine norites of type-1 and type-2 and N, S to olivine norites from northern and southern sides.

Appendix 18 (cont.)

Sample	246.362.8	246.196.3	264.156.5	264.162.4
Unit	wallrock	wallrock	wallrock	wallrock
Rock type[a]	tonalite	QFP	tonalite	tonalite
SiO_2	64.03	69.22	61.18	57.75
Al_2O_3	13.07	14.19	16.24	16.14
Fe_2O_{3TOT}	8.33	4.64	8.62	12.30
MgO	2.52	1.63	2.25	3.04
CaO	4.04	3.34	4.31	3.31
Na_2O	2.55	3.83	3.12	3.19
K2O	1.58	0.79	1.71	2.09
TiO_2	0.33	0.28	0.41	0.44
P_2O_5	0.22	0.00	0.00	0.00
MnO	0.07	0.06	0.05	0.06
Cr_2O_3	0.00	0.00	0.00	0.00
S	0.27	0.38	0.20	0.11
LOI	2.9	2.7	3.1	2.5
SUM	99.9	101.0	101.2	100.9
Li	12.40	11.80	13.60	18.30
Sc	19.9	13.6	25.5	32.9
Ti	1240	1480	2170	2330
V	89	88	150	184
Cr	14	11	9	11
Co	6.4	8.1	14.3	8.6
Ni	4	4	5	6
Cu	600	389	77	87
Zn	42	62	49	62
Ga	10.5	16.7	15.0	15.3
Rb	27.7	17.2	52.7	76.7
Sr	145	240	293	308
Y	15.2	18.5	27.9	26.8
Zr	43.9	78.9	48.1	40.0
Nb	3.03	4.18	7.38	6.27
Cs	1.52	1.83	2.30	4.55
Ba	216	244	251	238
La	7.93	11.10	19.50	12.30
Ce	16.5	31.1	43.0	31.9
Pr	1.95	2.86	5.37	4.35
Nd	7.62	11.30	20.70	17.20
Sm	1.72	2.53	4.22	3.59
Eu	0.267	0.464	0.578	0.566
Gd	1.76	2.48	3.69	3.14
Tb	0.319	0.420	0.616	0.559
Dy	2.24	2.81	4.13	3.85
Ho	0.518	0.628	0.911	0.880
Er	1.65	1.89	2.94	2.88
Yb	1.8	1.9	3.2	3.3
Lu	0.28	0.29	0.46	0.49
Hf	1.34	2.26	1.92	1.69
Ta	0.314	0.325	0.511	0.417
Tl	0.388	0.226	0.866	1.500
Pb	1.62	4.99	4.94	3.72
Th	1.10	3.17	3.75	1.40
U	4.250	2.970	2.290	1.670

(a) 1, 2 refer to olivine norites of type-1 and type-2 and N, S to olivine norites from northern and southern sides.

Appendix 19 Core photograph (a) and X-ray micro fluorescence derived map (b) of xenolith hosting network sulfides, sample 264.190.1.